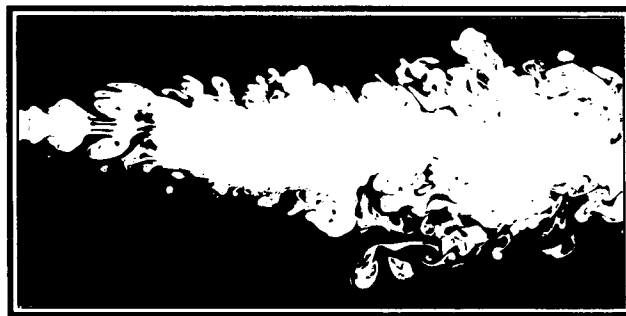# Studying Turbulence Using Numerical Simulation Databases

Proceedings of the 1987 Summer Program

Center for Turbulence Research

Report CTR-S87
December 1987

NASA
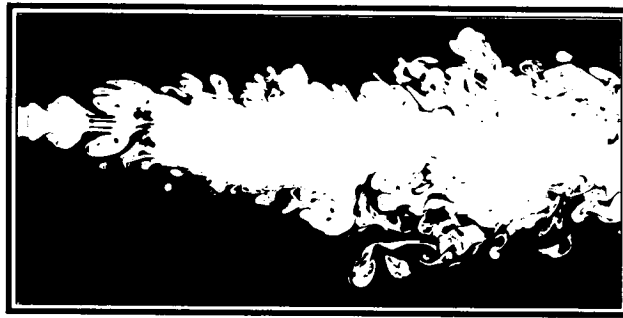
Ames Research Center   Stanford University

Studying Turbulence Using Numerical Simulation Databases

Proceedings of the 1987 Summer Program

Center for Turbulence Research

Report CTR-S87
December 1987

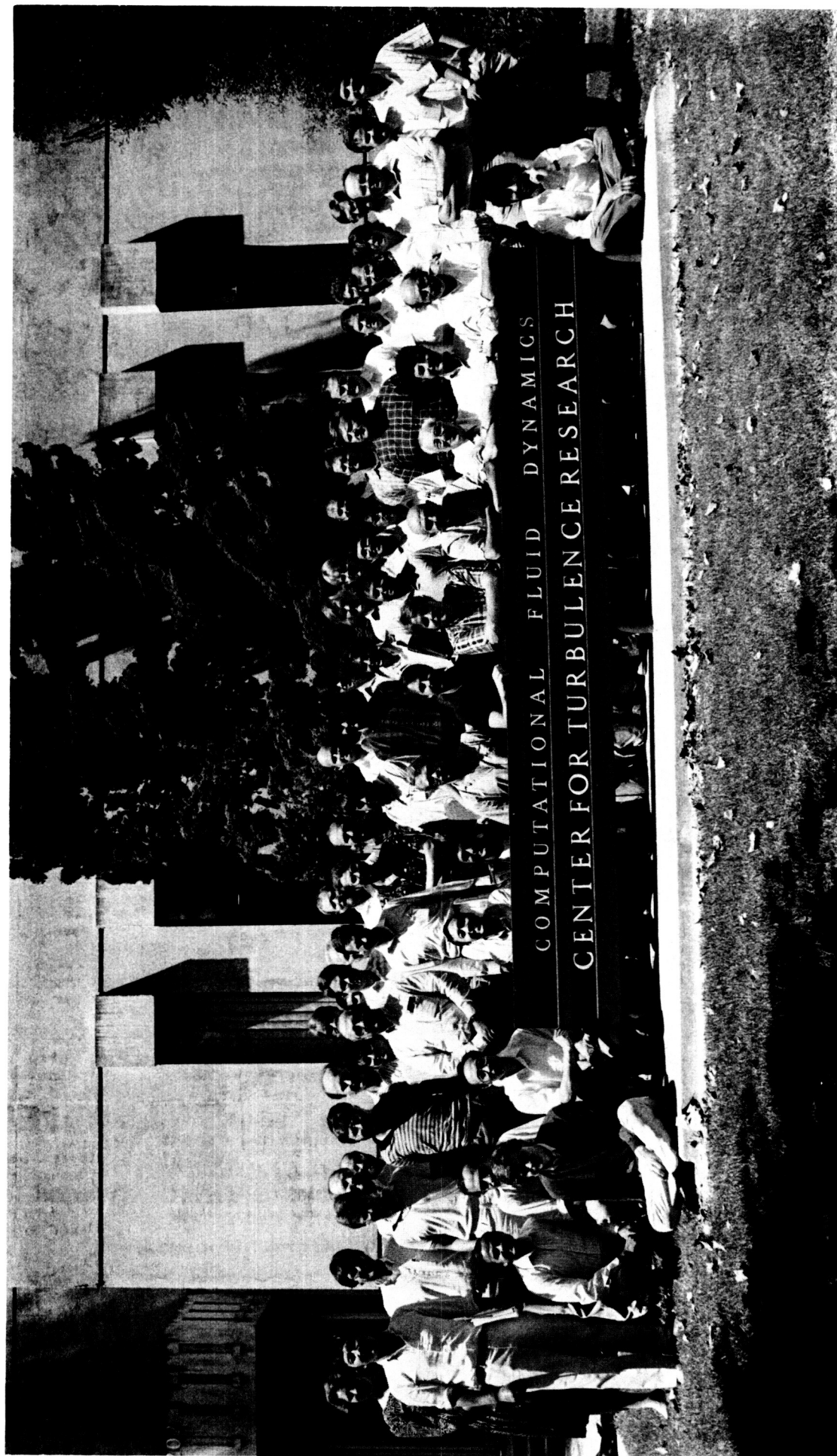COMPUTATIONAL FLUID DYNAMICS
CENTER FOR TURBULENCE RESEARCH

Roth House: residence for nearly half the 1987 Summer participants and the site of many gatherings.

CONTENTS

Reynolds Stress Modeling Group

Turbulence Structure Group

Appendix

Preface

The first Summer Program of the Center for Turbulence Research was held during the four week period July 13 to August 7, 1987. The program focused on the use of databases obtained from direct numerical simulations of turbulent flows, for study of turbulence physics and modeling.

Thirty-three participants from eight countries were selected on the basis of their research proposals. They were divided into five groups:

- Stochastic decomposition/chaos/bifurcation
- Two-point closure (or k-space) modeling
- Scalar transport/reacting flows
- Reynolds stress modeling
- Structure of turbulent boundary layers.

In addition to these participants, the program benefited from the week long participation of Robert Kraichnan and Evgeny Novikov. There were 8 tutorials and 4 seminars presented by leading experts in different areas of turbulence research.

The databases consisted of decaying and forced isotropic turbulence, homogeneous turbulence subjected to strain, homogeneous shear flow, fully developed turbulent channel flow and the turbulent boundary layer. The Reynolds numbers considered were low to moderate; Taylor micro-scale Reynolds number of about 50 in homogeneous flows and Reynolds number based on free-stream velocity and boundary layer thickness of about 3000-10000. Most simulation fields included fields of passive scalar contaminant as well as velocity.

The research reports that resulted from the 1987 summer program are included in the following pages. This is an account of a short term, but intensive, study of ideas and models of turbulent flows. Therefore, in most cases, the results should be considered as preliminary. It is expected that the studies will be continued and, in due course, the results will be submitted to the appropriate journals by the individual authors. In this volume the reports of each research group are clustered together, preceded by an overview written by the coordinator of that group.

Timely reporting of many of these projects occurred at the American Physical Society Fluid Dynamics Division Meeting in Eugene Oregon, Nov 22-24, 1987. Twenty abstracts based on the work accomplished during the summer program were presented at this meeting.

In our opinion, the Summer Program proved to be a valuable setting for exchange of conceptual ideas between participants with varied backgrounds and interests. The Summer Program demonstrated the viability of using simulation databases as a powerful tool in turbulence research, and the databases proved to be effective catalysts for interaction among turbulence researchers.

<div style="text-align: right">

Parviz Moin
William C. Reynolds
John Kim

</div>

Overview of research by the stochastic decomposition/chaos/bifurcation group

This group consisted of four loosely inter-related projects with the common objective of understanding the mechanics of wall-bounded turbulent flows. All projects used the un-processed channel flow database (Kim, Moin, Moser 1987) or the velocity two-point correlation tensor computed from it (Moin & Moser 1987).

The invited participants were:
  Professor Ronald J. Adrian (University of Illinois)
  Dr. Nadine Aubry (Cornell University)
  Dr. Julian C. R. Hunt (University of Cambridge)
  Professor Javier Jimenez (Universidad Politecnica, Madrid, & UAM-IBM, Spain)

The local participants were:
  Dr. Laurence R. Keefe (Center for Turbulence Research)
  Professor Parviz Moin (Stanford University & NASA Ames)
  Dr. Robert D. Moser (NASA Ames)

Hunt's self-similarity hypothesis for velocity correlations states that the two-point correlation of normal velocity v, when normalized by the intensity $\overline{v^2}$ at the point furthest from the wall is of the form $f(y/y_1)$. Using numerically generated correlations, this hypothesis was shown to be valid throughout a large portion of the boundary layer. A similar collapse was obtained for R_{uv} in the log layer. Hunt and coworkers had already shown that f is linear in shear free boundary layers. Comparison with their results clearly shows that shear reduces the correlation length of the normal velocity, in the normal direction. The variation of eddy scales in the spanwise direction was also investigated, and a strong dependence on shear was found. These results should be very useful in turbulence modeling and in other applications where two-point correlation data are used (e.g, see below).

The eigenfunctions of the spatial two-point correlation tensor were used in Aubry's dynamical systems representation of wall layer turbulence. In their previous work Aubry, Holmes, Lumley & Stone (1986) used eigenfunctions obtained from the experimental measurements of Herzog (1986) in the near wall region of a turbulent boundary layer. Employing these eigenfunctions, which appeared physically as roll-cells, they obtained a highly truncated solution of the Navier Stokes equations and used methods of dynamical system theory to analyze the results. The results exhibited intermittency which was associated with the bursting events in the sublayer. A similar analysis was performed at the CTR using the eigenfunctions computed from simulation databases (Moin & Moser 1987). The results were different from those of Aubry et al. In particular, limit cycle behavior was observed just prior to intermittency, rather than the fixed point behavior found previously. As a result the character of the intermittency is different and it is significantly more sensitive

to the bifurcation or eddy viscosity parameter. In view of the significance of this work in relating dynamical systems theory to the structure of turbulence, further work is required to determine the sensitivity of the results to various computational parameters and other inputs.

Two-point correlation data was also used to extend, to three dimensions, the work of Moin, Adrian & Kim (1987) on stochastic estimation of conditional eddies. The previous work applied only in planes transverse to channel flow. With stochastic estimation, one approximates conditional averages using the two-point correlation tensor. In addition, the theory was extended to include specification of conditions at more than one point. An important result of this investigation was the verification that linear stochastic estimation indeed provides an accurate representation of conditional eddies. It was also shown that two-point stochastic estimates of the conditional eddies provide reasonable representations of the instantaneous flow structures. This technique is capable of generating the asymmetric structures that occur in the instantaneous flow field. Using conditions obtained from shear layers in the instantaneous field (see below), a simplified model of the shear layers was proposed which consisted of inclined vortical structures surrounding each shear layer.

Perhaps the most dramatic observation in this group was the discovery that turbulent channel flow contains a high density of strong, and highly visible, shear layers. The shear layers are regions of strong spanwise vorticity protruding from the wall region into the outer layers. Apparently the dominance of these shear layers, at least for the low Reynolds numbers considered here, has been overlooked previously. More importantly, the patterns of these shear layers, depicted in contour plots of spanwise vorticity in planes normal to the wall, and in the flow direction, strongly resembled those in Jimenez's (1987) two-dimensional numerical solutions. Although in channel flow these shear layers are three dimensional, the generation mechanism appears to be the same as in the two-dimensional case. The shear layers were followed in time and this generation process was observed directly. Based on these observations a simple model was proposed to explain vorticity ejection from the sublayer and the production of the shear layers. This model is essentially equivalent to the mechanism responsible for the instability of 2-D Tollmien Schlichting waves. Finally, by reducing the size of the computational box, futile attempts were made to study the dynamics of one shear layer in isolation (in the absence of complex interactions with other structures). One of the by products of this latter study was an interesting numerical solution which displayed three-dimensional turbulence on one side of the channel, and essentially two-dimensional flow on the other. The average wall shear stress of the turbulent layer falls between the values characteristic of the 2-D non-linear solutions and the 3-D turbulent solutions.

Parviz Moin

REFERENCES

AUBRY, N., HOLMES, P., LUMLEY, J. L., AND STONE, E. 1986 The dynamics of coherent structures in the wall region of a turbulent boundary layer. *Sibley School of Mechanical and Aerospace Engineering* . Report No. FDA-86-15. Cornell Univ. Ithaca, NY.

JIMENEZ, J. 1987 Bifurcation and bursting in two-dimensional Poiseuille flow . *Phys. Fluids.* **30**, 3644.

KIM, J., MOIN, P. & MOSER, R. D. 1987 Turbulence statistics in fully developed channel flow at low Reynolds number. *J. Fluid Mech.* **177**, 133-166.

MOIN, P. & MOSER, R. D. 1987 Characteristic eddy decomposition of turbulence in a channel. Submitted for publication.

Stochastic estimation of conditional eddies in turbulent channel flow

By R. J. ADRIAN[1], P. MOIN[2,3] AND R. D. MOSER[2]

1. Background

In two recent studies, stochastic estimation algorithms were applied to numerical simulation data bases (Adrian & Moin 1987, Moin, Adrian & Kim 1987). The best (in the mean-square sense) estimate of the flow field in the vicinity of a point or points where certain data are given is the conditional average, $\langle \mathbf{u}(\mathbf{x}') \mid \mathbf{E}(\mathbf{x}) \rangle$, where $\mathbf{E}(\mathbf{x})$ denotes the data at point $\mathbf{x}$. In stochastic estimation one approximates the conditional averages by a restricted form, again determined so as to minimize mean square error. Linear stochastic estimation takes a form that is linear in the given data, $\mathbf{E}(\mathbf{x})$. In Adrian & Moin (1987), the homogeneous shear flow data base was used, and $\mathbf{E}(\mathbf{x})$ included the complete kinematic state at a point, consisting of the velocity field and the deformation tensor. In the study of Moin, et al. (1987), a turbulent channel flow data base was used, and $\mathbf{E}$ included only the velocity vector. In this latter study, the estimated eddy was obtained in cross-stream (y, z) planes. In both studies the probability density functions were used to specify the data, $\mathbf{E}$.

2. Multi-point stochastic estimation

The present studies contain two new elements: three- dimensional structure of inhomogeneous turbulence, and estimation using two-point events. The complete two-point correlation tensor, $R_{ij}(y, y', r_x, r_z)$ was recently computed by Moin & Moser (1987) from the channel-flow data base and was utilized in the present study. In addition, the stochastic estimation formulation was extended to include data at any number of points.

Consider any array of points $(\mathbf{x}_1, \mathbf{x}_2, \ldots, \mathbf{x}_n)$. The conditional averages of interest are conditional eddies defined by

$$\langle \mathbf{u}(\mathbf{x}') \mid \mathbf{u}(\mathbf{x}_1), \mathbf{u}(\mathbf{x}_2), \ldots \mathbf{u}(\mathbf{x}_N) \rangle$$

or, more briefly

$$\langle \mathbf{u}' \mid \mathbf{E} \rangle$$

where

$$\mathbf{E} = [\mathbf{v}_1 \le \mathbf{u}_1 < \mathbf{v}_1 + d\mathbf{v}_1 \text{ and} \ldots \text{and } \mathbf{v}_N \le \mathbf{u}_N < \mathbf{v}_N + d\mathbf{v}_N]$$

1 University of Illinois
2 NASA-Ames Research Center
3 Stanford University

is the N-point vector event consisting of $3N$ components. We wish to estimate $\langle \mathbf{u}' \mid \mathbf{E} \rangle$ as a linear function of the data $\mathbf{E}$. Nonlinear estimation usually results in a small correction (Adrian 1979, Adrian *et al.* 1987), so attention has been restricted to the linear estimate. Let us order the data vector as

$$\mathbf{E} = [u_{11}, u_{12}, u_{13}, u_{21}, \ldots, u_{N3}] = [E_1, E_2, \ldots E_{3N}]$$

The linear stochastic estimate of $\langle \mathbf{u}' \mid \mathbf{E} \rangle$ is

$$\hat{u}'_i = L_{ij} E_j. \tag{1}$$

Unless otherwise indicated, the summation convention is implied for repeated indices. Minimizing the mean square error results in the following system of equations for the estimation coefficients

$$\langle E_j E_k \rangle \, L_{ij} = \langle u'_i E_k \rangle, \qquad j, k = 1, 2, \ldots, 3N, \\ i = 1, 2, 3. \tag{2}$$

In the above equation, $L_{ij} = L_{ij}(\mathbf{x}', \mathbf{x}_1, \mathbf{x}_2, \ldots \mathbf{x}_N)$ and

$$\langle u'_i E_k \rangle = R_{ij}(\mathbf{x}', \mathbf{x}_\alpha) \qquad \alpha = 1 + \mathrm{INT}(k/3), \qquad j = k - 3\alpha + 1. \tag{3}$$

3. Objective

This investigation offered the opportunity to address, for the first time, several long-standing issues regarding linear estimation and coherent structures, and to answer more completely some questions that have been addressed partially, but never with the benefit of full, three-dimensional information. The objectives were:

a. Determine how well linear estimates approximate the field obtained by true conditional averaging, using events such as those in quadrant analysis.

b. Determine the extent to which the three-dimensional linearly estimated fields correspond to coherent structures, and the degree and manner in which they differ. When is it appropriate to interpret a linear estimate as a fluid entity, and when it must be considered to be only as a smoothed mathematical entity?

c. Evaluate the type and nature of the structural information gained by employing several different types of events.

d. Learn more about the 3-D structure of important coherent motions that occur in wall turbulence.

4. Results of the investigation

The validity of the linear stochastic estimation approximation of the conditional averages has been investigated previously for different types of conditional averages by comparison of experimentally measured conditional averages with their linear estimates. While experimental comparisons have been extensive (see Adrian *et al.* 1987), they have been limited to low dimensional results. In this investigation, a full
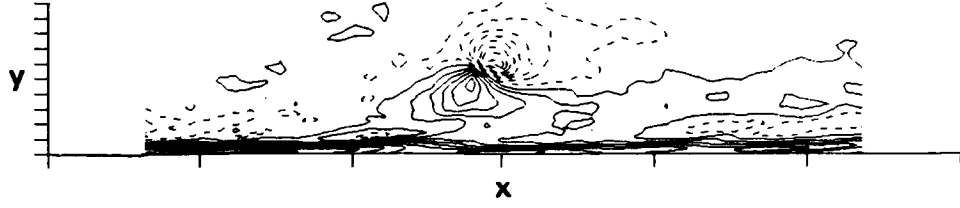
FIGURE 1. Conditional average of $\langle \omega_z'(\mathbf{x}') \mid Q2 \rangle$ using Kim and Moin (1986) $Q2$ event at $y^+ = 99$.
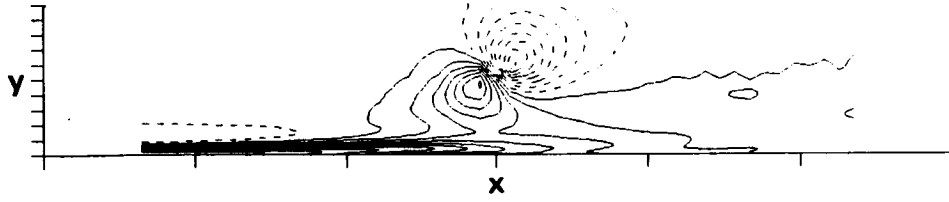
FIGURE 2. Linear stochastic estimate of $\langle \omega_z'(\mathbf{x}') \mid Q2 \rangle$ using Kim and Moin's (1986) $Q2$ event at $y^+ = 99$.

three-dimensional conditional field, determined using Kim & Moin's (1986) quadrant 2 conditional average, Figure 1, was compared to its linear estimate computed for the velocity vector $\mathbf{u}(\mathbf{x})$ conditional on the same quadrant 2 event in Figure 2. The former quantity $\langle \mathbf{u}' \mid Q2 \rangle$ is approximated in terms of the linear estimate by the following steps:

$$\langle u_i' \mid Q2 \rangle \doteq \int_{Q2} L_{ij}(\mathbf{x}, \mathbf{x}') u_j(\mathbf{x}) P(\mathbf{u}(\mathbf{x})) \, d\mathbf{u} = L_{ij}(\mathbf{x}, \mathbf{x}') \int_{Q2} u_j P(\mathbf{u}(\mathbf{x})) \, d\mathbf{u}, \quad (4)$$

where the integral extends over the range of $\mathbf{u}$ where the event $Q2 = \{u_1(\mathbf{x}) < 0, u_2(\mathbf{x}) < 0, \text{ and } uv(\mathbf{x}) < 10\overline{uv}(\mathbf{x})\}$ is satisfied.

Comparison of Figures 1 and 2 shows surprisingly close agreement between the linear estimate and the conditional average. Figure 3 shows contours of the u-component velocity in channel flow conditionally averaged, given Kim & Moin's (1986) Q2 event, and comparison with the linear estimate in Figure 4, again, shows good agreement. These results, coupled with the aforementioned experimental investigation, lead us to conclude that linear estimate is a reliable approximation of the conditional average.

To study the structure of channel-flow turbulence, the first step was to identify a structure that was judged to recur frequently and to be dynamically significant. To this end, the cube of velocity data available in a velocity field was scanned to locate the positions of maximum instantaneous Reynolds stress,uv. The velocity field in the vicinity of the maximum Reynolds shear stress was surveyed by examining many
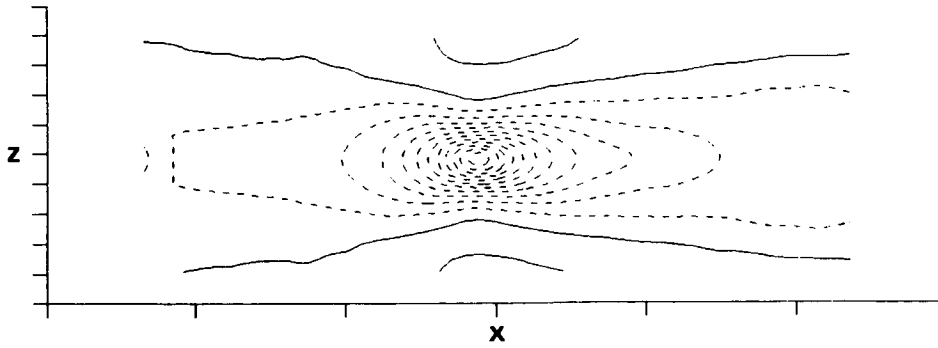
FIGURE 3.   Contours of $\langle u' \mid Q2 \rangle$ in the x-z plane passing through $\mathbf{x}$ $(y^+ = 99)$.
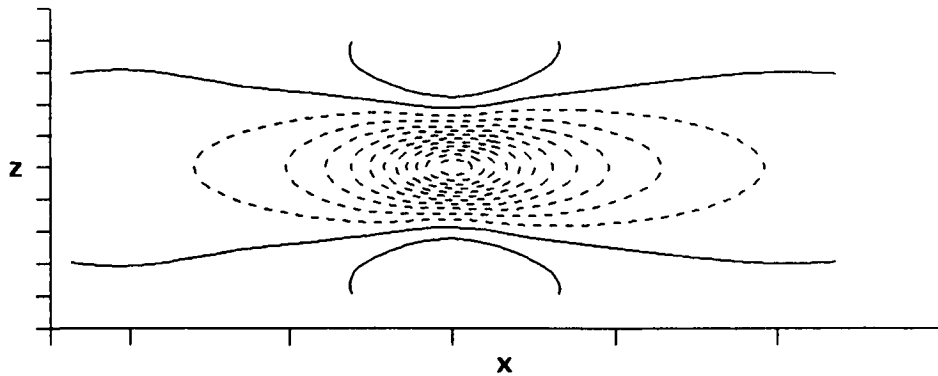
FIGURE 4.   Contours of the linear estimate of $\langle u' \mid Q2 \rangle$. Same plane as in Figure 3.

different quantities in many different planes, and a reasonably complete picture of the physical structure of the flow in this region was obtained.

The structure of the flow is illustrated in Figures 5 through 10. Figures 5 and 6 show the Reynolds stress in the x-z and x-y planes. They reveal two maxima occurring at $\mathbf{x}_1 = (30, 25, 20)$ and $\mathbf{x}_2 = (35, 25, 20)$, where the numbers in the parentheses refer to grid indices. The velocities at these maxima are denoted by $\mathbf{u}_1$ and $\mathbf{u}_2$. The right-most maximum is associated with the outflow of low-momentum fluid, and the left-most maximum is associated with the inflow of high-momentum fluid. This pair of $Q2/Q4$ events is associated with a region of organized transverse vorticity, Figure 7. The velocity field in the x-y plane in the neighborhood of this point is shown in Figure 8. The vorticity ω_z is associated with a shear layer that forms between the $Q2$ and $Q4$ events. This shear layer is visible in the velocity profile of Figure 8. A cross-section of the flow in the x-z plane passing through the $Q4$ event is shown in Figure 9. In the y-z plane, it is clear that $\mathbf{x}_1$ is located on the down-wash side of a streamwise vortex. The v-component of velocity in the vicinity of the $Q2/Q4$ event is shown in Figure 10.
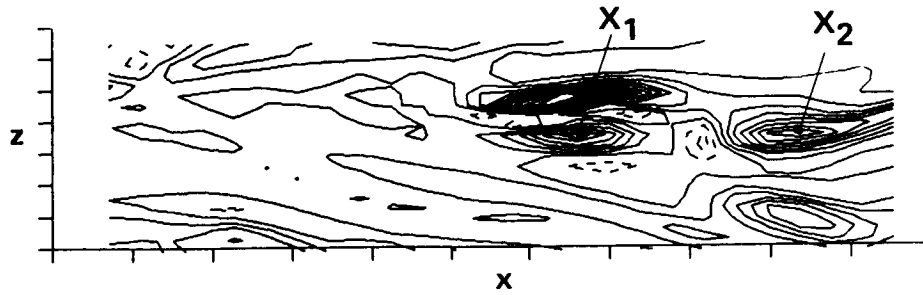
FIGURE 5. Instantaneous Reynolds shear stress contours in the x-z plane.
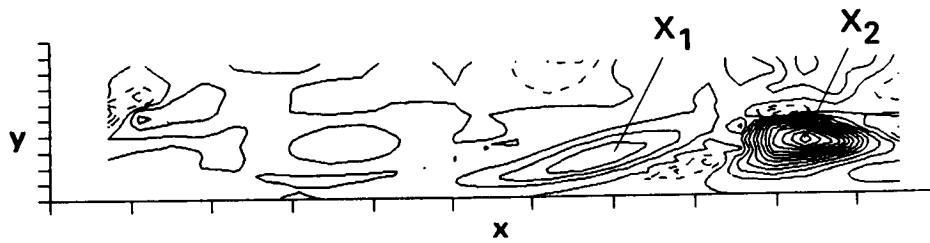
FIGURE 6. Instantaneous Reynolds shear stress contours in the x-y plane.
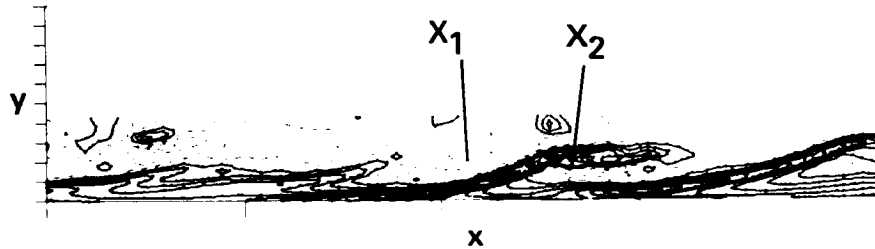
FIGURE 7. Contours of instantaneous ω_z in the x-y plane passing through x_1.

The degree to which the linear stochastic estimate is able to represent an instantaneous structure was evaluated by picking the velocity vectors at two points, x_1 and x_2 centered on the $Q2$ and $Q4$ events, respectively. Using these vectors as input to the two-point linear stochastic estimator, the fluctuating velocity profile was calculated from equations (1) and (2).

Figure 11 shows contours of the linearly estimated fluctuating ω_z. There is considerable similarity between these contours and the contours of the random realization in Figure 7. A notable difference is that, in the instantaneous realization, the vorticity changes sign twice below the shear layer (see Jimenez *et al.* in this volume). Comparison of the contours of the v-component of velocity plotted in Figure 12
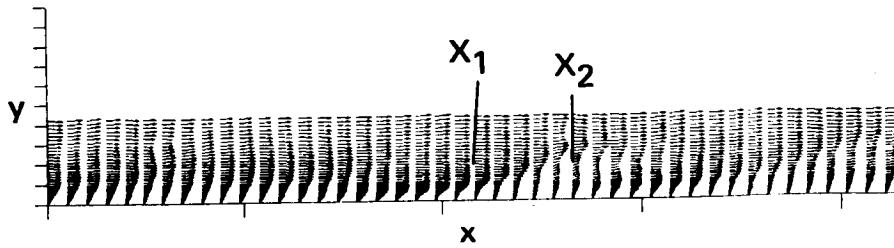
FIGURE 8.   Instantaneous total velocity vectors in the x-y plane passing through $\mathbf{x}_1$.
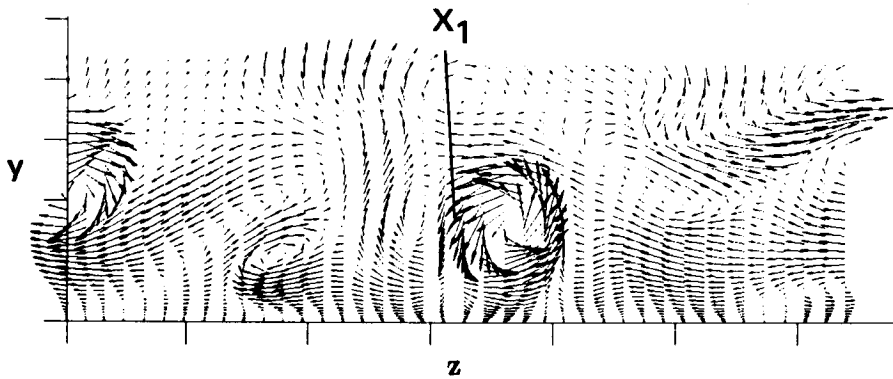
FIGURE 9.   Instantaneous velocity vectors in the y-z plane passing through $\mathbf{x}_1$.
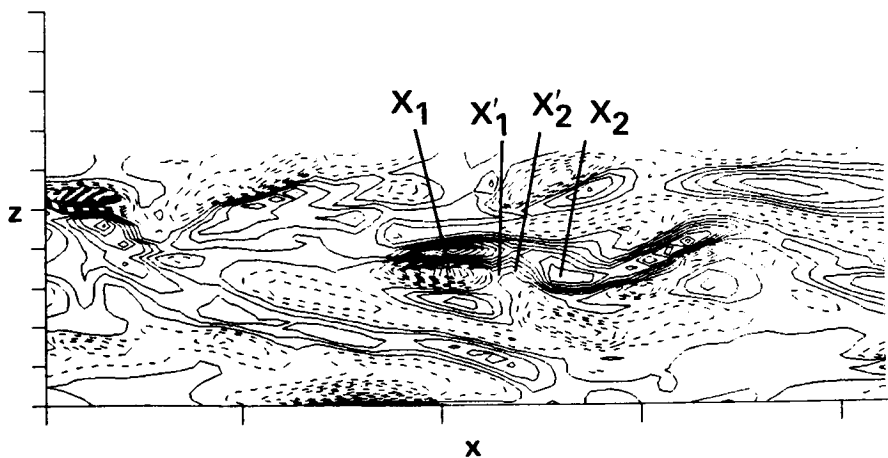
FIGURE 10.   Contours of the instantaneous v-component in the x-z plane passing through $\mathbf{x}_1$ at $y^+ = 30$.
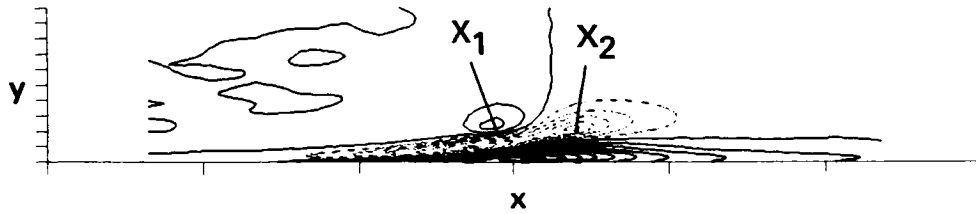
FIGURE 11.   Linear estimate of the ω_z in the x-y plane through x_1 given the $Q4$ event at x_1 and the $Q2$ event at x_2.
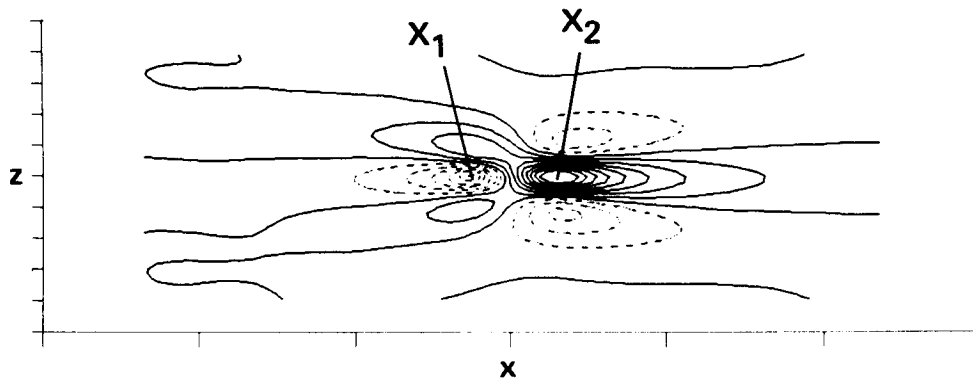
FIGURE 12.   Linear estimate of v-component in the x-y plane passing through x_1 given the $Q4$ event at x_1 and the $Q2$ event at x_2.

with the corresponding instantaneous contours plotted in Figure 10 is revealing. The instantaneous realizations are, of course, highly deformed, but they do reveal a region of large positive velocity surrounded by two regions of negative v-velocity in the downstream direction, and in the upstream direction an oppositely signed triplet, exactly as shown in the linear estimate. The velocity vectors in the y-z plane through x_1, Figure 13, show a strong impingement flow with a streamwise vortex present. Note that the vortical pattern reverses sign in a plane passing through x_2, resulting in flow away from the wall, in Figure 14.

A simplified sketch of the coherent region under investigation is shown in Figure 15. It consists of two pairs of streamwise vortices, one rotating so as to produce a $Q2$ event, i.e. low momentum fluid being pumped upwards, and the other pair lying farther upstream rotating so as to produce a $Q4$ event with high-momentum fluid being pumped downwards toward the wall. In the region between these pairs of vortices, the opposing flows of the $Q2$ and $Q4$ events generate a stagnation-point flow and an associated shear-layer tongue which has a narrow extent. This may be the origin of the region of large ω_z shown in Figures 7 and 11. It is also revealed in Figure 16, which shows (u, w) vectors in the x-z plane. It should be noted that the sketch in Figure 15 is composed of two pairs of symmetric vortices; however,
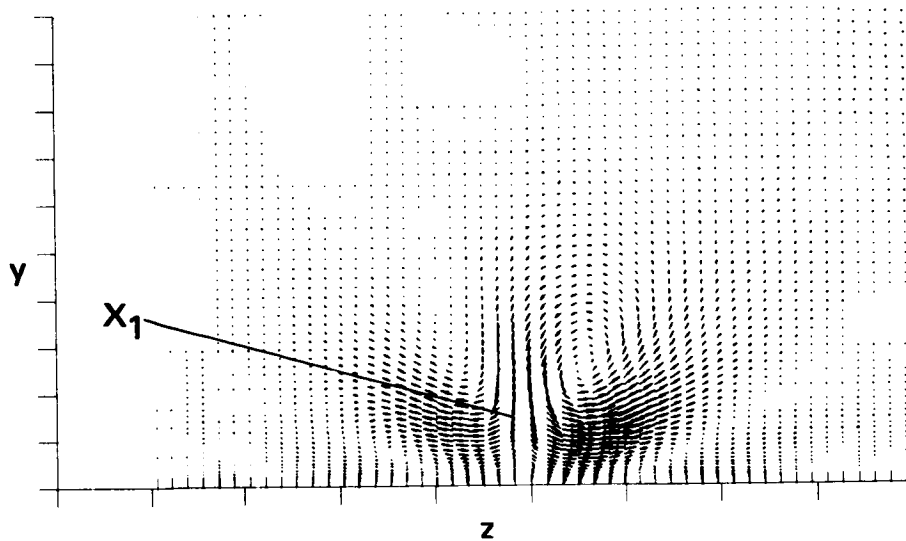
FIGURE 13. Linear estimate of (v, w) in the y-z plane passing through x_1 given the $Q4$ event at x_1 and the $Q2$ event at x_2.
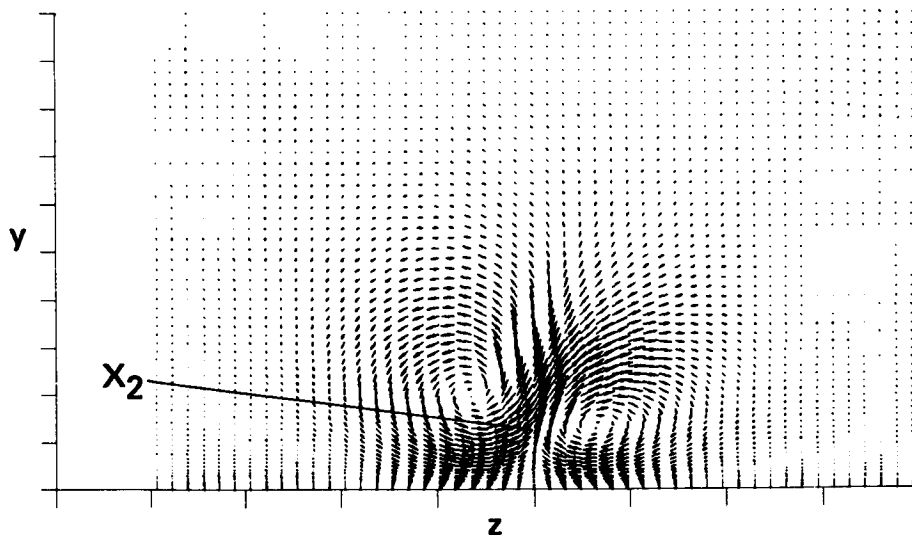
FIGURE 14. Linear estimate of (v, w) in the y-z plane passing through x_2 given the $Q4$ event at x_1 and the $Q2$ event at x_2.

the instantaneous as well as the estimated flow patterns show a pronounced single vortex followed by a pair. The sketch should be viewed as a simplified average portrait of the flow.

The question arises as to the effect upon the linear stochastic estimate of selecting different points and different combinations of velocity vectors at those points. In the
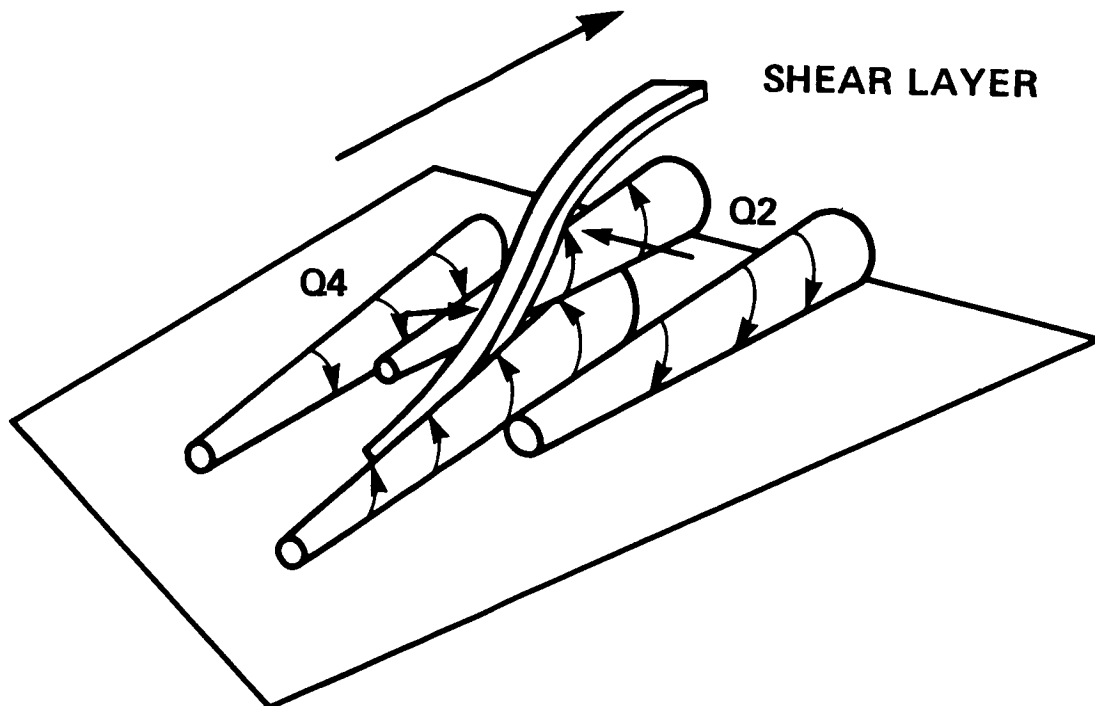
FIGURE 15. Sketch of the three-dimensional structure associated with the $Q4/Q2$ event.

preceding $Q4/Q2$ event, the events were far apart ($6\Delta x$), and they were characteristic of sweep and ejection events lying some distance away from the shear layer that they appeared to cause. Alternatively, one could concentrate on the shear layer. We chose to specify two points lying very close to the shear layer on either side of it: $\mathbf{x}_1 = (32, 26, 20)$ and $\mathbf{x}_2 = (33, 24, 20)$. We input the velocity vectors $\mathbf{u}_1$ and $\mathbf{u}_2$ taken from the instantaneous field at those points. The net effect was to specify approximately the average velocity between the points and the velocity derivatives $(\partial u_i/\partial x_j)$, since $(u_{i2} - u_{i1})/\Delta x_j$ is approximately the deformation tensor for small Δx_j.

Figure 17 shows contours of the linearly estimated v-component velocity that result from the specification of the shear event. Figure 10 shows the contours of the realization (points are marked as $\mathbf{x}_1$, $\mathbf{x}_2$). The comparison is good, but the strong lobe to the side of $\mathbf{x}_1$ is not captured.

Figure 18 shows the estimated z component of vorticity in the x-y plane. It compares well with Figure 11 for the $Q4/Q2$ event. In Figure 19, the velocity
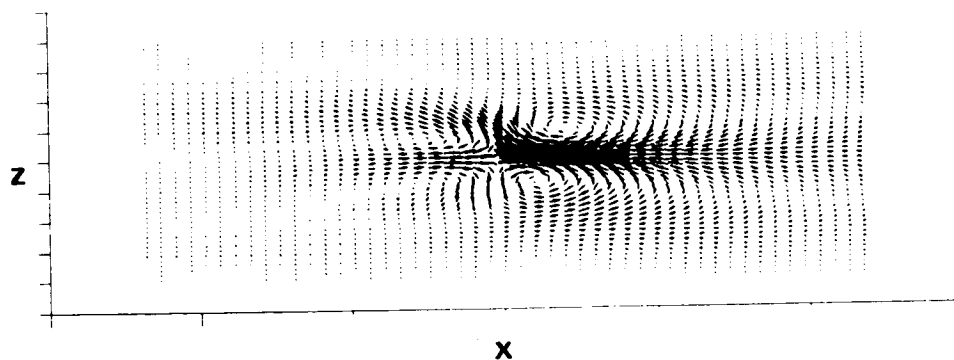
FIGURE 16.   Linearly estimated (u, w) vectors in the x-z plane passing through x_1 given the $Q4$ event at x_1 and the $Q2$ event at x_2.
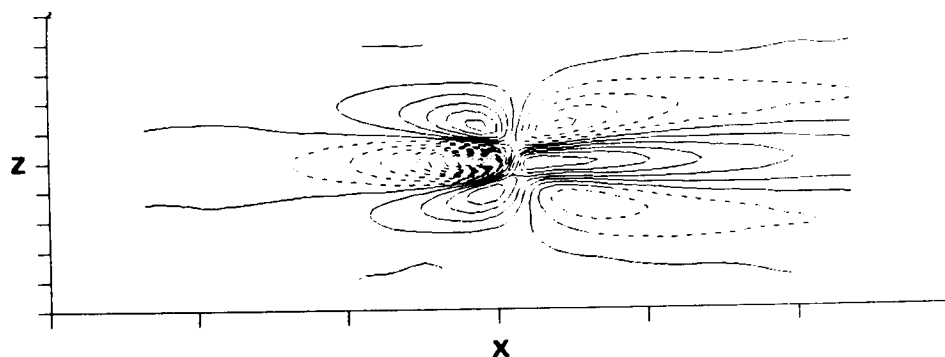
FIGURE 17.   Contours of linearly estimated v-components in an x-z plane, five grid points below x_1 ($y^+ = 21$) given the shear layer event.

vectors of the estimated eddy in the y-z plane passing through x_1 reveal a weak pair ov counter-rotating streamwise vortices near the wall, with a single strong vortex above them.

Finally, the foregoing results each utilized information at two points in the flow. The loss of velocity information incurred when velocity at only one point was specified was also investigated. Figures 20 and 21 show that the linear estimate based on the single-point $Q2$ event at $x_2 = (35, 25, 20)$ reveals only a single pair of streamwise vortices. This result suggests that two-point events provide the information needed to study the interaction between two characteristic structures.

5. Conclusion

The results of this investigation indicate that linear stochastic estimation can be used effectively in the study of numerical data bases consisting of three-dimensional vector fields, both velocity and vorticity. It is expected that pressure fields could
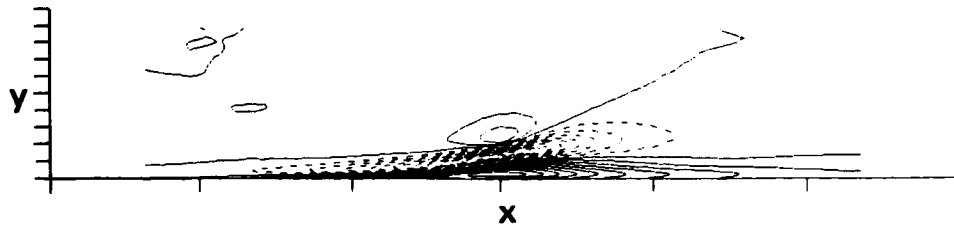
FIGURE 18. Linearly estimated ω_z in the x-y plane through x_1 given the shear layer event.
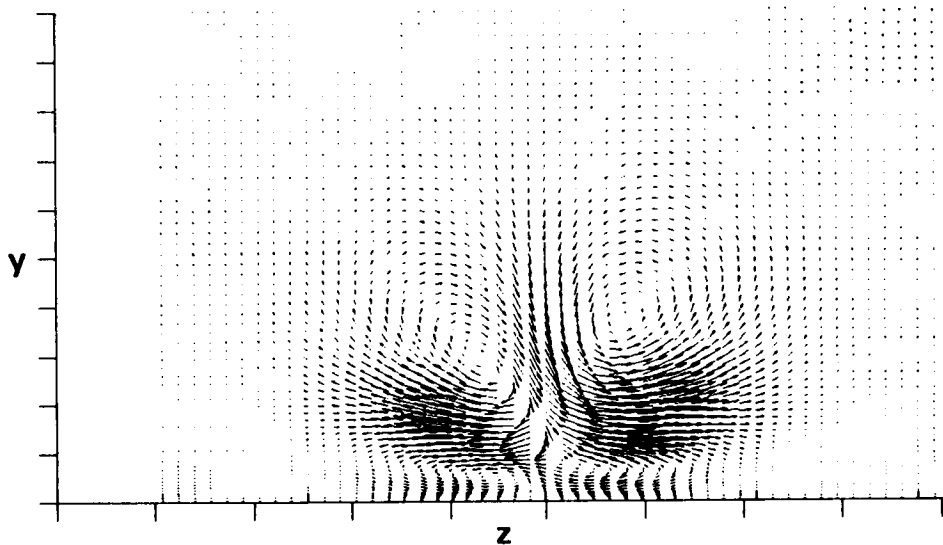
FIGURE 19. Linear estimate (v, w) in the y-z plane through x_1 given the shear layer event.

be studied with equal facility, although this avenue has not been explored. Linear stochastic estimation is surprisingly good at approximating conditional averages, at least to the extent that the size scales and the shapes of three-dimensional structures are revealed with relatively little distortion. The linear stochastic estimate is also surprisingly good at representing instantaneous realizations of flow in the turbulent wall layer. In part, this may be a consequence of the low Reynolds number of the flow investigated, and the fact that there are strong characteristic structures in the flow. Less energetic structures may not be represented with such fidelity.

Two-point stochastic estimation yields more structural information and more detail than single-point estimation. Interestingly, the locations of the two points are not too critical, provided velocity vectors input to the stochastic estimate are those that occur within the structure. This is indicated by the fact that the stochastic estimates using distant points ($Q4/Q2$ event) and neighboring points (shear event)
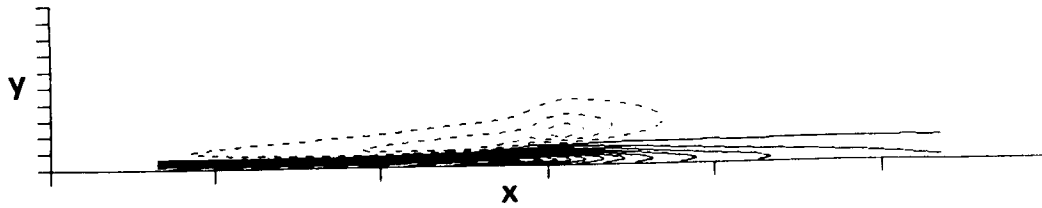
FIGURE 20.   Linear estimate of ω_z in the plane through x_2 given the single-point event $u_2(x_2)$.
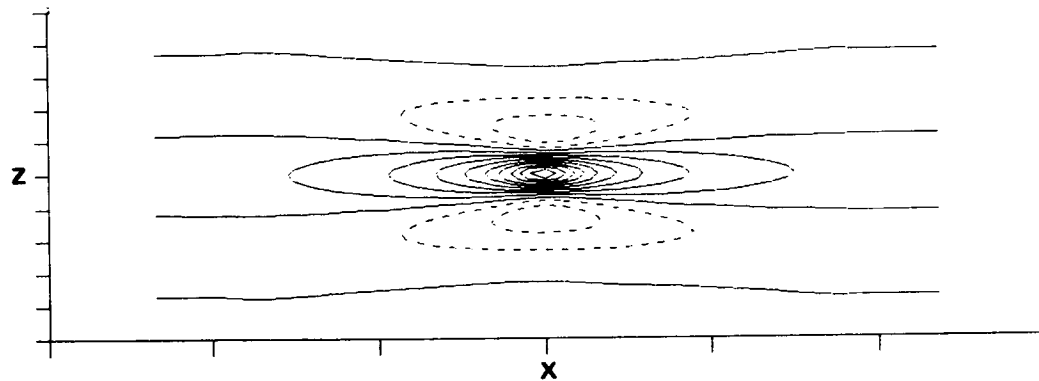
FIGURE 21.   Linear estimate of v-contours in the x-z plane through x_2 given the single-point event $u_2(x_2)$.

were very similar. Finally, the second point adds structural information which appears to represent interactions of flow structures in certain circumstances.

The structures we observed occurred repeatedly within the flow, but we cannot say much about their dominance or the probability of their occurrence without further systematic studies of their frequency. However, the combined $Q4/Q2$ event does appear to be associated with two pairs of streamwise vortices whose up-flows and down-flows create a stagnation point following an associated three-dimensional shear-layer tongue. Such flows can also occur as single events, i.e., $Q2$ or $Q4$ in isolation, and significant asymmetries may occur due to cross flows in the z-directions. Further work is needed to establish the three-dimensional structure of these systems.

Acknowledgments

REFERENCES

ADRIAN, R.J. 1979 Conditional Eddies in Isotropic Turbulence. *Phys. Fluids.* **22**, 2065–2070.

ADRIAN, R.J., CHUNG, M.K., HASSAN, Y., JONES, B.G., NITHIANANDAN, C.K., & TUNG, A.T. 1987 Experimental Study of Stochastic Estimation of Turbulent Conditional Averages. 6th *Turbulent Shear Flow Symposium, Toulouse, France.* Sept. 7–9, 1987, 6.1.1–6.1.7.

ADRIAN, R.J., & MOIN, P. 1987 Stochastic Estimation of Organized Turbulence Structure: Homogeneous Shear Flow. *to appear in J. Fluid Mech.*

MOIN, P., ADRIAN, R.J. & KIM, J. 1987 Stochastic Estimation of Organized Structures in Turbulent Channel Flow. 6th *Turbulent Shear Flow Symposium, Toulouse, France.* Sept. 7–9, 1987.

MOSER, R. & MOIN, P. 1987 Characteristic eddy decomposition of turbulence in a channel. *to be published.*

KIM, J. & MOIN, P. 1986 The Structure of the Vorticity Field in Turbulent Channel Flow. Part 2. Study of Ensemble-Averaged Fields. *J. Fluid Mech.* **162**, 339–363.

A low dimensional dynamical
system for the wall layer

By N. AUBRY[1] AND L. R. KEEFE[2]

Low dimensional dynamical systems which model a fully developed turbulent wall layer, for $y^+ \leq 40$ have been derived (Aubry *et al.* 1986, Aubry, 1987). The model is based on the optimally fast convergent proper orthogonal decomposition, or Karhunen–Loeve expansion, proposed by Lumley, 1967. This decomposition provides a set of eigenfunctions which are derived from the autocorrelation tensor at zero time lag. Those used in the previous studies were experimentally determined in a pipe flow at a Reynolds number 8750 based on the mean centerline velocity and the diameter of the pipe. (Herzog, 1986).

Via Galerkin projection, low dimensional sets of ordinary differential equations in time, for the coefficients of the expansion, were derived from the Navier Stokes equations. The energy loss to the unresolved modes was modeled by an eddy viscosity representation, analogous to Heisenberg's spectral model. In the previous work the equations of a ten dimensional system, consisting of one eigenfunction per wave number for the zero streamwise wave number, and six spanwise wave numbers corresponding to a periodic length of 333 wall units, were examined. The solution, which consisted of longitudinal rolls, exhibited an intermittent behavior(the zero mode decays to zero). The rolls are initially steady, but then oscillate with slowly growing amplitude until they "burst" into much more complicated features before recovering their initial state. The whole sequence then repeats. This is suggestive of the bursting event observed in visualization experiments (Kline *et al.*, 1967).

This approach may shed light on the basic dynamical mechanism of the fundamental bursting event. However, until recently, it was limited to the specific experimental flow (Herzog, 1986).

Another set of eigenfunctions and eigenvalues have been obtained from direct numerical simulation of a plane channel at a Reynolds number of 6600, based on the mean centerline velocity and the channel width (Moin & Moser, 1987). This new set of eigenfunctions is compared to those of Herzog (1986). The expansion still converges very quickly, since 75% of the kinetic energy is contained in the first eigenmode. Thus it still seems quite reasonable to truncate the expansion at the first mode. The energy content at the first eigenmode still drops faster with streamwise wave numbers than with spanwise wavenumbers, justifying, in a first approximation, no variations in the streamwise direction. However, the ratio between the streamwise and cross-stream length scales is not as large as was observed in the decomposition of Herzog, suggesting that few elongated patterns

1 Cornell University
2 Center for Turbulence Research

are present. The energy in cross- stream wavenumbers is slightly larger than in the experimental case and the peak in the spectrum is shifted to a higher wavenumber. Also, the peak magnitude of the numerically generated spectrum for $k_x = 0$ seems anomalously large. The contribution of the first eigenmode to the variance of the velocity fluctuations in the three directions is very similar in both cases. However, while the contribution of Herzog's first mode to the Reynolds shear stress is 50% near the wall, 95% at $y^+ = 20$, 78% at the upper edge of the layer, that of Moin and Moser exceeds 100% in the region $13 \leq y^+ \leq 25$ (120% at $y^+ = 25$). This apparent paradox occurs because the contribution of higher order modes to the Reynolds shear stress is negative in that region. The eigenfunctions themselves are quite similar in both cases, at least amongst those selected for inclusion in the dynamical system.

Using the new eigenvalues and eigenfunctions, a new ten dimensional set of ordinary differential equations has been derived using five non-zero cross-stream Fourier modes with a periodic length of 377 wall units. The coefficients in the equations are similar to those of the previous study. As in the previous work, the evolution equations are globally stable, since all the coefficients of the cubic terms are negative. This is due to the positive contribution of the first eigenmode to the Reynolds shear stress. The coefficients of the cubic terms are larger with the present data than in the previous studies. This appears to be caused by the higher proportion of Reynolds shear stress carried by the first mode.

The new dynamical system has been integrated for a range of the eddy viscosity parameter α. For large values, the solution goes to a stable fixed point, involving only the second and fourth Fourier mode. When α decreases, this fixed point undergoes a bifurcation to a limit cycle. As α decreases more, the solution becomes much more complicated and intermittent. In contrast, the results of the previous work showed a transition directly from a fixed point to an intermittent solution exhibiting the bursts discussed above. The intermittent solution in the present work exhibits the same basic features previously observed. In the previous work the solution cyclically visited the neighborhood of two different fixed points, being attracted to a double homoclinic orbit which connected them. In the new system the solution switches back and forth in a similar way between different orbits and limit cycles. When α decreases more, we observe much more disorganized motion.

This work is encouraging. Although we could not analyze in detail the bifurcation diagram during the short period of the program, we observed intermittency of the solution for some values of the parameter α. The appearance of limit cycles introduces periodic motions superposed to the intermittency. We plan more investigations in future work.

REFERENCES

AUBRY, N., HOLMES, P., LUMLEY, J.L., AND STONE, E. 1986 The dynamics of coherent structures in the wall region of a turbulent boundary layer. Sibley School of Mechanical and Aerospace Engineering Report No. FDA-86-15. Ithaca, NY: Cornell University.

AUBRY, N. 1987 A dynamical system/coherent structure approach to the fully developed turbulent wall layer. Ph.D. thesis. Cornell University.

HERZOG, S. 1986 The large scale structure in the near-wall region of turbulent pipe flow. Ph.D thesis. Cornell University.

KLINE, S.J., REYNOLDS, W.C., SCHRAUB, F.A. AND RUNDSTADLER, P.W. 1967 The structure of turbulent boundary layers.. *J. Fluid Mech..* **30(4)**, 741-773.

Self similarity of two point correlations in wall bounded turbulent flows

By J. C. R. HUNT[1], P. MOIN[2,3], R. D. MOSER[3] AND P. R. SPALART[3]

Computational results of Moin & Moser (1987) and Spalart (1986) for two-point correlations of the normal v component of turbulence at two points y, y_1 ($y_1 > y$), from the rigid walls bounding turbulent channel and boundary layer flows for Reynolds numbers 3200 and 7000 are shown to have an approximately self-similar form, when plotted in terms of y/y_1. It is found that

$$\frac{\overline{v(y)v(y_1)}}{\overline{v^2(y_1)}} = f(\frac{y}{y_1})$$

where $0 \le y/y_1 \le 1$, $f(0) = 0$, $f(1) = 1$, and where f is approximately independent of y_1, for y_1 ranging from about 20 ν/u_τ to half the channel width;

$$f \approx 2(y/y_1)^2 - (y/y_1)^3 \pm .1.$$

The same kind of self similarity has been predicted for and measured in shear free boundary layers. But in that case, where $f \approx y/y_1$, the mechanism is one of 'blocking' or 'splatting' at the wall. In these sheared wall layers, the shear *also* has an important effect. There are important implications from this research for modeling wall bounded shear flow.

---

1. Introduction and Objective

The structure of turbulence at a height y from a wall is affected by the local mean shear at y, $(\frac{\partial U}{\partial y})$, by the *direct* effect of the wall on the eddies, and by the action of other eddies close to or far from the wall. Some researchers believe that a single one of these mechanisms is dominant, while others believe that these effects have to be considered together.

It is important to understand the relative importance of these effects in order to develop closure models, for example for the dissipation or for the Reynolds stress equation, and to understand the eddy structure of cross correlation functions and other measures. The specific objective of this research project was to examine the two point correlation R_{vv} of the normal velocity component v near the wall in a turbulent channel flow and in a turbulent boundary layer. This component of

1 Univ of Cambridge

2 Stanford University

3 NASA Ames Research Center
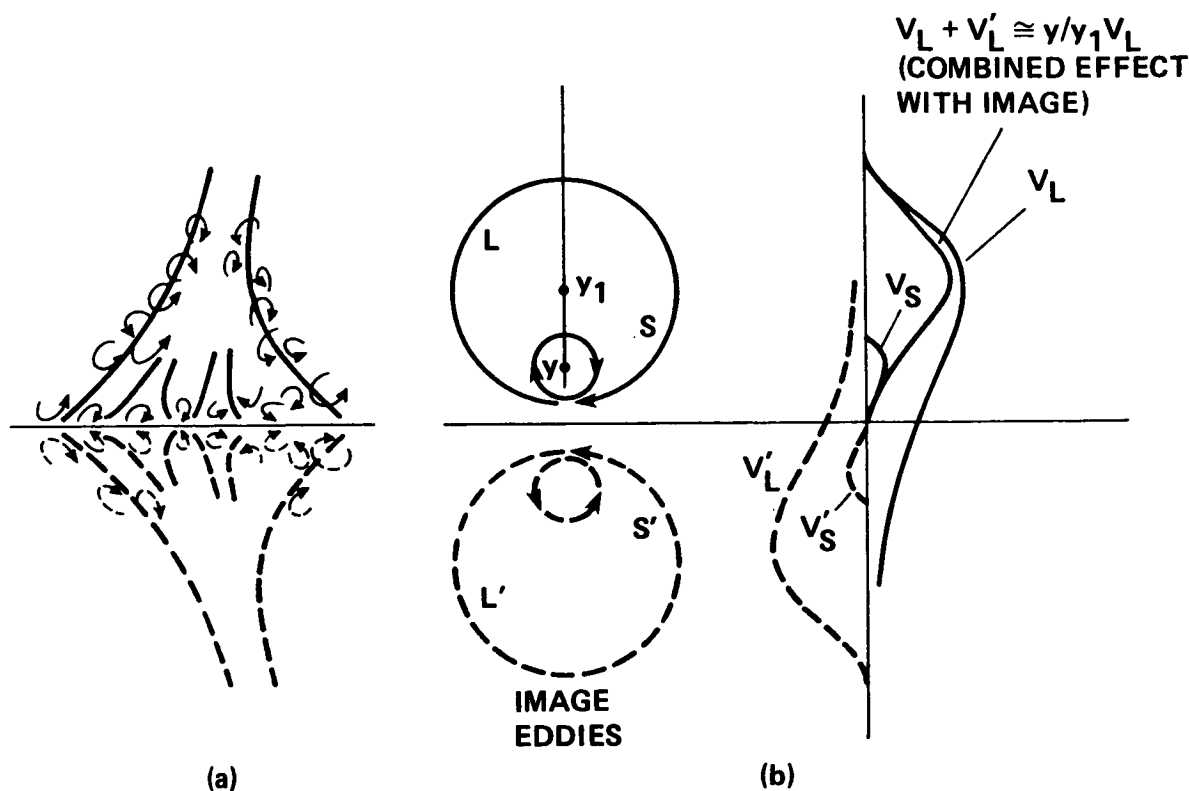
FIGURE 1. Diagram to illustrate eddy motion near the ground, *(a)* typical structure of an updraft or "thermal" plus the "image" updraft, *(b)* the relation between the velocity at y_1 and y. The large eddy L, with velocity v_L, is centered at height y_1. The small eddy S, with velocity v_S is centered at height y. (Their "images" are L' and S') The profiles are shown of the vertical velocity of the large and small eddies, of their images and of the combined effect of both.

turbulence is the most sensitive to the relative effects of shear (which amplifies v) and the blocking effect of the surface (where $v = 0$, even in inviscid flow).

Recent research on shear free turbulent boundary layers, (such as occur in thermal convection between boundaries or in turbulence near a free surface or turbulence near a density inversion layer) has shown how the blocking effect leads to a self-similar form for R_{vv} when expressed as a ratio with $\overline{v^2}(y_1)$ (i.e., normalized at the upper point),

$$R_{vv} \equiv \frac{\overline{v(y)v(y_1)}}{\overline{v^2}(y_1)} = f\left(\frac{y}{y_1}\right) \approx \frac{y}{y_1} \qquad y < y_1 \qquad (1.1)$$

The theory for the SFBL is valid when y_1 is much less than the turbulence scale far from the boundary. The explanation is given with the aid of figure 1. Let there be a large eddy (L) centered with maximum velocity at y_1 and a small eddy centered at y. Then the velocity at y_1, $v(y_1) \approx v_L$. The effect of the small eddy at y is small
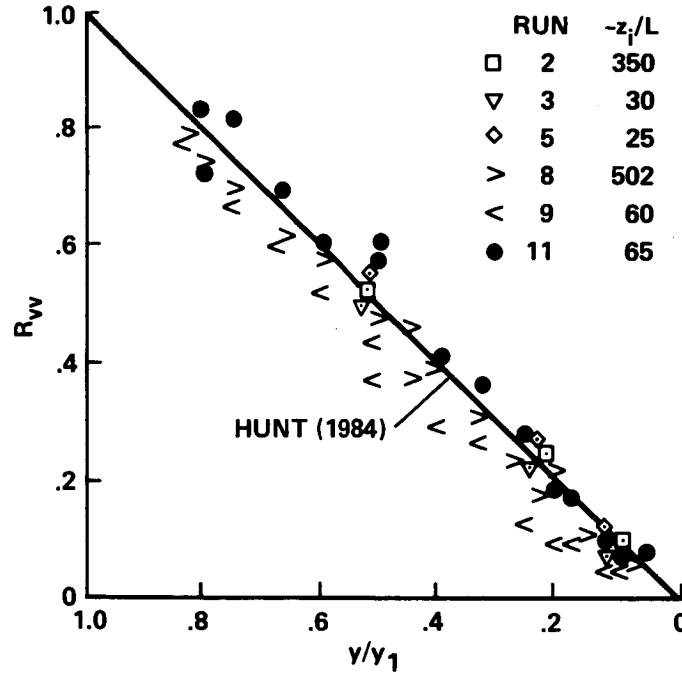
FIGURE 2. Measurements in the convective atmospheric boundary layer of the cross correlation of v at heights y and y_1, normalized by v^2 at y_1. The results are compared to the approximate form of the theoretical predictions of Hunt (1984), $\hat{R}_{vv} \approx y/y_1$. ($-z_i/L$ indicates the state of the convective boundary layer, the higher $-z_i/L$, the stronger the convection and the weaker the shear.) From Hunt, Kainal & Gaynor, (1987).

if y is less than about $y_1/2$. However, the velocity at y

$$v(y) = v_s + (y/y_1)v_L \tag{1.2}$$

has two components, from the small eddy and also from the large eddy. Because the vertical dependence of the large eddy is blocked by the surface, this component is reduced by a factor of about (y/y_1) for high Reynolds number turbulence. One can imagine an image vortex underneath the surface. Since the correlation between v_s and v_L is small if $y \leq y_1/2$ the correlation between $v(y)$ and $v(y_1)$ and thence the correlation, normalized at the upper point (N.U.P.) is

$$\hat{R}_{vv} \approx y/y_1. \tag{1.3}$$

It is interesting that the theory seems to agree with measurements for the atmospheric boundary layers during thermal convection. See figure 2 from Hunt, Kaimal & Gaynor 1987. The same general idea might be appropriate for a wall bounded shear flow at moderate Reynolds number, but now the velocity at height y is not a simple function of y/y_1. In general we expect the component of v_L to be given by

a function $g[(y - y_1)/L^v(y_1)]$, depending on the distance between y and y_1 and the scale of turbulence $L^v(y_1)$ at y_1. Therefore, we might predict:

$$\hat{R}_{vv} \approx g((y - y_1)/L^v(y_1)) \tag{1.4}$$

But in a wall-bounded flows $L^{(v)}(y_1)$ is proportional to y_1, (at least for unstable and neutral, but not for stably stratified flows). Therefore, we might expect,

$$g\left(\frac{y - y_1}{L^v(y_1)}\right) = g\left(\frac{y - y_1}{\alpha y_1}\right) \tag{1.5}$$

where $L^v(y_1) \approx \alpha y_1$, which can be written as another function, i.e.

$$\hat{R}_{vv} \approx f(y/y_1).$$

This is the first hypothesis to be tested.

We have argued that the wall "blocks" the normal component of the large-scale eddies centered above the wall at $y = y_1$. In a shear flow the streamwise u and normal v components of the turbulence are correlated at the height y_1, i. e., $R_{uv} \equiv \overline{uv}(y_1) \neq 0$. Therefore the cross-correlation between the normal velocity $v(y)$ at y ($< y_1$) and the horizontal velocity at y_1, $u(y_1)$, should steadily decrease near the wall as $y/y_1 \to 0$. If the scaling argument of (1.5) is valid one should expect that, in the log layer, where $y << y_1$, the $u - v$ correlation normalized by $\overline{uv}$ at y_1 has the form:

$$\hat{R}_{uv} \equiv \frac{R_{uv}(y_1, y)}{R_{uv}(y_1, y_1)} \approx f_{12}\left(\frac{y}{y_1}\right) \tag{1.6}$$

This is the second hypothesis to be tested.

In general, correlations involving the horizontal component are affected by the inactive or irrotational motions. Consequently, the presence of the wall exerts a weaker influence on these correlations.

The computations of the structure of homogeneous turbulence in a uniform, mean velocity gradient have shown that the main effect of the mean shear is to reduce the scale of the turbulence in the spanwise or z direction (Townsend 1976). Unlike many statistical effects this one is so strong that this channeling of turbulent eddies can be seen in the instantaneous pattern of streamlines, as derived from flow-visualization studies and direct simulations (e. g., Lee, Kim and Moin 1987).

The picture of these eddies in shear flow, indicated in figure 3, looks very different from the conventional circular vortex-like eddy of homogeneous isotropic turbulence; such as illustrated in figure 1. One suggestion is to represent the eddies as vertically-elongated structures with a defined spanwise scale a_3.

This suggests that the structure of the large eddy is approximately described by

$$v \approx f_v\left(\frac{y_2}{y_1}\right) g\left(\frac{r_3}{a_3}\right).v_L \tag{1.7}$$
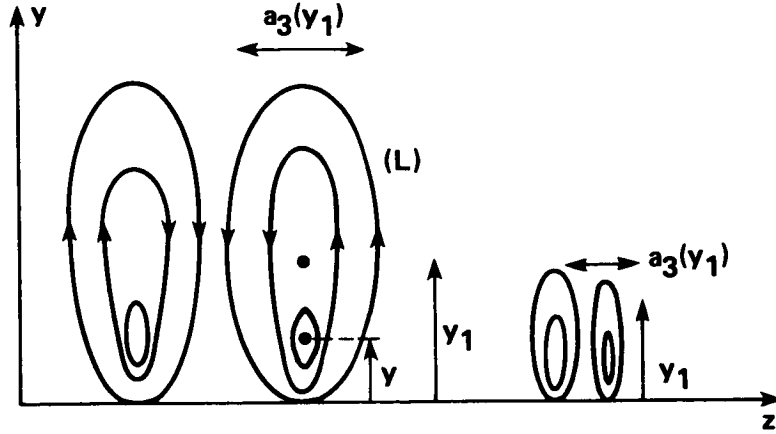
FIGURE 3. Schematic of spanwise structure of eddies in the boundary layer, showing how the spanwise scale (a_3) of the large eddy (L) at y_1 determines the spanwise scale closer to the wall (at y). Also, if y_1 is smaller, a_3 is also smaller.

(as opposed to the isotropic eddy structure where $v \approx f[(r_2^2 + r_3^2)/L^2]v_L$). Here $r_2 \equiv (y_1 - y)$ and r_3 are the distances from the center of the eddy. Thus at a height y, and spanwise displacement z,

$$v(y, r_3) = v_s + v_L f_v\left(\frac{y}{y_1}\right) g\left(\frac{r_3}{a_3}\right)$$

and therefore

$$\overline{v(y, r_3)v(y_1, 0)} \approx v_L^2 f_v\left(\frac{y}{y_1}\right) g\left(\frac{r_3}{a_3}\right).$$

This model also implies that

$$\hat{R}_{vv}(y, r_3) \equiv \frac{\hat{R}_{vv}(y, r_3)}{\hat{R}_{vv}(y, 0)} = \frac{\overline{v(y, r_3)v(y_1, 0)}}{\overline{v(y, 0)v(y_1, 0)}} \approx g\left(\frac{r_3}{a_3}\right) \qquad (1.8)$$

where the function g is independent of z. If the hypothesis (1.6) is valid we would also expect that

$$\hat{R}_{vu}(y, r_3) \equiv \frac{\hat{R}_{vu}(y, r_3)}{\hat{R}_{vu}(y, 0)} = \frac{\overline{v(y, r_3)u(y_1, 0)}}{\overline{v(y, 0)u(y_1, 0)}} \approx g\left(\frac{r_3}{a_3}\right)$$

Since the eddy structure (1.7) occurs only on strong shear flows, it is natural to suppose that a_3 depends on the *mean velocity gradient* dU/dy and the vertical turbulence intensity v' in the log layer. Near the wall the lateral structure is likely to be determined by instabilities within the wall layer. So we postulate that

$$a_3(y_1) \approx \alpha_s \frac{v'}{dU/dy(y_1)} + \alpha_w \frac{v'}{u_\tau}. \qquad (1.9)$$

This is the third hypothesis to be tested here.
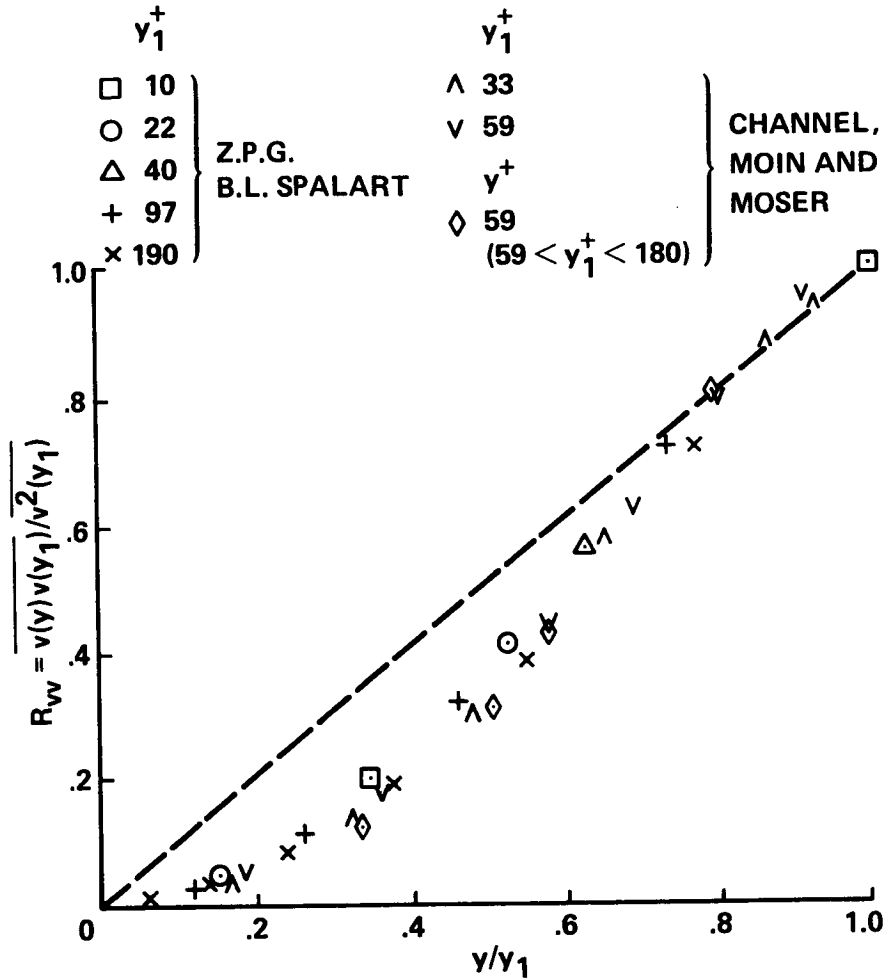
FIGURE 4.   Cross correlation of v at heights y and y_1, normalized by v^2 at y_1 computed from direct numerical simulations of the zero pressure gradient boundary layer (Spalart 1987), and the plane channel (Moin & Moser 1987). Also shown are the theoretical predictions of Hunt (1984) ($\hat{R}_{vv} \approx y/y_1$).

2. Preliminary results

In figure 4 we present a graph of $R_{vv}(y/y_1)$ combining the results of the computations of the zero pressure gradient (Z. P. G.) boundary layers (Spalart 1986) and of the channel flow (C.F.) (Moin & Moser 1987). The range of data is as follows: ZPG: $\delta u_\tau/\nu = 300$ (where δ is the boundary layer thickness) and

$$y^+ = 10,\ 22,\ 40,\ 97,\ 190$$

Channel Flow: $\delta u_\tau/\nu = 180$ (where δ is the channel half width) and

$$y_1 u_\tau/\nu = 33,\ 59,\ \dots\ 180$$

In figure 4 the results for the channel alone are plotted including the exceptionally small value of $y_1 = 5\nu/u_\tau$.

It appears that for these two wall bounded shear flows, the self similar plot of $\hat{R}_{vv}$ is a good description of the measurements. Comparing figures 2 and 4 indicates as good a 'collapse' as observed for shear free boundary layer. (But remember that figure 2 is a plot of experimental points in the atmosphere!). Note that the similarity hypothesis is more accurate for smaller values of y, as expected since the assumption that the small eddies at y and the large eddies as y_1 are uncorrelated, (i.e. $\overline{v_s v_L} \approx 0$) is more valid when y/y_1 is small.

It is particularly surprising that approximately the same curve describes the distribution of $\hat{R}_{vv}$ for points both within and well above the viscous sublayer. However very close to the surface within the sublayer we must expect that, since $v \propto y^2$ as $yu_\tau/\nu \to 0$, $R_{vv} \to (y/y_1)^2$ as $yu_\tau/\nu \to 0$.

However the computation of Kim, Moin or Moser (1987) have shown that some vertical eddying motion exists on a scale even smaller than $5\nu/u_\tau$ (because v is not exactly proportional to y^2). This is quite consistent with the fact that the two point correlation $\hat{R}_{vv}$ is greater than $(y/y_1)^2$ when $y_1 u_\tau/\nu = 5$.

These results show that there is a significant difference in the measured value of $\hat{R}_{vv}$ between these shear boundary layers (figures 4 and 5a) and the shear-free boundary layers in figure 2. They show that the effect of shear is to reduce the correlation length of the normal velocity in the normal direction. (But it is important to note that the smallest scale of v in a shear flow is in the spanwise or z-direction, Townsend (1976). So these curves of R_{vv} do *not* give a basis for estimating dissipation or the dissipation length scale.)

Figure 5b is added to show that if the conventional two point correlation is plotted against y/y_1, the points do not tend to zero as $y/y_1 \to 0$ and the curves do not have any general pattern.

In figure 5c we present the cross correlation of the Reynolds stress R_{uv} as defined by (1.6). These curves for different values of (y_1/δ) show that R_{uv} is not a universal function of (y/y_1) over the whole channel width. However, the three sets of curves for which y_1 is in the log layer, i.e., $30 \leq y+ \leq 100$ do exhibit a strong degree of similarity- (recall that the abscissa is being stretched by a factor of 3, and yet the curves are self similar).

It is interesting to note that the shape of the self similar curves of R_{uv} is markedly different to the curves for the normal velocity correlation, R_{vv}. The correlation is higher.

In figure 6, we present the cross correlation for the vertical velocity separated by a normal and spanwise spacing normalized by the correlation at the same height, but zero spanwise spacing i.e.,

$$\hat{R}_{vv}(y, r_3; y_1) = \frac{\hat{R}_{vv}(y, r_3, y_1)}{\hat{R}_{vv}(y, 0, y_1)} = \frac{\overline{v(y, r_3)v(y_1, 0)}}{\overline{v(y, 0)v(y_1, 0)}}$$

We also plotted the correlation of u and v defined as

$$\hat{R}_{vu}(y, r_3; y_1) = \hat{R}_{vu}(y, r_3; y_1)/\hat{R}_{vv}(y, 0, y_1)$$
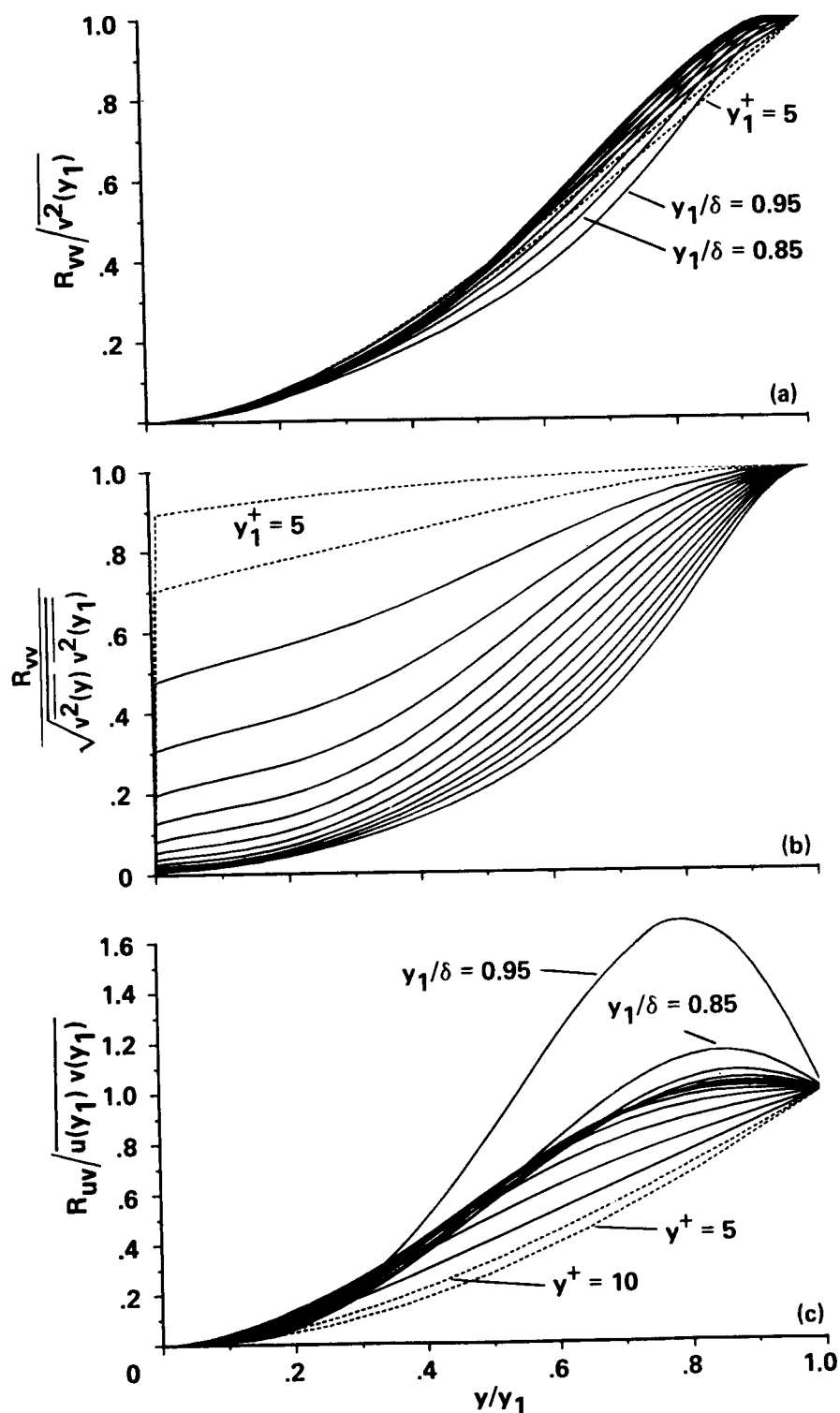
FIGURE 5.   Normalized cross correlations of velocities at y and y_1 from turbulent plane channel flow (Moin & Moser, 1987) for various values of y_1. *(a)* $\overline{v(y)v(y_1)}/\overline{v^2(y_1)}$, *(b)* $\overline{v(y),v(y_1)}/\sqrt{\overline{v^2(y)v^2(y_1)}}$, *(c)* $\overline{u(y)v(y_1)}/\overline{u(y_1)v(y_1)}$.
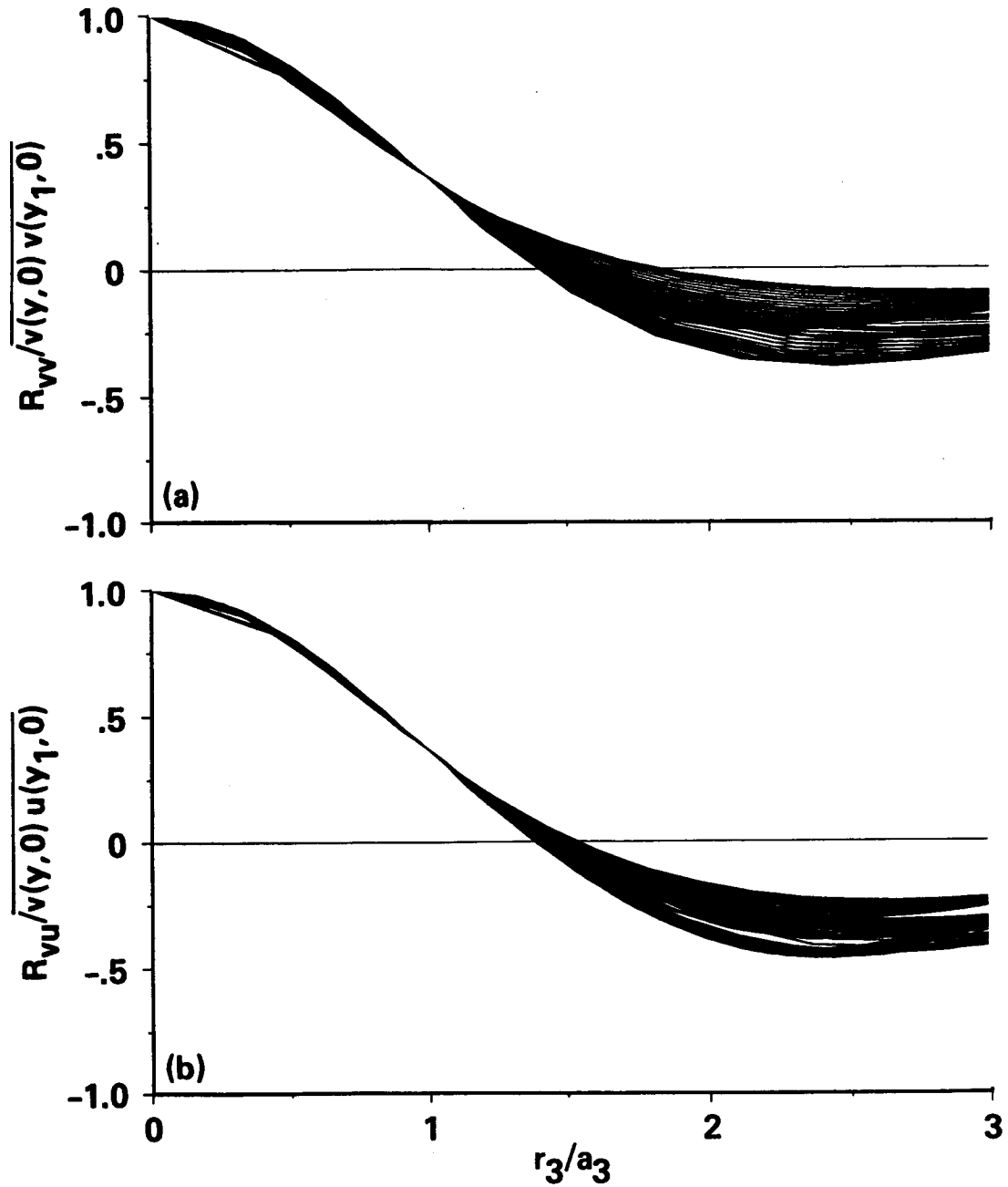
FIGURE 6. Normalized cross correlations of velocities at y and y_1 with separation in z (r_3) from turbulent plane channel flow (Moin & Moser, 1987) for various values of y_1. *(a)* $\overline{v(y,r_3),v(y_1,0)}/\overline{v(y,0)v(y_1,0)}$, *(b)* $\overline{v(y,r_3),u(y_1,0)}/\overline{v(y,0)u(y_1,0)}$. The value of a_3 is chosen for each curve to be the r_3 location at which the curve passes through $1/e$.
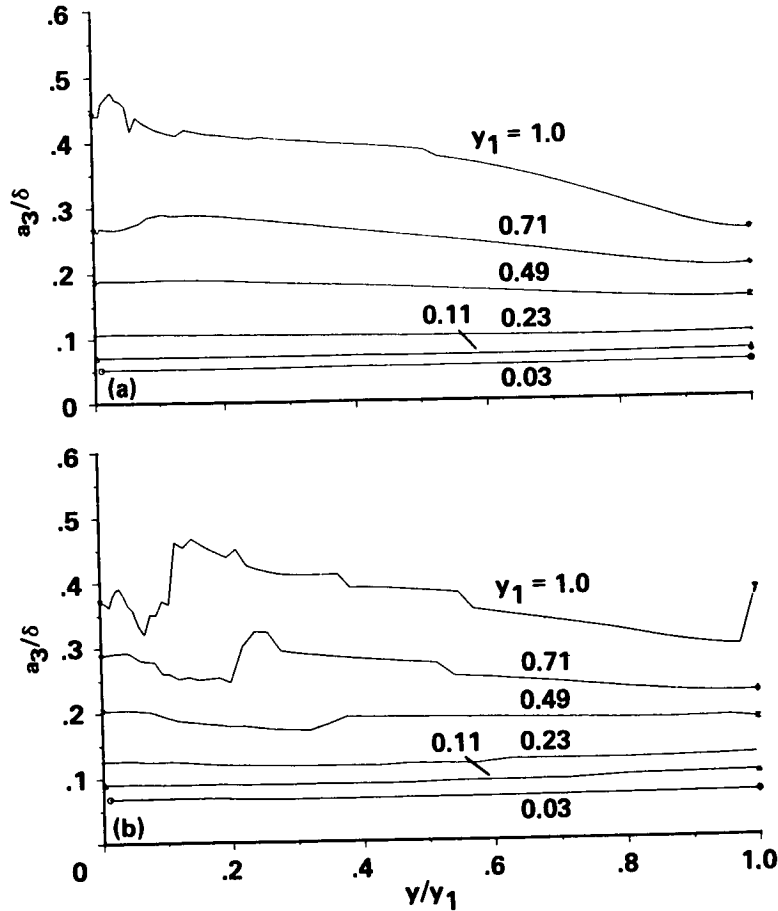
FIGURE 7.   Values of a_3 as a function of y/y_1 and y_1, *(a)* as used to scale R_{vv} (figure 6a), *(b))* as used to scale R_{vu} (figure 6b).

The curves are plotted as functions of r_3/a_3 for different y and y_1, where a_3 is defined as the value of r_3 where $\hat{R}_{vv} = 1/e = 0.36$ The results show firstly, the small variation of the form of the spanwise structure and the negligible variation of the spanwise scale of the eddies in these boundary layers. Using this particular correlation emphasizes this point quite nicely. This approximate invariance is found for values of $y_1/\delta \leq 0.8$. It is not true for y_1 at the centerline, $y_1/\delta \approx 1.0$.

Secondly, these results show how the scale a_3 increases with y_1. In Figure 7, we have plotted a_3^+ against y^+. It appears that this scale is of the order of 9 wall units near the wall and then begins to increase when $y_1^+ \geq 10$. This would be consistent with the ideas suggested in the introduction. A satisfactory curve fit could be (figure 8)

$$a_3^+ \approx (1.4\frac{\partial U^+}{\partial y^+} + 7)$$

$$\approx 0.3y^+ \quad \text{in the log layer.}$$
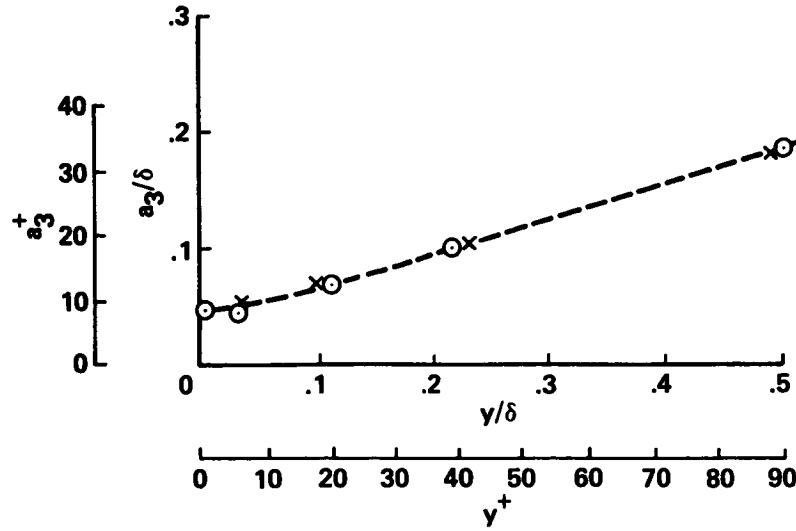
FIGURE 8.   Values of a_3 as used to scale R_{vv} (figures 6a and 7a), as a function of the reference height y_1. $\times$ – simulation results, o – the model $a_3 = 7 + (1.4\frac{du^+}{dy^+})^{-1}$.

This value of a_3^+ is of the same order but a little *greater* than the dissipation length scale L_ϵ (based on $\overline{v^2}$ in the log layer) where

$$L_\epsilon = \frac{\epsilon}{\overline{v^2}^{3/2}} \approx 0.18y$$

Other results have been computed for R_{uv}, R_{uu}. They also show equally strong channeling of the spanwise structure; though the value of a_3 for R_{uu} is about twice as great as for R_{vv}.

3. Implication and further work

The preliminary results show that even in the inhomogeneous turbulent boundary layer, the two-point correlation function may have self similar forms. The nature of these self similar functions can be inferred by using rapid-distortion theory. The results shows that the effects of shear and of blocking are equally important in the form of correlation functions for spacing normal to the wall. But for spanwise spacing, we have found that the eddy structure is quite different in these shear flows; this aspect of eddy structure is largely controlled by the shear and perhaps by small scale structures very close to the wall. So any theory for the turbulent structure must take both these effects into account.

The results suggest further study

a. Comparison with laboratory and atmospheric measurement.

b. The effects of curvature and pressure gradient should be investigated. We would still expect to see these self similar two point correlations.

c. Further theoretical calculations should be done using RDT Theory for uniform shear near a wall.

d. The two point correlation functions are likely to be self similar for other components and in other direction (eg. for the spanwise, z, spacing).

REFERENCES

HUNT J. C. R. 1984 *J. Fluid Mech.* **138**, 161-184.

HUNT J. C. R., KAIMAL J. C. & GAYNOR J.E. 1987 *Quart J. Roy Met. Jour.* (accepted).

KIM, J., MOIN, P. & MOSER, R. D. 1987 Turbulence statistics in fully developed channel flow at low Reynolds number. *J. Fluid Mech.* **177**, 133-166.

LEE, M., KIM, J. & MOIN, P. 1987 6th Turbulent Shear Flows Symposium, Sept 7-9 1987, Toulouse, France.

MOIN, P. & MOSER, R. D. 1987 Characteristic eddy decomposition of turbulence in a channel. In preparation.

SPALART, P.R. 1986 Direct simulation of a turbulent boundary layer up to $R_\theta =$ 1410. **NASA TM-89407.** (J. Fluid Mech. in press)

TOWNSEND A.A. 1976 *Structure of Turbulent Shear Flows.* Cambridge Univ. Press.

Ejection mechanisms in the sublayer of a turbulent channel

By J. JIMENEZ[1], P. MOIN[2,3], R. D. MOSER[3] AND L. R. KEEFE[4]

It has long been recognized that the structure of wall bounded turbulence in boundary layers and channels is three-dimensional (Kline et al., 1967). A generally accepted picture is that low velocity streaks are ejected from the wall layer and are responsible for a large fraction of turbulence production. (see e.g., Cantwell, 1981). The mechanism that triggers the initial ejection is, however, not understood, and there are indications that the processes controlling the behavior of the viscous sublayer, where these ejections originate, are different from those active in the outer parts of the boundary layer.

Recently, Jimenez (1987), while studying numerically the behavior of a *two-dimensional* channel flow, found a simple mechanism giving rise to spontaneous ejections of vorticity, and of the associated low momentum fluid, away from the wall and into the core flow. In that 2-D case, once the vorticity is ejected, it is stretched into long thin shear layers which periodically release part of their vorticity into the laminar core of the channel, where it is eventually dissipated by viscosity (figure 1). It should be stressed that the only vorticity component present in a 2-D flow is ω_z, and that this process is essentially different from any of the usually accepted mechanisms involving induction by hairpin vortices, which include important contributions from ω_x, and ω_y. As such, it was not expected that this complete picture would survive in fully developed three-dimensional channel flows, but one of our goals during this workshop was to check whether some aspect of it could still be useful in describing fully turbulent situations.

A particularly appealing possibility was that the same mechanism could contribute to the origin of the ejections in natural channels, especially since it was shown in Jimenez (1987) that the site of the basic ejection instability for the 2-D flow is the viscous sublayer, where it can reasonably be expected to be approximately independent of the three-dimensional phenomena occurring in the outer part of natural boundary layers.

The general behavior of the 2-D solution is that of a periodic train of nonlinear Tollmien-Schlichting (T-S) waves, of the kind described in (Herbert, 1976). This wave train is characterized by a succession of strong vorticity peaks at the wall, separated by regions of weaker, or even negative vorticity. This alternation of strong and weak vorticity generates local updrafts, corresponding to stagnation points in

1 Universidad Politecnica, Madrid, and UAM-IBM Scientific Center, Spain.
2 Stanford University
3 NASA Ames
4 Center for Turbulence Research
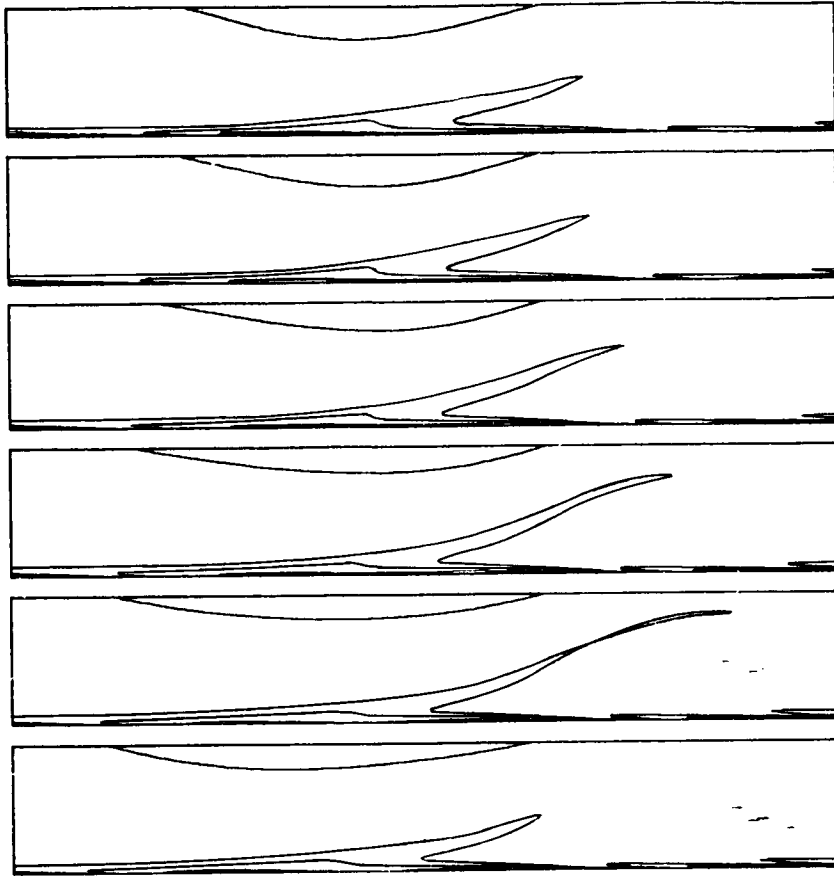
FIGURE 1.   Two dimensional ejection in the boundary layer of a 2-D channel. The periodic ejections from the train of nonlinear Tollmien- Schlichting waves are equivalent to a limit cycle of the system (from Jimenez, 1987). Flow runs from left to right, and time, from top to bottom. Axes move with primary T-S wave. Each frames spans from the lower wall to the channel centerline.

a frame of reference moving with the wave train, which tend to draw vorticity away from the wall, producing the protruding shear layers (see figure 2). The stability of this situation depends on the Reynolds number. Above $Re = Uh/\nu = 5500$, and for a wave number $\alpha = 1.0$, the uniform wave train becomes unstable and bifurcates into a limit cycle, giving rise to the periodic ejections described above. At a higher $Re = 9100$, it bifurcates again into more complicated dynamical behavior (a torus). Here, U refers to the center-line velocity of a parabolic profile with the same mass flux, and h, to the channel half width. Throughout this paper we will use this non-dimensionalization.

Our first step was to check the accuracy of the original 2-D calculations. To do that, some initial conditions from Jimenez (1987) were used with a 2-D version of the channel flow described in (Kim, Moin & Moser, 1987). Although both numerical codes are spectral, they are essentially independent, and differ in many important
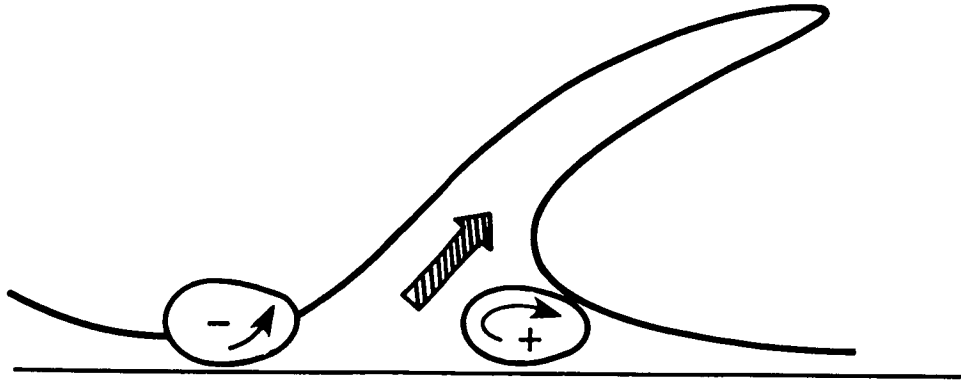
FIGURE 2. The basic mechanism for the two dimensional ejection of vorticity is the creation of an updraft between a pair of spanwise vortices of opposite sign (or unequal magnitude) in the sublayer.

details, including different dependent variables used in the integration. Nevertheless, the results of both codes did check in detail. The comparisons included a limit cycle ($Re = 7000$), and a torus ($Re = 9200$). In both cases, not only the qualitative nature of the results from both codes were similar, but the quantitative values of the wall stress, and of its oscillations as a result of the instability, agreed to within plotting accuracy.

The next step was to investigate the degree of similarity between nonlinear T-S waves and thin layers of z-vorticity present in natural channel flows. For that, we used a short time series of flow fields extracted from the numerical simulation described in (Kim, Moin & Moser, 1987). This is a fully resolved numerical simulation, $Re = 4200$, of a channel which is defined as $4\pi h$ periodic in the x direction, and as $4\pi h/3$ periodic in the z direction. The Reynolds number is based on the centerline velocity of a parabolic profile with the same mass flux. It was shown in that reference that its statistical properties are in good agreement with those of experimental flows, and we will consider it here as a "natural" turbulent channel.

The first surprising observation is that thin layers of z-vorticity are indeed a very common feature of this channel flow, and that they protrude from the wall in a manner which is strongly reminiscent of the features observed in the 2-D calculations (figure 3). To our knowledge, this is a new observation, although Kim (1987) had described the formation of thin layers of high vorticity magnitude as part of the evolution of an isolated "hairpin" vortex in the neighborhood of a channel wall.

There are some important differences between the structures observed in the channel and those in the 2-D calculations. To begin with, the "wavelength" seems to be shorter, with an average longitudinal separation between consecutive features of the order of 1 to $3h$. (200-600 wall units), while the 2-D nonlinear T-S waves can only exist, as equilibrium solutions, for wavelengths in a range between $4h$ and $6.5h$. Also, the channel layers penetrate less into the core of the channel, appearing to level off at a distance of $0.3h$. (35 wall units) away from the wall, while the 2-D
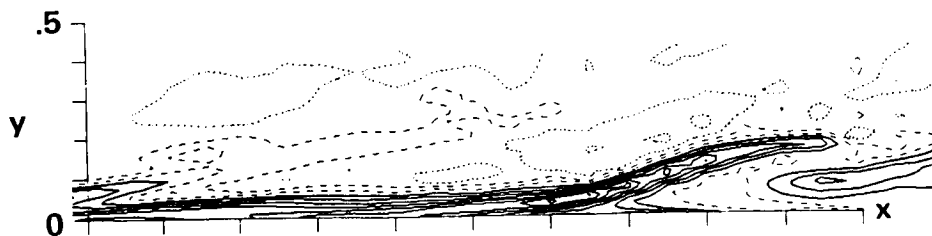
FIGURE 3. Lateral view of a train of projecting shear layers of z-vorticity in a natural, fully developed three dimensional channel flow. Note the similarity to the structures in the 2-D calculations. Dotted lines correspond to $\omega_z = -1, 0$; dashed: $\omega_z = 1, 2$; solid: $\omega_z = 3$ to 17. Average vorticity at the wall is $\omega_z = 7.67$.
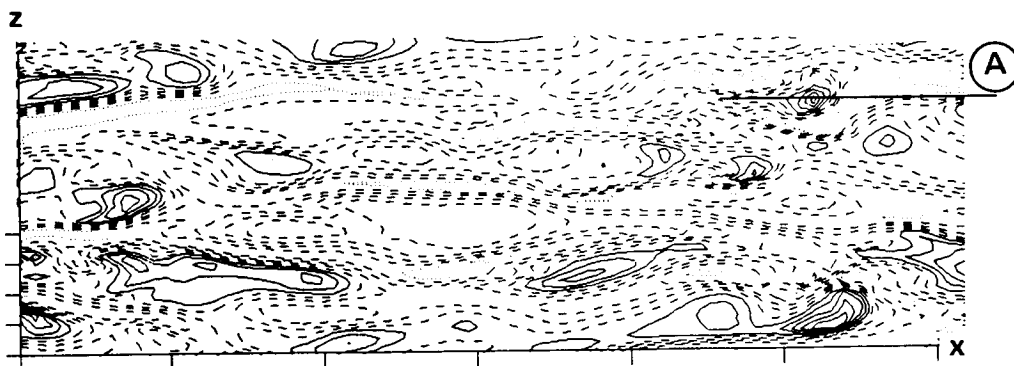
FIGURE 4. Distribution of spots of high spanwise vorticity in the viscous sublayer $(y^+ = 6)$. These spots are the roots of the structures in figure 3. The line marked "A" corresponds to the position of the cross section in figure 3.

solutions extend all the way to the channel center line. On the other hand, there is some evidence, in the natural flow, of weaker layers that do extend deeper into the core.

The main difference, however, is that the shear layers in the natural channel are three dimensional structures, with a spanwise extent of no more than $0.2h$, or about 35 wall units, at $y^+ = 6$ (and about twice as much at the wall). They appear to be rooted at the wall in elliptical "hot" spots in which the spanwise vorticity is at least 25% higher than its average wall value, and to extend into the channel with a characteristic S-shape , and an average ejection angle of a few degrees. These spots can be used to detect and count the protruding layers and to follow their motion (figure 4). They appear to move with a convection velocity of 60% of the center line velocity, or $0.47U$, where U refers to the centerline velocity of the laminar profile at the same mass flux. This last number is in surprisingly good agreement with the convection velocity of the 2-D nonlinear waves. Although the significance of this
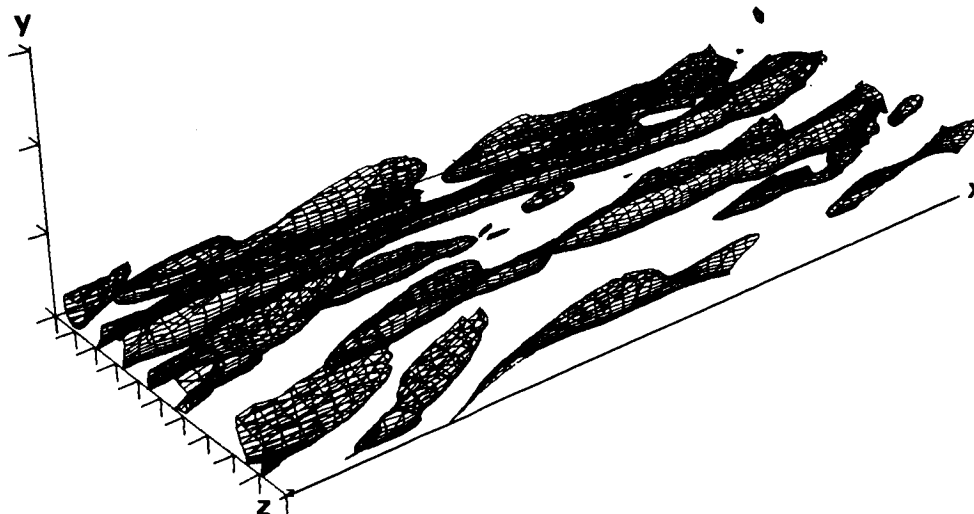
FIGURE 5. Three dimensional representation of z-vorticity structures extending away from the viscous sublayer. The vorticity iso-surface represented is approximately 25% higher than the average wall vorticity, and the first tick mark in the y-axis corresponds to $y^+ = 17$.

agreement is not clear, this convection velocity is quite high, showing that the spots are linked to some structure extending outside the viscous sublayer.

In fact, when these hot spots are followed into the flow in the form of three dimensional iso-surfaces of z-vorticity, they form a "forest" of leaning curving "necks" that covers much of the wall (figure 5). It is possible to follow the evolution of these structures as they move in time, and some of them were followed for fairly long periods, long enough for the structure to move several channel half widths. In the course of their life they reproduce, giving origin to new structures, and we were able to observe several of these reproduction processes. An example is given in figure 6, where time runs from top to bottom. In the first frame of this time sequence a structure has began to stretch, producing a small vorticity blob at its top end. In the next frame the blob has grown considerably, and a small patch of strong vorticity appears at the wall. Finally the vortex at the walls grows out into the boundary layer and fuses with the tip of the stretching layer. At this moment, the tip separates from its parent structure, forming what appears to be the "embryo" of a new spot. The last frame shows both spots as essentially independent units.

A closer examination of the vorticity field shows that there is a region of concentrated z-vorticity of opposite sign (negative), underneath the top part of the structure. These regions of reverse vorticity are visible in the lateral view of this same structure in figure 3. The whole reproduction process is strikingly reminiscent of the instability process for 2-D linear Tollmien-Schlichting waves (see Betchov & Criminale, 1967). Basically, vorticity is created at the wall and diffuses into the main flow through viscosity. In a frame of reference moving with the structure, the fluid below the critical layer is moving backwards, while that on top moves forward.
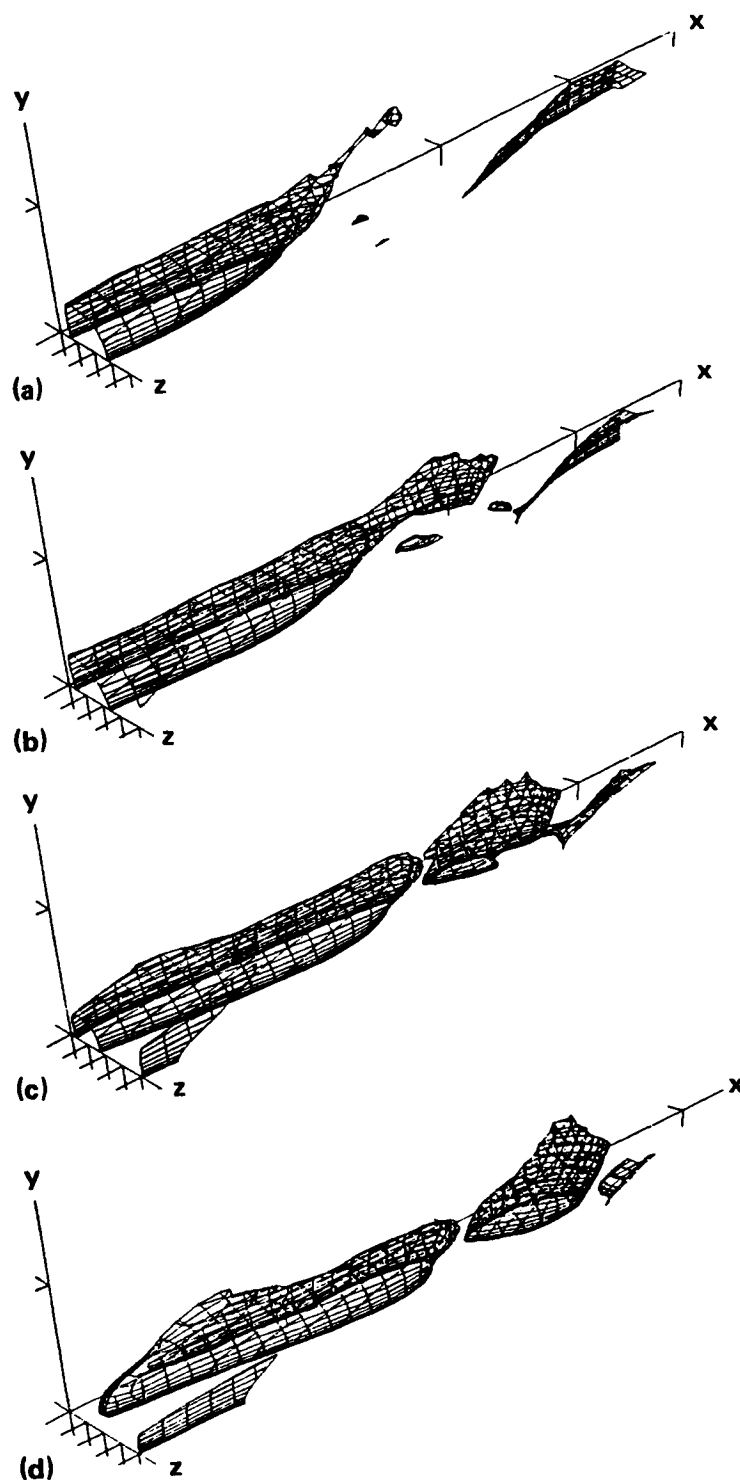
FIGURE 6.   Splitting process of a structure to create a new one. See text for explanation. Time difference between frames is approximately 6 wall units (ν/u_τ^2).

As a result, as the vorticity diffuses away from the wall, it takes a backwards pointing "V" shape that is visible in figure 3. Eventually, the positive vorticity in the main structure (above the critical layer) induces a negative vortex near the wall, to accommodate the no slip condition. This vorticity of opposite sign is convected backwards by the flow, as it diffuses outward, and forms a negative vortex layer underneath the original positive one. This new layer eventually overcomes the effect on the wall of the original structure, and begins to induce a new positive vortex. The moment that a strong vortex pair in formed in this fashion, underneath the original structure, an updraft is created that carries part of the positive and negative vorticity into the upper part of the structure. The negative vorticity in the rear cuts the connection between the head and the base of old structure (through viscous annihilation), while the positive vorticity connects with the head of the old structure to form a new one (see figure 7). Note that the mechanism invoked here, for the production of the updraft, is the same one proposed in figure 2 for the ejection of shear layers into the flow.

As noted previously, this is the mechanism responsible for the linear 2-D T-S waves, and it seems to explain approximately the behavior of z-vorticity in the splitting mechanism in figure 6. This suggests that the mechanism for the generation of ejections in the sublayer may be essentially two dimensional, although there are undoubtedly some three dimensional effects present, as shown by the fact that the structures do not spread laterally into spanwise bands. In fact a map of y-vorticity in the sublayer shows long active streaks, delimiting quiescent "corridors" between them (figure 8). The hot spots, and their associated shear layers seem to ride those corridors, as a necklace of beads. x-vorticity is also present in the sublayer, but it seems to be weaker, and harder to correlate with the structures studied here. Also, there is little doubt that, as the shear layers are ejected further into the main stream, longitudinal vorticity and three dimensional effects are important in their evolution.

The general picture of the sublayer suggested by this simplified model is a collection of patches of the high vorticity in the wall layer, which are lifted into little "ramps" corresponding to the shear layers described in this paper. Since the vortex lines cannot end in the middle of the flow, these ramps are linked to the wall by "sidewalls" which correspond to the regions of high y-vorticity observed in figure 8. It is easy to see that, if the ramps are constrained to be in between the streaks, the picture becomes something like the one in figure 9, and the induced longitudinal velocity fluctuations in the sublayer should consist of high velocity narrow streaks, bounding wider bands of lower velocity. This is precisely the pattern observed in experiments.

The remaining question is whether the three dimensional structure representing one of the protruding ramps can be studied in isolation. Numerical simulation provides a unique opportunity to attempt this, since the behavior of structures in natural channels is complicated by the interactions among the large number of them present in the flow, and since it is obviously difficult to isolate a single structure in a physical experiment. The numerical equivalent of isolating a single structure is
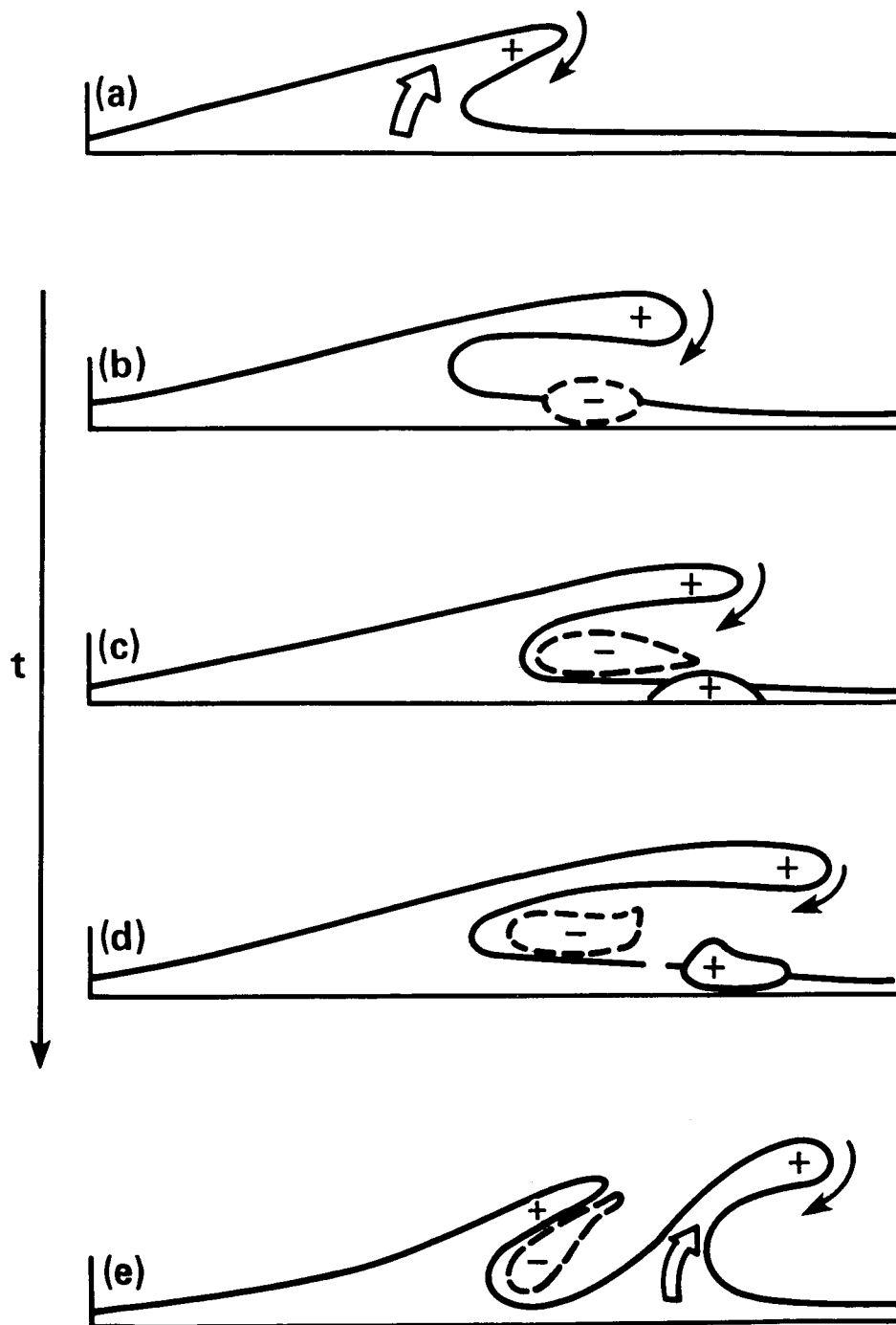
FIGURE 7.   Tentative mechanism for the splitting process of a structure. This 2-D mechanism corresponds roughly to the instability mechanism for Tollmien-Schlichting waves.
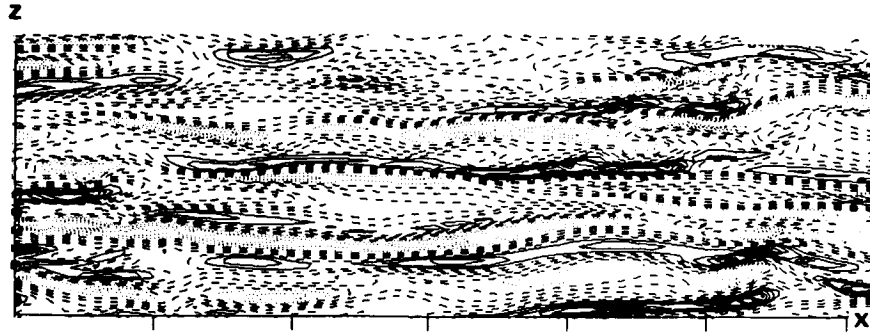
FIGURE 8. Streamwise streak pattern of y-vorticity in the sublayer. Conditions are identical to those of figure 4, and careful comparison with that figure shows that the vorticity spots reside in the relatively quiescent corridors between the high velocity streaks.
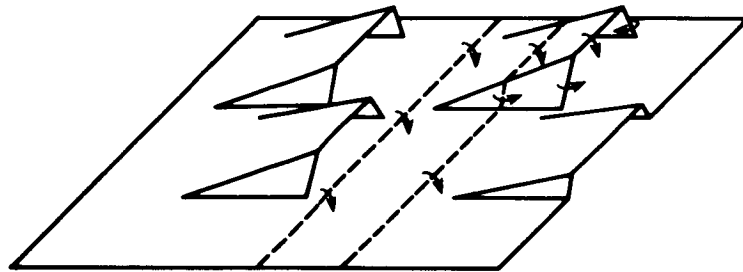
FIGURE 9. A model for the sublayer structures. The raised structures are lifted portions of wall vorticity, and are "supported" by vorticity sidewalls that are the origin of the y-vorticity streaks.

to use a computational box whose x-z extent is small enough to contain only one, or at most a few, structures. This was attempted in the course of the workshop.

Running at $Re = 7000$, we first tried computing a channel on a periodic box of $2\pi h \times 2\pi h$ (about 1800×1800 wall units). The initial conditions were extracted from the 2-D limit cycle solution, with the addition of a small 3-D perturbation. As expected, the flow became quickly three-dimensional, and the wall shear stress grew from the low value corresponding to the 2-D (Herbert) solution ($\omega_z = 3$), to that for a fully developed turbulent channel ($\omega_z = 12$). This solution was not followed for a long time, since it was not any easier to understand than any of the previously available flow fields. The remaining numerical experiments were carried out using computational boxes whose spanwise extent was $\pi h/8$, corresponding to approximately 113 wall units. Since the computational domain is periodic in both x and z, this corresponds to a periodic array of structures with a spanwise spacing close to the one found in natural flows. We tried different streamwise

FIGURE 10. z-vorticity field of a 3-D narrow channel, as described in the text. Note that the upper wall, at the top of the figure, is essentially two-dimensional, and smooth, while the lower one remains three-dimensional and "turbulent".

periods, none of which was completely successful. The most desirable boxes were the very short ones, that could be expected to contain a single structure (actually a doubly periodic array of them). However, attempts to introduce perturbations in boxes with streamwise periods of $\pi h/8$, and $2\pi h/5$ quickly decayed to laminar solutions. The most interesting box, up to now, has been one with an x-extent of $2\pi h$, and a spanwise one of $\pi h/8$. This flow cannot decay to laminar, since it is linearly unstable to two dimensional perturbations of this wavelength. Apparently, however, that domain is neither sufficiently stable to decay to a 2-D solution, nor sufficiently unstable to maintain a fully 3-D turbulent one. The result is a non-symmetric channel in which one wall (the top one in our case) sustains a roughly 2-D flow, while the other one has a turbulent, 3-D boundary layer, presumably forced by the 2-D solution at the top wall (see figure 10). This boundary layer contains ejection structures similar to those in 3-D natural layers, and which appear to be fairly typical, but the average shear stress at the wall falls in between the values characteristic of 2-D and 3-D solutions. At each particular moment, the computational box contains 3 or 4 sublayer structures, which are still too many for a simple model of the layer, but constitute, at this moment, the smallest system available for its study. Further experiments with boxes of different sizes are still in progress.

Summary

In summary, we present here a possible model for the inception of vorticity ejections in the viscous sublayer of a turbulent rectangular channel. We have shown that this part of the flow is dominated by protruding strong shear layers of z-vorticity, and have proposed a mechanism for their maintenance and reproduction which is essentially equivalent to that responsible for the instability of 2-D Tollmien-Schlichting waves. The efforts to isolate computationally a single structure for its study have failed up to now, since it appears that single structures decay in the absence of external forcing, but a convenient computational model has been identified in the form of a long and narrow periodic computational box containing at each

moment only a few structures. Further work in the identification of better reduced systems is in progress.

REFERENCES

BETCHOV, R. & CRIMINALE, W. 1967 *Stability of parallel flows.* Academic Press, Ch. II.

CANTWELL, B.J. 1981 Organised motion in turbulent flow . *Ann. Rev. Fluid Mech.* **13**, 457-515.

HERBERT, T. 1976 Periodic secondary motions in a plane channel . *Proc. 5th Int. Conf. Num. Methods in Fluid Dyn.* (A.I. Van de Vooren & P.J. Zandbergen, eds.). Springer, pp.235-240.

JIMENEZ, J. 1987 Bifurcations and bursting in two-dimensional Poiseuille flow. *Phys. Fluids,* in press.

KIM, J. 1987 Evolution of a vortical structure associated with the bursting event in channel flow. *Turb. Shear Flow 6,* Springer, pp. 221-233.

KIM, J., MOIN, P. & MOSER, R. 1987 Turbulence statistics in fully developed channel flow at low Reynolds number. *J.Fluid Mech.* **177**, 133-166.

KLINE, S.J., REYNOLDS, W.C., SCHRAUB, F.A. & RUNSTADLER, P.W. 1967 The structure of turbulent boundary layers. *J.Fluid Mech.* **30**, 741-773.

Overview of the K-space Group Projects

The projects of the K-space group consisted of six independent lines of inquiry with a common theme of the interaction among scales of motion in turbulence. The studies were almost entirely limited to homogeneous turbulence. In the following paragraphs I will give a brief overview of the six projects.

The invited participants were:
   Jean-Pierre Bertoglio (Ecole Centrale de Lyon)
   Julian Hunt (University of Cambridge)
   Paolo Orlandi (University of Rome)
   Roland Schiestel (Institut de Mecanique Statistique de la Turbulence)
   Akira Yoshizawa (University of Tokyo)
The local participants were:
   Jeffrey Buell (NASA Ames)
   Gary Coleman (Stanford University)
   Joel Ferziger (Stanford University)
   Robert Rogallo (NASA Ames)
   Alan Wray (NASA Ames)

Bertoglio wishes to test the accuracy of the assumptions within the EDQNM closure at a deeper level than has been previously done. An important step in the closure is the estimation of a Lagrangian time scale which is assumed to be a functional of $E(k)$. Bertoglio judges several candidate functionals by the degree to which they collapse the two-time velocity auto-correlations in direct simulations of isotropic turbulence. This approach appears very promising, and good collapse has been achieved at the higher wave numbers. This work is the continuation of a joint effort by Bertoglio, co-workers in France, and Squires and Ferziger at Stanford.

The EDQNM theory is purely statistical in nature, whereas many important turbulence problems are dominated by the presence of persistent coherent structures. Bertoglio's second goal is to determine how well EDQNM copes with such structures. An experimental program has been started in France using propellers to inject known coherent structures into a turbulent flow, and to conduct a parallel numerical simulation. Comparisons between experiment, simulation, and theory for this flow should illuminate any difficulties that the statistical theory has with imbedded coherency. During the workshop Bertoglio attempted to define initial conditions for such a simulation. The energy in the simulation peaked at the blade-passing frequency of the propellers while that in the experiment peaked at their rotation frequency. It should be a simple matter to solve that mystery, but there was simply not enough time during the workshop to do so.

Orlandi's project concerns the use of EDQNM as a subgrid (or supergrid) model for a large-eddy simulation. At a minimum, such models must accurately account for the energy transfer between the computationaly resolved and unresolved scales.

In EDQNM, the net transfer into wave number k is calculated as the integral over interacting triads (k,p,q) of a functional of E(k), E(p), and E(q). Orlandi has demonstrated that EDQNM accurately produces the transfer measured in a direct simulation of isotropic turbulence both when the full set of interactions is considered, and also when a subset (truncated spectrum) of interactions is considered. Then, if the spectrum of the unresolved scales can be estimated, EDQNM can account for their contribution to the energy transfer. In the simulation however, the effect of the unresolved scales must appear as additional terms in the *momentum* equations. The subgrid term is usually modeled by a gradient diffusion form with an eddy viscosity determined from the subgrid transfer (see the works of Kraichnan, Chollet, and Lesieur) . The supergrid term is presumably some sort of forcing but a gradient diffusion form, with negative eddy viscosity, does not seem physically correct. Another possibility is the application of a mean strain that is uniform in space but random in time. The art of driving simulations at the large scales, as was done by Hunt et al above, is currently not well understood (see the works of Siggia, Kerr, Pope, etc.). Orlandi also attempted to extend the EDQNM closure to homogeneous shear, but encountered numerical accuracy problems in the calculation of the five-dimensional integrals required.

While the EDQNM model appears to be reasonably accurate and tractable in isotropic turbulence, in anisotropic flows it is far less tractable, requires additional assumptions, and is much more expensive to compute. Because of this, the theory has not received much attention for anisotropic flows. These are however very important in the context of subgrid models for LES calculations because as the grid resolution increases, the subgrid contribution approaches homogeneity much more rapidly than it approaches isotropy. Coleman and Ferziger consider the possibility of a Galerkin approach to simplify the EDQNM calculation. The angular distribution of velocity correlations over spherical shells (which are, in the proper variables, uniform in isotropic flow) would be represented by the weighted sum of a small number of smooth basis functions. Coleman and Ferziger attempted to estimate the number of basis functions required by inspecting the angular distribution of the Reynolds stress spectrum tensor in a direct simulation of homogeneous sheared turbulence. The distributions were quite smooth and the authors speculated that they could be represented by a sum of two or three functions. There appear to be several important issues that were not covered in a general way: the choice of the coordinate system and the choice of the dependent variables. In any expansion technique the choice of variables, both dependent and independent, is crucial. In this case some clues might be extracted from rapid-distortion theory, from consideration of the principal axes of the stress and mean strain rate tensors, and from the manner in which the mean flow gradient enters the EDQNM equations.

The project of Hunt, Buell, and Wray concerns the relation between space and time spectra (or correlations), and their dependence on the reference frame (Eulerian or Lagrangian). In particular, they wanted to determine how the advection of small-weak scales by large-strong ones influences the Eulerian time spectra at high frequency and wave number. The results support the assertion of Tennekes that

such advection dominates the frequency spectrum at high frequency, but indicates that Hunt's earlier proposal relating the time-space spectrum to the space spectrum was over simplified. During the project Hunt reworked the analysis using a more realistic p.d.f. for the advecting velocity and derived a simple relation which agrees well with the simulation. Some anomalies were observed in the computed data; these appear to be a consequence of the small statistical sample of forced modes, the small range of spatial scales that could be retained, and the low Reynolds number that was required for adequate numerical resolution.

In Schiestel's model, the equation for the Reynolds stress spectrum tensor is integrated, in wave number space, over spherical shells rather than over the entire space as done in classical one-point Reynolds stress formulations. As a result, some scale information is retained. Within each shell, one must model the same quantities as in classical one-point closures (pressure-strain, dissipation, etc.) and in addition, model transfers between shells. These transfers are globally conservative and do not appear in the one-point approaches. Schiestel's goal during the summer program was to compare the models for these terms with data from direct simulations. He hoped to determine the accuracy of the models he is currently using, and to get some clues to aid in their improvement. As one would expect, some of the terms were modeled rather well while others were not, and, unfortunately, there was not enough time to consider improvements. The statistics taken from the simulations were rather noisy at the larger scales because of the small sample and sometimes biased at the small scales due to mesh anisotropy. But they are simply not available elsewhere, and appear to be precisely what Schiestel needs.

Over the past several years, Yoshizawa has worked out a formal two-scale expansion of the Navier-Stokes equations in which the interaction between the scales is weak. The scales are disparate in both space and time, and are separated by formally averaging over an intermediate scale at which Taylor series expansion of the large scales is assumed to be valid and averages of the small scales are assumed to be statistically converged. The interaction terms in general depend upon deterministic features of the large-scale field (its derivatives) and statistical features of the small-scale field (local correlations). The disparity of the spatial scales leads , at small scale, to homogeneous turbulence at lowest order, and the time scale disparity leads to its isotropy. The required statistics of the small scales are in turn modeled by the DIA formalism. At higher order the small scales become anisotropic. Within this framework (TSDIA) it is possible to find the form (formally, the asymptotic expansion) of terms that must be modeled in one-point closures, for example the diffusion of kinetic energy. A model is then postulated by replacing the gauge functions in the expansion with "model constants". It was Yoshizawa's hope to be able to test several of these models and to estimate the contribution of the higher-order terms, using simulation data to determine the constants. Unfortunately some model terms could not be computed because the required statistics had not been extracted from the database prior to the summer program and during the program no one was available to do so. In addition, the data that was available was not really adequate for the simultaneous determination of several constants. The sample was too small,

52

as was the Reynolds number. Yoshizawa was then forced to omit most of the new terms suggested by TSDIA. When this was done the models fit the data well (with one notable exception) with constants close to the values previously predicted. For example, the fact that rotation reduces the dissipation rate was correctly predicted. The exception was the case of turbulent diffusion in homogeneous shear of a passive scalar having a mean gradient in the stream direction. In this case the mean gradient itself changes with time but was in fact held fixed in the simulation used by Yoshizawa. A later simulation treated the case of changing mean gradient but it is not clear which case is appropriate for testing Yoshizawa's model.

Summary

All of the projects are, in my opinion, worthwhile and feasible, and will hopefully be pursued further. The progress made during the summer session was limited by the number of local participants available to interact directly with the computers. The group benefited greatly from discussions with Robert Kraichnan and Evgeny Novikov, and several projects were directly influenced by their suggestions. We at Ames benefited from each of these projects because in every case we were exposed to areas of research and ideas that we had not pursued in-house before.

Bob Rogallo

EDQNM closure: "A homogeneous simulation to support it", "A quasi-homogeneous simulation to disprove it"

By J.P. Bertoglio [1], K. Squires[2], and J.H. Ferziger[2]

It is known that two-point closures are useful tools for understanding and predicting turbulence. Among the various closures, the Eddy Damped Quasi-Normal Markovian (EDQNM) approach is one of the simplest and, at the same time, most useful. Nowadays, direct numerical simulations (DNS) can provide information that can be used to test the validity of two-point theories. It is the purpose of the present work to use DNS to validate, or improve upon, EDQNM.

In the first part of this work ("a homogeneous simulation to support it") we selected a case for which EDQNM is known to give satisfactory results: homogeneous isotropic turbulence. We then evaluated quantities which may be used to test the assumptions of two-point closure approximations: spectral Lagrangian time scales. Our goal is to make a careful and refined study to validate (and possibly improve) the EDQNM theory.

The aim of the second part of the work ("a quasi homogeneous simulation to disprove it") is, on the contrary, a test of EDQNM in a much more difficult situation. Our purpose is to build a reference case for which EDQNM is likely to give poor results. We present an attempt to generate a quasi-homogeneous turbulent field containing "organized" structures, by artificially injecting them in the initial conditions. The results of direct simulations using such initial conditions are expected to provide a challenge for EDQNM since this kind of field is simple enough to allow comparisons with two-point theories, but at the same time contains "coherent" structures which cannot be expected to be accurately accounted for by closures based on expansions about Gaussianity.

---

1. Lagrangian spectral times in isotropic turbulence

1.1 The Assumptions of EDQNM

In the EDQNM theory the growth of the third order moments is limited by the introduction of a damping term in the rate equation for the triple correlations. The damping coefficient $\mu(k,p,q)$ is essentially an inverse time scale for the decay of the triple correlation among the three wave-vectors of a triad. It is generally assumed that $\mu(k,p,q)$ is the sum of the inverse time scales for the individual wavenumbers:

$$\mu(k,p,q) + \nu(k^2 + p^2 + q^2) = \eta(k) + \eta(p) + \eta(q)$$

1 Ecole Centrale de Lyon
2 Stanford University

and $\eta(k)$ is specified phenomenologically.

For flows at Reynolds numbers sufficiently high to contain an inertial subrange, the damping coefficient must have the form (Orszag 1970)

$$\eta(k) = a\epsilon^{\frac{1}{2}} k^{\frac{2}{3}}$$

The form proposed by Pouquet et al(1975) for an arbitrary energy spectrum:

$$\eta(k) = \lambda [\int_0^k p^2 E(p)dp]^{\frac{1}{2}} + \nu k^2$$

is more commonly used. The value of constant λ is generally taken to be 0.355.

According to this expression the time scale at wavenumber k depends only on wavenumbers smaller than k (i.e. only the large eddies influence the damping). There is however no reason, on physical grounds, to assume that the effect of the smaller scales can be neglected. Indeed, in order to devise a two-point closure compatible with the RNG approach of Yakhot and Orszag, Kraichnan (1987) recently introduced a model in which it is assumed that only the small scales affect the damping. In fact, neither type of expression can be completely correct, and during his stay at the Center for Turbulence Research (CTR) 1987 summer program Kraichnan suggested the following possibility of building a time scale that depends on all scales:

$$\eta(k) = \lambda_a [\int_0^k p^2 E(p)dp]^{\frac{1}{2}} + (\nu + \nu_>(k))k^2$$

where $\nu_>(k)$ is given by :

$$\nu_>(k) = \lambda_b \int_k^\infty \frac{E(p)dp}{\eta(k) + \eta(p)}$$

where λ_a and λ_b are constants. It can be shown that these two new constants must satisfy the following relation:

$$\lambda_a = \lambda - 2(1 - \log 2)\frac{\lambda_b}{\lambda}$$

in order that the new form reduces to the old one in the case of an inertial range.

During the CTR Summer Program, we tested the new form for the damping by introducing it into the EDQNM computation code written by Orlandi. We found no significant differences from the results obtained using the classical form, as long as λ_a/λ remains larger than 0.5. We noticed a small effect on the skewness, (see figure 1); the other quantities remain unaffected.
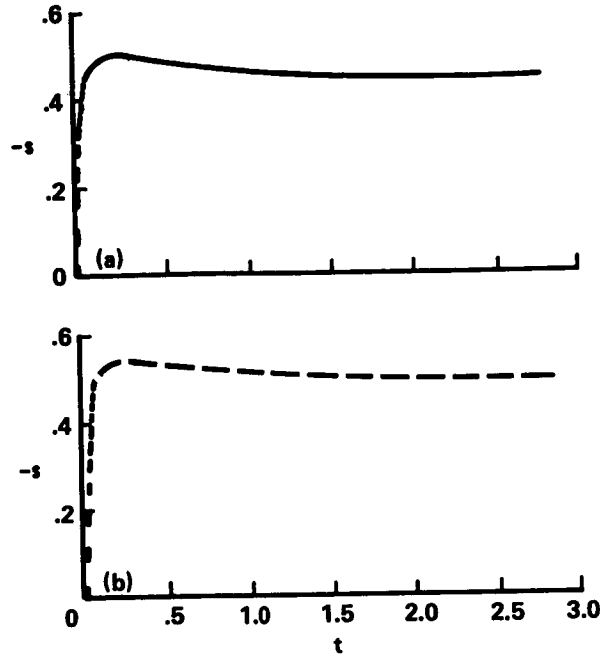
FIGURE 1. Evolution of the skewness in time. Comparison of EDQNM results obtained with different formulations for the damping. (a) damping given by Pouquet et al (1975); (b) damping suggested by Kraichnan (with $\lambda_a/\lambda = .5$).

1.2 Evaluation of $\eta(k)$ using direct numerical simulation.

In order to test the expression for $\eta(k)$ used in EDQNM against actual turbulence time scales, we have to deduce a spectral time scale from the simulation results. Comparisons between EDQNM and the Direct Interaction Approximation suggest evaluating the time scale using two-time correlations of the velocity field. The proper time scale must be invariant under an arbitrary Galilean transformation since the triple correlations must not be affected by convective effects. The time scale must therefore be a Lagrangian time scale derived from Lagrangian two-time correlations, as suggested by LHDIA. For practical reasons, we used the two-time correlations introduced by Kaneda (1981):

$$R_{ij}(\mathbf{x}, t'|t; \mathbf{x}', t'|t') = \langle u_i(\mathbf{x}, t'|t) u_j(\mathbf{x}', t'|t') \rangle$$

where $u_i(\mathbf{x}, t'|t)$ is the velocity at time t of the fluid particle whose trajectory passes through $\mathbf{x}$ at time t'. One could also use the two-time correlations defined by Kraichnan in the LHDIA or ALHDIA theories, or work with the response tensor, but the evaluation of Kaneda's correlations is simpler.

Spectral information is obtained by Fourier transforming with respect to the initial position of the particles.

To deduce the Lagrangian correlations from the results of a DNS, one has to

follow particle trajectories. This is done using Squires' code, which was developed for the study of particle dispersion.

1.3 Results

Two direct numerical simulations of homogeneous isotropic turbulence were used. Both used Rogallo's code. In the first case, a 64x64x64 grid was used. In the second, a 128x128x128 grid was introduced in order to increase the Reynolds number.

We present here only a limited number of results. For a more detailed study see the paper by Lee, Squires, Bertoglio, and Ferziger (1987). A study preliminary to this work was performed in Lyon using Large Eddy Simulation on a 16x16x16 grid.

In the DNS, it would have been desirable to place particles at each point of the computational grid, but doing so would have increased the cost of the computation prohibitively. The number of markers is therefore much smaller than the number of grid points. Marker placements were of two types. First, to ensure accurate large scale statistics, markers were placed on a 16x16x16 equally spaced grid. This provides a set of widely spaced particles. To obtain data on the small scales, a second set, consisting of 8x8 lines of 64 particles was used.

In figure 2a, the Lagrangian correlations obtained from the 128x128x128 run are given as functions of the dimensional separation time $t - t'$. As expected, the correlations corresponding to large wavenumbers decrease rapidly.

The correlations can also be plotted as functions of the time normalized by the candidate time scale; an accurate time scale should collapse the results to a single curve. figure 2b shows that, when the classical time scale is used, the collapse is good at high wavenumbers but not as good at low wavenumbers. When Kraichnan's expression is used (with $\lambda_a = \lambda/2$), the collapse is slightly improved at low wavenumbers, and remains acceptable at high wavenumbers (figure 2c).

1.4 Problems and future orientations

The major problem encountered is the lack of sufficient sample at high wavenumbers. The number of particles used (8x8x64) was probably not large enough to allow conclusive results concerning the highest wavenumbers in the simulation.

In the comparison between Lagrangian and Eulerian correlations, another problem appears. As expected, for short times and at high k, the Eulerian correlation decreases faster than the Lagrangian one; however, for long times, the trend appears to be reversed. In fact , for large values of the separation time, the significance of Fourier transforming with respect to the initial positions of the markers must be questioned. One could try to use another definition for the spectral time scale in this case. However, we believe that information deduced from the small time behavior is sufficient for the purposes of our study.

It would be interesting to extend the present study to anisotropic flows, as almost no information is available about the effects of mean velocity gradients or anisotropy on the damping. The easiest anisotropic case to investigate would be turbulence submitted to uniform solid body rotation since, in this case, steady coordinates (in the rotating frame) can be used. Due to the lack of time, we could not investigate this case during the summer program. It should be the subject of future work.
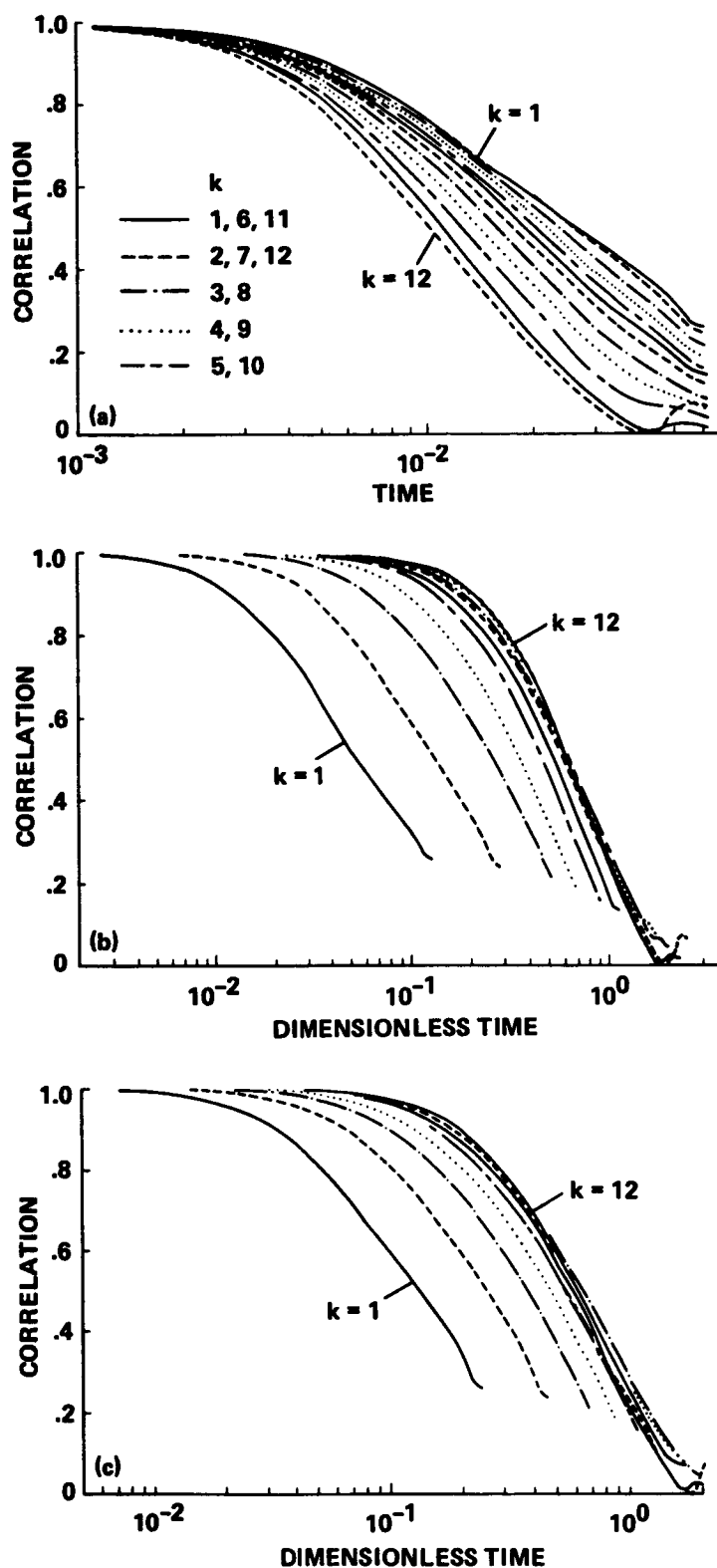
FIGURE 2.   Two-time Lagrangian correlations as a function of the time separation at different values of the wavenumber. (a) un-normalized time separation, (b) time separation normalized using Pouquet's formula, (c) time separation normalized using Kraichnan's formula.

In the case of isotropic fields, interest in studying the damping term is quite limited, since it is known that the existing formulations lead to satisfactory predictions of the decay of isotropic turbulence. This is, to a certain extent, true, (and is the reason why our goal is the study of anisotropic turbulence). However we believe that, even though limited to isotropic turbulence, the results of the present study are valuable. In the study of homogeneous isotropic turbulence containing a gap or a peak in the spectrum, for example, the accuracy of the expression for the damping is of greater importance. Since the choice of the damping term has an important effect on the "localness" of the triadic interaction in k space, a better expression for η could provide interesting information concerning localized interactions and, possibly, insight about the effect of the presence of coherent structures on the energy cascade (see Kraichnan, 1987). Furthermore, we believe that, in large-eddy simulation, the influence of the subgrid terms on the Lagrangian time scales should be investigated.

2. A quasi-homogeneous field containing "organized" structures

2.2 Aim of the study and initial conditions.

The first part of the work was devoted to the study of a case in which EDQNM is known to perform well: isotropic turbulence. The aim of the second part is significantly different. It consists of an attempt to simulate a case which, although simple enough to be handled by closures with reasonable computation times, is likely to provide a severe test of EDQNM.

Our goal is to get insight into the ability of two-point closures to account for situations in which coherent structures are present. How are the predictions of EDQNM affected by the presence of organized eddies?

The existence of coherent structures in wall bounded flows is well known. Wall bounded flows would, however, require a large amount of computational effort to be predicted by EDQNM, and at least at first, simpler situations have to be studied.

The basic idea of the present work is therefore to artificially inject coherent structures into a "quasi-homogeneous" turbulent field (quasi-homogeneous meaning periodic rather than homogeneous).

During the summer program we tried to define initial conditions for a simulation of a flow containing "coherent" structures in a periodic cubic box. The results of such a simulation could provide reference data to test EDQNM.

In an attempt to create such a turbulent field, an experiment has been devised in Lyon. This experiment consists of generating organized structures in grid turbulence by using a grid equipped with small rotating propellers. One hundred counter-rotating propellers are used in this experiment (one at each node of the grid); see figure 3. The results (see Michard et al, 1986) display interesting behavior, in particular, a spike appears in the spectrum; see figure 4.

Large Eddy Simulations on 16x16x16 grids, run in Lyon, using initial conditions containing four vortices embedded in a random field, show that some experimental tendencies can be predicted, and, to a certain extent, understood (for example, the existence of a periodic distribution of anisotropy). However, due to the lack

FIGURE 3. Grid equipped with propellers (Michard et al,1986).
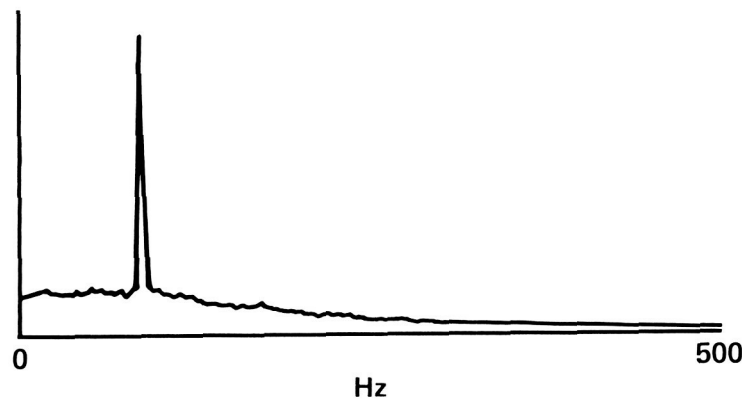
FIGURE 4. Experimental one-dimensional energy spectrum of Michard et al (1986).

of resolution of this coarse grid, it has not been possible to inject a peak in the spectrum in the flow direction.

The work done at CTR consists in building an initial field that contains such a peak. We used a 64x64x64 mesh. A few simulation runs were started to test the initial field. After several attempts, it was decided to define the initial conditions in terms of the vorticity field. In the 64x64x64 box, four vortex-containing cells, corresponding to the wakes of four propellers, were defined. In each cell three vortices are introduced, centered on helical lines corresponding to the wakes of the three blades of each propeller. In order to ensure zero circulation in each cell, another vortex was introduced on the centerline. A representation of this initial field is given in figure 5.

This field was embedded in a random fluctuating field. For this random field, we
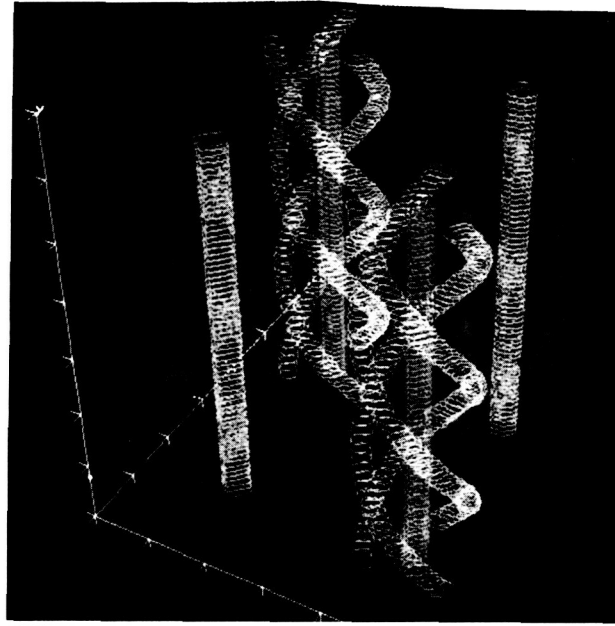
FIGURE 5.   Representation of the initial "coherent structures" used in the simulation. These are the idealized wakes of the counter-rotating propellers shown in figure 3.

ORIGINAL PAGE IS
OF POOR QUALITY
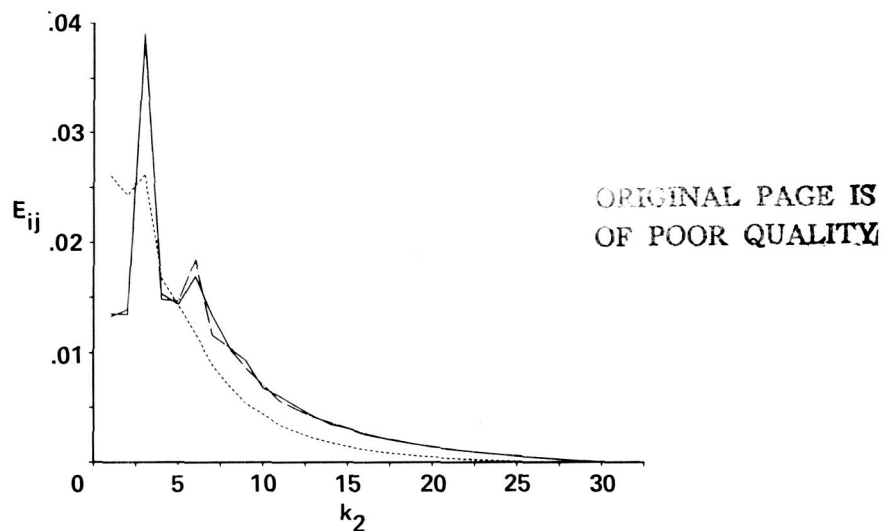
FIGURE 6.   Initial one dimensional spectra (vortex field + isotropic turbulence, averaged over the entire $x_1 - x_3$ space). The mean flow is in the x_2 direction. —— E_{11}, - - - - E_{22}, — — E_{33}.

used the one created by Lee & Reynolds (1985) with $N = 64$, and $Re = 51.13$.

The initial spectrum, in the k_2 direction, is given in figure 6. A small peak appears at the wavenumber corresponding to the blade passing frequency.

2.2 Results and directions for future work.

The peak in figure 6 is relatively weak, although the energy contained in the vorticity field is not small compared to the total energy of the field. However, it must be pointed out that the plotted spectrum is an average over the X,Z plane, and one should investigate the behavior of the one-dimensional spectra obtained at a given point in the X,Z plane.

It is worth noting that the peak appears at the blade passing frequency (due to the construction of the initial conditions) whereas the experimental spike is found at the rotation frequency of the propellers. During the simulation, the computed peak evolved only slightly and no subharmonic spike appeared at the rotation frequency. The simulations were, however, limited to one hundred time steps due to time constraints; longer runs are necessary to see the expected behavior.

Another experimental feature is that there is an axisymmetric contraction downstream of the grid. This axisymmetric contraction was introduced to amplify the intensity of the peak. Without it, the peak would die immediately; in fact, the amplification was much stronger than expected. The axisymmetric contraction should probably be included in the simulation. It is hoped that this work will be completed in the near future. It could provide a challenge for EDQNM, as preliminary studies show that the experimental decay of the peak is overpredicted by the closure. The existence of a reference field deduced from the simulation would be highly valuable since precise analysis of the mechanism occurring in the experiment is hard to deduce from the measured quantities.

2.3 Acknowledgements

REFERENCES

KANEDA Y. 1981, *J. Fluid Mech.*, **107**, 131.

KRAICHNAN R.H. 1987 *Phys. Fluids*, **30**, 1583.

LEE, C.H., SQUIRES, K., BERTOGLIO J.P. & FERZIGER, J.H. 1987 *to be presented at the 6th Turb. Shear Flow Symp., Toulouse.*

LEE, M.J. & REYNOLDS, W.C. 1985 *Stanford University Report TF-24.*

MICHARD ET AL. 1986 *European Turb. Conf., Euromech, Lyon, July 1986.*

POUQUET A., LESIEUR M., ANDRE J.C. AND BASDEVANT C. 1975 *J. Fluid Mech.*, **72**, 305.

ORSZAG S.A. 1970 *J. Fluid Mech.*, **41**, 363.

Validation of EDQNM for subgrid and supergrid Models

By P. Orlandi [1]

1. Introduction

The advantage of two-point closure models over one-point closure models is that they retain one of the most important turbulence characteristics, the energy transfer mechanism among eddies of different sizes. These models require closure hypotheses on the higher order terms. Among the different models derived by the direct-interaction approximation, DIA, of Kraichnan the simplest one is the eddy-damped quasi-normal Markovianized, EDQNM, theory of Orszag (1970). It requires a very simple numerical scheme to solve the so-called triadic integral. This closure is based on the quasi-normal approximation in the equation for the third-order cumulants where fourth-order terms are replaced by products of second order terms. The approximation gives an unrealistic increase of the third order cumulant and leads to negative energies. The introduction of an eddy damping term eliminates that unphysical effect.

2. Isotropic Turbulence

When a particular transformation (Crocco & Orlandi, 1985) for the wave numbers is introduced, the EDQNM expression of the energy transfer term is

$$T(k) = \frac{1}{k} \int_0^1 d\beta \int_{1-\beta}^{1+\beta} d\gamma [k^3 \Sigma(k, \beta k, \gamma k) + (\frac{k}{\beta})^3 \Sigma(k, k/\beta, \gamma k/\beta)] \qquad (1)$$

where the integration is to be performed only in a triangle in the (β, γ) plane. $\Sigma(k, p, q)$ is given by

$$\Sigma(k, p, q) = k^3 pq B(k, p, q) D(k, p, q) \left[\frac{E(p)}{p^2} - \frac{E(k)}{k^2} \right] \frac{E(q)}{q^2} \qquad (2)$$

where $B(k, p, q)$ is a geometrical factor and $D(k, p, q)$ is the relaxation frequency that results from the Markovianization of a certain integral:

$$D(k, p, q) = \frac{1 - e^{-[\eta(k)+\eta(p)+\eta(q)]t}}{\eta(k) + \eta(p) + \eta(q)}$$

The damping function $\eta(k)$ completes the EDQNM closure and the expression generally adopted is

$$\eta(k) = \nu k^2 + \lambda \left(\int_0^k p^2 E(p) dp \right)^{\frac{1}{2}}$$

1 University of Rome
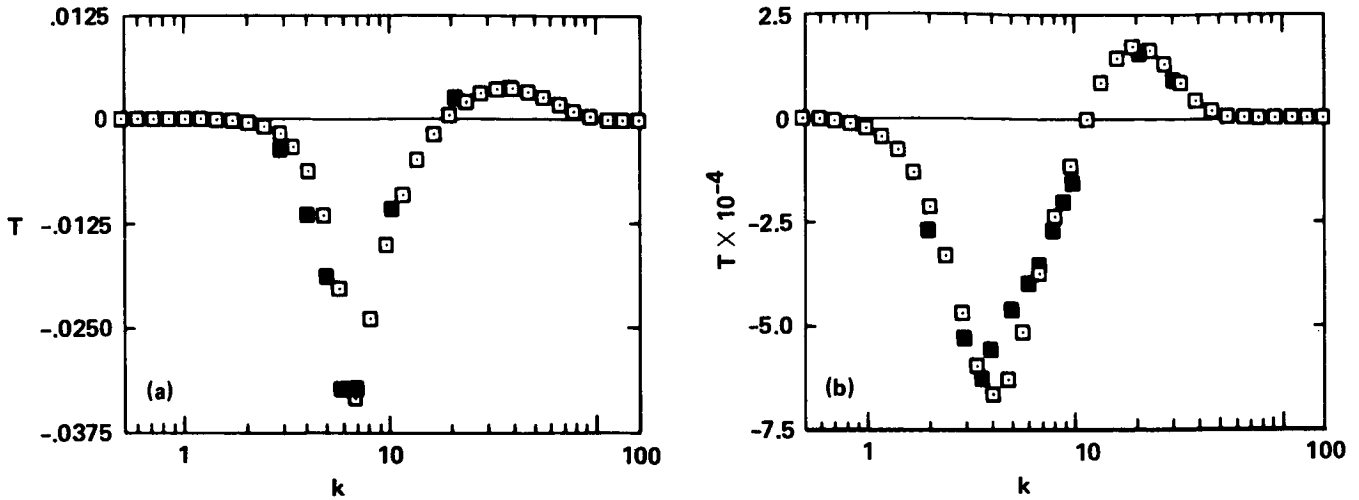
FIGURE 1. Energy transfer distribution: (a) $t = 0.54$, (b) $t = 4.34$, □ EDQNM , ■ DS.

Comparisons between EDQNM and direct simulation, DS, are possible only at very low Reynolds numbers. In the past these comparisons were limited to the evolution in time of globally averaged quantities such as turbulent energy , dissipation and skewness . In the first part of the CTR summer program a detailed comparison of the energy transfer between scales in a DS and the transfer given by EDQNM has been made. Only the accurate prediction of the energy transfer distribution is sufficient to demonstrate that the EDQNM closure describes correctly the complex mechanism of energy transfer among different scales. An even better check of the closure would be obtained by comparison of the detailed interaction distribution $\Sigma(k, p, q)$ in the (β, γ) plane. This has been done by Wray, but the evaluation of $\Sigma(k, p, q)$ within a DS requires $O(N^2)$ operations and the calculation was thus limited to a simulation of only $N = 32^3$ nodes. The resulting Σ distribution was very sparse and it was difficult to infer a continuous distribution from a single realization. Once the transfer $T(k)$ is determined, the energy spectrum evolution is obtained by solving

$$\frac{\partial E(k)}{\partial t} + 2\nu k^2 E(k) = T(k) \ . \tag{3}$$

Starting from the initial spectrum used in the DS, (3) together with (1) and (2) have been solved. figure 1 shows the energy transfer term at two different times and indicates very good agreement with the DS results.

The ability of the EDQNM closure to produce accurate transfer spectra encourages its use as a closure model (subgrid or supergrid) in a DS. A simulation at high Reynolds numbers, with an inertial range extending for at least one decade, might then be obtained by introducing both a subgrid and a supergrid model to account for the transfer between the computed scales and the unresolved scales both at low and high wave numbers. The energy spectrum is then subdivided into three regions
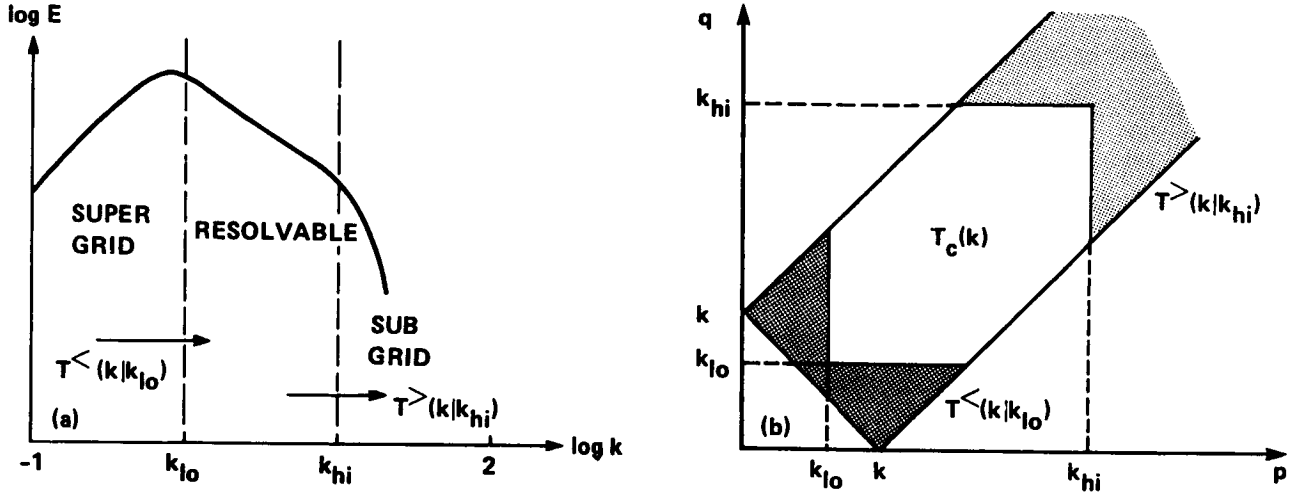
FIGURE 2.   (a) Partition of the energy spectrum into resolved and unresolved scales. (b) Partition of the domain of integration for $\Sigma(k, p, q)$.

as figure 2a shows. In the DS range $k_{lo} < k < k_{hi}$ the energy transfer can be decomposed into two parts,

$$T(k) = T_c(k) + T_{sgs}(k|k_{lo}, k_{hi}),$$

where $T_c(k)$ is the transfer due to interactions between wave numbers within the DS, $T_{sgs}(k|k_{lo}, k_{hi})$ is the transfer due to interactions involving wave numbers $p, q < k_{lo}$ (supergrid $T^<(k|k_{lo})$), and interactions involving wave numbers $p, q > k_{hi}$ (subgrid $T^>(k|k_{hi})$). The transfers due to interactions outside the DS are evaluated by (1). figure 2b shows the contribution of supergrid and subgrid ranges to the integral (1). When k is very close to k_{hi}, interactions between sub- and supergrid scales occur, and these can be easily calculated.

The integral (1) is calculated by discretizing the triangle into quadrilaterals of different sizes whose areas are related to the number of points per octave used to represent the energy spectrum. Thus, at each point inside the domain in the (β, γ) plane, $\Sigma(k, p, q)$ represents the interaction of wave numbers p and q. When $T^<(k|k_{lo})$ (supergrid) is calculated, $\Sigma(k, p, q)$ is set to 0 unless p or q is less than k_{lo}. In a similar way when $T^>(k|k_{hi})$ is calculated, $\Sigma(k, p, q)$ is set to 0 unless p or q is greater than k_{hi}.

To compare the transfers due to unresolved scales obtained by the EDQNM integral with those obtained by DS, the flowfield of a DS with a 128^3 resolution has been considered and the transfers across several cutoff wave numbers k_c, have been calculated. Figures 3 and 4 show that the distributions of $T(k)$, $T^<(k|k_c)$, and $T^>(k|k_c)$ obtained from DS are in very good agreement with those calculated by EDQNM at both small and large times. As a result of this very good agreement it is hoped that a DS can be used to simulate decaying turbulence at high Re. At
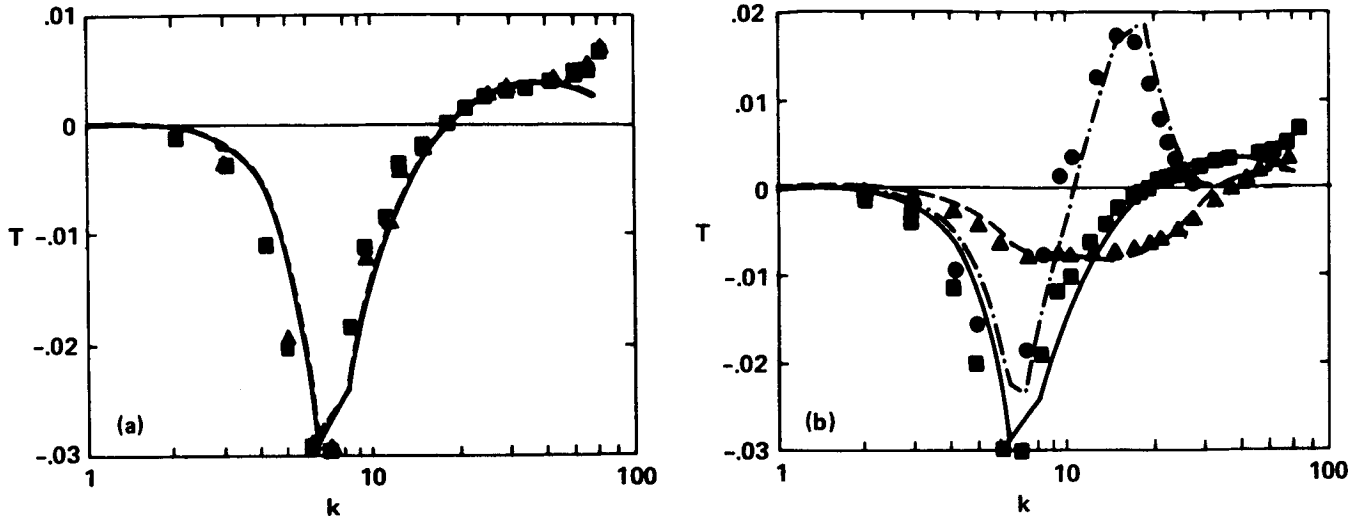
FIGURE 3.   Energy transfer distribution at $t = 0.54$ (a) $k_c = 4$, (b) $k_c = 16$:
EDQNM ——— $T(k)$, —·— $T^>(k|k_c)$, ———— $T^<(k|k_c)$; DS □ $T(k)$, ○ $T^>(k|k_c)$,
△ $T^<(k|k_c)$.
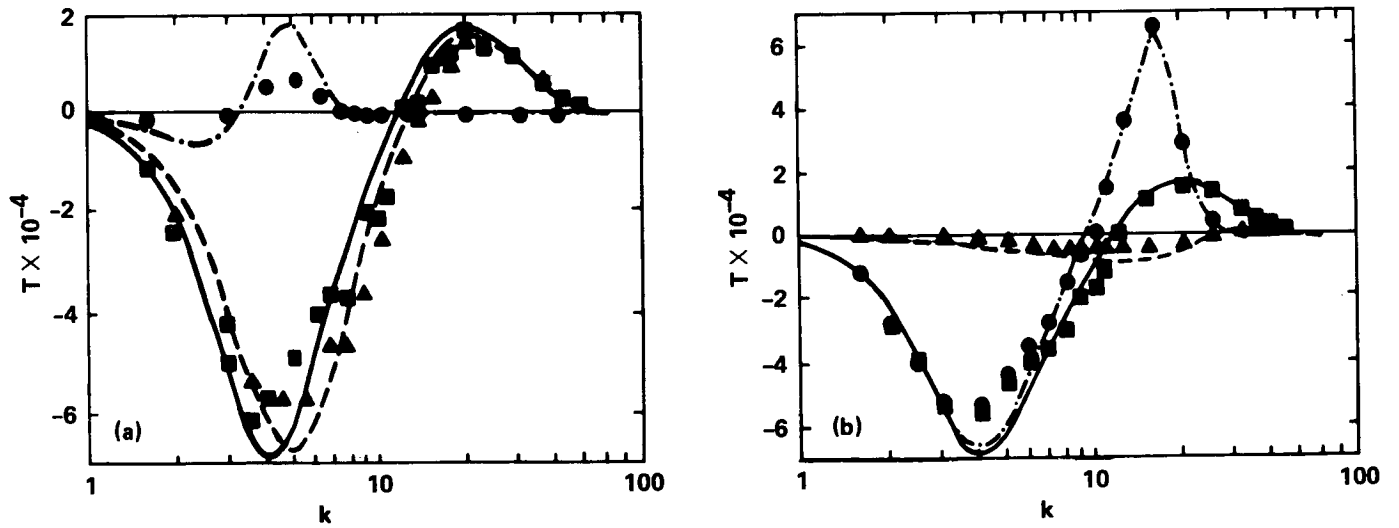
FIGURE 4.   Energy transfer distribution at $t = 4.34$ (a) $k_c = 4$, (b) $k_c = 16$:
EDQNM ——— $T(k)$, —·— $T^>(k|k_c)$, ———— $T^<(k|k_c)$; DS □ $T(k)$, ○ $T^>(k|k_c)$,
△ $T^<(k|k_c)$.

each time step the EDQNM calculation with $k_{min} \ll k_{lo}$ and $k_{max} \gg k_{hi}$ gives
the transfers $T^<(k|k_{lo})$ and $T^>(k|k_{hi})$ necessary to drive the simulation at the large
scales and remove energy at the small ones.

Table 1.

Comparison between RDT and DS

case RR128: $S = 28.28, \nu = 0.01$

	$St = 0$	$St = 2$		$St = 4$		$St = 6$		$St = 8$		$St = 10$	
		RDT	DS	RDT	DS	RDT	DS	RDT	DS	RDT	DS
q^2	20.89	15.42	15.12	18.74	20.42	24.77	25.70	33.34	31.11	44.42	34.76
$\overline{u_2'^2}/q^2$	.373	.428	.477	.502	.628	.534	.724	.544	.779	.525	.819
$\overline{u_3'^2}/q^2$	.329	.242	.195	.181	.068	.166	.027	.170	.012	.191	.007
$\overline{u_1'^2}/q^2$	.308	.329	.328	.316	.304	.299	.249	.286	.207	.284	.174
$\overline{u_2'u_3'}/\sqrt{\overline{u_2'^2}\,\overline{u_3'^2}}$	.0	.535	.596	.579	.740	.558	.797	.528	.812	.498	.820

Case S64NJ: $S = 10.00, \nu = 0.02$

	$St = 0$	$St = 2$		$St = 4$		$St = 6$	
		RDT	DS	RDT	DS	RDT	DS
q^2	20.89	4.29	5.19	4.10	5.02	4.81	5.16
$\overline{u_2'^2}/q^2$	.373	.452	.461	.535	.598	.601	.699
$\overline{u_3'^2}/q^2$	.329	.259	.165	.166	.047	.125	.018
$\overline{u_1'^2}/q^2$	.308	.302	.374	.299	.355	.273	.283
$\overline{u_2'u_3'}/\sqrt{\overline{u_2'^2}\,\overline{u_3'^2}}$	.0	.539	.843	.607	.645	.602	.471

3. Anisotropic Turbulence (rapid distortion case)

In the case of anisotropic turbulence the expression for the energy transfer term is much more difficult to derive and it is not clear whether the eddy damping term should have a tensorial or a scalar form. The time evolution of the correlations consists in part of interactions between turbulence and mean fields and in part of higher correlations. If interactions among the turbulent fields (slow terms) are neglected, a calculation based on rapid-distortion theory, RDT, is possible. It is convenient to work in a reference frame in which, for turbulence with some symmetry, all the second order correlations can be derived from three quantities N_1, N_2, N_3. In the simple case of a shear flows with $S = \partial U_2/\partial x_3$ the equations are (Craya 1958):

$$\frac{\partial N_1}{\partial t} + 2\nu k^2 N_1 - 2S \frac{k_2 k_3}{k^2} N_1 - S k_2 \frac{\partial N_1}{\partial k_3} = \Omega_1(k, \theta, \varphi),$$

$$\frac{\partial N_2}{\partial t} + 2\nu k^2 N_2 - 2S \frac{k_1}{k} N_3 - S k_2 \frac{\partial N_2}{\partial k_3} = \Omega_2(k, \theta, \varphi), \qquad (4)$$

$$\frac{\partial N_3}{\partial t} + 2\nu k^2 N_3 - S \frac{k_2 k_3}{k^2} N_3 - S \frac{k_1}{k} N_1 - S k_2 \frac{\partial N_3}{\partial k_3} = \Omega_3(k, \theta, \varphi),$$
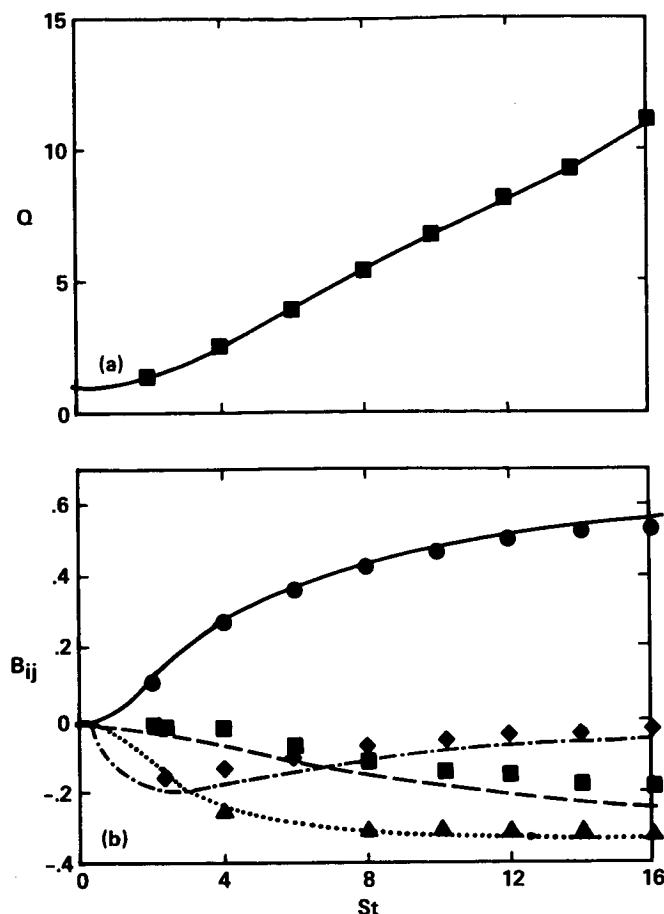
FIGURE 5.   Evolution of (a) turbulent kinetic energy, (b) Reynolds-stress anisotropy tensor. The present results are: ——— B_{22}, - - - - B_{11}, ······· B_{33}, —·— B_{23}. The solid symbols are the corresponding DS results.

where $\Omega_l(k,\theta,\varphi)$ are the non-linear terms that are discarded in RDT. Introducing the modified wave number system (k_1,k_2,k_3+Stk_2) the system of equations (4) can be easily solved.

Lee et al (1987) performed a DS by following the isotropic decay of an initial spectrum until it reaches a value for the skewness of about -0.5. This field was then used as the initial condition for a highly sheared simulation. Flow field structures similar to those found near the walls of a channel are obtained even when the non-linear terms are neglected. We calculated this case by using EDQNM for the isotropic decay and RDT for the high shear evolution. figure 5 shows good agreement between the present results and those obtained by DS. A further comparison between the RDT calculations and cases S64NJ and RR128 of Rogers et al (1986) has been completed. Table 1 shows that due to the predominant effect of the viscosity on the shear, the RDT calculation predicts the behavior of the total energy also at the later times, St, but it does not predict well the time evolution of

each component. This is consistent with the analysis done by Brasseur during the CTR summer school. He analyzed the effects of the slow pressure terms and found that these withdraw energy from $\overline{u_2'}^2$, transfer it to $\overline{u_3'}^2$ and from there to $\overline{u_1'}^2$ .Our calculation shows a faster decay of the $\overline{u_3'}^2$ than the one obtained by DS. On the contrary $\overline{u_1'}^2$ agrees with the DS because the amount of energy it is receiving from $\overline{u_2'}^2$ is comparable to the amount of energy it is transfering to $\overline{u_3'}^2$.

4. Conclusions

From these preliminary calculations we conclude that the two-point EDQNM closure accurately describes the behavior of second order moments. This closure can be applied as subgrid and supergrid models for Large Eddy Simulations at higher Reynolds numbers. In the case of homogeneous anisotropic turbulence, when the non-linear terms are introduced the calculation becomes quite onerous but is still considerably less expensive than the calculation of a DS. The major merit of two-point closure models is that they can be easily applied to flows at Reynolds numbers that are unreachable by a DS. Work is in progress to derive expressions for the non-linear terms that give good global conservation properties.

REFERENCES

CRAYA A. 1958 Contribution a l'analyse de la turbulence associee' a des vitesse moyennes . *Publications Scientifiques et Techniques du Ministere de l'Air.*

CROCCO L. & ORLANDI P. 1985 A transformation for the energy-transfer term in isotropic turbulence . *J. Fluid Mech..* **16**, 405-424

LEE M.J., KIM J. & MOIN P. 1987 Turbulence structure at high shear rate . *Proceedings of the Sixth Symposium on Turbulent Shear Flows Toulouse.*

ORSZAG S.A. 1970 Analytical theories of turbulence . *J. Fluid Mech..* **41**, 363-386

ROGERS M., MOIN P.& REYNOLDS W.C. 1986 The structure and modelling of the hydrodynamic and passive scalar fields in homogeneous turbulent shear flow . *Stanford University Report No TF-25.*

Angular distribution of turbulence in wave space

By G. Coleman[1], J.H. Ferziger[1], J.P. Bertoglio[2]

1. Introduction

As experience with the one-point closure models for turbulence in current use has not been completely satisfactory, people have begun to search for other ways to predict turbulent flows. One alternative that has been suggested is large eddy simulation (LES) which, together with its more exact relative, direct numerical simulation (DNS), has had considerable success in the prediction of turbulent flows. These methods are beginning to serve as partial substitutes for turbulence experiments.

It is perhaps natural that people should regard these new methods as panaceas. More careful consideration will lead one to be more cautious. DNS and LES have been applied only to the simplest low Reynolds number turbulent flows. The prospects for a large increase in the range of applicability of DNS in the near future are very small. For LES, the prospects are somewhat brighter.

The range of flows that has been treated with LES to date is only a little broader than that treated by DNS. The Reynolds numbers are somewhat higher but the geometries are almost as restricted. Three items pace the growth of LES applications. The first is computational resources: speed, memory (both fast and archival), and number of processors available. The second is numerical methods; there is, and perhaps always will be, a need for faster algorithms applicable to a wide range of geometries. Finally, there are the subgrid models required by LES; this is the focus of the present work.

In simulations done to date, the Reynolds numbers were such that most of the turbulence energy resided in the resolved scales. Under these circumstances, the results are relatively insensitive to the quality of the model used for the subgrid scale (SGS) component of the turbulence. As one pushes LES to higher Reynolds numbers or more complex flows, the model quality becomes a more important issue. It is safe to say that, if the models in current use are applied to these more difficult flows, the results will be of reduced quality. Thus the development of improved SGS models must be of highest priority if LES is to become an engineering tool.

SGS models in current use are, for the most part, based on the same ideas as one-point closure models. To obtain significant improvements, new ideas will probably be needed. It is here that turbulence theories may have a role to play.

1 Stanford University
2 Ecole Centrale de Lyon

2. Turbulence theories

There is a wide range of turbulence theories. The modern ones deal with the distribution of the turbulence in Fourier or wavenumber space. Use of Fourier transforms implies that their applicability is limited to homogeneous turbulence; however, their importance lies in the fact that they contain information about the length scales of turbulence, something notably lacking in one-point closure models. Extensions to inhomogeneous flows may be possible, but it is unlikely that these theories will ever be applied directly to the complex engineering flows. Nonetheless, they may be of use in the development of SGS models. In particular, one may be able to regard the turbulence as locally homogeneous and apply the theory to the prediction of the SGS turbulence. The objective is to obtain the best of both worlds: the ability of LES to simulate inhomogeneous flows and that of theory to provide length scale information.

In selecting a candidate turbulence theory on which to base an SGS turbulence model, one should be guided by the following principles. The theory should be successful in predicting homogeneous flows. The computation time should not be too large. Finally, it should be capable of simplifications that will render it practical for use as an SGS model.

There is no space to review turbulence theories here. Let it suffice to say that, of the theories that we considered, the Eddy Damped Quasi-Normal Markovian (EDQNM) model appears to have the brightest prospects. It meets the criteria set forth in the preceding paragraph to a higher degree than its competitors. The EDQNM model is based on simplifications of the moment equations in Fourier space. The quasi-normal assumption replaces the fourth order moments by their values for a Gaussian distribution. Eddy damping is introduced to restore some of the important interactions removed by the quasi-normal hypothesis. Finally, the Markovian assumption removes history effects that complicate the analysis. The result is a system of non-linear integral equations for the second moments in Fourier space. These are also the Fourier transforms of the two-point correlation functions; hence this is a two-point closure method.

Solving the equations of EDQNM is not trivial. In the absence of further simplifications, it is necessary to solve a coupled system of non-linear integral equations in three dimensional wave space. This has been done for homogeneous flows with excellent results. However, when using EDQNM as an SGS model for an inhomogeneous flow, it is necessary to solve these equations at each point at every time step. Although EDQNM has been applied as an SGS model for homogeneous isotropic turbulence, it is clearly impractical for more complex flows without additional simplifications. Such simplifications have been used. For isotropic turbulence, one can integrate over angles analytically and reduce the equation to one involving a single independent variable. In other flows, the symmetries can be used to provide other, less dramatic, simplifications. In the work reported here, we investigated possible simplifications in the homogeneous flow of most direct relevance to engineering applications: homogeneous sheared turbulence.

3. Angular Distributions

One way to simplify EDQNM is to assume that the distributions of the second moments in wave space can be represented as a sum of a small number of simple functions. The equations could then be reduced to a set of non-linear algebraic equations for the parameters. This would greatly reduce the cost of EDQNM and could render it practical for use as an SGS model for inhomogeneous flows.

It is well-known that, in the inertial subrange, the spectral distribution of the energy obeys a power law. The viscous range can be represented by using a cutoff, the details of which should not be important at high Reynolds numbers. Since the full simulation data we will use as the basis of the current work is at Reynolds numbers lower than those at which the model is to be applied, and the spectral distributions are nearly always smooth, it was felt that there is little point in investigating the distributions in wavenumber. We therefore concentrated on the angular distribution in wave space; caution is required because the results obtained may not apply at higher Reynolds numbers.

The data on which our analysis is based represent isotropic turbulence which has been sheared at a rate $S = d\overline{u}/dy$ until $St = 12$; the initial turbulence Reynolds number based on microscale was approximately 50. The data, originally generated by Mike Rogers, were supplied to us in the form of the Fourier-transformed velocity field by Moon J. Lee.

The data were converted from Cartesian to spherical coordinates in wave space. The k_y direction was chosen as the pole of the spherical system while the k_z direction was chosen as the origin for the azimuthal angle.

The angular distribution of the converted data was examined. At each wavenumber, contours of each of the significant second moments (E_{11}, E_{22}, E_{33}, and E_{12}) and the total energy were plotted as functions of the two spherical angles; only results at the largest wavenumber for which an entire shell was available will be presented here. The distribution was found to be smooth enough that it can probably be represented as a sum of a small number of functions. The energy is concentrated near the poles, indicating the presence of small scales in the k_y direction caused by shear-thinning of the eddies.

In order to further determine what is needed to fit the angular distribution, we plotted the energy components on lines on which one of the angles is held fixed. Figure 1 shows the results as a function of azimuthal angle for fixed polar angle while figure 2 shows the energy as a function of polar angle for fixed azimuthal angle. The distribution in polar angle can be fit with the first two terms of a Fourier series while the distributions in azimuthal angle appear to require three terms. Thus, approximately six terms should suffice to fit the angular distribution of each component. If the distribution in wavenumber can be assumed, a total of eighteen parameters should be the upper limit of what is needed to represent the subgrid turbulence. With further experience, we may be able to reduce the number somewhat. We estimate that using an eighteen parameter algebraic SGS model would approximately double the cost of LES, a not unreasonable price if the Reynolds numbers can be increased sufficiently.
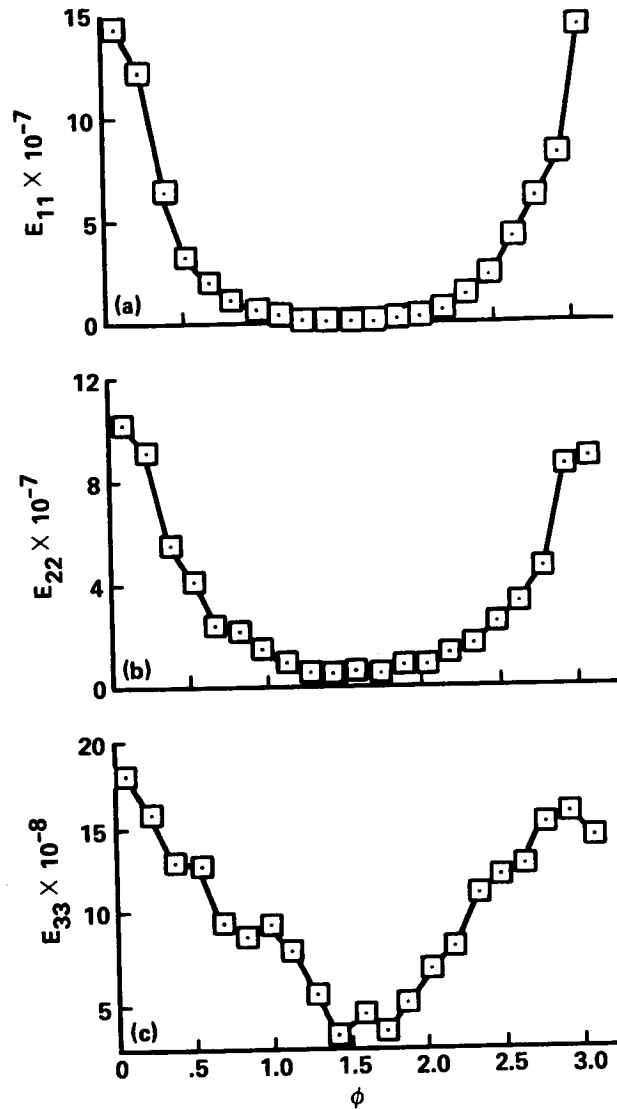
FIGURE 1.   Distribution of Reynolds stresses over azimuthal angle ϕ at constant polar angle $\theta = 1.1794$.

4. Future Work

We intend to continue the work described above. We will attempt to fit the distribution of the second moments with a few functions as described above and determine how many parameters are needed more precisely. At some later date, we will try to perform an EDQNM calculation of homogeneous sheared turbulence using the parameter set suggested by these fits. The results will be compared to the original data used in this work and with the results of an EDQNM calculation carried out in the usual way.
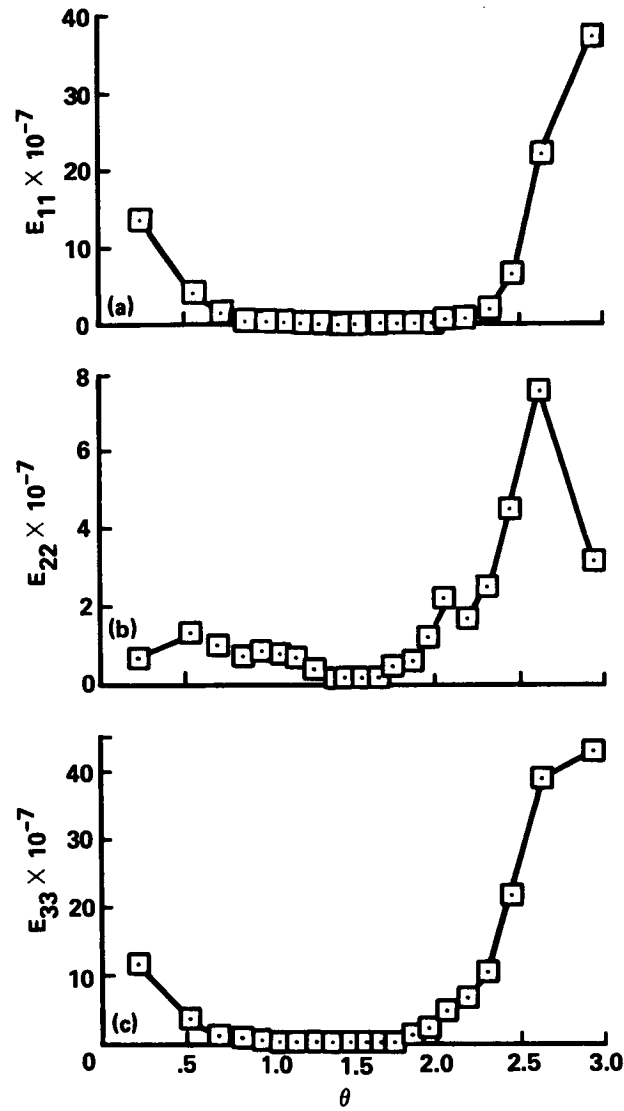
FIGURE 2. Distribution of Reynolds stresses over polar angle θ at constant azimuthal angle $\phi = 1.5708$.

Acknowledgements

Big Whorls Carry little whorls

By J.C.R. Hunt[1], J.C. Buell[2], and A.A. Wray[2]

The space-time structure of homogeneous isotropic turbulence has been studied using a direct spectral simulation on a 64^3 mesh at a microscale Reynolds number of $Re_\lambda = 48$. Steady body forces were applied to a few low-wavenumber modes to make the flow statistically stationary. The results for the two-point space-time correlations of velocity and pressure (R_{11} and R_{pp}) show that the auto-correlations of u and p are positive and have about the same integral time scales, and that the spatial correlation $R_{pp}(r) \simeq R_{11}(0, r, 0)$. The form of $R_{pp}(r)$ and the result that $\overline{p^2}/(\rho u_0^2)^2 \simeq 1.0$ agree fairly well with the Hinze/Batchelor (Hinze 1975) results. The three-dimensional energy spectrum for small space-time scales of velocity and pressure are consistent with the concept of large eddies advecting the small scales with a random Gaussian velocity (rms value of one component is u_0): the wavenumber (k), frequency (ω) and the energy spectrum $\mathcal{E}(k,\omega)$ are related to the spatial energy spectrum $E(k)$ by the formula

$$\mathcal{E}(k,\omega) = E(k) \exp\left[-\tfrac{1}{2}\omega^2/(aku_0)^2\right]/(\sqrt{2\pi}(aku_0)),$$

where $a \simeq 0.4$-0.5. The same form is found for the pressure spectrum. Extrapolating this result to high Reynolds number implies that in the inertial range the frequency spectra are $\phi_{11}(\omega) \propto (\epsilon u_0)^{2/3}\omega^{-5/3}$ (Tennekes 1975), and $\phi_{pp}(\omega) \propto (\epsilon u_0)^{4/3}\omega^{-7/3}$.

1. Introduction

1.1 Background to the project

Recent reports on the structure of turbulence and its dynamics have tended to emphasize the representation and the dynamics of the *spatial* structure rather than the temporal structure of the turbulent velocity field. However, closer examination of dynamical theories (e.g., Kraichnan's, described by Leslie 1981) show that they are always based on certain assumptions about the temporal structure, which have not been subjected to detailed examination or computation.

The temporal structure of turbulence also needs to be understood in order to develop models for the effects of turbulence and fluctuating pressure fields on the generation of surface and internal waves (Carruthers & Hunt 1986) and on dispersion of pollutants, particles and bubbles. One of the ways of developing practical models for these problems is first to develop a stochastic representation of the velocity field.

1 University of Cambridge

2 NASA Ames Research Center
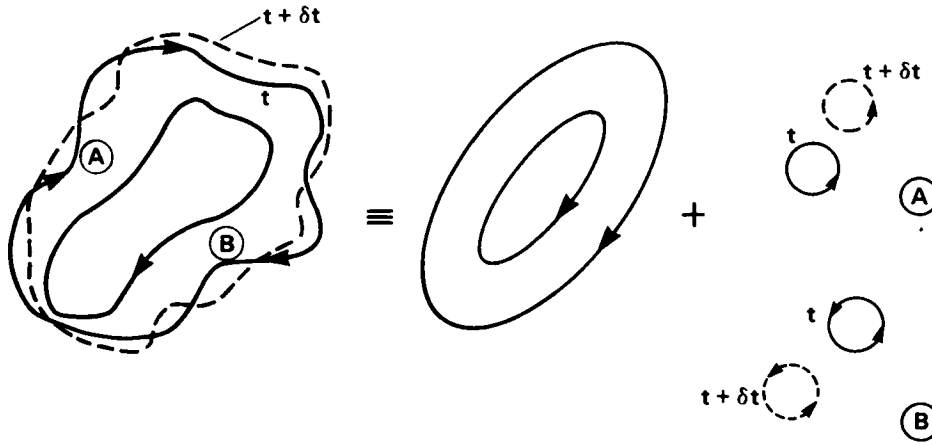
FIGURE 1.   Flow field composed of large scale eddies and small scale eddies that are transported by the large scales. The small eddies also deform on a larger time scale.

The current research on the *spatial* structures (such as that of Moin 1987 and Moin, Adrian & Kim 1987) needs to be supplemented by information on how the turbulent velocity field evolves in *time*. (Some initial suggestions were put forward by Turfus & Hunt 1986, but they will be superceded by the present work.)

The clearest recent account of the temporal structure of turbulence is given by Tennekes (1975) and Tennekes & Lumley (1979). Essentially, the current understanding is that the largest scales of turbulence with velocity and length scales u_0 and L are unsteady and change on a time scale L/u_0. Meanwhile, smaller eddies on a scale ℓ with velocity $u(\ell)$ (defined by the structure function $\overline{[|u(x) - u(x + r)|^2]}^{1/2}$, where $|r| = \ell$), have two time scales: the Eulerian time scale

$$\tau_E(\ell) \sim \ell/u_0, \tag{1.1a}$$

for the eddy to be advected by the large eddies past an observing point (moving with the mean flow), and the Lagrangian time scale

$$\tau_L(\ell) \sim \ell/u(\ell), \tag{1.1b}$$

for the velocity field on a scale (ℓ) to change as it is advected by the large scale eddies. See figure 1.

Thus at a point (moving with the mean flow), the dominant time-dependent phenomenon (which determines $\partial u/\partial t$) is the rapid, random movement of small scale eddies past the observer by the large eddies. On the other hand, for a point moving *with the fluid*, the only change of velocity is the slow change caused by the dynamical processes at the scale ℓ. These differences are best defined by the *Eulerian* microscale

$$\tau^{(E)} = \left[\overline{(\partial u/\partial t)^2}\Big/\overline{u^2}\right]^{-1/2}, \tag{1.2a}$$

and the *Lagrangian* microscale, following a material element,

$$\tau^{(L)} = \left[\overline{(d\mathbf{u}/dt)^2}\Big/\overline{\mathbf{u}^2}\right]^{-1/2}. \tag{1.2b}$$

For high Reynolds number turbulence these can be related to the basic time scale L/u_0 by

$$\tau^{(E)} \sim Re^{-1/2}L/u_0, \tag{1.3a}$$

and

$$\tau^{(L)} \sim Re^{-1/4}L/u_0, \tag{1.3b}$$

where $Re = u_0L/\nu$. Tennekes (1975) found that these estimates were consistent with the grid turbulence measurements of Shlien & Corrsin (1974). Another important consequence of Tennekes's analysis is that for high Reynolds number turbulence in the inertial subrange, the frequency spectrum $\phi_{11}(\omega)$ of one component of the velocity, say u_1, measured at a point (moving with the mean flow) has a form which is different from the universal Lagrangian form

$$\phi_{11}^{(L)}(\omega) = C_\omega^L \epsilon \omega^{-2}, \tag{1.4a}$$

namely

$$\phi_{11}^{(E)}(\omega) = C_\omega^E (\epsilon u_0)^{2/3} \omega^{-5/3}, \tag{1.4b}$$

where C_ω^E is a constant for a given flow. Since this form depends on the large scales which do not have (even approximately) a universal character, it is not likely that C_ω^E is a universal constant, unlike the constant for the one-dimensional wavenumber spectrum $\phi_{11}(k_1)$ or energy spectrum $E(k)$. The prediction (1.4b) has not to our knowledge been properly tested experimentally or computationally.

No detailed analyses have been developed for the four-dimensional wavenumber-frequency spectrum tensor $\Psi_{ij}(\mathbf{k},\omega)$ or its equivalent energy spectrum $\mathcal{E}(k,\omega)$, defined by

$$\Psi_{ij}(\mathbf{k},\omega) = \frac{1}{(2\pi)^4} \int \int \int \int \overline{u_i(\mathbf{x},t)u_j(\mathbf{x}+\mathbf{r},t+\tau)}e^{i(\mathbf{k}\cdot\mathbf{r}+\omega\tau)}d\mathbf{r}d\tau, \tag{1.5a}$$

and

$$\mathcal{E}(k,\omega) = \int_{|\mathbf{k}|=k} \Psi_{ii}(\mathbf{k},\omega)dA(\mathbf{k}). \tag{1.5b}$$

Note that

$$E(k) = \int_{-\infty}^{\infty} \mathcal{E}(k,\omega)d\omega. \tag{1.5c}$$

However, Carruthers & Hunt (1986) made a rash speculation based on Tennekes's time scale argument (in order to estimate internal wave generation) that

$$\Psi_{ij}(\mathbf{k},\omega) \simeq \Phi_{ij}(\mathbf{k})\delta(\omega \pm ku_0), \quad \text{where} \quad \Phi_{ij}(\mathbf{k}) = \int_{-\infty}^{\infty} \Psi_{ij}(\mathbf{k},\omega)d\omega. \tag{1.6}$$

Measurements have been made of one-dimensional space-time correlations $R(r, \tau)$ of velocity and pressure fluctuations in grid turbulence and in boundary layers (Favre *et al.* 1956; Wills 1971), and in a pipe (Sabot & Comte-Bellot 1976). The general features have been described by formulae of the form (in coordinates moving with the mean flow)

$$R_{11}(r_1, \tau) \simeq R_{11}(r) F(\tau, r, u_0, L)$$

where $F(\tau = 0) = 1$, and F decreases with r more slowly as τ increases. See Hinze (1975 p. 416). Similar forms are observed for fluctuating pressure. Wills (1971) also took the Fourier transform of these measurements and calculated the one-dimensional wavenumber-frequency spectra $\phi_{pp}(k_1, \omega)$. When converted into a frame moving at the same mean speed as the travelling pressure field, he found that his result could be expressed as

$$\phi_{pp}(k_1, \omega) = \phi(k_1) f\left(\frac{\omega}{k_1 u_0}\right), \qquad (1.7)$$

where $f \simeq \exp\left(-\frac{1}{2} \frac{\omega^2}{k_1^2 u_0^2}\right)$, and u_0 is the rms value of the streamwise velocity component (at $y/\delta \simeq 0.5$). Moser & Moin (1984) computed space-time correlations for channel flow.

An interesting quantity that can be derived from these correlations is the Eulerian time scale $T_{ii}^{(E)}$ (in a frame moving with the mean flow) of the ith velocity component. [Since the measurements are not extensive enough for $T^{(E)}$ to be computed from *integrals* of $R_{11}(\tau)$, $T^{(E)}$ has to be estimated from the value of τ at which $R_{11} \simeq 1/e$.] The results of Favre and Moser & Moin indicate that the value of $T_{ii}^{(E)}$, normalized in terms of the rms velocity and the integral length scale L_1^{ii} in the flow direction has a range of values given by

$$\beta^{(E)} = T_{ii}^{(E)} \sqrt{\overline{u_i^2}} \Big/ L_1^{ii}, \qquad (1.8)$$

where $1 \leq \beta^{(E)} \leq 2$. Snyder & Lumley (1971) inferred a value of $\beta^{(E)} \simeq 3$ from their measurements of small particles in grid turbulence.

Using the same normalization for the Lagrangian integral time scale $T_{ii}^{(L)}$, defined by

$$\beta^{(L)} = T_{ii}^{(L)} \sqrt{\overline{u_i^2}} \Big/ L_1^{ii}, \qquad (1.9)$$

experiments and simulations indicate that $\beta^{(L)} \simeq 1$ for grid turbulence (Snyder & Lumley 1971), and boundary layer turbulence (Durbin & Hunt 1980). A random Fourier mode representation for homogeneous turbulence has produced a value of $\beta^{(L)} \simeq 1/3$-$1/2$.

So the current position is that the magnitudes of $\beta^{(E)}$ and $\beta^{(L)}$ are *not* well defined.

1.2 Aims of the project

The aim of the research presented here is to explore the space-time structure of homogeneous turbulence by computing and then interpreting the two-point spectra and correlations of the velocity and pressure fields. Many of these statistics are of considerable practical importance, as indicated in the previous section. In particular it is of interest to compare the different time and length integral scales and microscales for Eulerian and Lagrangian quantities, and to compare the space and time spectra.

2. Some Theoretical Ideas for Guiding Interpretation

2.1 Velocity spectra

2.1.1 Simple non-interacting eddies

Consider a set of smooth eddies on a line, each located at a position x_n, with a spatial scale ℓ_n, a turnover time ω_n^{-1}, and a random phase ϵ_n. We consider, for simplicity, one component of turbulence, u_1; then a typical form for u_1 is

$$u_1(x,t) = \sum_{n=0}^{N} a_n \exp\left[-\frac{(x-x_n)^2}{2\ell_n^2}\right] \cos(\omega_n t + \epsilon_n), \qquad (2.1)$$

where a_n are random amplitude coefficients which are independent, $\overline{a_n a_m} = \delta_{nm}\overline{a_n^2}$. We assume the mean of ω_n is $\overline{\omega_n}$, and its random element has variance $\sigma_{\omega_n}^2$.

The cross correlation at points x and $x + r$ and times t and $t + \tau$, when averaged over a length $X \sim \sum \ell_n$ and over a sufficiently long time, is

$$R_{11}(r,\tau) = \frac{\sqrt{\pi}}{2X} \sum_{n=0}^{N} \overline{a_n^2}\ell_n \exp\left(-\frac{r^2}{4\ell_n^2}\right) \exp(-\tfrac{1}{2}\sigma_{\omega_n}^2 \tau^2) \cos(\overline{\omega_n}\tau). \qquad (2.2a)$$

So in general the space-time correlation is not simply related to the spatial correlation $R_{11}(r)$. But, for the case of just one eddy scale L, where $N = 0$, R_{11} reduces to

$$R_{11}(r,\tau) = \frac{\sqrt{\pi}}{2X} a_0^2 L \exp\left(-\frac{r^2}{4L^2}\right) \exp(-\tfrac{1}{2}\sigma_{\omega_0}^2 \tau^2) \cos(\omega_0\tau), \qquad (2.2b)$$

or

$$R_{11}(r,\tau) = R_{11}(r,\tau = 0)f(\tau).$$

Then the time and space correlations are separable. Similarly the wavenumber and frequency spectra are not linked, for this type of flow field.

2.1.2 Small eddies moved by a large-scale velocity field

Now consider a set of small eddies moved by a random large scale velocity U. These might be the small scale components of turbulent flow. Again, take one dimension: Let

$$u = \sum_{m=-M}^{M} \sum_{n=-N}^{N} a_{nm} \exp\left[i(k_n x + \omega_m t)\right], \qquad (2.3)$$

where $\omega_m = U k_m + \omega'_m$, a_n is again a set of random amplitude coefficients, and ω'_m is the frequency in the advected frame.

Let the probability density function of U be $p(U)$. Then

$$R_{11}(r,\tau) = \int \sum_{m=-M}^{M} \sum_{n=-N}^{N} |a_{nm}^2| \exp\left[i(k_n r + k_n \tau U + \omega'_m \tau)\right] p(U) dU. \qquad (2.4)$$

It is interesting to consider two possibilities for $p(U)$.

(a) $p(U)$ is Gaussian with variance U_0^2:

$$R_{11}(r,\tau) = \sum_{m=-M}^{M} \sum_{n=-N}^{N} |a_{nm}^2| e^{ik_n r} e^{-\frac{1}{2}\tau^2 k_n^2 U_0^2} e^{i\omega'_m \tau}. \qquad (2.5)$$

Then the one-dimensional wavenumber frequency spectrum is

$$\psi(k_1,\omega) = \frac{1}{(2\pi)^2} \sum_{m=-M}^{M} \sum_{n=-N}^{N} \int_{-\infty}^{\infty} |a_{nm}^2| e^{i(k_n-k_1)r} dr \int_{-\infty}^{\infty} e^{(-\frac{1}{2}\tau^2 k_n^2 U_0^2 - i(\omega-\omega'_m)\tau)} d\tau$$

$$= \sum_{m=-M}^{M} |a_{k_1 m}|^2 \exp\left[-\frac{(\omega-\omega'_m)^2}{2k_1^2 U_0^2}\right] \Big/ \left(\sqrt{2\pi}|k_1|U_0\right).$$

$$(2.6)$$

For high wavenumbers, the advective time scale $(k_1 U_0)^{-1}$ is much less than the time scale for the eddies to change as they move. Consequently $|\omega'_m| \ll |k_1 U_0|$. By taking large enough values of N to give a dense distribution of Fourier modes, a spatial spectrum $\phi(k_1)$ from $\psi(k_1,\omega)$ can be defined. From (2.6),

$$\psi(k_1,\omega) = \phi(k_1) \exp\left(-\frac{\omega^2}{2k_1^2 U_0^2}\right) \Big/ \left(\sqrt{2\pi}|k_1|U_0\right). \qquad (2.7)$$

Note that

$$\overline{u^2} = \int_{-\infty}^{\infty} \phi(k_1) dk_1 = \int_{-\infty}^{\infty} \int_{-\infty}^{\infty} \psi(k_1,\omega) dk_1 d\omega. \qquad (2.8)$$

In a three-dimensional isotropic velocity field, $\omega_n = \mathbf{U} \cdot \mathbf{k}_n + \omega'_n$, and for a Gaussian distribution of the 3-D large-scale velocity $\mathbf{U}$, it can be shown that the relation between the k-ω energy spectrum and the k energy spectrum is

$$\mathcal{E}(k,\omega) = E(k) \exp\left(-\frac{\omega^2}{2k^2 U_0^2}\right) \Big/ \left(\sqrt{2\pi} k U_0\right), \qquad (2.9)$$

where $U_0^2 = \frac{1}{3}\overline{|\mathbf{U}|^2}$.

(b) The large-scale velocity has a constant magnitude (forwards or backwards):

In this case $p(U) = \frac{1}{2}\left[\delta(U - U_0) + \delta(U + U_0)\right]$, and this leads to

$$R_{11}(r,\tau) = \sum_{n} |a_n^2| e^{ik_n r} e^{i\omega_n_0 \tau} \cos(\tau k_n U_0),$$
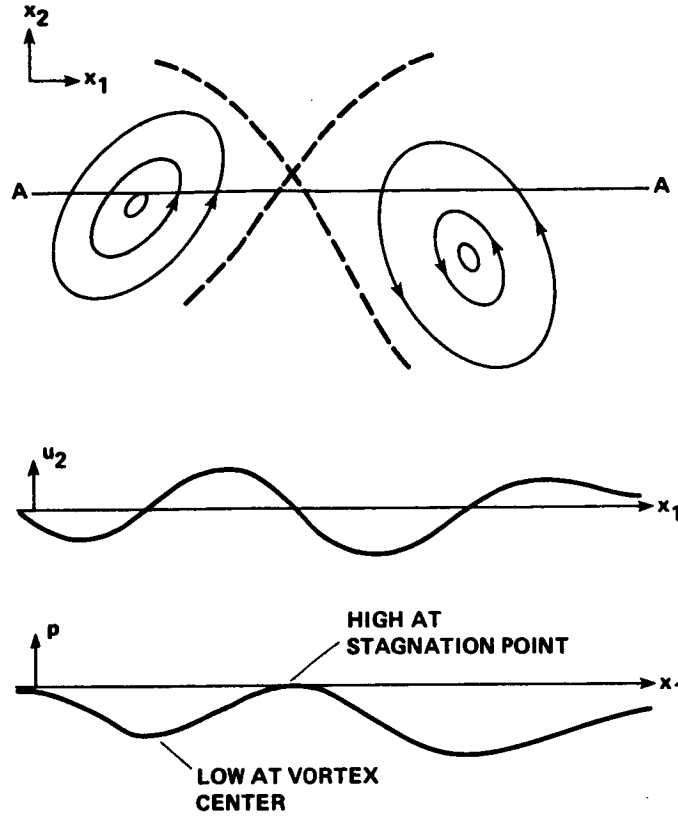
FIGURE 2.   Similarity of the length scales of velocity and pressure fields induced by large vortices.

and

$$\psi(k_1, \omega) = \phi(k_1)\frac{1}{2}\left[\delta(\omega - k_1 U_0) + \delta(\omega + k_1 U_0)\right].\qquad(2.10)$$

2.2 Pressure

For large eddies having a form similar to vortices (such as analyzed by Townsend 1976), the large scale distribution of pressure across the eddy, say in the x_1 direction, has a distribution similar to that of $u_2(x_1)$ (figure 2). Consequently, the pressure correlation $R_{pp}(r_1)$ is expected to have the same scale and form as $R_{22}(r_1)$.

The pressure fluctuations at small scales have been found in previous investigations (e.g. George *et al.* 1982) to be *caused* by the motions of eddies on that scale, and not (for example) by interactions between small scales and large scales. The former (which is observed) gives $\phi_{pp}(k_1) \propto \epsilon^{4/3} k_1^{-7/3}$, while the latter gives $\phi_{pp}(k_1) \propto (U_0^2/L^2)\epsilon^{2/3} k_1^{-11/3}$. Thus it is expected that, as the large scale eddies *advect* the small eddies, they also advect the small scale pressure fluctuations. Therefore the k-ω power spectrum of pressure fluctuations is *expected* to have the

form

$$\mathcal{E}_{pp}(k,\omega) = E_{pp}(k)\exp\left(-\frac{\omega^2}{2k^2U_0^2}\right)\bigg/(\sqrt{2\pi}kU_0). \qquad (2.11)$$

This is close to the values measured by Wills (1971).

3. Method

To obtain the frequency spectra and time correlation of a turbulent velocity field, a long time record is necessary; a decaying turbulent field is not appropriate because the amplitude decay does not allow a long enough time record. It is necessary to generate a statistically stationary velocity field.

The method used in these computations is to introduce a *steady* nonuniform force field $\mathbf{F}(\mathbf{x})$ at the largest scale of the flow (defined to be 2π in all three directions), which induces a mean flow at this scale. The mean flow is unstable, allowing instabilities to grow. This leads to a chaotic structure with motions at all scales down to the Kolmogorov microscale. If the initial conditions are chaotic, the force field will maintain the turbulence, but not necessarily at the original amplitude. Given a spatially periodic flow (whose maximum scale is fixed) any steady force distribution will eventually give rise to a stationary turbulent flow. This flow is determined by $\mathbf{F}$ and the viscosity ν.

The computations were performed on a $N_x \times N_y \times N_z$ mesh with periodic boundary conditions. The force spectrum $E_f(k)$ is chosen to have contributions from values of $k = \sqrt{2}$, i.e., $\mathbf{k} = (\pm 1, 0, \pm 1)$, $(\pm 1, \pm 1, 0)$, and $(0, \pm 1, \pm 1)$. To generate isotropic turbulence, all the moments of the body force $\mathbf{F}(\mathbf{x})$ would have to satisfy isotropy conditions. This could only be done approximately, by ensuring that moments up to second order of the Fourier coefficients of $\mathbf{F}$, $\hat{\mathbf{f}}$, satisfied isotropy. We also specified that $\overline{\hat{f}_1\hat{f}_2\hat{f}_3} = 0$. $\mathbf{F}$ was chosen to be solenoidal to avoid the generation of large pressure fluctuations. For each $\mathbf{k}$ such that $|\mathbf{k}| = \sqrt{2}$ the amplitude of the forcing was set so that $\sqrt{\hat{f}_i(\mathbf{k})\hat{f}_i^*(\mathbf{k})} = 0.2$. The viscosity ν was .02.

The 3-D Navier-Stokes equations were solved under the above conditions using the spectral code of Rogallo (1981) modified to include the body force $\mathbf{F}$. The primary results of the computation were the time-dependent, 3-D spatial Fourier coefficients of the velocity, $\hat{\mathbf{u}}$, and pressure, $\hat{p}$, fields, defined by

$$u_j(\mathbf{x},t) = \sum_{k_1=-N_x/2}^{N_x/2} \sum_{k_2=-N_y/2}^{N_y/2} \sum_{k_3=-N_z/2}^{N_z/2} \hat{u}_j(\mathbf{k},t)\exp(i\mathbf{k}\cdot\mathbf{x}), \qquad (3.1)$$

where $N_x = N_y = N_z = 64$. A similar definition applies to $\hat{p}(\mathbf{k},t)$.

After storing $\hat{u}_j(\mathbf{k},t)$ at M time intervals Δt_s, the individual time series are filtered with a cosine "window" within the period $T = M\Delta t_s$. Fourier transforms in time yield the 3-D space-time Fourier coefficients $\hat{\hat{u}}_j(\mathbf{k},\omega_m)$, defined by

$$\hat{u}_j(\mathbf{k},t) = \sum_{m=-M/2}^{M/2} \hat{\hat{u}}_j(\mathbf{k},\omega_m)\exp(i\omega_m t), \qquad (3.2)$$

where $\omega_m = 2\pi m/T$.

The time interval Δt_s used for the computation of frequency spectra and time correlations must be small enough to resolve the shortest time variation *at a point*. This minimum Eulerian time scale $\tau_{min}^{(E)}$ is defined by the fast large eddies carrying, at a velocity u_0, the smallest scale eddies ℓ_{Kol} past the point, i.e., $\tau_{min}^{(E)} \sim \ell_{Kol}/u_0$. (It is $Re_\lambda^{-1/2}$ times the magnitude of the Eulerian microscale!) In our computations Δt (based on CFL limitations) turned out to be less than $0.1\tau_{min}^{(E)}$, thus we took $\Delta t_s = 10\Delta t$.

The flow was initiated by suddenly imposing the force field on a given initial random isotropic velocity field $u(x, t = 0)$. It was found that $\overline{u_j^2}$ initially increased or decreased, but eventually oscillated with small amplitude about a stationary value; then the time series were collected to obtain the statistics.

From the Fourier coefficients, space-time spectra and correlations may be computed, using the normalized length (2π) of the box.

(i) The wavenumber-frequency (k, ω) energy spectrum tensor,

$$\Psi_{ij}(k, \omega) = \overline{\hat{u}_i(k, \omega)\hat{u}_j^*(k, \omega)}, \tag{3.3}$$

and similarly for $\Psi_{pp}(k, \omega)$.

(ii) The energy spectrum tensor,

$$\Phi_{ij}(k) = \overline{\hat{u}_i(k, t)\hat{u}_j^*(k, t)}. \tag{3.4}$$

(iii) The energy spectra (summing over spherical shells in wavenumber space; the equivalent integral expressions for a continuum of wavenumbers are given in (1.5)),

$$\mathcal{E}(\bar{k}, \omega) = \sum_{\bar{k}-\frac{1}{2}<|k|\leq\bar{k}+\frac{1}{2}} \Psi_{ii}(k, \omega), \tag{3.5a}$$

$$E(\bar{k}) = \sum_{\bar{k}-\frac{1}{2}<|k|\leq\bar{k}+\frac{1}{2}} \Phi_{ii}(k). \tag{3.5b}$$

(iv) The one-dimensional space-time correlation,

$$R_{ij}(r, \tau) = \sum_k \sum_m \Psi_{ij}(k, \omega)e^{i(k\cdot r+\omega_m\tau)}. \tag{3.6}$$

(v) One-dimensional spectra,

$$\Theta_{ij}(k_1, \omega) = \sum_{k_2} \sum_{k_3} \Psi_{ij}(k, \omega). \tag{3.7}$$

4. Results of the computations

Table 1 gives most of the major statistics of the computed turbulent flow. Note that the Reynolds number based on the Taylor microscale, λ, is only 48, so that we

do not expect to see many features of high Reynolds number turbulence. However the Reynolds number is large enough so that the effects of *advection* of small scales can be investigated. Note also that the turbulent velocity field is not quite isotropic; the lack of isotropy in the moments $(\overline{u_1^2}/\overline{u_2^2} \simeq 1.1)$ for a given realization is of the same order as that usually found in wind tunnel experiments. This probably means that the forcing is not quite isotropic. The ratio of the integral scales L'_{11}, L'_{22}, computed from the one-dimensional correlations $R_{11}(r_1,0,0)$, $R_{22}(r_1,0,0)$, is 1.64. This is less than the value of 2.0 required by isotropy. By comparison the *decaying* strained turbulence computed on a 128^3 mesh by Rogallo (1981) and others was effectively defined to be isotropic at its initiation.

Figure 3 shows the unfiltered and filtered time variations of typical large scale and small scale Fourier coefficients. Note the rather sudden changes in the small scale filtered velocity. The time scale τ_k for such a change is consistent with large scales advecting the small scales $\left(\tau_k \sim 2\pi/(u_0 k)\right)$.

Figure 4a shows the contours of the energy spectrum $\mathcal{E}(k,\omega)$, and figure 4b the various statistics of the variation of $\mathcal{E}(k,\omega)$ with ω for different values of k. The mean and skewness are close to zero. The standard deviation defined by

$$\sigma_{\mathcal{E}} = \left[\int_{-\infty}^{\infty} \omega^2 \mathcal{E}(k,\omega)d\omega \Big/ \int_{-\infty}^{\infty} \mathcal{E}(k,\omega)d\omega\right]^{1/2} \tag{4.1}$$

is described by the formula $\sigma_{\mathcal{E}} = aku_0$, where $u_0 = \sqrt{\frac{1}{3}\overline{u_i^2}}$. The flatness (or kurtosis) is close to 3. Consequently $\mathcal{E}(k,\omega)$ can be approximated by

$$\mathcal{E}(k,\omega) = E(k)\exp\left[-\frac{\omega^2}{2(aku_0)^2}\right] \Big/ \left(\sqrt{2\pi}(aku_0)\right), \tag{4.2}$$

where $a \simeq 0.51$ for $kL_1 \leq 10$, and $a \simeq 0.4$ for $kL_1 \geq 15$ (figure 4c). A similar result for the k-ω energy spectrum for pressure has been found with $a_p \simeq 0.51$ for $kL_1 \leq 10$, and $a_p \simeq 0.45$ for $kL_1 \geq 15$. This result for $\mathcal{E}_{pp}(k,\omega)$ is in approximate agreement with the space-time correlation measurements of Wills (1971) for pressure fluctuations on the wall below a boundary layer.

An important consequence of (4.2) is that by assuming its validity at high Reynolds number we can *calculate* the Eulerian frequency spectra for the velocity $\phi_{11}(\omega)$ and the pressure $\phi_{pp}(\omega)$. Since $\phi_{11}(\omega) = \frac{1}{3}\int \mathcal{E}(k,\omega)dk$ and $E(k) = \alpha_k \epsilon^{2/3} k^{-5/3}$, where α_k is the Kolmogorov constant, we have

$$\phi_{11}(\omega) = \frac{\frac{1}{3}\Gamma(\frac{5}{6})a^{2/3}}{2^{2/3}\sqrt{\pi}}\alpha_k(\epsilon u_0)^{2/3}\omega^{-5/3}.$$

Taking $a = 0.51$ yields

$$\phi_{11}(\omega) = 0.085\alpha_k(\epsilon u_0)^{2/3}\omega^{-5/3}. \tag{4.3}$$
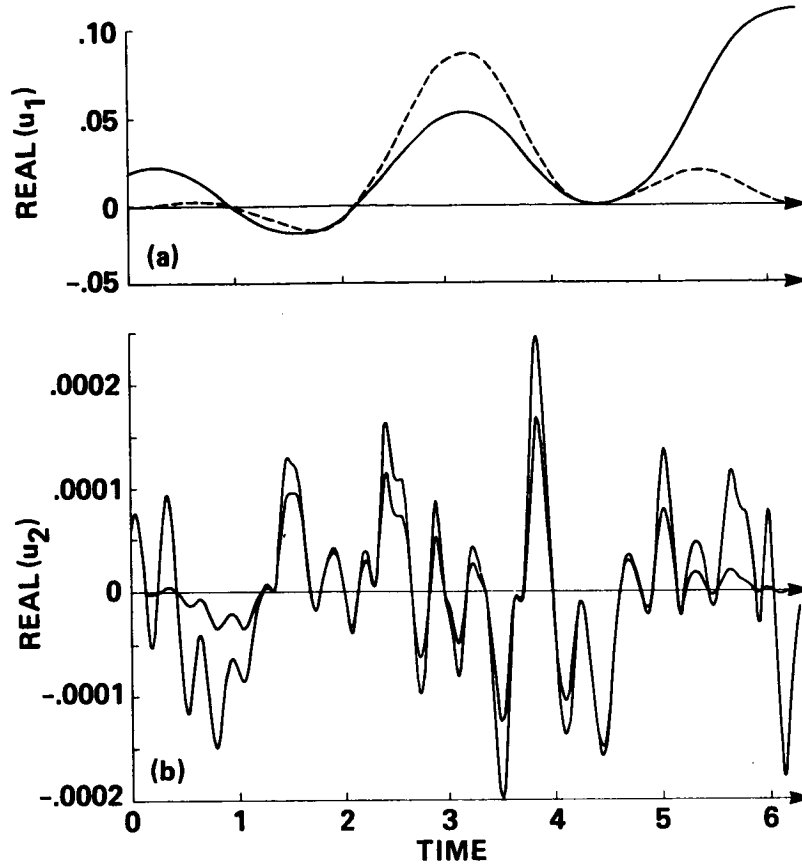
FIGURE 3. Typical time variation of computed Fourier coefficients over the period of time used for frequency calculations. The real part of $\hat{u}_i(k_x, k_y, k_z)$ is shown. The data is filtered to allow processing by discrete Fourier transform methods: the filtering is most apparent at the interval boundaries. (a) data at low wavenumber, $\hat{u}_1(1,1,1)$: ——— unfiltered, - - - - filtered; (b) filtered and unfiltered data at high wavenumber, $\hat{u}_2(4,4,19)$.

Similarly if $E_{pp}(k) = \alpha_{kp}\epsilon^{2/3}k^{-7/3}$ (George *et al.* 1984), we deduce that

$$\phi_{pp}(\omega) = \frac{\Gamma(\frac{7}{6})a_p^{4/3}}{2^{1/3}\sqrt{\pi}}\alpha_{kp}(\epsilon u_0)^{4/3}\omega^{-7/3}.$$

Taking $a_p = 0.51$ yields

$$\phi_{pp}(\omega) = 0.17\alpha_{kp}(\epsilon u_0)^{4/3}\omega^{-7/3}. \tag{4.4}$$

The result (4.3) has the same form as proposed by Tennekes (1975), while (4.4) appears to be new.
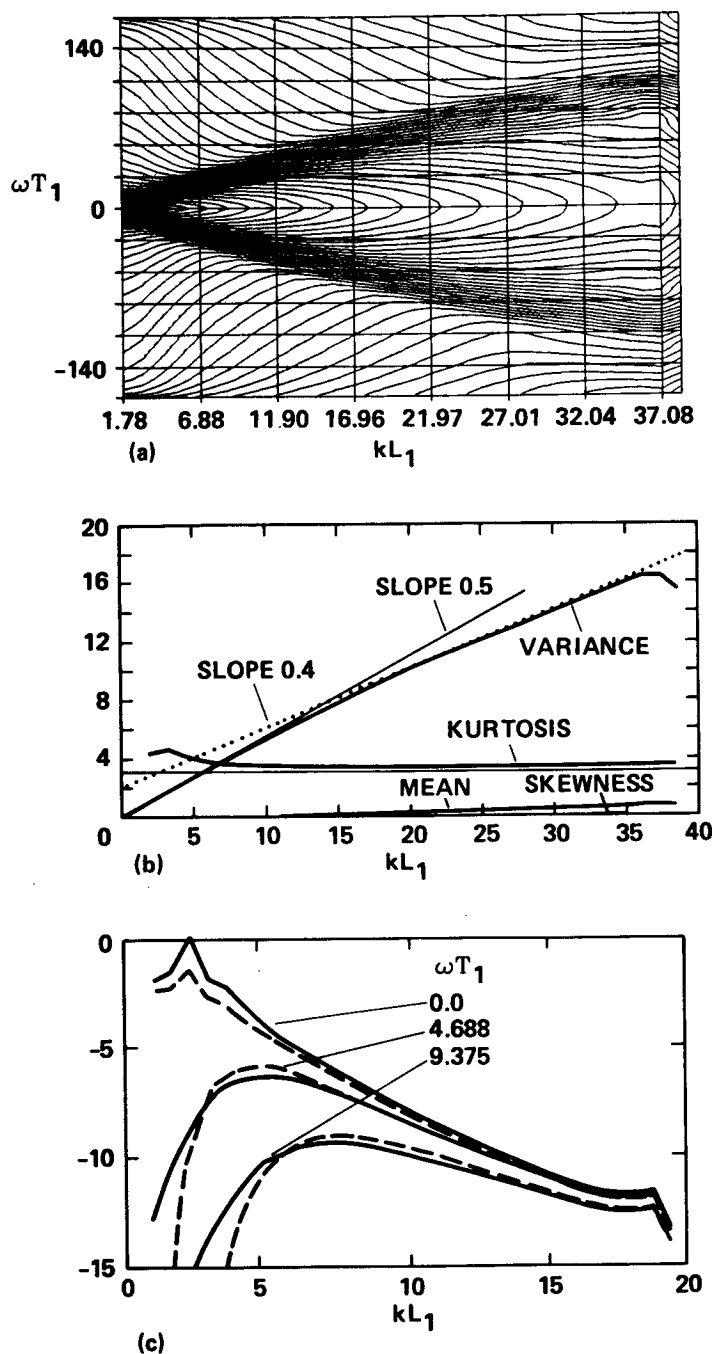
FIGURE 4. Space-time spectrum of energy. (a) Contours of the energy spectrum $\mathcal{E}(k,\omega)$. k is normalized on L_1, and ω on u_0/L_1. Contours are in factors of $\sqrt{10}$. (b) Moments of the frequency distribution of the energy spectrum. Note particularly the variance $\sigma_{\mathcal{E}}$ and the kurtosis $K_{\mathcal{E}}$. (c) Relation between the space-time spectrum and the space spectrum: ——— $\mathcal{E}(k,\omega)$, - - - - (4.2). Results are from a later simulation.
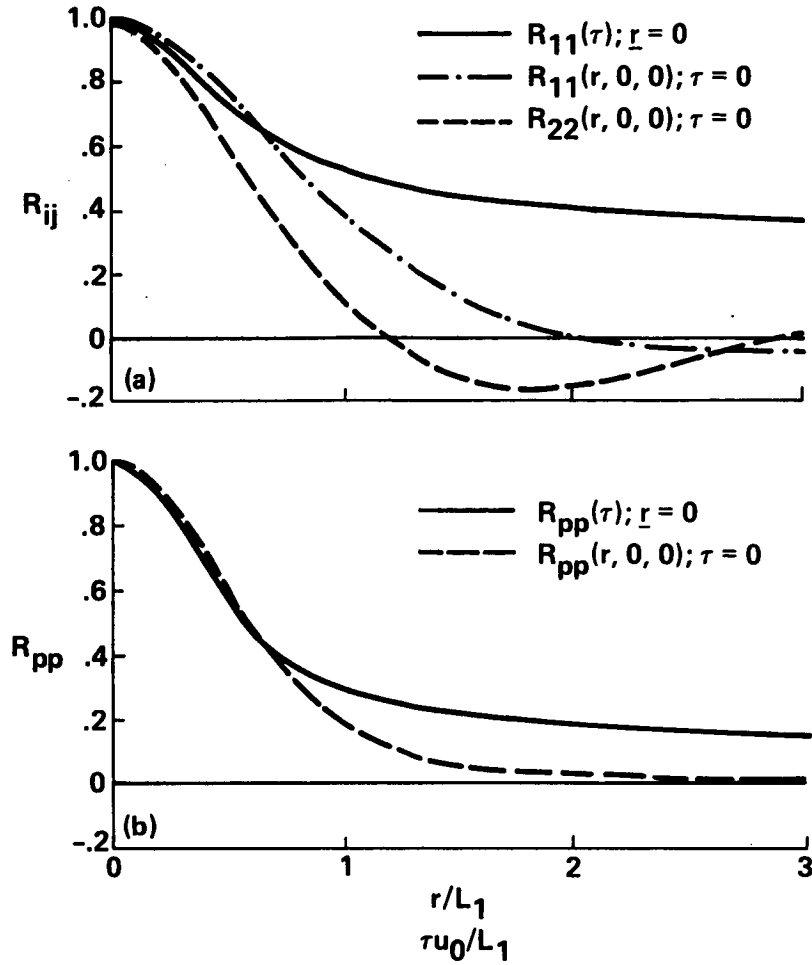
FIGURE 5.   Auto-correlations in space and time for isotropic turbulence: (a) velocity, (b) pressure.

Figure 5 shows the longitudinal and transverse correlations of the velocity and pressure fields. Note that for the velocity, the auto correlation curve $R_{11}(\tau)$ has the same form as the longitudinal spatial correlation, $R_{11}(r_1)$, and is positive, at least for $r_1/L_1 \leq 2.5$. These curves are normalized on an integral length scale derived from the energy spectrum (Monin & Yaglom 1971, p. 55),

$$L_1 = \frac{3\pi}{4} \int_0^\infty k^{-1} E(k) dk \bigg/ \int_0^\infty E(k) dk.$$

For these experiments $L_1/2\pi \simeq 0.25$, i.e., about a quarter of the box size. It is convenient to define length and time scales from these one-dimensional correlations by a similar procedure as in many experiments. Because of the finite box size, the one-dimensional integral scales are estimated from the value of the space or time variable where the correlation is $1/e$ of the variance. So $R_{11}(r = L_{11}^{(1)}) =$
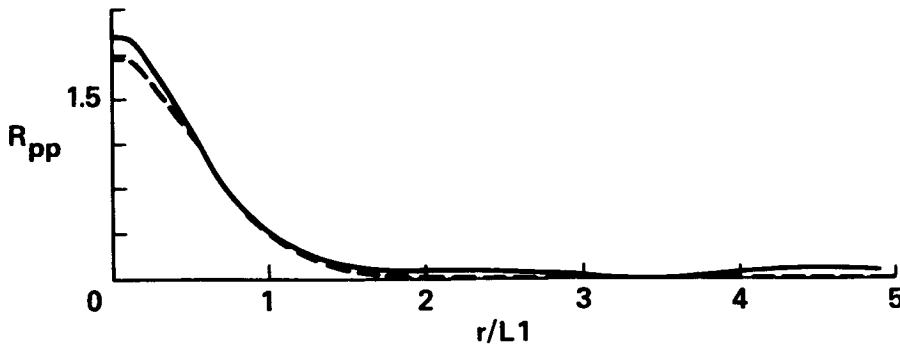
FIGURE 6.   Comparison of the unnormalized pressure auto-correlation with the Hinze/Batchelor theory: —— computed, - - - - theory of Batchelor (1951). Results are from a later simulation.

$(1/e)R_{11}(r = 0)$. On this basis our computed longitudinal length and time scales are

$$L_{11}^{(1)} = 1.25L_1,$$

and

$$T_1^{(E)} \simeq 1.5L_1/u_0.$$

This value of $T_1^{(E)}$ is greater than the value of $1.15L_1/u_0$ obtained by Kyle Squires (private communication) in *decaying* turbulence at $Re_\lambda = 35$. Both estimates are less than the value of 3 inferred by Snyder & Lumley (1971).

The pressure time and space correlations $R_{pp}(\tau)$ and $R_{pp}(r_1)$ are plotted in figure 5b. Note that $R_{pp}(r_1)/R_{pp}(0)$ has a similar form as $R_{22}(r_1,0,0)$ in that the curves become negative when $r/L_1 > 1.5$ for the former and $r/L_1 > 1.3$ for the latter. A plausible physical explanation can be based on the typical form of the large eddies discussed in §2.2. Note that, as for the velocity, the autocorrelation of the pressure fluctuations is positive. An important result is that the mean square pressure fluctuation is given by

$$\overline{p^2}/(\rho u_0^2)^2 \simeq 1.0.$$

This ratio is higher than the estimates made by Batchelor (1951) for low Reynolds number wind tunnel turbulence (0.34), and for high Reynolds number turbulence by Hinze (1975) (0.5), and George et al. (1984) (0.42).

A significant agreement with the theory of Batchelor (1951) is shown in figure 6 where the theoretical value of $R_{pp}(r_1)$ (using $R_{11}(r_1)$ from a later simulation having lower anisotropy) is compared with computational results. The agreement is quite good except near $r = 0$.

The final results, figure 7, were the power spectra E_1 to E_4 for the four quantities: $\nabla p + (\mathbf{u} \cdot \nabla)\mathbf{u}$, ∇p, $\frac{\partial \mathbf{u}}{\partial t}$, and $\frac{D\mathbf{u}}{Dt}$. For high Reynolds number turbulence, where the viscous terms are small, the first and third spectra should be equal and also the
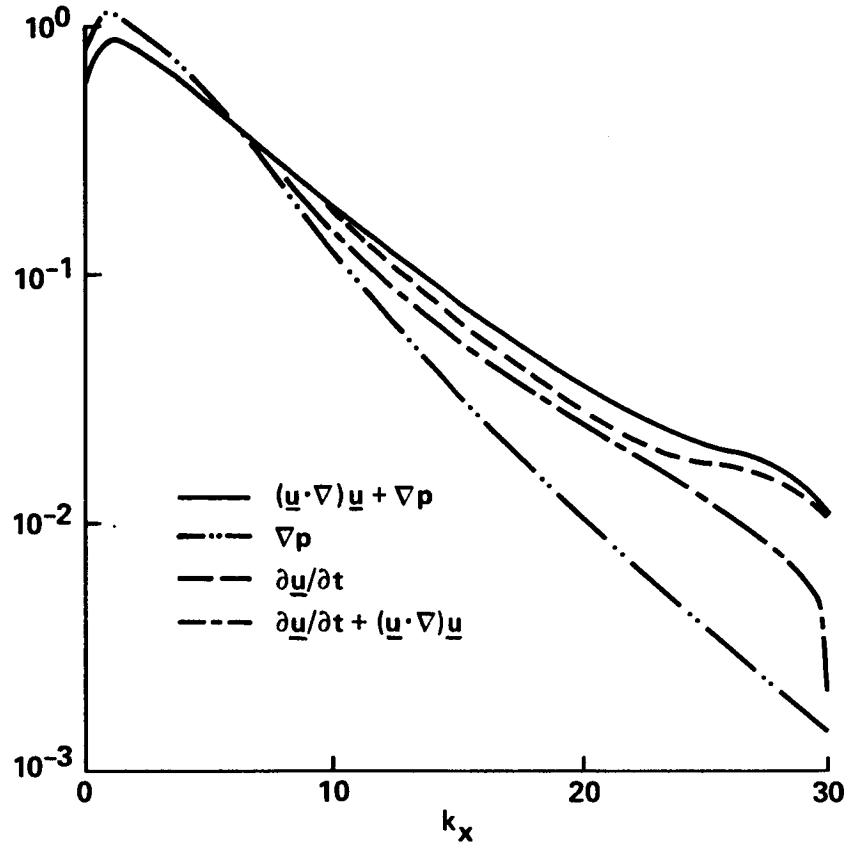
FIGURE 7. Power spectra of the terms in the Navier-Stokes equations.

second and fourth. Furthermore if the eddies are advected past an observer faster than they evolve by nonlinear or viscous processes, then following Tennekes (1975) $\frac{\partial u}{\partial t}$ and $E_3(k)$ should be much greater than $\frac{Du}{Dt}$ and $E_4(k)$ for large k. However the computations showed that E_3 and E_4 were of comparable magnitude (within 20%). But we did find that the ratio E_1/E_2 increased from about 1 to 8 as kL_1 increased from 8 to 36. This is consistent with the advective contribution to $(u \cdot \nabla)u$ being much greater than the local nonlinear contribution (which largely determines ∇p). We also found that E_4 (i.e. $\frac{Du}{Dt}$) was about 2 or 3 times as great as E_2 (∇p), even for $kL_1 \simeq 20$, showing that the contribution of viscous stresses to E_4 and $\frac{Du}{Dt}$ is dominant.

These viscous stresses are probably the explanation for why E_3 is of the same order as E_4. But if the viscous stresses are so relatively large, is this consistent with the small eddies being apparently advected by the large eddies? A possible explanation is that the small eddies are like slowly decaying vortices advected by the large eddies. Within the small eddies the viscous term $\nu\nabla^2 u$ may be *greater* than the advective acceleration term $(U \cdot \nabla)u$. But the time for the decay of say an extended line vortex with core size k^{-1} is *much longer* than $(\nu k^2)^{-1}$. Therefore we

draw the surprising conclusion that, for turbulence in this Reynolds number range, the locations of the viscous stresses is associated with relatively large values of $\frac{\partial u}{\partial t}$ suggesting that first there is not necessarily a local instantaneous balance between the large straining and dissipation, and second the small eddies decay as they are advected by the large eddies. Perhaps the generation of small scale turbulence occurs on *shorter time scales* than its decay.

5. Conclusions and Further Work

1. The central hypothesis to be tested in this project of large scale eddies (or Whorls) advecting (or carrying) small scale eddies (or whorls), was supported, if not completely confirmed. [Perhaps we should change one word in L.F. Richardson's rhyme: replace 'Big whorls *have* little whorls ...' with '... *carry* ... '!]

2. The computations raised numerous questions. To clarify the advection process we need to compute the probability distribution of the large eddies, and for the pressure correlations the probability distribution of the strain rates. We found that the pressure correlation agrees fairly well with the Hinze/Batchelor theory which is based on a quasi-normality assumptions for velocity moments.

3. In these simulations the turbulence was driven by a steady forcing function **F**. The generality of the results is not clear until we explore further the effect of the magnitude and spectral distribution of **F**. Also, do the initial conditions matter? However there are encouraging signs of agreement with other kinds of simulations and with measurements. These comparisons need to be pursued.

4. The computations have given rise to some important new physical ideas; the connection between the advection of small eddies and the advection of small scale pressure fluctuations; the structure of the large scale pressure field; and, finally, perhaps some insight into the temporal pattern of the movement and decay of small scale eddies.

5. There will be several applications of these computations to other areas of turbulence research, including practical applications. It will be possible to compute the effects of turbulence on the generation of internal and surface waves, and to develop representations of the space-time structure of turbulence, either as a 3-D stochastic field, or by means of conditional eddy techniques. Such representations are being used to compute the motions of particles in turbulent flows, where it is too expensive to use direct simulations.

Table 1

Numerical and physical parameters

Number of mesh points: 64^3

Number of time samples: 288

Total disk storage used: 604 Mbytes

Boxsize: 2π

Force field: $F' = \left[\frac{1}{(2\pi)^3} \int |\mathbf{f}|^2 d\mathbf{x}\right]^{1/2} = 0.69$

Kinematic viscosity: $\nu = .02$

Properties of flow field

Velocity field: $\frac{1}{2}\overline{u_i^2} = 1.94$

$$u_0 = \left(\frac{1}{3}\overline{u_i^2}\right)^{1/2} = 1.14$$

Lengthscale: $L_1 = \frac{3\pi}{4} \int_0^\infty k^{-1} E(k)dk / \int_0^\infty E(k)dk = 1.25$

Taylor microscale: $\lambda = \left[5\int_0^\infty E(k)dk / \int_0^\infty k^2 E(k)dk\right]^{1/2} = 0.84$

Kolmogorov microscale: $\ell_{\mathrm{Kol}} = \left(\nu^3/\epsilon\right)^{1/4} = 0.064$

Reynolds number: $Re_\lambda = u_0\lambda/\nu = 48$

Dissipation rate: $\epsilon/(u_0^3/L_1) = (15/Re_\lambda)(L_1/\lambda) = 0.47$

Skewness: $\frac{1}{3}\sum_{i=1}^{3} \overline{\left(\frac{\partial u_i}{\partial x_i}\right)^3} / \left[\overline{\left(\frac{\partial u_i}{\partial x_i}\right)^2}\right]^{3/2} = -0.50$

Normalized force: $F'L_1/u_0^2 = 0.66$

'Integral' length scales estimated from 1-D correlations:

Velocity: $L_{11}^{(1)}/L_1 = 1.25, \qquad L_{22}^{(1)}/L_1 = 0.76$

Pressure: $L_{pp}^{(1)}/L_1 = 0.75$

'Integral' time scales: $T_1^{(E)}/(L_1/u_0) = 1.5$

$$T_2^{(E)}/(L_1/u_0) = 1.3$$

REFERENCES

BATCHELOR, G. K. 1951 *Proc. Camb. Phil. Soc.*, **47**, 359-374.

CARRUTHERS, D. J. & HUNT, J. C. R. 1986 *J. Fluid Mech.*, **165**, 475-501.

DURBIN, P. A. & HUNT, J. C. R. 1980 *J. de Macanique*, **19**, 679-95.

FAVRE, A. J., CRANGLIO, J. J. & DUMAS, R. 1956 *J. Fluid Mech.*, **2**, 313-342.

GEORGE, W. K., BEUTHER, P. D. & ARNDT, R. E. A. 1984 *J. Fluid Mech.*, **148**, 155-191.

HINZE, J. O. 1975 Turbulence . *McGraw-Hill, New York*.

LESLIE, D. C. 1981 Developments in the Theory of Turbulence . *Oxford University Press*.

MONIN A. S. & YAGLOM, A. M. 1971 Statistical Fluid Mechanics, vol. 2 . *M.I.T. Press*.

MOSER, R. D. & MOIN, P. 1984 Direct numerical simulations of curved channel flow . *NASA TM 85974*.

MOIN, P. 1987 *AIAA paper 87-0194.*

MOIN, P., ADRIAN, R. J. & KIM, J. 1987 Stochastic estimation of the structure in turbulent channel flow . 6th *Symposium on Turbulent Shear Flows, Toulouse.*

ROGALLO, R. S. 1981 Numerical experiments in homogeneous turbulence . *NASA TM 81315.*

SABOT, J. & COMTE-BELLOT, G. 1976 *J. Fluid Mech.*, **74**, 767-796.

SHLIEN, D. J. & CORRSIN, S. 1974 *J. Fluid Mech.*, **62**, 255-271.

SNYDER, W. H. & LUMLEY, J. L. 1971 *J. Fluid Mech.*, **48**, 41-71.

TENNEKES, H. 1975 *J. Fluid Mech.*, **67**, 561.

TENNEKES, H. & LUMLEY, J. L. 1979 A first course in turbulence 2nd edition . *M.I.T. Press*

TOWNSEND, A. A. 1976 Structure of turbulent shear flow 2nd edition . *Cambridge University Press.*

TURFUS, C. & HUNT, J. C. R. 1987 In *Advances in Turbulence*, ed. G. Comte-Bellot & J. Mathieu.

WILLS, J. A. B. 1971 *J. Fluid Mech.*, **20**, 417-432.

Study of one-dimensional spectral dynamic equations of the Reynolds stresses in homogeneous anisotropic turbulence: Application to split-spectrum modeling

By R. Schiestel[1]

The CTR numerical data base generated by direct simulation of homogeneous anisotropic turbulence has been used to calculate all of the terms in the spectral balance equations for the turbulent Reynolds stresses. The aim is not only to test the main closure assumptions used in the split-spectrum model, but also to try to devise improved hypotheses deduced from the statistical information.

1. Description of the Split-Spectrum Model

1.1 Framework

The split-spectrum approach is a very simple way to introduce some spectral information into one-point closure formalisms. The starting point is the spectral equation for the Reynolds stress tensor $\Phi_{ij}(\mathbf{k})$ originating from equations for the two-point velocity correlations. The one-dimensional spectral equations are then obtained by spherical integration in Fourier space. The split-spectrum scheme is developed (Launder & Schiestel 1978, and Schiestel 1987) on the basis of partial integration of the spectral equations over wavenumber intervals. The transport equations for the partial stresses (figure 1) can be written formally:

$$\frac{dR_{ij}^{(m)}}{dt} = \underbrace{P_{ij}^{(m)}}_{A} + \underbrace{F_{ij}^{(m-1)} - F_{ij}^{(m)}}_{B} + \underbrace{\Psi_{ij}^{(m)}}_{C} - \underbrace{D_{ij}^{(m)}}_{D} \; , \tag{1}$$

where

$$R_{ij}^{(m)} = \int_{k_{m-1}}^{k_m} \varphi_{ij}(k)dk, \quad \text{and} \quad \varphi_{ij}(k) = \oint \Phi_{ij}(\mathbf{k})dA(k). \tag{2}$$

This multiple component splitting is such that the usual Reynolds stress R_{ij} is given by

$$R_{ij} = \sum_{m=1}^{M} R_{ij}^{(m)}. \tag{3}$$

The different terms on the right side of (1) represent the following processes in spectral slice m:

---

1 Institut de Mecanique Statistique de la Turbulence
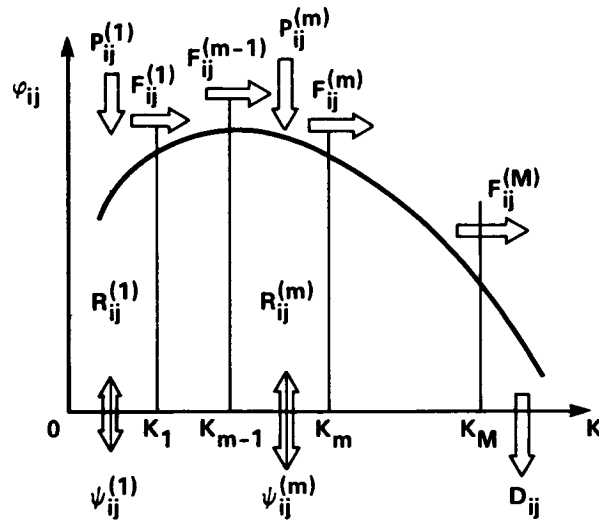
FIGURE 1. Decomposition of wave space into discrete slices.

A) production of $R_{ij}^{(m)}$ by mean velocity gradients;

B) net turbulent flux into the slice including inertial cascade transfer, transfer due to mean strain, and the effect of time varying k_m;

$$F_{ij} = {}_N F_{ij} + {}_L F_{ij} - \varphi_{ij} \frac{\partial k_m}{\partial t}$$

C) redistribution by pressure-velocity correlations including the fast and slow parts;

D) viscous dissipation.

The definition of the time varying wavenumbers k_m, which is related to the energy spectrum, and the hypotheses on energy transfer across the spectrum are used to derive transport equations for the energy flux $F = \frac{1}{2} F_{jj}$. In practical applications M is usually 2 or 3 but here, for the purpose of testing hypotheses, we consider the wavenumber intervals given by the discrete mesh of the simulation.

1.2 Hypotheses

All of the main closure hypotheses can be tested by using the simulation data. These are:

• rapid pressure-strain term:

   The relaxation-of-production approximation is

$$_L \Psi_{ij}^{(m)} \approx -C_2 \left(P_{ij}^{(m)} - \frac{P_{ll}^{(m)}}{3} \delta_{ij} \right) \tag{4}$$

• slow pressure-strain term:

The local-return-to-isotropy approximation is

$$_N\Psi_{ij}^{(m)} \approx -C_1 \frac{\epsilon}{K}(R_{ij}^{(m)} - \frac{R_{ll}^{(m)}}{3}\delta_{ij}) \tag{5}$$

Although this looks like Rotta's model, the behavior can be very different.

- inertial transfer of energy:

The Kovasznay model for the transfer of energy is

$$_N\mathcal{F} \approx \gamma_K \mathcal{E}^{3/2} k^{5/2} \tag{6}$$

where $\mathcal{E}(k) = \frac{1}{2}\varphi_{jj}(k)$

- energy transfer due to mean strain, $\Lambda_{ij} = \partial \overline{u_i}/\partial x_j$:

$$_L\mathcal{F} \approx -\frac{2k}{5}\varphi_{ij}\Lambda_{ij} \tag{7}$$

- slow transfer for stress components:

$$_N F_{ij} \approx {}_N\mathcal{F}(a\frac{\varphi_{ij}}{\mathcal{E}} + \frac{2(1-a)}{3}\delta_{ij}) \tag{8}$$

- rapid transfer for stress components:

A proposal of D. Jeandel and J. Mathieu is

$$_L F_{ij} \approx \frac{k}{20}[\varphi_{li}(\Lambda_{lj} + \Lambda_{jl}) + \varphi_{lj}(\Lambda_{li} + \Lambda_{il})] - \frac{k}{5}\varphi_{lm}\Lambda_{lm}\delta_{ij} \tag{9}$$

These closure hypotheses are among the simplest ones that can be formulated. Our goal is to use the results of the simulations to determine the accuracy of these models and, when the models must be improved, to suggest the form of more sophisticated approximations.

2. Use of the simulation data

2.1 Methodology

The simulation database provides the Fourier transform of the velocity field $\widehat{u}_i(\mathbf{k})$ for one realization of the flow field. The equation for the Reynolds stress spectrum tensor $\Phi_{ij}(\mathbf{k}) \equiv \widehat{u}_i(\mathbf{k})\widehat{u}_j(-\mathbf{k})$ can be written in terms of velocity Fourier modes:

$$\frac{\partial\Phi_{ij}}{\partial t} + \underbrace{\Lambda_{il}\Phi_{lj} + \Lambda_{jl}\Phi_{il}}_{P_{ij}} - \underbrace{\frac{2\Lambda_{lm}k_l}{k^2}(k_i\Phi_{mj} + k_j\Phi_{im}) - \Lambda_{lm}\frac{\partial}{\partial k_m}(k_l\Phi_{ij})}_{_L\Pi_{ij} \qquad\qquad _LT_{ij}}$$

$$-\underbrace{\frac{ik_mk_l}{k^2}[k_i\widehat{u}_j(-\mathbf{k})\widehat{u_lu_m}(\mathbf{k}) - k_j\widehat{u}_i(\mathbf{k})\widehat{u_lu_m}(-\mathbf{k})]}_{_N\Pi_{ij}}$$

$$+\underbrace{ik_m[\widehat{u}_j(-\mathbf{k})\widehat{u_iu_m}(\mathbf{k}) - \widehat{u}_i(\mathbf{k})\widehat{u_ju_m}(-\mathbf{k})]}_{_NT_{ij}} + \underbrace{2\nu k^2\Phi_{ij}}_{\epsilon_{ij}} = 0 \tag{10}$$

R. Schiestel
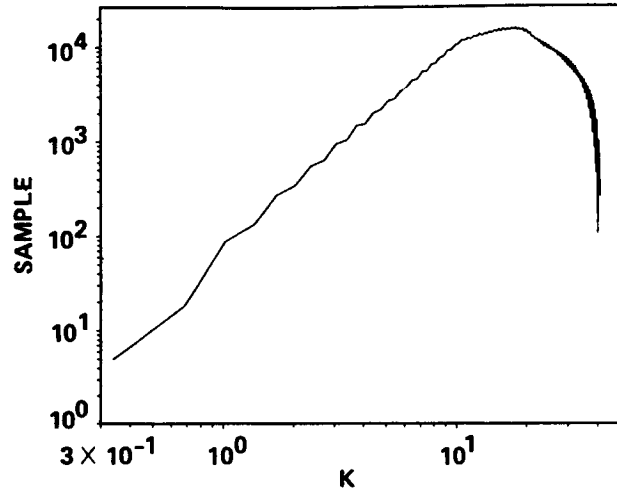
FIGURE 2. Typical variation of statistical sample with scale. Case PXB4 is shown.

One-dimensional spectra are then obtained by summing over the sample within spherical shells. Thus we readily get the necessary terms to test hypotheses (4) to (9).

$$R_{ij}^{(m)} = \sum_{(m)} \Phi_{ij} \quad {}_N\Psi_{ij}^{(m)} = \sum_{(m)} {}_N\Pi_{ij} \quad {}_NF_{ij}^{(m)} = \sum_{(m)} {}_NT_{ij}$$
$$P_{ij}^{(m)} = \sum_{(m)} P_{ij} \quad {}_L\Psi_{ij}^{(m)} = \sum_{(m)} {}_L\Pi_{ij} \quad {}_LF_{ij}^{(m)} = \sum_{(m)} {}_LT_{ij} \qquad (11)$$

This treatment has been carried out using an adaptation of Rogallo's (1981) computer code. The program computes the balance of each component of the Reynolds stress spectrum tensor, the sums (11), and performs the comparisons (4) to (9) using flow fields from the stored database.

The transfer term, ${}_LT_{ij}$ in (10), is difficult to compute because derivatives with respect to wavenumber can not be accurately calculated within the context of the simulation. In the simulation, a coordinate system moving with the mean flow was used to remove such derivatives. The problem of evaluating ${}_LT_{ij}$ has been avoided by considering the gross flux ${}_LF_{ij}$. Using

$$\int {}_LT_{ij}d\mathbf{k} = \oint \Lambda_{lm} \frac{k_l k_m}{k} \Phi_{ij} dA(k)$$

we find

$$_LF_{ij}^{(m)} = \frac{1}{\delta k} \sum_{(m)} \Lambda_{ln} \frac{k_l k_n}{k} \Phi_{ij}$$

The simulation shell sample varies with wave number (figure 2). For low wave numbers the sample increases as k^2 (spherical shell), but due to the anisotropy of the wave-space grid the sample decreases at high wave numbers even before the limit of resolution is reached. In this case, we do not obtain true spherical averages because some directions are privileged.

2.2 Test cases.

In order to reach some degree of generality, it is necessary to consider a number of different flows. The following test cases from the CTR database have been considered:

uniform shear
   RR1288
isotropic decay
   HIE1
simple strains and relaxation from them
   HIA9 PXB4 B4R1 B4R6 (plane strain)
   HIC6 AXL6 L6R1 L6R6 (axisymmetric contraction)
   HID6 P6R1 P6R6   (axisymmetric expansion)
successive strains and relaxation from them
   M2V1 M2V1R1 M2V1R5
   K3V1 K3V1R1 K3V1R5
   M2U1 M2U1R1 M2U1R5

The shear case is from Rogers et al (1986) and the remaining fields are from Lee & Reynolds (1985).

3 Comparisons and discussion

3.1 Homogeneous shear

The spectra of the various terms in the transport equation for $\overline{u^2}$ are shown in figure 3a. All of the terms have been filtered using a $(\frac{1}{4}, \frac{1}{2}, \frac{1}{4})$ molecule to reduce noise, however the rapid transfer term remains rather noisy.

Figure 3b compares the gross-flux, linear "fast" part and non-linear "slow" part to their approximations given by (6) and (7). The Kovasznay hypothesis overestimates the non-linear transfer (possibly due to the lack of an inertial range in the simulation). The free model constants are taken as unity here and in the following figures and we direct our attention to how well the spectral shape of the model conforms to that of the modelled term. All values are normalized using the appropriate powers of kinetic energy and dissipation rate.

The fast pressure term and the slow pressure term are compared in figure 3c to their approximations given by (4) and (5). The results are encouraging.

The linear transfer is overestimated by (9), but the sign of the approximation is generally correct and the shape of the curve is acceptable. The model (8) for the slow-transfer tensor approximation, with $a = 1$, is often nearly satisfied. This is illustrated for the $\overline{u^2}$ component in figure 3d. Figure 3e shows the ratio of the right side of (4) to the left side and can be interpreted as the variation of C_2 with wavenumber and with stress component. The jumps simply reflect the fact that the zero crossings of the data are not predicted exactly by the model. For components $\overline{u^2}$, $\overline{v^2}$, $\overline{w^2}$, and $\overline{uv}$ the mean value of $C_2 = 0.6$ that is frequently used in classical one-point closure can be inferred. The same ratio for (5) is presented in figure 3f. We see that the coefficient C_1 increases continuously with k, implying a more rapid return to isotropy at high wavenumbers.
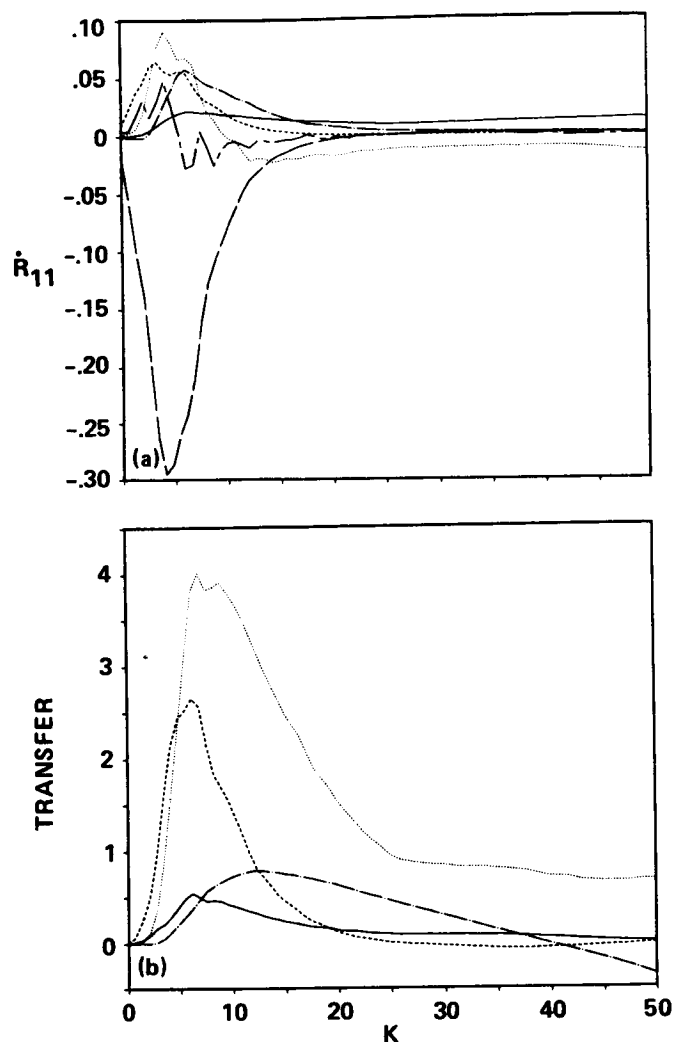
FIGURE 3. Homogeneous shear turbulence. Case RR1288 is shown. (a): budget for R_{11}; —--- production, ---- fast pressure-strain, —·— slow pressure-strain, —··— fast transfer, ······ slow transfer, ——— dissipation. (b): gross energy transfer, fast part; ——— data, ---- model (7), slow part; —·— data, ······ model (6).

3.2 Simple strains.

Comparisons like those above are presented in figures 4a to 4d for the case of a plane strain. The models for the pressure terms compare favorably, but the model (8) seems inadequate for the slow transfer terms. Similiarly, the model (6) overestimates the nonlinear transfer of energy. The coefficients C_1 and C_2 both increase slowly with k and are different for each component of the tensor.

3.3 Successive strains and relaxation
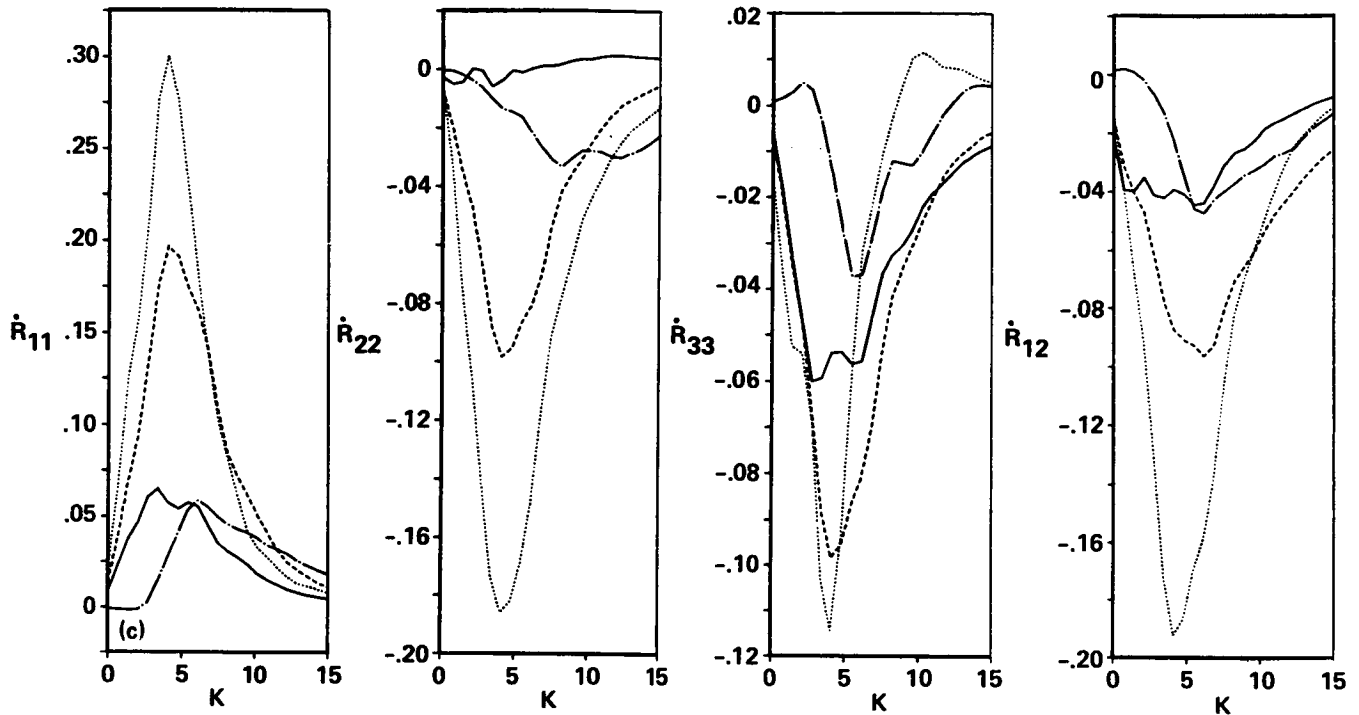
FIGURE 3 (CONTINUED). (c): pressure-strain terms, fast part; ——— data, — — — — model (4), slow part; — · — data, ········· model (5).

This is an interesting case and is particularly relevant for the multiple-scale approach. The M2V1 flow (figure 5) is the result of a strong axisymmetric contraction followed by a plane strain. The M2V1R1 flow (figure 6) is the relaxation of M2V1 when the straining ceases. Most of the remarks in section 3.2 are still applicable. In this particular case the simulation exhibits an increase of the Reynolds stress anisotropy at the beginning of decay. This paradoxical effect can be produced by (5) when the coefficient C_1 increases with wavenumber (this occurs for example in figure 6b) and when the initial spectral distribution is such that anisotropies at large and small scales are more or less compensating (this occurs in M2V1). Then a rapid return to isotropy of the fine scales reveals the anisotropy of the larger scales which was hidden temporarily (Schiestel 1986). Such a behavior cannot be obtained with one-point models using the Rotta hypothesis. Some spectral information is necessary to describe this phenomenon.

4. Concluding remarks.

Numerical simulations of turbulent flows provide a large amount of data, a thought provoking wealth of information.

The main advantage of this type of comparison is that a great variety of flows can be considered, and this is necessary to test closure hypotheses. Moreover various
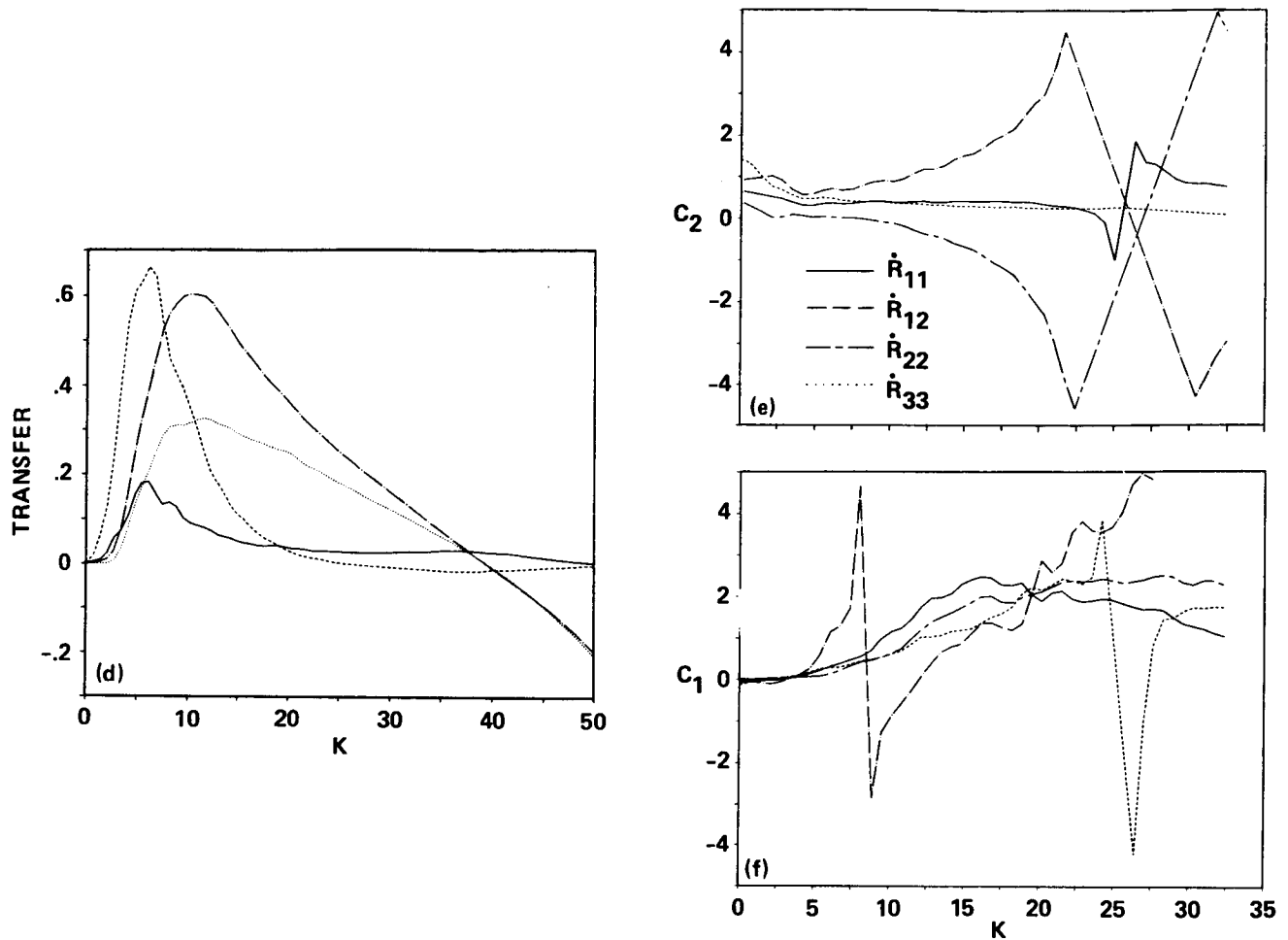
FIGURE 3 (CONCLUDED).   (d): gross transfer of R_{11}, fast part; ——— data, – – – – model (9), slow part; — $\cdot$ — data, $\cdots\cdots$ model (8). Variation of the pressure-strain model coefficients for each component of R_{ij}: (e) fast part, (f) slow part.

initial conditions can be introduced in the calculation, even if they are not experimentally feasible. Various statistical information can be easily extracted from the data. All the terms in the spectral equations can be calculated, and this is particularly interesting for terms involving pressure correlations that cannot be measured. The limited Reynolds numbers of the simulations and the statistical noise caused by a small sample, particularly at the large scales, causes some difficulty in the interpretation of the results, but the method of approach proved to be a powerful tool for testing and improving spectral closures.

REFERENCES

LAUNDER, B.E. AND SCHIESTEL, R. 1978 *C.R. Academy of Science, Paris.* **t. 286,** **ser A,** 709-712.

SCHIESTEL, R. 1987 *Phys. of Fluids,* **30(3)**, 722-731.

LEE, M.J. AND REYNOLDS, W.C. 1985 Numerical experiments on the structure of homogeneous turbulence . *Stanford University Report TF-24.*

ROGERS, M.M., MOIN, P. AND REYNOLDS, W.C. 1986 The structure and modeling of the hydrodynamic and passive scalar fields in homogeneous turbulent shear flow . *Stanford University Report TF-25.*

ROGALLO, R.S. 1981 Numerical experiments in homogeneous turbulence . *NASA TM 81315.*

SCHIESTEL, R. 1986 *C.R. Academy of Science, Paris.* **t. 302, ser II, no.11,** 727-730.
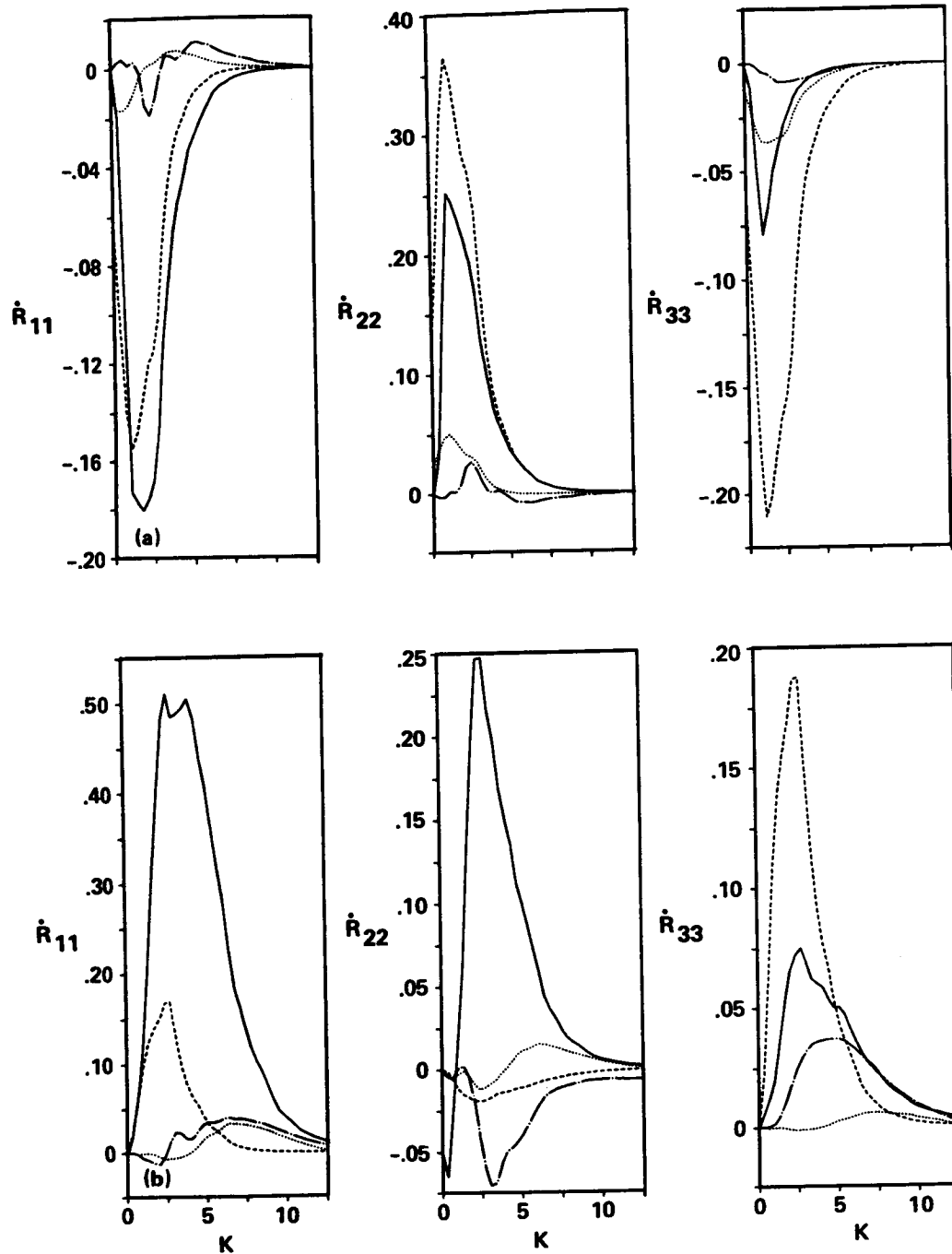
FIGURE 4. Homogeneous turbulence subjected to plane strain. Case PXB4 is shown. Evaluation of models for the pressure-strain and transfer terms. (a): pressure-strain, fast part; ——— data, ———— model (4), slow part; ——·— data, ········ model (5). (b): transfer, fast part; ——— data, ———— model (9), slow part; ——·— data, ········ model (8).
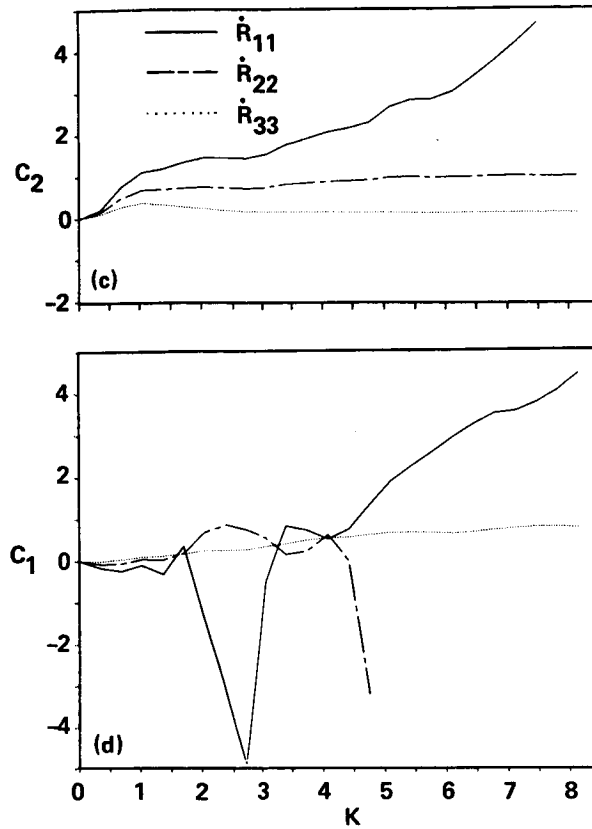
FIGURE 4 (CONCLUDED). Variation of the pressure-strain model coefficient for each component of R_{ij}: (c) fast part, (d) slow part.
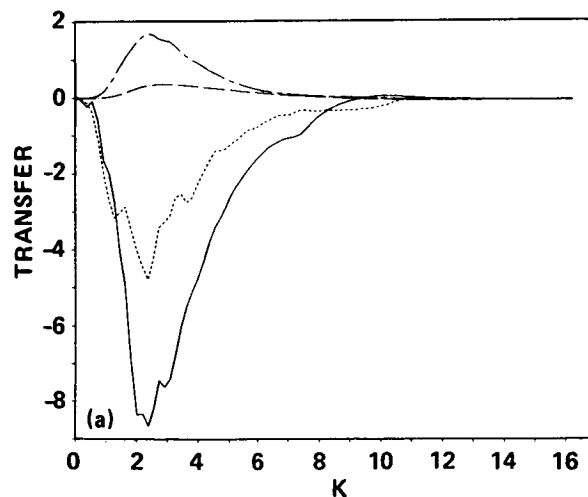
FIGURE 5. Homogeneous turbulence subjected to complex strains. Case M2V1 is shown. (a): gross energy transfer, fast part; ———— data, - - - - model (7), slow part; —·—— data, ——— model (6).
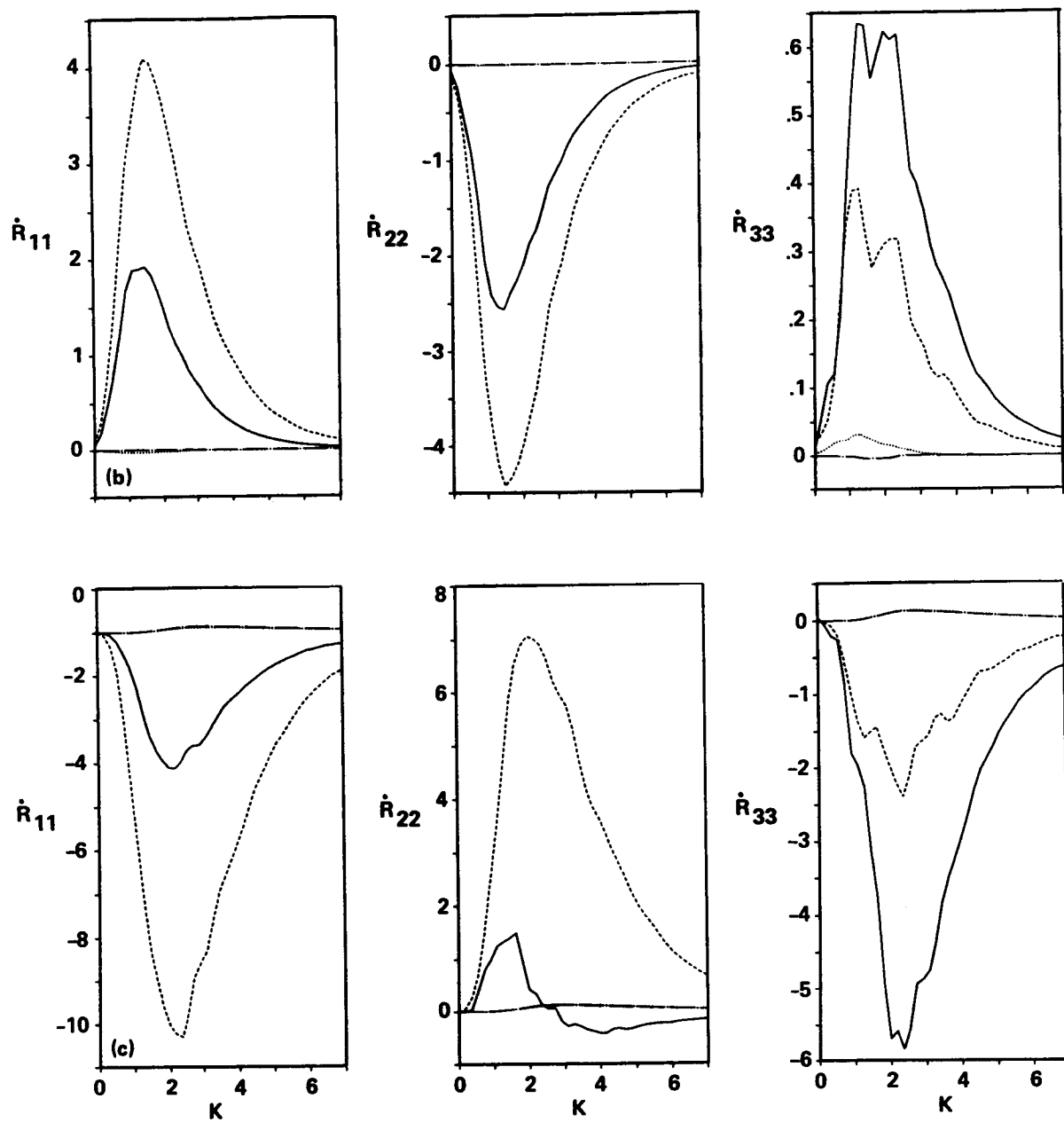
FIGURE 5 (CONTINUED). Evaluation of models for the pressure-strain and transfer terms. (b): pressure-strain, fast part; ——— data, - - - - model (4), slow part; — · — data, ········ model (5). (c): transfer, fast part; ——— data, - - - - model (9), slow part; — · — data, ········ model (8).
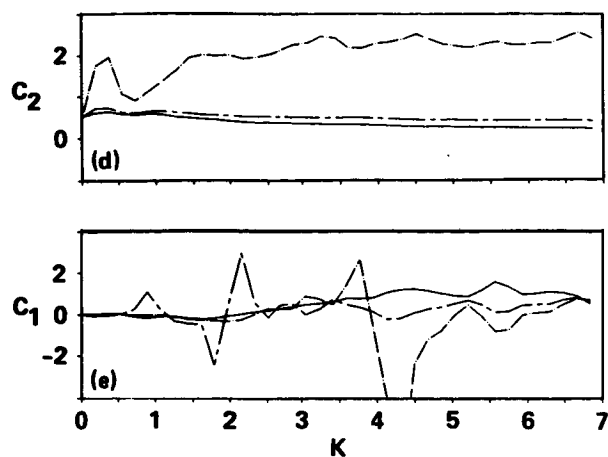
FIGURE 5 (CONCLUDED). Variation of the pressure-strain model coefficient for each component of R_{ij}: (d) fast part, (e) slow part. ——— R_{11} term, — — — R_{22} term, — · — R_{33} term.
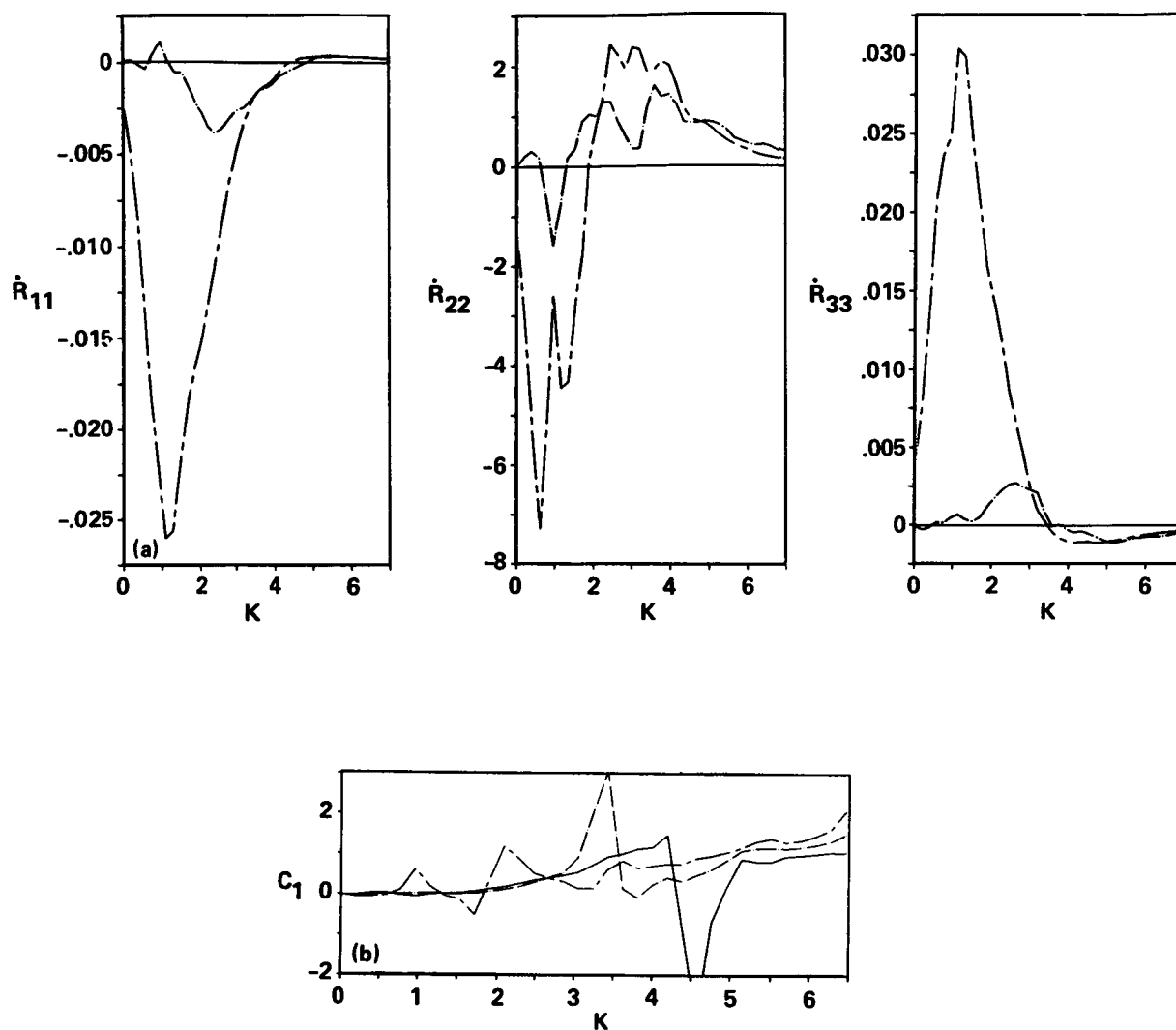
FIGURE 6. Relaxation of homogeneous turbulence subjected to complex strains. Case M2V1R1 is shown. (a): Slow pressure-strain; —·— data, — — — model (5). (b): Variation of the slow pressure-strain model coefficient for each component of R_{ij}: ——— R_{11} term, — — — R_{22} term, —·— R_{33} term.

Modeling scalar flux and the energy and dissipation equations

By A. Yoshizawa[1]

Closure models derived from the Two-Scale-Direct-Interaction Approximation have been compared with data from direct simulations of turbulence. In the working session, we have restricted our attention to 1) anisotropic scalar diffusion models, 2) models for the energy dissipation equation, and 3) models for energy diffusion.

---

1. Anisotropic eddy-diffusivity model for turblent scalar flux

The scalar flux is represented by a gradient diffusion model

$$\overline{u_i'\theta'} = -D_{ij}\frac{\partial\bar\theta}{\partial x_j}$$

with a diffusivity tensor D_{ij} that depends on the mean strain and vorticity tensors (Yoshizawa, 1985).

$$D_{ij} = C_K\frac{k_\theta^2\epsilon}{\epsilon_\theta^2}\delta_{ij} - \frac{k_\theta^3\epsilon}{\epsilon_\theta^3}[C_{KA}(\frac{\partial\bar u_i}{\partial x_j} + \frac{\partial\bar u_j}{\partial x_i}) + C'_{KA}(\frac{\partial\bar u_i}{\partial x_j} - \frac{\partial\bar u_j}{\partial x_i})].$$

The accuracy of the model is shown in table 1 by comparison at several times t of the actual fluxes with the modeled fluxes in a direct numerical simulation of homogeneous turbulence in uniform shear S having a uniform scalar gradient. The scalar diffusivities D_{22}, D_{12}, and D_{21} are represented well by the model but D_{33} and D_{11} are not. The performance of the model might be improved by the inclusion of unsteady terms in C_K suggested by the TSDIA analysis.

$$C_K \longrightarrow C_K + a\frac{1}{\epsilon_\theta}\frac{\partial k_\theta}{\partial t} + b\frac{k_\theta}{\epsilon_\theta^2}\frac{\partial\epsilon_\theta}{\partial t} + c\frac{k_\theta}{\epsilon_\theta\epsilon}\frac{\partial\epsilon}{\partial t}$$

Table 1. Evaluation of the Scalar Diffusion Model from case C128U of Rogers, Moin, and Reynolds (1986)
($C_K = .187$, $C_{KA} = .132$, $C'_{KA} = .06$)

St	D_{22}		$-D_{12}/D_{22}$		$-D_{21}/D_{22}$		D_{33}/D_{22}		D_{11}/D_{22}	
	model	data	model	data	model	data	model	data	model	data
8	.068	.090	1.97	2.38	1.32	1.20	.737	1.98	.936	5.58
10	.102	.108	2.74	2.63	1.27	1.23	.695	1.98	.826	6.52
12	.150	.146	2.54	2.56	1.24	1.23	.663	1.82	.760	6.60
14	.205	.194	2.60	2.45	1.17	1.23	.649	1.77	.717	6.44
16	.250	.265	2.51	2.21	1.19	1.15	.634	1.66	.746	5.77

1 University of Tokyo

2. A model for the dissipation of kinetic energy

Here we contrast the familiar $k - \epsilon$ model (model 1),

$$\frac{D\epsilon}{Dt} = C_{\epsilon 1}\frac{\epsilon}{k}P - C_{\epsilon 2}\frac{\epsilon^2}{k} + \frac{\partial}{\partial x_i}(C_{\epsilon\epsilon}\frac{k^2}{\epsilon}\frac{\partial\epsilon}{\partial x_i}),$$

$$C_{\epsilon 1} \simeq 1.4, \ C_{\epsilon 2} \simeq 1.9, \ C_{\epsilon\epsilon} \simeq 0.07,$$

with the model derived via the TSDIA approach (model 2; Yoshizawa, 1987) ,

$$\frac{D\epsilon}{Dt} = C_{\epsilon 1}\frac{\epsilon}{k}P - C_{\epsilon 2}\frac{\epsilon^2}{k} + C'_{\epsilon 1}k(\frac{\partial\overline{u}_i}{\partial x_j} - \frac{\partial\overline{u}_j}{\partial x_i})^2 + \bullet\bullet\bullet \ ,$$

$$C_{\epsilon 1} = C_{\epsilon 2} \simeq 1.70.$$

Note that for both models, the eddy-viscosity approximation implies that

$$C_{\epsilon 1}\frac{\epsilon}{k}P = C_{\epsilon 1}C_\nu k(\frac{\partial\overline{u}_i}{\partial x_j} + \frac{\partial\overline{u}_j}{\partial x_i})^2 \ ,$$

where $C_\nu \simeq 0.09$. For homogeneous turbulence in uniform shear S, model 1 reduces to

$$\frac{\partial\epsilon}{\partial t} = C_{\epsilon 1}\frac{\epsilon}{k}P - C_{\epsilon 2}\frac{\epsilon^2}{k} \ ,$$

and model 2 reduces to

$$\frac{\partial\epsilon}{\partial t} = C_{\epsilon 1}\frac{\epsilon}{k}P - C_{\epsilon 2}\frac{\epsilon^2}{k} + 2C'_{\epsilon 1}kS^2 \ .$$

These two models were tested against the homogenous shear turbulence fields of Rogers et al (1986) for $8 \leq St \leq 14$. The resulting "constants" were found to be $.97 \leq C_{\epsilon 1} \leq 1.2$ for model 1, and $1.7 \leq C_{\epsilon 1} \leq 1.9$, $-.025 \leq C'_{\epsilon 1} \leq -.018$ for model 2. Note that the negative value of $C'_{\epsilon 1}$ implies that the effect of rotation, given by the third term of the model, acts to reduce the dissipation rate. The simulation data also support the relationship $C_{\epsilon 1} = C_{\epsilon 2} \simeq 1.7$ suggested by TSDIA.

3. A model for the diffusion of kinetic energy

The diffusion term

$$D_k = \frac{\partial}{\partial x_i}(\frac{1}{2}\overline{u'_i u'_j u'_j} + \overline{p' u'_i})$$

in the equation for kinetic energy is usually modeled as (model 1)

$$D_k = -\frac{\partial}{\partial x_j}(C_K\frac{k^2}{\epsilon}\frac{\partial k}{\partial x_j}),$$
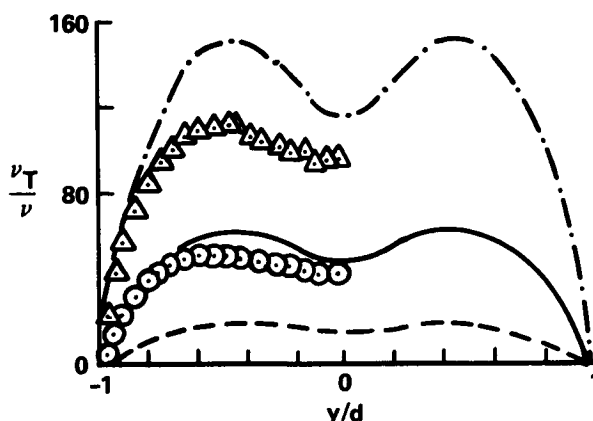
FIGURE 1. The eddy viscosity distribution in turbulent channel flow. Experimental data of Hussain & Reynolds: $\triangle\ R = 32300$, o $R = 13800$. Model: — · — $R = 32454$, ——— $R = 12581$, - - - - $R = 3666$.

whereas the TSDIA analysis (Yoshizawa, 1982) indicates the presence of a cross-diffusion term

$$D_k = -\frac{\partial}{\partial x_j}(C_{KK}\frac{k^2}{\epsilon}\frac{\partial k}{\partial x_j}) + \frac{\partial}{\partial x_j}(C_{K\epsilon}\frac{k^3}{\epsilon^2}\frac{\partial \epsilon}{\partial x_j}).$$

These models have been compared with the turbulent channel flow data of Kim et al (1987) (hereafter KMM) for $100 < y^+ < 180$. The Reynolds number is 3300, based on channel half-height and centerline velocity, and the centerline is at $y^+ = 180$.

When the data was fit with a single term of the model, the constants were estimated to be $.11 \leq C_{KK} \leq .12$ when $C_{K\epsilon}$ was set to zero, and $.06 \leq C_{K\epsilon} \leq .08$ when C_{KK} was set to zero. At high Reynolds number, the eddy viscosity distribution $(\nu_T = \overline{u'v'}/S)$ has maxima off the centerline of the channel. The cross-gradient term in model 2, when incorporated into a $k - \epsilon$ model, can produce the off-axis maxima whereas model 1 cannot. However, at the low Reynolds number of the simulation, the eddy viscosity did not exhibit the off-centerline maxima strongly enough to allow the two constants to be found simultaneously from the data alone.

If the constants are taken as $C_{KK} = .08$ and $C_{K\epsilon} = .03$, the locations of the maxima and their values are reproduced. The data of KMM indicate a maximum $\nu_T/\nu = 16$ at $y/d = \pm.5$ while the model gives a maximum of 18 at $y/d = \pm.47$. A comparison of the eddy-viscosity distribution of model 2 and experimental data at higher Reynolds numbers is shown in figure 1.

REFERENCES

KIM, J., MOIN, P. & MOSER, R. 1987 Turbulence statistics in fully developed channel flow at low Reynolds number . *J. Fluid Mech..* **177**, 133-166.

ROGERS, M., MOIN, P., & REYNOLDS, W.C. 1986 The structure and modeling of the hydrodynamic and passive scalar fields in homogeneous turbulent shear flow . *Stanford University Report TF-25.*

YOSHIZAWA, A. 1982 Statistical evaluation of the triple velocity correlation and the pressure-velocity correlation in shear turbulence . *J. Phys. Soc. Jpn..* **51(7)**, 2326-2337.

YOSHIZAWA, A. 1985 Statistical analysis of the anisotropy of scalar diffusion in turbulent shear flow . *Phys. Fluids.* **28(11)**, 3226-3231.

YOSHIZAWA, A. 1987 Statistical modeling of a transport equation for the kinetic energy dissipation rate . *Phys. Fluids.* **30(3)**, 628-631.

Overview of the scalar transport/reacting flows group

This group conducted five projects aimed at developing improved modeling capabilities for turbulent flows with scalar transport or chemical reaction. Two projects used existing data bases selected from previous simulations of incompressible homogeneous flows, both with and without mean deformation; two modified the basic program for homogeneous incompressible turbulence to account for simple chemical reactions; and one modified the code to include a Boussinesq buoyancy term.

The invited participants were:
Dr. William T. Ashurst (Sandia National Laboratories)
Dr. Sherif El-Tahry (General Motors Research Laboratories)
Prof. James C. Hill (Iowa State University)
Mr. Mark J. Jennings (Illinois Institute of Chicago)
Mr. Andrew D. Leonard (Iowa State University)
Prof. Wolfgang Kollman (University of California, Davis)
Dr. Thomas Morel (Integral Technologies)
Mr. Masood Mortazavi (University of California, Davis)

The local participants were:
Mr. Scott D. Abrahamson (Stanford University)
Prof. Joel H. Ferziger (Stanford University)
Prof. William C. Reynolds (Stanford University and NASA Ames)
Dr. Robert S. Rogallo (NASA Ames)
Dr. Michael M. Rogers (NASA Ames)
Mr. Christopher J. Rutland (Stanford University)
Mr. Kyle D. Squires (Stanford University)
The principal accomplishements of each project are summarized below.

Pressure gradient statistics in homogeneous shear

Using the data base for homogeneous shear, Kollman, Mortazavi, Squires and Rogers examined one-point probability density functions for the pressure gradient, conditioned on components of the fluctuating velocity and vorticity. The objective was to develop a firm basis for modeling quantities needed in pdf treatments of turbulent flows.

They found that the expectation value of the fluctuating pressure gradient, conditioned on a turbulence velocity component, is linear in the velocity component over the range of velocity where an adequate sample existed. In contrast, the expectation values of pressure gradient conditioned with vorticity were found to be very small, indicating that the pressure gradient is statistically independent of the vorticity. It thus appears that the conditioned pressure gradient term in homogeneous shear

flow can be modeled as $< (1/\rho)\partial p/\partial x_i | u_1, u_2, u_3, \omega_1, \omega_2, \omega_3 > = \alpha_{1i}u_1 + \alpha_{2i}u_2$, where $\alpha_1 < 0$ and $\alpha_2 > 0$. This model is likely to be useful in pdf modeling of turbulence.

Modeling turbulent scalar transport

Morel, Jennings, and Abrahamson explored Morel's ideas for non-local modeling of turbulent scalar transport using integrals formed from two-point correlation functions. For homogeneous turbulent shear flow they examined quantity $I_{ij}(t) = \int Q_{kk}(\mathbf{r},t) r_i r_j d^3\mathbf{r}$ where $Q_{ij}(\mathbf{r},t) = \overline{u_i(\mathbf{x},t)u_j(\mathbf{x}+\mathbf{r},t)}$. Morel's conjecture was that the component of turbulent transport of a scalar ϕ in the ith direction might be modeled as $T_{\phi_i} = C\,\Phi_{,j} I_{ij}$ where Φ is the mean scalar field. This is of the form $T_{\phi_i} = -D_{ij}\Phi_{,j}$ which Rogers et $al.$ (1986) found fit their direct simulations of homogeneous turbulent shear flow. However, Morel's model gives a symmetric D_{ij}, whereas Rogers found that D_{ij} is non-symmetric. Thus, while Morel's model predicted the correct trends for the diagonal terms, it did not predict the off-diagonal terms. Further study of these ideas is planned by Morel and Jennings.

Buoyant convection

The Rogallo code for homogeneous turbulence was modified by Ashurst and Rogers to include a Boussinesq forcing term in the momentum equation. The objective was to study the effects of buoyancy on the relationships between vorticity and strain rate in homogeneous shear flow.

An unstable temperature gradient was imposed in the gravitational direction and the turbulence development was studied and compared to a zero gravity isotropic decaying case. A computational box that was twice as long in the gravitational direction as horizontal was employed to permit the simulation to be run longer before the flow structures were affected by the imposed periodic boundary conditions. The simulations were begun from developed initial isotropic fields at $Re_\lambda = 7.8$ and run on a $64 \times 32 \times 32$ grid. The Rayleigh number based on the Taylor microscale varied from 21 to 93, and the Prandtl number was 0.7.

As expected, the Boussinesq term eventually caused the velocity fluctuations and length scales in the gravity direction to grow. The relationship between the vorticity and the eigenvectors of the strain-rate tensor in the buoyant fields was qualitatively similar to that observed in incompressible homogeneous shear flow and isotropic decaying turbulence studied previously (Ashurst et $al.$ 1987). Specifically, the vorticity has a large probability of aligning with the intermediate strain-rate eigenvector direction and at large strains this intermediate strain-rate is extensional. This direction has a low probability of being aligned with the gravitational direction. The temperature field also behaves like the passive scalar fields in incompressible shear flow in that the local temperature gradient is most likely to be aligned with the most compressive eigenvector of the strain-rate tensor. In addition, the scalar dissipation (conditioned on the kinetic energy dissipation) resembles the behavior in incompressible shear flow, exhibiting a near linear dependence at large values. These results should be useful to developers of models for buoyant turbulent convection.

Premixed flame in homogeneous turbulence

El-Tahry, Rutland, Ferziger, and Rogers modified the Rogallo code for homogeneous turbulence to study premixed turbulent flames in decaying isotropic incompressible turbulence. The objective was to to determine the effect of turbulence on flame structure and speed speed over a range of Damkohler number. The results, though preliminary, are be of interest to combustion modelers.

They considered the reaction A → B, where A denotes premixed reactants and B denotes products. A temperature-dependent reaction rate was used, with the Arrhenius parameters adjusted to yield a flame width of about ten gridpoints (to resolve the structure) and a 15°C temperature rise across the flame (to allow treatment as incompressible). In order to keep the flame thin compared to the turbulence scales and still resolve the flame structure, the Reynolds number had to be kept small, and the Taylor microscale Reynolds number was only about 5 in their simulations. The Damkohler number was approximatrely 1.5. A 128 × 128 × 128 grid was employed, with a uniform initial chemical distribution (premixed reactants) and a Gaussian temperature distribution sufficient to ignite the reaction. A purely laminar case was run for reference purposes.

The resulting flame front exhibited the characteristics of a wrinkled laminar flame; the local flame structure was everywhere similar to that of a laminar flame, with isotherms approximately parallel at about the same spacing as in the laminar case. The wrinkling of the instantaneous flame front appeared well correlated with the local velocity fluctuations and resulted in a mean flame thickness of about twice the local (laminar) flame thickness. The increased reaction area led to turbulent flame speeds about 20% larger than the laminar flame speed. As the flame propagated through the decaying hydrodynamic field it slowed due to the decaying turbulence intensity (decreasing roughly linearly with the rms turbulence intensity) and thickened slightly, perhaps due to the increasing turbulent length scales.

The probability distribution of the mean reactant mass fraction at different positions through the mean flame location agrees with the wrinkled laminar flame model of Bray and Moss (1977), consisting of two delta functions representing pure reactant and pure product joined by a region of low probability proportional to the inverse of the reactant mass fraction gradient.

Diffusion flame in homogeneous turbulence

Hill, Leonard and Rogers modified Rogallo's code to begin a study of a simple diffusion chemical reaction in incompressible homogeneous turbulence. The objective was to determine the influence of vorticity and strain rate on the structure and propagation of the reaction zone (flame).

They considered a simple irreversible chemical reaction A + B + C → P + C occuring in isotropic turbulence with the reaction rate proportional to the product of the local concentrations of non-premixed reactants A and B through a constant reaction rate coefficient. P denotes the product, and C is an inert diluent. The mass fractions of the four species were computed along with the hydrodynamic field on a 64 × 64 × 64 grid. The initial chemical composition consisted of alternating slabs

of pure reactants A + C and B + C. The Schmidt number was unity for all species. Two runs with different reaction rates resulted in Damkohler numbers based in the initial mean reactant concentration, turbulence intensity, and integral velocity scale of 2 and 10.

The instantaneous reaction front appeared more convoluted in this study than in the premixed flame calculation described previously, presumably due at least in part to the higher Reynolds number of this simulation. The structure of surfaces of constant reactant concentration appear to be well correlated with the local velocity field. The simulation indicates that the dissipation microscale of the concentration fields is not greatly affected by the Damkohler number, suggesting that the diffusive effects can be treated reasonably well by correctly modeling an equivalent non-reacting flow.

These observations may be helpful in reaction for modeling. Hill and Leonard are continuing this work, and plan to study the effects of mean strain and shear on the flames, variation of the reactant Schmidt numbers, sensitivity to initial conditions and non-stoichiometric mixtures.

W.C. Reynolds, M. M. Rogers

REFERENCES

ASHURST, WM. T., KERSTEIN, A. R., KERR, R. M. & GIBSON, C. H. 1987 Alignment of vorticity and scalar gradient with strain rate in simulated Navier-Stokes turbulence. *Phys. Fluids.* **30**, 2343-2353.

BRAY, K.N. & MOSS, J.B. 1977 *Acta Astron.*,4.

ROGERS, M. M., MOIN, P. & REYNOLDS, W. C. 1986 The structure and modeling of the hydrodynamic and passive scalar fields in homogeneous turbulent shear flow. *Dept. Mech. Eng. Report No. TF-25.* Stanford University, Stanford, California.

Direct numerical simulation of buoyantly driven turbulence

By Wm. T. ASHURST[1] AND M. M. ROGERS[2]

Abstract

Numerical simulations of homogeneous turbulence subject to buoyant forcing were performed. The presence of a mean temperature gradient combined with a gravitational field results in a forcing term in the momentum equation. The development of the turbulence was studied and compared to the decay of similar fields in the absence of gravity. In the buoyantly driven fields, the vorticity is preferentially aligned with the intermediate eigenvector of the strain-rate tensor and the local temperature gradient is more likely to be aligned with the most compressive eigenvector. These relationships are qualitatively similar to those observed in previous shear flow results studied by Ashurst *et al.* (1987). A tensor diffusivity model for passive scalar transport developed from shear flow results in Rogers, Moin & Reynolds (1986) also predicts this buoyant scalar transport, indicating that the relationship between the scalar flux and the Reynolds stress is similar in both flows.

Discussion

During the workshop period, calculations were made with 64 by 32^2 grids in order to examine the effect of forcing the velocity field with scalar fluctuations. With the Boussinesq assumption of a zero divergent velocity field, the modifications to the Rogallo (1981) code were simple. The buoyant forcing develops flow patterns at large length scales in the gravity direction. Because of this, a grid which is longer in the gravitational direction is used. The flow is analyzed at a time before the large scales feel the effect of the periodic boundary conditions. Calculations were made with and without gravity, that is forcing and no forcing.

The Rayleigh number based on the Taylor microscale of the velocity field, λ, is defined as $Ra_\lambda = (g/T_0)|\frac{\partial T}{\partial z}|\lambda^4 Pr/\nu^2$, where z is the gravitational direction and g is the gravitational acceleration. The Prandtl number, Pr, was taken to be 0.7 and the Taylor-microscale Reynolds number was 7.4. In the field analyzed here $Ra_\lambda = 93$ and the ratio $Ra_\lambda/(Re^2 Pr)$ is 2.4.

Previous work by Ashurst *et al.* (1987) indicated a coupling between the vorticity field and the eigenvectors of the strain-rate tensor (ordered so that $\alpha \geq \beta \geq \gamma$) as determined from single point analysis of the alignment between the vorticity vector and the strain-rate directions. This analysis was repeated for the buoyantly driven fields and similar results were found in that vorticity has a large probability to

1 Sandia National Laboratories
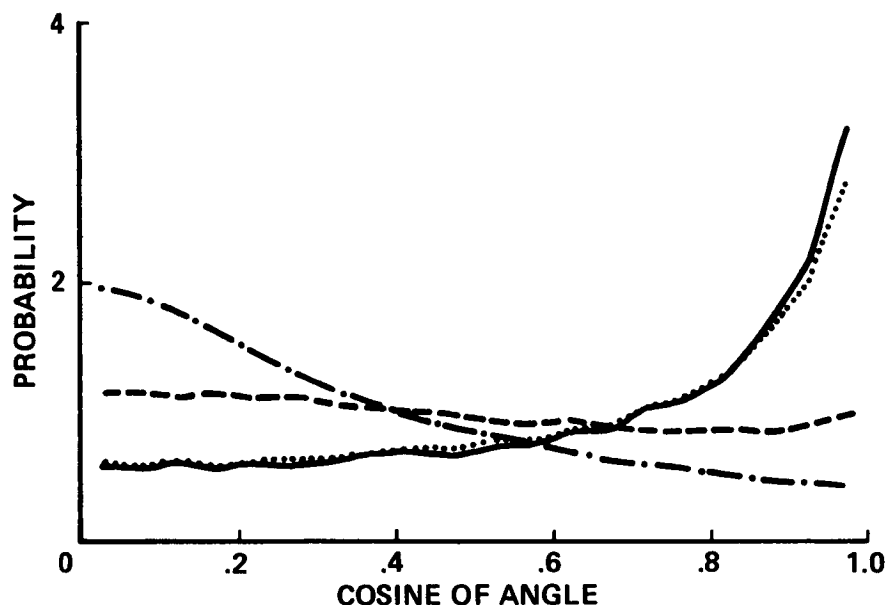
2 NASA-Ames Research Center

FIGURE 1. Pdf of the cosine of the angle between the vorticity and the principal strain-rate directions. $----\,\omega\cdot\alpha$, $\cdots\cdots\,\omega\cdot\beta$, $---\,\omega\cdot\gamma$, $-\!\!-\!\!-\,\omega\cdot\beta$ for $\beta > 0$. Note the increased probability for alignment with the intermediate strain-rate, β.

align with the intermediate strain-rate direction (Figure 1) and at large strains this intermediate strain-rate is extensional. In this buoyant flow we find that both the vorticity and the intermediate strain-rate are more likely not to point in the gravitational direction which is consistent with the fact that the plumes present in this flow tend to produce vorticity normal to the gravitational direction.

The behavior of the temperature gradient is also similar to that observed in homogeneous turbulent shear flow. Figure 2 presents the alignment of the temperature gradient with the three strain-rate eigenvectors. The most probable direction is the most compressive strain-rate direction with a peak value that is twice that found in previous passive scalar simulations.

Figure 3 presents scalar dissipation values conditioned on the energy dissipation value. As in the passive scalar shear flow results there is an increasing power-law dependence with increasing strain-rate.

A comparison between the heat flux observed in the simulations studied here with flux predictions from the model developed in Rogers, Moin & Reynolds (1986) is shown in Figure 4. The qualitative agreement is good and slight adjustments to the fitting function used for the single model constant could improve the results further. It is not surprising that the fitting function may require modification because it was developed from homogeneous shear flow results at $Re_\lambda \approx 100$ and therefore a significant extrapolation is required to the field examined here with $Re_\lambda = 7.4$.
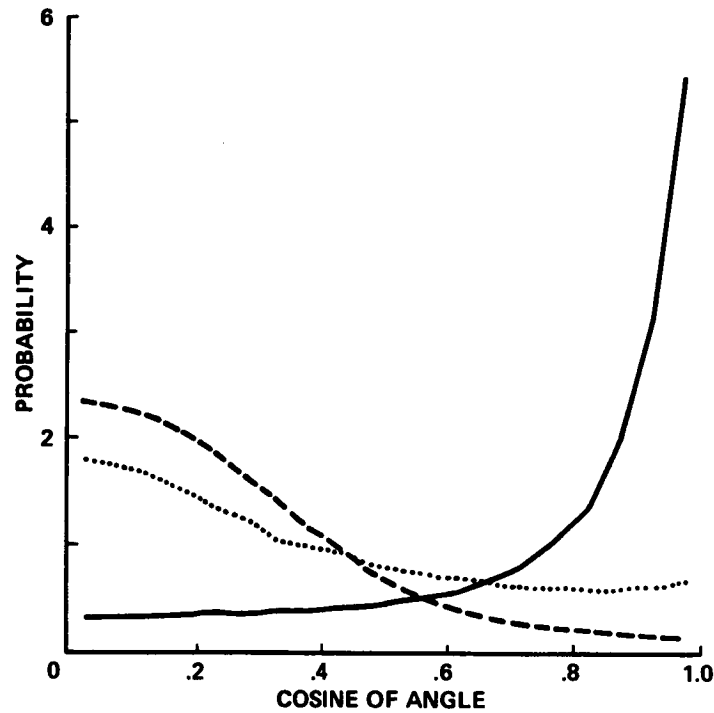
FIGURE 2. Pdf of the cosine of the angle between the temperature-gradient vector and the principal strain-rate directions. $---$ $\nabla T \cdot \alpha$, $\cdots\cdots$ $\nabla T \cdot \beta$, $\longrightarrow$ $\nabla T \cdot \gamma$. Note the increased probability for alignment with the most compressive strain-rate, γ.
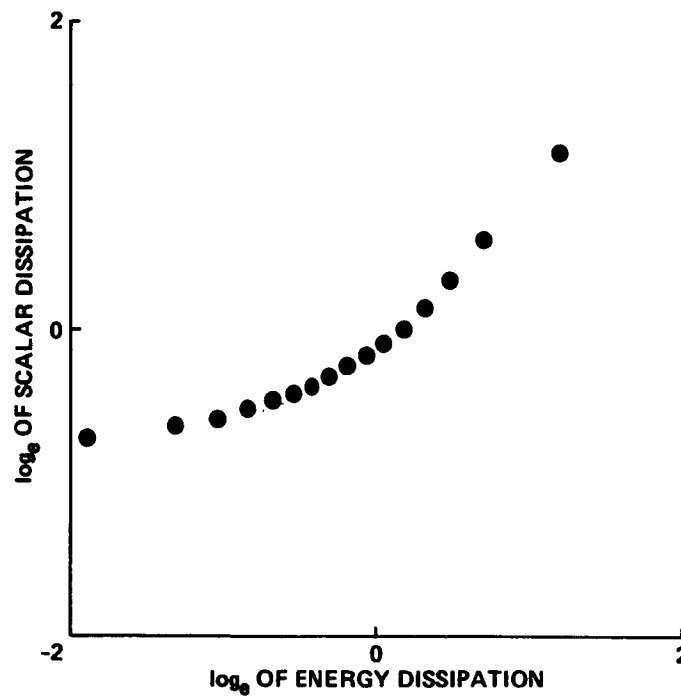
FIGURE 3. Mean scalar dissipation ($D\nabla T \cdot \nabla T$) conditioned on energy dissipation reveals a changing power-law dependence.
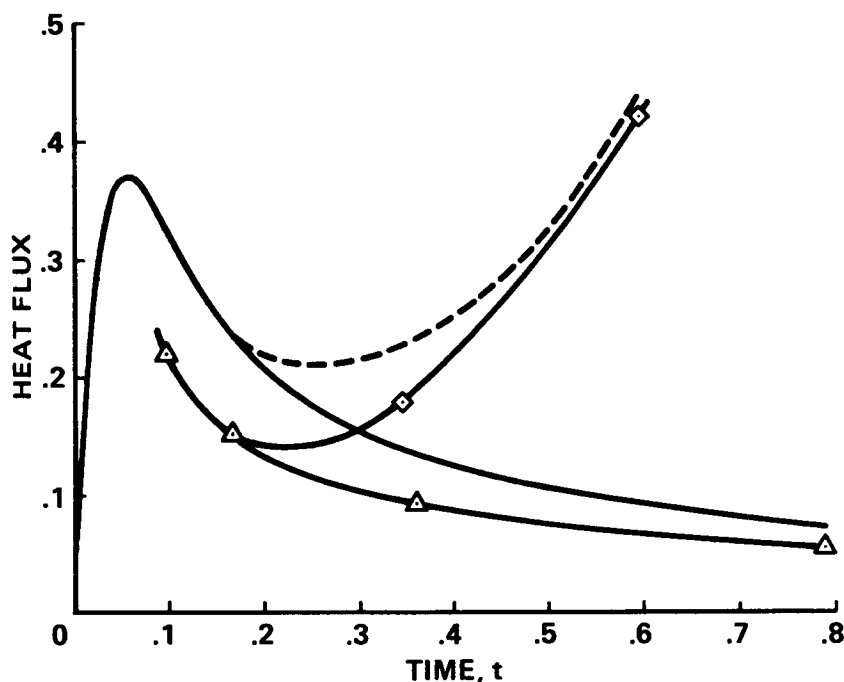
FIGURE 4.   Comparison between the heat flux from the numerical simulations and that predicted by the model developed in Rogers, Moin & Reynolds (1986). ――――― simulation g=0, ‒ ‒ ‒ ‒ simulation g=30, △ model g=0, ◇ model g=30.

In conclusion, much of the behavior of this buoyantly driven homogeneous turbulence resembles the behavior of homogeneous turbulent shear flow, despite the different production mechanisms of these two flows.

REFERENCES

ASHURST, WM. T., KERSTEIN, A. R., KERR, R. M. & GIBSON, C. H. 1987 Alignment of vorticity and scalar gradient with strain rate in simulated Navier-Stokes turbulence. *Phys. Fluids.* **30**, 2343-2353.

ROGERS, M. M., MOIN, P. & REYNOLDS, W. C. 1986 The structure and modeling of the hydrodynamic and passive scalar fields in homogeneous turbulent shear flow. *Dept. Mech. Eng. Report No. TF-25.* Stanford University, Stanford, California.

ROGALLO, R. S. 1981 Numerical experiments in homogeneous turbulence. *NASA Tech. Memo. 81315.*

Premixed turbulent flame calculation

By S. EL-TAHRY[1], C. J. RUTLAND[2], J. H. FERZIGER[2] AND M. M. ROGERS[3]

The importance of turbulent premixed flames in a variety of applications has led to a substantial amount of effort towards improving our understanding of these flames. Although these efforts have increased our understanding, many questions remain. For example, there is contradicting evidence concerning the role of the turbulent length scales on turbulent flame speed. There are a variety of proposals that attempt to correlate the turbulent flame speed with the turbulence velocity (*e.g.*, Bray, 1980 and zur Loye and Bracco, 1987). As in non-reacting turbulent flows, the main impediment is the inability to both adequately control experiments and to adequately measure the quantities of interest in the experiments. With recent advances in supercomputers and the accompanied development of direct numerical simulation (DNS) it might now be possible to alleviate some of these difficulties.

There are a variety of questions that are currently being raised in turbulence combustion modeling work for which DNS can provide answers. For example, what is the instantaneous structure of a premixed turbulent flame? Flame structures are difficult to obtain experimentally because of the fine resolution required. Knowledge of the flame structure can aid in closing the viscous dissipation term in the equation for the variance of relevant scalars (for a related example see Pope and Anand, 1985). It is anticipated that in the thin flame mode of combustion (*i.e.*, when the turbulence strain rate is small compared to the reciprocal of the chemical time scale), the flame structure is similar to an undisturbed laminar flame. We need to test this assumption under a variety of circumstances such as different chemical systems, different Lewis numbers, and different ratios of turbulent velocity to laminar flame speeds (u'/S_L).

A fundamental question that can be addressed with DNS is what factors control the turbulent flame speed (S_T). For example, what are the turbulence characteristics that control S_T and what is the form of the correlation of these characteristics? In DNS we know the values of all quantities at each grid point at every time step. In addition, both Eulerian and Lagrangian (*i.e.*, following the flame surface) analyses can be conducted and parameters can be switched on and off. Thus with DNS more information can be gained than is possible experimentally and many questions can be addressed. However, there are limitations to DNS and these are reviewed next.

The first limitation of all DNS is the range of scales which can be resolved. Small grid spacing is required to resolve small scales and large domain size is needed to capture the large scales. Computer resources limit this range and hence limit

1 General Motors Research Laboratory
2 Dept. of Mech. Engng., Stanford University
3 NASA-Ames Research Center
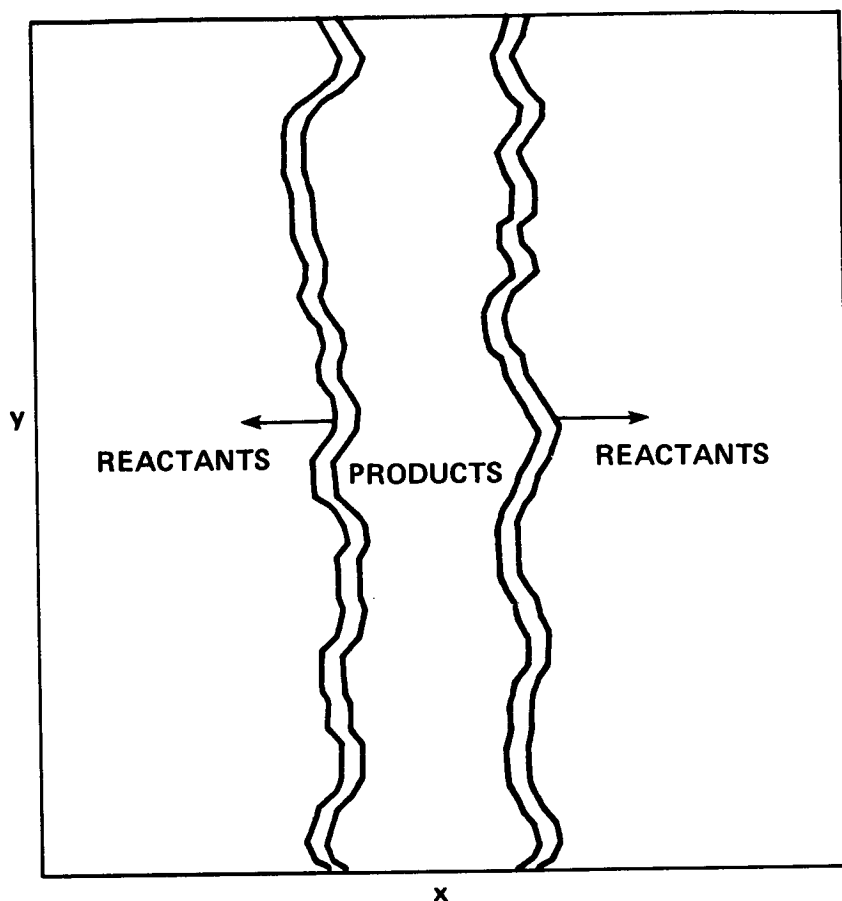
FIGURE 1. Schematic of the flame geometry.

the maximum Reynolds number of the computations. In the presence of premixed flames there is a more stringent condition on the Reynolds number that arises if calculations are to be made in the more interesting thin flame regime that occurs at high Damkohler numbers (Da). We define Da based on the strain rate of the turbulence *i.e.*,

$$Da = \frac{\lambda S_T}{\delta u'} ,$$

where λ and δ are the Taylor microscale and the flame thickness, respectively. Then, it is generally accepted that the thin flame regime is achieved with Da greater than unity. To reveal the extra constraint on the Reynolds number in the thin flame regime, we can rewrite Da as

$$Da = \left(N_1 Re_L^{-0.75}/N_2 n\right)^2 , \tag{1}$$

where N_1 is the number of grid lines spanning the computational domain along a coordinate direction, N_2 is the number of grid points that will span the flame

thickness, Re_L is the Reynolds number based on the integral length scale and n is the number of integral length scales present in the computational domain.

In deriving (1) we used the standard relations between the turbulent scales, hence the equation is to be used only for order-of-magnitude purposes, particularly at small Reynolds numbers. We notice that N_1 is constrained by the maximum job size that can be run and N_2 is limited by resolution considerations. We cannot set n too low; otherwise the large eddies become too large for the computational domain before there has been sufficient time for the flame to develop and propagate. Thus, the only avenue available to obtain large Damkohler numbers is to reduce Re_L.

The other relevant constraints on the DNS calculations are the periodic boundary conditions and the limitation to incompressible flows. These constraints are particular to the computer code that is used in the present study (Rogallo, 1981) and in principle can be eliminated. The former constraint may not be too significant. The latter constraint, however, precludes studying important aspects, such as the influence of the flame on the turbulence and the effect of hydrodynamic flame instabilities on the flame structure. The present work is an initial effort in studying thin premixed flames using DNS. We attempt to address some of the questions raised earlier and we do so under the mentioned constraints.

The problem considered is shown schematically in Figure 1. It consists of a planar flame sheet, located in the y-z plane, initiated at the midpoint of the x-direction. The chemical kinetics model used is a hypothetical, single-step kinetics with a single reactant A going to a product B. The equations which govern the thermal and chemical states are the conservation equations for species A mass fraction, Y_A, and the temperature, T. These are:

$$\frac{DY_A}{Dt} = \gamma_Y \nabla^2 Y_A - bY_A \exp(-T_a/T) \tag{2}$$

$$\frac{DT}{Dt} = \gamma_T \nabla^2 T - bHY_A \exp(-T_a/T) , \tag{3}$$

where D/Dt is the substantial derivative, γ_Y and γ_T are the (uniform and constant) diffusivities of mass and heat, respectively, b is a pre-exponential factor, T_a is the activation temperature, and H is the enthalpy of the reaction. In the present calculation we have taken the diffusivities of mass and heat to be equal (*i.e.*, the Lewis number is unity). For Lewis number not equal to unity, a term involving species diffusion should be added to the temperature equation. The value of H was selected so as to yield a temperature rise of 15° across the flame. This ensured a small density variation due to the reaction so that our assumption of a divergence-free velocity field is acceptable. The values of b and T_a were selected to give a flame thickness spanning about 10 grid lines and an inner flame region spanning about 4 grid lines. The values of these quantities were established by trial and error using a laminar flame code.

To implement (2) and (3) in the DNS code (Rogallo, 1981), the source terms had to be added to the already existing scalar equations and a chemical time step
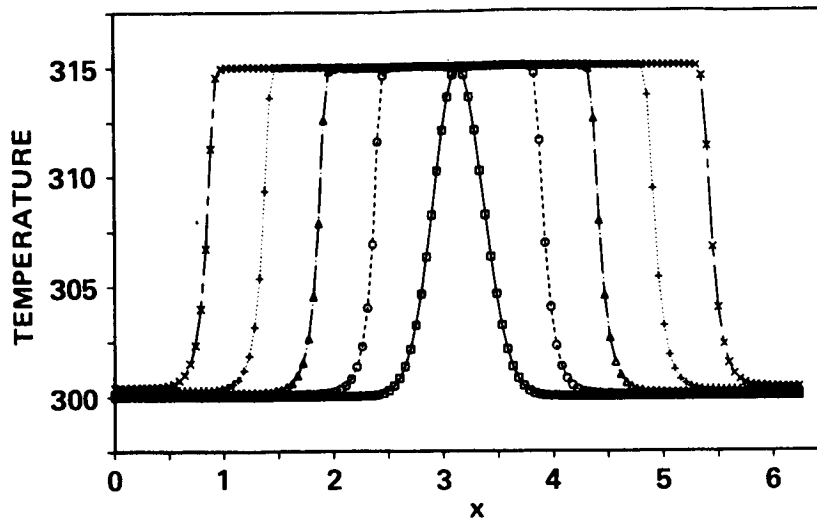
FIGURE 2.   Laminar temperature profiles at 400 step intervals.
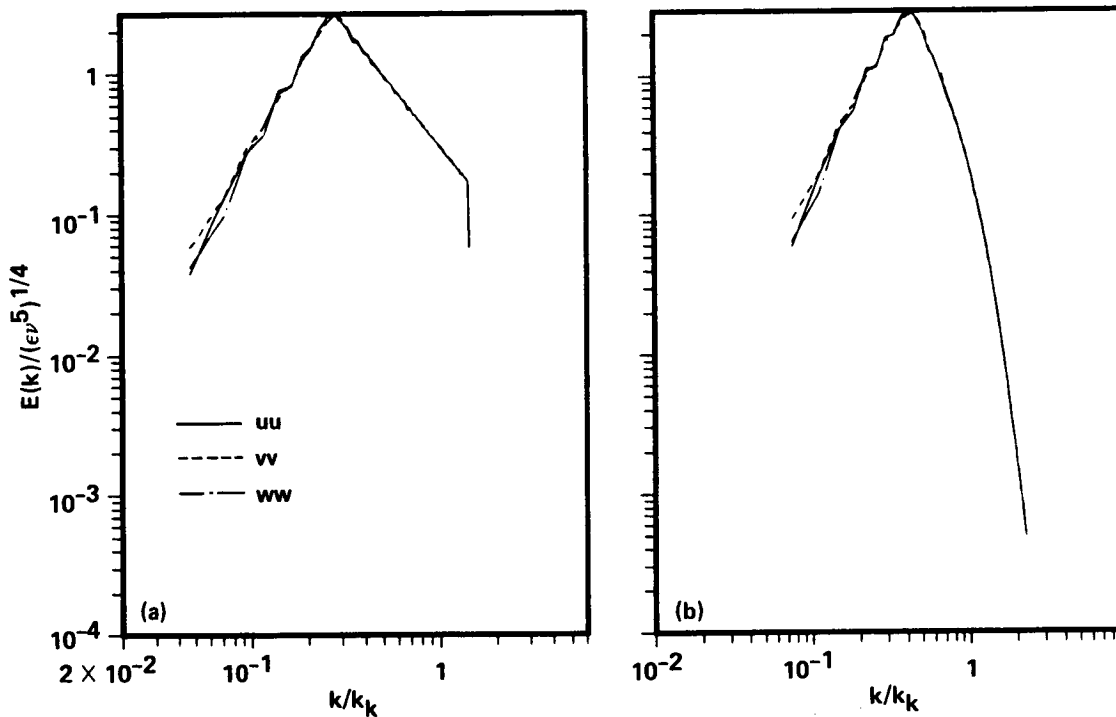
FIGURE 3.   Velocity energy spectra (a) Initial spectra (b) Spectra after 50 steps, at the beginning of the reacting part of the calculation.

stability constraint had to be implemented. The calculations were performed with a $128 \times 128 \times 128$ grid.

To test the accuracy of the flame calculation with the DNS code, a laminar flame

(a)

(b)
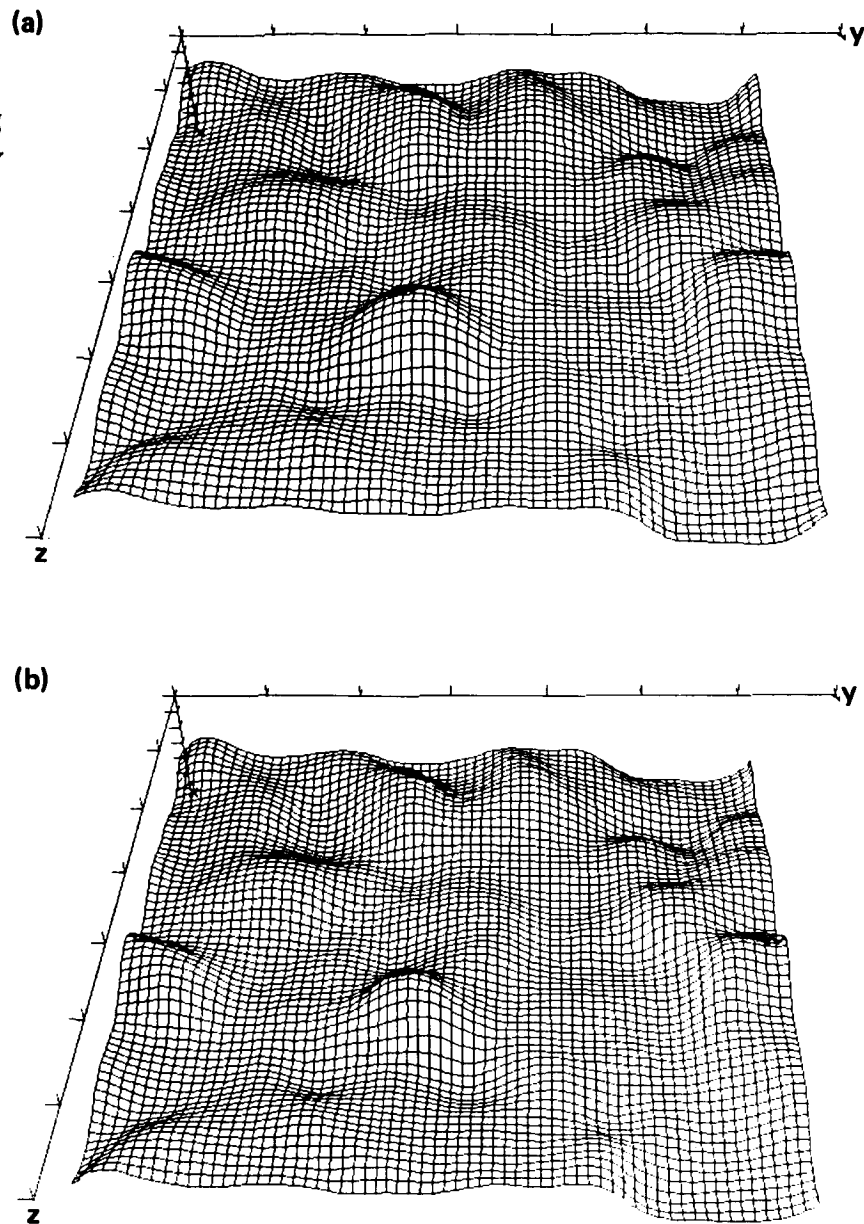
FIGURE 4. Constant temperature surfaces (a) $T = 302°$ (b) $T = 314°$.

propagation calculation was made on the same geometry as depicted in Figure 1 and the results were compared to the results of a similar calculation made with an accurate laminar flame code. The results of the laminar flame calculations made with the DNS code are shown in Figure 2. The figure shows the temperature profiles at 400 step intervals which begin at $t = 0$ with a Gaussian distribution. It is seen that after 400 time steps the profile has significantly steepened relative to the initial conditions and the flame thickness has approximately stabilized (*i.e.*, the initial conditions are forgotten). Comparison of the flame speeds obtained from the two
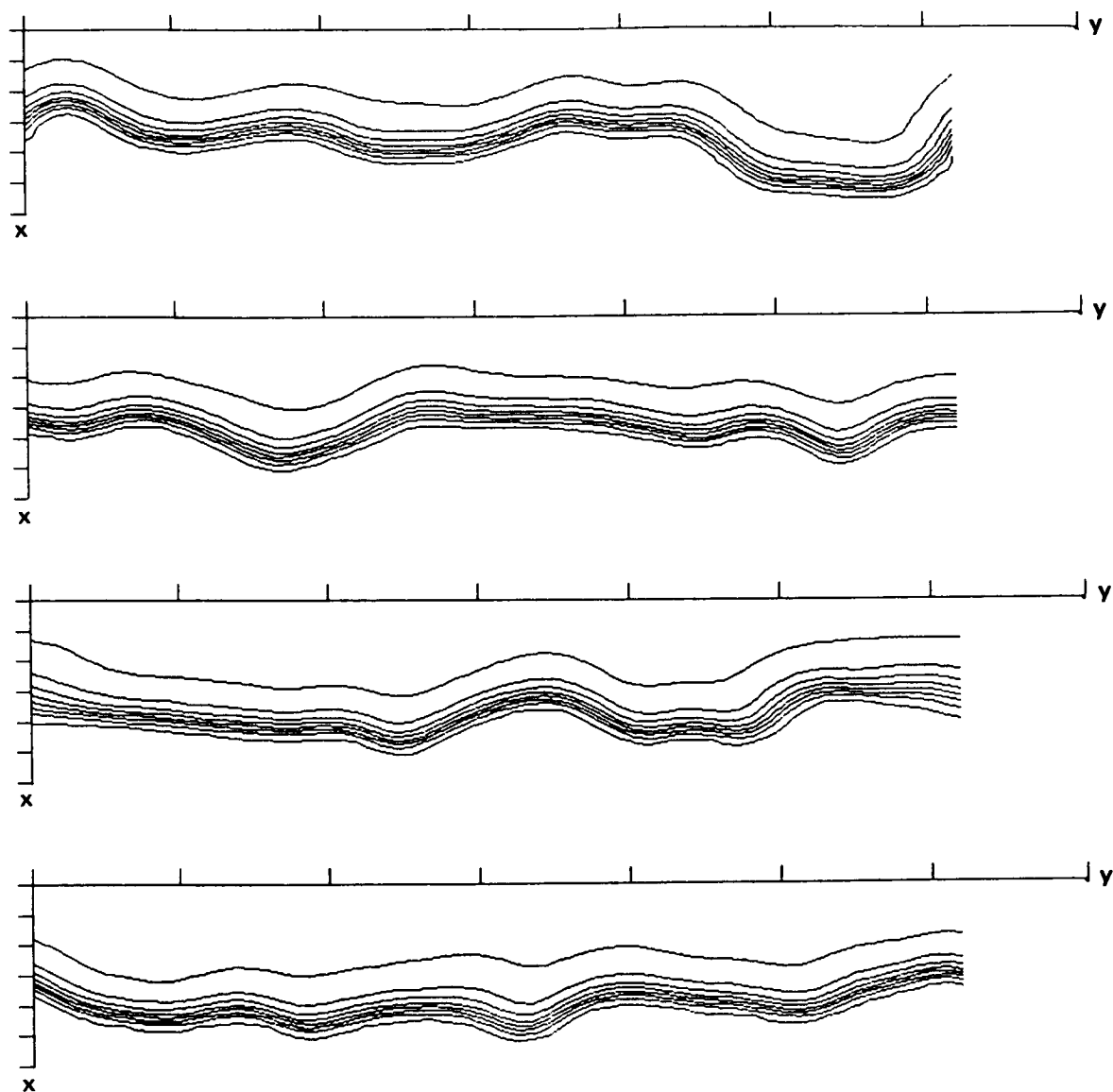
FIGURE 5. Temperature contours in x-y planes (a) z station $= 0$ (b) z station $= 1/4$ (c) z station $= 1/2$ (c) z station $= 3/4$.

codes were found to be within 2% of each other. This is good agreement considering that only about 10 grid points were within the flame and that no de-aliasing was attempted for the non-linear source terms.

For the turbulent combustion calculations, the underlying hydrodynamic field was an unforced isotropic turbulence. To achieve a developed turbulence spectrum at the start of the chemistry calculations, the latter calculations were initiated after developing the hydrodynamics field for 50 time steps. The turbulence spectrum at $t = 0$ and after 50 time steps are shown in Figure 3. The Reynolds number based
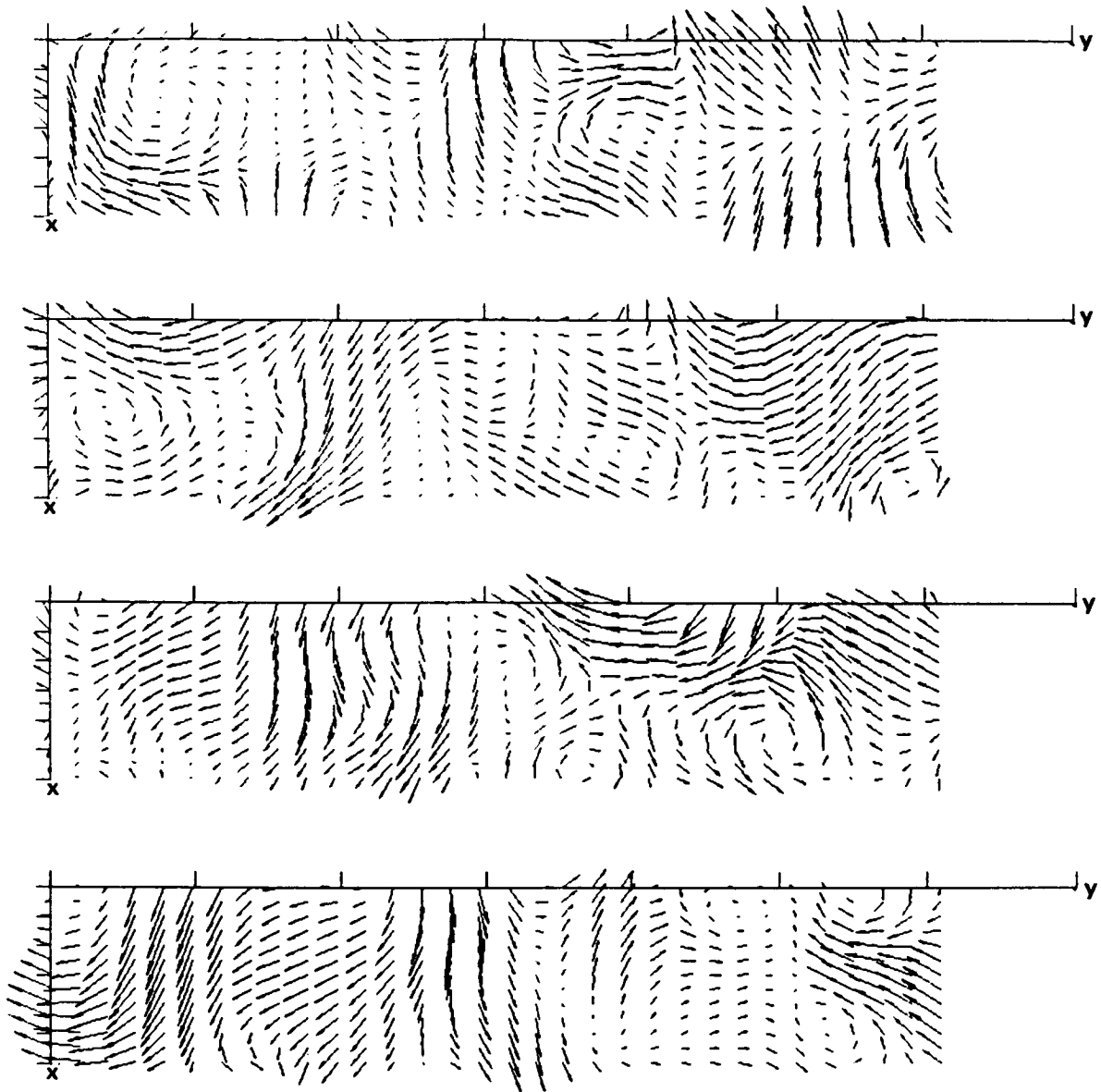
FIGURE 6. Velocity vectors in x-y planes (a) z station $= 0$ (b) z station $= 1/4$ (c) z station $= 1/2$ (c) z station $= 3/4$.

on the Taylor microscale was approximately 5, Da was approximately equal to 1.5 and u'/S_L was of the order 0.53. This meant that we expect a thin flame with low turbulence (*i.e.*, the wrinkled flame regime).

We start reviewing the results by examining the flame structure. Figure 4 shows the constant temperature surfaces for $T = 302°$ and $T = 314°$ (the unburned temperature is $300°$ and the burned temperature is $315°$). The surfaces are seen to have a wavy topology consistent with what is expected in the wrinkled flame regime. Figure 5 shows contours of constant temperatures in x-y planes taken at
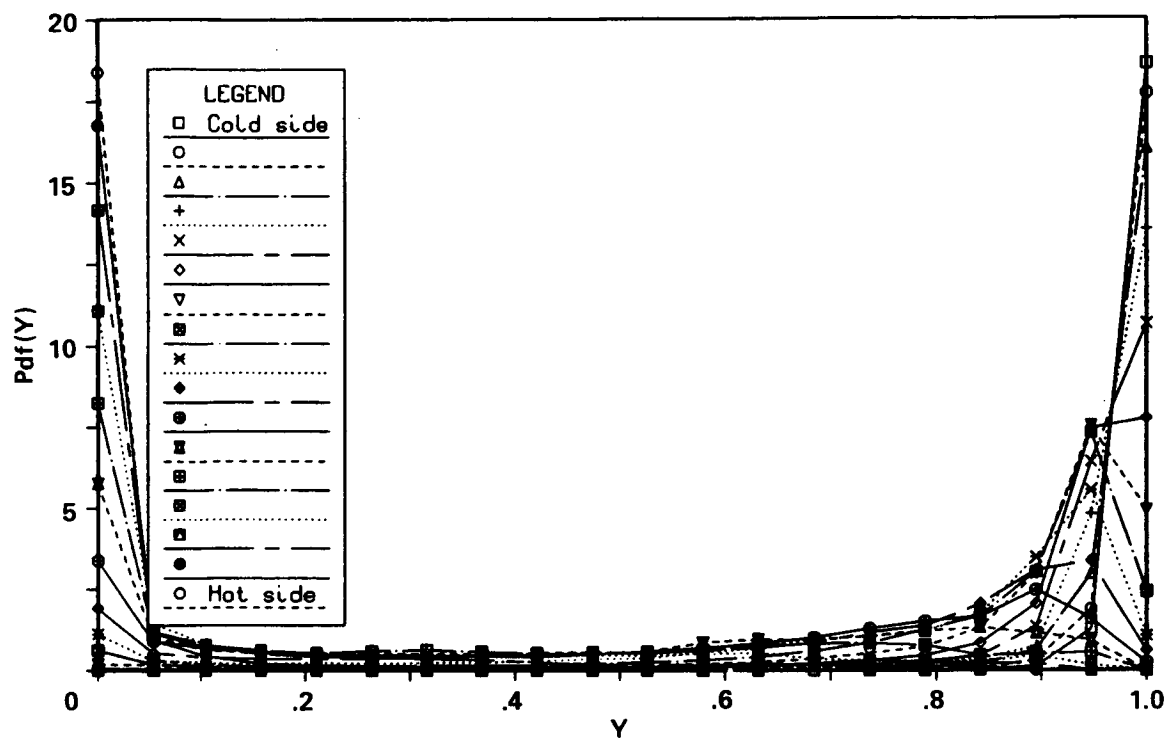
FIGURE 7. PDF of the mean reactant mass fraction.

the 0, 1/4, 1/2, and 3/4 stations in the z-direction. Here the wrinkled structure is more evident and the wrinkling seems to be occurring at several scales. The flame thickness is found to vary with location. This variation is caused by the inclination of the local flame front relative to the section plane. Thus the flame appears thicker than it is along a normal to the flame front. The flame thickness in the thin regions were found to be comparable to the thickness of the laminar flame calculated earlier. At thirteen locations tested the flame structure was also found to be similar to the laminar flame structure. This result agrees with the first-order solution derived by Clavin and Williams (1979). However, their second-order solution modifies the laminar profile.

Figure 6 shows the velocity vector field in x-y planes at the same z-locations as Figure 5. In these figures the flame wrinkling appears for the most part to follow the velocity field. We can also see that on the scale of the flame thickness the strain rate is small. This qualitatively verifies that we are in the thin flame regime.

The probability density function (PDF) for the reactant mass fraction is shown in Figure 7 at various x-locations. These PDFs were generated by collecting data from the homogeneous planes (y-z planes) at the specified x locations, dividing it into 20 bins and averaging the data in each bin. The distributions are seen to be qualitatively similar to the PDF of the laminar flamelet model proposed by Bray and Moss (1977). According to this model the PDF consists of two delta functions located at $Y_A = 0$ and $Y_A = 1$ which are joined by a region of low probability
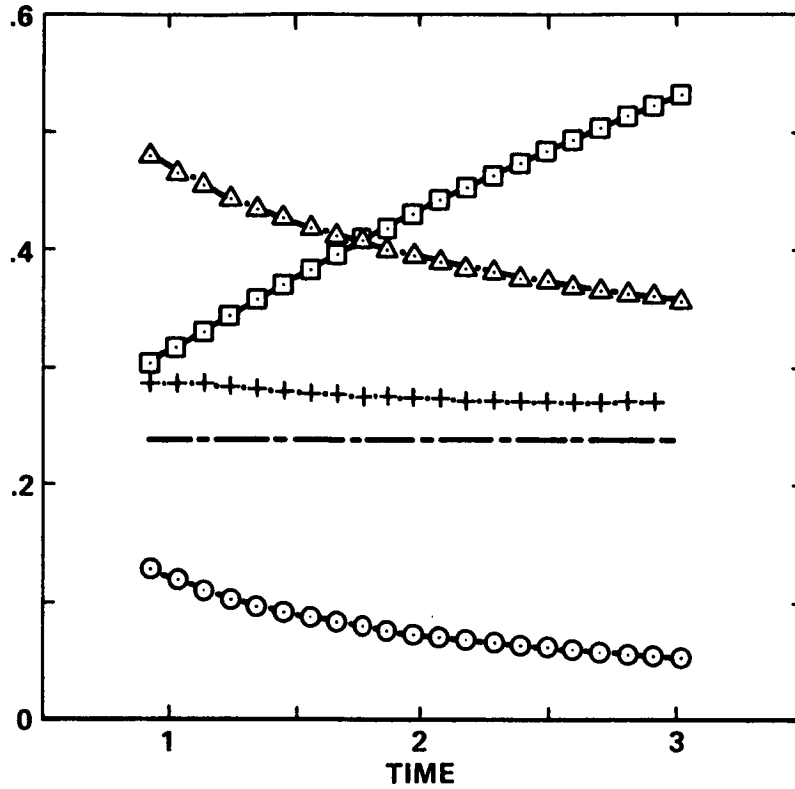
FIGURE 8.   Various scales and velocities as a function of time. □ Taylor microscale; ○ u'; △ Reynolds number/10; + Turbulent flame speed; — - — Laminar flame speed.

that has its PDF proportional to the inverse of the gradient of Y_A. We notice from Figure 7 that, because the gradients on the cool side of the flame are small, the probability density function tends to be higher at the large values of Y_A. There is, however, a peculiar behavior of the PDFs at some of the x-locations where we observe a maximum of the PDF at values of Y_A of around 0.9. This probably indicates that the wrinkling of the flame is not much larger than the flame thickness. This is supported by the contour plots in Figure 5.

Next we will examine the dependence of the turbulent flame speed on u'. Figure 8 depicts the variation of λ, u', Re_λ and the turbulent flame speed S_T with time. The laminar flame speed is also included for comparison. The hydrodynamic quantities display the expected behavior *i.e.*, u' and Re_λ decrease with time, while λ increases. Hence, Da will increase with time which means that we remain in the wrinkled flame regime for the duration of the calculation. The variation of the turbulent flame speed with u' is shown in Figure 9. We find S_T increasing with u' but the increase is much slower than suggested by the commonly used formula

$$S_T = S_L + c'u' \ , \tag{4}$$
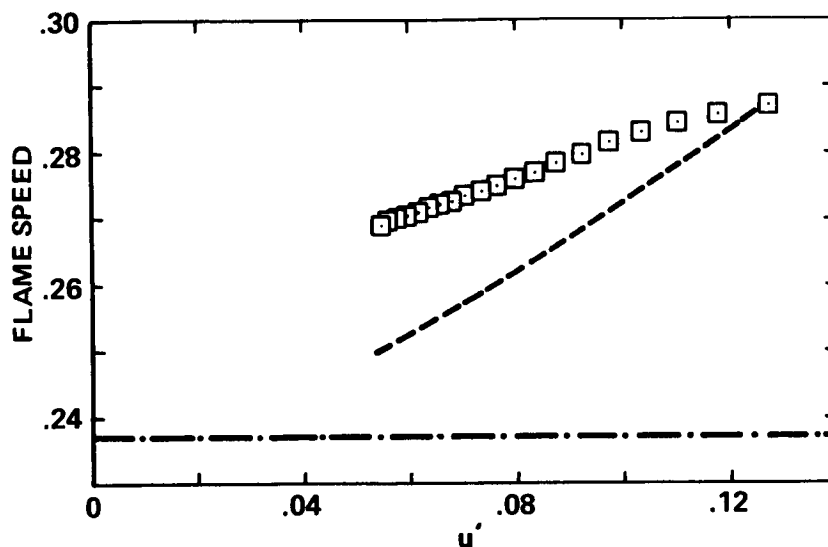
FIGURE 9. Flame speed vs. u'. $\square$ Turbulent flame speed; - - - - Williams' equation; — · — Laminar flame speed.

where c' is a constant. Tabaczyski *et al.* (1974) use $c' = 1$, Witze and Mendes-Lopez (1986) suggest a value of 2.2. For other suggestions see zur Loye and Bracco (1987). Our results are closer to the theoretically obtained formula given by Clavin and Williams (see Williams 1985) for weak turbulence

$$S_T = S_L \left[\frac{1}{2} (1 + \sqrt{1 + 8c(u'/S_L)^2}) \right]^{1/2} , \qquad (5)$$

where c is a constant of order unity. This equation is also plotted in Figure 9 using $c = 1.2$ to match the first data point. Within the range of our data the magnitude of S_T/S_L given by equation (5) is fairly close to our calculated values. However, the trend is not, indicating that S_T probably depends on more than just u'. It is interesting to note that in equations (4) and (5) and most other suggestions in the literature, there is no dependence of S_T/S_L on heat release or Reynolds number (there are some exceptions *e.g.*, Abdel-Gayad and Bradley (1976) give an expression that involves the Reynolds number). Hence the flame speeds calculated with the DNS code should also be representative of flames with large density variation and large Reynolds numbers. However, as implied earlier, the differences in the various proposed equations for the flame speed may be due to not including all of the relevant parameters on which the flame speed depends. We should try to investigate these systematically.

Finally, the development of the mean temperature profiles is shown in Figure 10. The profiles suggest that the turbulent flame thickness is about twice the laminar flame thickness. We also observe that the flame thickness increases with flame travel. This may be due to the increase of the turbulent length scale with time.
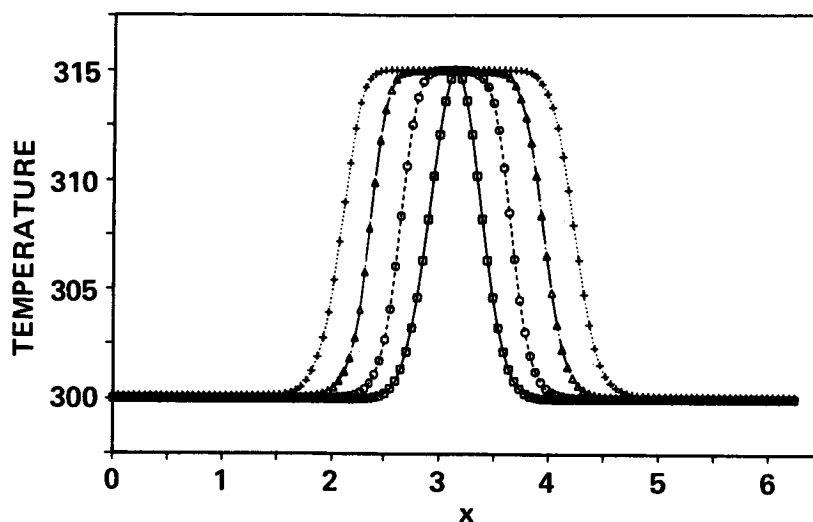
FIGURE 10.   Mean turbulent temperature profiles at 200 step intervals.

Our plans to continue the work on this project include more analysis of the case we have presented here. In particular, we will examine scales and structures relating to the turbulent diffusion of the reactant mass fraction. We will also calculate the area of the wrinkled flame front and compare this to the turbulent flame speed. Further work in this area will include turbulent calculations with a mean strain-rate so that we can examine the effects of anisotropy on flame propagation.

REFERENCES

ABDEL-GAYAD, R. G. & BRADLEY, D. 1976 *Sixteenth Symposium (International) on Combustion*, The Combustion Institute.

CLAVIN, P. & WILLIAMS, F.A.   1979 Theory of premixed-flame propagation in large-scale turbulence. *J. Fluid Mech.* **90**, 589-604.

BRAY, K.N. 1980 Turbulent Flows with Premixed Reactants. *In Turbulent Reacting Flows*, ed. P.A. Libby, F.A. Williams, Springer Verlag, Berlin.

BRAY, K.N. & MOSS, J.B.   1977 *Acta Astron.*,**4**.

POPE, S.B. & ANAND, M.S.   1985 *Twentieth Symposium (International) on Combustion*, The Combustion Institute.

ROGALLO, R.S.   1981   Numerical Experiments in Homogeneous Turbulence. *NASA Technical Memorandum Number 81315.*

TABACZYNSKI, R.J., FERGUSON, C.R. & RADHAKRISHANAN, K. 1974 *SAE Paper Number 740191, SAE Trans.*,**83**.

WILLIAMS, F.A. 1985 *Combustion Theory*, Benjamin-Cummings, Reading, Mass.

WITZE, P.O. & MENDES-LOPES, J.M.C.   1986 *SAE Paper Number 861531.*

ZUR LOYE, A.O., & BRACCO F.V.   1987 *SAE Paper Number 870454.*

Modeling of turbulent transport as a volume process

By MARK J. JENNINGS[1] AND THOMAS MOREL[2]

Introduction

One of the issues in turbulence modeling is the representation of turbulent transport of Reynolds-averaged quantities, both mean values and turbulent statistics. The process of turbulent transport is one of dispersion due to the fluctuating turbulent motions, which span a wide range of spatial scales. In the current models of turbulence, some of the transport terms are calculated from transport equations for the terms themselves. Specifically, the turbulent transport of a quantity ϕ due to velocity-ϕ correlations may be calculated from higher-order equations obtained by manipulation of the ϕ-equation and the momentum equation. However, each such equation introduces additional transport terms due to velocity and pressure correlations.

At any selected level of turbulence modeling, there remains a number of these correlations, and those are almost universally being modeled by gradient diffusion, analogous to the laminar diffusion, with an isotropic scalar diffusivity. More recently, Rogers, Mansour and Reynolds (1987) have proposed a model which employs tensorial diffusivity for heat transfer. The analogy of turbulent transport with laminar diffusion is only distant. This is in part because the seemingly random turbulent motions responsible for the transport can be relatively large compared to the scale of the entire flow region and thus they can communicate with adjacent flow regions. Also, in strained flows these motions have preferred directions and consequently their contributions are not isotropic.

The objective of this work has been to give consideration to an alternative class of methods for the representation of turbulent transport, which would incorporate the effects of (1) the surrounding finite volume, and (2) preferred lines of communication within the flow. These methods, if successful, should have the potential of removing the drawbacks of the current gradient diffusion models.

In a broader sense, all of the turbulence correlations appearing in the Reynolds-averaged equations are the result of non-linear interactions of turbulent motions of various scales. Their modeling has traditionally followed the path of representation in terms of local variables, be it mean gradients or other turbulence correlations. This approach has been moderately successful, although much work remains. It is likely that modeling of terms other than turbulent transfer would also benefit from the consideration of the surrounding volume and of the preferred directions

1 Illinois Institute of Technology
2 Integral Technologies

of strained turbulence. In fact, some work along these lines has already been done, *e.g.*, by Miklavic and Wolfshtein (1987).

Conceptual model of turbulent transport

One concept for alternative description of turbulent transport is to represent it as net convection by fluctuating turbulent motions, which exchange small volumes of fluid between neighboring points. It is assumed that one needs to consider only points that are close enough to be able to influence each other directly. This is based on the premise that the spatial extent of turbulent transport is controlled by the extent over which the motions are coherent. That implies that the turbulent transport of any quantity is directly linked to the coherence and dynamics of the fluid motions. A further premise is that the influence of mean shear on the turbulent transport of a scalar quantity ϕ (which appears in the governing equations of velocity-ϕ correlations as a consequence of manipulation of the momentum equation) is accounted for indirectly, through the action of mean shear on the velocity fluctuation field, resulting in its distortion, anisotropy, and preferred lines of communications within it. The turbulent transport of the scalar can then be deduced from the interaction of the distorted turbulent velocity field with the spatial distribution (gradients) of the mean scalar Φ.

Assuming that the above premises are valid, one may proceed to search for an appropriate formulation of the transport term, which would properly represent this physical picture. Consider two small volumes, one centered on a given point $\mathbf{x}$ and the other on some arbitrary point $\mathbf{x}'$ in the neighborhood of $\mathbf{x}$. These two volumes interact and exchange fluid carrying the scalar. Based on the discussion above, we propose to model the scalar transport in terms of the mean field Φ by

$$T\phi_i(\mathbf{x},t) = C \int [\Phi(\mathbf{x},t) - \Phi(\mathbf{x}',t)] X D \frac{V}{L} \frac{r_i}{r} \frac{1}{4\pi r^2} d^3\mathbf{r} , \qquad (1)$$

where $\mathbf{r} = \mathbf{x} - \mathbf{x}'$, X is a dimensionless spatial function descriptive of the velocity fluctuation field, V/L is the time scale of turbulent motions with V being a velocity scale and L an integral length scale, D is a scalar function of r/L discussed below, and r_i/r is the direction cosine of the vector $\mathbf{r}$ in the i-direction. The factor $1/(4\pi r^2)$ is introduced to represent the decaying influence of a volume as the distance r increases. The introduction of the direction cosine into the relationship implies that the contribution to transport between any two given points in the flow is directed along the vector connecting these points. The function D is included to represent changes in the convected scalar during the transit time $\tau = r/L$ due to diffusion.

The general nature of equation (1) is such that the transport calculated using that expression can produce counter-gradient flux in certain types of non-homogeneous flows. Furthermore, this term is in general non-isotropic (depending on the function X) and thus is more general than commonly used scalar diffusivity models.

A key element in the model is the selection of the function X. Building on the premises of this approach, it seemed worthwhile to investigate the usefulness of basing this function on the two-point velocity correlation Q_{rr} which correlates the

velocity component along the vector r. Such a correlation can be shown to be related to the commonly used two-point correlation Q_{ij}

$$Q_{ij} = \overline{u'_i(\mathbf{x}, t)u'_j(\mathbf{x}', t)} \tag{2}$$

by a relation

$$Q_{rr} = \frac{r_i r_j Q_{ij}}{r^2} . \tag{3}$$

The scalar Q_{rr} is a function of the spatial position. In an isotropic flow this function has spherical contours centered on the correlating point and its value decays along any ray extending from the origin according to the longitudinal correlation function $f(r)$. In a shear flow this function is much more complex, as will be discussed below.

Two-point velocity correlations

Homogeneous shear flow

To test the ideas proposed above, advantage was taken of the available data produced through direct numerical simulations of turbulent flows at Stanford University and at NASA-Ames. One such flow was the homogeneous shear flow calculated by Rogers *et al.* (1986), specifically the flow C128U. Analysis was made of the two-point correlations at dimensionless time $St = 12$. At that instant, the flow may be characterized by $Sq^2/\epsilon = 11$, $q^4/\epsilon\nu = 800$, $\nu_t/\nu = 13$, $P/\epsilon = 1.7$, where S is the mean shear rate dU/dy, $q^2/2$ is the turbulent kinetic energy, ϵ is the turbulent dissipation rate, P is the production rate, ν is the molecular kinematic viscosity, and ν_t is the effective turbulent kinematic viscosity. This is a fully-developed turbulent flow, albeit at fairly low Reynolds number as evidenced by the low value of ν_t/ν. The ratio of longitudinal length scale λ_1 to the computational grid spacing in the x-direction was about 5, and the computational domain spanned 128 nodes in all three directions. The simulation included a cross-stream vertical gradient of a passive scalar with molecular Prandtl number of 0.7.

Using the data base, two-point velocity-velocity and velocity-scalar correlations were obtained. The two-point $u_1 u_1$, $u_1 \phi$, $u_2 u_2$, and $u_2 \phi$ correlations are shown in Figures 1-4 for the x-y and y-z planes through the correlating point. Inspection of the contours shows a distinct similarity between the two types of correlations. The $u_1 \phi$ correlation appears to be strongly influenced by the $u_1 u_1$ correlation. The $u_2 \phi$ contours are somewhat similar to the $u_2 u_2$ contours, although there also appears to be some influence from the $u_1 u_2$ correlation. This tends to support the view that two-point velocity correlations are relevant to scalar transport.

An interesting, and perhaps surprising observation, is that the contours of the $u_2 u_2$ correlation have no inclination, while the $u_1 u_1$ and $u_3 u_3$ correlation contours are very strongly inclined in a direction that is consistent with the mean shear and with the orientation of the flow structures (hairpins) that develop in the flow. This surprising behavior of the vertical fluctuations has been previously observed in experiments, *e.g.*, in a boundary layer by Kovasznay *et al.* (1970) and in homogeneous
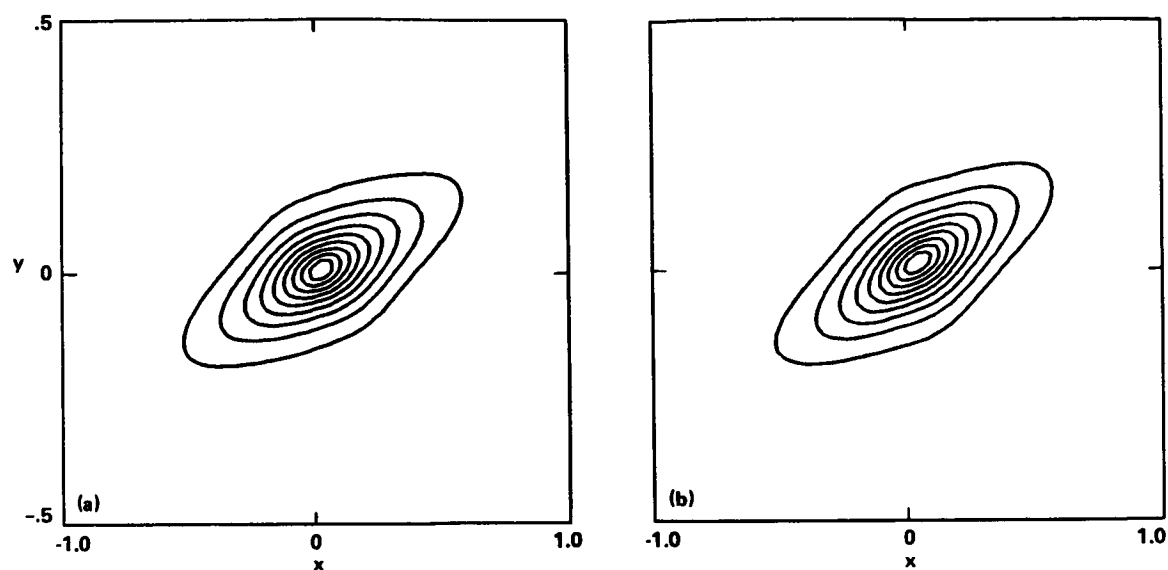
FIGURE 1. Comparison of velocity-velocity and velocity-scalar correlations in a homogeneous shear flow with a vertical mean temperature gradient. Note compressed x-scale. (a) x-y plane, $u_1 u_1$ and (b) x-y plane, $u_1 \phi$.
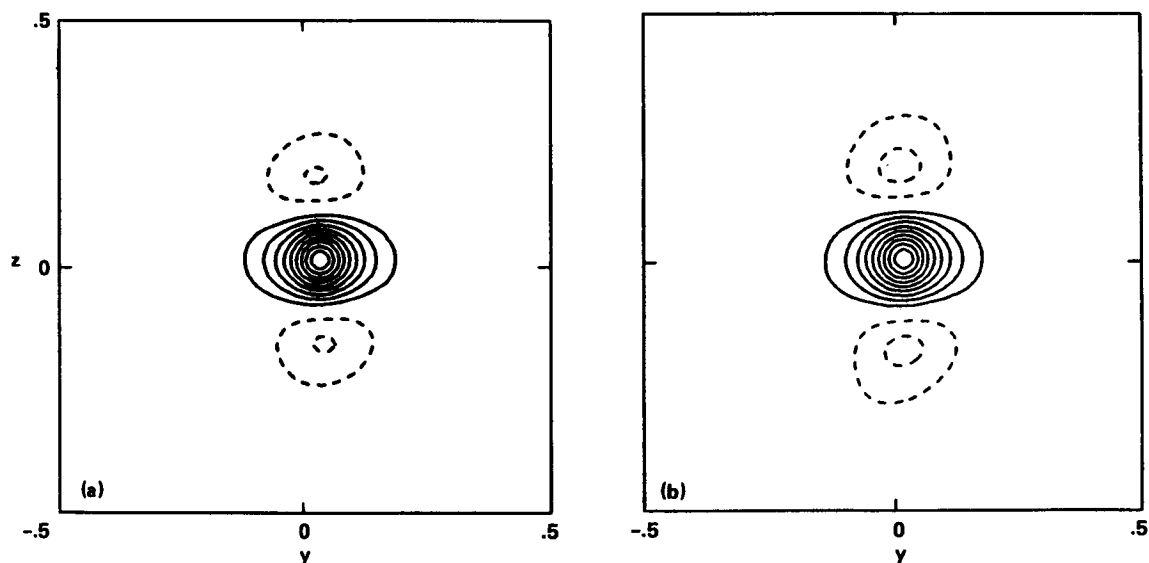
FIGURE 2. Comparison of velocity-velocity and velocity-scalar correlations in a homogeneous shear flow with a vertical mean temperature gradient. (a) y-z plane, $u_1 u_1$ and (b) y-z plane, $u_1 \phi$.

shear layer by Townsend (1970). The contours of the $u_1 u_2$ correlation, being related to both u_1 and u_2, have an inclination which lies between the $u_1 u_1$ and $u_2 u_2$ inclinations.

The contracted correlation Q_{rr}, defined in equation (3), is a linear combination of
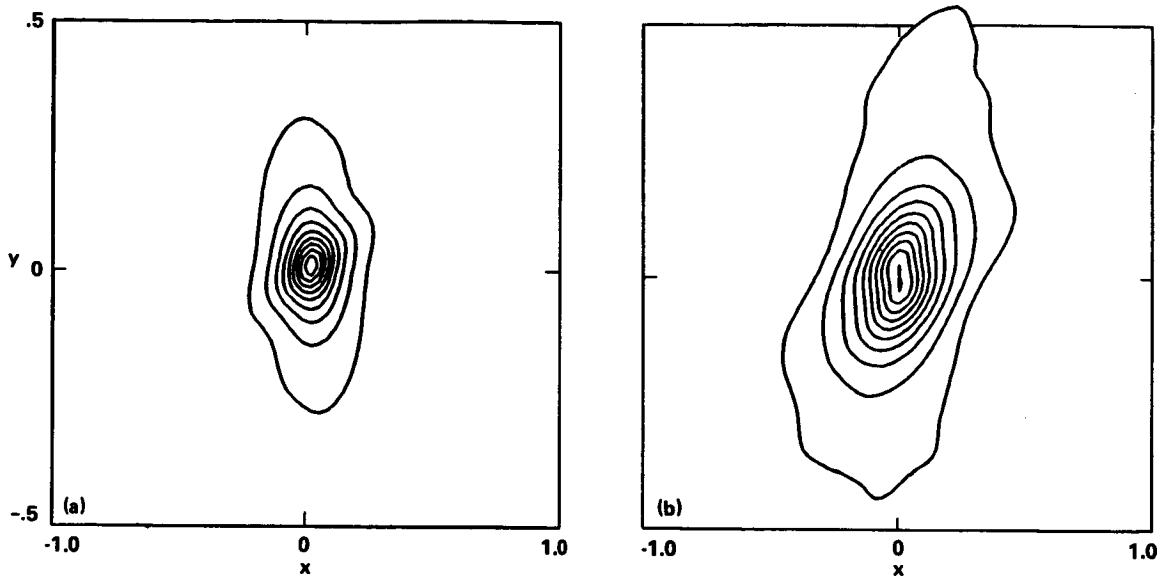
FIGURE 3. Comparison of velocity-velocity and velocity-scalar correlations in a homogeneous shear flow with a vertical mean temperature gradient. Note compressed x-scale. (a) x-y plane, $u_2 u_2$ and (b) x-y plane, $u_2 \phi$.
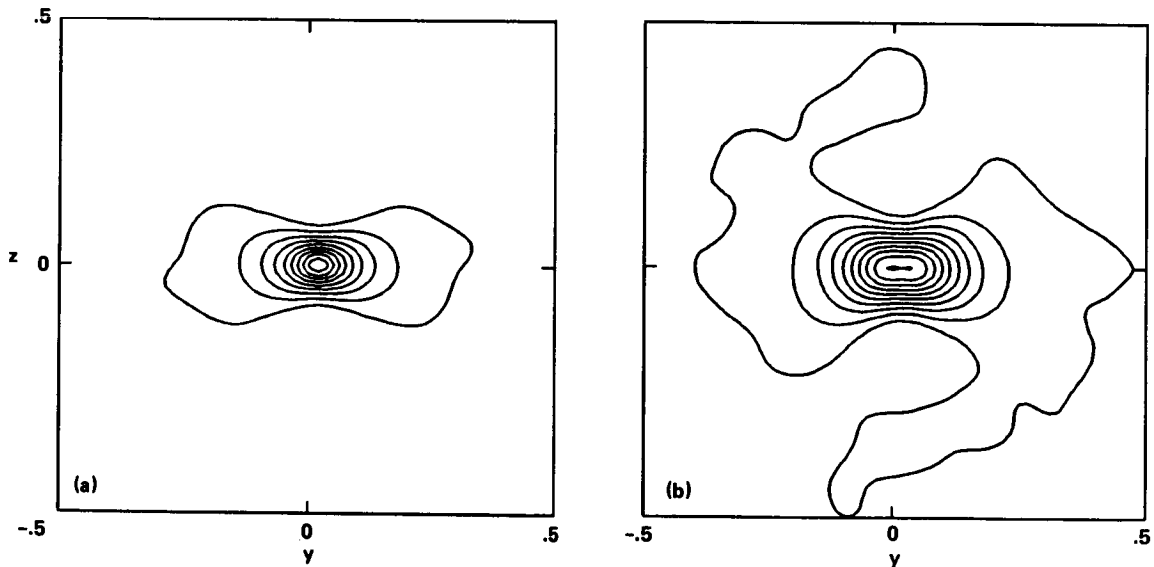
FIGURE 4. Comparison of velocity-velocity and velocity-scalar correlations in a homogeneous shear flow with a vertical mean temperature gradient. (a) y-z plane, $u_2 u_2$ and (b) y-z plane, $u_2 \phi$.

the individual velocity correlations. Its contours are shown in Figure 5 for the three planes x-y, y-z, and x-z. It may be seen that this correlation is very different from the individual components Q_{ij}. Its values are mostly positive with only very weak
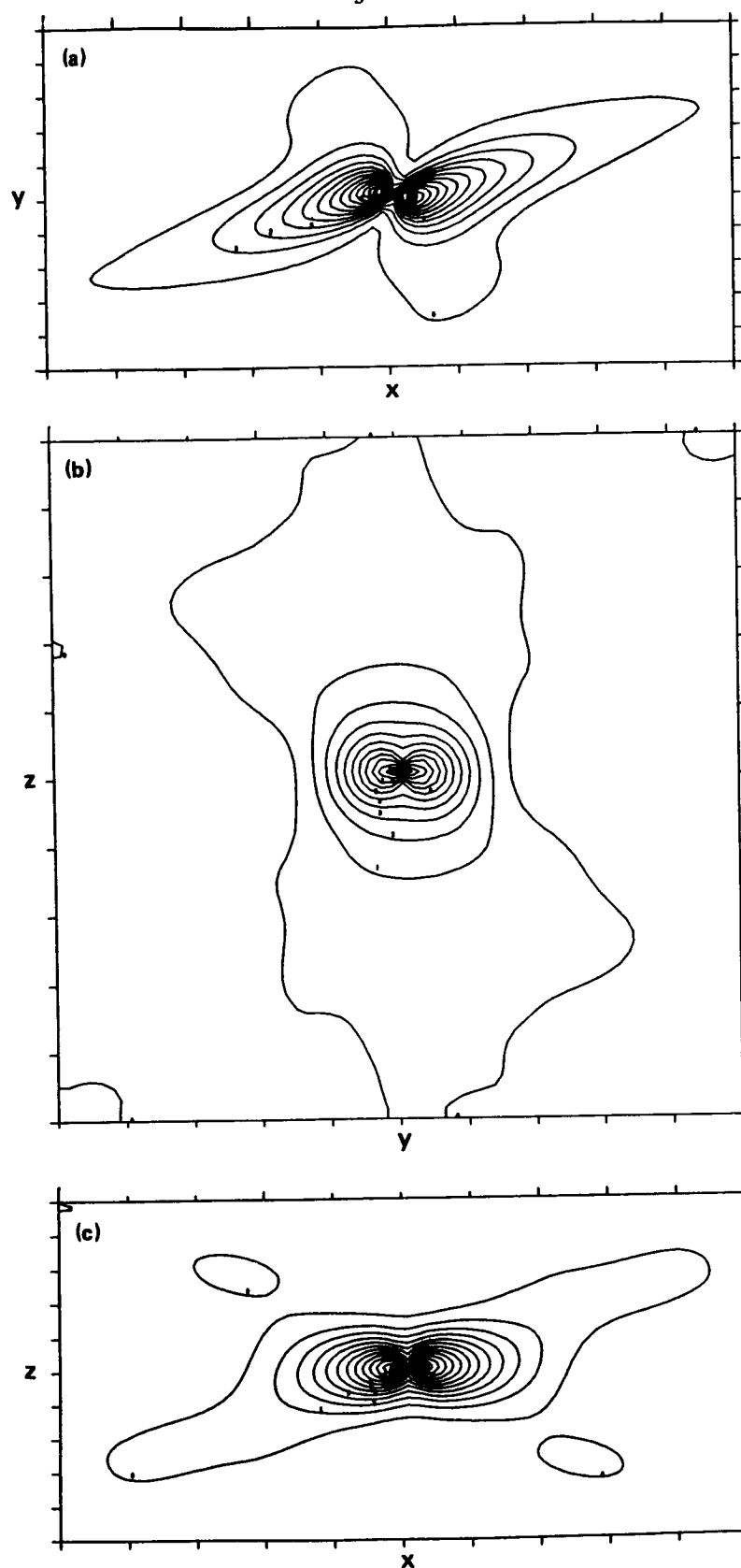
FIGURE 5. Contracted two-point correlation Q_{rr}. (a) x-y plane; (b) y-z plane and (c) x-z plane.

negative lobes. In the x-y plane (Figure 5a) this correlation has a very distinctive shape. This is partly caused by the fact that Q_{rr} has a singular behavior at the origin, where its value depends on the direction from which this point is being approached. The butterfly-like shape seen in this plane is mainly produced by the contributions from the Q_{12} and Q_{21} correlations, and it is absent in the other two planes. In the spirit of the discussion above, this shape of the correlation volume may be interpreted as an indication of the preferred lines of communication set up in a strained turbulent field. It is seen that the preferred communication is along a direction close to the mean flow direction, while a very poor communication is set up along a direction inclined about 70 degrees from the x-direction. This anisotropy may be expected to have a major effect on turbulent transport and perhaps on other processes as well. The correlation volume reflects the effects of the dominant turbulent motions and should be consistent with their orientation and shape; in the case of the homogeneous shear flow these are hairpin-shaped, and their relationship to the correlation volume shape is not immediately obvious.

In the case of homogeneous shear flow equation (1) simplifies to

$$T\phi_i = \frac{c}{4\pi} \, \Phi_{,j} V \int Q_{rr} r_i r_j \frac{dr}{r^2} \qquad (4)$$

or

$$T\phi_i = -D_{ij}\Phi_{,j} \, . \qquad (5)$$

Evaluating the integral in equation (4) over the entire domain one obtains a tensorial diffusivity D_{ij}. The values calculated for this particular flow are given below:

$$(D_{ij}/D_{22})_{model} = \begin{pmatrix} 1.80 & -0.23 & 0.05 \\ -0.23 & 1.00 & -0.04 \\ 0.05 & -0.04 & 1.00 \end{pmatrix}$$

$$(D_{ij}/D_{22})_{simulation} = \begin{pmatrix} 6.5 & -2.4 & 0.0 \\ -1.1 & 1.0 & 0.0 \\ 0.0 & 0.0 & 1.8 \end{pmatrix} \, .$$

The first of the two tensors is that calculated by the present model, the second one has the values deduced by Rogers *et al.* (1986) from the direct simulation. The model values are seen to exhibit correct trends, with high values of D_{11} and with negative off-diagonal contributions D_{12} and D_{21}. However, the magnitudes of the departures from isotropy are not predicted well. By contrast, scalar diffusivity models contain only diagonal terms that are equal in magnitude.

Channel flow

To complement the data presented above, a brief study was made of a two-point correlation in a channel flow simulation data of Kim, Moin and Moser (1987). The Reynolds number based on wall friction velocity u_τ and channel half-width H was 180. The contours of the $u_1 u_1$, $u_2 u_2$, $u_3 u_3$ and $u_1 u_2$ two-point correlations at

distances of one-quarter and one-half H from the wall were computed. At the one-quarter H location, $u_1 u_1$ and $u_3 u_3$ contours are stretched and inclined towards the channel wall. The $u_2 u_2$ contours are seen to be affected by the presence of the wall, especially those at lower correlation levels which are farther away from the origin. This general behavior is also seen at the half H point, except that the wall effects are diminished and some similarities with the homogeneous shear flow begin to emerge.

Summary

An alternative type of modeling has been proposed for the turbulent transport terms in Reynolds-averaged equations. During the Summer Program, one particular implementation of the model has been considered, based on the two-point velocity correlations. The model was found to reproduce the trends but not the magnitude of the non-isotropic behavior of the turbulent transport. Some interesting insights have been developed concerning the shape of the contracted two-point correlation volume. This volume is strongly deformed by mean shear from the spherical shape found in unstrained flows. Of particular interest is the finding that the shape is sharply waisted, indicating preferential lines of communication, which should have a direct effect on turbulent transfer and on other processes.

Acknowledgements

REFERENCES

KIM, J., MOIN, P., & MOSER, R. D. 1987 Turbulence statistics in fully developed channel flow at low Reynolds number. *J. Fluid Mech.* **177**, 133-166.

KOVASZNAY, L. S. G., KIBENS, V. & BLACKWELDER, R. F. 1970 Large-scale motion in the intermittent region of a turbulent boundary layer. *J. Fluid Mech.* **41**, 283-325.

MIKLAVIC, S. J. & WOLFSHTEIN, M. 1987 A quasi-isotropic model of the two-point temperature-velocity correlation and its application to the modeling of the turbulent heat flux, to be published.

ROGERS, M. M., MANSOUR, P. & REYNOLDS, W. C. 1987 An algebraic model for the turbulent flux of a passive scalar, to be published.

ROGERS, M. M., MOIN, P. & REYNOLDS, W. C. 1986 The structure and modeling of the hydrodynamic and passive scalar fields in homogeneous turbulent shear flow. *Dept. Mech. Eng. Report No. TF-25.* Stanford University, Stanford, California.

TOWNSEND, A. A. 1970 Entrainment and structure of turbulent flow. *J. Fluid Mech.* **41**, 13-46.

Analysis of non-premixed turbulent reacting flows

By ANDY D. LEONARD[1] AND JAMES C. HILL[1]

Studies of chemical reactions occurring in turbulent flows are important in the understanding of combustion and other applications. Some situations, hypersonic reacting flows for example, are difficult to study experimentally and will benefit from direct numerical simulations. Current numerical methods are limited in their applications due to the numerical resolution required to completely capture all length scales but, despite the fact that "realistic" combustion cannot be solved completely, numerical simulations can be used to give insight into the interaction between the processes of turbulence and chemical reaction (Jou and Riley, 1987).

The objectives of this work were (1) to investigate the effects of turbulent motion on the effects of chemical reaction to gain some insight on the interaction of turbulence, molecular diffusion and chemical reaction to support modeling efforts, and (2) to develop efficient strategies for evaluation of multi-point probability density functions (pdfs) and develop other post-processing tools. For lack of time, only the first objective was actually addressed.

A direct turbulence simulation spectral code (Rogallo 1981) was modified to include the effects of chemical reaction and applied to an initial value problem of chemical reaction between non-premixed species. Preliminary results show the dissipation microscale of the scalar variance to be independent of Damkohler number. The influence of hydrodynamics on the instantaneous structure of the reaction was investigated.

The specific problem under consideration is the isothermal, irreversible chemical reaction of two initially segregated species, of the type

$$A + B \rightarrow P \qquad (1)$$

occurring in a decaying homogeneous isotropic turbulent flow. The concentration of one reacting species follows the mass conservation equation

$$\frac{\partial A}{\partial t} + \mathbf{u} \cdot \nabla A = D_A \nabla^2 A - KAB \qquad (2)$$

and the turbulent velocity field obeys the Navier-Stokes equations

$$\frac{\partial \mathbf{u}}{\partial t} + \mathbf{u} \cdot \nabla \mathbf{u} = -\frac{1}{\rho} \nabla p + \nu \nabla^2 \mathbf{u} . \qquad (3)$$

The reaction-rate coefficient, K, is constant, and so the situation can be thought of as an isothermal diffusion flame. The turbulent velocity and the concentration of

---

1 Department of Chemical Engineering, Iowa State University
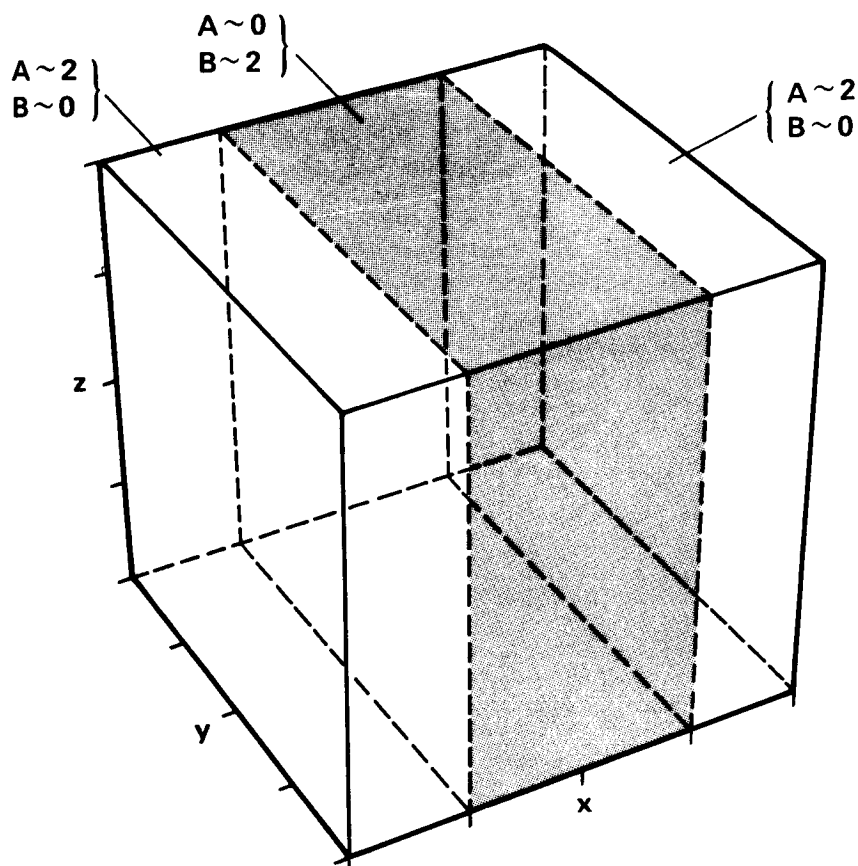
FIGURE 1. Schematic diagram of initial conditions for reactants A and B.

chemical species were all calculated using direct numerical simulation. A pseudo-spectral method was used with aliasing errors removed. It was necessary to add the term for chemical reaction in equation (2) to an existing program for the direct simulation (Rogallo 1981; see also Lee and Reynolds 1985). The Courant-Freidricks-Lewy stability criterion was appropriately modified to include the effect of reaction on the scalar field equation, and some modifications were needed to obtain diagnostics for the scalar field.

Two calculations were performed on a mesh of 64x64x64 points. Three velocity components and four scalar components were calculated in each simulation, including the reactant species (denoted as A and B), the product species (denoted as P) and the non-reacting species (denoted as C). Two different values of the reaction-rate coefficients were used in the study. The Damkohler numbers (dimensionless reaction-rate coefficients) based on the initial mean reactant concentration, turbulence intensity and the integral velocity length scale were 10 and 2 for the two runs. The Schmidt number for all species was unity. The initial conditions for the reactant species are illustrated in Figure 1. Initial values of A and C were identical. The turbulence was freely decaying from an arbitrarily chosen initial energy spectrum.
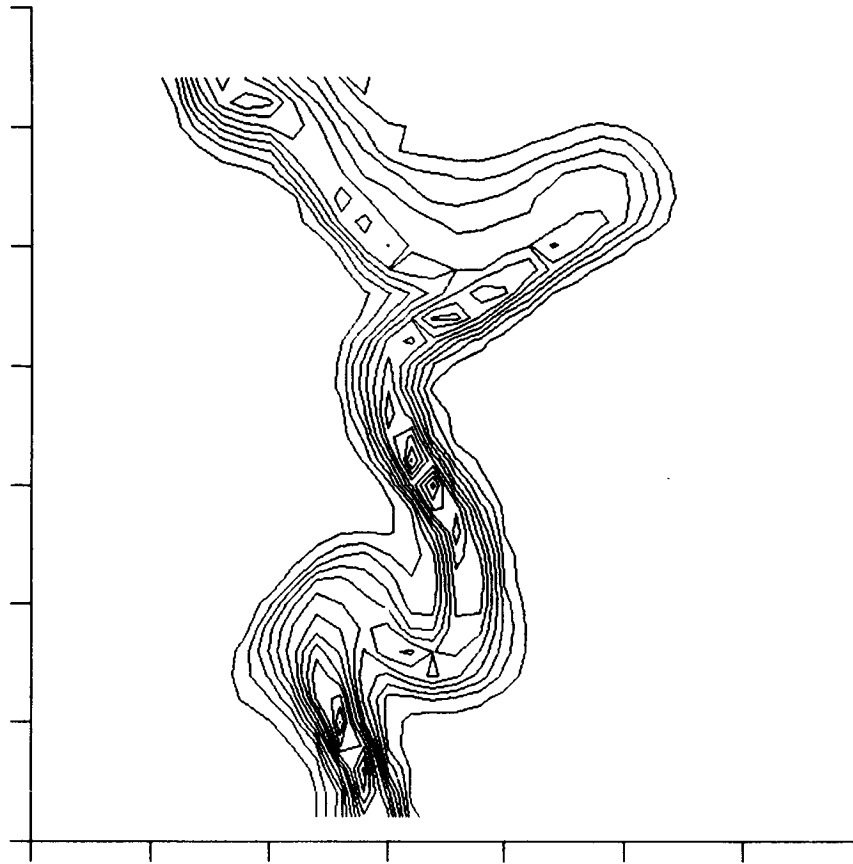
FIGURE 2.   Reaction term in equation (2), KAB, for $t = 1.1$ and $Da = 10$. The contour interval is 0.2.

The initial Reynolds number based on the Taylor microscale was 24. Velocity fields were initialized using random numbers scaled to fit a given energy spectrum that was nearly Gaussian in form. The simulations were carried out for 400 steps for the case with the higher reaction rate and for 300 steps for the case with the lower reaction rate.

Modification of the program, small-scale calculations to verify the changes, and running the 64x64x64 calculations required three weeks to complete. Several data sets were saved with the full set of Fourier coefficients for the scalar and velocity fields, so that the IRIS workstation and interactive graphics programs could be used to examine the spatial dependence of the fields in physical space at a single value of time. Many of the results are only qualitative at this writing.

Our proposal was to examine the local scalar dissipation rates and the local reaction rates to determine the influence of vorticity or rate of strain on the reaction and the structure of the scalar field. Consequently, the region where the reaction occurs was the focus of attention. The location of this region is marked by the value of the term KAB in equation (2) and is clearly shown in Figure 2. The region was
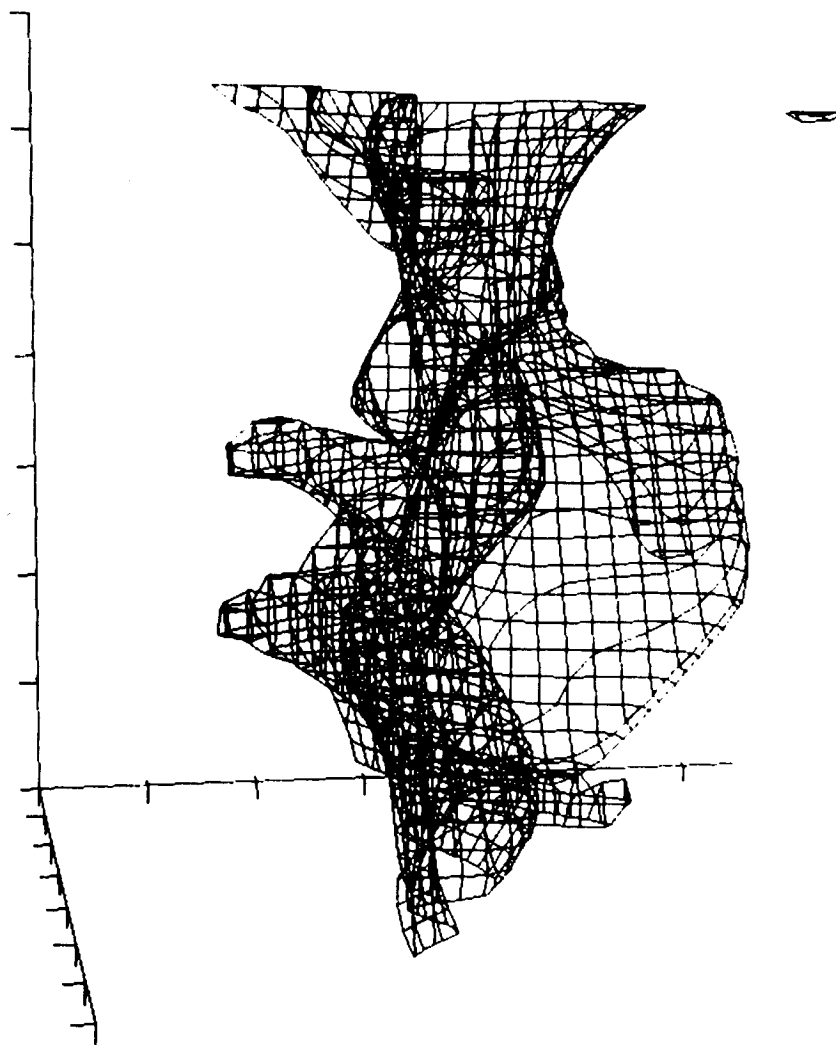
FIGURE 3. Surface where the conserved scalar $A - B$ equals zero.

also marked by the product species concentration and high values of the magnitude of the gradients of reactant species concentrations as the reaction was nearly diffusion limiting, due to the high reaction rates. The reactant species, therefore, remain highly segregated over the course of the reaction with sharp gradients in the reaction zone. The thickness of the zone is about four grid points at the higher Damkohler number. The reaction zone is distorted by the turbulent motion and the reaction rate and product concentrations are not uniform within the reaction zone. The regions of high reaction rate correlate only roughly with regions of high product concentration.

An attempt was made to determine the influence of the hydrodynamics on the structure of the reaction zone. Surfaces at which the concentration of the conserved scalar $A - B$ equals zero appear to be good indicators of the location of the reaction
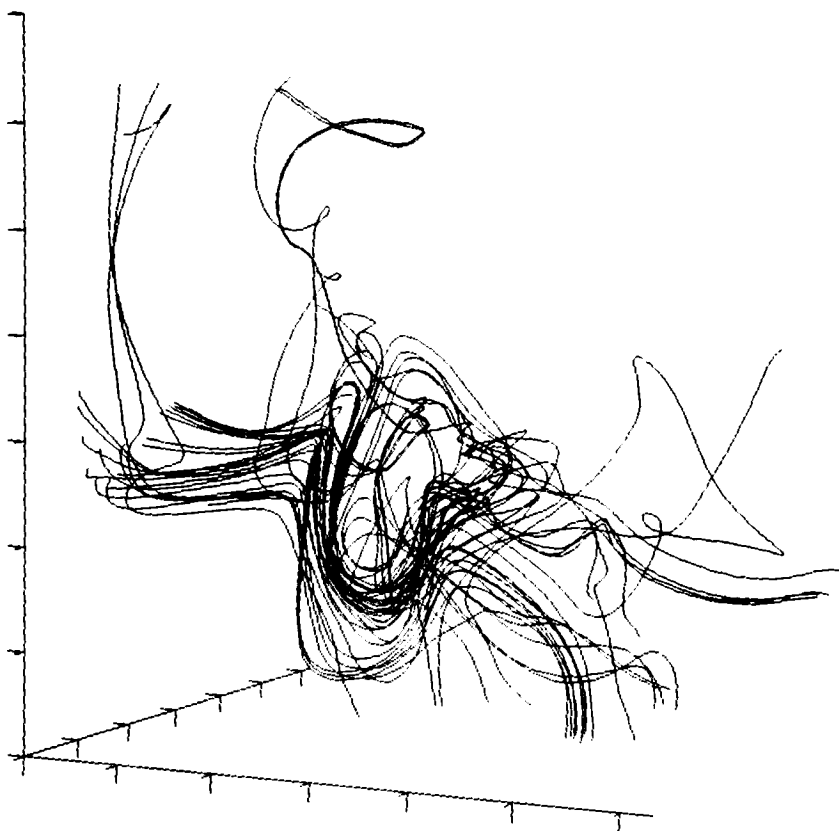
FIGURE 4.   Vortex lines passing through points near one of the finger-like structures in Figure 3.

zone. These surfaces show fingers of reactant pushing into the reaction zone (Figure 3). Vortex lines passing through a group of points located near one of the fingers are shown in Figure 4. The vortex lines are suggestive of the idea that a vortex ring is producing the finger by eduction, but the evidence is inconclusive and needs more extensive investigation.

The results of the simulations supported earlier findings (Leonard and Hill, 1987) that the dissipation microscale of the concentration fields is not greatly affected by the Damkohler number (Table 1). Modeling the effects of dissipation is a weakness of some theories, as the process is not local. These findings suggest that diffusive effects can be treated reasonably well by correctly modeling an equivalent non-reacting flow.

The work done at the summer program was a beginning of an effort to look closely at the influence of hydrodynamics on the instantaneous structure of the reaction. Previous work (Leonard and Hill, 1987) had looked primarily on volume-averaged quantities to test closure theories (Toor 1969; Patterson, 1981). The effect of strain rate on the reaction has yet to be investigated. Further work is planned for analysis

Da	λ_A $t_e = 0$	λ_A $t_e = 1$
0	1.46	1.02
2	1.46	1.00
10	1.46	0.94

$$Da = K\overline{A_0}u_0'/L_0 \quad \lambda_A^2 = 6\overline{a^2}/|\overline{\nabla a}|^2 \quad t_e = L_0/u_0'$$

Table 1. Effect of Da on dissipation microscale of reactant A.

of the simulations performed during the CTR summer program and for additional simulations to study the effects of parameters such as different molecular diffusivities for reactant species, non-stoichiometric ratio of reactant concentrations, steady (forced) turbulence, external mean shear or strain, and different initial velocity conditions.

Acknowledgements

REFERENCES

JOU, W.-H. & RILEY, J. J. 1987 On Direct Numerical Simulations of Turbulent Reacting Flows. *AIAA-87-1324*.

LEE, M. J. & REYNOLDS, W. C. 1985 Numerical Experiments on the Structure of Homogeneous Turbulence. *Dept. Mech. Eng. Report TF-24*. Stanford University, Stanford, California.

LEONARD, A. D. & HILL, J. C. 1987 Direct Numerical Simulation and Simple Closure Theory for a Chemical Reaction in Homogeneous Turbulence. *U.S.-France Joint Workshop on Turbulent Reactive Flows*, Rouen, France.

PATTERSON, G. K. 1981 Application of Turbulence Fundamentals to Reactor Modelling and Scaleup. *Chem. Eng.Commun.* **8**, p 25.

TOOR, H. L. 1969 Turbulent Mixing of Two Species With and Without Chemical Reaction. *Ind. Eng. Chem. Fundam.* **8**, p655.

ROGALLO, R. S. 1981 Numerical Experiments in Homogeneous Turbulence. *NASA TM-81315*.

A statistical investigation of the single-point pdf of velocity and vorticity based on direct numerical simulations

By M. MORTAZAVI[1], W. KOLLMANN[1] AND K. SQUIRES[2]

Vorticity plays a fundamental role in turbulent flows. However, most closure models presently available do not treat vorticity in an explicit fashion. Hence it is suggested to investigate the dynamics of vorticity in turbulent flows and the effect on single-point closure models. The approach is to use direct numerical simulations of turbulent flows to investigate the pdf of velocity and vorticity.

The pdf of velocity and vorticity is governed by a transport equation, which contains terms describing the dynamical processes of vortex stretching, viscous dissipation, and the effect of fluctuating pressure gradients as conditional fluxes in velocity-vorticity and physical spaces. These fluxes, together with appropriate boundary conditions, determine the evolution of the pdf from an initial state. Analysis of these fluxes shows that they cannot be represented in terms of the single-point pdf only, but require structural information in terms of two-point pdf's or two-point correlations. A direct way of getting information on the conditional fluxes is the statistical evaluation of results obtained from direct numerical simulations of turbulent flows, presently possible only at relatively low Reynolds numbers. This was carried out for a homogeneous shear flow.

Consider a point $(\mathbf{x}, t)$ in a turbulent flow field. Let $v_i(\mathbf{x}, t)$ and $w_i(\mathbf{x}, t)$ be a realization of velocity and vorticity at the chosen point. The quantity (Lundgren 1967)

$$\hat{f} \equiv \delta(\mathbf{v}(\mathbf{x}, t) - \mathbf{V})\delta(\mathbf{w}(\mathbf{x}, t) - \mathbf{W}) \tag{1}$$

denotes the fine-grained pdf of velocity and vorticity at $(\mathbf{x}, t)$. The expectation of $\hat{f}$ is then the pdf at $(\mathbf{x}, t)$,

$$f(\mathbf{V}, \mathbf{W}; \mathbf{x}, t) \equiv < \hat{f} > , \tag{2}$$

where $<>$ denotes an ensemble average. The fine-grained pdf is conserved

$$\partial_t \hat{f} + \frac{\partial}{\partial V_i} (\partial_t v_i \hat{f}) + \frac{\partial}{\partial W_i} (\partial_t w_i \hat{f}) = 0 , \tag{3}$$

where $\partial_i = \partial/\partial x_i$ and $\partial_t = \partial/\partial t$. Averaging of (3) and the use of the balances for an incompressible Newtonian fluid, in the absence of body forces, lead to the pdf transport equation:

1 Dept. of Mech. Engng., University of California, Davis
2 Dept. of Mech. Engng., Stanford University

$$\partial_t f + V_i \partial_i f = \frac{\partial}{\partial V_i}(< \frac{1}{\rho}\partial_i p | \ldots > f) + \nu\nabla^2 f - \frac{\partial^2}{\partial V_i \partial V_j}(\nu < \partial_k v_i \partial_k v_j | \ldots > f)$$

$$-2\frac{\partial^2}{\partial V_i \partial W_j}(\nu < \partial_k v_i \partial_k w_j | \ldots > f) - \frac{\partial^2}{\partial W_i \partial W_j}(\nu < \partial_k w_i \partial_k w_j | \ldots > f)$$

$$-\frac{\partial^2}{\partial x_j \partial W_i}(V_i W_j f) - \frac{\partial^2}{\partial W_i \partial V_k}(< w_j v_i S_{jk} | \ldots > f)$$

$$-\frac{\partial^2}{\partial W_i \partial W_k}(< w_j v_i \partial_j w_k | \ldots > f) - \frac{\partial}{\partial V_i}(< f_i | \ldots > f)$$

$$-\epsilon_{ijk}\frac{\partial}{\partial W_i}(< \partial_j f_k | \ldots > f) , \tag{4}$$

where ... denotes the condition $(\mathbf{v} = \mathbf{V}, \mathbf{w} = \mathbf{W})$ and $S_{ij} \equiv \frac{1}{2}(\partial_i v_j + \partial_j v_i)$ denotes the rate of strain.

This transport equation contains three dynamically different groups of terms. The conditional flux of f due to the fluctuations of the pressure gradient

$$F_i \equiv < \frac{1}{\rho}\partial_i p | \mathbf{v} = \mathbf{V}, \mathbf{w} = \mathbf{W} > \tag{5}$$

acts on f in velocity space only, since the vorticity transport equation does not contain the pressure in explicit form. This implies that

$$\lim_{|\mathbf{V}|\to\infty} F_i f = 0$$

no matter what value $\mathbf{W}$ for vorticity is considered. In this preliminary report, we will focus our attention on F_i.

The conditional fluxes caused by the fluctuating pressure gradient, vortex stretching and viscous stresses are functions of the point $(\mathbf{x}, t)$ and the conditioning variables $(\mathbf{V}, \mathbf{W})$. Hence, they are functions of up to ten independent variables. Consequently, we consider conditional expectations with increasing number of conditions in order to begin with a manageable number of independent variables. Integration of equation (5) over vorticity space leads to

$$\int F_i(\mathbf{V}, \mathbf{W})f(\mathbf{V}, \mathbf{W})d\mathbf{W} = f^{\mathbf{V}}(\mathbf{V})\int F_i(\mathbf{V}, \mathbf{W})f(\mathbf{W}|\mathbf{V})d\mathbf{W}$$

and thus

$$F_i^{\mathbf{V}}(\mathbf{V})f^{\mathbf{V}}(\mathbf{V}) = \int F_i(\mathbf{V}, \mathbf{W})f(\mathbf{V}, \mathbf{W})d\mathbf{W} ,$$

where

$$F_i^{\mathbf{V}}(\mathbf{V}; \mathbf{x}, t) = \int F_i(\mathbf{V}, \mathbf{W}; \mathbf{x}, t)f(\mathbf{W}|\mathbf{V}; \mathbf{x}, t)d\mathbf{W}$$

denotes the conditional flux in velocity space irrespective of vorticity and $f(\mathbf{W}|\mathbf{V})$ the conditional pdf of vorticity given velocity. Then,

$$F_i^{\mathbf{V}}(\mathbf{V};\mathbf{x},t) = <\frac{1}{\rho}\partial_i p | \mathbf{v} = \mathbf{V}>. \tag{6}$$

Integration over parts of the velocity space leads furthermore to expectations conditioned with a single variable,

$$F_i^j(V_j;\mathbf{x},t) = <\frac{1}{\rho}\partial_i p | v_j = V_j>. \tag{7}$$

These quantities are most easily accessible to numerical evaluation and they constitute, therefore, the starting point for the investigation.

The direct simulation of a homogeneous linear shear flow carried out by Rogers and Moin (1987) and Rogers, Moin and Reynolds (1986) (case C128U12) was the data base for the evaluation of the pdf's and the conditional fluxes. This was done in three steps: (1) conditioning with one velocity component; (2) conditioning with one vorticity component; (3) conditioning with two variables (two velocity components, one velocity and one vorticity component or two vorticity components).

In the plots that follow, iso-probability contour lines are equally spaced, with high values near the center. The important aspect is the shape of the contour lines, and so the flow-dependent levels and coordinate ranges are omitted. Samples are collected in discrete bins, which produces the rather jagged look to the diagrams. The plotting package used plots the curves over the full range of velocity fluctuation values encountered, ranging from the minimum to the maximum. The abscissa and ordinate range from their minimum to maximum values so their zeros are not exactly in the center of the figure. At each extreme there is only one data point, and hence no conclusion can be drawn on the statistical behavior there. Areas with inadequate statistical sample, and hence highly uncertain values, are shaded.

The joint pdfs of the pressure-gradient component $\partial_1 p$ and one velocity component V_1, V_2, or V_3 are shown in Figures 1–3. The skewed shapes of the iso-probability contours show that $\partial_1 p$ is weakly correlated positively with V_1 and more strongly correlated negatively with V_2; the correlation with V_3 is zero by symmetry. The conditional pdfs of ∂p_1 are shown in Figures 4–6. They show that the conditioned probabilities are of the same form at different values of V_i, with a mean value (expectation) that varies with the conditioning velocity. The conditional expectations $<\partial_1 p | v_i>$ are shown in Figure 7. Note that they are linear in the velocity components over the range of adequate sample, an observation of importance in modeling. Figure 8 shows contours of the expectation of $\partial_1 p$ conditioned on both V_1 and V_2. Note that these contours are straight in the region of adequate sample, consistent with the linear behavior found in Figure 7, and that the rate of change with respect to each velocity component is independent of the velocities.

The joint pdfs of pressure-gradient components and single vorticity components show no discernable correlation between the two. Consequently, the expectation values of the fluctuation pressure gradient, conditioned on the local fluctuation
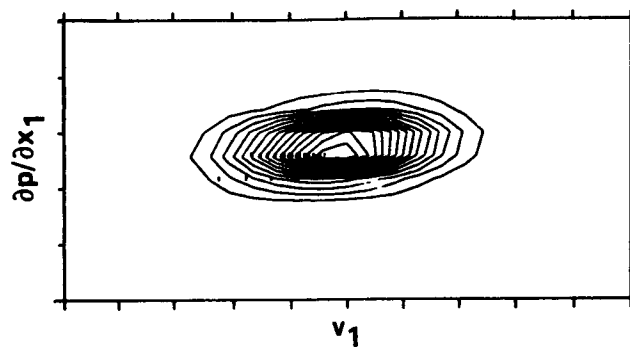
FIGURE 1.   Iso-probability lines of $f(v_1, \partial_1 p)$ in a linear shear flow.
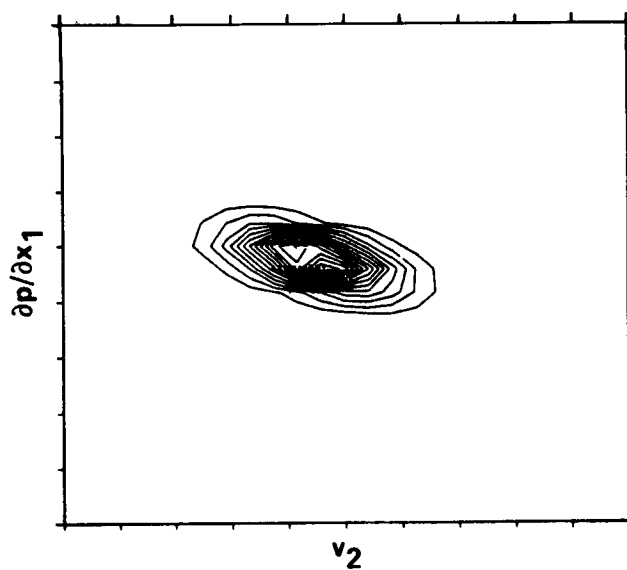
FIGURE 2.   Iso-probability lines of $f(v_2, \partial_1 p)$.
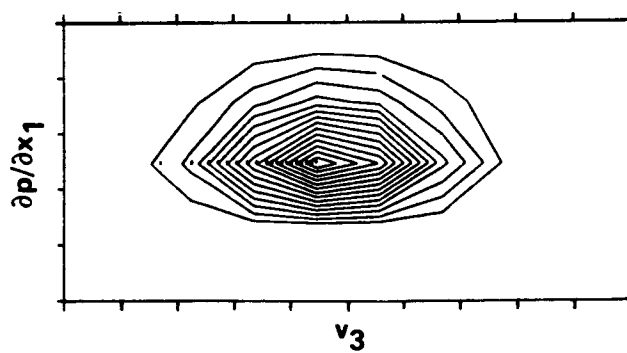
FIGURE 3.   Iso-probability lines of $f(v_3, \partial_1 p)$.
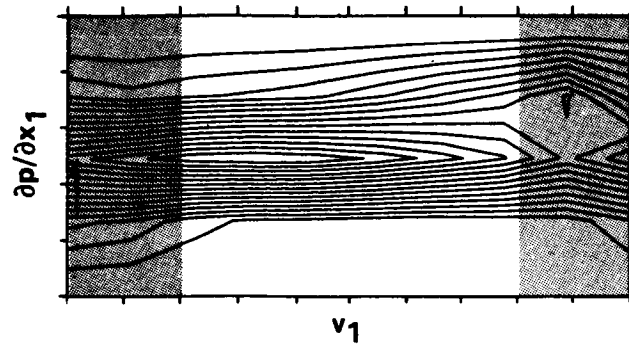
FIGURE 4. Iso-probability lines of the conditional pdf $f(\partial_1 p|v_1)$.
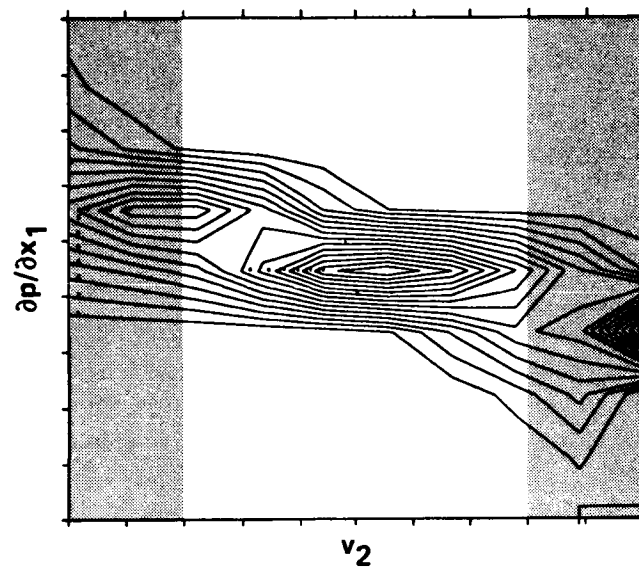
FIGURE 5. Iso-probability lines of the conditional pdf $f(\partial_1 p|v_2)$.
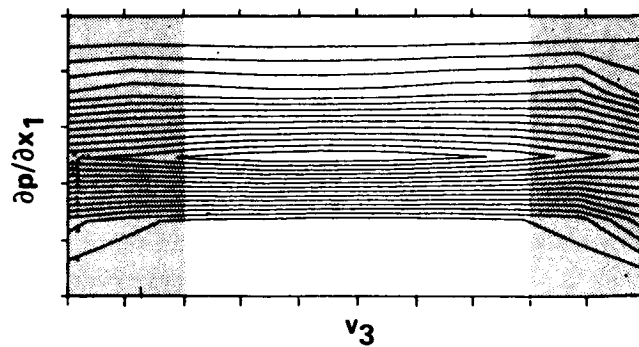
FIGURE 6. Iso-probability lines of the conditional pdf $f(\partial_1 p|v_3)$.
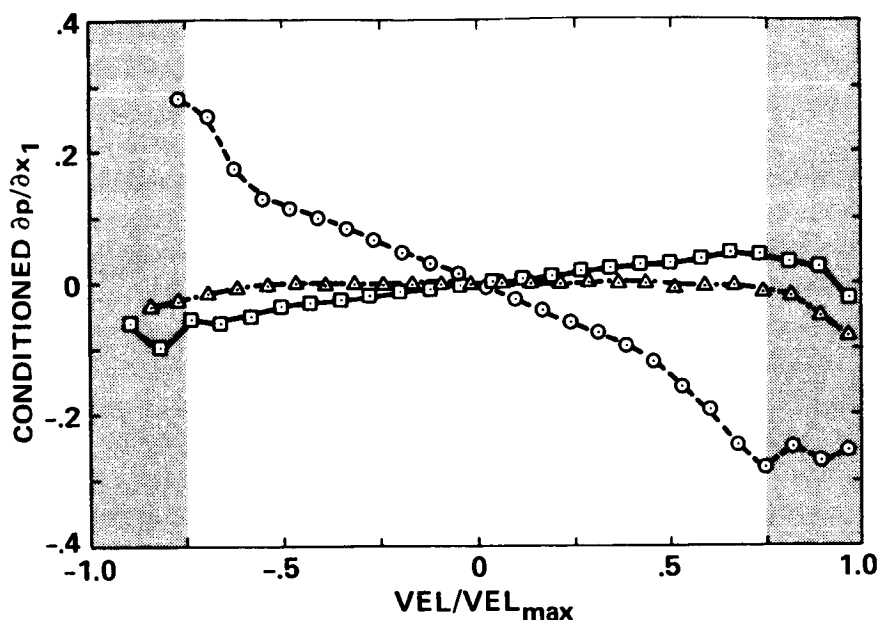
FIGURE 7. Rescaled conditional expectations $< \partial_1 p | v_\alpha >$. ——— $\alpha = 1$; ---- $\alpha = 2$; —·— $\alpha = 3$.

vorticity, are essentially zero. For example, Figure 9 shows the contours of the expectation of the streamwise pressure gradient $\partial_1 p$ conditioned on the velocity component V_2 and the streamwise vorticity component W_1. Note that the expectation is independent of vorticity. Figure 10 shows the expectations of the streamwise pressure gradient, conditioned on the vorticity components W_1 and W_2. The variations at either end are due to inadequate sample, and the flat portion in the middle is at zero, indicating no dependence on the vorticity.

In summary, this preliminary study of homogeneous shear flow has shown that the expectation of the fluctuating pressure gradient, conditioned with a velocity component, is linear in the velocity component, and that the coefficient is independent of velocity and vorticity. In addition, the work shows that the expectation of the pressure gradient, conditioned with a vorticity component, is essentially zero.

REFERENCES

LUNDGREN, T.S. 1967 *Phys. Fluids*, **10**, 969.

ROGERS, M. M. & MOIN, P. 1987 The structure of the vorticity field in homogeneous turbulent flows. *J. Fluid Mech.* **176**, 33-66.

ROGERS, M. M., MOIN, P. & REYNOLDS, W. C. 1986 The structure and modeling of the hydrodynamic and passive scalar fields in homogeneous turbulent shear flow. *Dept. Mech. Eng. Report No. TF-25.* Stanford University, Stanford, California.
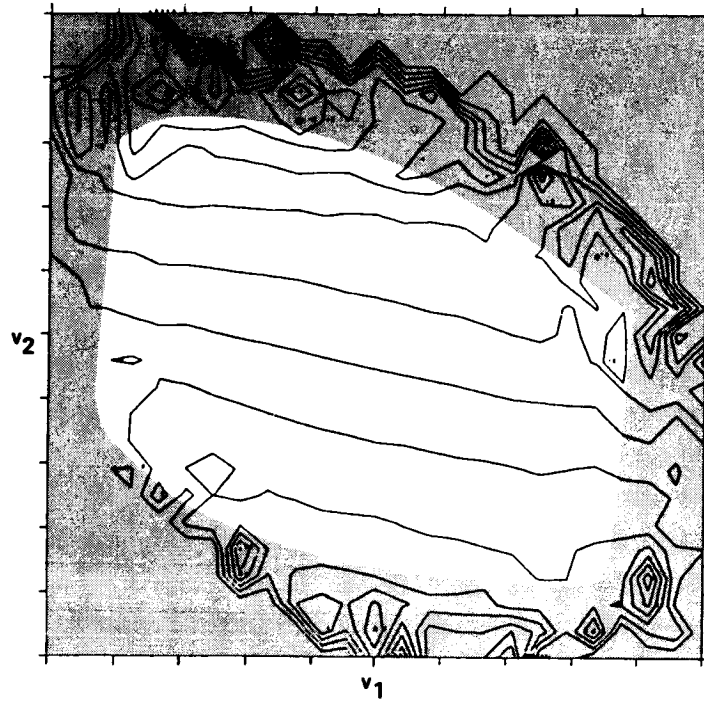
FIGURE 8. Conditional expectation $< \partial_1 p | v_1, v_2 >$
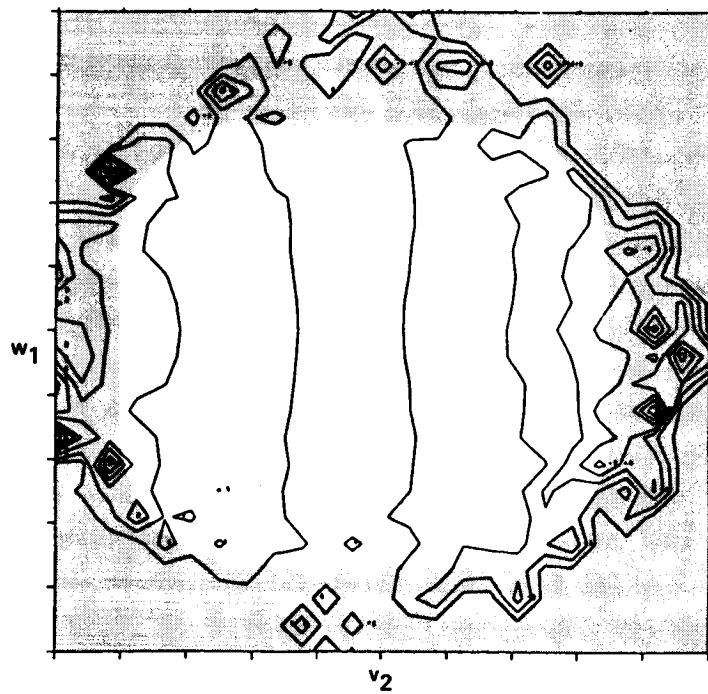
FIGURE 9. Conditional expectation $< \partial_1 p | v_2, w_1 >$
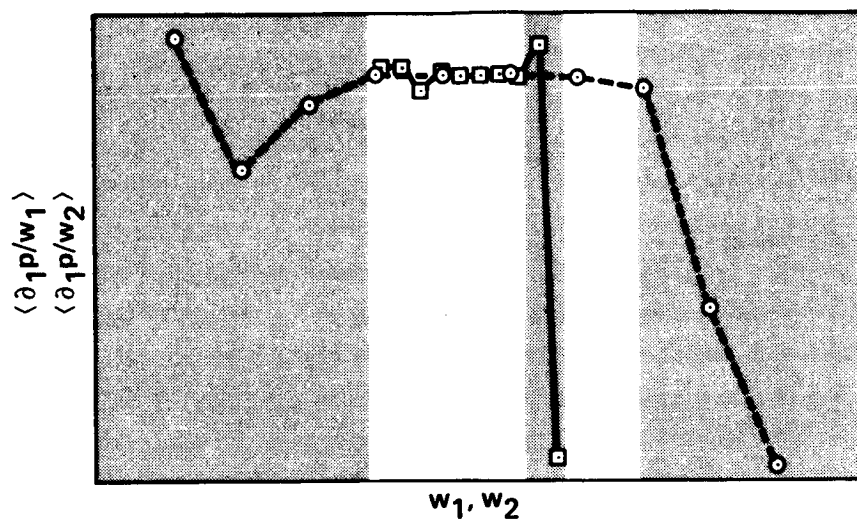
FIGURE 10.   Conditional expectations $< \partial_1 p | w_\alpha >$. ——— $\alpha = 1$; - - - - $\alpha = 2$.

Overview of Research by the Reynolds Stress Modeling Group

It is well recognized that full turbulence simulations will be limited for the forseeable future to simple fundamental flows. In order to compute flows of engineering interest, turbulence models will have to be used in formulating the governing equations. These models are a pacing item in the development of a computational fluid dynamics capability. Traditional model development had relied on formulating a closure model, then the model is used in a simulation to assess its validity. No direct experimental measurements are available for the pressure-strain, because of the difficulty in measuring these terms, and therefore no direct assessment of the models was possible. Direct simulation data can be used to compute the terms that need to be modeled and direct comparison with closure formulas can be achieved. This process should lead to a more systematic way of testing models. The objectives of the Turbulence Modeling Group were to develop and test closure models.

The invited participants in the modeling group were:
Prof. P. Bradshaw (Imperial College)
Prof. J. G. Brasseur (Clemson University)
Dr. J. Y. Chen (Sandia National Laboratories)
Prof. H. Ha Minh (IMF-CNRS)
Prof. J. C. Hunt (Cambridge)
Prof. C. G. Speziale (ICASE; NASA Langley)
Prof. D. Vandromme (CORIA-CNRS)
Dr. J. Weinstock (NOAA/ERL/Aeronomy Laboratory)
Prof. M. Wolfshtein (Technion)

The local participants were:
Dr. M. J. Lee (NASA Ames)
Dr. S. Lele (NASA Ames)
Dr. N. N. Mansour (NASA Ames)
Mr. U. Piomelli (Stanford University)
Dr. M. W. Rubesin (NASA Ames)
Mr. K. Shariff (NASA Ames)
Dr. T.-H Shih (Center for Turbulence Research)
Dr. J. R. Viegas (NASA Ames)

As expected, most of the work was devoted to the assessment of existing turbulence models. While some of this work had already been carried out by investigators at Ames (e.g. Mansour, Kim and Moin, 1987, to appear in J.F.M.) for the model of Launder, Reece and Rodi (1975), the summer school provided an opportunity for various other modelers to test their models against full turbulence simulation data.

Weinstock & Shariff evaluated the theory of Weinstock (1981, 1982, 1985) for the slow term. They found that many of the features of the slow term are reproduced by the theory. The data indicates that the "Rotta" coefficient varies between component and changes significantly with strong temporal variations of the kinetic energy; these features are well predicted by the theory.

Wolfshtein & Lele studied the structure of two-point correlations (velocity-velocity, velocity-scalar, and scalar-scalar) with view towards improving turbulence models. They tested the linear two-point correlation model of Naot, Shavit & Wolfshtein (1973) and found that it is necessary to relate the two-point correlations not only to the Reynolds stresses, but also to all mean velocity and mean scalar gradients.

Shih, Mansour & Chen evaluated non-linear models for the return and the rapid pressure-strain terms (Shih and Lumley, 1985, and Shih, Mansour & Moin, 1987, to be published). In general, the models of the pressure strain term performed well for the cases of homogeneous turbulence under axisymmetric contraction, but all models were marginal for the cases of homogeneous turbulence under plain strain.

In addition to testing the models by direct comparison, Shih, Mansour & Chen used Reynolds stress models to predict the homogeneous shear case of Rogers, Moin and Reynolds (1987). Rubesin, Viegas, Vandromme, and Ha Minh coded a Reynolds stress model to compute channel flows at different Reynolds numbers. It was found that existing models that are linear in the anisotropy tensor perform poorly for these cases, while second-order models perform well for the homogeneous shear case but were not tested for the channel cases.

In addition to model testing, efforts were devoted by Bradshaw, Mansour, & Piomelli to testing certain approximations to the pressure strain term. In particular, the usual approximation to the rapid term where the local mean velocity gradient is used outside the integral solution of the Poisson equation was tested using the channel data. It was found that away from the wall this approximation works well, but close to the wall it will fail. The reason for the failure is attributed to the fact that close to the wall the velocity gradient varies rapidly as compared to the correlation length of the fluctuating velocity gradients.

A detail study of a homogeneous shear flowfield was carried out by Brasseur, & Lee where the intercomponent energy transfer by pressure-strain-rate was investigated. It was found that the rapid and slow parts of the turbulent pressure were uncorrelated; providing strong justification for current modeling procedures. In addition, instantaneous events of high transfer regions were studied in details. These events were found to be highly localized in space and are imbedded in regions of concentrated vorticity.

In order to gain insight into the effects of rotation on the dissipation rate, Speziale, Mansour & Rogallo carried a direct numerical simulation of decaying isotropic turbulence in a rapidly rotating frame. It was found that the primary effect of rotation is to shut off the energy transfer so that the turbulence dissipation is substantially

reduced. It was found that the anisotropy tensor remains essentially unchanged while the energy spectrum underwent a pure viscous decay. Rapid distortion theory analysis reveals that the rate of change of the vorticity field is $O(\Omega)$ so that no Taylor-Proudman reorganization of the flow to a two-dimensional state was observed. Suggestions are made towards including the effects of rotation on the dissipation rate.

Finally, a recent mixing length formula proposed by Hunt et al. (1987) was tested by Hunt, Spalart & Mansour, for a wide range of turbulent wall-bounded shear flows. It was found that the formula works well for all y^+, but fails in the neighborhood of regions where $dU/dy = 0$.

REFERENCES

HUNT, J. C. R., STRECTH, D. D., BRITTER, R. E. 1986 Length scales in stably stratified flows and their use in turbulence models, Proc. *I.M.A. Conference on stably stratified flow and dense gas dispersion*, Chester, April 9–10.

LAUNDER, B. E., REECE, G. J., & RODI, W. 1975 *.J. Fluid Mech.*, **68**, *537*.

NAOT, D., SHAVIT, A. AND WOLFSHTEIN, M. 1973 . *Phys. of Fluids.* **16**, 738-743.

SHIH, T.-H., & LUMLEY, J.L. 1985 . Rep. FDA-85-3, Sibley School of Mech. and Aero. Engrg., Cornell University.

WEINSTOCK, J. 1981 . *J. Fluid Mech.* **105**, 369–396.

WEINSTOCK, J. 1982 . *J. Fluid Mech.* **116**, 1-29.

WEINSTOCK, J. 1985 . *J. Fluid Mech.* **154**, 429–447.

On Local Approximations of the Pressure-Strain Term in Turbulence Models

By P. BRADSHAW[1], N. N. MANSOUR[2] and U. PIOMELLI[3]

The reason for the success of the approximation that uses the mean velocity gradient $\partial U/\partial y$ outside the integral solution of the Poisson equation for pressure, and sets the gradient equal to its value at the point where the pressure is being calculated, has been explored. This approximation is implicit in most existing turbulence models, where the pressure-strain terms are assumed to be functions of local variables rather than of the proper spatial integrals. Direct simulation data for the channel were used to evaluate spatial correlations of pressure and velocity gradients. The results show that a correlation coefficient of about -0.5 between the rapid pressure and its Laplacian (proportional to $\partial v'/\partial x$); this is in favor of the local assumption. Analysis of the solution to the Poisson equation indicates that the assumption will be valid when the mean velocity gradient varies slowly as compared to the correlation length of the fluctuating velocity gradients.

1. Introduction

The pressure-strain "redistribution" terms in the Reynolds-stress transport equations, which are mean products of the pressure fluctuation and various components of the fluctuating rate of strain, have received much attention from turbulence modelers for two reasons: first, the pressure-strain terms in the shear stress equations are the largest of the terms that need to be modelled in those all-important equations; secondly, little experimental data is available to properly assess the models.

In an experimental setup, pressure fluctuations within a boundary layer cannot be measured with any assurance of accuracy, because the velocity fluctuations induce pressure fluctuations on any solid probe inserted in the flow, and these spurious fluctuations are usually larger than those in the undisturbed flow. Using the instantaneous velocity field in the entire domain, turbulence simulations (numerical solutions of the full time-dependent Navier-Stokes equations without any modeling approximations) can be used to deduce statistics of measurable and of "unmeasurable" quantities such as those we will discuss in the next section. We shall discuss in this paper an approximation to the pressure-strain term which is commonly used in modeling the Reynolds-stress transport equations.

1 Imperial College
2 NASA Ames Research Center
3 Stanford University

2. Local approximation to the pressure

For an incompressible flow the fluctuating pressure can be obtained from the velocity field by solving the Poisson equation

$$\frac{\partial^2 p}{\partial x_j \partial x_j} = -2\frac{\partial U_i}{\partial x_j}\frac{\partial u'_j}{\partial x_i} - \left(\frac{\partial u'_i}{\partial x_j}\frac{\partial u'_j}{\partial x_i} - \overline{\frac{\partial u'_i}{\partial x_j}\frac{\partial u'_j}{\partial x_i}}\right) \tag{1a}$$

with the boundary condition at the walls

$$\frac{\partial p}{\partial y} = \frac{1}{Re}\frac{\partial^2 v'}{\partial y^2}. \tag{1b}$$

Equation (1a) shows that any correlations of the pressure with other fluctuating quantities will have a part proportional to the mean velocity gradients $\partial U_i/\partial x_j$ and a part depending only on velocity fluctuations. These are called the "rapid" and "slow" parts respectively, because only the former will respond at once to a change in the mean velocity field. An inhomogeneous boundary condition makes the split less obvious. However, for the case of the fully developed channel the volume integrals of each of the terms on the right hand side of (1a) will integrate to zero and pressure in this case can be split in three parts: the rapid pressure p^1, which satisfies

$$\frac{\partial^2 p^1}{\partial x_j \partial x_j} = -2\frac{\partial U_i}{\partial x_j}\frac{\partial u'_j}{\partial x_i} \tag{2a}$$

with the boundary condition at the walls

$$\frac{\partial p^1}{\partial y} = 0; \tag{2b}$$

the slow pressure p^2, which is the solution to:

$$\frac{\partial^2 p^2}{\partial x_j \partial x_j} = -\left(\frac{\partial u'_i}{\partial x_j}\frac{\partial u'_j}{\partial x_i} - \overline{\frac{\partial u'_i}{\partial x_j}\frac{\partial u'_j}{\partial x_i}}\right) \tag{3a}$$

with the boundary condition at the walls

$$\frac{\partial p^1}{\partial y} = 0; \tag{3b}$$

and, finally, the Stokes pressure p^S, which is the solution to Laplace's equation with the boundary condition (1b) at the walls.

The pressure-strain terms that appear in the Reynolds stress equations are linear in p, so that the total term will be equal to the sum of the rapid pressure-strain, slow
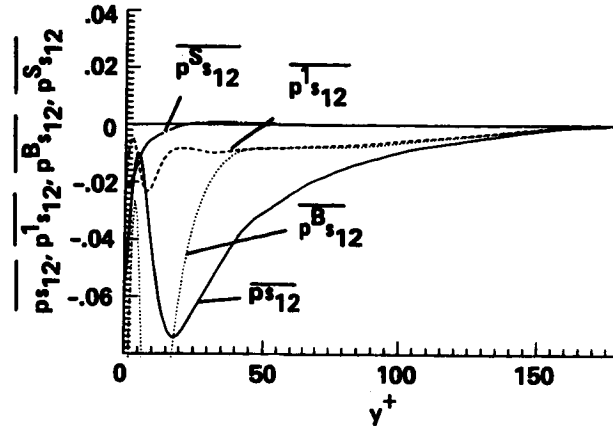
FIGURE 1. Pressure-strain term in the $-\overline{uv}$ transport equation.

pressure-strain and Stokes pressure-strain. The solution of (2a) with the boundary condition (2b) at the walls is

$$p^1 = -\frac{1}{4\pi} \int_V 2 \frac{\partial U_i}{\partial x_j} \frac{\partial u'_j}{\partial x_i} G d\mathcal{V} \tag{4}$$

in which G is Green's function with homogeneous Neumann boundary conditions at the walls. Note that most modelers neglect the surface integral terms that should be added to (4) if non-homogeneous Neumann conditions are used for the pressure. The use of the homogeneous boundary condition (2b) at the walls for the rapid pressure is consistent with (4) and the approximation used by the modelers. Although, by (4), the rapid pressure is an integral of the weighted mean velocity gradients over the entire domain, in modeling the assumption is often made that p^1 depends only on the local mean velocity gradient, which allows one to take the mean velocity gradients outside of the integral in (4) to yield the following approximation for the pressure:

$$p^B = -\frac{1}{4\pi} 2 \frac{\partial U_i}{\partial x_j} \int_V \frac{\partial u'_j}{\partial x_i} G d\mathcal{V}. \tag{5}$$

Direct experimental measurement of either p^1 or p^B is impossible, but the use of direct simulation results allows us to test the approximation (5) directly by computing the integrals in (4) and (5) and comparing the approximate value p^B with p^1. The purpose of the present paper is to examine the results of this comparison for channel flow at low Reynolds number.

3. Results

The results of the direct numerical simulation of fully developed channel flow at $Re_\tau = 180$ (Kim, Moin and Moser, 1987) were used to compute all the statistics presented in this work.
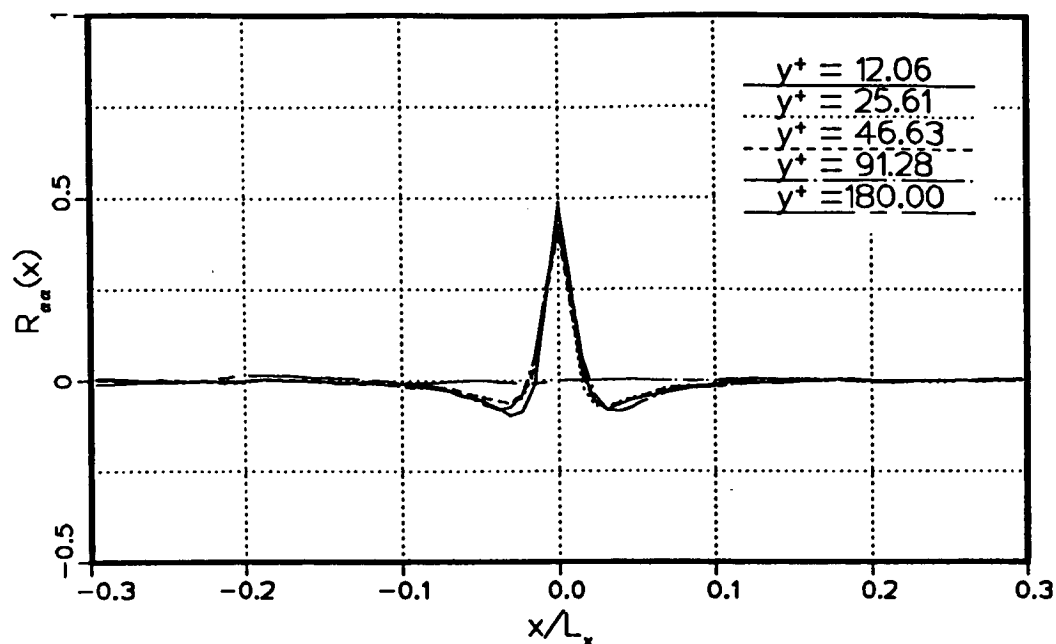
FIGURE 2. Two point correlation of the rapid-pressure term with $\partial v / \partial x$.

Figure 1 shows the contribution of the rapid pressure-strain term in the $-\overline{u'v'}$ transport equation. All results are normalized by $\rho u_\tau^4 / \nu$: on this scale the maximum rate of production of turbulent energy, which occurs where $\tau = \tau_w / 2$, *i.e.* at about $y^+ = 12$, is 0.25. Note that the plotted terms are negative if $-\overline{u'v'}$ is being reduced and positive if it is being increased by the pressure-strain redistribution.

The accuracy of the local approximation to the pressure-strain terms is surprisingly good: differences between the exact and approximate values are generally within the scatter of the statistical averaging, except in the viscous sublayer $(y^+ < 30)$. The rapid pressure-strain contribution to the other Reynolds stress transport equations shows similar trends.

To further investigate the reasons for the success of the approximation outside of the sublayer, as well as to ascertain the causes of its failure inside it, we examined the correlation coefficient between the rapid pressure p^1 and various components of the fluctuating strain-rate tensor for varying distances from the wall.

The most noticeable feature of the simulation results is the high correlation between pressure and velocity gradients. In particular, the coefficient of correlation between p^1 and $\partial v' / \partial x$ (Figure 2) is numerically as large as 0.5. This implies a correlation coefficient of -0.5 between the pressure and its Laplacian. The relatively high value for p^1 is noteworthy. It is not high enough to legitimize the p^B
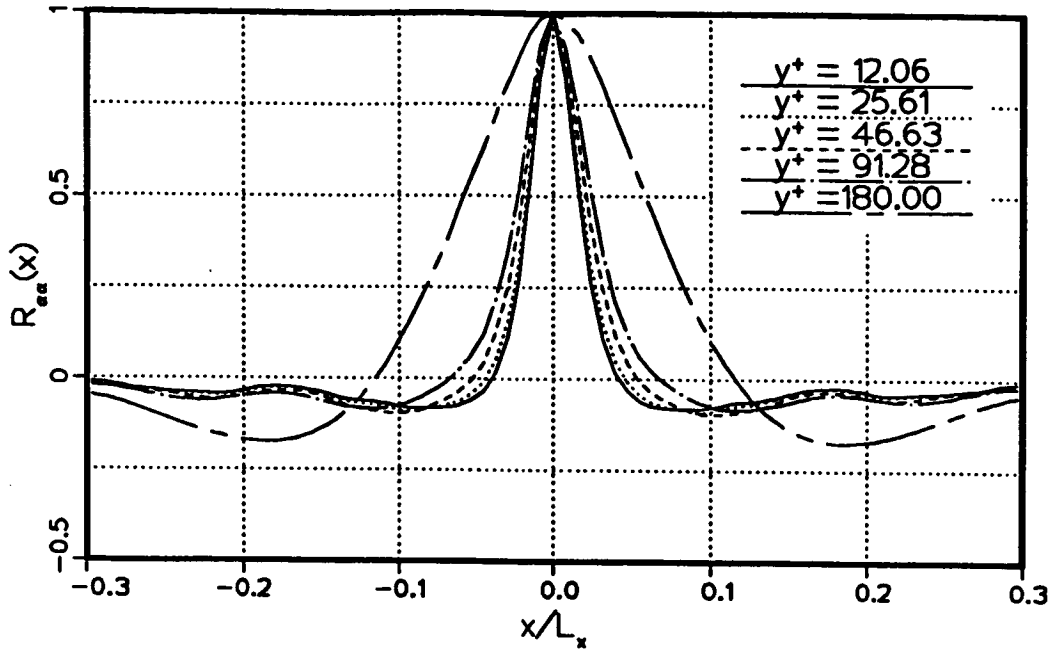
FIGURE 3. Two point auto-correlation of the rapid-pressure.

approximation directly, but it suggests that the rapid pressure is not so dependent on contributions from distant parts of the flow as its governing Poisson equation nominally implies. A demonstration of this dependency is the rapid increase of the length scale of p^1 near the channel centerline, which can be inferred from the auto-correlation of p^1, Figure 3. Near the centerline the source term in the Poisson equation for p^1, being proportional to the mean shear, vanishes; contributions to p^1 on the centerline, therefore, must necessarily come from regions off the centerline, and have their high wavenumber parts attenuated by distance.

For homogeneous flows in the x and z directions, the pressure-strain term can be written as follows:

$$\overline{p^1 \frac{\partial u_i'}{\partial x_j}} = \int_{-\infty}^{\infty} \int_{-\infty}^{\infty} \overline{p^1(x,y,z) \frac{\partial u_i'}{\partial x_j}(x,y,z)} dx dz. \tag{6}$$

Substitution of (4) into (6) gives

$$\overline{p^1 \frac{\partial u_i'}{\partial x_j}} = \int_{-1}^{1} \int_{-\infty}^{\infty} \int_{-\infty}^{\infty} \int_{-\infty}^{\infty} \int_{-\infty}^{\infty} \frac{\partial U}{\partial y}(y') \times$$
$$\overline{\frac{\partial v'}{\partial x}(x - x', y', z - z') \frac{\partial u_i'}{\partial x_j}(x,y,z)} G(x', y, y', z') dx dz dx' dz' dy' \tag{7}$$

whereas the local approximation (5) yields

$$\overline{p^B \frac{\partial u_i}{\partial x_j}} = \frac{\partial U}{\partial y}(y) \int_{-1}^{1} \int_{-\infty}^{\infty} \int_{-\infty}^{\infty} \int_{-\infty}^{\infty} \int_{-\infty}^{\infty}$$

$$\frac{\partial v'}{\partial x}(x - x', y', z - z')\frac{\partial u_i'}{\partial x_j}(x, y, z)G(x', y, y', z')dx'dz'dxdzdy'. \quad (8)$$

The two inner integrals in (7) and (8) represent the two-point correlation between $\partial v(y')/\partial x$ and $\partial u_j(y)/\partial x_i$, weighted by Green's function G, as a function of y and y'. This correlation can be expected to vanish as $y - y'$ increases, since Green's function decreases as $y - y'$ increases and the velocity gradients are not correlated over large distances. As long as the length scale of this correlation is small with respect to the length over which the mean shear can be considered constant, the local approximation will hold. In the logarithmic region the mean shear varies slowly $(\partial^2 U/\partial y^2 \sim 1/y^2)$ and the local approximation holds. At the sublayer edge, where the velocity gradient changes significantly, this is not true and the local approximation fails.

4. Conclusions

The results of numerical simulations of turbulent channel flows have been used to examine the validity of the local approximation of the pressure-strain term in the Reynolds stress transport equation.

Outside of the viscous sublayer the local approximation compares very well with the exact pressure strain. This agreement is due, at least in part, to the high correlation between the rapid pressure and its Laplacian, which suggests that only the nearer parts of the flow contribute to the rapid pressure at a point.

In the viscous sublayer the distance over which the mean shear can be considered constant is comparable to the length scale in the normal direction of the correlations of velocity gradients, leading to failure of the local approximation.

REFERENCES

KIM, J., MOIN, P. & MOSER, R. D. 1987 Turbulence statistics in fully developed channel flow at low Reynolds number. *J. Fluid Mech.* **177**, 133–166.

Local Structure of Intercomponent Energy Transfer in Homogeneous Turbulent Shear Flow

By JAMES G. BRASSEUR† AND MOON J. LEE‡

Intercomponent energy transfer by pressure–strain-rate was investigated for homogeneous turbulent shear flow. The rapid and slow parts of turbulent pressure (decomposed according to the influence of the mean deformation rate) are found to be uncorrelated; this finding provides strong justification for current modeling procedure in which the pressure–strain-rate term is split into the corresponding parts. Issues pertinent to scales involved in the intercomponent energy transfer are addressed in comparison with those for the Reynolds-stress and vorticity fields. A physical picture of the energy transfer process is described from a detailed study of instantaneous events of high transfer regions. It was found that the most significant intercomponent energy transfer events are highly localized in space and are imbedded within a region of concentrated vorticity.

1. Introduction

Statistical quantities in turbulent flows have underlying them local, random events whose dynamical evolution determines the structure of the average. Here, *event* refers to a local concentration of a statistical quantity in an instantaneous turbulent field and *significant events* are those which provide major contributions to the average.

The pressure–strain-rate term is the most controversial in current modeling procedure for the Reynolds-stress transport. The poor understanding of the role played by pressure in intercomponent energy transfer is in part for want of reliable data from laboratory measurements of fluctuating pressure. With the advent of supercomputer, 'data' from full turbulence simulations of building-block flows such as homogeneous turbulence are now available. In this paper, we analyse significant events associated with the intercomponent energy transfer by interaction between fluctuating pressure and strain rate in homogeneous turbulent shear flow.

Homogeneous turbulence is chosen for the present study due to the unambiguous statistical description of intercomponent energy transfer as the correlation between the fluctuating pressure and strain rate. In this study, we consider those local events which do not average to zero. Velocity times pressure-gradient, which appears in the instantaneous Reynolds stress equation, may be written as the sum of transport and trace-free terms. In homogeneous turbulence, the trace-free term (pressure–strain-rate) alone survives on the spatial average due to the requirement of the

---

† Department of Mechanical Engineering, Clemson University, Clemson, SC 29634
‡ NASA-Ames Research Center, Moffett Field, CA 94035

translational invariance. In inhomogeneous turbulence, the split of the velocity–pressure-gradient is not unique (Lumley 1975). We hope to extend the inquiry in the future to homogeneous turbulence subjected to irrotational mean strains and to inhomogeneous wall-bounded turbulence.

2. Preliminaries

The transport equation for the Reynolds-stress tensor $\overline{u_i u_j}$ in homogeneous turbulence is given by (Lee & Reynolds 1987)

$$\frac{dR_{ij}}{dt} = P_{ij} + O_{ij} + T_{ij} - D_{ij} \tag{1}$$

where $P_{ij} = -(S_{ik}R_{jk} + S_{jk}R_{ik})$ is the production-rate tensor, $O_{ij} = -(\Omega_{ik}R_{jk} + \Omega_{jk}R_{ik})$ the kinematic rotation term, $T_{ij} = \frac{2}{\rho}\overline{ps_{ij}}$ the pressure–strain-rate term and $D_{ij} = 2\nu\,\overline{u_{i,k}u_{j,k}}$ the 'dissipation-rate' tensor (**u** and p are the fluctuating vector velocity and pressure, respectively; an overbar denotes a statistical average, repeated indices imply summation and a comma followed by an index means differentation). Here, $S_{ij} = \frac{1}{2}(U_{i,j} + U_{j,i})$ and $\Omega_{ij} = \frac{1}{2}(U_{i,j} - U_{j,i})$ are the mean strain-rate and rotation-rate tensors, respectively, and s_{ij} is the turbulent strain-rate tensor. Notice that the kinematic rotation and pressure–strain-rate terms are trace-free ($O_{ii} = 0$ and $T_{ii} = 0$), and hence they do not contribute to production of the turbulent kinetic energy. These terms represent intercomponent transfer of turbulent kinetic energy by the mean rotation rate and by interaction between fluctuating pressure and strain rate, respectively.

For homogeneous shear flow with mean velocity $\mathbf{U} = (Sy, 0, 0)$, equations for the component energy can be written as

$$\left.\begin{aligned}
\frac{d}{dt}\overline{u^2} &= -S\,\overline{uv} & -S\,\overline{uv} & +T_{11} - D_{11}, \\
\frac{d}{dt}\overline{v^2} &= -S\,\overline{uv} & +S\,\overline{uv} & +T_{22} - D_{22}, \\
\frac{d}{dt}\overline{w^2} &= & & +T_{33} - D_{33}, \\
\frac{d}{dt}\overline{uv} &= -\frac{S}{2}\left(\overline{u^2} + \overline{v^2}\right) & +\frac{S}{2}\left(\overline{u^2} - \overline{v^2}\right) & +T_{12} - D_{12},
\end{aligned}\right\} \tag{2}$$

where $S = dU/dy$ is the imposed 'shear rate' uniform in space and constant in time.† Turbulent shear flow with unidirectional mean velocity has the characteristic that, on the average, turbulent kinetic energy is produced by the mean strain rate in the streamwise component u as much as in the gradient-direction component v (i.e. $P_{11} = P_{22} = -S\overline{uv}$), and the kinematic rotation term rotates the turbulence structure in the xy-plane by transferring energy $-S\,\overline{uv}$ from v-component to u-component. The principal axes of the production-rate tensor are aligned at 45°

---

† For notational convenience, we occasionally shift from (x_1, x_2, x_3) and (u_1, u_2, u_3) to (x, y, z) and (u, v, w).

with those of the mean strain-rate tensor, stretching the principal ellipsoid of the Reynolds-stress tensor, while the kinematic rotation term is perpendicular to the Reynolds-stress tensor, only tilting the principal ellipsoid.

It is suggested by experimental measurements (Harris, Graham & Corrsin 1977; Tavoularis & Corrsin 1981) and numerical simulations (Rogallo 1981; Rogers, Moin & Reynolds 1986; Lee, Kim & Moin 1987) that homogeneous turbulent shear flow approaches an asymptotic growth state in which most turbulent kinetic energy is concentrated in the u-component, followed by w, then v. The u-component loses energy to those in the spanwise (w) and gradient directions (v) through the pressure–strain-rate correlations: $T_{11} < 0$, $T_{22} > 0$ and $T_{33} > 0$. Examination of the process by which the pressure–strain-rate redistributes energy between components and the mechanism by which the spanwise component receives the greater share is the primary purpose of this study.

The equations for fluctuating momentum flux ($u_i u_j$), which lead to (2) on the average, contain local products of fluctuating pressure and strain rate which by continuity sum to zero at a point ($ps_{ii} = 0$). The pressure–strain-rate term may therefore be associated with local as well as average intercomponent transfer of kinetic energy. The role of fluctuating pressure as causing the local transfer of kinetic energy between components can be observed more clearly in the instantaneous Fourier-transformed equations; pressure alters the directional distribution of the energy associated with individual Fourier modes without modifying their energy content (Batchelor 1953, §5.2).

The present investigation makes use of the full simulation of homogeneous turbulent shear flow (Rogers *et al.* 1986). The simulation was carried out by using a pseudospectral code developed by Rogallo (1981) with periodic boundary conditions on a grid with $128 \times 128 \times 128$ node points. Run R128 (vid. Rogers *et al.*) was analysed for fields at $\beta = 4$ and 8 ($\beta = St$ is the total shear). The run was made by imposing a homogeneous shear rate on an initially isotropic turbulence with an energy spectrum $E(k)$ of a top-hat profile. As the flow developed, reasonable values of velocity-derivative skewness were attained and the largest scales approached the size of the computational domain near $\beta = 16$. The Taylor-microscale Reynolds number ranged from 43 to 74 for $\beta = 4$–8, and the ratio of turbulence time scale to that of the mean field (Sq^2/ϵ where $q^2 = R_{ii}$ and $\epsilon = \frac{1}{2}D_{ii}$) increased from 5.4 to 8.8 between $\beta = 4$ and 8.

3. Characteristics of rapid and slow pressures

The Poisson equation for fluctuating pressure in homogeneous shear flow

$$-\frac{1}{\rho}\nabla^2 p = 2S\,u_{2,1} + u_{i,j}u_{j,i} \tag{3}$$

can be decomposed into two parts, *rapid* and *slow* pressures:

$$-\frac{1}{\rho}\nabla^2 p_{\mathrm{r}} = 2S\,u_{2,1} \quad \text{and} \quad -\frac{1}{\rho}\nabla^2 p_{\mathrm{s}} = u_{i,j}u_{j,i}. \tag{4}$$
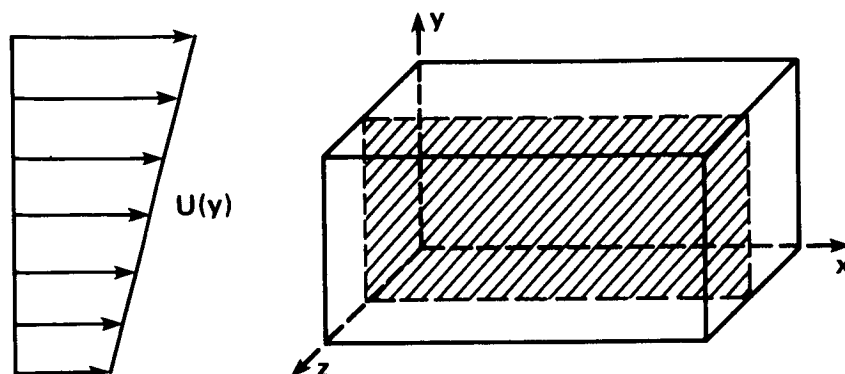
FIGURE 1. The hatched area in the one-eighth (1/8) of the whole computational domain indicates the xy-plane over which the two-dimensional contours in figures 2, 3 and 5 are displayed. The streamwise extent of this $64 \times 64 \times 64$ subdomain is twice those in the spanwise and gradient directions.

From this decomposition it is apparent that the rapid pressure responds directly to the mean velocity gradient, whereas the slow pressure is affected only indirectly by the mean, via the fluctuating velocity gradients.

In accord with this, the pressure–strain-rate term may be separated into *rapid* and *slow* parts:

$$T_{ij} = \Pi_{ij} + \Phi_{ij} \tag{5}$$

where

$$\Pi_{ij} = \frac{2}{\rho}\, \overline{p_r s_{ij}} \quad \text{and} \quad \Phi_{ij} = \frac{2}{\rho}\, \overline{p_s s_{ij}}. \tag{6}$$

In Reynolds-stress transport closures (e.g. Launder, Reece & Rodi 1975; Lumley 1978) these terms have been modeled separately, the slow pressure–strain-rate term typically with a 'return-to-isotropy' model. Order-of-magnitude arguments would suggest that the slow pressure resides in scales of the same order as the energy-containing eddies and the rapid pressure in somewhat larger scales, albeit it is not obvious in what scales the pressure–strain-rate events are likely to reside.

At an earlier time ($\beta = 4$), the rapid pressure variance $\overline{p_r^2}$ is 70% of the complete pressure variance $\overline{p^2}$ and reaches 87% at a later time ($\beta = 8$), indicating increasingly dominant contribution of the rapid part to the complete pressure fluctuations.[†] These figures compare with values in turbulent channel flow (e.g. Kim, Moin & Moser 1987) of 50% in the sublayer to 30% outside (P. Bradshaw 1987, private communication). In the homogeneous shear flow, r.m.s. rapid pressure p_r' dominates r.m.s. slow pressure p_s' by a factor of two at both times.

---

† It has been suggested (P. Bradshaw 1987, private communication) that the term 'complete pressure' be adopted to describe the sum of rapid and slow pressures to avoid confusion with either the full pressure (mean plus fluctuating parts) or the total pressure (static plus dynamic pressures).
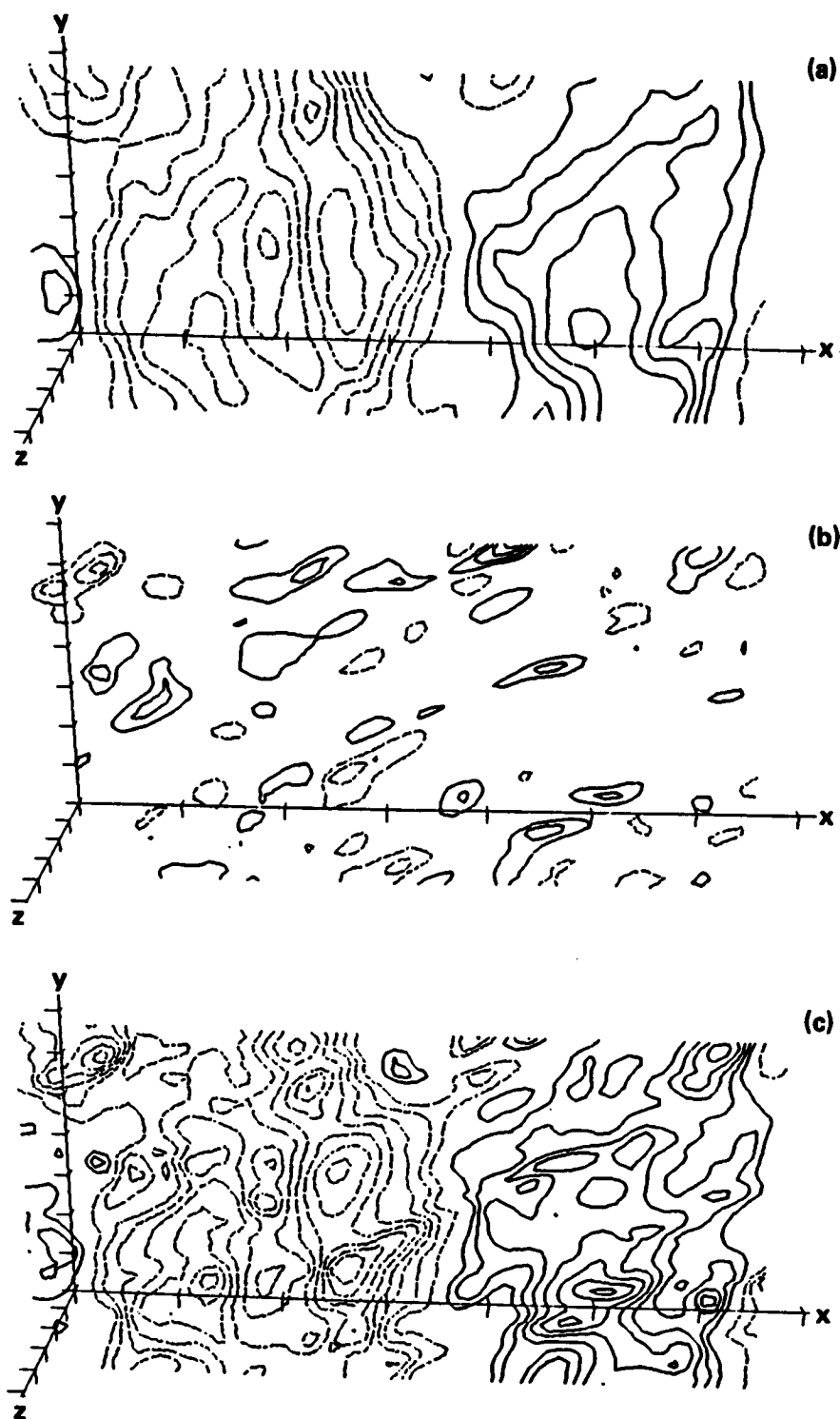
FIGURE 2. Contours of constant pressure on the xy-plane in figure 1 ($\beta = 8$): (a) rapid pressure, p_r; (b) slow pressure, p_s; (c) complete pressure, $p = p_r + p_s$. ——, negative; ----, positive.
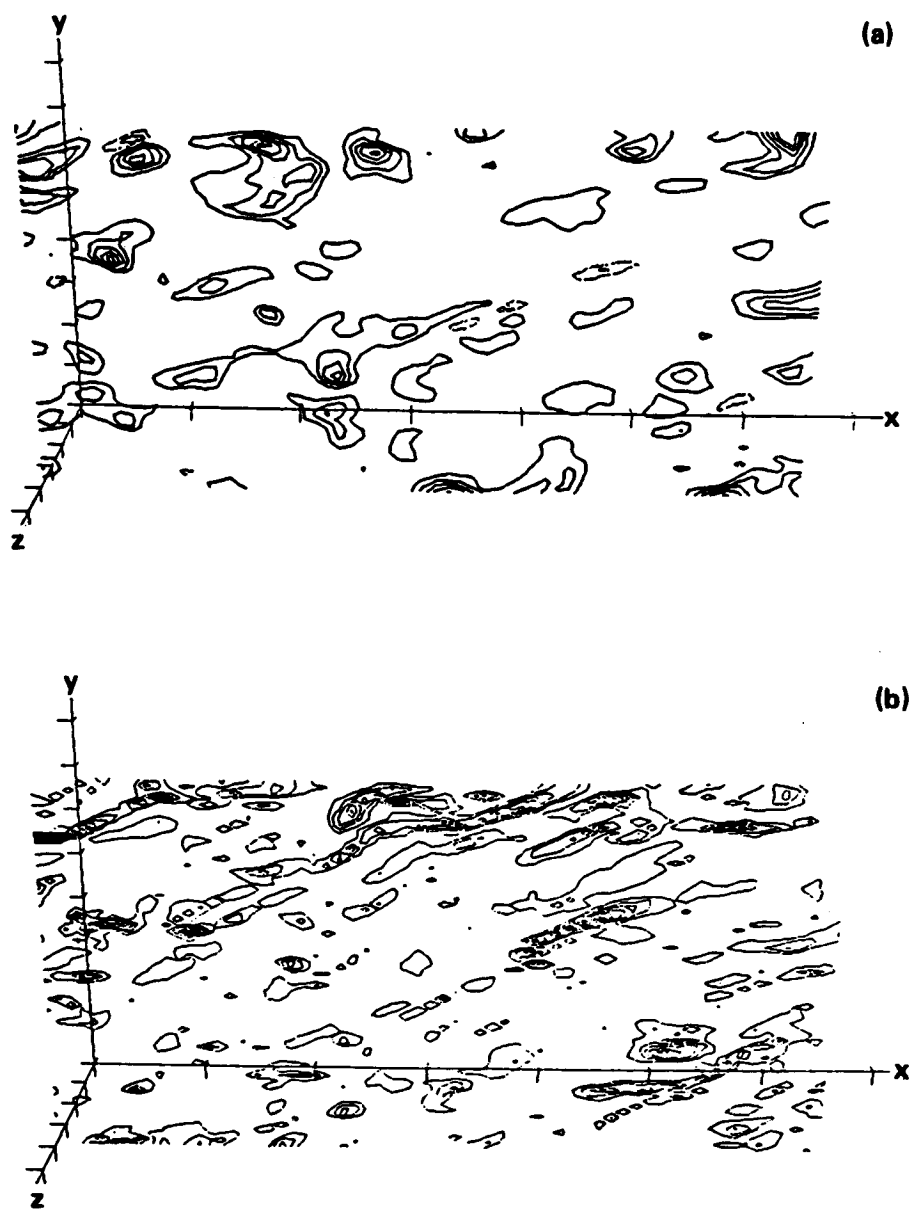
FIGURE 3. Contours on the xy-plane in figure 1 ($\beta = 8$): (a) fluctuating Reynolds stress uv (——, negative; ----, positive); (b) fluctuating vorticity magnitude, $|\omega|^2$.

It was found that the correlation coefficient between the rapid and slow pressures is very small (0.05 at $\beta = 4$ and 0.002 at $\beta = 8$). Note that this fact provides strong support for the modeling procedures in which the pressure–strain-rate term is divided into the rapid and slow parts (Launder *et al.* 1975; Lumley 1978). Since the correlation coefficient between the rapid and slow pressures is almost zero, one would inquire whether they are concentrated in different regions in space.

β	Π_{11}	Φ_{11}	T_{11}	Π_{22}	Φ_{22}	T_{22}	Π_{33}	Φ_{33}	T_{33}
4	-35.9	-16.8	-52.6	-5.2	17.6	12.4	41.1	-0.8	40.3
8	-29.7	-26.1	-55.8	-4.1	24.3	20.2	33.8	1.7	35.5

$\beta = St$; $T_{ij} = \Pi_{ij} + \Phi_{ij}$ where $\Pi_{ij} = \frac{2}{\rho}\overline{p_r s_{ij}}$ and $\Phi_{ij} = \frac{2}{\rho}\overline{p_s s_{ij}}$.

TABLE 1. Components of pressure–strain-rate in homogeneous shear flow.

To address this question, instantaneous pressure fields were studied in detail. Figure 1 shows a schematic of an xy-plane (consisting of 64 × 64 data points) midway in the spanwise z-direction in a 64 × 64 × 64 subdomain where primary attention is to be paid for the following discussion.† Figures 2(a–c) show contours of constant rapid, slow and complete pressures at $\beta = 8$. It is discernible that variation of rapid pressure is much larger than that of slow pressure. Even more obvious is the substantial difference in scale. Figure 2(a) (and three-dimensional contour plots not shown here) illustrates that rapid pressure is roughly constant in planes perpendicular to the x-axis and the streamwise variation is sinusoidal with about two wavelengths occupying the whole computational domain. On the other hand, figure 2(b) shows spotty distribution of slow pressure. Therefore, the product of this very-large-scale structure of rapid pressure and the much-smaller-scale slow pressure results in a relatively-small-scale structure with average near zero: $\overline{p_r p_s}/(p'_r p'_s) \simeq 0$.

Figures 3(a, b) display contours of constant values of instantaneous Reynolds stress (uv) and fluctuating vorticity magnitude ($|\omega|^2$), respectively. Comparison with figure 2(b) suggests that slow pressure is concentrated in scales of roughly the same size as the Reynolds stress. In contrast, vorticity resides in scales considerably smaller in the transverse and more elongated in the direction of principal axes of the mean deformation-rate tensor. This is consistent with the observation of Rogers & Moin (1987) that vorticity concentrates in 'legs' of hairpin-like vortex structures as they are stretched and rotated by the mean shear.

4. Intercomponent energy transfer processes (events)

Statistical averages of the diagonal components of the rapid, slow and complete pressure–strain-rate tensor at $\beta = 4$ and 8 are presented in table 1. Statistically, the pressure–strain-rate transfers energy out of u ($T_{11} < 0$) into v and w ($T_{22} > 0$ and $T_{33} > 0$); the w-component receives the greater amount ($T_{33} > T_{22}$). The rapid term removes energy from u at a rate twice that of the slow term at $\beta = 4$ and at about the same rate at $\beta = 8$; however, the ratios between components of rapid transfer rate ($\Pi_{11}:\Pi_{22}:\Pi_{33}$) are nearly the same at both times.

† Only one-eighth of the whole 128 × 128 × 128 dataset could be processed at a time on an IRIS workstation used for graphical display at the NASA-Ames Research Center. The strongest pressure–strain-rate events at $\beta = 8$ were observed in and near the plane shown.
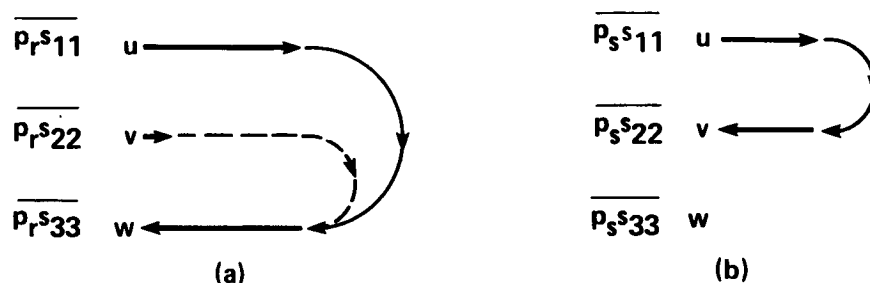
FIGURE 4. Schematic representation of intercomponent energy transfer process by pressure–strain-rate covariances ($\beta = 8$): (a) rapid transfer; (b) slow transfer. The directions of energy transfer are those suggested by the statistical averages.

The relative rate of gain or loss of energy in each component is illustrated schematically in figure 4. On average, both rapid and slow terms remove energy from u. Most of the net energy received by w is due to the rapid term, whereas the v-component receives its energy mostly via the slow term (see table 1). This would suggest, as indicated by the arrows, that the rapid term transfers energy from the u-component to the w-component (and a little from v to w), but the slow term delivers energy from the u-component directly to the v-component. The instantaneous field, however, shows that this is not the case.

Figures 5(a–c) show contours of constant slow pressure–strain-rate components at $\beta = 8$ on the xy-plane illustrated in figure 1. [N.B.: Negative values are contoured with solid lines and positive with dashed.] It can be observed that intercomponent energy transfer is highly localized in relatively few strong events.† Two-point correlations (not shown) suggest that the average spatial scale of the rapid transfer event is roughly twice that of the slow transfer event.

By comparing pressure–strain-rate contours in each of the three components, it is possible to determine the net sender and net receiver in each energy transfer event. Four events are identified for this purpose. Events (A) and (B) represent the greatest contributions to the energy transfer out of the u-component by the slow term.‡ Event (A) is by far the strongest, reaching peak values twice that in (B). In this event, most of the energy from the u-component is transferred to the w-component and only a small amount of energy is transferred from u to v. Surrounding this event is a region of rather powerful energy transfer from the v-component into w-component. The w-component therefore receives energy both from u and v. A similar energy transfer process is seen in event (B), although most of the u-energy is transferred directly to w, with smaller amounts from u to v and v

---

† The rise in ps_{11} from zero is exceptionally abrupt. A three-dimensional view of constant ps_{11}-contours suggests that the transfer of energy from the u-component is concentrated in about ten primary events scattered within the 64 × 64 × 64 subdomain.

‡ For the rapid transfer, two other exceptionally strong pressure–strain-rate events exist in addition to events coinciding with the two slow events.
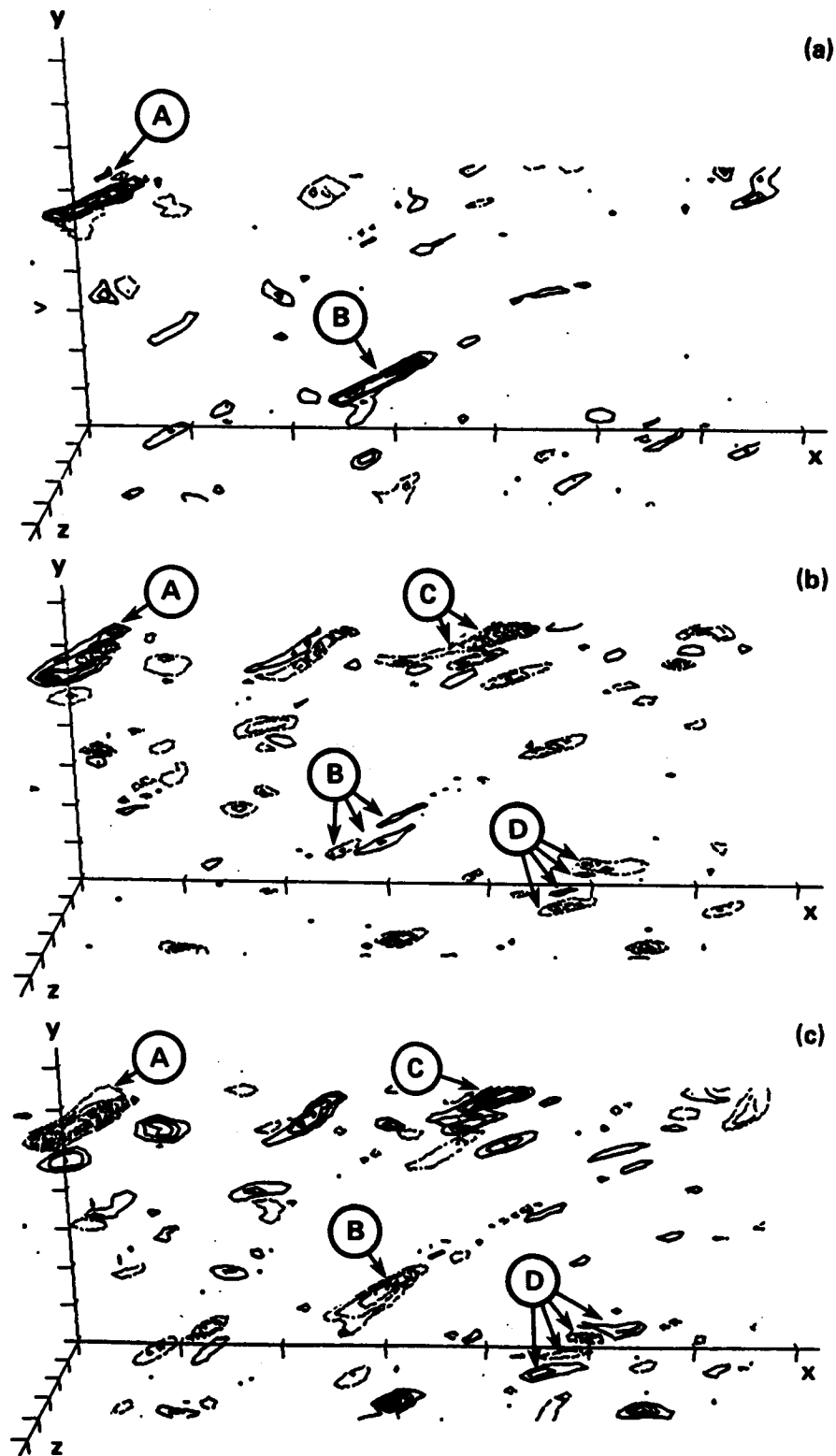
FIGURE 5. Contours of slow pressure–strain-rate on the xy-plane in figure 1 ($\beta = 8$): (a) $p_s s_{11}$; (b) $p_s s_{22}$; (c) $p_s s_{33}$. ——, negative; ----, positive. Four significant events are labeled (A), (B), (C) and (D) (see text).
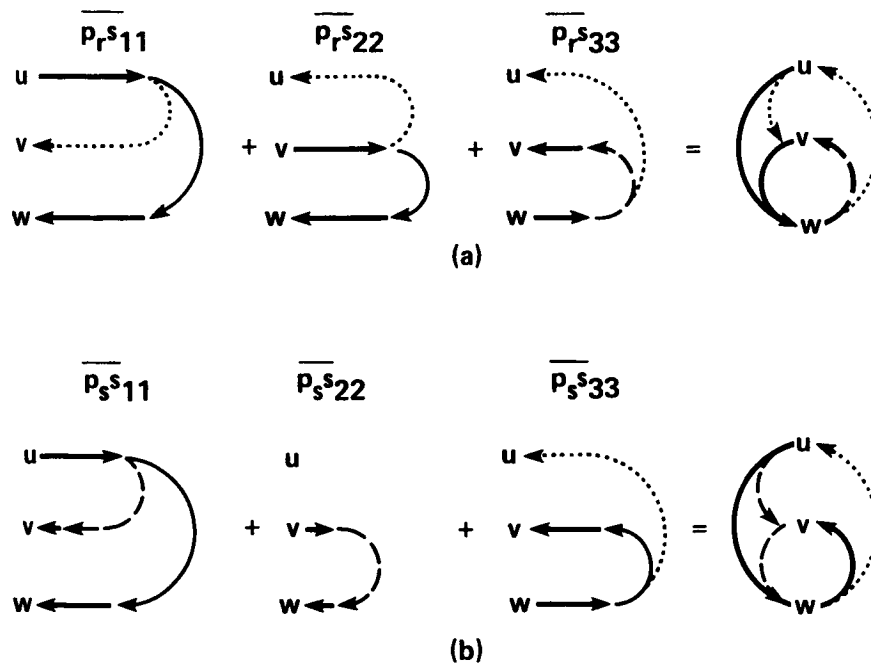
FIGURE 6. Schematic of the intercomponent energy transfer process as deduced from the instantaneous pressure–strain-rate field ($\beta = 8$): (a) rapid transfer; (b) slow transfer. A composite picture (on the right) is developed from sum of the individual energy transfer processes of the three components.

to w. Therefore, the slow term transfers most of the energy from u to w rather than to v (as might be implied by figure 4). In addition, a great deal of energy transfer takes place between v and w, independent of transfer from u. In event $\copyright$, for example, energy is transferred directly from the w-component to the v-component, and in event $\textcircled{D}$ energy flows back and forth between w and v.

Our interpretation of the instantaneous events in the rapid and slow pressure–strain-rate fields is schematically summarized in figure 6. The slow term transfers energy from u primarily to w with a small amount to v, and some energy from v is transferred to w; however, more energy enters v from w than vice versa. As shown to the right of figure 6, the net process is an indirect transfer of energy from u to v through w with significant energy transfer between v and w. The rapid term moves energy from u again primarily into w. However, there is considerably greater energy transfer to w from v. The w-component appears to receive a significant portion of its energy from the v-component, while transferring a lesser amount back to v. Compared with the slow process, the rapid term to a much greater extent transfers energy back to u from both v and w. The transfer processes in both rapid and slow parts are clearly more involved than those inferred from the statistics only (cf. fig. 4).

FIGURE 7. Three-dimensional contours of constant vorticity $(\beta = 8)$: (a, b) ω_x, positive (solid contour) and negative (mesh contour); (c, d) ω_z, all negative (solid contour, higher values of $|\omega_z|$; mesh contour, lower values). (a, c) side view looking towards the xy-plane; (b, d) top view looking towards the xz-plane. (Very little positive ω_y exists in this region.)
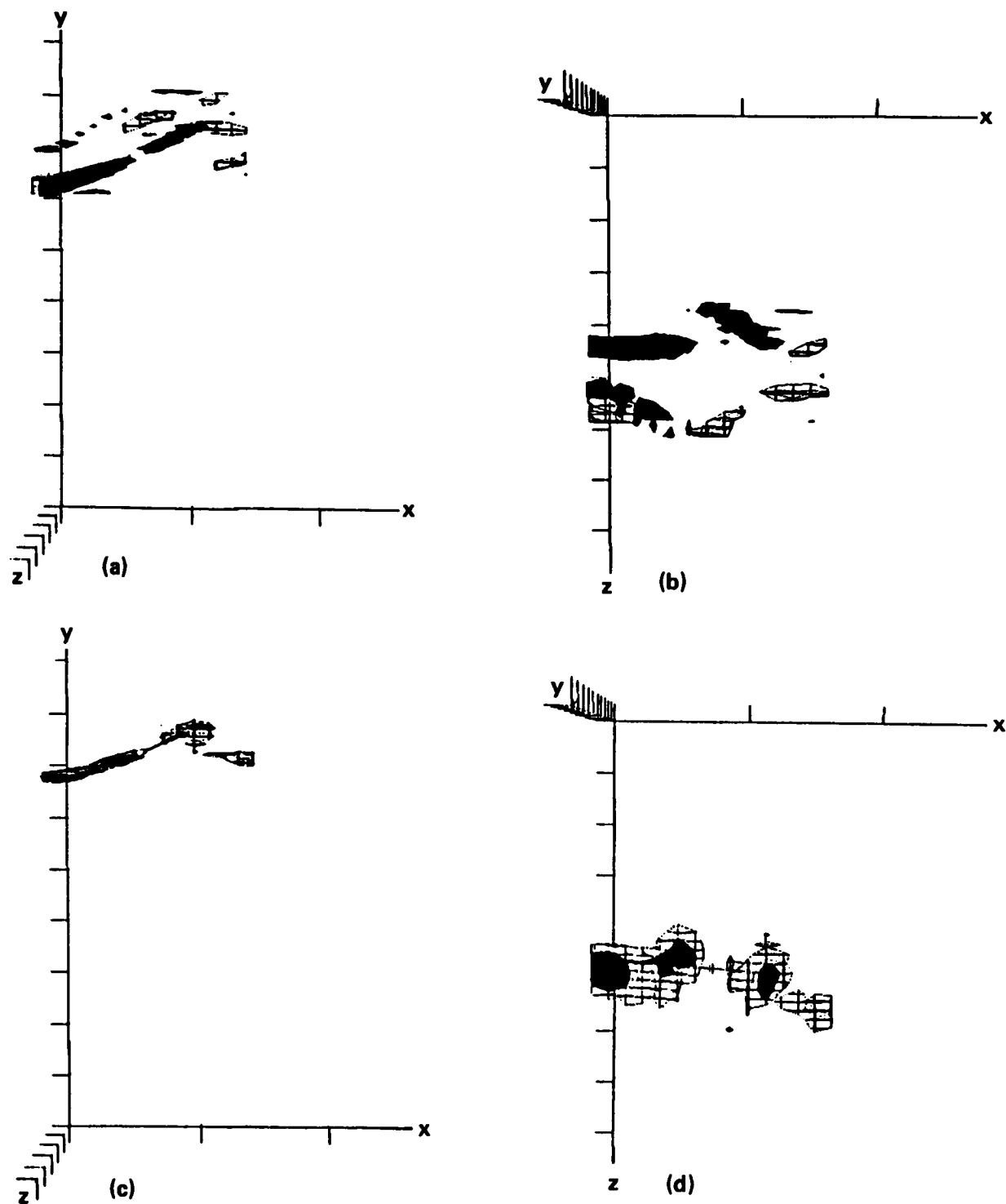
5. Instantaneous structure of the most significant event

In their study of a sheared Taylor-Green cellular flow, Corrsin & Kollmann (1977) reported that intercomponent energy transfer from the streamwise to the transverse components is associated with local stagnation points. To understand the physical mechanisms by which the intercomponent energy transfer proceeds in homogeneous turbulent shear flow, the structure of the velocity field in the neighborhood of significant energy transfer events was investigated.

Event $\textcircled{A}$ in figure 5 shows the strongest energy transfer from the streamwise component in the $64 \times 64 \times 64$ subdomain at $\beta = 8$. Recall that this event is associated with a region of concentrated vorticity (fig. $3b$). Upon close examination, we found a rather complex three-dimensional vortical structure in which the energy transfer event is embedded. In the xy-plane of figure $3(b)$, the fluctuating vorticity magnitide in event $\textcircled{A}$ turns out to be all spanwise vorticity ω_z (ω_x and ω_y are zero there!), indicative of the existence of a local shear layer. This is confirmed through three-dimensional contour plots of ω_x and ω_z near event $\textcircled{A}$ as shown in figure 7 (very little ω_y exists in this region).

The two vorticity components are viewed looking from the side along the z-axis at the xy-plane (figs. $7a$, c) and looking from the top down at the xz-plane (figs. $7b$, d). There exists a sheet of negative spanwise vorticity ($\omega_z < 0$) relatively thin in the y-direction in comparison with its spanwise extent (figs. $7c$, d). Surrounding this sheet-like structure is a region of strong ω_x of two tube-like structures, one with positive and the other with negative streamwise vorticity (figs. $7a$, b). The spanwise separation of the two vortex tubes was estimated to be about 20 viscous units ($\sqrt{\nu/S}$), consistent with the typical hairpin vortices observed by Rogers & Moin (1987) in the same flow. The vortical structure in the region of event $\textcircled{A}$ then appears to consist of the remnants of an inverted hairpin vortex with a local sheet of spanwise vorticity occupying the region in between.

Notice the gap in the spanwise vorticity shown in figure $7(d)$. Examination of the velocity vectors shows the existence of a local stagnation point in this gap, apparently a consequence of the velocity field induced locally by the vortical structure. Figure $8(a)$ shows the top view of the three-dimensional region in which ps_{11} is concentrated compared with streamwise (fig. $7b$) and spanwise vorticity (fig. $7d$). The peak in ps_{11} (solid volume) occupies this gap in the ω_z-field, suggesting the energy transfer out of the u-component is, for this powerful event, associated with a local stagnation point, itself associated with neighboring vortical structures embedded in the turbulent field. Interestingly, instantaneous Reynolds stress (fig. $8b$), like streamwise vorticity, is concentrated in regions which straddle the ps_{11}-event.

As we have observed, the structure of high pressure–strain-rate concentration interacts strongly with coherent vortical structure where the Reynolds-stress eddies are energetic. In view of its importance of the pressure–strain-rate term in Reynolds-stress transport modeling, it would be of considerable value to investigate how the intercomponent energy transfer by the pressure–strain-rate takes place in association with dynamics of the coherent vortical structures.
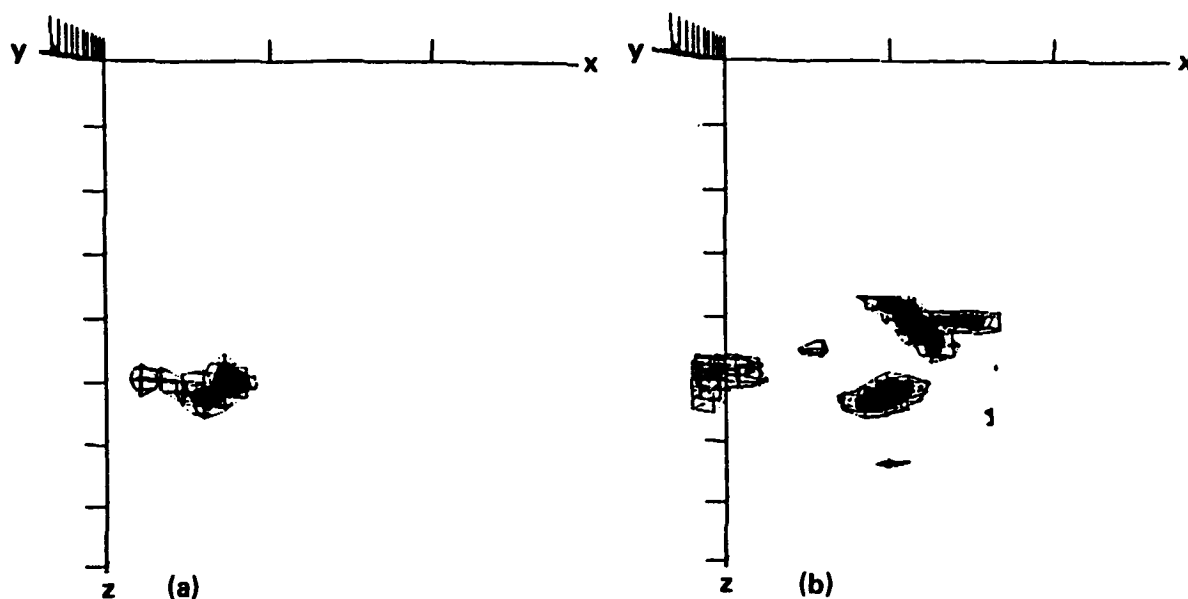
FIGURE 8. Three-dimensional contours in top view looking towards the xz-plane ($\beta = 8$): (a) pressure–strain-rate, ps_{11}; (b) Reynolds stress, uv. In both plots, contours shown are all negative (solid contour, higher values in negative; mesh contour, lower values).

The authors would like to thank R. J. Adrian, P. Bradshaw, A. K. M. F. Hussain, W. Kollmann, S. K. Lele, M. M. Rogers and K. Shariff for many useful discussions during the 1987 Summer Program sponsored by the Center for Turbulence Research. J. G. B. would like to acknowledge former helpful discussions with S. Corrsin.

REFERENCES

BATCHELOR, G. K. 1953 *The theory of homogeneous turbulence.* Cambridge University Press: Cambridge, England.

CORRSIN, S. & KOLLMANN, W. 1977 Preliminary report on sheared cellular motion as a qualitative model of homogeneous turbulent shear flow. In *Turbulence in Internal Flows*, a 1976 Project SQUID Workshop (ed. S. N. B. Murthy), pp. 11–33. Hemisphere Publ. Corp.: Washington, D.C.

HARRIS, V. G., GRAHAM, J. A. H. & CORRSIN, S. 1977 Further experiments in nearly homogeneous turbulent shear flow. *J. Fluid Mech.* **81**, 657–687.

KIM, J., MOIN, P. & MOSER, R. D. 1987 Turbulence statistics in fully developed channel flow at low Reynolds number. *J. Fluid Mech.* **177**, 133–166.

LAUNDER, B. E., REECE, G. J. & RODI, W. 1975 Progress in the development of a Reynolds-stress turbulence closure. *J. Fluid Mech.* **68**, 537–566.

LEE, M. J., KIM, J. & MOIN, P. 1987 Turbulence structure at high shear rate. In *Proc. Sixth Symp. on Turbent Shear Flows*, Toulouse, France, Sept. 7–9, 1987 (ed. F. Durst *et al.*), pp. 22.6.1–22.6.6.

LEE, M. J. & REYNOLDS, W. C. 1987 Structure and modeling of homogeneous turbulence in strain and relaxation processes. (Submitted to *J. Fluid Mech.*)

LUMLEY, J. L. 1975 Pressure-strain correlation. *Phys. Fluids* **18**, 750.

LUMLEY, J. L. 1978 Computational modeling of turbulent flows. *Adv. Appl. Mech.* **18**, 123–176.

ROGALLO, R. S. 1981 Numerical experiments in homogeneous turbulence. *NASA Tech. Memo.* 81315.

ROGERS, M. M. & MOIN, P. 1987 The structure of the vorticity field in homogeneous turbulent flows. *J. Fluid Mech.* **176**, 33–66.

ROGERS, M. M., MOIN, P. & REYNOLDS, W. C. 1986 The structure and modeling of the hydrodynamic and passive scaler fields in homogeneous turbulent shear flow. *Dept. Mech. Engng. Rep.* TF–25, Stanford University: Stanford, California.

TAVOULARIS, S. & CORRSIN, S. 1981 Experiments in nearly homogeneous turbulent shear flow with a uniform mean temperature gradient. *J. Fluid Mech.* **104**, 311–347.

A General Form for the Dissipation Length Scale in Turbulent Shear Flows

By J. C. R. HUNT [1], P. R. SPALART [2] and N. N. MANSOUR [2]

It has been found that, for a wide range of turbulent wall- bounded shear flows with mean velocity profile $U(y)$, the length scale L_ϵ determining the dissipation is approximately described in terms of distance from the wall y, the mean shear dU/dy, and the variance of the normal component of turbulence $\overline{v^2}$, by the formula

$$L_\epsilon^{-1} \approx \frac{A_B}{y} + A_S \; \frac{dU/dy}{\sqrt{\overline{v^2}}}$$

where $L_\epsilon = \epsilon/(\overline{v^2})^{3/2}$. To match with shear-free boundary layers, $A_B \simeq 0.27$, and with the log layer, $A_S \simeq 0.46$. The shear flows tested here were: boundary layers over a flat plate, sink flow, oscillatory flow and channel flow. The use of $\sqrt{\overline{v^2}}$ as a velocity scale minimizes the effects of Reynolds number. However, the formula fails within a distance of order L_ϵ for the regions where $dU/dy = 0$.

---

1. Introduction

The estimation of the rate of dissipation of turbulent energy ϵ is a critical feature of many computations of turbulent shear flows. However, current methods based on a heuristic differential equation for ϵ are not always accurate and almost never understood in physical terms. In particular, the relative effects of the distance (y) from a <u>boundary</u> and the shear dU/dy on the eddies is not clear.

The essential point in thinking about the rate of dissipation ϵ is that it is controlled by the <u>steepest gradients</u> of the energy-containing eddies. Therefore we need to be able to define the smallest integral or macroscales.

The aim of the research described here is to specify the relevant velocity components and macroscale L_ϵ that enable ϵ to be estimated. (For previous discussion, see Hunt, Stretch & Britter, 1986.)

Recent theoretical and experimental research on shear-free turbulent boundary layers (Hunt, 1984) ("SFBL", where $dU/dy \simeq 0$), has demonstrated how the

1 Univ. of Cambridge
2 NASA Ames Research Center

smallest "macro" scale is that of the normal velocity component $L_{11}^{(2)}$, and that $L_{11}^{(2)} \simeq 1.7y$. If we are to use this length to estimate ϵ, we recall that in a SFBL. ϵ is approximately invariant with distance from the wall $(\partial \epsilon / \partial y \simeq 0)$. It is also found by theoretical (or scaling) arguments that $\overline{v^2} = C_B \epsilon^{2/3} y^{2/3}$, where C_B is a constant. The linear analysis of Hunt (1984) gives a value for $C_B = 1.8$, while the measurements in the atmospheric convective boundary layer give $C_B = 2.5$.

Therefore in the SFBL it is natural to define the dissipation scale as

$$L_\epsilon \equiv \frac{(\overline{v^2})^{3/2}}{\epsilon} \simeq C_B^{3/2} y \tag{1.1}$$

It is convenient to express (1.1) as

$$L_\epsilon^{-1} = A_B y^{-1} \tag{1.2}$$

So we take A_B as ranging from $(1/2.5)^{3/2} = 0.25$ to $(1/2.0)^{3/2} = 0.35$. Note that the horizontal scale of the vertical fluctuations $L_{11}^{(2)}$ in the SFBL is about $1.7y$, so L_ϵ is about $L_{11}^{(2)}$.

By contrast in a uniform shear, the length scales, including L_ϵ, are largely determined by the shear dU/dy and the velocity fluctuations, so that

$$L_\epsilon = C_s \sqrt{\overline{v^2}} / (dU/dy)$$

where C_s is a dimensionless parameter of order unity. Recent numerical simulations on the time evolution of turbulence in a homogeneous shear flow by Rogers et al. (1986), Lee, Kim & Moin (1987), and Rogallo (1981) show that the parameter C_s depends on the initial conditions (in particular $L_{11}^{(2)}(dU/dy)/\sqrt{\overline{v^2}}$, and the total strain $(=t \, dU/dy)$. However, for a wide class of <u>actual</u> shear flows the effective value of $t \, dU/dy$ only varies over a range of about 3 (Townsend, 1976). So we can expect that there is an approximately constant value for

$$C_s = \frac{L_\epsilon \mid dU/dy \mid}{(\overline{v^2})^{1/2}} = \frac{1}{A_S} \tag{1.3}$$

What happens in a shear flow near a boundary? Dissipation of turbulent energy is driven by the straining of small eddies by slightly larger eddies. So the dissipation length scale L_ϵ depends on the smaller of the two effects of the boundary and the shear. So we take the <u>harmonic mean</u> of (1.2) and (1.3)

$$L_\epsilon^{-1} = \frac{A_B}{y} + A_S \frac{\mid dU/dy \mid}{\sqrt{\overline{v^2}}} \tag{1.4}$$

Taking $A_B \simeq 0.27$, then A_S can be calculated from the log layer (assuming at high Reynolds number $\sqrt{\overline{v^2}} = 1.3u_*$), and a local equilibrium between production and dissipation of turbulence energy. We obtain

$$A_S \simeq 0.46 \qquad (1.5)$$

In the research performed at the CTR, L_ϵ has been computed using the data from direct simulations of a number of wall-bounded flows. We make a comparison here with (1.4), using (1.1) to define L_ϵ

2. Preliminary results

In Fig. 1a L_ϵ/δ is plotted against y/δ for the flat plate boundary layer (Spalart, 1986b); in Fig. 1b, for the sink boundary layer (Spalart, 1986a); in Fig. 2 for the oscillating boundary layer (Spalart & Baldwin, 1987), where the flow reverses, and in Fig. 3 for the channel flow (Mansour, Kim & Moin, 1987).

Where the results for L_ϵ have been computed for different values of the Reynolds number (e.g., Fig. 1), the normalization (1.1) reduces the profiles of L_ϵ/δ to a form that is approximately independent of Re. If L_ϵ were defined on the basis of $\epsilon/(\overline{u_i^2})^{3/2}$, this would not be so. In Figs. 1 through 3, we have used the technique of extrapolating the values of $\overline{u^2}$ to their values as $Re \to \infty$, by suitable extrapolation of the high wave number spectrum (Spalart, 1986b; Perry et al., 1986). This method apparently works well even for transitional turbulence, such as occurs in the oscillating boundary layer near reversal.

All the results agree well in the log regions (where L_ϵ is proportional to y) for which the coefficient A_B was defined. But the results show that the formula (1.4) applies well beyond the log region. This implies that dU/dy is controlling the scale. The structure of turbulence must be rather similar if the constant is so good! But, note that, at the edge of the boundary layer or in a reversing boundary layer, where $dU/dy = 0$, the model is not satisfactory. The local turbulent scale is determined by advection of evolution from previous time. (Effects that are approximately incorporated in the ϵ equation!)

3. Further work

Apparently the proposed formula (1.4) has some generality. But we still do not know what aspect of the turbulent structure exactly corresponds to the length L_ϵ. The research of Lee and Hunt (in progress) on R.D.T. near a wall may help explain more about the relative role of blocking and shear, as will the related research on two-point correlations.

The use of R.D.T. to study the linear interactions will not really tell us how shear and blocking affect the nonlinear transfer. That may only come from more

detailed computations and models of the spectra (e.g., by the studies of scale transfer by Schiestel, D.I.A. by Yoshizawa, or the large-scale/small-scale interactions using R.D.T. by Kida & Hunt).

REFERENCES

HUNT, J. C. R., STRECTH, D. D., BRITTER, R. E. 1986 Length scales in stably stratified flows and their use in turbulence models, Proc. *I.M.A. Conference on stably stratified flow and dense gas dispersion*, Chester, April 9–10.

HUNT, J. C. R. 1984 Turbulent structure in thermal convection and shear-free boundary layers. *J. Fluid Mech., 161 – 184.*

KIDA, S. & HUNT, J. C. R. 1987 Submitted to *J. Fluid Mech.*

LEE, M., KIM, J., MOIN, P. 1987 Turbulence structure at high shear rate. *Proc. 6th Symp. Turbulent Shear Flows*, Sep. 7-9, Toulouse.

MANSOUR, N. N., KIM, J. & MOIN, P. 1987 Reynolds stress and dissipation rate budgets in a turbulent channel flow, to appear in *J. Fluid Mech.*

PERRY, A. E., HERBERT, S. & CHUNG, M. S. 1986 A theoretical and experimental study of wall turbulence. *J. Fluid Mech.*. **165**, 163.

ROGERS, M. M., MOIN, P. & REYNOLDS, W. C. 1986 report No. TF-25, Dept. Mechanical Eng., Stanford Univ., Stanford, Ca.

ROGALLO, R. S. 1981 Numerical experiments in homogeneous turbulence. NASA TM 81315, Ames Research Center, Moffett Field, Ca.

SPALART, P. R. 1986a Numerical study of sink flow boundary layers. *J. Fluid Mech.*. **172**, 307.

SPALART, P. R. 1986b Direct Simulation of a turbulent boundary layer up to $R_\theta = 1410$. NASA TM 89407, to appear in *J. Fluid Mech.*

SPALART, P. R. & BALDWIN, B. S. 1987 Direct simulation of a turbulent oscillating boundary layer. *Proc. 6th Symp. Turbulent Shear Flows*, Sep. 7-9, Toulouse.

TOWNSEND, A. A. 1976 **The structure of turbulent shear flow**. Cambridge University Press, Cambridge, England.
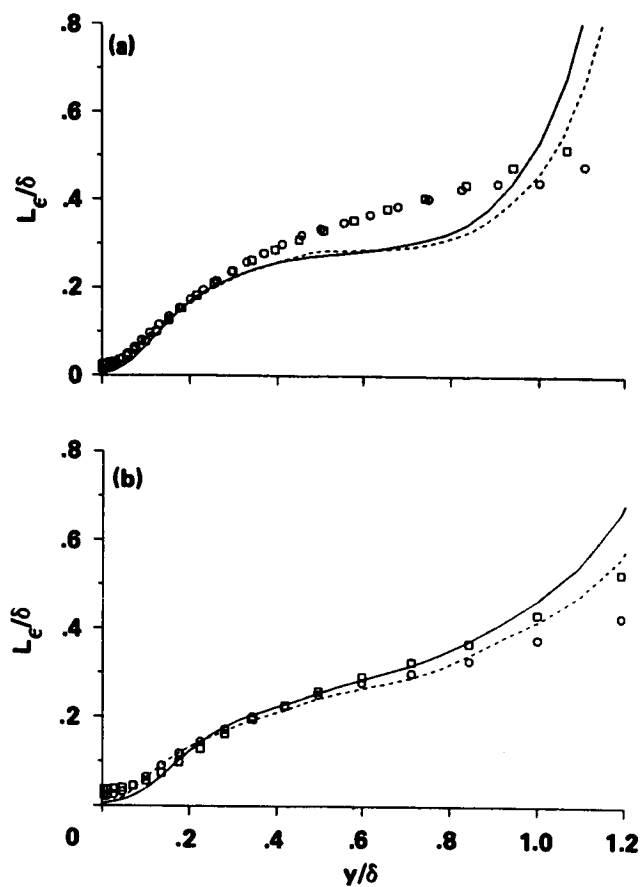
FIGURE 1. Distribution of the dissipation length scale as function of the distance to the wall.

a) Flat-plate boundary layer.

formula Eq. 1.4: ——— $R_\theta = 670$, - - - - $R_\theta = 1410$.

Simulations $(\overline{v^2}^{3/2}/\epsilon)$: □ $R_\theta = 670$, ○ $R_\theta = 1410$.

b) Sink flow boundary layer.

formula Eq. 1.4: ——— $K = 2.5 \times 10^{-6}$, - - - - $K = 1.5 \times 10^{-6}$.

Simulations $(\overline{v^2}^{3/2}/\epsilon)$: □ $K = 2.5 \times 10^{-6}$, ○ $K = 1.5 \times 10^{-6}$.

FIGURE 2.   Oscillating boundary layer, $Re = 1000$. Formula Eq. 1.4: ——— ;
Simulations $(\overline{v^2}^{3/2}/\epsilon)$: •

FIGURE 3.   Channel Flow, $Re_\delta = 3,300$. Formula Eq. 1.4: ——— ; Simulations
$(\overline{v^2}^{3/2}/\epsilon)$: ○

Test Code for the Assessment and Improvement of Reynolds Stress Models

By M. W. RUBESIN[1], J. R. VIEGAS[1], D. VANDROMME[2] and H. HA MINH[3]

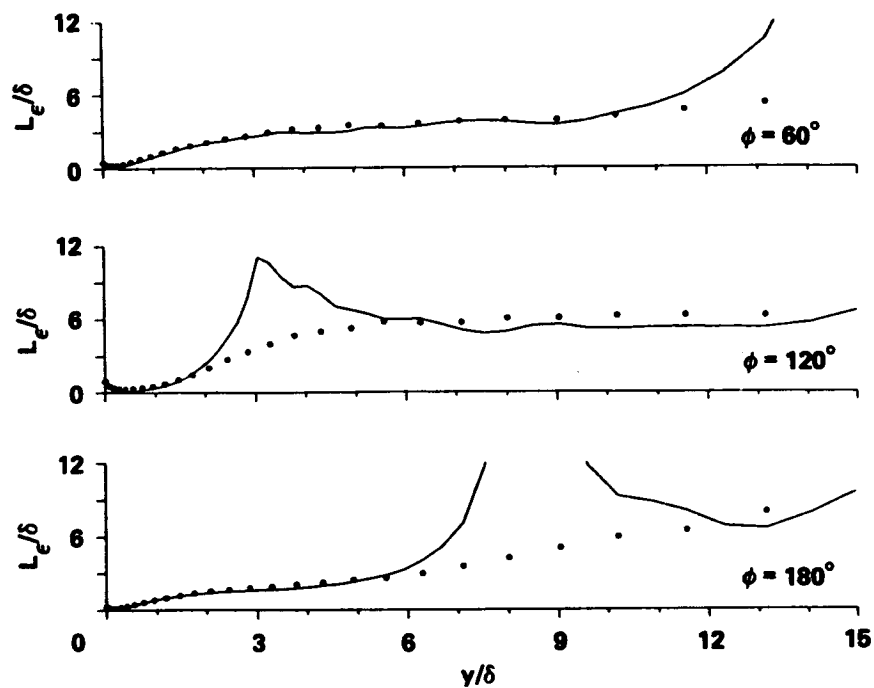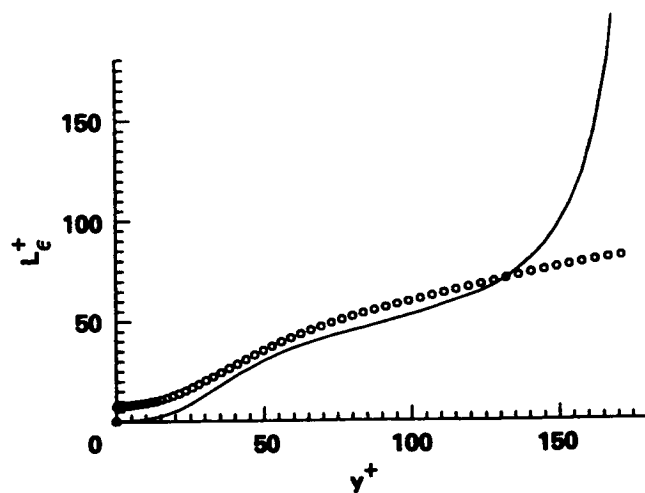An existing two-dimensional, compressible flow, Navier-Stokes computer code, containing a full Reynolds stress turbulence model, has been adapted for use as a test bed for assessing and improving turbulence models based on turbulence simulation experiments. To date, the results of using the code in comparison with simulated channel flow and over an oscillating flat plate have shown that the turbulence model used in the code needs improvement for these flows. They also show that direct simulation of turbulent flows over a range of Reynolds numbers are needed to guide subsequent improvement of turbulence models.

1. Introduction

Various turbulence models are suggested in the literature to close the different terms in the Reynolds stress budget, each with its advocates and its critics. To properly assess these models, direct simulation of turbulent flows can be used to compute the terms in the Reynolds stress budget and directly compare the model expressions with the terms (see Mansour *et al.*, 1987). Direct comparison is not enough, however, because perfect agreement can rarely be achieved, and for a complete evaluation, the models should be used in an actual computation of the flow. A code previously developed by the authors (see. Vandromme *et al.*, 1983) has been modified to simulate the channel flow of Kim *et al.* (1987) and the oscillating flat plate of Spalart & Baldwin (1987). The code is based on a bidiagonal predictor-corrector time marching algorithm (MacCormack, 1981) that has been modified to solve the nonconservative equations that result from the introduction of Reynolds stress turbulence models. This algorithm has been used to calculate several complex compressible flows, including shock wave-boundary layer interactions (HaMinh *et al.*, 1985, and Viegas & Rubesin, 1983). Because the code is quite robust and can accept turbulence modeling changes conveniently, it was decided to adapt it to the low speed conditions of the existing turbulence simulations rather than to write a new code. For the selected cases of flow in a channel (Kim *et al.*, 1987) or over an oscillating infinitely long flat plate (Spalart & Baldwin, 1987), meshes having the

---

dimensions of 5 (axial) and 50 (transverse) were employed. The small number of mesh points in the axial direction are adequate for these problems since there are no variations of dependent variables, except for pressure, in this direction. The code uses two mesh points at each of the upstream and downstream boundaries to define the conditions there. Computations with this mesh arrangement for the channel flow took about 1 minute of Cray cpu time for about 1000 iterations and about 10000 iterations to reach steady state. The code, when used to yield time-accurate oscillating plate solutions, took about an hour of cpu time to reach a steady periodic state.

2. Results and Discussion

To test the code's ability to handle low speed flows, both the channel and the oscillating plate were first run with laminar flow. The numerical results in both cases agreed quite well with the corresponding analytical solutions (Schlichting, 1960). When the same flow cases were run with the turbulence model developed by Vandromme et al. (1983), it was found that the numerical results did not agree with the statistical output from the simulations.

2.1 Channel Flow

The channel flow computations at Re=2800 gave results that differed considerably from the statistical quantities corresponding to the simulation of Kim et al., (1987). For example, Fig. 1a shows a comparison of the distribution of the turbulent shear stress, normalized by the wall shear as a function of the distance from the surface in wall parameters. The solid symbols are the output from the simulation, whereas, the open symbols represent the computed results from the modeled equations. The difference between the results indicate that the current model in the code needs considerable improvement. When similar computations were performed for channel flows with higher Reynolds numbers, namely, Re=13000 and 50000, the stresses shown in Figs. 1b and 1c resulted. Here the solid symbols are the same as on Fig. 1a and are used as reference for the levels of the computed results, the open symbols. These figures indicate that the current model in the code shows a large sensitivity to the Reynolds number of the channel flow. If the LES calculations of Moin and Kim (1982) are examined, it is noted that the maximum Reynolds shear stress at Re=13800 found there is about 0.86. This is larger than the corresponding value of 0.7 in the complete simulation at Re=2800, and is in the same direction of increased normalized shear stress with higher channel Reynolds number exhibited by the turbulence model shown in Figs. 1a and 1b. There exist questions regarding the near wall treatments of the subgrid model in the LES, and this suggests that the process of improving the turbulence model to handle these Reynolds number effects could benefit from additional accurate channel flow simulations at Reynolds numbers higher than 2800.

Another aspect of the process of using the simulated results to improve statistical turbulence models becomes evident in Fig. 2. Here is shown the rate of dissipation
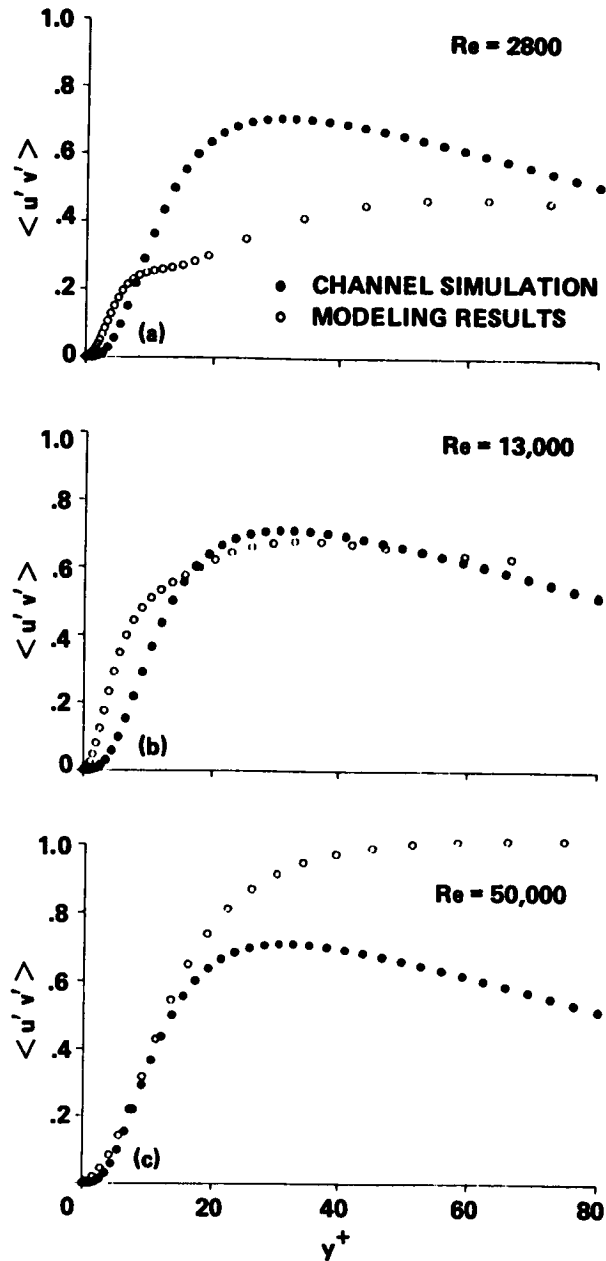
FIGURE 1. Dimensionless Reynolds shear stress in the near wall region of the channel. a) $Re = 2800$. b) $Re = 13000$. c) $Re = 50000$.

in the equation for the normal stress, $\overline{uu}$, expressed in dimensionless form. Again, the open and closed symbols represents the results of the model calculations and the simulations, respectively. The figure shows considerable difference between the two computations, and at first glance suggests difficulties with the particular model used for the turbulence dissipation rate. It was found (Mansour, Kim and Moin,

FIGURE 2.   Distribution of dimensionless dissipation rate in $\overline{uu}$ equation.

1987), however, that the model used in the computations evaluated with the moments found from the simulations, rather than from the modeled computations, gave results quite close to those of the simulations. Thus the error of the modeled computations shown on this figure result from the errors of the Reynolds stresses used in the evaluation of the dissipation rather than the functional form of the dissipation m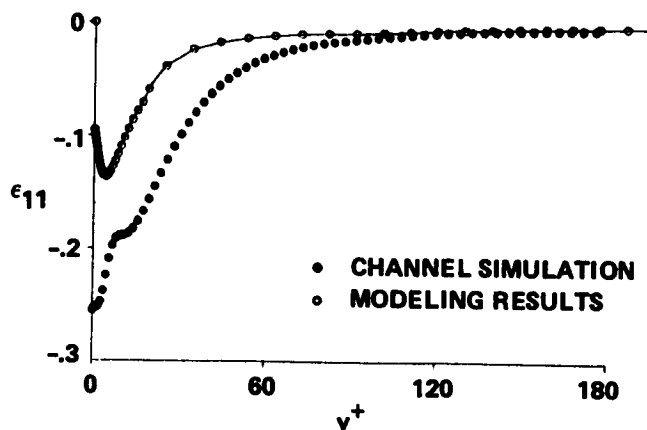odel. This is an example of the highly interactive behavior of elements of turbulence models and indicates that model improvements must be made simultaneously in all elements of the model so that it improves in the aggregate. The wealth of information available in the simulations should facilitate this process in future studies.

2.2 Oscillating Flat Plate

Representative results of the comparison of the computation of the flow over an oscillating flat plate with the direct simulation of Spalart & Baldwin (1987) are shown in Fig. 3. Here are shown the time-dependent skin friction over a cycle of time for the model computations as well as the simulation. Although the computed results are periodic and show similar phase relationships as do the simulation, there are significant differences between the results which, again, indicate the weaknesses of the current turbulence model.

3. Future Directions

The authors plan to continue to use direct turbulence simulations to improve the Reynolds stress model used in the code. The directions this will take depends a great deal on the availability of simulations for a range of Reynolds numbers. The range in Reynolds number is needed to minimize the number of assumptions used
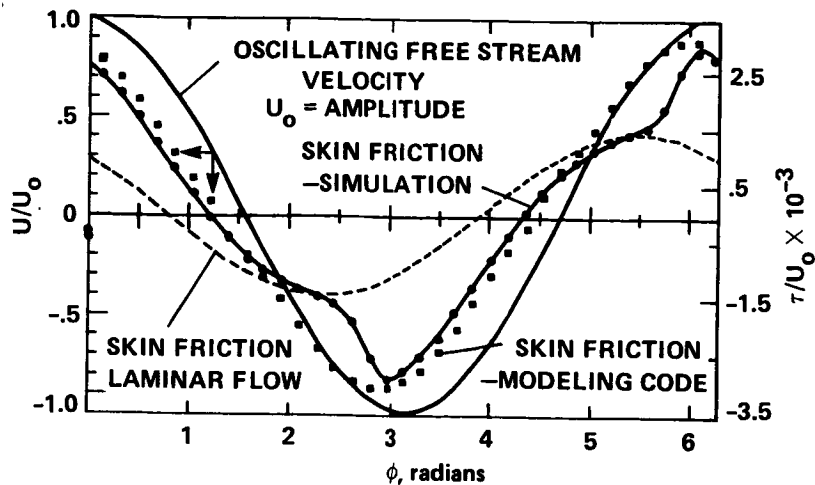
FIGURE 3. Skin friction as function of phase angle ϕ for an oscillating flat plate. Comparison of model results with simulation data.

regarding the functional form of of the various coefficients in the turbulence model. A test for the universality of these coefficients will be agreement with simulation data from a variety of flow fields.

REFERENCES

HaMinh, H., Rubesin, M.W., Vandromme, D., and Viegas, J. R., 1985 On the Use of Second Order Closure Modeling for the Prediction of Turbulent Boundary Layer/Shock Wave Interactions: Physical and Numerical Aspects, *International Symposium on Computational Fluid Dynamics*, Tokyo, Japan, Sept. 9–12.

Kim, J., Moin, P., and Moser, R., 1987 Turbulence Statistics in Fully Developed Channel Flow at Low Reynolds Number . *J. Fluid Mech.* **177**, 133 – 166.

MacCormack, R. W., 1981 A Numerical Method for Solving the Equations of Compressible Viscous Flows, AIAA Paper 81-0110.

Mansour, N.N., Kim, J. and Moin, P., 1987 Reynolds-stress and Dissipation Rate Budgets in a Turbulent Channel Flow, to appear in *J. Fluid Mech.*

Moin, P. and Kim, J., 1982 Numerical Investigation of Turbulent Channel Flow. *J. Fluid Mech.* **118**, 341 – 377.

Spalart, P. R., and Baldwin, B. S. 1987 Direct Simulation of a Turbulent Oscillating Boundary Layer, NASA TM 89460, May.

Schlichting, H., 1960 **Boundary Layer Theory**, Mc-Graw Hill, New York.

Vandromme, D., HaMinh, H., Viegas, J. R., Rubesin, M. W., and Koll-

MANN, W., 1983 Second Order Closure for the Calculation of Compressible Wall Bounded Flows with an Implicit Navier-Stokes Solver, *Fourth Symposium on Turbulent Shear Flows*, Karlsruhe, GFR, Sept. 12-14.

VIEGAS, J. R., AND RUBESIN, M. W. 1983 Wall-Function Boundary Conditions in the Solution of the Navier-Stokes Equations for Complex Compressible Flows, AIAA 83-1694.

Reynolds Stress Models of Homogeneous Turbulence

By T. -H. SHIH[1], N. N. MANSOUR[2], and J. Y. CHEN[3]

Existing and new models for the rapid and the return terms in the Reynolds stress equations have been tested in two ways. One, by direct comparison of the models with simulation data. The other, by simulating the flows using the models and comparing the predicted Reynolds stresses with the data. We find that existing linear models can be improved and that non-linear models are in better agreement with the simulation data for a wide variety of flows.

1. Introduction

Homogeneous flows are considered to be basic flows in the study of complex turbulent flows. These flows are the simplest turbulent flows, yet, the pressure-strain and the dissipation rate terms in the Reynolds stress equations do not vanish in these flows. These terms need to be modeled for closure of the Reynolds stress equations, and are usually recombined into a so-called rapid pressure-strain and a return term. On the other hand, the terms related to turbulence diffusion (for example, the triple correlation tensor and pressure transport terms, which will complicate the turbulence modeling) do not appear in homogeneous flows, this allows us to concentrate on two of the important terms to be modeled. There exist several models developed for these terms, we have for example, for the rapid term, the models of Naot, Shavit and Wolfshtein (1970), Launder, Reece and Rodi (1975, hereafter referred to as LRR), Shih and Lumley (1985, hereafter referred to as SL), Reynolds (1987), and others; for the return term, the models of Rotta (1951), Lumley (1978, hereafter referred to as Lumley) and a second-order form by Shih, Mansour and Moin (1987, hereafter referred to as SMM).

The research conducted at the CTR this summer concentrated on testing some existing and new models developed for the rapid and the return terms. These models were tested in two ways. First, we compared these models directly with numerical simulation data, since direct evaluation of these terms is possible using the full simulation data. Second, we used these models in a finite difference code for the Reynolds stress equations and compared the solutions of the modeled Reynolds stress equations with numerical simulation data.

1 Center for Turbulence Research
2 NASA Ames Research Center
3 Sandia National Laboratories

2. Reynolds stress Closure Models

2.1 Reynolds stress equation

For homogeneous turbulence, the Reynolds stress equations read as follows,

$$\langle u_i u_j \rangle_{,t} = -\langle u_j u_k \rangle U_{i,k} - \langle u_i u_k \rangle U_{j,k}$$
$$+ (\langle p u_{i,j} \rangle + \langle p u_{j,i} \rangle)/\rho - 2\nu \langle u_{i,k} u_{j,k} \rangle$$

where, $\langle \ \rangle$ stands for ensemble averaging. In this equation, the second line, i.e. the pressure strain correlation tensor and dissipation tensor must be modeled. The usual approach is to recombine the terms in the equations as follows:

$$\langle u_i u_j \rangle_{,t} = P_{ij} + \Pi^1_{ij} + \Pi^2_{ij} - (2/3)\langle \epsilon \rangle \delta_{ij}$$

where P_{ij} is the production term,

$$P_{ij} = -(\langle u_j u_k \rangle U_{i,k} + \langle u_i u_k \rangle U_{j,k})$$

and Π^1_{ij} and Π^2_{ij} are called the rapid and the return term respectively and are defined as

$$\Pi^1_{ij} = (\langle p^1 u_{i,j} \rangle + \langle p^1 u_{j,i} \rangle)/\rho$$

$$\Pi^2_{ij} = (\langle p^2 u_{i,j} \rangle + \langle p^2 u_{j,i} \rangle)/\rho - 2\nu \langle u_{i,k} u_{j,k} \rangle + (2/3)\langle \epsilon \rangle \delta_{ij}$$

where $\langle \epsilon \rangle = \nu \langle u_{i,k} u_{i,k} \rangle$, the pressures p^1 and p^2 are solutions to the rapid and the slow Poisson equations (for more details see SL).

2.2 Models

Based on realizability, Shih and Lumley (1985) and Reynolds (1987) proposed the following model for the rapid term,

$$\Pi^1_{ij} = (1/5 + 2\alpha_5)\langle q^2 \rangle (U_{i,j} + U_{j,i})$$

$$-2/3(1 - \alpha_5)(P_{ij} - 2P\delta_{ij}/3)$$

$$+(2/3 + 16\alpha_5/3)(D_{ij} - 2P\delta_{ij}/3)$$

$$+(6/5)b_{ij}P + (2/15)(P_{ij} - D_{ij}) \tag{2.1}$$

$$+(2/5)[(\langle u_i u_k \rangle U_{j,q} + \langle u_j u_k \rangle U_{i,q})\langle u_k u_q \rangle$$

$$-\langle u_i u_p \rangle \langle u_j u_q \rangle (U_{p,q} + U_{q,p})]/\langle q^2 \rangle$$

where,

$$D_{ij} = -(\langle u_j u_k \rangle U_{k,i} + \langle u_i u_k \rangle U_{k,j})$$

$P = P_{ii}/2$ is the turbulent kinetic energy production,

$$\alpha_5 = -(1/10)(1 + 0.8F^{1/2}) \qquad\qquad \text{(SL)}$$

$$\alpha_5 = -(1/10)\left\{1 + 3.5[1 - (1 - F)^{1/4}]\right\} \qquad \text{(SMM)}$$

If we retain in Eq. (2.1) the first three lines and set $\alpha_5 = -1.45455$, we get the linear model of LRR.

A general form of the model for the return term is suggested by Lumley (1978), and Shih (1984):

$$\Pi_{ij}^2 = -\langle\epsilon\rangle\{(2 + C_f F^\xi)b_{ij} + \gamma[b_{ij}^2 + (1/3 + 2II)b_{ij} + 2II\,\delta_{ij}/3]\} \qquad (2.2)$$

where

$$C_f = (1/9)\exp(-7.77/\sqrt{Re})\{72/\sqrt{Re}$$
$$+ 80.1\ln[1 + 62.4(-II + 2.3III)]\}$$

$$II = -b_{ij}b_{ji}/2$$

$$III = b_{ij}b_{jk}b_{ki}/3$$

$$\gamma = \gamma_0(1 - F^\eta)$$

$$Re = \langle q^2\rangle^2/(9\langle\epsilon\rangle\nu)$$

$$F = 1 + 9II + 27III$$

$$\xi = 0, \quad \gamma_0 = 0, \quad C_f = 1 \qquad\qquad \text{(Rotta, 1951)}$$

$$\xi = 1, \quad \gamma_0 = 0 \qquad\qquad\qquad\qquad \text{(Lumley)}$$

$$\xi = 17/20, \quad \eta = 1/20, \quad \gamma_0 = -2 \qquad \text{(SMM)}$$

3. Model Testing

3.1 Direct comparison with simulation data

The data for homogeneous strain of Lee and Reynolds (1985) and for homogeneous shear of Rogers, Moin and Reynolds (1986) were used to directly compare the model expression with the simulation results. For all simulated shear flows, the non-linear rapid model Π_{ij}^1, Eq. (2.1), and the non-linear return model Π_{ij}^2, Eq. (2.2), are in good agreement with the simulation data. The linear rapid model (launder, Reece and Rodi, 1975) and the linear return model (Lumley, 1978) are also included for comparison. Here, we present two typical flows: C128U†(with a

moderate shear rate $S = 28.284$) and C128W† (with a high shear rate $S = 56.568$). Fig.1 - Fig.4 show the comparison between the models and the simulation data. We find that the non-linear rapid model works well in each component of the Reynolds stress equations (see Fig. 1 and Fig. 2), while the linear rapid model (LRR) does not work well for the $\langle uu \rangle$ and $\langle vv \rangle$ components. On the other hand, Lumley's linear return model works very well in all simulated shear flows as indicated in Fig. 3 and Fig. 4. But, we find that the non-linear return model, Eq. (2.2), works at least as good as Lumley's linear model in all simulated shear flows, in addition, the non-linear model works better in relaxation from simple strains (typical comparisons are shown in Figs 5-7). The return to isotropy cases (or relaxation cases), after irrotational strain, of Lee and Reynolds (1985) provide a critical evaluation of the return model. We find that the return term models work well in all relaxation flows from axisymmetric contractions, but the agreement between the model expression and the data deteriorates in some relaxation flows from plane strains and axisymmetric expansions. Fig.5 shows a typical relaxation from an axisymmetric contraction. Fig.6 and Fig.7 show relaxations from the plane strain and axisymmetric expansion respectively. The failure of the return term models in some relaxation flows from plane strain (Fig. 6.1) and axisymmetric expansion (Fig. 7.1) is due to the inability of the current models to reflect the effect of the initial condition on the relaxation process.

3.2 Predictions using the modeled Reynolds stress equations

In this section, we choose the homogeneous shear case (C128W, high shear $S = 56.568$) of Rogers, Moin and Reynolds (1986) to evaluate the performance of the rapid and return term models in predicting the Reynolds stresses. However, in order to integrate the Reynolds stress equations, we need a model equation for the dissipation rate $\langle \epsilon \rangle$. A standard transport model equation for $\langle \epsilon \rangle$ (Lumley,1978) was used in conjunction with the models of SL, Lumley, and SMM. The $\langle \epsilon \rangle$ equation of LRR was used in conjunction with the LRR model.

Figures 8.1 and 8.2 show the Reynolds stresses and dissipation rate as predicted using the models of SMM (Eqs. 2.1 and 2.2). The model predicts well the shear stress and the streamwise component of the Reynolds stress but slightly overpredicts the cross stream components. Similar results were obtained using the models of SL and lumley for the rapid and return terms (See Fig. 9b). Figure 9a shows the results using the linear models of LRR. In this case the Reynolds stresses are overpredicted by a significant amount.

4. Future Work

From this study, we conclude that the models given by Eq.(2.1) and Eq.(2.2) are appropriate at least for homogenous turbulent shear flows. The linear models are unable to predict the high shear case, and are expected to have severe limitations for more general cases. The nonlinear models were developed based on a general

---

† The name of the flow cases are those of Rogers, Moin and Reynolds (1986)

realizability conditions, we should be able to use them to model other flows. In particular, these models should be extended to inhomogeneous flows and should be evaluated in a similar manner.

REFERENCES

LAUNDER, B. E., REECE, G. J., & RODI, W. 1975 .*J. Fluid Mech.*, **68**, *537*.

LEE, M. J., & REYNOLDS, W. C. 1985 . Rep. No. TF-24, Stanford University.

LUMLEY, J. L. 1978 . *Adv. Appl. Mech.* **18**, *123*.

SHIH, T.-H., MANSOUR, N. N., & MOIN, P. 1987 . Second Order Modeling of Homogeneous Turbulence and Comparison with Numerical Simulations, to be published.

NAOT, D., SHAVIT, A., & WOLFSHTEIN, M. 1970 . *Israel J. Tech.* **8**, *259*.

REYNOLDS, W.C. 1987 . Fundamentals of Turbulence for Turbulence Modeling and Simulation, *Lecture Notes for Von Karman Institute*, March 16-17.

ROGERS, M.M., MOIN, P., & REYNOLDS, W.C. 1986 . Rep. No. TF-23, Stanford University.

ROTTA, J.C. 1951 . *Z. Phys.* **129**, *547*.

SHIH, T.-H. 1984 . Second order modeling of scalar turbulent flows Ph.D Thesis, Sibley School of Mech. and Aero. Engrg., Cornell University.

SHIH, T.-H., & LUMLEY, J.L. 1985 . Rep. FDA-85-3, Sibley School of Mech. and Aero. Engrg., Cornell University.

FIGURE 1. Rapid Pressure strain terms for homogeneous shear, $S = 28.284$ (case C128U of Rogers, Moin and Reynolds, 1986). Comparison of models with data.

FIGURE 2.   Return Pressure strain terms for homogeneous shear, $S = 28.284$ (case C128U of Rogers, Moin and Reynolds, 1986). Comparison of models with data.
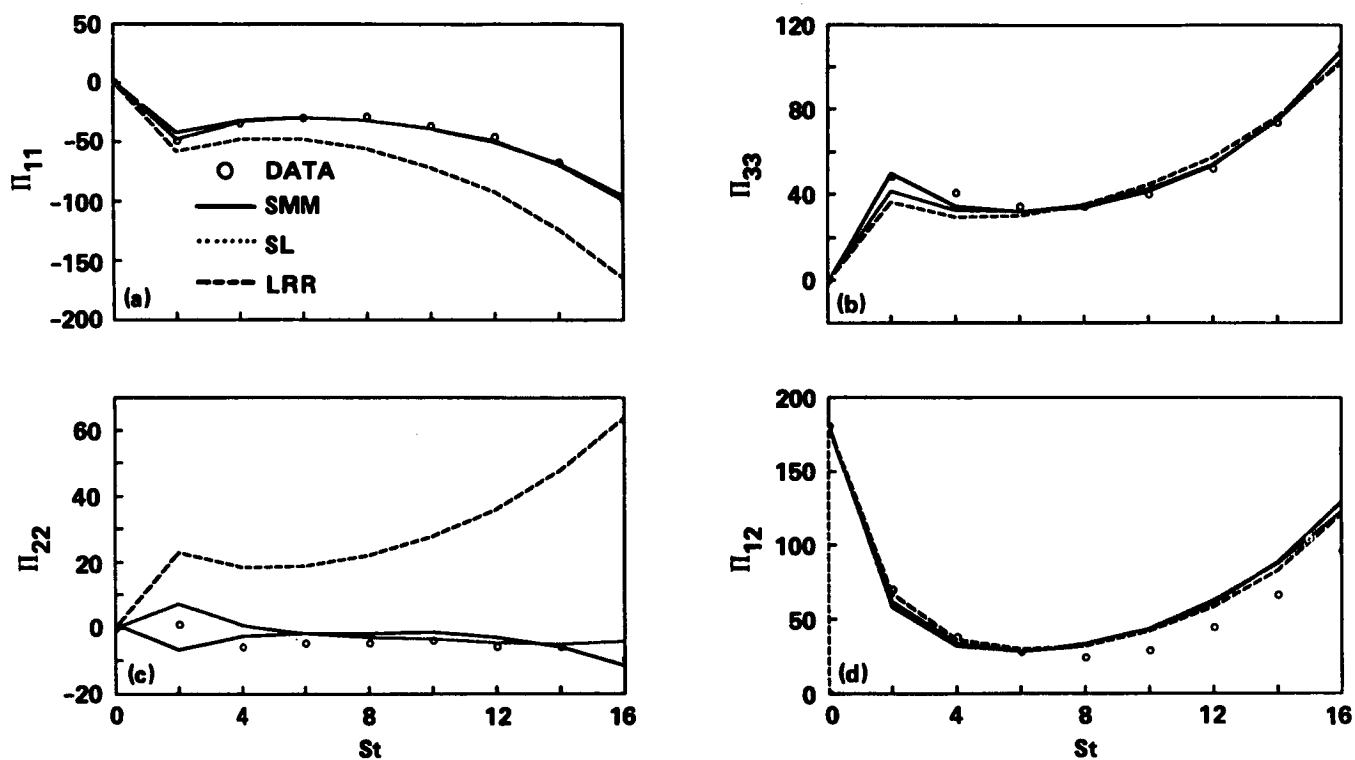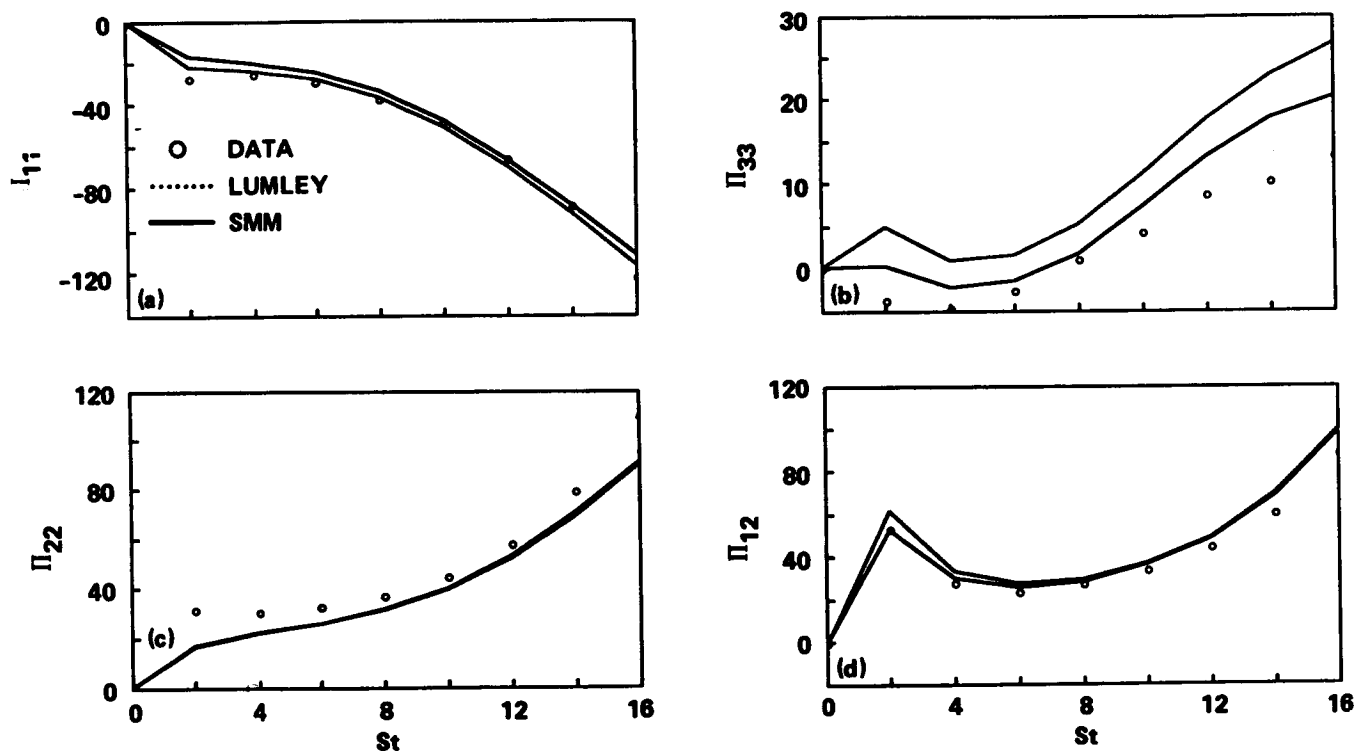
FIGURE 3.   Rapid Pressure strain terms for homogeneous shear, $S = 56.568$ (case C128U of Rogers, Moin and Reynolds, 1986). Comparison of models with data.
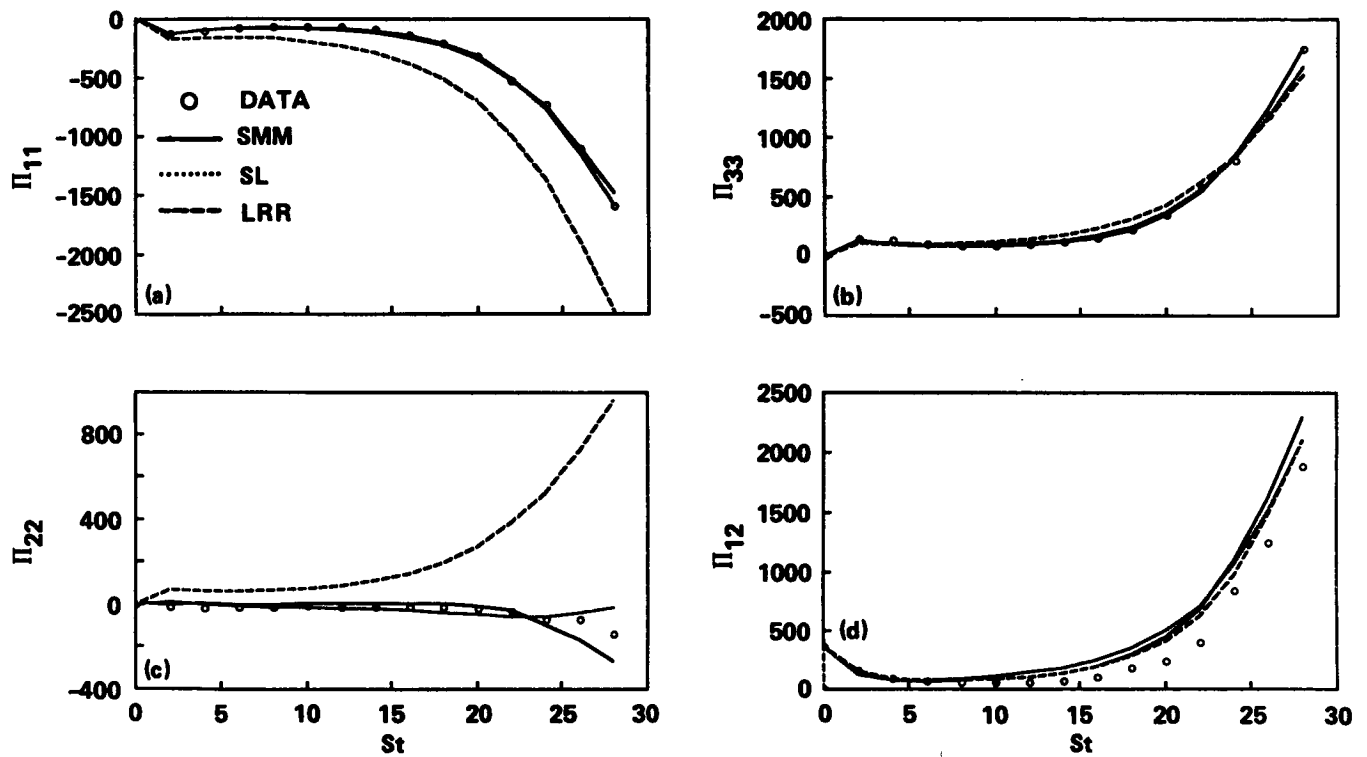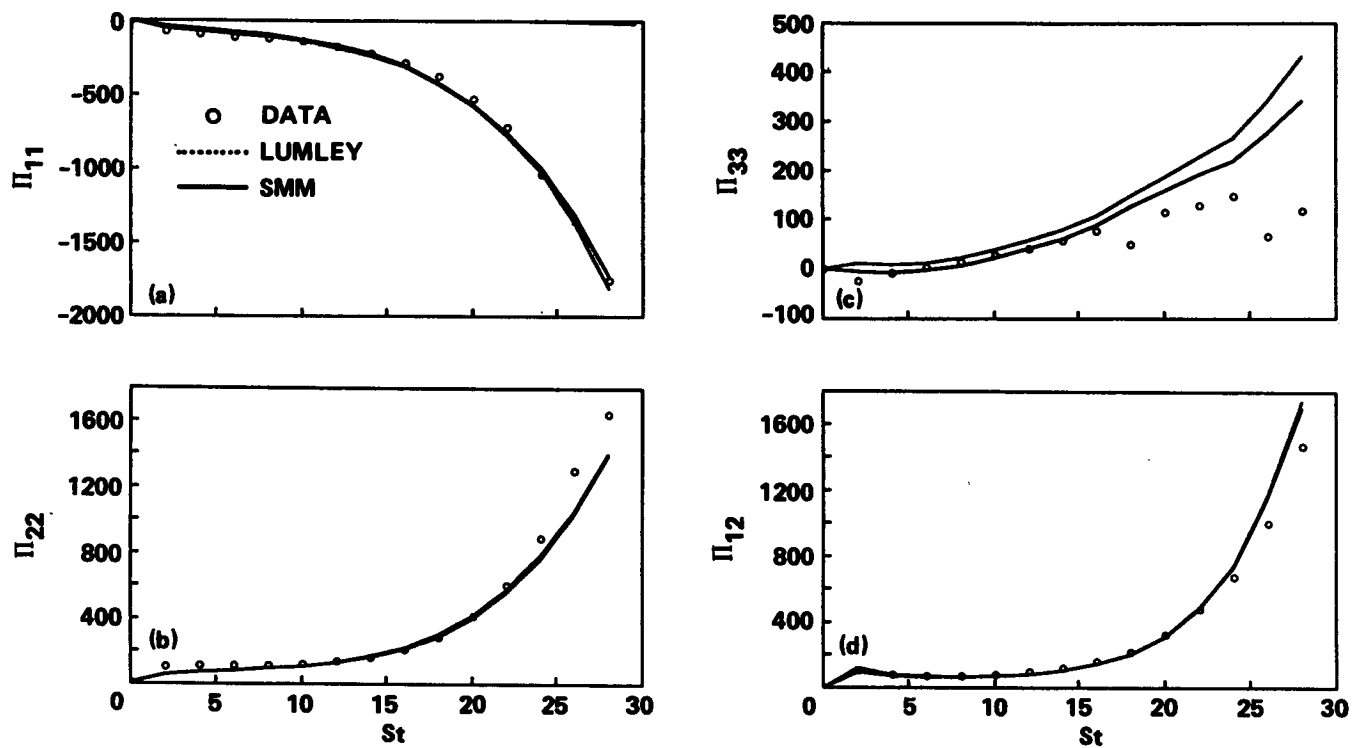
FIGURE 4. Return Pressure strain terms for homogeneous shear, $S = 56.568$ (case C128U of Rogers, Moin and Reynolds, 1986). Comparison of models with data.
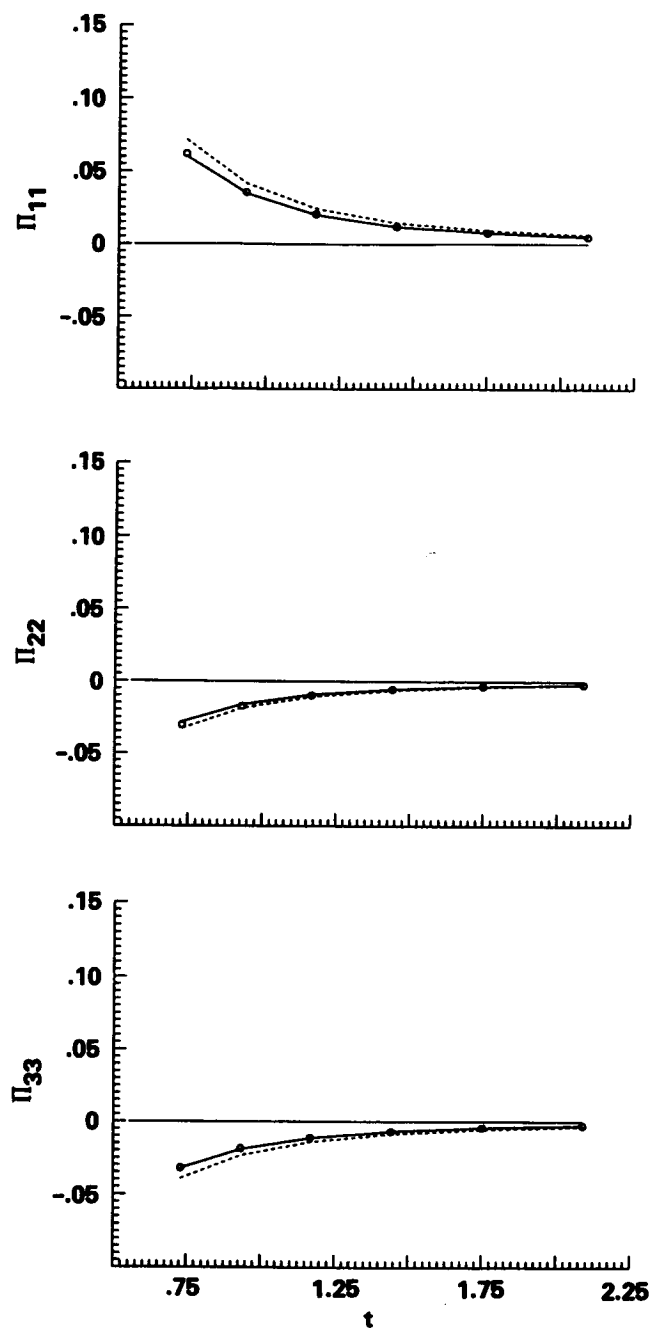
FIGURE 5.   Return Pressure strain terms for return from axisymmetric contraction (case M2R of Lee and Reynolds, 1985). Comparison of models with data. o Data, - - - - SMM, ⋯⋯ Lumley.

FIGURE 6. Return Pressure strain terms for return from plane strain (cases E4R, a), and A2R, b), of Lee and Reynolds, 1985). Comparison of models with data. o Data, - - - - SMM, ········ Lumley.

FIGURE 7. Return Pressure strain terms for return from axisymmetric expansion (cases P3R, a), and O3R, b), of Lee and Reynolds, 1985). Comparison of models with data. ○ Data, – – – – SMM, ⋯⋯⋯ Lumley.
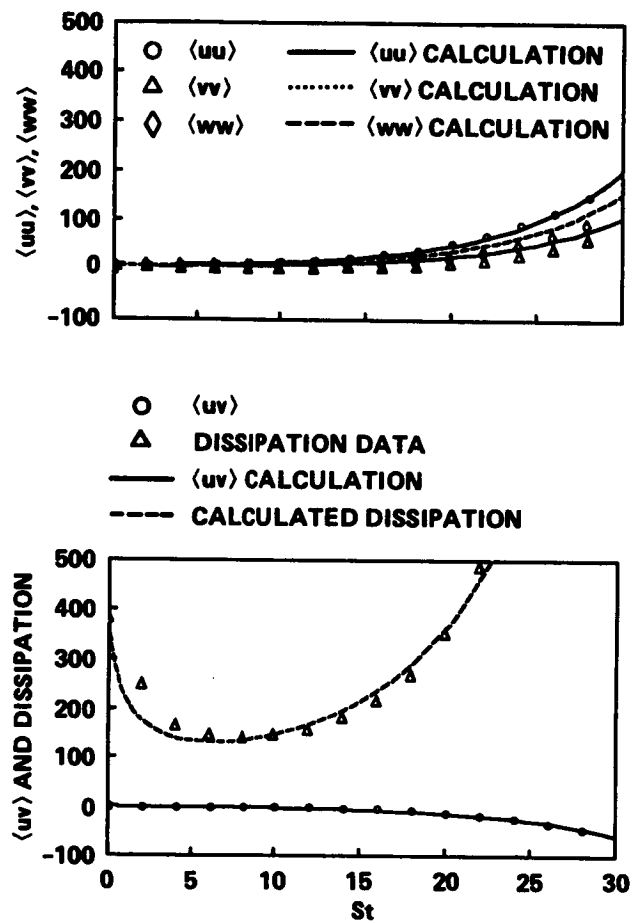
FIGURE 8. Reynolds stresses and dissipation rate for homogeneous shear, $S =$ 56.568 (case C128W of Roger, Moin and Reynolds, 1986). Comparison of prediction using SMM with data.
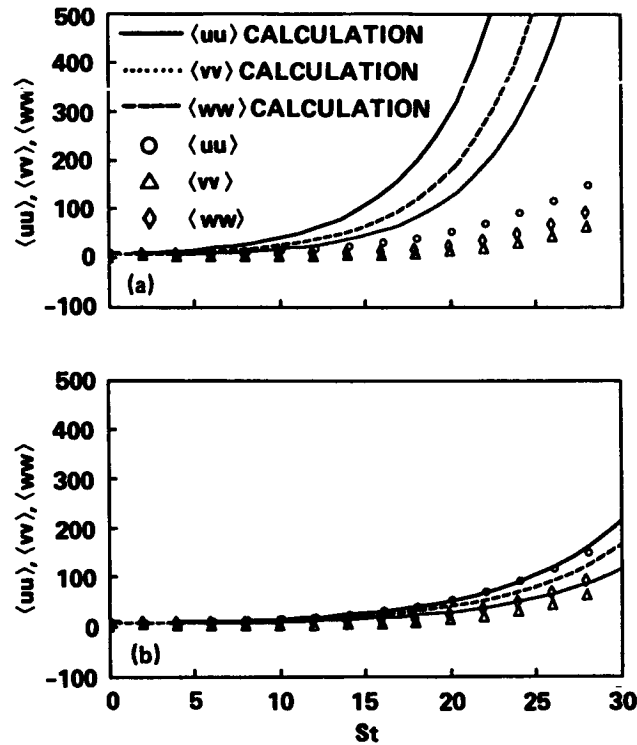
FIGURE 9.   Reynolds stresses development for homogeneous shear, $S = 56.568$
(case C128W of Roger, Moin and Reynolds, 1986).

a) Comparison of prediction using LRR with data.

b) Comparison of prediction using SL with data.

The Decay of Isotropic Turbulence in a Rapidly Rotating Frame

By C. G. SPEZIALE[1], N. N. MANSOUR[2], and R. S. ROGALLO[2]

A direct numerical simulation of the decay of initially isotropic turbulence in a rapidly rotating frame was conducted. This 128x128x128 simulation was completed for a Reynolds number $Re_\lambda = 15.3$ and a Rossby number $Ro_\lambda = 0.07$ based on the initial turbulent kinetic energy and Taylor microscale. The numerical results indicate that the turbulence remains essentially isotropic during the major part of the decay (i.e., beyond the point where the turbulent kinetic energy has decayed to less than 10% of its initial value). The rapid rotation has the primary effect of shutting off the energy transfer so that the turbulence dissipation (and hence the rate of decay of the turbulent kinetic energy) is substantially reduced. Consequently, the anisotropy tensor remains essentially unchanged while the energy spectrum undergoes a nearly linear viscous decay — the same results that are predicted by Rapid Distortion Theory which is only formally valid for much shorter elapsed times. Surprisingly, no Taylor-Proudman reorganization of the flow to a two-dimensional state is observed. The implications that these results have on turbulence modeling are discussed briefly along with prospective future research.

1. Results

The research conducted this summer at the CTR concentrated on the development of improved Reynolds stress models for the description of rotating turbulent flows. It is envisioned that such models could also have important applications in the description of curved turbulent flows as a result of the analogy that can quite often be drawn between rotation and curvature.

In order to gain insight into the effects of rotation, a direct numerical simulation of decaying isotropic turbulence in a rapidly rotating frame was conducted. A Reynolds number of $Re_\lambda = 15.3$ based on Taylor microscale and a Rossby number of $Ro_\lambda = 0.07$ were considered (this Rossby number is more than an order of magnitude smaller than those which were considered previously). This direct simulation yielded some surprising results. As has been shown in previous numerical simulations and experiments (see Bardina, Ferziger and Rogallo 1985, and Wigeland and Nagib 1978), the turbulence remained isotropic after the rotation was imposed.

---

1 ICASE, NASA Langley Research Center

2 NASA Ames Research Center
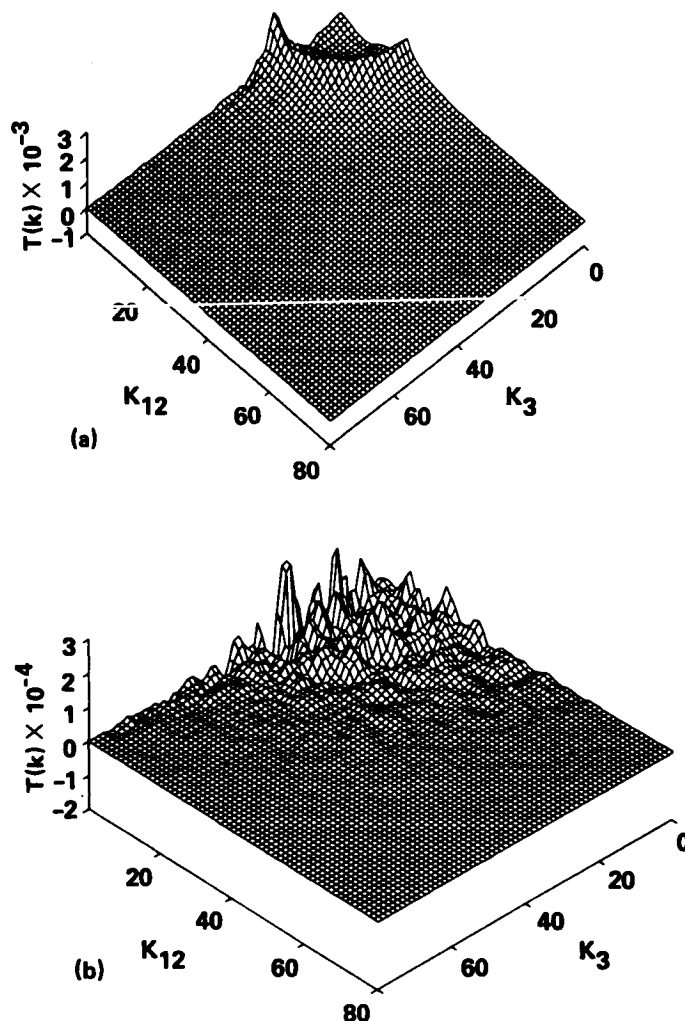
FIGURE 1.   Transfer spectra as function of $k_{12} = \sqrt{k_1^2 + k_2^2}$ and k_3. a) Initial distribution (isotropic decay). b) Shortly after the rotation is started $(t\epsilon_0/q_0^2)$.

The rotation killed the energy transfer (through the generation of inertial waves; see Fig. 1) and the turbulence underwent a pure viscous decay as would be predicted by Rapid Distortion Theory (RDT). More precisely, the energy spectrum, $E(k,t)$, decayed in time in good agreement with the formula,

$$E(k,t) = E(k,t_0)\exp\left[-2\nu k^2(t - t_0)\right] \tag{1}$$

where ν is the kinematic viscosity (see Fig. 2). Equation 1 is obtained from RDT for this problem. The surprising finding was that Eq. (1) remained an excellent approximation even after the turbulent kinetic energy had decayed to only 10% of its initial value. As a result of the energy transfer being suppressed, the turbulence
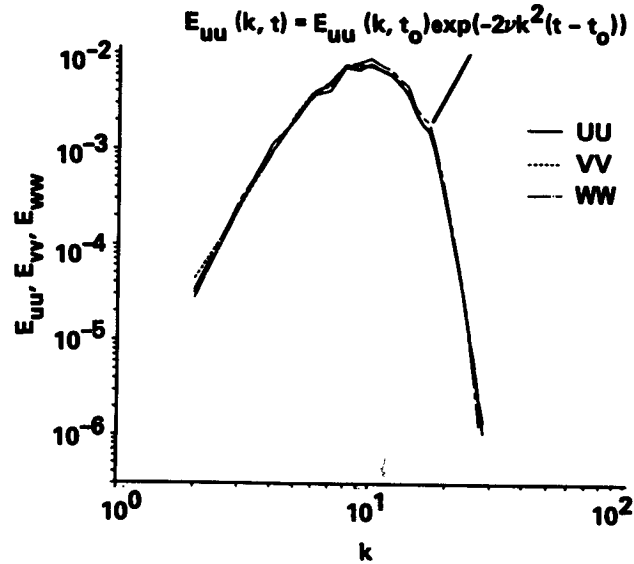
FIGURE 2.   Energy spectra, E_{uu}, E_{vv} and E_{ww} $(q^2/q_0^2 = 0.03)$.

decayed slower in the rotating frame (see Fig. 3). Although the integral length scales showed the development of mild anisotropies, there was no discernable Taylor-Proudman reorganization to a two-dimensional flow. The tensor,

$$A_{ij} = \frac{\nu}{\epsilon} \overline{u'_{k,i} u'_{k,j}} \tag{2}$$

which is normalized by the dissipation rate ϵ, remained isotropic (under a complete Taylor-Proudman reorganization, the velocity gradient along the axis of rotation $u_{,3} \mapsto 0$ as the rotation rate $\Omega \mapsto \infty$ and, hence $A_{33} << A_{11}, A_{22}$). It can be shown that the RDT solution does not undergo a Taylor-Proudman reorganization since the Fourier transform of the velocity,

$$\hat{u}_i(k,t) \propto A(k)\exp(i\alpha(k)\Omega t) \tag{3}$$

and, hence, in the limit as $\Omega \mapsto \infty$,

$$\frac{1}{\Omega}\frac{\partial \omega_i}{\partial t} = O(1) \tag{4}$$

where ω_i is the vorticity vector.

In order for the Taylor-Proudman theorem to apply, $(1/\Omega)\partial \omega_i/\partial t$ must vanish as $\Omega \mapsto \infty$. Since RDT becomes a better approximation for longer instants of time as Ω gets larger (for a given turbulence level), it appears that no Taylor-Proudman

FIGURE 3.   Effect of rotation on the decay of the turbulent kinetic energy.

reorganization will occur in a rapidly rotating isotropic turbulence. Previous investigators (c.f., Bardina, Ferziger and Rogallo 1985) had speculated that such a reorganization to a two-dimensional flow could occur.

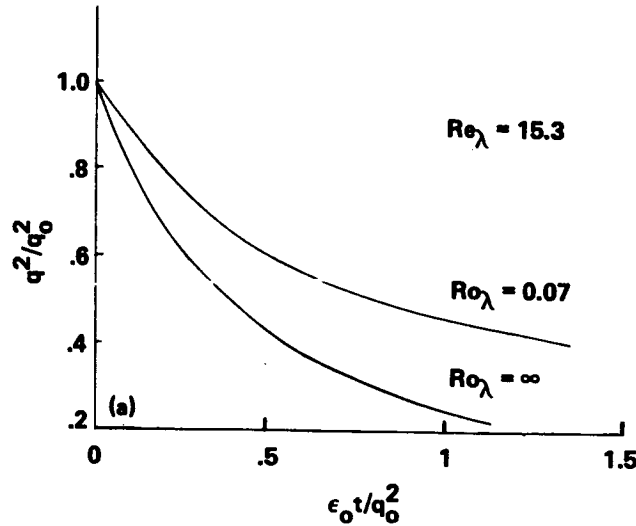Since the results of these direct simulations on rotating isotropic turbulence clearly demonstrate (in support of Wigeland and Nagib 1978, and Bardina, Ferziger and Rogallo 1985) that there is a reduction in the dissipation rate with increasing rotation rate, it is clear that modifications need to be made in the dissipation rate equation. All of the commonly used dissipation rate equations (c.f., Launder, Reece and Rodi 1975) predict that for a given mean flow, a system rotation has no effect on the evolution of the dissipation rate in contradiction of experimental and numerical simulation data. A recently proposed model by Bardina, Ferziger and Rogallo (1985) given by,

$$\dot{\epsilon} = -C_1 \frac{\epsilon^2}{q^2} - C_2 \Omega \epsilon \tag{5}$$

for an isotropic turbulence (where ϵ is the dissipation rate, q^2 is the trace of the Reynolds stress tensor, and $C_2 = 11/3$ and $C_1 = 0.15$ are empirical constants) was tested. It was found that this model, which compared favorably with the data of Wigeland and Nagib (1978) performed very poorly at the rapid rotation rates considered herein (see Fig. 4). Consequently, it appears that the dependence of the dissipation rate equation on Ω is unlike in Eq. (5). Furthermore, it is not clear at this time how such a modified dissipation rate equation could be generalized to anisotropic turbulent flows. Any smooth function of the invariants,

$$\Omega_{ij}\Omega_{ij}, \Omega_{ij}^2 \tau_{ij}, \Omega_{ij}^2 S_{ij}, \tag{6}$$
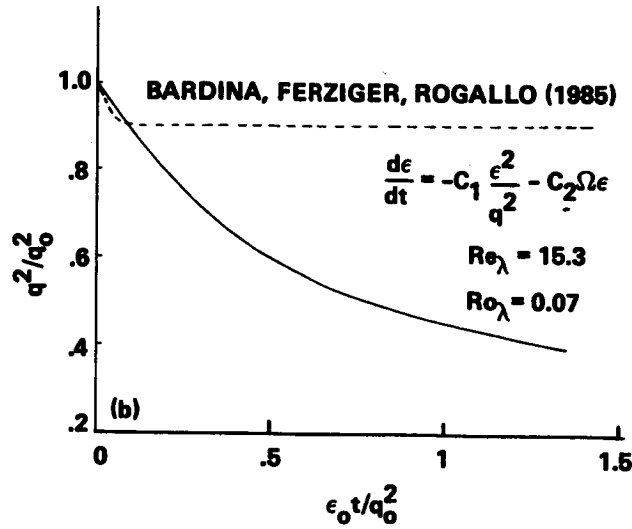
FIGURE 4. Comparison of the decay of the turbulent kinetic energy with the model of Bardina, Ferziger & Rogallo (1985).

where,

$$\Omega_{ij} = \frac{1}{2}\left(U_{i,j} - U_{j,i}\right), \quad S_{ij} = \frac{1}{2}\left(U_{i,j} + U_{j,i}\right) \tag{7}$$

U_i is the mean velocity, and τ_{ij} is the Reynolds stress tensor, reduce to functions of Ω in the limit of rotating isotropic turbulence (a model containg $\Omega_{ij}^2 S_{ij}$ was proposed by Pope 1978). Work on the development of a more general dissipation rate equation which can account for rotation in inhomogeneous turbulent flows was begun during the summer program and will continue in the future.

2. Future work

The time development of the energy spectrum for an isotropic turbulence is given by,

$$\dot{E}(k,t) = T(k,t) - 2\nu k^2 E(k,t) \tag{8}$$

where $T(k,t)$ is the energy transfer. The equation for the dissipation rate, ϵ, can be derived by multiplying Eq.(8) by $2\nu k^2 dk$ and integrating over all wave numbers,

$$\dot{\epsilon} = 2\nu \int_0^\infty k^2 T(k,t)dk - 4\nu^2 \int_0^\infty k^4 E(k,t)dk \tag{9}$$

The commonly used model for the right-hand-side of Eq. (9) is given as follows:

$$2\nu \int_0^\infty k^2 T(k,t)dk - 4\nu^2 \int_0^\infty k^4 E(k,t)dk = -C_1 \frac{\epsilon^2}{q^2} \tag{10}$$

where q^2 is twice the turbulent kinetic energy. Any modification to the above model that takes into account the effect of rotation, has to reflect the fact that the first term in Eq. (10) vanishes for high rotation rates.

Work was begun on the development of improved second-order closure models. In all of the currently popular second-order closure models it is assumed that the deviatoric part of the velocity pressure-gradient correlation $_D\Pi_{ij}$ and the deviatoric part of the dissipation rate corelation $_DD_{ij}$ are functions of τ_{ij}, S_{ij}, and Ω_{ij}. Hence, we considered the most general model of the form

$$_D\Pi_{kl} + _DD_{kl} = f_{kl}(\tau_{ij}, S_{ij}, \Omega_{ij}) \tag{11}$$

Equation (8) should be subjected to the constraints:

(i) Form invariance under a change of coordinates (c.f., Smith 1971).

(ii) Material frame-indifference in the limit of two-dimensional turbulence (see Speziale 1981).

and the fact that $_D\Pi_{ij}$, and $_DD_{ij}$ are traceless. This led to the most general form,

$$
\begin{aligned}
_D\Pi_{kl} + _DD_{kl} =& \beta_1 \frac{\epsilon}{q^2}(\tau_{kl} - \frac{2}{3}k\delta_{kl}) + \beta_2 k S_{kl} + \beta_3 \frac{\epsilon}{q^4}(\tau_{km}\tau_{ml} - \frac{1}{3}\tau_{mn}\tau_{mn}\delta_{kl}) \\
&+ \beta_4 \frac{q^4}{\epsilon}(S_{km}S_{ml} - \frac{1}{3}S_{mn}S_{mn}\delta_{kl}) \\
&+ \beta_5(\tau_{km}S_{ml} + \tau_{lm}S_{mk} - \frac{2}{3}\tau_{mn}S_{mn}\delta_{kl}) \\
&+ \frac{\beta_6}{q^2}(\tau_{km}\tau_{mn}S_{nl} + \tau_{lm}\tau_{mn}S_{nk} - \frac{2}{3}\tau_{mn}\tau_{np}S_{pm}\delta_{kl}) \\
&+ \beta_7 \frac{q^2}{\epsilon}(\tau_{km}S_{mn}S_{nl} + \tau_{lm}S_{mn}S_{nk} - \frac{2}{3}\tau_{mn}S_{np}S_{pm}\delta_{kl}) \\
&+ \beta_8 \frac{1}{\epsilon}(\tau_{km}\tau_{mn}S_{nr}S_{rl} + \tau_{lm}\tau_{mn}S_{nr}S_{rk} - \frac{2}{3}\tau_{mn}\tau_{np}S_{pr}S_{rm}\delta_{kl}) \\
&+ 2(1 - \beta_9)(\tau_{km}\Omega_{lm} + \tau_{lm}\Omega_{km}) + \beta_9 \frac{1}{q^2}(\tau_{km}\tau_{mn}\Omega_{nl} + \tau_{lm}\tau_{mn}\Omega_{nk})
\end{aligned}
\tag{12}
$$

The coefficients β_i are functions of the invariants. This model is substantially simpler than previous attempts at general representations which contained several redundant terms (c.f., Reynolds 1987 for a summary of such previous representations). In the limit of a two component turbulence, Realizability (Shih 1987, private communication) requires that

$$
\begin{aligned}
\beta_1 =& 2 - \frac{1}{2k^2}\tau_{kl}\tau_{lk}\beta_3 \\
\beta_2 =& 0 \\
\beta_4 =& 0 \\
\beta_5 =& -(\frac{1}{k}\tau_{kl}\tau_{lm}S_{mk}\beta_6 + \frac{k}{\epsilon}\tau_{kl}S_{lm}S_{mk}\beta_7 + \frac{1}{\epsilon}\tau_{kl}\tau_{lm}S_{mn}S_{nk}\beta_8)/\tau_{pq}S_{pq}
\end{aligned}
\tag{13}
$$

and hence, in the first approximation this model has only five undetermined constants. This model will be investigated in the future in collaboration with Dr. T.-H. Shih. It is interesting to note that this model is consistent with the numerical results of this study which predict that an initially isotropic turbulence in a rotating frame decays isotropically.

REFERENCES

BARDINA, J., FERZIGER, J. H. & ROGALLO, R. S. 1985 Effect of rotation on isotropic turbulence: computation and modeling. *J. Fluid Mech.* **154**, 321 – 336.

LAUNDER, B. E., REECE, G. J. & RODI, W. 1975 Progress in the development of a Reynolds-stress turbulence closure. *J. Fluid Mech.* **68**, 537 – 566.

POPE, S. B. 1978 An explanation of the turbulent round jet / plane jet anomaly. *AIAA J.* **16**, 279 – 281.

REYNOLDS, W. C. 1987 Fundamentals of turbulence for turbulence modeling and simulation, Lecture Notes for Von Karman Institute, March 16-17.

SMITH, G. F. 1971 On isotropic functions of symmetric tensors, skew-symmetric tensors and vectors. *Int. J. Engng. Sci.* **9**, 899 – 916.

SPEZIALE, C. G. 1981 Some interesting properties of two-dimensional turbulence. *Phys. Fluids.* **24**, 1425 – 1427.

WIGELAND, R. A. & NAGIB, H. M. 1978 Grid-generated turbulence with and without rotation about the streamwise direction. *IIT Fluids and Heat Transfer Rep.* R78-1, Illinois Inst. of Tech., Chicago, Illinois.

Evaluation of a Theory for Pressure-Strain Rate

By J. WEINSTOCK[1], and K. SHARIFF[2]

A theoretical expression for the slow part (the non-linear fluctuation part) of the pressure-strain rate is compared with simulations of anisotropic homogeneous flows. The objective is to determine the quantitative accuracy of the theory and to test its prediction that the generalized Rotta coefficient, a non-dimensionalized ratio of slow term to the Reynolds stress anisotropy, varies with direction and can be negative. Comparisons are made between theoretical and simulation values of the slow term itself and of the generalized Rotta coefficients. The implications of the comparison for two-point closure theories and for Reynolds stress modeling are pointed out.

1. Introduction and background

The slow pressure-strain rate correlation Φ_{ij}^s is a key term that occurs in Reynolds stress modeling. Until recent years it was almost universally modeled according to Rotta's (1951) prescription as

$$\Phi_{ij}^s = -C\frac{\epsilon}{q^2} \; b_{ij}, \qquad \text{(empirical model)}$$

where $b_{ij} = <u_i' u_j'> -[1/3(q^2\delta_{ij})]$, u_i' is the fluctuating velocity along direction i, $q^2 = <u_i u_i>$ is twice the turbulent kinetic energy density, ϵ is the rate of turbulent kinetic energy dissipation, and C is an empirical constant referred to as Rotta's constant. However, Lumley (1978) has shown that C cannot be constant and more recently, it has been shown (Weinstock, 1981; 1982; 1985) that C is neither constant nor the same for different directional components ij. These variations occur because $\Phi_{ij}^{(s)}$ depends on more than one scale of the turbulence field, and, in addition, the scales vary with direction.

One way to account for the effect of all scales is for the slow term to be derived by a two-point closure theory. Such a derivation has been carried out (Weinstock, 1981; 1982; 1985), a principal result of which was that Φ_{ij}^s can be expressed as an integral over scalar energy spectra $E_{ij}(k)$. Standard closures such as the DIA (Kraichnan, 1959) and EDQNM (e.g., Cambon et al., 1981; Bertoglio, these proceedings) are much more ambitious, and correspondingly complex, since they determine the energy spectrum itself. Here, $E_{ij}(k)$ is taken from simulations. It is hoped that the relative simplicity will allow the present theory to be applied to a wider class of flows – including those with relatively large anisotropies after suitable modeling of

1 NOAA/ERL/Aeronomy Laboratory
2 NASA Ames Research Center

the scalar spectra. This is encouraged by a "universal" character found for the theoretical Φ_{ij}^s in which its dimensionless (Rotta) coefficients are very insensitive to the shape of the energy spectrum in the small k (energy producing) region, provided that the Reynolds number is not too small. We believe that such a universality is crucial for predictive modeling of flows.

The theoretical Φ_{ij}^s to be tested is given by

$$\Psi_{ij}^s = -C_{ij}\epsilon b_{ij}, \qquad \text{(No sum on } i \text{ and } j) \tag{1a}$$

$$C_{\alpha\alpha} = 1.08 \left(\frac{2\pi}{3}\right)^{\frac{1}{2}} \left(\frac{1}{\epsilon k_o^{1/3} q b_{\alpha\alpha}}\right) \int_0^\infty dk_1 \int_0^\infty dk_2$$

$$\times \ \frac{k_1^2 k_2^2 E(k_2)[E_{\alpha\alpha}(k_1) - \frac{1}{3}E(k_1)]}{\left(k_1^2 + k_2^2\right)^{4/3}} H(k_1, k_2), \tag{1b}$$

$$E(k) = \frac{1}{2} \ [E_{11}(k) + E_{22}(k) + E_{33}(k)],$$

$$H(k_1, k_2) \approx \left[2 - \frac{2.4k_2^2}{k_1^2 + k_2^2} - 0.08\left(\frac{4k_1 k_2}{k_1^2 + k_2^2} - 1\right) + \frac{2}{3}\left(1 - \frac{2k_1^2}{k_1^2 + k_2^2}\right)\right],$$

where the C_{ij} are dimensionless coefficients referred to as generalized Rotta coefficients, $E_{\alpha\alpha}(k)$ is the scalar spectrum for kinetic energy along direction α, $k_o = (3\beta)^{3/2}\epsilon/q^3$, and β is the Kolmogorov constant. The various numerical factors arise from angular integrations of spectra in wave space. The specific angular dependence of the spectra had to be modeled to make this possible. The off-diagonal elements C_{12}, C_{13}, C_{23} are given elsewhere (Weinstock, 1981) and have not been evaluated. A much simpler form of $C_{\alpha\alpha}$ for use in Reynolds stress modeling is obtained by use of the model spectrum $E_{\alpha\alpha} = \beta\epsilon_{\alpha\alpha}^{2/3}k^{-5/3}$ for $k_o \leq k \leq k_\nu$, and $E_{\alpha\alpha} = \beta\epsilon_{11}^{2/3}k^m k_o^{-m-5/3}$ for $k < k_o$, where k_ν is the viscous "cut-off" wavenumber. We refer to this $E_{\alpha\alpha}$ as the model spectrum.

Our primary goal is to test expression (1) by comparison with computer simulations. This test has also implications for standard two-point closures in general, since such closures have in common with our closure the neglect of a two-time fourth-order velocity cumulant.

Our article is outlined as follows: Straight forward comparisons are given in Sec. 2 where values of $\Phi_{\alpha\alpha}^s$ and $C_{\alpha\alpha} = -\Phi_{\alpha\alpha}^s/(\epsilon b_{\alpha\alpha})$ obtained directly from simulations are compared with (1b). Improvements and generalizations of the theory suggested by simulations are in Sec. 3, and Sec. 4 contains suggestions for further simulation tests.

2. Comparison between theory and simulation

The theory was compared with several simulations of homogeneous shear and straining flows. Typical examples are given in Figures 1 through 3 for two cases of homogeneous shear ($S = U_{1,2}$, simulation runs C128U and C128X of Rogers, Moin

FIGURE 1. Slow pressure strain components for homogeneous shear (moderate shear case C128U of Rogers, Moin & Reynolds, 1986). (a) Comparison of theory with simulation for the diagonal components. (b)-(d) Generalized Rotta coefficients as computed from the simulation data and using the simulation spectra in the theory.

and Reynolds 1986) and for plane strain (strain directions are 2 and 3, simulation run PXA of Lee and Reynolds 1985). For the shear cases the horizontal axis is the total shear, St. For the plane strain case the horizontal axis is the eddy turnover time. Figures 1 show the evolution of $\Phi^s_{\alpha\alpha}$ scaled on the initial dissipation rate, and $C_{\alpha\alpha}$ for run C128U, Figures 2 for run C128X and Figures 3 for plane strain run PXA. Each graph includes simulation and theoretical values.

(a)

●   **THEORY 11**
■   **THEORY 22**
▣   **THEORY 33**
——   **SIMULATION 11**
·········   **SIMULATION 22**
- - - -   **SIMULATION 33**

(b)-(d)

● **INTEGRATION OF SIMULATION SPECTRA**
△ **SIMULATION**

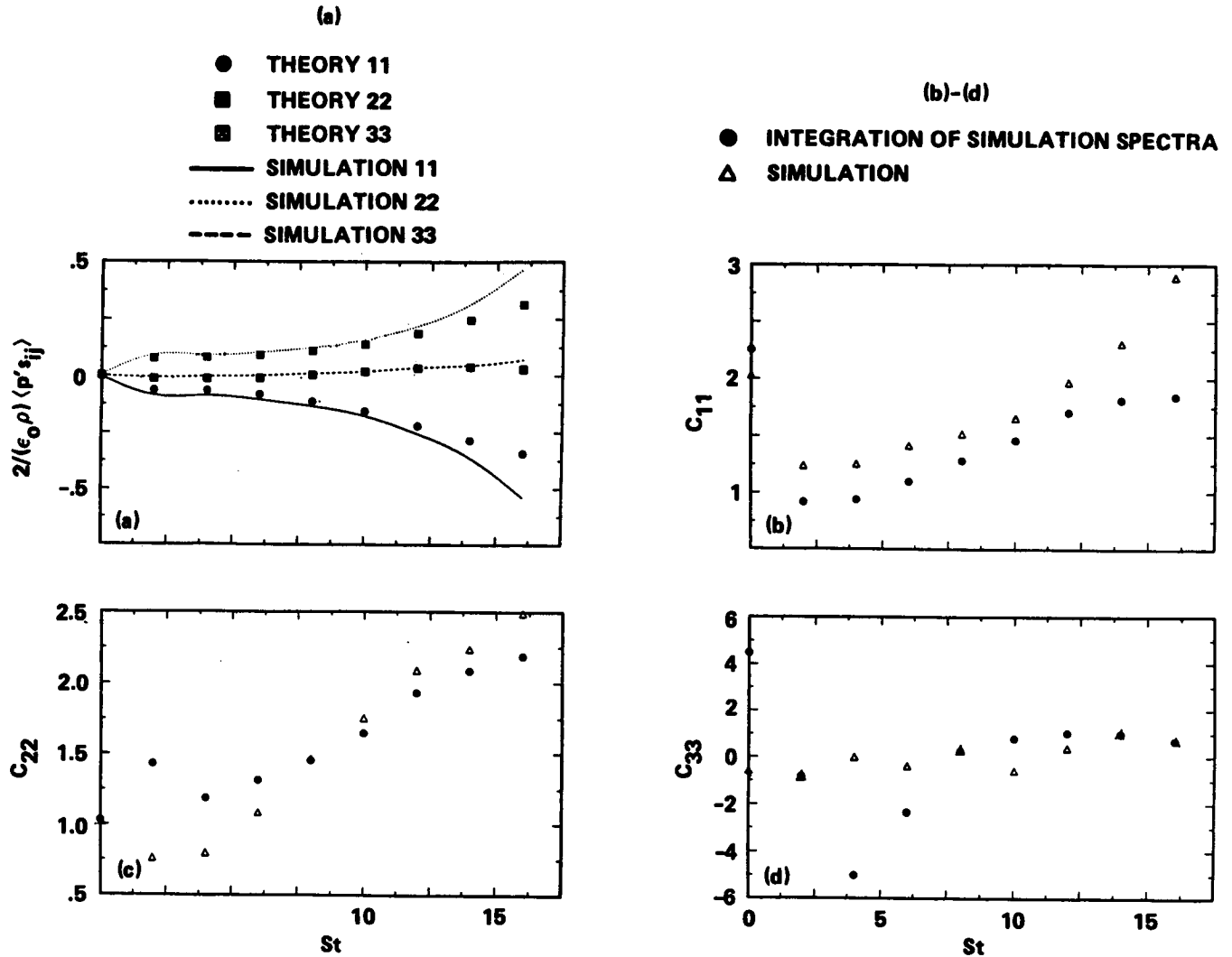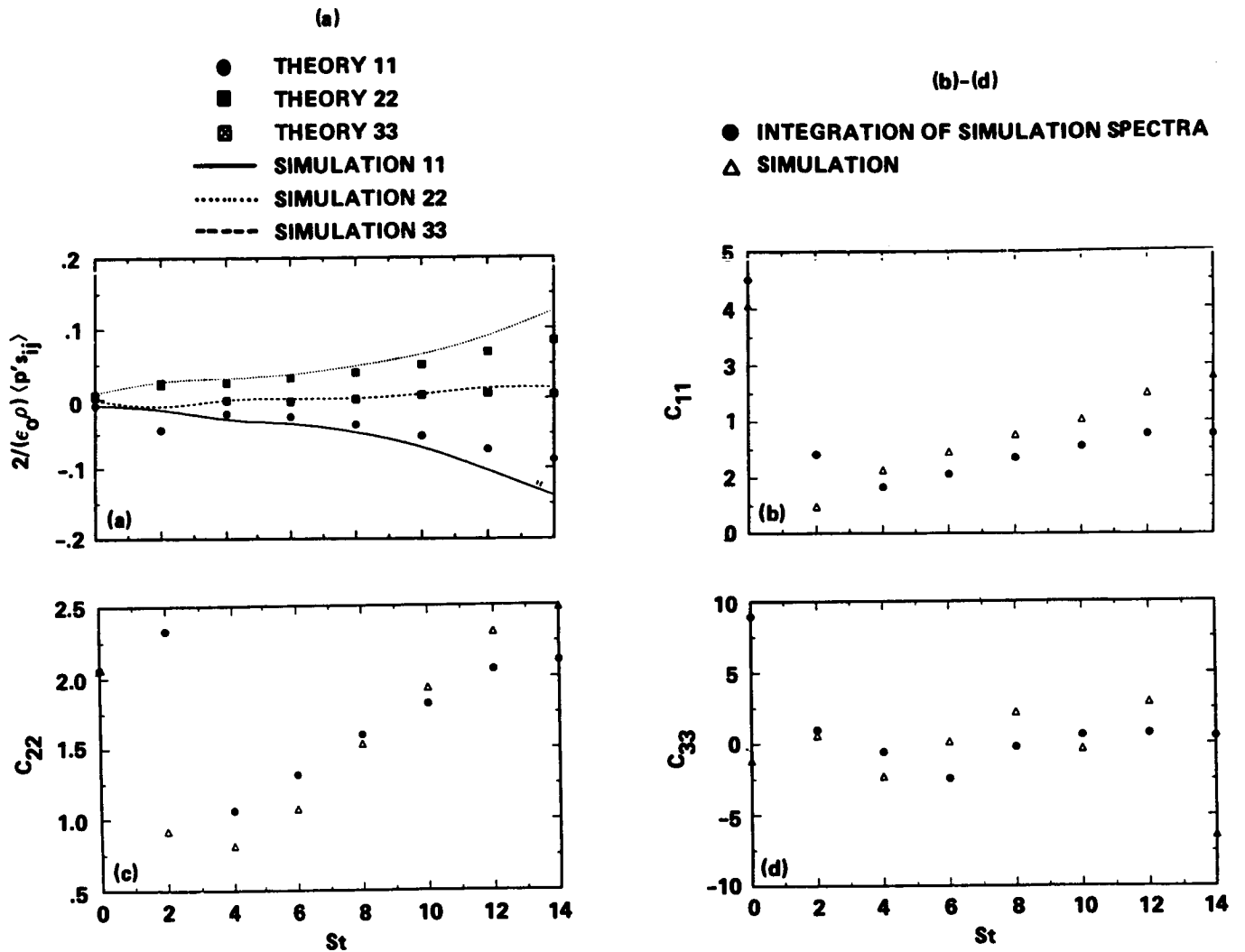
FIGURE 2. Slow pressure strain components for homogeneous shear (high shear case C128X of Rogers, Moin & Reynolds, 1986). a) Comparison of theory with simulation for the diagonal components. b)-d) Generalized Rotta coefficients as computed from the simulation data and using the simulation spectra in the theory.

(a) Dominant features of the (slow) pressure-strain rate

The simulation data show the following features:

- $C_{\alpha\alpha}$ varies between components.
- The normal components C_{11}, C_{22}, C_{33} each vary greatly during the simulations. For example, C_{11}, in plane strain run PXA, varies from -5 To +10 (in the unstrained direction). The Reynolds number defined as $q^4/(\nu\epsilon)$ varied between 39.1 nad 69. Another example is that C_{22} varies from 0.6 to 2.5 in homogeneous shear flow (C128U).
- C_{11} can be negative for many conditions. However, this does not imply that

(a)

● THEORY 11
■ THEORY 22
▣ THEORY 33
——— SIMULATION 11
········· SIMULATION 22
— — — SIMULATION 33

(b)-(d)

● INTEGRATION OF SIMULATION SPECTRA
△ SIMULATION

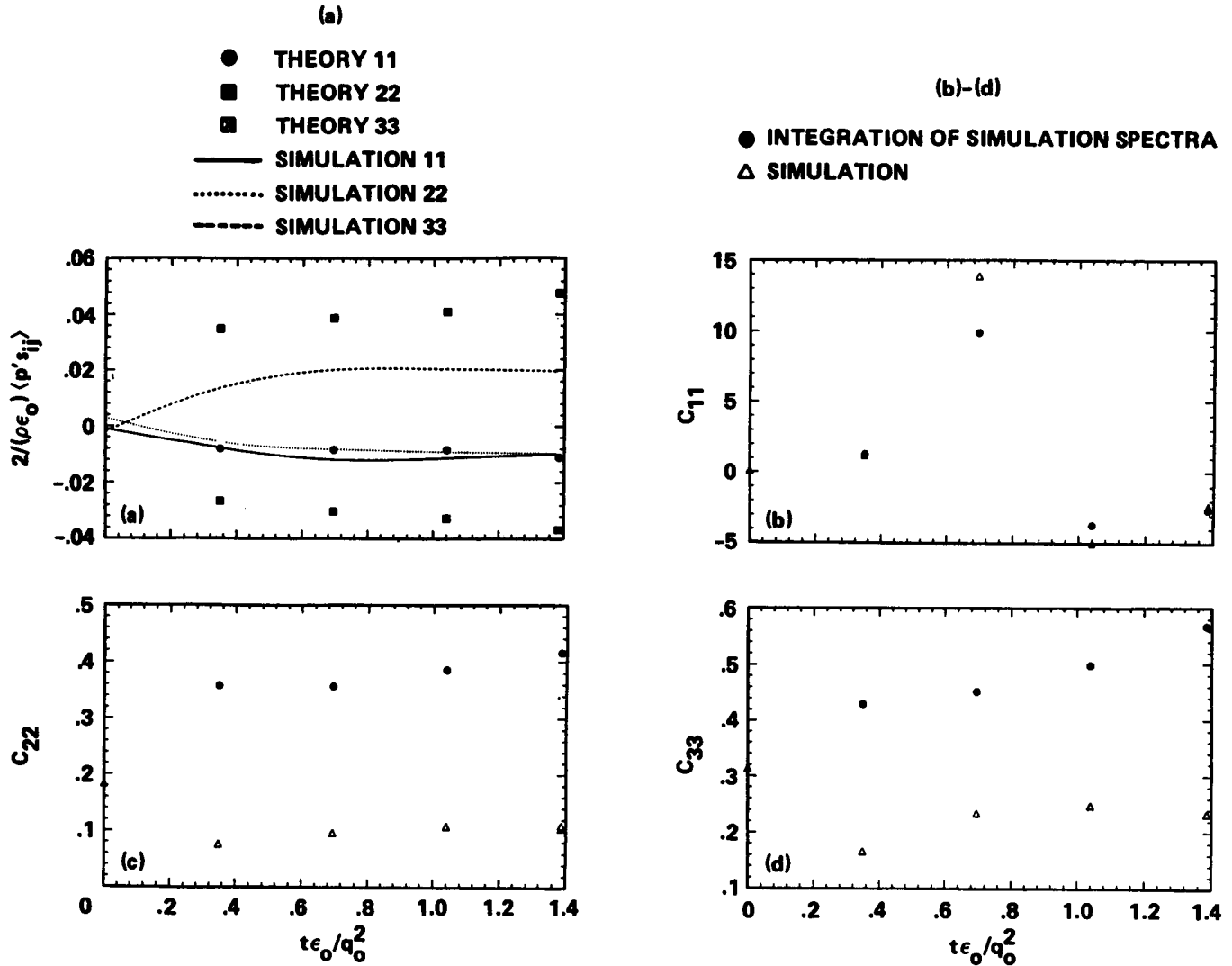FIGURE 3.   Slow pressure strain components for homogeneous plane strain (case PXA of Lee & Reynolds, 1985). a) Comparison of theory with simulation for the diagonal components. b)-d) Generalized Rotta coefficients as computed from the simulation data and using the simulation spectra in the theory.

the flow will not return to isotropy were the mean deformation to be removed at that instant. The Lumley return to isotropy tensor, of which the pressure strain rate is only a part, determines this.

Each of these qualitative features is predicted by the theory. There is good quantitative agreement of the pressure strain rate for the shear cases, discounting times larger than $St = 12$ where the "box" size has an important influence. The agreement is weaker for the case of plane strain. In the comparisons for the generalized Rotta coefficients $C_{\alpha\alpha}$, the theoretical $C_{\alpha\alpha}(\alpha = 1, 2, \text{or } 3)$ generally follows the trend of the simulations; being small whenever the simulation $C_{\alpha\alpha}$ is small and large when-

ever the $C_{\alpha\alpha}$ is large, and most notably, passing through zero at the same time that the simulation $C_{\alpha\alpha}$ (see Figure 3b) does.

During straining flows, the values of $C_{\alpha\alpha}$ in the strained directions, were always overpredicted by the theory. This discrepancy might be accounted for by the strong temporal variations of $b_{\alpha\alpha}$ which violates the present assumptions in the theory which limit it to slow variations of $b_{\alpha\alpha}$ and low mean strain-rate. Indeed, when estimates are made to account for time-scale variation of $b_{\alpha\alpha}$ by calculating the change in the Lagrangian time-scale that is used to derive (16), the discrepancies are reduced. However, for modeling purposes the original, unextended theory may be sufficient.

(b) Unexpected features of $\Phi_{\alpha\alpha}^s$

- Simulations show that $C_{\alpha\alpha}$ can be very small (much less than unity) in straining flows for a wide range of anisotropies. This smallness was unexpected, although it is contained in the theory. Small $C_{\alpha\alpha}$ implies that intercomponent energy transfer is a very weak process in straining flows.
- $C_{\alpha\alpha}'$ can vary significantly with strong temporal variations of kinetic energy.
- Surprising is the extent of difference between C_{11} and C_{33} in homogeneous shear flows (Figures 1b and 1d).

These features are also found in the theory with small quantitative discrepancies.

3. Improvement and generalization of the theory

(i) An intriguing proposition is to derive $\Phi_{ij}(\mathbf{x}) = < p^s(\mathbf{x}')S_{ij}(\mathbf{x}' + \mathbf{x}) >$, the two-point correlation of the slow pressure-strain, from the theory. This was suggested by Brasseur and obtained from simulations by Brasseur and Lee, Schiestel and Rogallo (these proceedings). This correlation provides a more severe and detailed test of closure theory than does $C_{\alpha\alpha}$. It also provides a direct link between spatial structures and Reynolds stress modeling. The theoretical $\Phi_{ij}(\mathbf{x})$ was worked out during the summer school, but was not compared with simulations at the time; for example, one component of $\Phi_{ij}^s(\mathbf{x})$ is

$$\Phi_{22}^s(x_1) = -\left(\frac{2\pi}{3}\right)^{\frac{1}{2}} \frac{1}{k_o^{1/3}q} \int_0^\infty dk \int_0^\infty dk_a \int d\theta \sin\theta \cos(kx_1 \cos\theta)$$

$$\times \frac{k^2 k_a^2 E(k_b) H}{(k^2 + k_a^2)^{4/3}} \left[\sin^2\theta E_{22}(k_a) - \frac{5}{2}\sin^2\theta \quad \cos^2\theta \quad E_{11}(k_a) - \frac{5}{8}\sin^4\theta \quad E_{33}(k_a)\right]$$

where

$$k_b^2 = (k^2 + k_a^2)\left[1 + \frac{4}{3}\frac{k^2 k_a^2}{(k^2 + k_a^2)^2}\right]$$

(ii) Extend the theory to include spatial and temporal variations.

(iii) Revise the model scalar spectra $E_{\alpha\alpha}(k)$ to account for small Reynolds number.

As pointed out by Bertoglio the theory does not account for deformation of wave vectors by the mean strain rate and should be modified accordingly.

(iv) Attempt to model the rapid pressure-strain rate, by a k-space closure.

(v) Compare the theoretical pressure-strain rate with a $k-$ space model of Schiestel (these proceedings).

4. Suggestions for future simulations

(a) Regarding the pressure-strain rate:

(i) Compare the theoretical two-point pressure-strain $< p^s(\mathbf{x}')S_{ij}(\mathbf{x}' + \mathbf{x}) >$ with simulation.

(ii) Generalize the theoretical $< p^s S_{ij} >$ to apply to channel flow, and then test with simulations.

(iii) Using simulations, calculate the two-time fourth-moment velocity cumulant. Determine the time scale for its decay. In particular, determine if this time scale is shorter than the time scale for decay of second-moment correlations. Such an ordering of time scales is basic for k-space closure theories in general, and also for the present theory.

(b) Regarding a theory for modeling inhomogeneous flows:

(i) Compare simulation values of $< u'_i u'_j u'_k >$, $< \theta u'_i u'_j >$, $< \theta^2 u' >$, $< u'_i u'_j \partial p/\partial x_k >$, $< \theta u'_i \partial p/\partial x_j >$ with the eddy-damped quasi-Gaussian approximation (EDQG) and with a recent theory. These quantities are basic to modeling weakly inhomogeneous and stratified flows.

(ii) Verify whether or not the cumulant of $< (\mathbf{u}' \cdot \nabla \mathbf{u}')_i u'_i u'_i >=< u'^2 > \nabla < u'^2_i >$. This was derived by a theory and, if true, contradicts the quasi-Gaussian assumption for inhomogeneous flows.

acknowledgment

REFERENCES

CAMBON, C., JAENDEL, D. & MATHIEU, J. 1981 . *J. Fluid Mech.* **104**, 247–262.

KRAICHNAN, R. 1959 . *J. Fluid Mech.* **5**, 497–543.

LEE, M. J. & REYNOLDS, W. C. 1985 Numerical experiments on the structure of homogeneous turbulence. *Report No. TF-24*. Mech. Engrg., Stanford Univ.

LUMLEY, J. L. 1978 . *Adv. Appl. Mech.* **18**, 123–176.

ROGERS, M. M., MOIN, P., & REYNOLDS, W. C. 1986 The structure and modeling of the hydrodynamic and passive scalar fields in homogeneous turbulent shear flow. *Report No. TF-25*. Mech. Engrg., Stanford Univ.

ROTTA, J. 1951 . *Z. Phys.* **129**, 547–572.

WEINSTOCK, J. 1981 . *J. Fluid Mech.* **105**, 369–396.

WEINSTOCK, J. 1982 . *J. Fluid Mech.* **116**, 1-29.

WEINSTOCK, J. 1985 . *J. Fluid Mech.* **154**, 429–447.

Relations Between Two-Point Correlations and Pressure Strain Terms

By MICHA WOLFSHTEIN [1] and SANJIVA K. LELE [2]

We study the structure of the two-point spatial correlations (velocity-velocity, velocity-scalar and scalar-scalar) with a view to improve turbulence closure models. The linear model for the two-point correlations proposed by Naot et al. provides a method of including the information about the turbulence structure in the turbulence models. We test the assumptions and adequacy of this model against the homogeneous shear flow simulation data base. The model performs poorly in some details and we suggest how it may be improved. We also test the models for rapid pressure-strain terms in a variety of flows including axisymmetric expansion and contraction flows, homogeneous shear flow, channel flow and boundary layer.

Introduction

Two-point correlations are often considered to include much information on the structure of turbulence, and on the modeling of various terms in the equations governing turbulent quantities such as the Reynolds stresses or the turbulent heat fluxes. In particular, the rapid pressure-velocity gradient terms in the Reynolds stress equations or pressure-temperature term in the heat flux equations, as well as the viscous decay terms of these equations may be exactly calculated if the corresponding two-point correlations are known with sufficient accuracy. It was therefore the purpose of the present project to study the two-point correlations, and to improve turbulence closure models for pressure terms by a better understanding of the two-point correlations.

The report is organized in three sections. The first section contains some general observations on two-point correlations; Section 2 contains the assessment of linear two-point correlation models, which is followed by our study of linear pressure-strain models in Section 3. Finally, some conclusions from the present work are presented.

1. Two-point correlations

Two-point correlations (velocity-velocity, velocity-scalar, scalar-scalar) were examined for homogeneous shear and channel flows. The primary focus was on the homogeneous shear case due to its simplicity. The numerical data base generated by Rogers et al. (1986) provided the "raw data." The C128 simulation series was studied in most detail. The simplest case is that of scalar-scalar correlation in a

---

1 Israel Inst. of Tech.

2 Center for Turbulence Research

homogeneous shear flow. The flow is in the x-direction, with a uniform velocity gradient in the y-direction. Uniform scalar gradients were applied in the x-, y-, and z-directions, further referred to as scalars A, B, and C, respectively. Details of the simulations may be found in Rogers et al. (1986). Contour plots of the scalar-scalar two-point correlations in the x-y plane at nondimensional time $St = 12$ are shown in Figs. 1a, b, and c for the three corresponding temperature gradients. All cases show an inclination of about $15°$-$20°$ with respect to the x-axis. This inclination appears to represent the influence of dU/dy (mean shear). At earlier nondimensional times the correlations show a steeper angle. This behavior is similar to that observed by Rogers et al. (1986) for vorticity correlations. Correlation contours in the y-z plane (not shown) are nearly elliptical, with the direction of the scalar gradient defining the major axis. The influence of mean shear is also clearly evident in the contours of the velocity-scalar correlations $\overline{uB}$ and $\overline{wC}$ when plotted in the x-y plane (not shown). The influence of the mean scalar gradient on the velocity-scalar correlations is better seen in the y-z plane. In Fig. 2 the correlations $\overline{vB}$ and $\overline{wC}$ are plotted in the y-z plane at nondimensional time $St = 12$. The correlations decrease more slowly in the direction of the applied scalar gradient, a feature also noted in the scalar-scalar correlations.

The contours of the velocity-velocity two-point correlations $\overline{uu}, \overline{vv}$ and $\overline{ww}$ in plane x-y are shown in Fig. 3. While the $\overline{uu}$ and $\overline{ww}$ show an inclination of about $22°$ the $\overline{vv}$ does not show this orientation. This suggests a strong influence of the mean velocity gradient dU/dy on the velocity-velocity two point correlations. It may be noted that the derivation of the linear pressure-strain models (as presented by Naot et al.) assumes no direct dependence of the two point correlations on the mean velocity gradients.

Finally, the channel flow results of the two-point correlations with separation vector in the y-direction show asymmetries not possible in the homogeneous shear case. The influence of the wall appears to be quite persistent and leads to asymmetries in the correlations. It may be noted that some of these features are well described by a model proposed by Hunt (details may be found in his report in the present volume).

The principal conclusion from this part of the study is that the two-point correlations (velocity-velocity, velocity-scalar, and scalar-scalar) show strong dependence not only on their single-point analogs but also on the mean velocity gradients and mean scalar gradient. Thus models which inadequately represent these dependencies may not be very successful.

2. Linear two-point correlation model

The two-point correlations may be represented by a model in which they are linearly related to the corresponding single-point correlations by arbitrary functions of r, the magnitude of the separation vector only. One such function is required for scalar-scalar correlation, two for scalar-velocity correlations, and six for velocity-velocity correlations (but three of these are related to the other three by continuity relations. Such models have been proposed by Naot et al. (1973) for the velocity-velocity correlations and by Miklavic and Wolfshtein (1987) for the velocity-scalar

and scalar-scalar correlations. We tried to fit the data for the homogeneous shear case to this model. Typical results for scalar-velocity correlation functions are shown in Fig. 4 for functions G and R.

The different curves correspond to different combinations of profiles of the two-point correlations (from simulations) used to obtain the model function. Considering function G, which contains the isotropic part of the correlation, most (but not all) profiles appear to give similar results for small separations, but not for large separations. The function R representing the non-isotropic part has small values for the small separations, and becomes important only for larger separations, and there it shows unacceptable scatter. Three velocity-velocity model functions (not shown) show a very similar behavior.

We did not have sufficient time to test the validity of the linear two-point correlation model in other flow fields. However, examination of the governing equations, as well as results on the rapid pressure-strain term (to be described in Section 3) suggest that the two-point correlation model may perform reasonably well for axially-symmetrical turbulence (in particular for compression).

The linear models tested here can be considerably improved by accounting for the dependence of the two-point correlations on the mean velocity gradients, and in addition on the mean scalar gradient for correlations involving the scalar fields. Our study suggests that both the irrotational and rotational components of the mean deformation rate should be included in such extensions. Detailed exploration of these possibilities was not conducted.

3. Linear pressure-strain model

We considered here the model of Naot, Shavit and Wolfshtein (1973, hereafter referred to as NSW) or that of Launder, Reece and Rodi (1975, hereafter referred to as LRR) (the two models are identical, although the derivation is quite different). In both models the rapid pressure-strain terms are related to the Reynolds stresses and velocity gradients by a single coefficient ϕ (for NSW) or C_2 (for LRR). The test here was to calculate the value of ϕ corresponding to different Reynolds stress components from the simulation data base for the rapid term in various flows.

In Figs. 5a and b, the calculated value of the NSW coefficient ϕ is plotted against total strain for the axisymmetric expansion and contraction flows, respectively. The data base used was from Lee et al. (1985) and the simulation details may be found there. The scatter is acceptable, but (at least in the compression) the value of ϕ changes with the strain (which corresponds to time in this case). This situation is typical for all the compression cases studied, but not to all expansion cases.

In the case of shear flows it was impossible to get a single value of ϕ (from different Reynolds stress components, indicated as the subscript on ϕ in the figures). The behavior of the homogeneous shear flow is very similar to the plane channel and boundary layer shown in Figs. 6a and b, respectively. The ϕ values obtained from different stress components differ a lot amongst each other but do not change much with the distance from the wall (in the log- layer). These results make the linear model unsuitable for shear flows. However, if we do not require tensorial symmetries

in the model, it is possible to use different values of ϕ for different components. In this case it may be possible to use such a linear model.

We tried to seek a correlation of the total pressure terms with the three model constants suggested by NSW. The coefficients β, γ, Λ were computed for the homogeneous shear case. This model appears to be a logical choice, as most coefficients do not change rapidly as a function of the nondimensional time St.

An even better result is obtained if we consider the combined total pressure velocity and viscous decay terms.

Conclusions

We now summarize our conclusions from the present work. Linear two-point correlation models appear to be imperfect even for simple turbulent flows. For shear flows it is necessary to relate the two-point correlations not only to the Reynolds stresses, but also to *all* mean velocity gradients and mean scalar gradients. Even so, it may be necessary to use nonlinear modeling to account for asymmetries.

The current linear models for the pressure-strain terms (in the models considered) can work only if different values of the coefficient ϕ are used for each direction, but then the evolution of ϕ and its spatial variation is a serious problem. Considerable improvement may be obtained if we consider the total pressure-strain terms. The models work even better when the total pressure-strain terms are combined with the viscous decay terms.

With everything said, we should bear in mind that all these conclusions are based on low Reynolds number turbulence. It is desirable to confirm these conclusions by comparison with Large Eddy Simulations at higher Reynolds numbers.

REFERENCES

LAUNDER, B. E., REECE, G. J., & RODI, W. 1975 Progress in the development of a Reynolds stress turbulence closure. *J. Fluid Mech.* **68**, 537-566.

LEE, M. J. & REYNOLDS, W. C. 1985 Numerical experiments on the structure of homogeneous turbulence. *Report No. TF-24*. Mech. Engrg, Stanford Univ.

MIKLAVIC, S. J. AND WOLFSHTEIN, M. 1987 A quasi-isotropic model of the two-point temperature-velocity correlation and its application of the modeling of the turbulent heat flux. *Proceedings of the Sixth Symposium on Turbulent Shear Flows*, Toulouse, France.

NAOT, D., SHAVIT, A. AND WOLFSHTEIN, M. 1973 Two-point correlation model and the redistribution of Reynolds stress. *Phys. of Fluids.* **16**, 738-743.

ROGERS, M. M., MOIN, P., & REYNOLDS, W. C. 1986 The structure and modeling of the hydrodynamic and passive scalar fields in homogeneous turbulent shear flow. *Report No. TF-25*, Mech. Engrg, Stanford Univ.

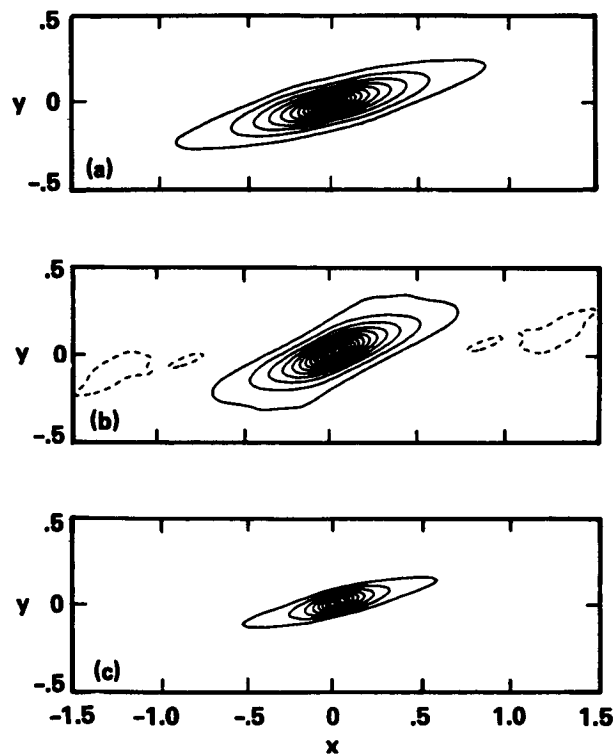FIGURE 1.   Iso-correlation contours of scalar-scalar two-point correlation in x-y plane at $St = 12$. a) Scalar gradient in x-direction (Scalar-A); b) Scalar gradient in y-direction (Scalar-B); c) Scalar gradient in z-direction (Scalar-C).
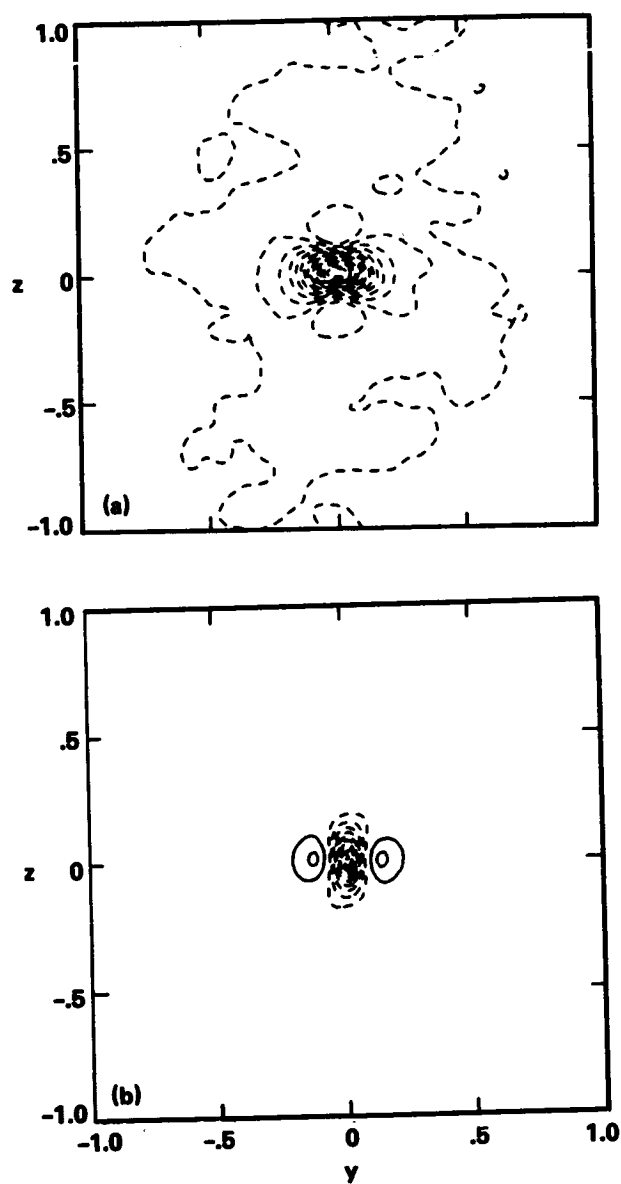
FIGURE 2.   Iso-correlation contours of velocity-scalar two-point correlation in y-z plane at $St = 12$. a) $\overline{vB}$ correlation; b) $\overline{wC}$ correlation.
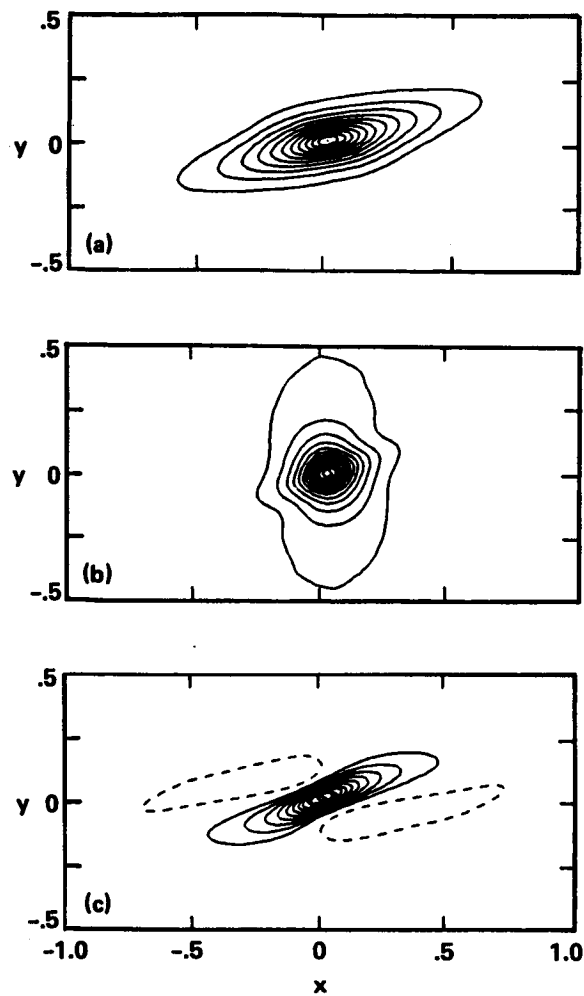
FIGURE 3. Iso-correlation contours of velocity-velocity two-point correlation in x-y plane at $St = 12$. a) $\overline{uu}$ correlation; b) $\overline{vv}$ correlation; c) $\overline{ww}$ correlation.
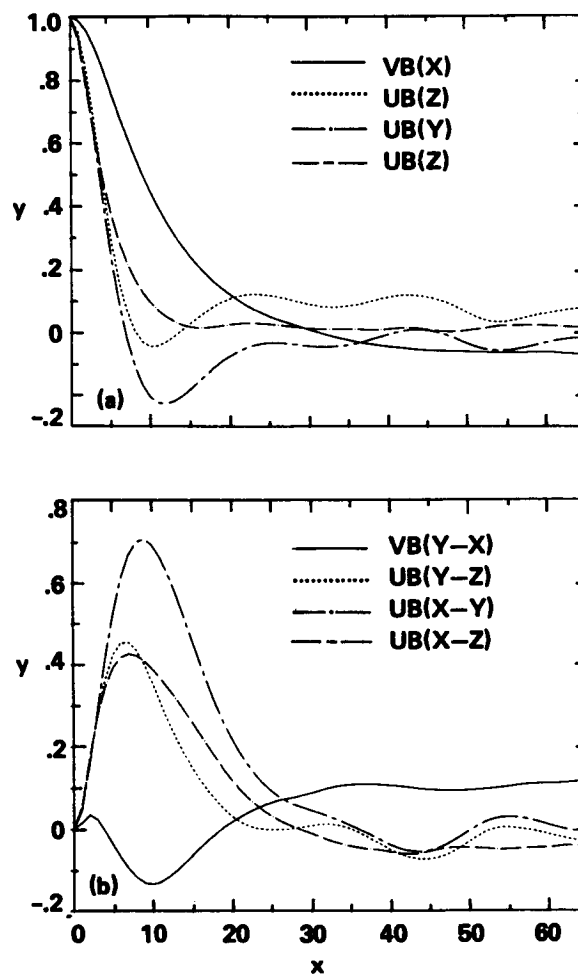
FIGURE 4.   Two-point scalar-velocity correlation model functions for uniform shear flow at $St = 12$. a) Different estimates of the model function G; b) Different estimates of the model function R.

FIGURE 5.   Values of the NSW coefficient ϕ in velocity-velocity two-point correlation model for axisymmetric turbulence. a) Expansion flow; b) Contraction flow.

FIGURE 6. Values of the NSW coefficient ϕ in velocity-velocity two-point correlation model. a) Channel flow; b) Boundary layer.

Overview of Research by the Turbulence Structure Group

Unlike the other groups, the people in the Turbulence Structure group were primarily experimentalists with the exception of Landahl. The Summer Program thus provided a 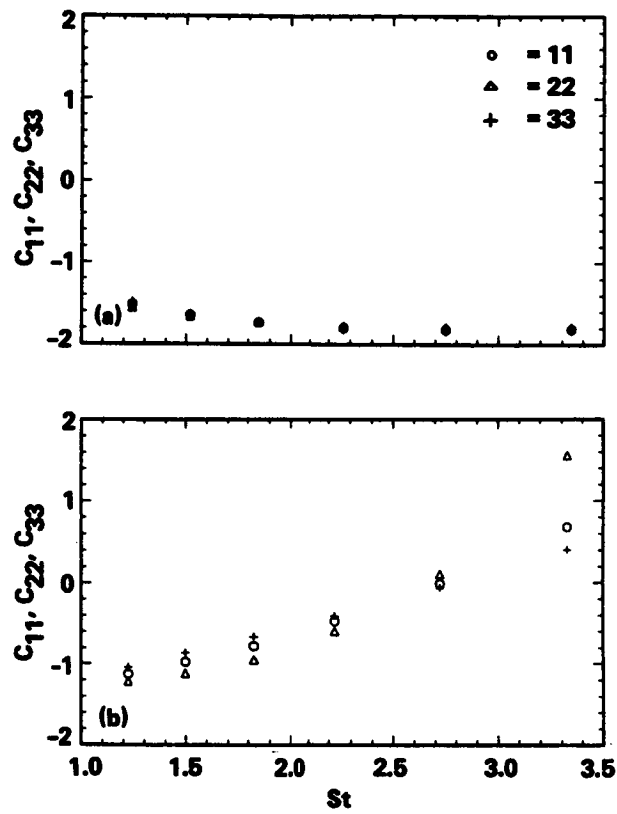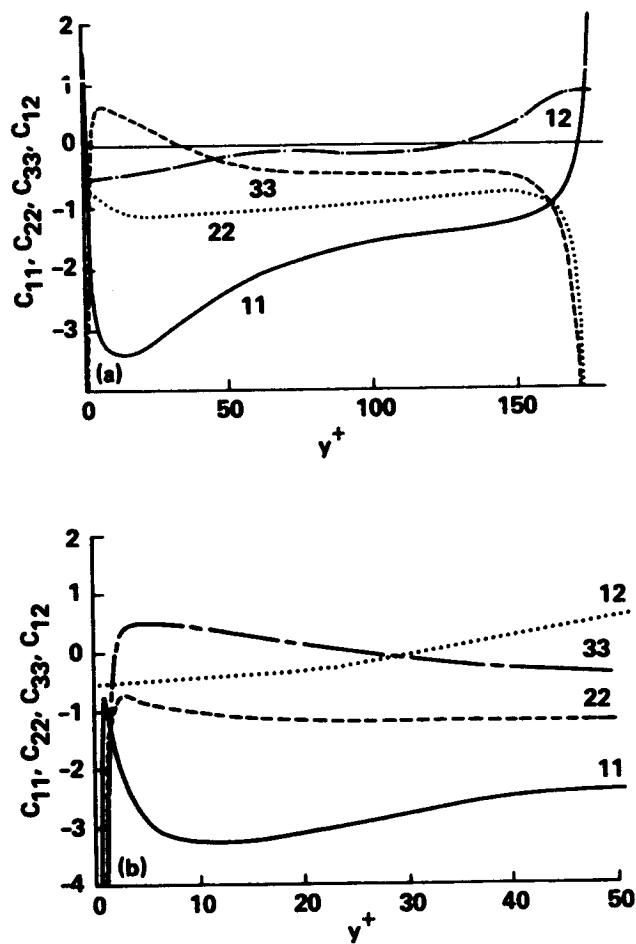unique opportunity for these experimentalists to assess the numerical data in comparison with their own experimental data, and to extend their previous work using full 3D turbulence fields. The Group expressed a particular interest in investigating temporal evolutions in addition to the spatial variations of the organized turbulence structures.

The invited participants were:
Dr. Henrik Alfredsson (K. T. H., Sweden)
Dr. Arne Johansson (K. T. H., Sweden)
Professor Ron Blackwelder (U. S. C.)
Dr. Jerry Swearingen (U. S. C.)
Professor Yann Guezennec (O. S. U.)
Mr. Dan Henningson (F. F. A., Sweden)
Professor Fazle Hussain (U. Houston)
Mr. Jinhee Jeong (U. Houston)
Professor Marten Landahl (M. I. T.)
Mr. Kenny Breuer (M. I. T.)

The local participants were:
J. Kim (NASA Ames)
P. Spalart (NASA Ames)
G. Coleman (Stanford University and NASA Ames)
U. Piomelli (Stanford University and NASA Ames)
S. Robinson (Stanford University and NASA Ames)

During the first two days of the Summer Program, the following items were identified as unifying themes for the group:

- Detect significant structures
- Compare with experimental results
- Observe space-time evolutions
- Implement improved averaging schemes
- Investigate flow instability

With these unifying themes in mind, the Group was divited into several teams and each team proceeded to investigate the organized structures in wall-bounded shear flows using the databases generated by Kim, Moin & Moser (channel) and

by Spalart (boundary layer). Data were prepared in time intervals short enough ($\Delta t^+ = 3$) to accomodate the study of the temporal evolution.

The most significant result from the Turbulence Structure Group as a whole concerned the temporal evolution of the organized structures in wall-bounded shear flows. Several different detection schemes, ranging from a simple visual method to rather sophisticated iteration procedures, were used to detect the organized structures. The resulting structures were slightly different from each other, since each scheme emphasized different aspects of the structures; however, these structures were also related to each other in many respects. For example, the internal shear layer investigated by Alfredsson and Johansson was generally observed between the structures associated with fourth- and second-quadrant events investigated by Guezennec (see Fig. 1). In all cases, the structures retained their coherence for much longer time than expected, and consequently, they could be tracked over a long streamwise extent. Typically, the organized structures persisted over a period on the order of $t^+ \approx 100$, and they could be tracked in space on the order of $x^+ \approx 1000$. The pictures emerging from these investigations suggest that the organized structures do not go through violent break-up processes, as perceived from previous studies, but rather diffuse slowly into incoherent motions. The spatial structure, however, was highly localized in space with small-scale motions within the structure. When such a structure passes a fixed probe in space, it can leave signatures that might look like a violent break-up process. To confirm this conjecture, it would be worthwhile in a future study to perform *in situ* comparison between the spatial distribution of a detected structure and the temporal signature at a fixed point when the structure passes by.

Brief summaries of each team effort are given in the following:

Johansson, Alfredsson and Kim studied the formation and evolution of shear-layer-like flow structures in the buffer region of wall-bounded turbulent shear flow that were associated with turbulence production. The structures were found to retain their coherence over streamwise distances on the order of 1000 viscous length units, and propagated with a constant velocity of about 10.5 u_τ throughout the near wall region. The shear-layer structures were found to be important contributors to the turbulence production: the conditionally averaged production at the center of the structure was almost twice as large as the long-time mean value. Individual shear layers often showed a strong spanwise asymmetry which was lost in conventional conditional averaging procedures.

Breuer, Landahl and Spalart performed numerical simulations, in which structures similar to those described by Alfredsson and Johansson were used as initial velocity fields, surrounded by a laminar boundary layer. The objective of this study was to investigate the dynamics of such structures in isolation, which made them easier to detect and follow in time. It was found that the structure associated with a fourth-quadrant event upstream of a second-quadrant event grew much more rapidly than that associated with a second-quadrant event upstream
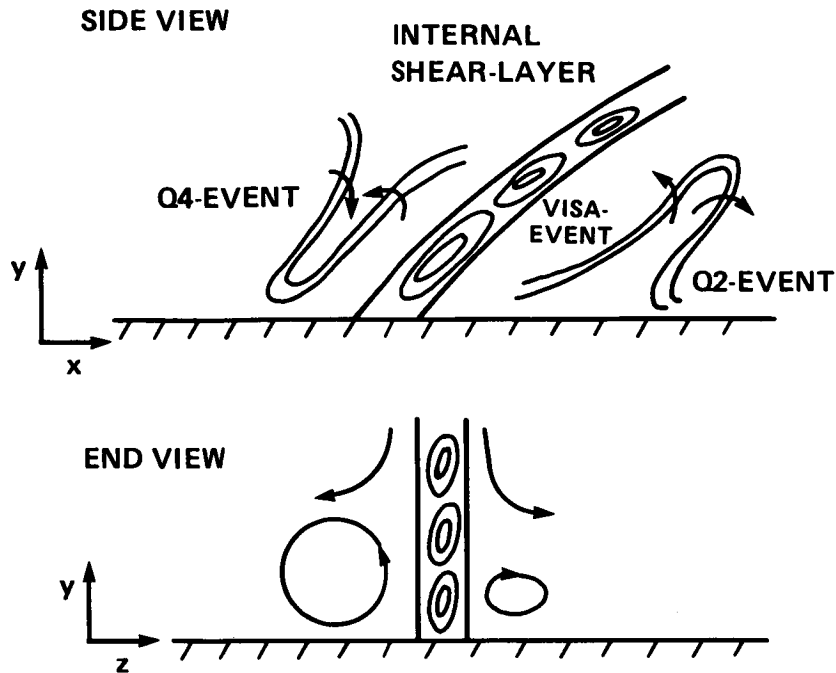
FIGURE 1. Coordinator's view on the organized structures in the wall-bounded shear flow.

of a fourth-quadrant event. This is consistent with the fact that one finds more energetic events of the former type than of the latter in turbulent flows.

Guezennec, Piomelli and Kim implemented several ensemble-averaging techniques (VITA, quadrant technique, techniques based on wall shear, etc) to determine organized structures in the wall-bounded flows. The results were in good agreement with his experimental results. It was found that the size of the detected structures in wall units was a function Reynolds number, and approximately scaled with the boundary layer thickness. Since detected instantaneous structures responsible for turbulence producing events were mostly asymetric, the ensemble-averaging process was improved by taking the asymmetry of the turbulence structures into consideration. The resulting structures were strongly asymmetric, suggesting that conventional ensemble-averaging schemes are misleading in that respect. It was also observed that these structures were persistent over a time on the order of 50 viscous time units.

Hussain, Jeong and Kim applied a conditional sampling technique designed to detect coherent vorticity through an iteration procedure to the above mentioned databases, as well as to a homogeneous shear flow field, to educe coherent structures from each flow. Many characteristics of the detected structures were quite similar to those of the mixing layer observed experimentally by Hussain and his colleagues: the topology consisted of saddles and centers, the saddle region being the location of maximum incoherent Reynolds shear stress and maximum shear production. The

effect of shear on the coherent structure was also investigated by comparing the structure obtained in the wall region (high shear) with that obtained in the outer layer (low shear).

Hussain (in collaboration with Kim and Spalart) also studied the propagation speeds of the velocity, pressure and vorticity by examining cross-correlations between two fields at different times. It was found that the propagation speeds for velocity and vorticity were almost the same throughout the channel and boundary layer. The propagation speeds were constant ($0.55\ U_c$) in the wall region ($y^+ < 15$) and slightly less than the local mean outside this region. The value $0.55\ U_c$ is very close to the value obtained visually by Alfredsson and Johansson. The propagation speed for the pressure was also constant in the wall region but much higher than the others ($0.75\ U_c$), whereas in the outer layer it was almost the same as the others.

Hussain (in collaboration with Kim and Coleman) investigated the Taylor hypothesis of frozen turbulence by directly evaluating the terms involved. Three different propagation speeds — mean velocity, local velocity and filtered local velocity — were used for the evaluation. It was found that the hypothesis was surprisingly good except very close to the wall region. It was also found that the departure from the hypothesis was not directly associated with large-scale structures. It should be an worthwhile effort to pursue further to examine which neglected terms contribute most to the departure from the hypothesis in the wall region.

Swearingen, Blackwelder and Spalart investigated flow instabilities associated with shear layers by examining the structure of the normal shear layer ($\partial u/\partial y$) and the spanwise shear layer ($\partial u/\partial z$). They found that a strong shear and an inflectional velocity profile existed surrounding the low speed region, and more importantly, they persisted up to $60\ \nu/u_\tau^2$ indicating sufficient time for an instability to develop. The low-speed streaks developed an oscillatory motion which increased in time (also indicative of instability) and eventually the undulating portion of the streaks appeared to break up into chaotic motion.

Landahl, Kim and Spalart examined the basic hypothesis of his "active-layer" model for wall-bounded turbulence. The model assumes that the non-linear (fluctuation-fluctuation) terms are large only in a thin layer near the wall, and hence, the turbulence in the region outside the active inner layer can be modeled as a linear response driven by the active layer. Preliminary investigation indicated that the non-linear effects were indeed strongest near the wall with a maximum around $y^+ = 20$ and, outside the near-wall region, they involved primarily the cascading mechanism to dissipative scales of motion. This model may lead to a reasonably simple procedure for determining the Reynolds stresses and other statistical quantities through a comparatively simple linear calculation making use of a universal model for the non-linear processes in the near-wall region.

Henningson, Landahl and Kim used a kinematic wave theory to investigate the cause of the rapid growth of waves observed at the wingtip of a turbulent spot in plane Poiseuille flow. It was found that the qualitative behavior of the

wave motions was well described by Landahl's breakdown criterion: that is, using the breakdown criterion together with the requirement of exponential growth, the qualitative behavior of normal group velocity was able to select a wave number, wave angle and phase velocity comparable to those observed in the simulation.

J. Kim

Shear-layer structures in near-wall turbulence

By A. V. Johansson[1], P. H. Alfredsson[1], and J. Kim[2]

The structure of internal shear layer observed in the near-wall region of turbulent flows is investigated by analyzing flow fields obtained from numerical simulations of channel and boundary-layer flows. It is found that the shear layer is an important contributor to the turbulence production. The conditionally averaged production at the center of the structure was almost twice as large as the long-time mean value. The shear-layer structure is also found to retain its coherence over streamwise distances on the order of a thousand viscous length units, and propagates with a constant velocity of about 10.6 u_τ throughout the near wall region.

1. Introduction

The formation and evolution of shear-layer-like structures in the near-wall region of turbulent flows have been recognized to be intimately coupled to turbulence production. Most of the information on these structures has been obtained from flow visualizations, although probe measurements have provided a limited quantitative information. Computer-generated data bases, obtained from numerical simulation of turbulent flows which contain velocities and pressure fields in three-dimensional space and time, make it possible to study these structures in more detail, especially regarding their space-time evolution.

The main body of the results presented here has been obtained from simulation data for turbulent channel flow at a Reynolds number of 180 (based on half-channel height and the friction velocity) with a grid of 128 × 129 × 128 points. The grid spacing in terms of viscous units was 17.7 in the streamwise and 5.9 in the spanwise direction.*

Very strong and dynamically important (for the process of turbulence production) shear-layers have been shown to exist in the buffer region of near-wall turbulent flows, and are related to the lift-up of low-speed streaks from the viscous sublayer. A characteristic feature of these shear layers is, by definition, a high value of the instantaneous velocity gradient $\partial u/\partial y$, but since these structures become highly inclined due to the mean shear, the streamwise velocity gradient ($\partial u/\partial x$) across the shear-layer also becomes large. In experimental investigations, a fixed observer

---

1 Department of Mechanics, The Royal Institute of Technology, S-10044 Stockholm, Sweden.

2 NASA-Ames Research Center.

* x, y, and z denote the streamwise, normal, and spanwise coordinates normalized by the viscous length scale. Similarly, u, v, and w denote the corresponding fluctuating parts of the velocity normalized by the friction velocity u_τ. Also, other quantities are normalized by viscous scales unless stated otherwise explicitly.

will see a high value of the temporal derivative of the streamwise velocity and a large change in u as the shear-layer passes by. This feature is utilized in the so-called VITA (variable interval time averaging) technique which has been used in various experimental investigations (see, Blackwelder & Kaplan, 1976, and Johansson & Alfredsson, 1982, for example) to detect shear-layer structures in boundary layers and channel flows. With this detection scheme, an event is considered to occur when the variance of u averaged over a "short" time T exceeds a chosen threshold level, k, times the long-time- averaged variance (i.e., u_{rms}^2). The detection position is normally chosen in the buffer region. In the analysis of computer-generated data bases, a spatial counterpart, VISA, is used, where the averaging length will be denoted as L (see Kim, 1985). In the present study, this method was extended by an event-centering technique (see Section 2).

Results for the channel-flow case will be presented in Section 2 concerning the three-dimensional spatial structure of the internal shear layer as well as their propagation characteristics and their development in time. These results will be compared with previously published data obtained from the Göttingen oil channel (Johansson, Alfredsson & Eckelmann, 1987) for a comparable Reynolds number. Comparisons concerning frequency of occurrence of shear-layer structures will also be made with hitherto unpublished oil-channel data by Johansson, Alfredsson & Eckelmann. In Section 3, some results from turbulent boundary-layer flow at two different Reynolds numbers will also be presented. A short summary and conclusions are given in Section 4.

2. Channel-flow results

The first step in the detection of shear-layer structures in the buffer region was to compute the locally averaged variance (or VISA-variance) for various xz-planes. For the following channel-flow results, the detection was applied at $y = 15$ with a threshold level (k) of 1.0. The resulting regions of high variance, indicating the existence of strong shear layers, give a spatially spotty picture (Fig. 1). In Fig. 1 the variance was averaged over 11 grid points in the x-direction, corresponding to about 200 viscous length units, and about 30 regions with levels above 1.0 can be observed. In the present approach, these regions were identified, i.e., their maxima were located and followed from their formation to their disappearance for a time sequence of 141 viscous time units (t_*). Each time step was separated by three viscous time units.

As examples, the space-time history of three high-variance islands marked by A, B, and C in Fig. 1 is shown in Fig. 2, where consecutive plots are separated by $12t_*$. Event C is here followed over more than $70t_*$, during which it has traveled approximately 900 viscous units, corresponding to 5 channel half-heights. However, the shear layer can be identified over considerably larger distances. The mean survival time of the shear layers, such as those indicated in Fig. 1, was approximately $50t_*$, but some strong shear layers could be followed throughout the entire extent of the time studied $(141t_*)$.

If the events in Fig. 1 and those detected at $y = 15$ near the opposite wall are divided into intervals of the maximum variance amplitude, the low amplitude will
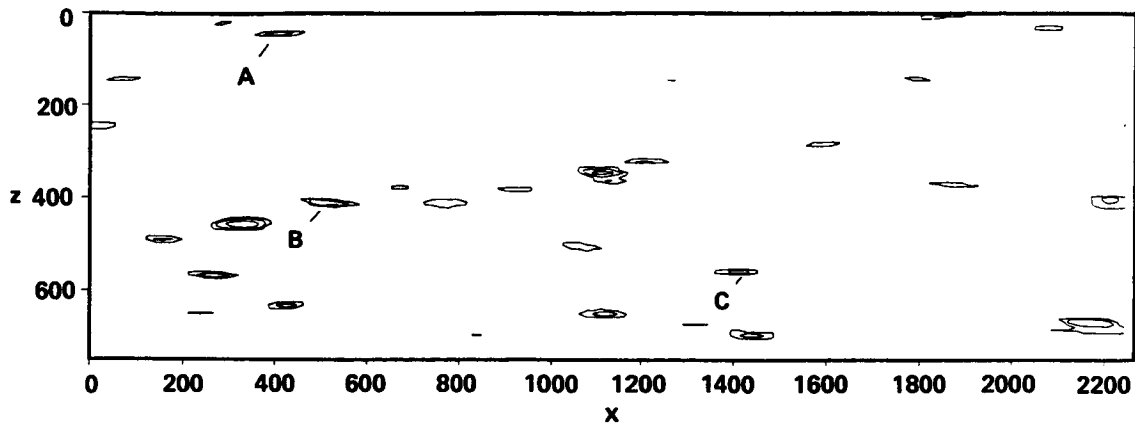
FIGURE 1. Contours of the streamwise velocity variance averaged over a distance of 200 viscous length units at $y=15$. Contours start at 1.0 with an increment of 0.5.
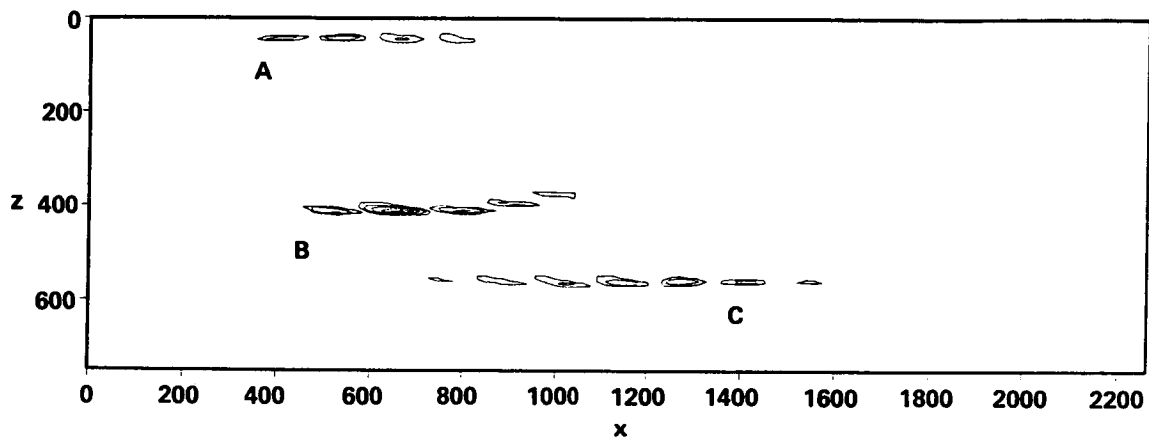

FIGURE 2. The space-time development of the variance associated with the events marked A, B and C in Fig. 1. Time separation between plots is 12 viscous time units.

dominate: i.e., at a given time there are many events (regions of high variance) with a maximum variance just above the threshold. This is illustrated by the open symbols in Fig. 3. On the other hand, if all these events are traced in time to locate the time at which the shear layer is strongest, i.e., the time for which the event has its largest variance amplitude, the picture becomes different (+ symbols in Fig. 3). The most probable variance maximum is now found in the interval 1.5 – 2.0, and values close to 3.5 were observed.

The propagation velocity of the shear layers could be determined (see Fig. 4) from their space-time history, and was found to be 10.6 with a standard deviation of ±1.0. This is substantially lower than the value 13.0 obtained from an experimental investigation (Johansson, Alfredsson & Eckelmann, 1987) at about the same Reynolds number (10 % higher). In that study, the VITA-detection was carried out
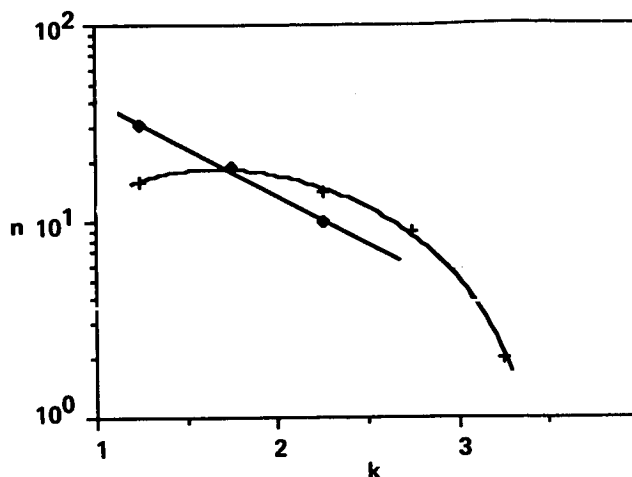
FIGURE 3.   Variance amplitude distribution of the events in Fig. 1 (also included are the events detected at the opposite side of the channel: ◇, the amplitude at the time of detection, +, the maximum amplitude of each event when followed over its life-cycle.

at $y = 15$, and a second probe was positioned at various y and x-positions downstream of the detector probe (e.g., at $y = 20$). However, the averaging time was $10t_*$, which would correspond to a shorter averaging length than that used in the present analysis of the numerical data. Also, there is an inherent difference between spatial and temporal data evaluation.

The significance of these flow structures for the flow dynamics in the near-wall region depends on their frequency of occurrence (or probability to occur within a given area). In order to enable comparisons with experimental results obtained with a stationary probe, the average number of detections per z-position was determined and normalized by the streamwise extent of the domain (2260) divided by the propagation velocity (10.6). This means that a shear layer, if signified by a region of high variance extending over several z-positions, gets counted several times, but gives the equivalent of the number of detections per unit time for a fixed probe. Also, the averaging length was converted to an equivalent averaging time by use of the propagation velocity. The agreement is excellent (see Fig. 5) between the present results obtained in this manner and the experimental results (unpublished results by Johansson, Alfredsson, & Eckelmann). One should bear in mind that the scaling used here is immaterial, since the Reynolds number is approximately the same for the two sets of data.

Johansson, Alfredsson & Eckelmann (1987) studied the spatial structure in the symmetry plane of the shear layers. Their results are shown in Fig. 6, where contour lines of the streamwise disturbance velocity normalized with the local rms-value are plotted in the xy-plane. These results may be compared with the corresponding results (Fig. 7a) obtained from the computer-generated data base for channel flow.
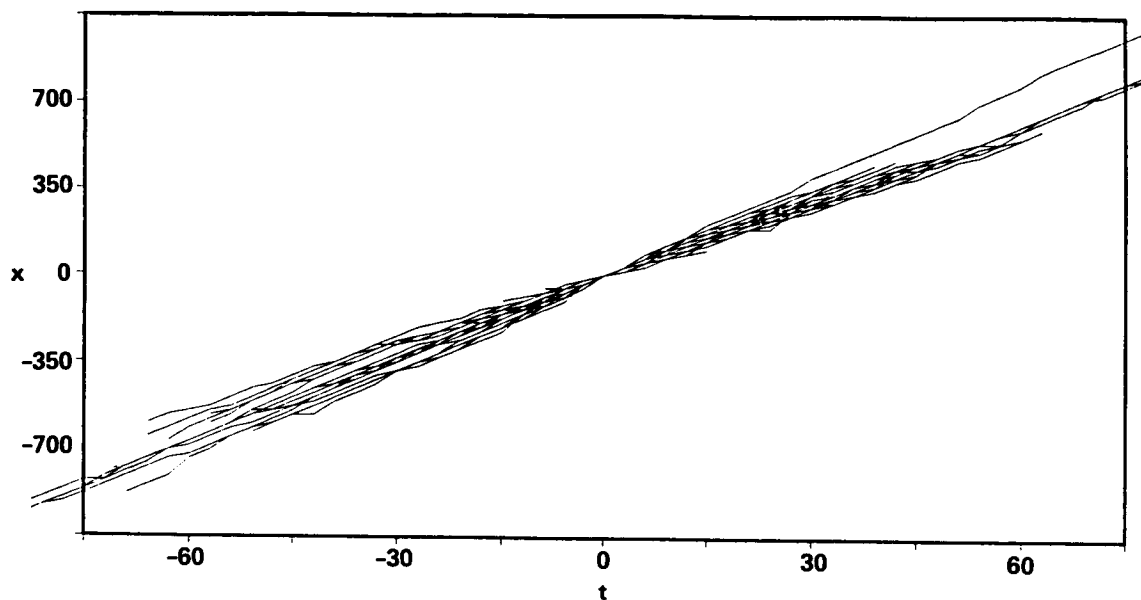
FIGURE 4. Streamwise position of the maximum variance as fuction of time for 60 diffrent events. The plot is centered around the maximum value of the variance for each event. The slope of these lines gives the propagation velocity of the shear layers.

Note that the same contour levels are used in Figs. 6 and 7a. An ensemble average of 60 events detected at both sides of the channel at one time-step are shown. The ensemble averaging here involves centering of the individual realizations in both the x (as in conventional conditional averaging) and the z-direction. Hence, boxes 600 long, 200 wide, and 180 high (the entire half-channel height) in viscous units centered around the point of maximum variance (at $y = 15$) are averaged. The agreement between the experimental and simulation data is seen to be good. In the following, conditional averages (denoted by $< >$) will be presented in absolute scale, i.e., normalized by u_τ (or other appropriate viscous scales).

Figs. 7b and c show the conditionally averaged u and v in the xy-plane. An interesting feature is that, close to the wall, the lifted low-speed fluid is pushed back towards the wall, resulting in a so-called wall-ward interaction. It is also quite evident that there is strong streamwise shear associated with the detected structure and that the regions of coherent velocity are confined below $y \approx 50$. The corresponding results in the xz-plane for $y = 15$ are shown in Fig. 8. The spanwise scale of the primary low- and high-speed regions is seen to be about 50, which is the same as the distance between high- and low-speed streaks in the viscous sublayer. The maximum deviation from the long-time mean in the low- speed region in Fig. 8a is almost twice as large as on the high-speed side of the shear layer. Similarly, the amplitude of the normal velocity is also much higher on the downstream side, which also gives a strong uv-peak in that region (Fig. 8c). The uv-contribution on the sweep side is practically negligible at this y-location.
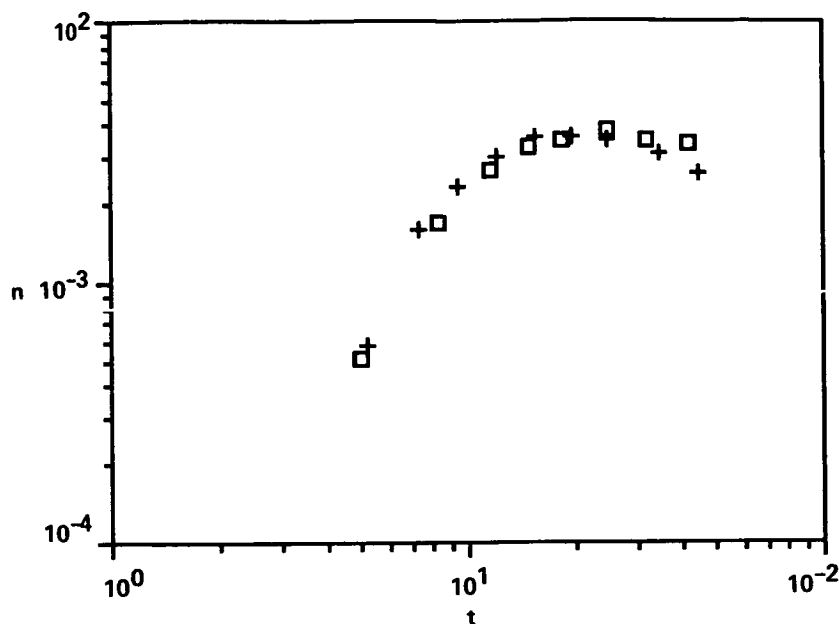
FIGURE 5. Number of events that would be detected per unit time by a stationary probe. Simulation (□) and measurements in the Göttingen oil channel (+) at about the same Reynolds number.

It was found that spanwise centering of the events is essential to obtain reasonable quantitative estimates of the associated Reynolds stress contributions, as is illustrated by Figs. 9a,b. In the latter, no such centering was applied, and the resulting maximum uv is drastically reduced on the ejection side. It should be noted that (to the present authors' knowledge) all previous results, experimental as well as numerical, presented in the literature have been obtained without spanwise centering. The reduction with no spanwise centering can be attributed to the resulting jitter in the spanwise separation between the uv-peak and the detector position, and the fact that the spanwise scale of the uv-peak is rather small.

In conventional conditional averaging procedures, with or without spanwise centering, symmetric patterns are the result of homogeneity of the flow in the spanwise direction. Instantaneous shear-layer structures, on the other hand, often tend to develop strong asymmetries as they propagate downstream. This can give large values of the spanwise gradient of the streamwise velocity at the center of the shear layer. The average of the (absolute) spanwise gradient at the detection point for the events shown in Figs. 7 and 8 was found to be about 0.20 of the mean gradient at the wall, or 2/3 of the local mean gradient. In reality, it is more likely to find an asymmetric structure than the symmetric pattern in Fig. 8a. In order to retain the spanwise asymmetry, often found in the individual events and also in the conditional average, an asymmetry was imposed by switching the z-coordinate according to the sign of the spanwise gradient at the detection point (Fig. 10). The resulting averages illustrate a mechanism for creation of high streamwise gradients
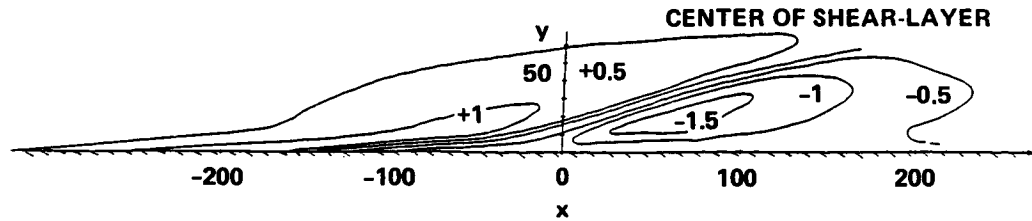
FIGURE 6. Conditionally averaged shear-layer structure in the near wall region in channel flow at Re=200 (Johansson, Alfredsson & Eckelmann, 1987) showing streamwise velocity disturbance ($< u > /u_{rms}(y)$) in the symmetry plane. Events detected by VITA with T^+=10 and k=1.
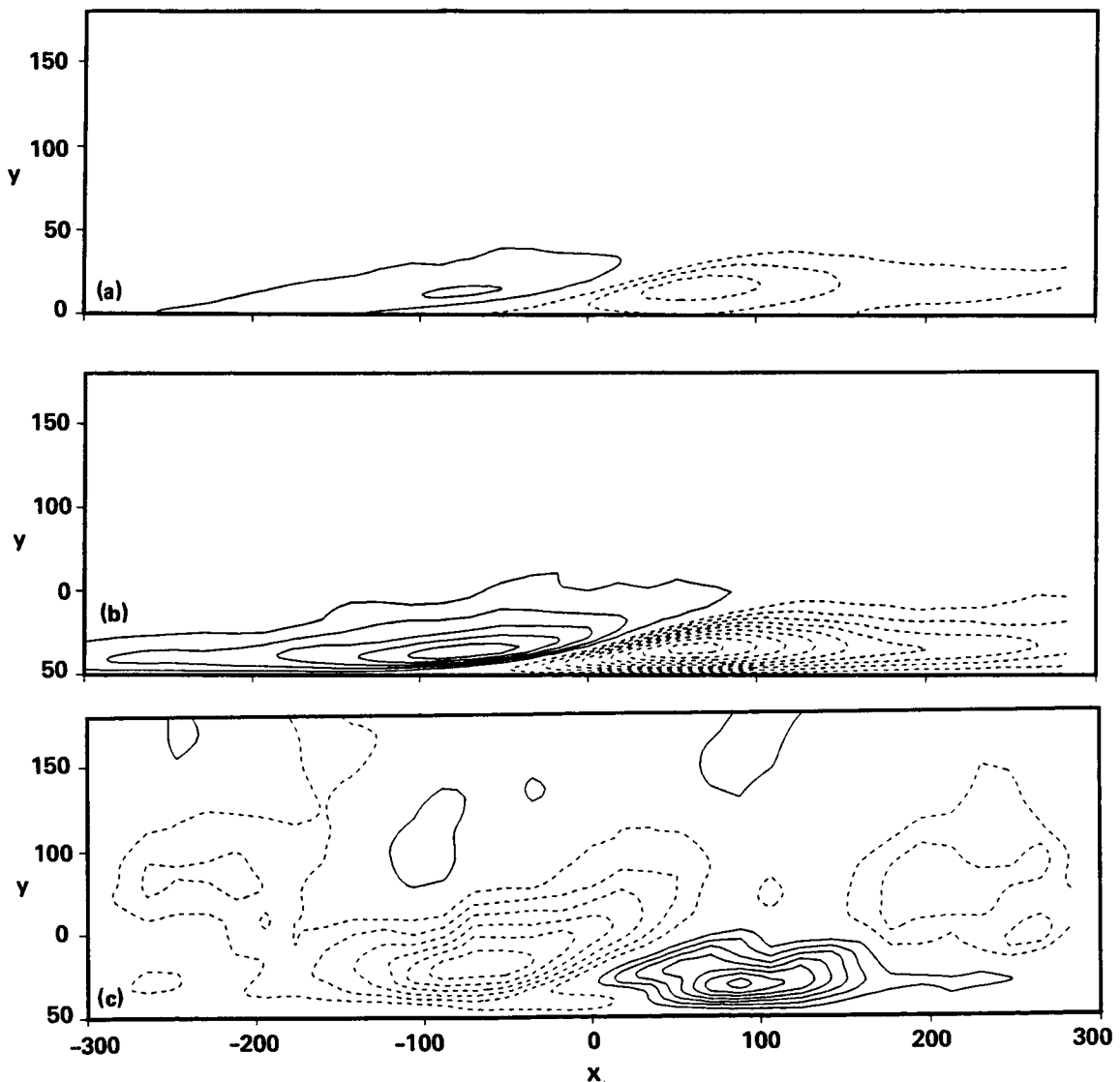
FIGURE 7. Ensemble averaged VISA-events detected with L=200 and k=1. Full drawn lines and broken lines denote positive and negative contours, respectively. (a) $< u > /u_{rms}(y)$, contour increment is 0.5. (b) $< u >$, contour increment is 0.5. (c) $< v >$, contour increment is 0.1.

FIGURE 8.   Contours in the (x, z)-plane at $y=15$ of the conditionally averaged shear layer structure. Detection parameters: $L=200$ and $k=1$ (same data as in Fig. 7). (a) $< u >$, contour increment is 0.5. (b) $< v >$, contour increment is 0.1. (c) $< uv >$, contour increment is 0.5.

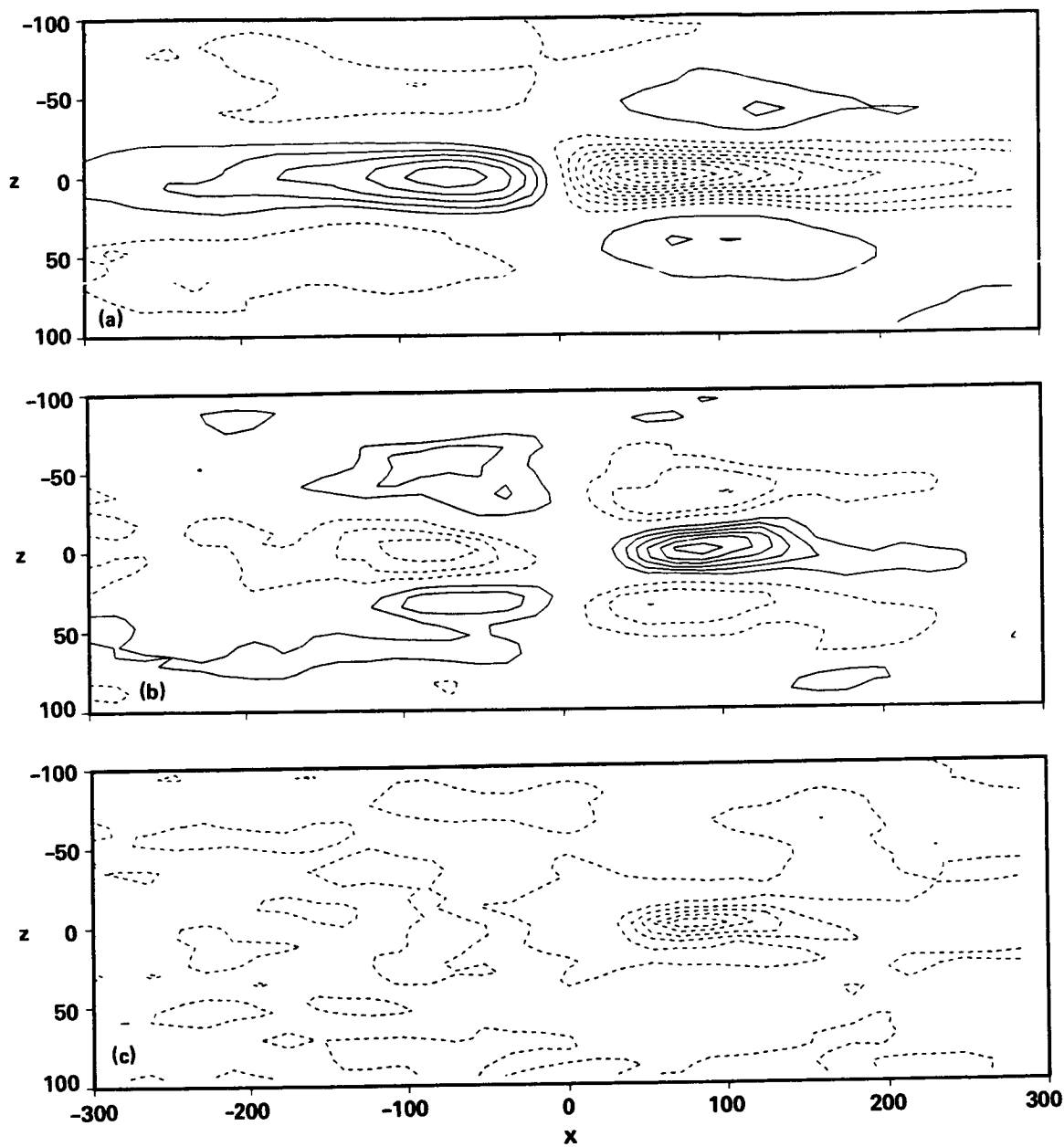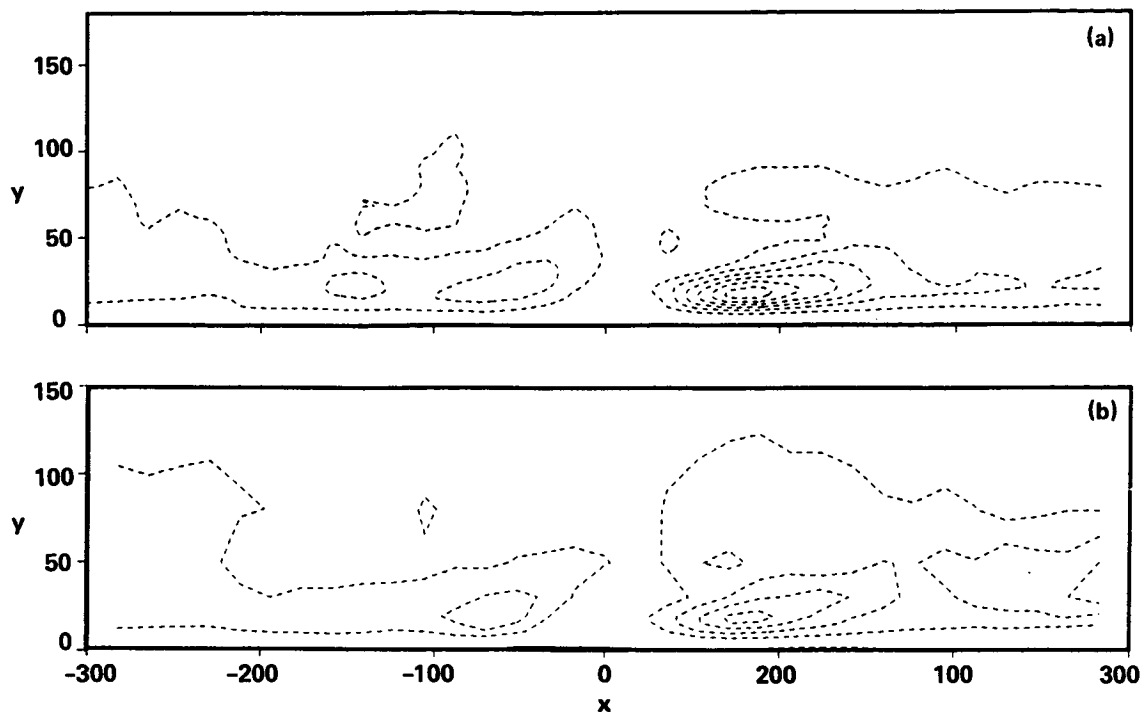FIGURE 9. Conditionally averaged uv ($L=200$, $k=1$, contour increment is 0.5). (a) with alignment in spanwise direction (b) without alignment.
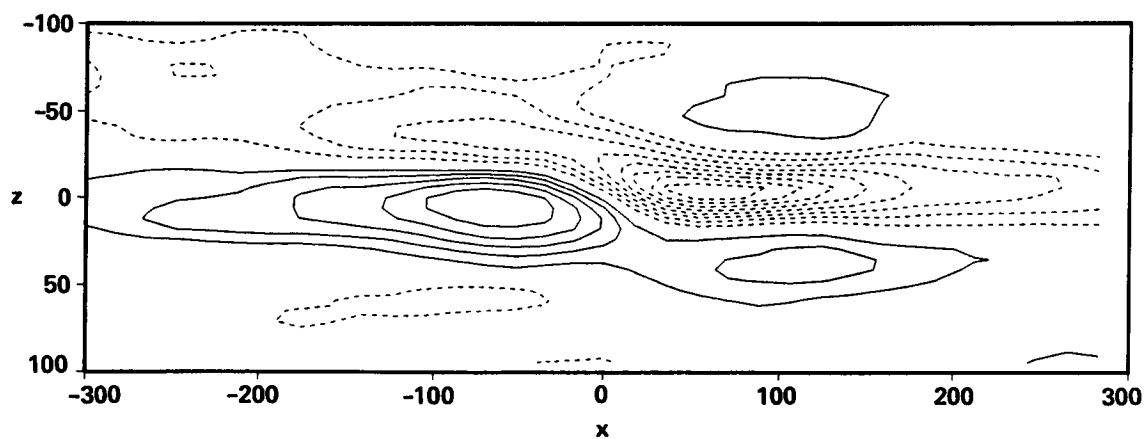
FIGURE 10. Conditionally average ($< u >$) detected with the VISA-criterion ($L=200$ and $k=1$) and the asymmetry condition (same data as in Fig. 8a). Data is at $y=15$ and contour increment is 0.5.

through spanwise motions of the high- and low-velocity regions. Such gradients play a relatively important role for the generation of conditionally averaged turbulence production (as will be discussed below).

The often occurring asymmetric features of the shear layers are illustrated by the space-time development of a single event in Fig. 11, where the frame of reference is chosen so that the center of the shear layer is stationary. The xy- plane view clearly shows the sharpening of the shear layer due to the action of the mean shear, whereas the planar view illustrates a meandering of the high- and low-speed regions, resulting in steep streamwise and spanwise gradients.

A key issue for the importance of coherent structures in turbulent flows is their role in the turbulence-production process. One can show that the conditionally averaged production of turbulent kinetic energy for a plane two-dimensional flow can be written as

$$
<P> = - <uv> \frac{dU}{dy} - \overline{u^2} < \frac{\partial u}{\partial x} > -\overline{uv}(< \frac{\partial u}{\partial y} > + < \frac{\partial v}{\partial x} >)
$$
$$
- \overline{v^2} < \frac{\partial v}{\partial y} > -\overline{w^2} < \frac{\partial w}{\partial z} > .
$$

(1)

The only term that remains in the long-time-averaged sense is $< uv > dU/dy$. However, the total conditionally averaged production (Fig. 12a) is substantially higher than what can be accounted for by this term (Fig. 12b). This is mainly due to strong gradients in the x- and y-directions of the conditionally averaged streamwise velocity (Fig. 12c). The largest of these terms is the second term in Eq. (1), which is illustrated in Fig. 13 where the production terms have been averaged over an area of 300×40 (streamwise and spanwise extent, respectively). Integrating the conditional production out to $y = 30$ gives an average over this volume which is almost twice as large as the long- time mean value. Moreover, the dissipation of turbulence energy is large in the vicinity of the shear layer (Fig. 14). It is noteworthy here that the conditionally averaged $\partial u/\partial z$ does not enter the left-hand-side expression of Eq. (1). Hence, although there exist high values of the spanwise gradient of u at the edges of the shear layers, they do not in themselves imply contributions to the associated turbulence production.

3. Boundary-layer results

Computer-generated data bases for a turbulent boundary-layer flow at two different Reynolds numbers were also analyzed. These data bases are described in detail in Spalart (1987). In order to investigate whether the size of the near-wall structures shows any significant Reynolds number variation, the ensemble-averaging procedure was carried out for momentum-thickness Reynolds numbers (Re_θ) of 670 and 1410 (Figs. 15a,b). One may note that the structure is somewhat larger in terms of viscous units for the higher Reynolds number, especially on the sweep side. This Reynolds number dependence indicates that there is some influence of the outer flow on the scale of inner-layer structures, and hence some interaction between the outer and inner regions of the flow. However, the influence is rather weak, and the structures are mainly determined by the conditions at the wall.
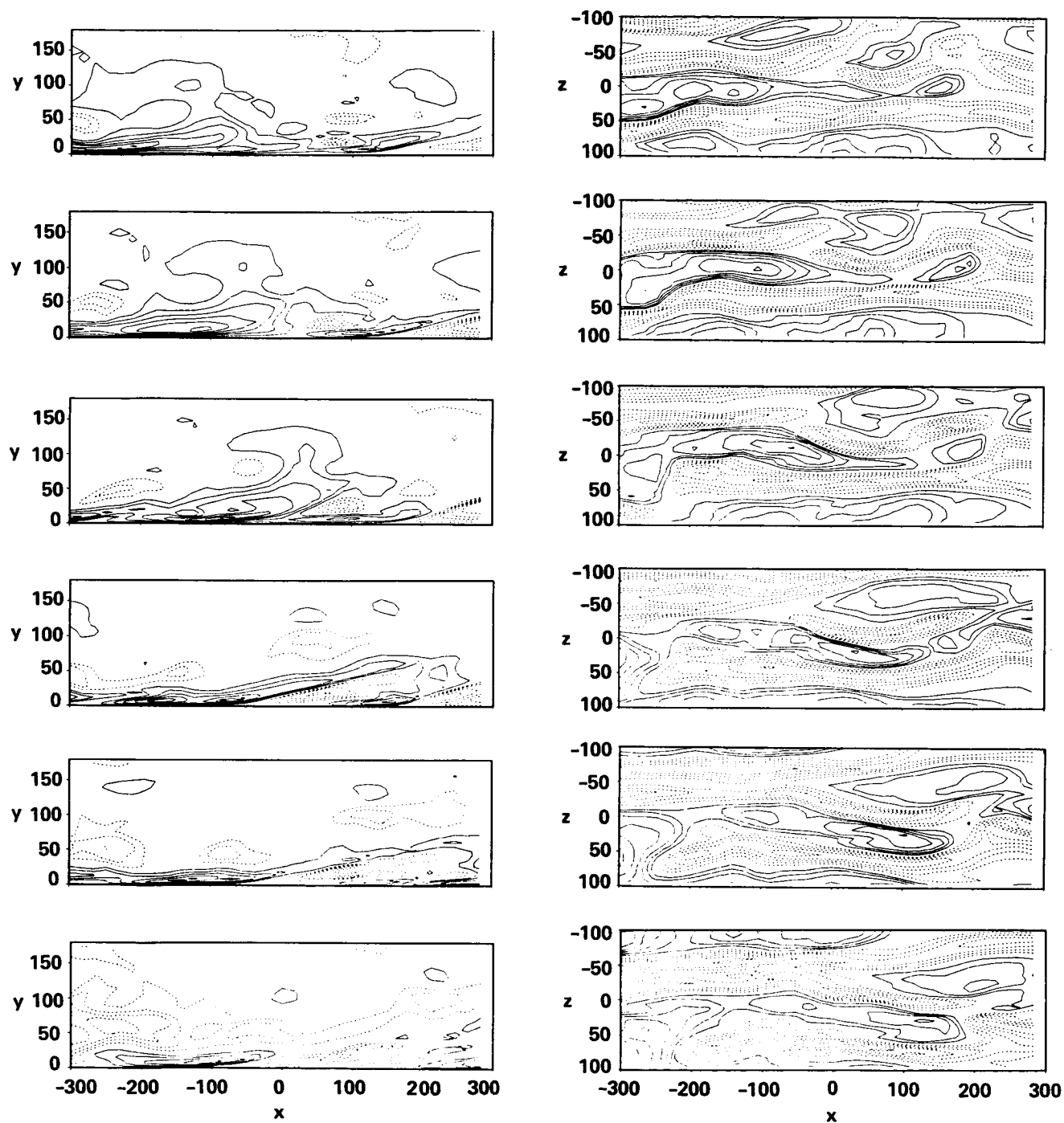
FIGURE 11. (x, y)- and (x, z)-plane of event B in Fig, 1 followed in time. Time increment between plots is 12 viscous units.
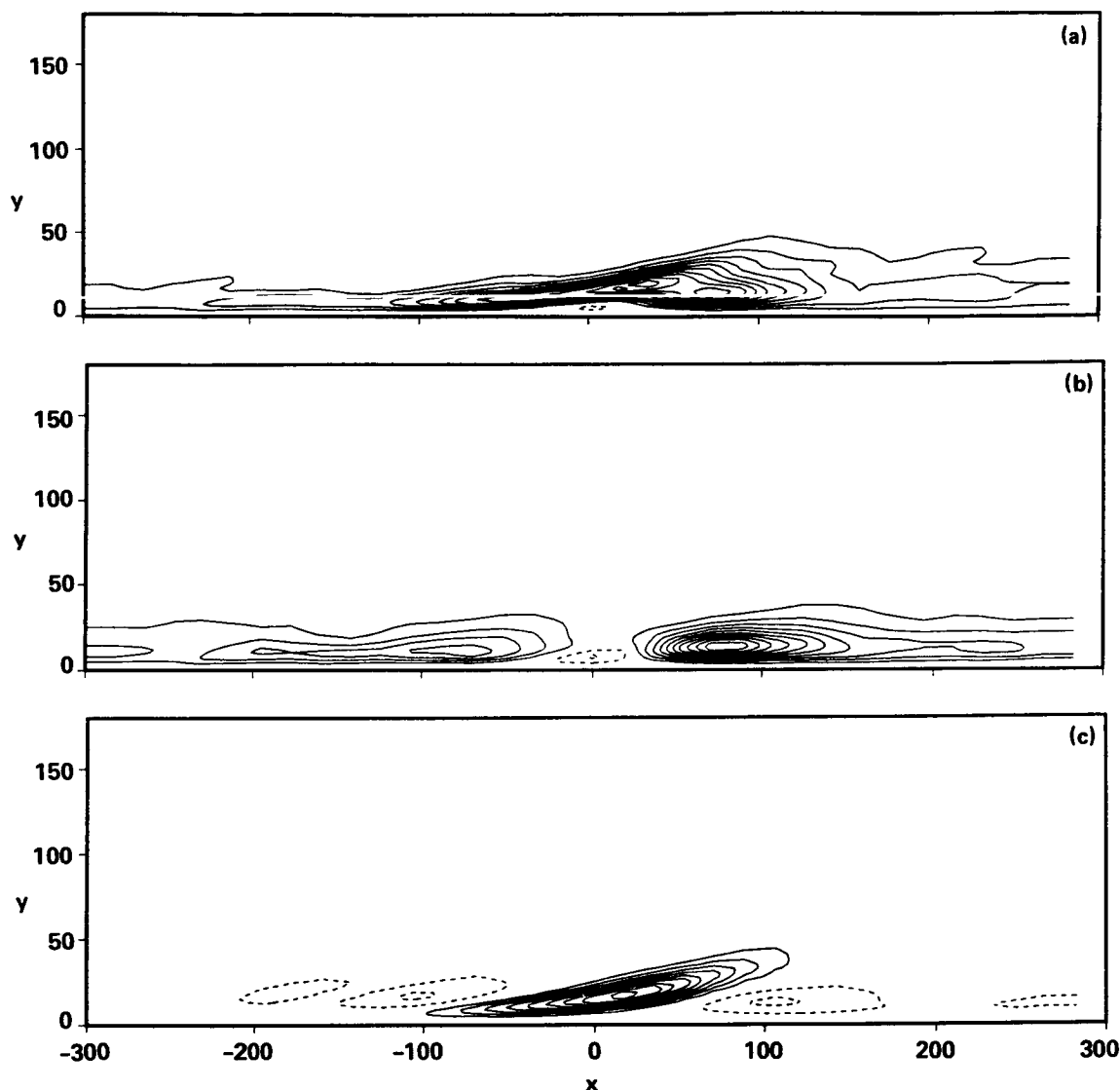
FIGURE 12. Energy production in the symmetry plane of the shear layer (contour increment is 0.1). (a) Total conditional averaged production $< P >$. (b) Reynods-stress induced production $< -uv > dU/dy$. (c) $< P > - < -uv > dU/dy$.

4. Conclusions

- Shear-layer structures are found frequently in near-wall turbulence and often have many features in common with the conditionally averaged structure obtained with the VITA or VISA methods.

- Coherent shear-layer structures in the near- wall region ($y^+ < 15$) were found to propagate with a velocity of about $10.6u_\tau$, and retained their coherence over streamwise distances on the order of a thousand viscous length units.

- Shear-layer structures were found to be important contributors to the turbulence production, and a substantial part of the conditionally averaged production was
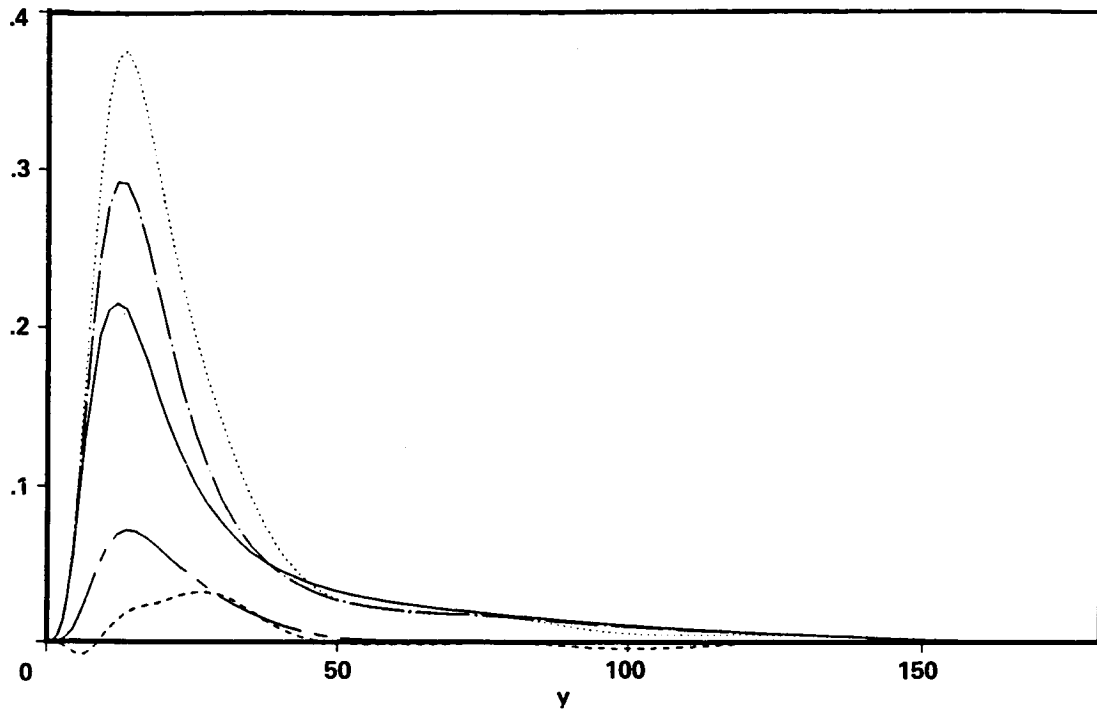
FIGURE 13. Energy production averaged over area around center of event: ———— , $-\overline{uv}dU/dy$; ········ , $< P >$; —————— $-\overline{uv} < \partial u/\partial y >$; —·—· , $- < uv > dU/dy$; chndsh $-\overline{u^2} < \partial u/\partial x >$.
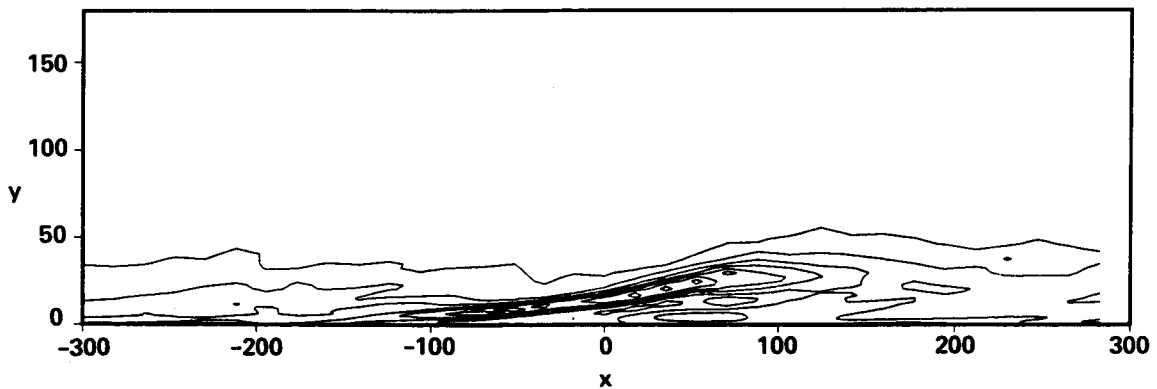
FIGURE 14. Dissipation of turbulent energy in the symmetry plane of the conditional averaged structure in Fig. 7. Contour increment is 0.1.
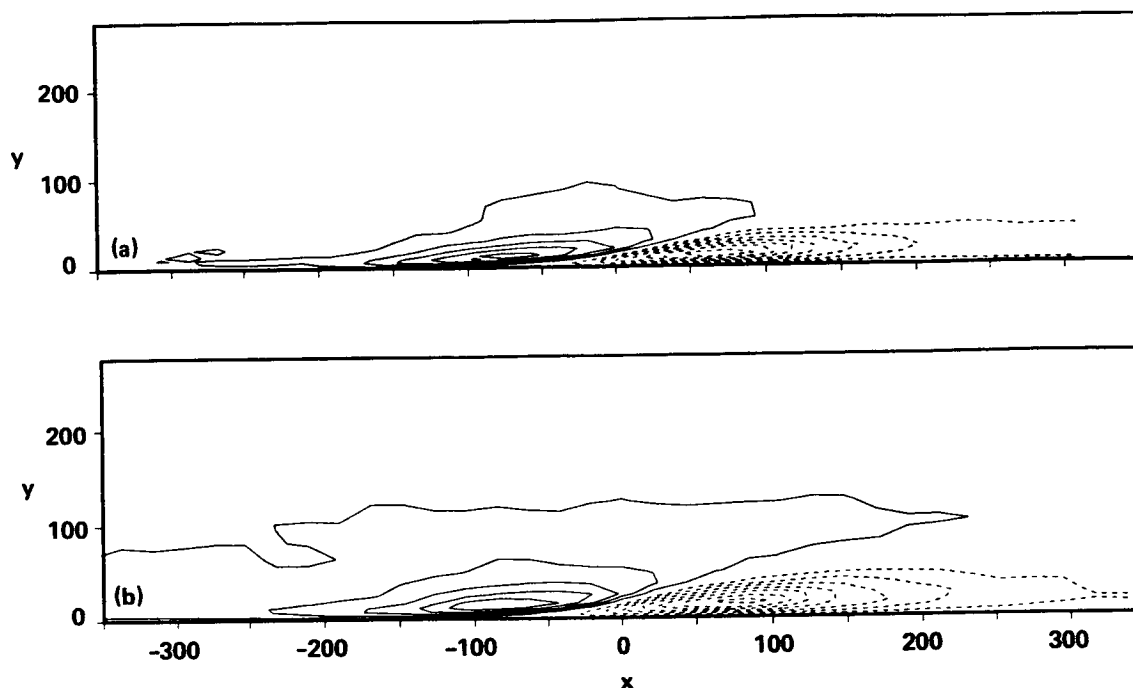
FIGURE 15.   Conditionally averaged u obtained from boundary layer simulations ($k=1$): (a) $Re_\theta=670$, $L=211$; (b) $Re_\theta=1410$, $L=232$.

shown to be generated by strong gradients in the streamwise disturbance velocity.

- The dominant associated uv-contribution was found to be associated with an ejection type of motion on the downstream side of the shear layer.
- Individual shear layers often develop a strong asymmetry (which is lost in conventional averaging procedures) as they propagate downstream.

We are grateful to Dan Henningson for much valuable assistance with the computers and many lively discussions. We also wish to thank Philippe Spalart for providing the boundary-layer data, and Kenny Breuer and Marten Landahl for many fruitful discussions.

REFERENCES

ALFREDSSON, P. H., & JOHANSSON, A. V. 1984 Time scales in turbulent channel flow. *Phys. Fluids.* **27**, 1974.

BLACKWELDER, R. F., & KAPLAN, R. E. 1976 On the wall structure of the turbulent boundary layer. *J. Fluid Mech..* **76**, 89.

JOHANSSON, A. V., & ALFREDSSON, P. H. 1982 On the structure of turbulent channel flow. *J. Fluid Mech..* **122**, 295.

JOHANSSON, A. V., ALFREDSSON, P. H., & ECKELMANN, H. 1987 On the evolution of shear-layer structures in near- wall turbulence. in *Advances in Turbulence* (G. Comte-Bellot and J. Mathieu, eds.), Springer-Verlag.

KIM, J. 1985 Turbulence structures associated with the bursting event. *Phys. Fluids.* **28**, 52.

SPALART, P. 1987 Direct simulation of a turbulent boundary layer up to $R_\theta = 1410$. NASA Technical Memorandum 89407.

The Simulation of Coherent Structures in a Laminar Boundary Layer

By KENNY BREUER[1], MARTEN T. LANDAHL[1], AND PHILIPPE R. SPALART[2]

Introduction

Coherent structures in turbulent shear flows have been studied extensively by several techniques, including the VITA technique (Alfredsson & Johansson 1984, Blackwelder & Kaplan 1976, Johansson, Alfredsson & Eckelmann 1987) which selects rapidly accelerating or decelerating regions in the flow. "Positive" events (in which the streamwise velocity increases while passing a fixed probe) have been found (Alfredsson & Johansson 1984, Johansson, Alfredsson & Eckelmann 1987) to be inclined shear layers with a strong associated Reynolds stress. If these structures are responsible for a large part of turbulence production, then an important question is how are they formed and how do they evolve in the flow.

Present study

The motivation for the present work is the idea that the evolution of coherent structures in a turbulent flow follows simple dynamics which are not dominated by the turbulent flow field. This idea has been studied by Russell and Landahl (1984, also Landahl 1984) who developed some approximate models for the dynamics of such structures, but in order to study them more completely a full-scale calculation is necessary. Based on the assumption that the dynamics of the shear layer's evolution are largely independent of the random part of the flow, one should be able to capture the essential features by looking at the evolution of a disturbance in a laminar boundary layer. This approach has recently been illustrated in Acarlar & Smith's study of hairpin vortices (1987).

A localized disturbance was studied numerically using a three-dimensional, unsteady Navier-Stokes code (Spalart 1986). The mean flow considered was a Blasius boundary layer and the initial velocity perturbation, shown at one y-location in figure 1, was the same as that used by Russell & Landahl (1984), consisting of two pairs of counter-rotating vortices. Landahl (1984) has shown that such a flow would result from an instantaneous peak of $u'v'$, and so one would expect to find perturbations of this kind following high Reynolds-stress production in a turbulent

flow. Analytically, the disturbance has the following form:

$$u' = 0$$

$$v' = \frac{Axy^3(1 - 2z^2)}{l_z}\, e^{-(x^2+y^2+z^2)}$$

$$w' = \frac{-Axz(3y^2 - 2y^4)}{l_y}\, e^{-(x^2+y^2+z^2)}$$

where A is the amplitude of the disturbance and the coordinates are scaled by some characteristic lengths l_x, l_y, and l_z. For the cases presented, the scaling used was $l_x = 5$, $l_y = 1.2$, $l_z = 6$, and A was chosen to be 0.2. This gave an initial perturbation in v and w of about 2% and a streamwise and spanwise extent of about 10 (all velocities are normalized by the free stream, and all lengths by the displacement thickness at the point of generation). The starting Reynolds number, Re_{δ^*}, was chosen to be 945. Some calculations were also performed with a negative amplitude, $A = -0.2$, representing an initial condition of downward flow, followed by upward motion, and simulating a "negative" VITA event. Several grid resolutions and box sizes were used to ensure that there was no grid dependence. Most of the results reported here were calculated on a 64^2 grid in the horizontal planes with 40 Jacobi modes in the vertical direction. The solution at all times remains symmetric with respect to the $z = 0$ plane.

Results and discussion

Figures 2 and 3 show the evolution of the streamwise velocity perturbation u' (all of the results presented here are plotted in a frame of reference moving at $0.4U_\infty$, chosen so as to 'freeze' the structure in the plotting window). At $T = 0.0$ there is no longitudinal component of the disturbance but one quickly develops as the liftup of slower fluid creates a velocity defect region, followed by a accelerated region of fluid pulled down from the upper part of the boundary layer. Because of the mean shear, the fluid elements further from the wall will be advected faster than those closer to the wall resulting in the stretching out and intensification of the structure in the streamwise direction as it propagates downstream. This is clearly seen in the second frame, $T = 81.4$, where a strong internal shear layer has formed. The shear layer is not quite symmetric as the ejection side (downstream, where v' is positive) is somewhat stronger than the sweep side (upstream, where fluid moves toward the wall) which is in agreement with the results of Johansson, Alfredsson and Eckelmann (1987) in a turbulent flow. At a later time $T = 116.9$, the breakdown of the shear layer is becoming evident from the greatly increased amplitude and the appearance of finer scales in the disturbance velocities, although the exact nature of the breakdown is as yet unclear.

The spanwise structure of the disturbance close to the wall is seen in figure 3. What is especially striking here is the development of long "streaks" of alternating high and low speed fluid. The streak spacing is closely related to the spanwise dimension of the original disturbance.

The Reynolds stress distribution is shown in figure 4. As one would expect, $-u'v'$ increases as the disturbance grows and it is primarily concentrated in the two regions ahead and behind the shear layer. The downstream peak is stronger, consistent with the larger perturbation levels in that region. The Reynolds-stress distribution is also remarkably consistent with the structure seen in the fully turbulent flow (Johansson & Alfredsson 1982).

Figure 5 shows the amplitude of the disturbance as it propagates downstream. Two results are plotted: the solid line is the shear-layer disturbance ($A = 0.2$), while the dashed line indicates the growth of the "inverse disturbance" ($A = -0.2$). While this disturbance does grow, its growth seems to be linear, in contrast to the shear layer which grows exponentially. This dramatic difference serves to show that it is the structure of the disturbance, and not only its initial amplitude that leads to the rapid growth. One possible reflection of this in experimental results is that the frequency of detection for negative VITA events is considerably lower than for positive events. While the results are not shown here, the negative case also develops a long streaky structure and at later times an unstable shear-layer structure does develop off the center-line, perhaps hinting that it too will undergo a rapid growth when that mechanism becomes dominant.

Summary

The evolution of a localized disturbance in a laminar boundary layer shows strong similarity to the evolution of coherent structures in a turbulent wall-bounded flow. Starting from a liftup-sweep motion, a strong shear layer develops which shares many of the features seen in conditionally-sampled turbulent velocity fields. The structure of the shear layer, Reynolds stress distribution and wall pressure footprint are qualitatively the same, indicating that the dynamics responsible for the structure's evolution are simple mechanisms dependent only on the presence of a high mean shear and a wall and independent of the effects of local random fluctuations and outer flow effects. As the disturbance progressed, the development of streak-like high- and low-speed regions associated with the three-dimensionality of the disturbance was also observed.

Acknowledgments

REFERENCES

ACARLAR, M. S. & SMITH, C. R. 1987 "A study of hairpin vortices in a laminar boundary layer". *J. Fluid Mech.* **175**, 1.

ALFREDSSON, P. H. & JOHANSSON, A. V. 1984 "On the detection of turbulence-generating events". *J. Fluid Mech.* **139**, 325.

BLACKWELDER, R. F. & KAPLAN, R. E. 1976 "On the wall structure of the turbulent boundary layer". *J. Fluid Mech.* **76**, 89.

JOHANSSON, A. V. & ALFREDSSON, P. H. 1982 "On the structure of turbulent channel flow". *J. Fluid Mech.* **122**, 295.

JOHANSSON, A. V., ALFREDSSON, P. H., & ECKELMANN, H. 1987 "On the evolution of shear-layer structures in near-wall turbulence". *Advances in Turbulence*, Comte-Bellot, G. & Mathieu, J. editors, Springer-Verlag, p. 383.

LANDAHL, M. T. 1984 "Coherent structures in turbulence and Prandtl's mixing-length theory". *Z. Flugwiss. Weltraumforsch.* **8**, **4**, 233.

RUSSEL, J. M. & LANDAHL, M. T. 1984 "The evolution of a flat eddy near a wall in an inviscid shear flow". *Phys. Fluids.* **27**, **3**, 557.

SPALART, P. R 1986 Numerical simulation of boundary layers. Part 1. Weak formulation and numerical method. NASA TM 88222.
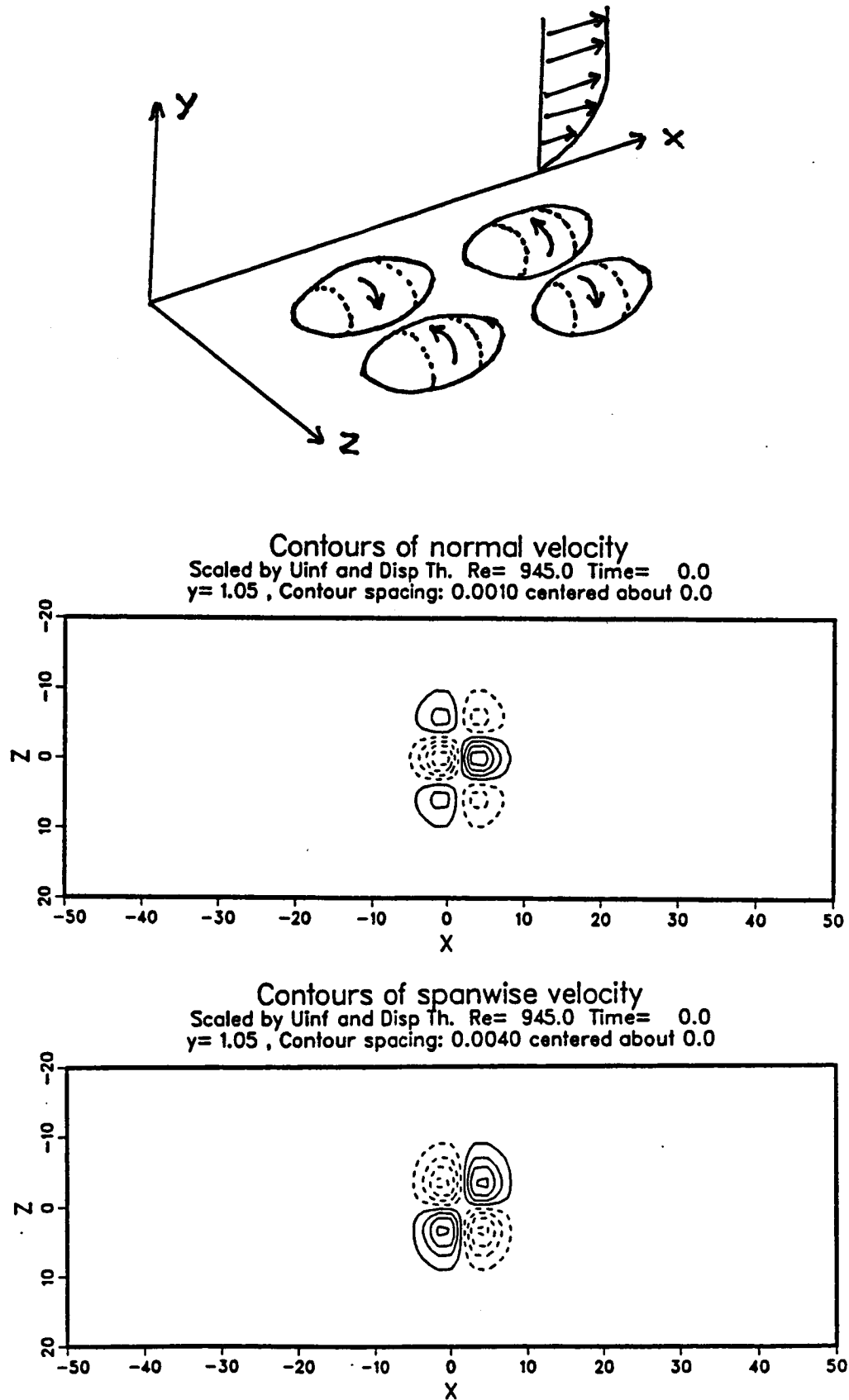
FIGURE 1. Initial disturbance. a) Sketch of vorticity field; b) and c) velocity contours.
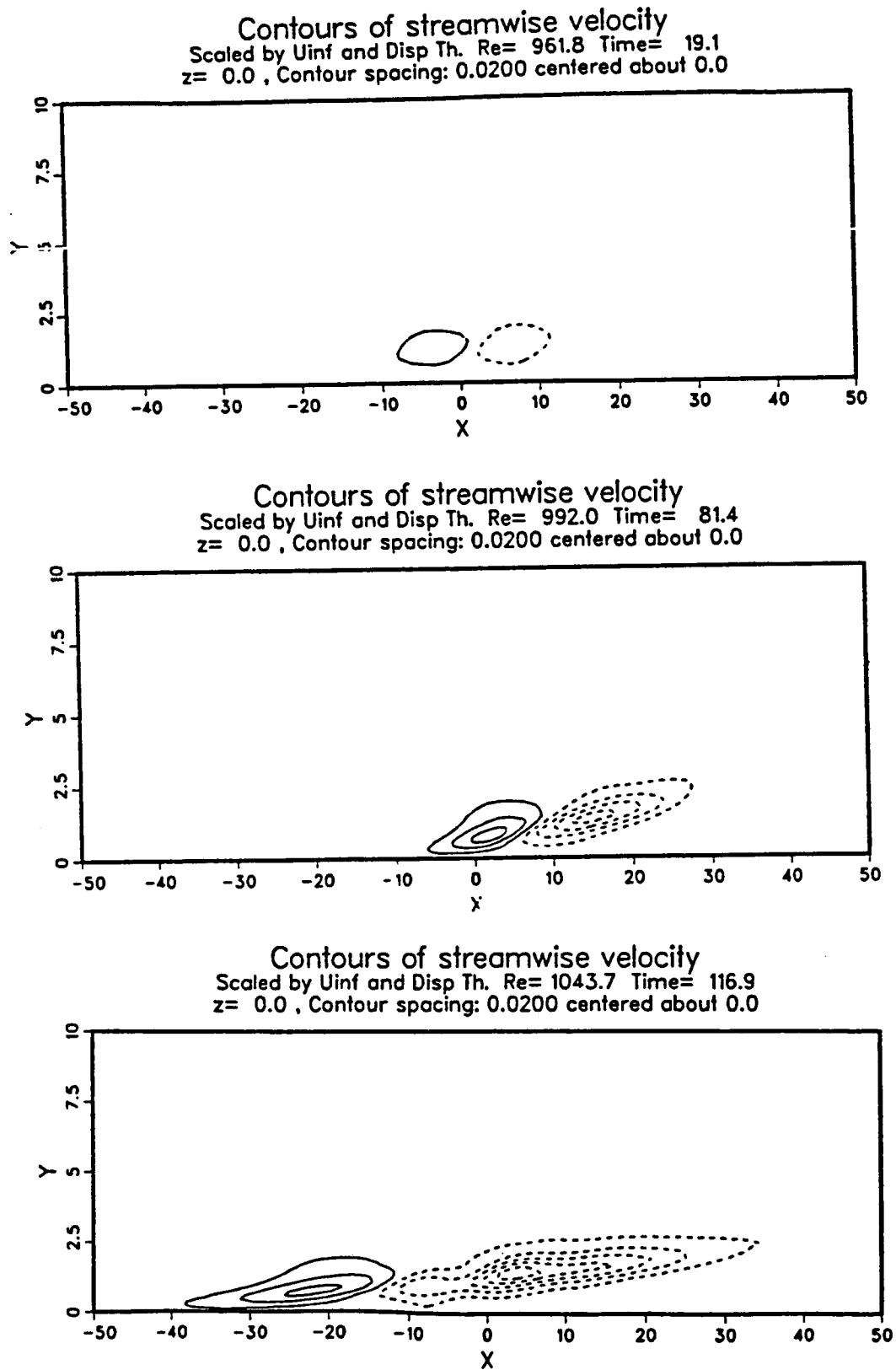
FIGURE 2.   Streamwise-velocity contours at different times. Side view.
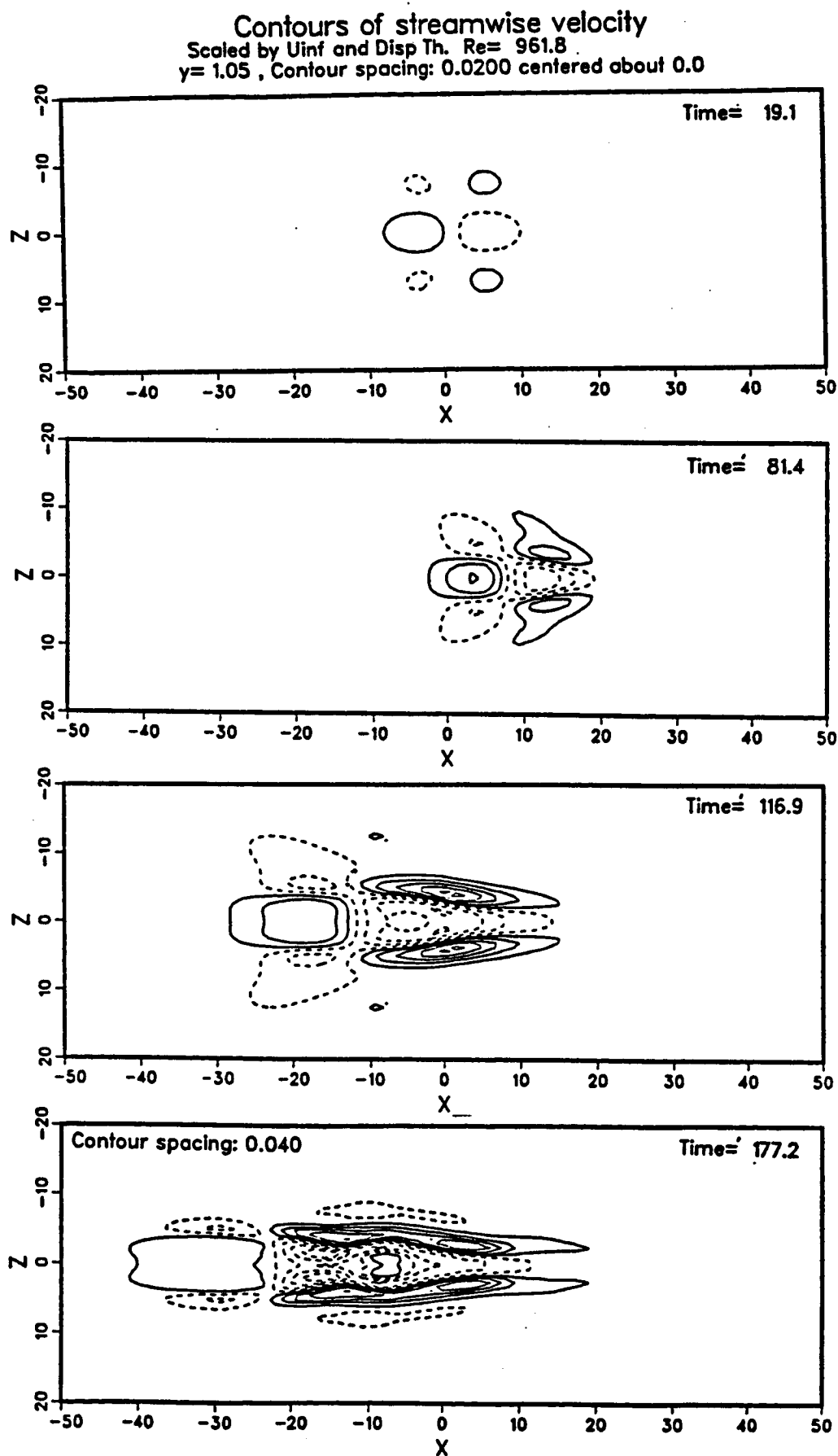
FIGURE 3. Streamwise-velocity contours at different times. Plan view.

Contours of uv
Scaled by Uinf and Disp Th. Re= 961.8 Time= 19.1
z= 0.0 , Contour spacing: 0.0001 centered about 0.0

Contours of uv
Scaled by Uinf and Disp Th. Re= 992.0 Time= 81.4
z= 0.0 , Contour spacing: 0.0001 centered about 0.0

Contours of uv
Scaled by Uinf and Disp Th. Re= 1043.7 Time= 116.9
z= 0.0 , Contour spacing: 0.0001 centered about 0.0

FIGURE 4. Reynolds-stress contours at different times. Side view.

Amplitude of Localized Disturbance
Normalize by Uinf and Disp. Th
Solid line: A = 0.2, Dotted Line: A = −0.2
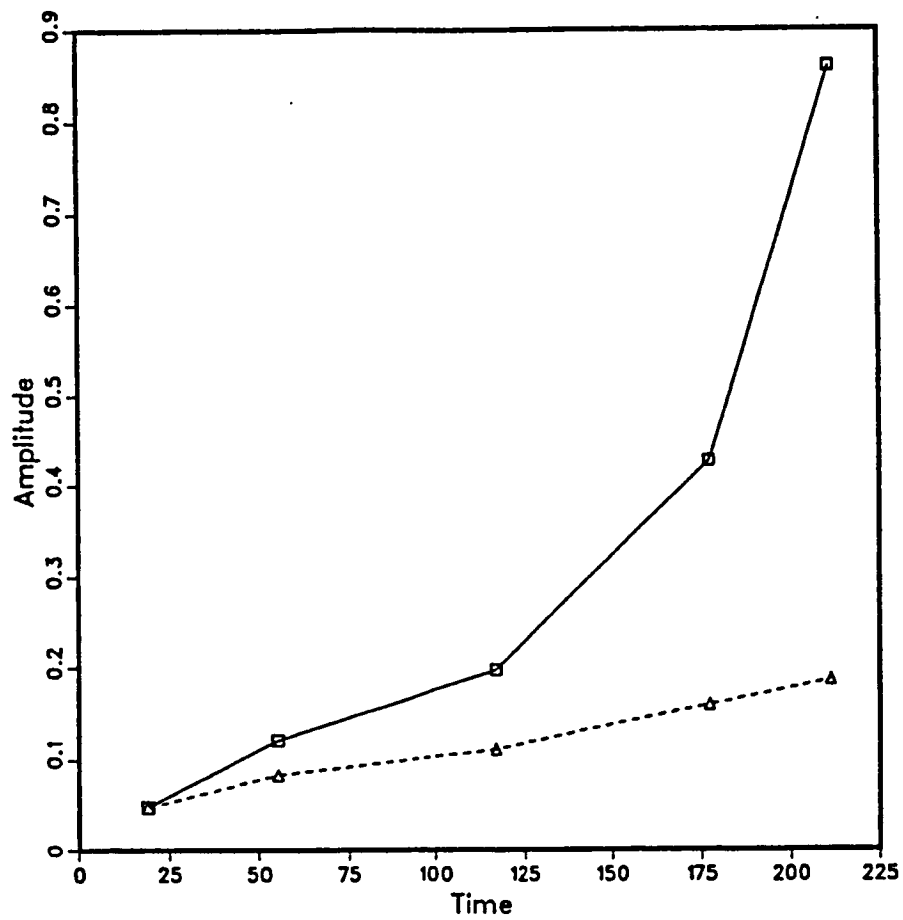
FIGURE 5. Evolution of the disturbance amplitude.

Conditionally-Averaged Structures in Wall-Bounded Turbulent Flows

By Yann G. Guezennec,[1] Ugo Piomelli[2] and John Kim[3]

The quadrant-splitting and the wall-shear detection techniques were used to obtain ensemble-averaged wall layer structures. The two techniques give similar results for Q4 events, but the wall-shear method leads to smearing of the Q2 events. Events were found to maintain their identity for very long times ($\sim 50t^+$). The ensemble-averaged structures scale with outer variables. Turbulence producing events were associated with one dominant vortical structure rather than a pair of counter-rotating structures. An asymmetry-preserving averaging scheme was devised that allowed to obtain a picture of the "average" structure which more closely resembles the instantaneous one.
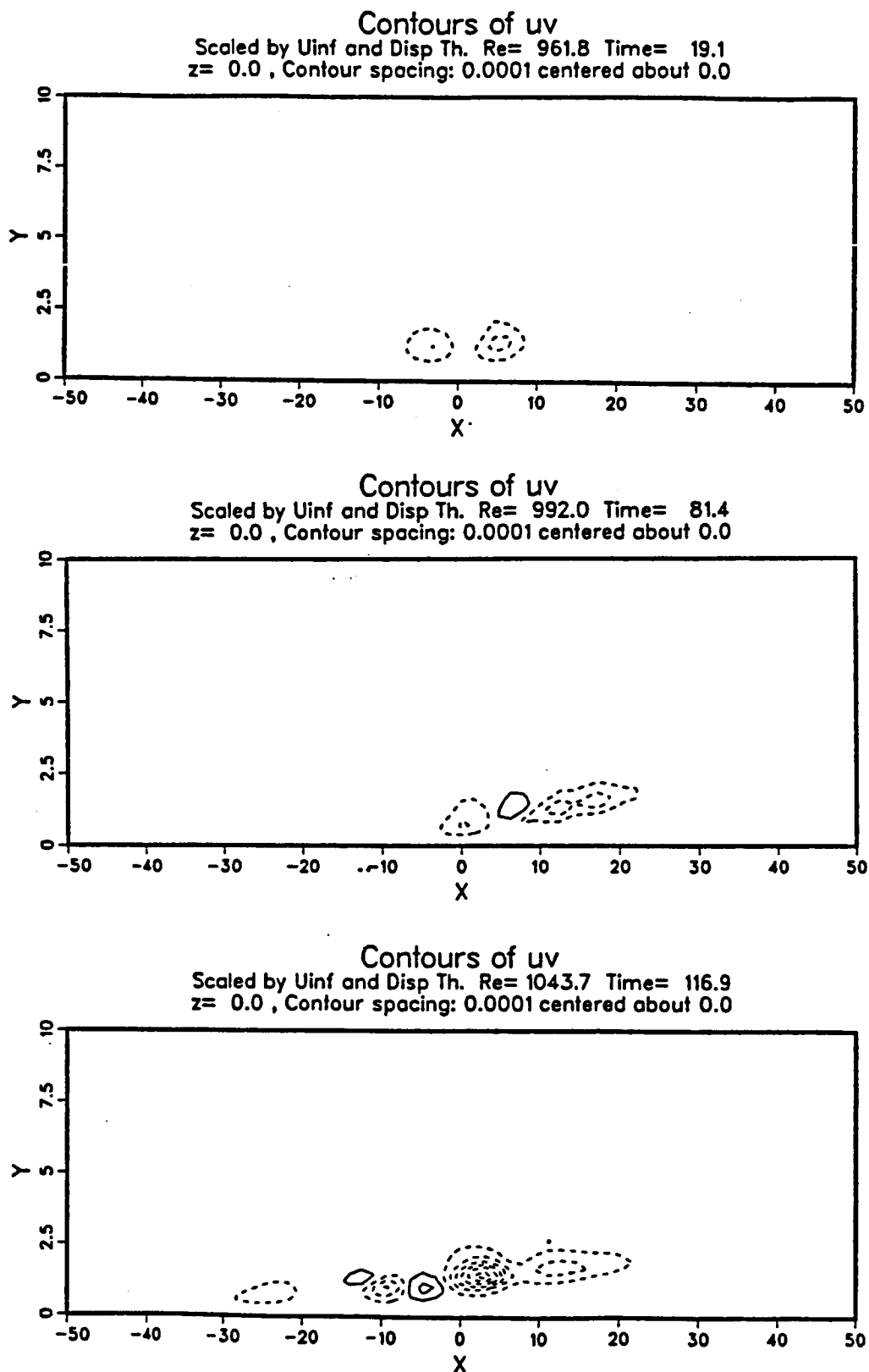
1. Objectives

It was our goal to study coherent structures found in turbulent channel and boundary layer flows using the direct numerical simulation data bases.

Specifically, the following issues were examined:

- Comparison between the ensemble-averaged structures detected by the quadrant-splitting technique and those obtained by the wall-shear detection scheme.
- Scaling of the size of these ensemble-averaged structures with Reynolds number.
- Tracking of individual events (quadrant detected and wall-shear detected) in time to determine their propagation velocity and their persistence.
- Comparison between the structures obtained by ensemble-averaging and those observed instantaneously in the flow.
- Design of better detection and averaging procedures to yield average structures more representative of the instantaneous ones.

2. Procedure

Most of the present results were obtained from the direct numerical simulation of a turbulent channel flow at a Reynolds number $Re_\tau = 180$ based on channel halfwidth δ and friction velocity (Kim, Moin and Moser, 1987). Some additional results were also obtained from the direct numerical simulation of a turbulent boundary layer at $Re_\theta = 670$ based on momentum thickness θ and friction velocity (Spalart, 1987).

1 Ohio State University

2 Stanford University

3 NASA-Ames Research Center

PRECEDING PAGE BLANK NOT FILMED

Coherent structures, defined here as large contributors to the turbulence production process, were detected using two techniques. The first one was the quadrant-splitting technique, which identified events characterized by a fluctuating Reynolds stress larger than 3.5 times the product of the long-term r.m.s. of the streamwise (u') and normal (v') velocity fluctuations. The detection was performed at $y^+ = 12$ and events were sorted into second (Q2) and fourth (Q4) quadrant in the usual manner.

The second detection technique was the wall-shear technique used experimentally by Nagib and Guezennec (1986). With this technique, Q4 events were detected whenever the fluctuating instantaneous wall stress $\tau'_{12} \sim \partial u'/\partial y|_w$ exceeded its r.m.s. intensity by more than 2.8 times while the spanwise shear $\tau'_{32} \sim \partial w'/\partial y|_w$ was small (less than half its r.m.s. intensity). Q2 events were detected in a similar fashion when $-\tau'_{12}$ was over 1.8 times its r.m.s. value. The difference in threshold values for the Q2 and Q4 events was necessary to detect a similar number of events and is consistent with the positive skewness of the wall shear probability distribution.

For both techniques, centering in the streamwise (x) and spanwise (z) direction was performed whenever several neighboring points met the detection criteria by selecting only the one at which the perturbation was maximum. Ensemble averages of the three velocity components were performed for each type of event and detection technique. An average of 100 events were detected with each scheme for the channel flow data, and 500 for the boundary layer data (due to the larger spatial extent of the computational box). Results of the ensemble-averaging procedure were examined by vector maps in various cross-cuts through the events.

3. Results

3.1 Validation of wall-shear detection technique

Results obtained with the two detection technique were compared in the channel flow case. Figure 1 shows such a comparison for a streamwise cut through the centerline of the Q4 event. The two techniques yield essentially the same result. Comparisons were also performed for various spanwise cuts (not shown here) and confirmed this result. Figure 2 represents a similar comparison for the Q2 event. Although the patterns are qualitatively the same, the quadrant splitting technique yields a much more localized perturbation in the streamwise direction. The wall-shear detection technique is not as selective for this type of event, resulting in a lack of registration in the streamwise direction. This is consistent with the fact that the Q2 events represent motion away from the wall, and are less detectable by their imprint on the wall than the Q4 events. However, spanwise cross-cuts (not shown here) are quite similar with both techniques, indicative of little smearing in the spanwise direction.

3.2. Scaling of ensemble-averaged structures

The effect of the Reynolds number on the size of the ensemble-averaged structures was then examined. In order to compare with the experimental results of Wark, Nagib and Guezennec (1987), in which only two velocity components were

FIGURE 1. Ensemble-averaged perturbation velocity maps of the fourth quadrant events. The maximum velocity fluctuations in figure are approximately equal to $5u_\tau$. (a) Events detected by quadrant splitting technique; (b) events detected by wall shear technique.
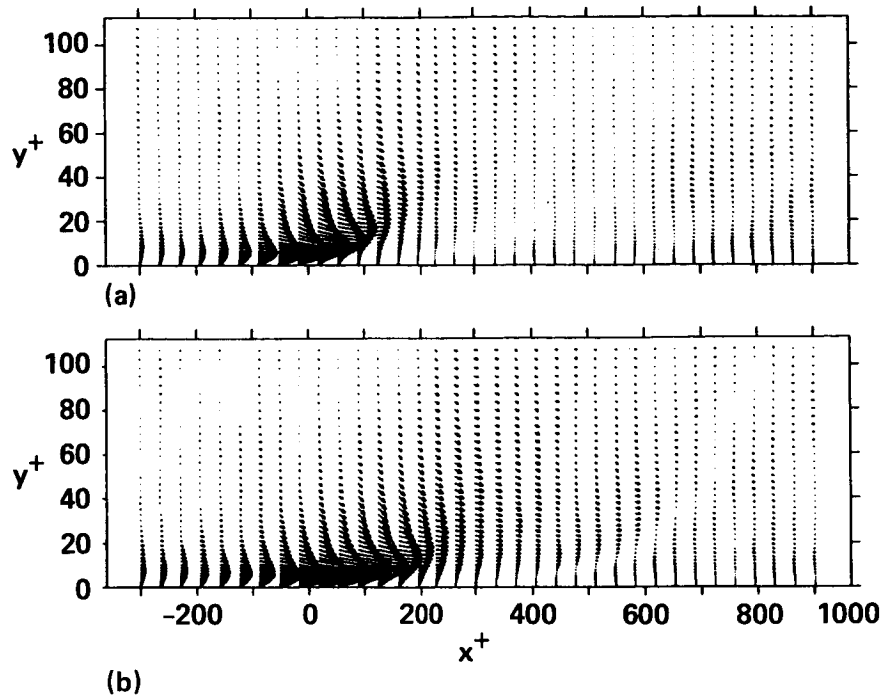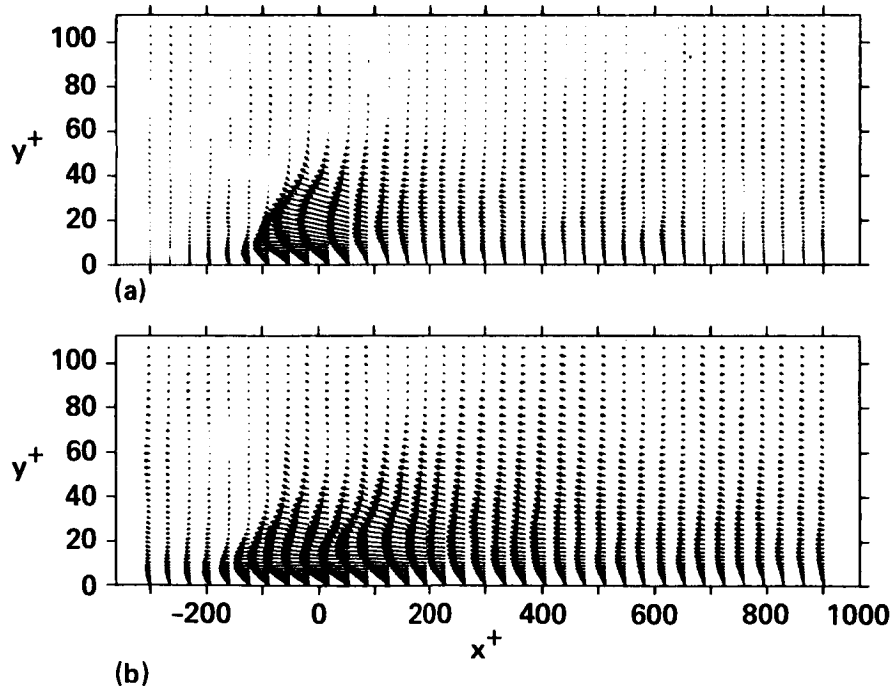

FIGURE 2. Ensemble-averaged perturbation velocity maps of the second quadrant events. The maximum velocity fluctuations in figure are approximately equal to $5u_\tau$. (a) Events detected by quadrant splitting technique; (b) events detected by wall shear technique.
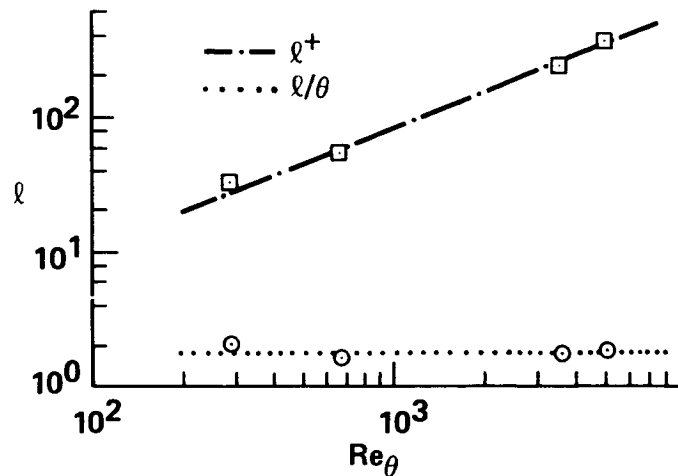
FIGURE 3. Reynolds number dependence of the transverse characteristic scale of the ensemble-averaged structures.

measured, a procedure similar to theirs was used to estimate the characteristic span-wise length scale. At the streamwise location of the detection point, the streamwise velocity perturbation was integrated over the height of the structure to yield a local "perturbation displacement thickness". This procedure was repeated at various spanwise positions. The characteristic spanwise length scale was then arbitrarily chosen as the distance away from the centerline where this perturbation displacement thickness became zero. This distance was checked visually to correspond approximately to the center of the vortical structures detected. This procedure was applied to the events detected by the gradient technique. Q2 and Q4 events also yielded comparable results. Figure 3 shows the variation of this length scale, ℓ, with Reynolds number, Re_θ. The lowest Reynolds number (250) corresponds to the channel flow data and the second point (670) correspond to the boundary layer simulation. The upper two point were determined experimentally by Wark *et al.* (1987). When the size is non-dimensionalized with inner variables (u_τ and ν), it increases with Reynolds number. On the other hand, it remains constant when non-dimensionalized with outer variables (θ) over a twenty-fold increase in Reynolds number.

3.3. Propagation velocity and persistence

Quadrant-type events were tracked in successive time frames to determine their propagation velocity and persistence. Time frames were 3 viscous time units apart, so that the identification and matching of corresponding events in successive time frames was unambiguous. The coordinates of each event were then recorded as a function of time. Events were found to propagate in the streamwise direction with very little meandering in the spanwise direction. Figure 4 illustrates the space-time trajectories of the individual Q2 (top) and Q4 (bottom) events. The average slope of these trajectories represent the propagation velocity of the events and was found
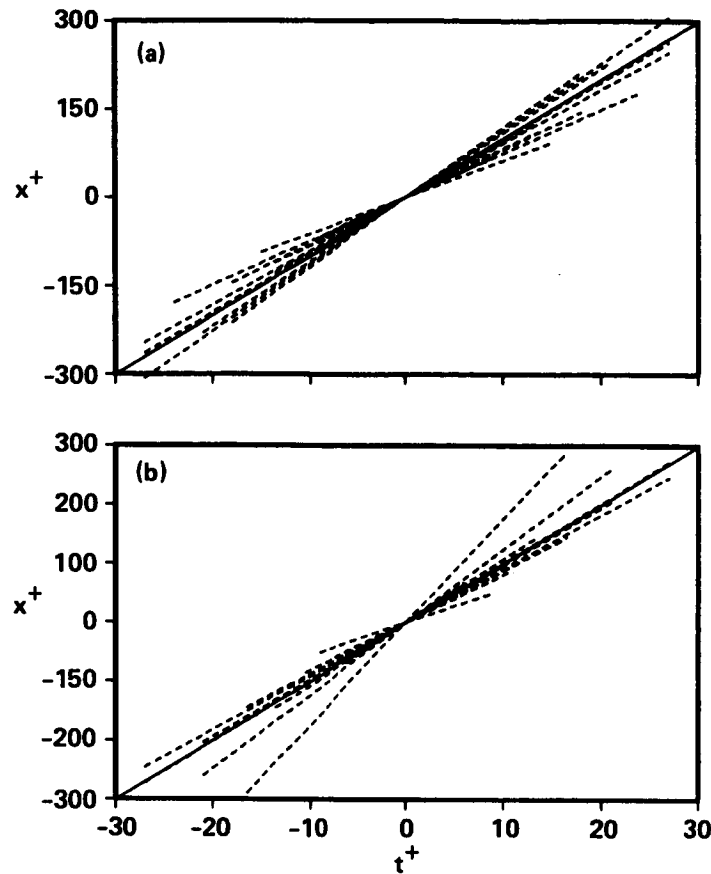
FIGURE 4. Space-time trajectories of events. (a) Second quadrant; (b) fourth quadrant.

to be $9.3u_\tau$ for the Q2-type and $10.3u_\tau$ for the Q4-type events. The local mean velocity at this y-location was $9.5u_\tau$. Moreover, it should be noted that the events maintain their identity for a rather long time (of the order of 40 to 60 viscous time units). This indicates that they do not break up under some rapid instability once they have been formed. The high frequency oscillations observed in laboratory measurements with a fixed probe are linked to their localized spatial extent and propagation velocity. Similar tracking was also performed for wall-shear detected events. They were also found to propagate at similar speeds and persist for similar durations. This finding confirms that large wall-shear fluctuations are the imprint of structures residing in the buffer or logarithmic layer and has important implications for numerical modeling of the wall layer.

3.4. Link between instantaneous and ensemble-averaged structures

Cross-stream vector maps of each individual quadrant event were examined to understand the relation between the instantaneous structures and those obtained from the ensemble-averaging process. While the averaged event resulted in a symmetric pair of counter-rotating vortical structures, due to the homogeneity of the

flow in the spanwise direction, individual realizations differed greatly from this pattern, in terms of size and strength of the structures and, in particular, of symmetry. An example of such difference between the ensemble-averaged pattern and a typical realization is shown in Figure 5. The instantaneous field shows the presence of a strong vortical structure on one side and of a weak one on the other side. Based on this visual evidence, a procedure to measure this asymmetry was designed. Circulation was computed around a closed path (square for simplicity) on each side of the detection point to measure the strength of each vortical structure. Since these structures appear in different sizes, the circulation Γ was computed around four separate integration contours as illustrated in Figure 5b. For each contour the circulation was averaged over both sides and all events to determine the choice of an appropriate contour size. The results are shown in Figure 6 for the Q2 events. The second contour contains the entire structure, and the average circulation Γ_{av} is maximum; along the larger paths the average circulation decreases due to the effect of viscosity. Based on these observations, the second path was chosen and the asymmetry of the event was estimated by the difference $\Delta\Gamma$ of the circulation between the two sides. The normalized probability density function of this measure of asymmetry is shown in Figure 7 as a function of $\Delta\Gamma$ normalized by Γ_{av} (the probability density function was normalized so that its integral is 1 over the whole distribution). This symmetry parameter has a bi-modal distribution, indicating that the most likely event is strongly one-sided, *i.e.* associated with one dominant vortical structure. Similar results were obtained for the Q4 events.

3.5. New ensemble-averaging technique

Based on the result of the previous section, a new ensemble-averaging procedure was designed that recognizes the asymmetry of the individual structures. For each event, the stronger side was identified by the procedure described above and the individual structures were "flipped" about the centerline if necessary, so that the strong structure was always on the same side. The ensemble averaging procedure was then carried out as usual. The comparison between the conventional procedure and this new one is shown in Figure 8 for the Q2 event. The average event is now characterized by only one dominant vortical structure associated with a strong Q2 motion on the centerline. It is worthy to notice the presence of a rather strong Q4 motion on the other side of the structure. This is consistent with the observation that Q4 and Q2 events appear often in pairs side by side. This average structure resembles more closely the individual realizations (there is of course an equal probability of finding its mirror image). The fact that strongly asymmetric structures (or possibly even single structures) are more likely to occur has an important implication on their dynamics. For example, the mutual induction effect for lifting away from the wall commonly used to describe their evolution loses some of its appeal.

4. Conclusions

In summary, the following conclusions have been reached:

- The wall-shear detection technique works well for the fourth quadrant events, but leads to substantial streamwise smearing of the second quadrant events. Events
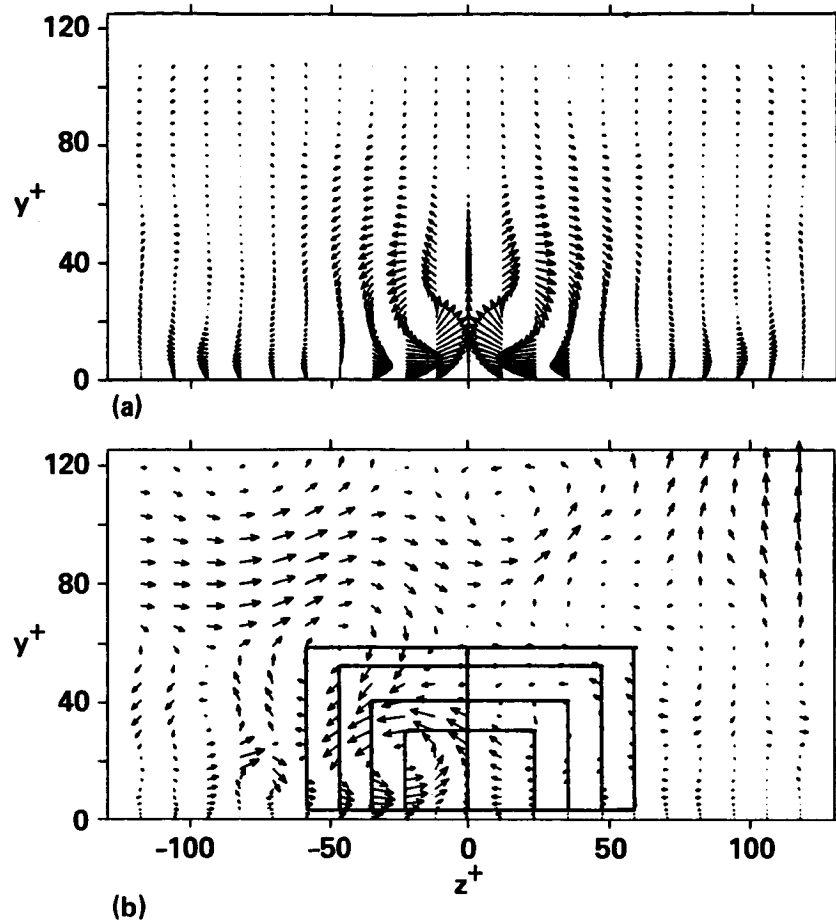
FIGURE 5. Comparison between the ensemble-averaged structure (top) and a typical instantaneous structure of a second quadrant event (bottom), highlighted with circulation integration paths. The maximum velocity fluctuations are approximately equal to u_τ in the top figure and to $2u_\tau$ in the bottom figure.

detected by both techniques have, however, similar spanwise structures.

- Turbulence producing events (regardless of the method of detection, *i.e.* wall-shear, quadrant-splitting or VITA/VISA events, which represent the interaction of two opposite quadrant events) propagate at a speed of approximately $10u_\tau$ in the wall region ($y^+ \leq 15$), with the sweeps being slightly faster than the ejections. They retain their coherence over a period of the order of $50t^+$ and over a streamwise extent of the order of $500\ell^+$. It is therefore unlikely that strong instabilities convected with these structures lead to their catastrophic break up.

- The size of ensemble-averaged structures scales with outer variables, *i.e.* it appears to follow the growth of the logarithmic layer with the Reynolds number. Therefore, they become more and more distinct from the wall layer as the Reynolds number increases. However, it must be noted that this scaling applies to the ensemble-averaged structures, and possibly stems from the fact that a larger
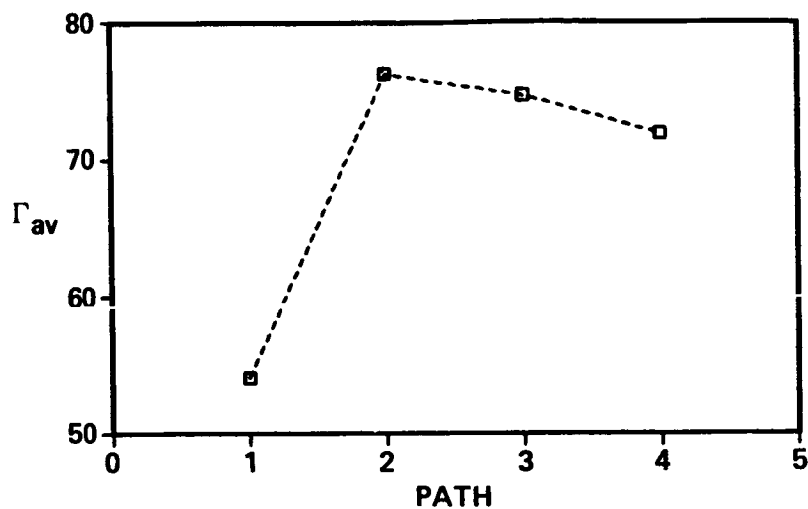
FIGURE 6. Average strength of vortical structures for different integration paths.
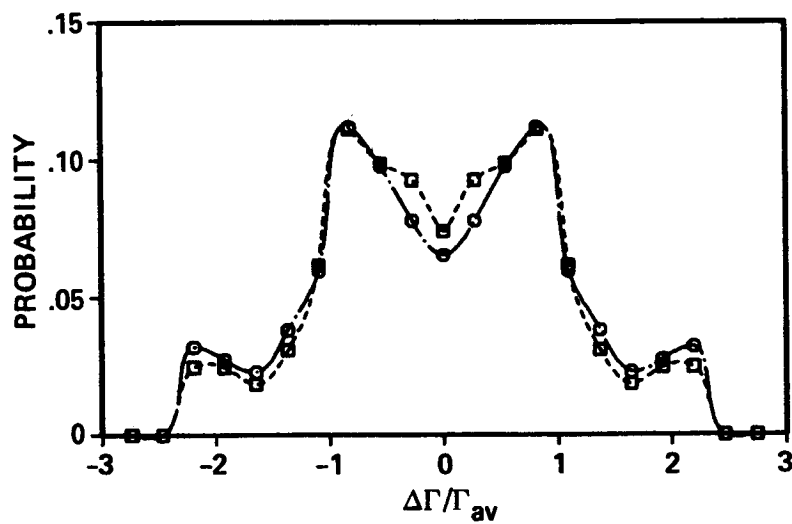
FIGURE 7. Probability density of the asymmetry of vortical structures. Second quadrant event.
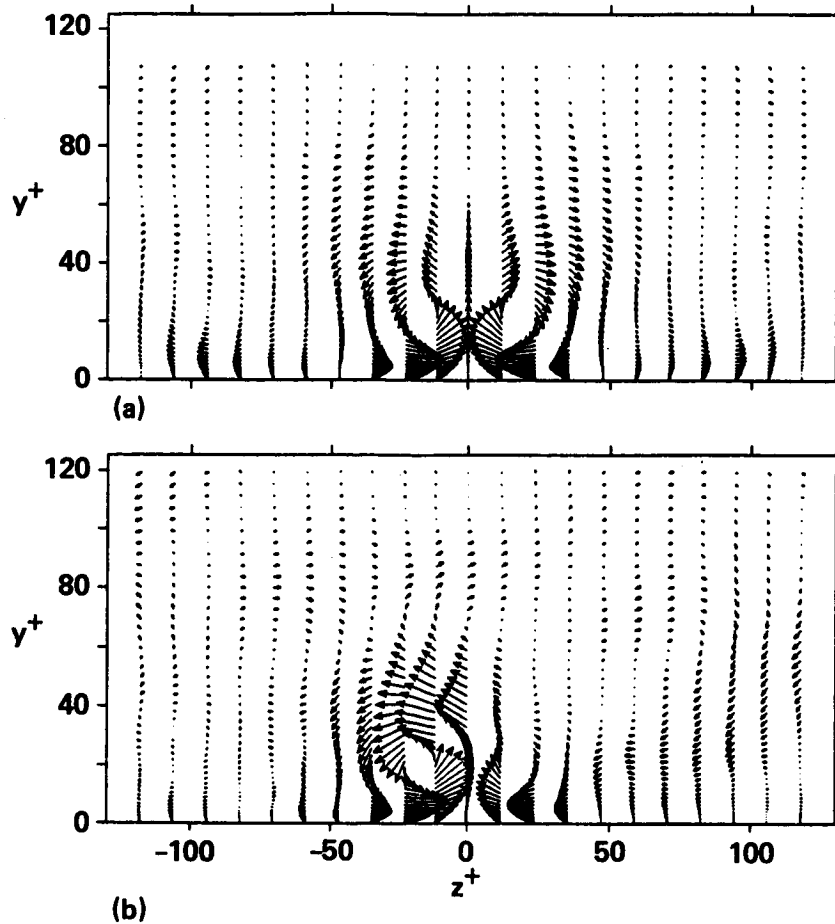
FIGURE 8. FIGURE 8. Ensemble-averaged structures for the second quadrant event. The maximum velocity fluctuations in figure are approximately equal to u_τ. (a) Conventional averaging technique; (b) modified averaging technique.

range of individual sizes exists at higher Reynolds numbers. This indicates the need to perform more high Reynolds number experiments (physical or numerical) to distinguish more clearly the hierarchy of scales associated with the coherent structures.

• Turbulence producing events were found to be associated with one dominant vortical structure rather than a pair of counter-rotating structures. This represents the first step in obtaining "sharper" ensemble averages which are more representative of the instantaneous flow topology. The correct kinematic description of these structures will undoubtedly lead to a better understanding of their dynamics, and more accurate structural information to be incorporated in turbulence models.

REFERENCES

KIM, J., MOIN, P. & MOSER, R. 1987 Turbulence statistics in fully developed channel flow at low Reynolds number. *J. Fluid Mech.*. **177**, 133-160.

NAGIB, H.M. & GUEZENNEC, Y.G. 1986 On the Structure of Turbulent Boundary Layers. Proceedings of the Tenth Symposium on Turbulence, University of Missouri, Rolla.

SPALART, P.R. 1986 Direct Simulation of a Turbulent Boundary Layer up to $Re_\theta =$ 1410. NASA T.M.89407.

WARK, C.E., NAGIB, H.M. & GUEZENNEC, Y.G. 1987 Documentation of Turbulence Producing Structures in Regular and Manipulated Boundary Layers. Proceedings of the IUTAM Meeting on Turbulence Control, Bangalore, India.

Structure of Turbulent Shear Flows

By A.K.M.F. HUSSAIN[1], J. JEONG[1] AND J. KIM[2]

Introduction

The accuracy and spatial resolution of numerically simulated databases for turbulent shear flows, like those generated at NASA/Ames, far exceed those typically available in laboratory experiments. While there are limitations of the simulations, in particular regarding low Reynolds number (a technological constraint) and limited duration of flow that can be computed (an economic constraint), the simulations have also the advantage that they enable the scientists to "measure" quantities (such as enstrophy, pressure, dissipation, helicity, and pressure-strain rate correlation) which are virtually impossible to measure accurately in the laboratory (see Hussain, 1983, 1986). Simulations provide quantitative measures of flow fields free from the effects of probe interference and from errors introduced by invoking Taylor's hypothesis. The simulations thus accord heretofore unavailable unique opportunities for research into the structure of turbulence; such was our goal and the centerpiece of our effort during the 1987 summer school of Stanford-NASA CTR.

Our research covered three different topics:

(1) Eduction of coherent structures,

(2) Measurement of propagation velocities of perturbations (such as velocity, pressure, and vorticity) in turbulent shear flows, and

(3) Direct evaluation of the Taylor hypothesis.

In the following, we summarize our activities during the summer school in each of these three categories. However, most of our effort was devoted to item (1), which will occupy the bulk of this report. Recognizing that very little time was available to either complete the post-processing or to even adequately digest the results obtained, we venture to point out a few apparent interesting observations and surprises, make some tentative conclusions and suggest specific areas of continuing collaboration between NASA-Ames and University of Houston.

A. Eduction of coherent structures

Coherent structures, an embodiment of our search for order in disorder, has been the focus of much of the research in turbulent shear flows in the past two decades. The overwhelming majority of coherent structure studies has been based on flow visualization, which is not only qualitative but can even be grossly misleading (Hussain, 1986). We need hard quantitative data regarding the distributions of properties over the spatial extent of the structures and the dynamical roles of these

1 University of Houston

2 NASA-Ames Research Center

structures. These structures being defined in terms of coherent vorticity (Hussain, 1980), the requirement of vorticity measurement presents a severe constraint. A first simplification of this problem was to measure one component of vorticity only and in one plane only—that in the azimuthal plane. The initial approach was to perform phase-locked measurements triggered on the periodicity of the flow event or of a forcing signal (Cantwell & Coles, 1983; Hussain & Zaman, 1980; Hussain, Kleis & Sokolov, 1980). Note that structures in natural (unexcited) shear flows undergo jitters of two kinds: initiation and evolutionary jitters. Via excitation, initiation of structure formation can be controlled, but the evolutionary jitter remains uncontrolled. Thus eduction, even in periodically induced structures, must use a local trigger at the measurement location instead of an upstream trigger—a major drawback of Cantwell & Coles' data.

The next step was to develop a scheme for eduction of coherent structures in an unexcited flow by using a local footprint of passing structures (Zaman & Hussain, 1984). In parallel, efforts were devoted to develop an algorithm that can educe structures in any fully developed turbulent flow without requiring any trigger signal. This resulted in a scheme which utilizes the measurement signal itself. Such a technique (to be explained below) was first developed for eduction of structures in the fully developed region of an axisymmetric jet (Tso, 1983) and was further refined to educe structures in a turbulent plane wake (Hayakawa & Hussain, 1985). This generic and robust scheme, which can be applied to data in any transitional and turbulent shear flow, was also successfully applied to numerical simulation and experimental data in a plane mixing layer (Metcalfe et al., 1985). The close agreement between structures educed from numerical and experimental data is strong evidence of the robustness of the scheme as well as a validation of the simulation.

Our goal in this area continues to be: (i) eduction of coherent structure topology in different turbulent flows, (ii) understanding of turbulence phenomena in terms of entrainment, mixing, production, and dissipation, and (iii) the dynamical role and significance of coherent structures in various turbulent shear flows. This provides the motivation for eduction of coherent structures from direct simulations of turbulent flows. While the coherent structure topology and dynamics in the wall region of a turbulent boundary layer would not be expected to be different from those in the wall region of a channel, the outer layer structures must be noticeably different between the two flows. Hence the motivation for studying coherent structures in a flat plate boundary layer and a channel flow. These new data would establish how coherent structures in the wall-bounded flows are different from coherent structures in free shear flows, which have been studied extensively at University of Houston. Having decided to especially focus on the coherent structures near the wall, which are responsible for the most interesting events in wall-bounded shear flows, it was necessary to separate the effects of the wall from those of shear. Hence the goal of eduction of coherent structures in homogeneous shear flows.

The simulation data in a low Reynolds number, fully turbulent channel flow (Kim, Moin & Moser, 1987), in a flat plate boundary layer (Spalart, 1987), and in two homogeneous shear flows (Rogers & Moin, 1987; Lee & Reynolds, 1985) are used to

educe coherent structures in these flows.

Eduction methodology:

Even though the eduction procedure, in principle, is based on the 3D vorticity information in a flow field, experimental limitation forced us to implement the procedure on one component of vorticity, namely the spanwise vorticity, ω_z. In order to permit meaningful comparison with experimental data, our earlier eduction from numerical simulation was also based on only the ω_z field of the simulation (Metcalfe et al., 1985).

The eduction procedure is briefly outlined here. Readers can find further details in our earlier papers. The eduction steps are as follows: (i) select a small y-range where coherent structures are to be studied and obtain $\omega_z(x, y)$ data from simulations in various z-planes, but centered at the middle of this y-range (x, y, z are longitudinal, transverse, and spanwise coordinates, respectively); (ii) smooth the $\omega_z(x, y)$ data using a zero-phase shift filter; (iii) detect structures which are strong (i.e., peak vorticity above a threshold ω_{t_1}) and of a sufficiently large size; (iv) look for z-symmetry of these vorticity concentrations; (v) accept ω_z data from a plane of symmetry (being careful not to accept two planes of the same structure).

The phase average of all realizations containing similar structures yields a coherent structure. Note that a coherent structure is a stochastic quantity and may not be observed instantaneously. The center (marked by the peak value) of smoothed ω_z contours is only a first guess, and is a useful reference for initial alignment of various realizations, but may have nothing to do with the true center, which must be determined from the ensemble averaging after proper alignment.

The eduction continues as follows: (vi) align ω_z with respect to the peaks of smoothed contours and obtain the ensemble average — this is the *zeroth iteration ensemble average* Ω_0; (vii) obtain cross correlation $R_{\omega_1 \Omega_0}$ of each realization with the ensemble average; (viii) shift the center of each realization by the location in (x, y) for peak correlation; (ix) reject realizations requiring excessive shifts; (x) obtain ensemble average of the realizations by aligning them with respect to the new centers—this is the *first iteration ensemble average*; (xi) reject realizations that produce excessively low correlation peaks; (xii) continue the iteration until all shifts required for alignment fall below a size and all correlation peaks are above a set level; (xiii) identify the locations of revised centers of finally accepted realizations in the unsmoothed data records and obtain ensemble average after aligning with respect to these centers—this final ensemble average is the coherent structure; (xiv) the departure of each *unsmoothed* realization from the ensemble average denotes incoherent turbulence.

In the eduction, we set ω_{t_1} in terms of the local maximum of mean $\omega_z(y)$. In case of the channel flow, the structures educed were those centered at $y^+ = 125, 50, 30$, and 15.

The educed velocity vector patterns in the (x, y)-plane for the four locations are shown in Figs. 1(a-d). All the four contours show some similarities, characterized by saddles and centers. We had anticipated the structure at $y^+ = 125$ (note $y^+ = 180$ at the centerline of the channel) to resemble to some extent the mixing layer structure
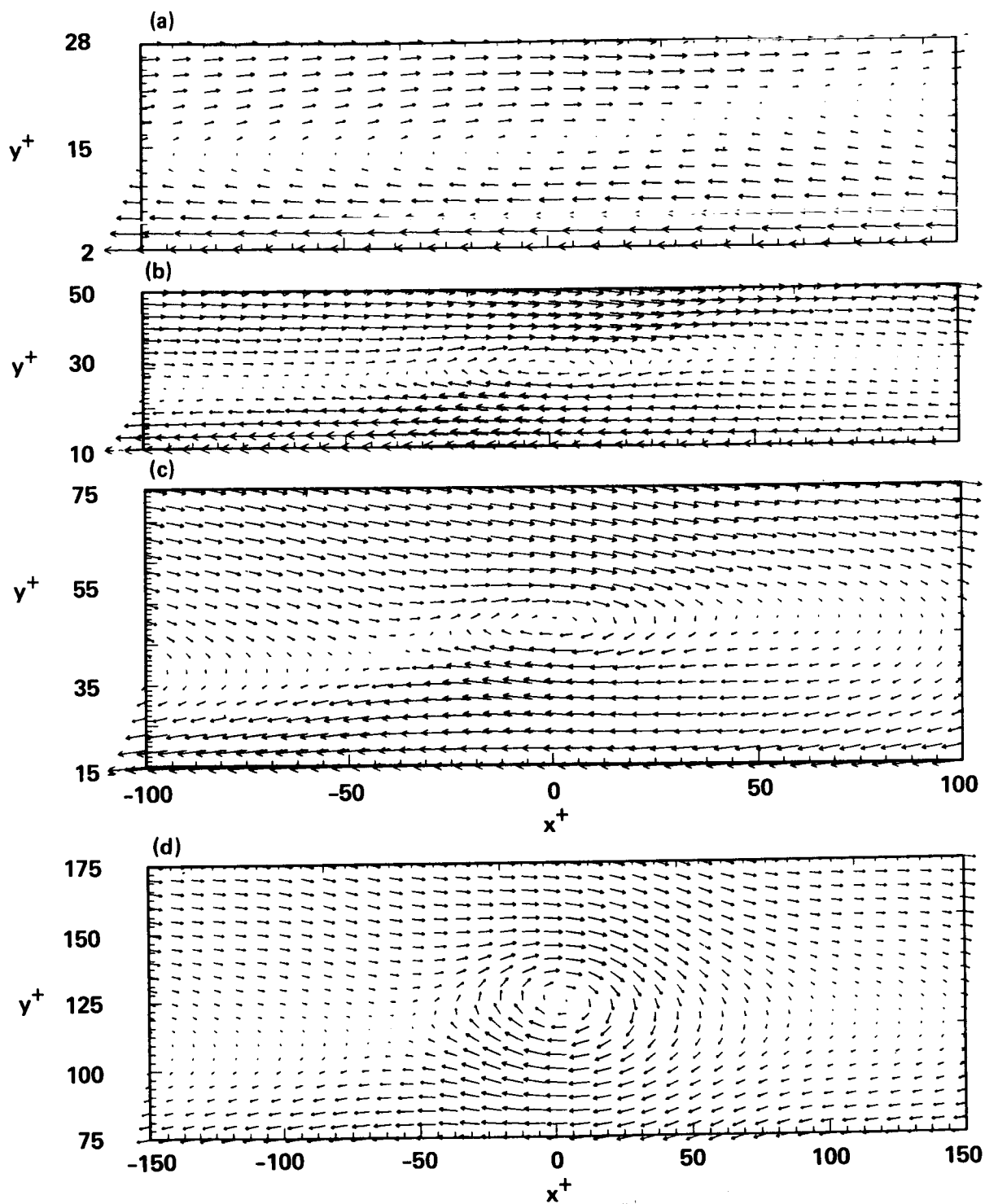
FIGURE 1.   Educed velocity vector patterns in (x, y)-plane: (a) Centered at $y^+ = 15$; (b) $y^+ = 30$; (c) $y^+ = 50$; (d) $y^+ = 125$. Note that the y-scales are stretched at different factors for each figures.

studied extensively before (see Hussain & Zaman, 1985; Metcalfe et al., 1985), but the near wall structures appear to be different presumably due to the effects of the wall and high shear. For this reason we present detailed data for structures centered at both $y^+ = 125$ and $y^+ = 15$. The results for $y^+ = 15$ are presented in Figs. 2(a-m) as contours of coherent vorticity $< \omega_z >$; coherent longitudinal and transverse velocities $< u >$ and $< v >$; coherent pressure $< p >$; incoherent turbulent kinetic energy $< q_r^2 >$; incoherent Reynolds stress $-< u_r v_r >$; incoherent pressure $< p_r^2 >$; coherent strain rate $< S >=< \partial u/\partial y > + < \partial v/\partial x >$; coherent shear production $< P_S >= - < u_r v_r >< S >$; coherent normal production $< P_N >= - < u_r^2 > \partial < u > /\partial x - < v_r^2 > \partial < v > /\partial y$; total production $< P_T >=< P_S > + < P_N >$; coherent pressure works $< p >< S_{11} >$, $< p >< S_{22} >$. Note that the y-scale is expanded relative to the x-scale in order to reveal the details of the flow field and that two vorticity contours are duplicated in all figures to provide a common reference. The corresponding contours for $y^+ = 125$ in the channel flow are shown in Figs. 3(a-m).

We have started educing structures at four transverse locations in the Spalart's boundary layer as well as one location each in the homogeneous shear flows. For the purposes of this preliminary report, we limit our discussions primarily to the case of channel structures centered at $y^+ = 15$.

In the frame of the advected coherent structure, the flow above it moves downstream and the flow below it moves upstream. The structure advection velocity being about 60% of the centerline velocity, the downstream stagnation point is closer to it than the upstream one. One would thus expect the normal production at the front to be higher than at the back, as is indeed the case (Fig. 3j). Note that nearer to the center of the channel, the shear is weak and more nearly uniform across the structure. That is why the two saddles are nearly equidistant from the center, and the normal productions are equal on both the front and the back.

The coherent pressure contour extends in the transverse direction considerably beyond the structure boundary as denoted by coherent vorticity. This is to be expected from the fact that pressure is an integral property, being the solution of a Poisson equation with the source term due to gradients of the velocity field. Note that the minimum of coherent pressure is at around the structure center, but does not exactly coincide with it.

One striking feature is the fact that longitudinal pressure work is mostly negative (hence of the right sign) at $y^+ = 125$ but mostly positive at $y^+ = 15$ (hence of the wrong sign). That is, the pressure work transfers kinetic energy away from the longitudinal component in the outer layer as is commonly presumed on the basis of time average kinetic energy balance (see Tennekes & Lumley, 1972), and it transfers kinetic energy into the longitudinal component (contrary to expectation) near the wall. This is consistent with the result of Moin & Kim (1982), in which they attributed it to the "splatting" motions of large eddies in the near-wall region.

Since the shear layer below the advecting structure (near the wall) has a higher velocity gradient than the one above the structure (toward the centerline), one would expect the shear production $< P_S >$ to be higher on the left- than on the

right-hand side of the structure. Data show the two regions to have comparable levels of $< P_S >$, suggesting that the incoherent Reynolds stress $< u_r v_r >$ is higher at the top right-hand side of the structure. Note that both $< P_N >$ and $< P_S >$ are coordinate dependent and it is their sum which is invariant under rotation (Hussain, 1983). The total production $< P_T >$ is higher at the top on the right- hand side.

Concluding remarks

The success of the eduction scheme in extracting coherent structure details in the fully turbulent channel flow is demonstrated. In the plane of z-symmetry the coherent structure characteristics are quite similar to those in the free mixing layer—more so in the outer regions than near the wall. The topology consists of saddles and centers, the saddle region being the location of maximum incoherent Reynolds stress $-< u_r v_r >$, and maximum shear production. One interesting difference from the mixing layer case is that the center in the wall-bounded case is not necessarily characterized by a high level of incoherent turbulence intensity.

While we need to devote more time to compare our channel data with those in jets, wakes and shear layers, some of the measures have not been obtained yet in the free shear flows: for example, contours of dissipation, pressure work, etc. These measurements and simulations are planned in the future. One noticeable difference between the educed structures at $y^+ = 125$ and $y^+ = 15$ is that the structure in the former case is more rounded while in the latter case it is much more sheared. In order to determine the role of shear while eliminating any effect of the wall, it would be worthwhile to educe these structures in homogeneous shear flows with different shear rates. This work is in progress now.

While we do not expect any noticeable difference in the near-wall coherent structure characteristics between channel flow and flat plate boundary layer, the outer layer structures can be quite different in the two flows on two accounts. In the boundary layer, the outer structures should all be of the same sign and be bounded by irrotational (nonturbulent) fluid which they entrain. In the case of the channel, the outer region should consist of structures originating from both walls and can be significantly different as a result of interaction of these structures of oppositely-signed circulations.

When all these data are completed, we will be able to identify the similarities and differences among structure topologies in the channel flow, the boundary layer and homogeneous shear flow. We then hope to be able to comment specifically on the role of the nonturbulent freestream, on the role of shear, and on the role of the wall.

Future extensions

We propose to extend this work to include the following:
(1) Starting from the plane of symmetry, march ahead on either side to track the coherent vortical structure and educe structure details in local planes and then reconstruct the three-dimensional structure.
(2) Educe structures with circulation opposite to the direction of mean shear. This is important in the outer region of the channel where structures migrate from
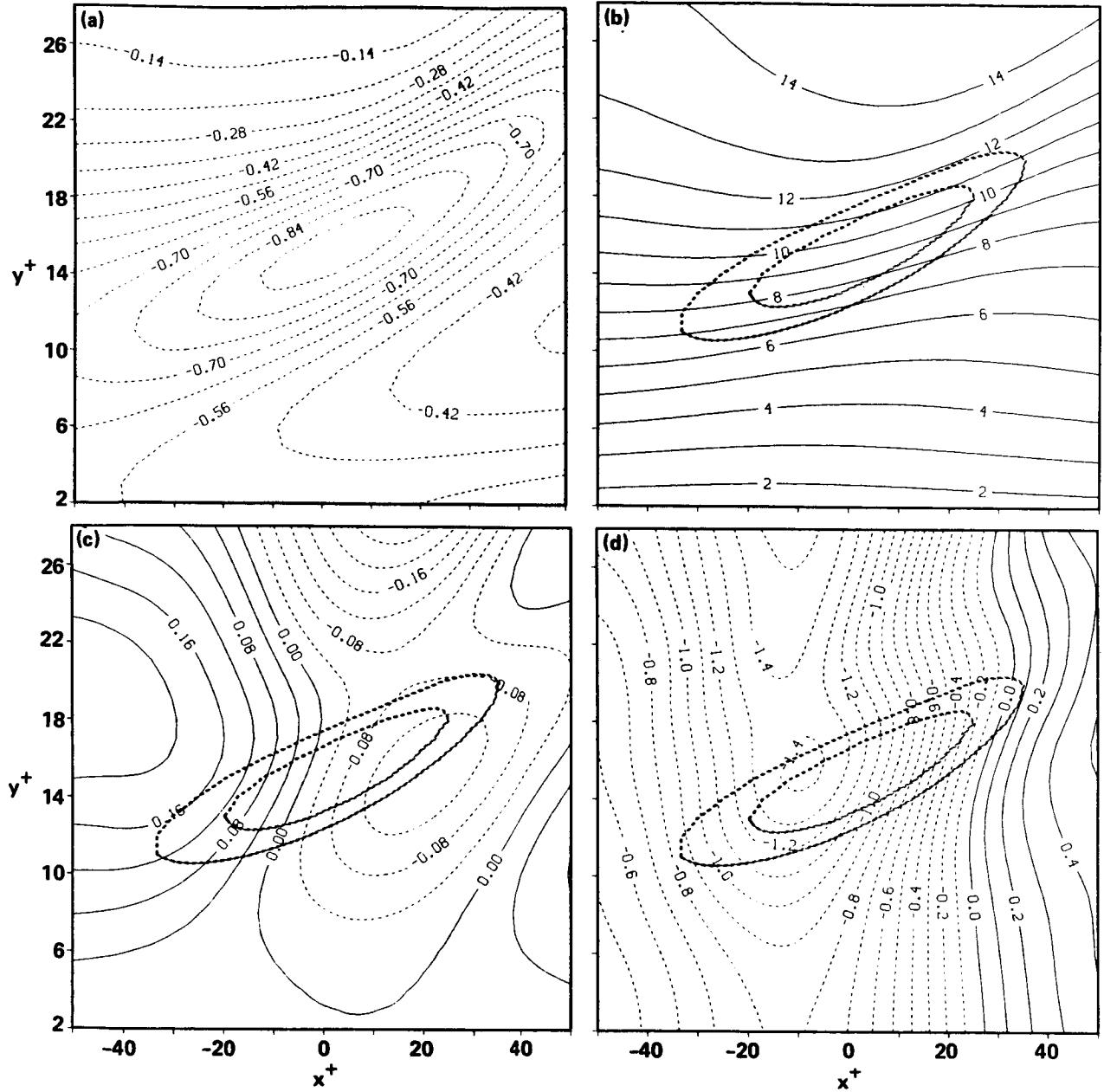
FIGURE 2. Educed turbulence structures centered at $y^+ = 15$. Note that the y-scales are stretched to reveal the details of the structures. (a) $< \omega_z >$; (b) $< u >$; (c) $< v >$; (d) $< p >$; (e) $< q_r^2 >$; (f) $-< u_r v_r >$; (g) $< p_r^2 >$; (h) $< S >=< \partial u/\text{partialy} > + < \partial v/\partial x >$; (i) $< P_S >= - < u_r v_r >< S >$; (j) $< P_N >= - < u_r^2 > \partial < u > /\partial x - < v_r^2 > \partial < v > /\partial y$; (k) $< P_T >=< P_S > + < P_N >$; (l) $< p >< S_{11} >$; (m) $< p >< S_{22} >$.

FIGURE 2.   ... continued.
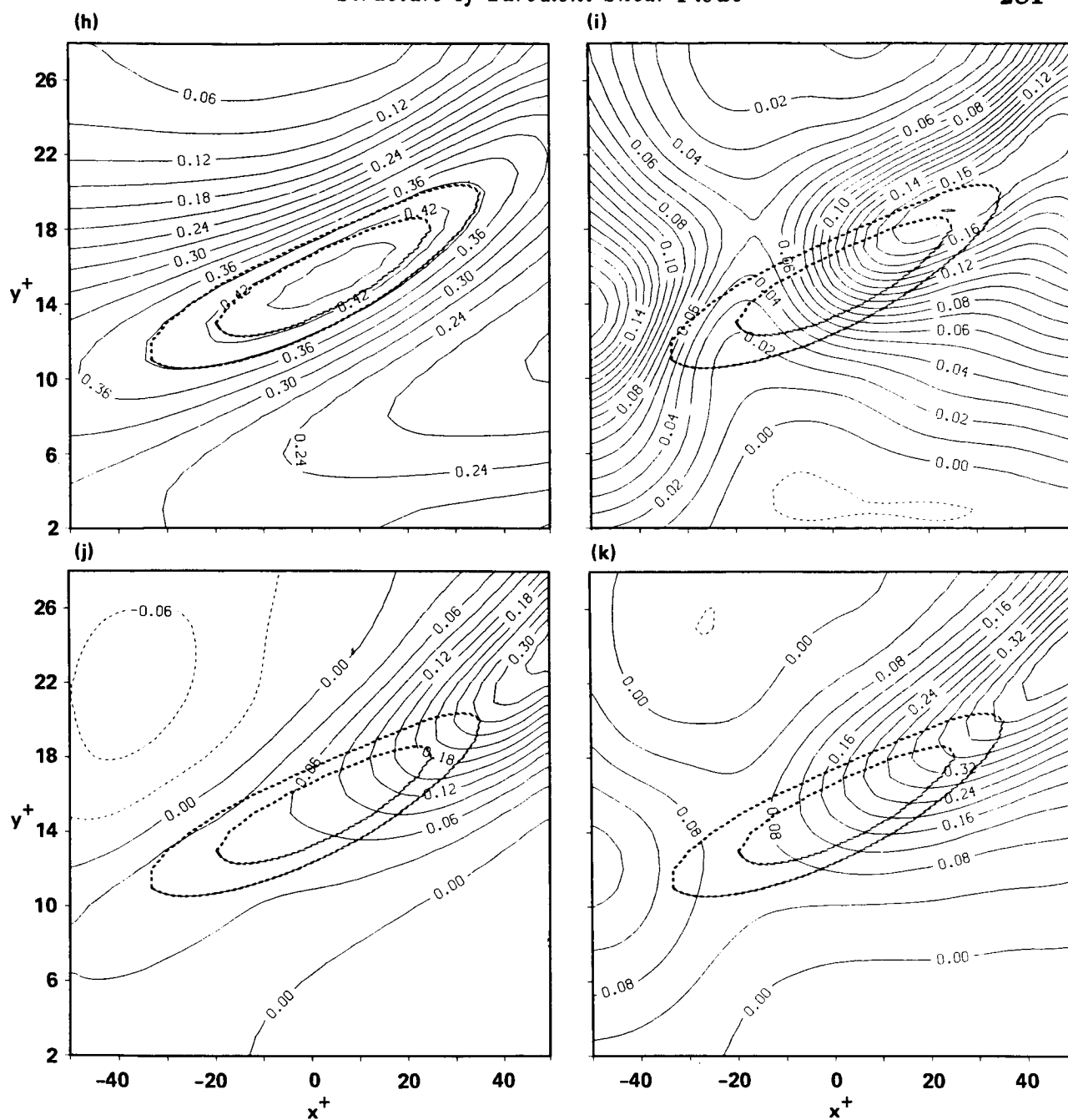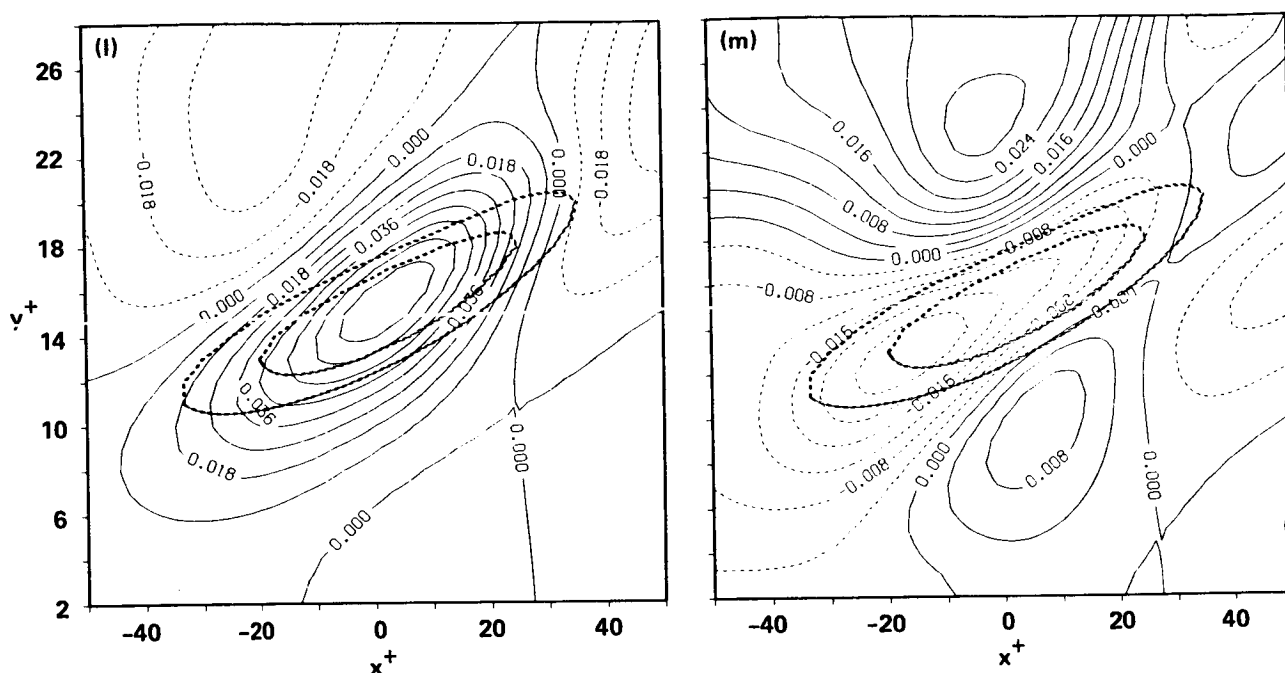
FIGURE 2.   ... continued.

FIGURE 2. ... continued.

the opposite wall.

(3) Complete eduction on the basis of total vorticity $|\omega|$ rather than the spanwise vorticity ω_z.

(4) Address clearly the mechanisms of entrainment, mixing, production, intercomponent transport, enstrophy cascade and dissipation associated with the educed three-dimensional coherent structure.

(5) Educe other significant coherent structures and evaluate the dynamical role and significance of coherent structures in the three flows studied.

(6) Study the evolution of a turbulent hairpin vortex in a laminar boundary layer and a laminar channel flow with a velocity profile matching that of a turbulent flow. Study the same in a flow with laminar and turbulent homogeneous shear.

(7) Study the dynamics and evolution of an an artificially induced bursting coherent structure in fully turbulent channel flow and flat plate boundary layer.

B. Propagation velocities

The direct simulation data provide an excellent opportunity for determination of propagation velocities of pressure, velocity and vorticity perturbations in turbulent shear flows. In the case of the turbulent boundary layer or channel flow, in particular, varying values of propagation velocities have been reported in the literature. In addition to being of fundamental interest, the propagation velocity is of direct concern in understanding coherent structure topology and dynamics.

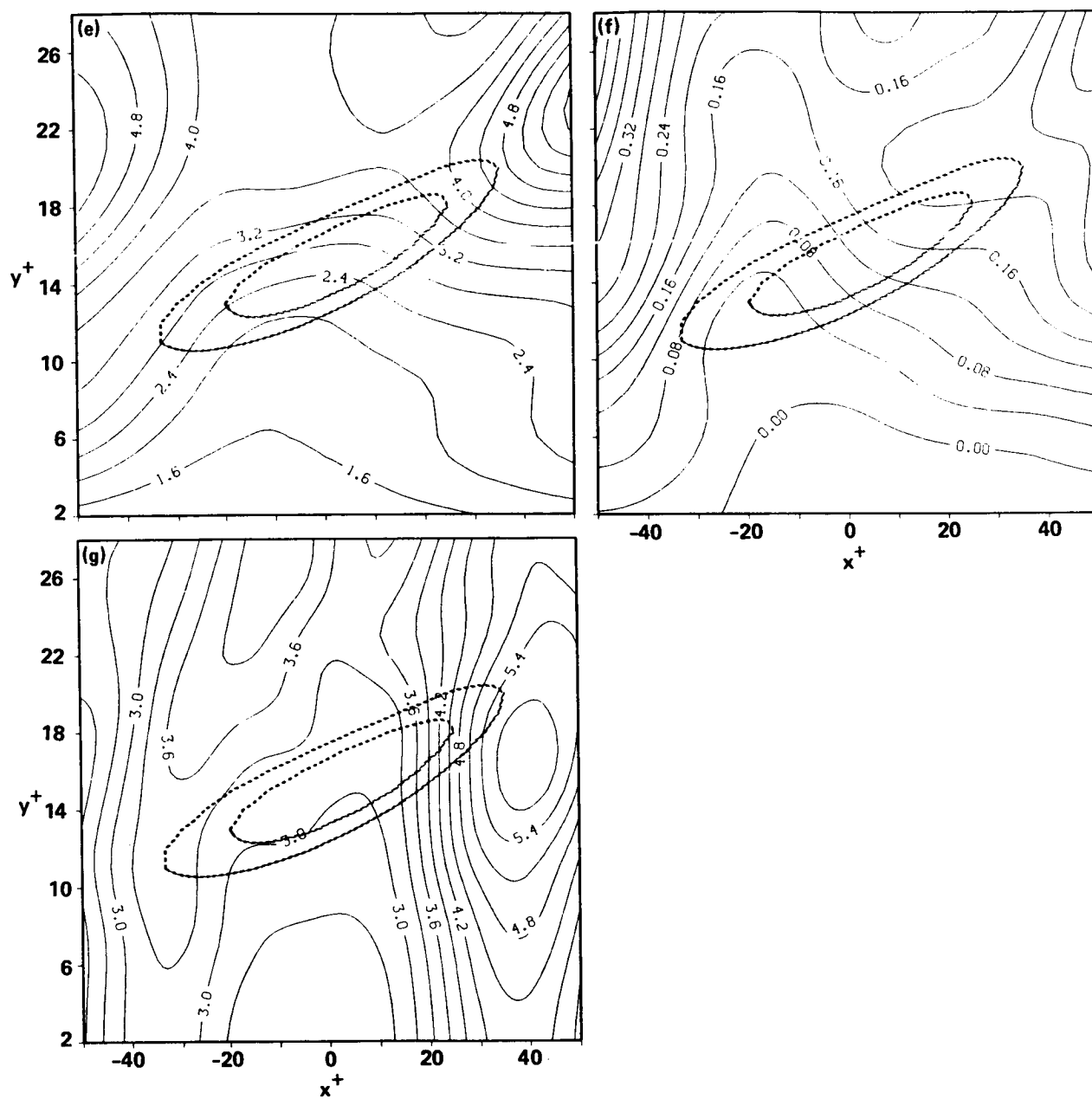If instantaneous fields of simulation data are considered at two instants t_1 and t_2
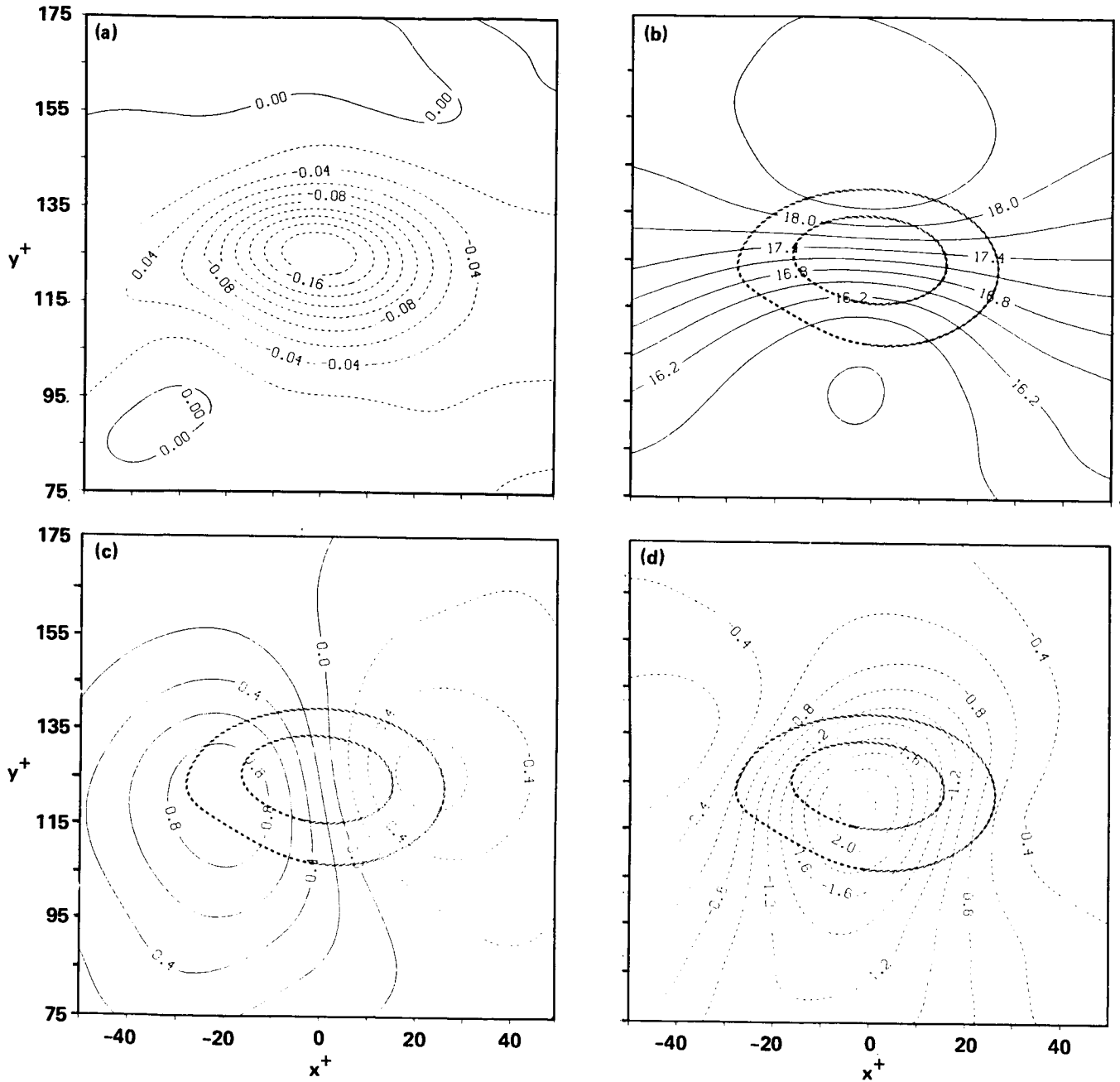
FIGURE 3. Educed turbulence structures centered at $y^+ = 125$. Note that the y-scales are stretched to reveal the details of the structures. (a) $< \omega_z >$; (b) $< u >$; (c) $< v >$; (d) $< p >$; (e) $< q_r^2 >$; (f) $-< u_r v_r >$; (g) $< p_r^2 >$; (h) $< S >=< \partial u/partialy > + < \partial v/\partial x >$; (i) $< P_S >= - < u_r v_r >< S >$; (j) $< P_N >= - < u_r^2 > \partial < u > /\partial x - < v_r^2 > \partial < v > /\partial y$; (k) $< P_T >=< P_S > + < P_N >$; (l) $< p >< S_{11} >$; (m) $< p >< S_{22} >$.

FIGURE 3.   ... continued.

FIGURE 3.   ... continued.

FIGURE 3. ... continued.

and they are cross-correlated, then from the locations $(\delta x_m, \delta y_m)$ of cross- correlation peak, one can obtain streamwise and transverse propagation velocities U_c, V_c as follows:

$$U_c = \frac{\delta x_m}{(t_2 - t_1)}$$

$$V_c = \frac{\delta y_m}{(t_2 - t_1)}$$

As a first step, we have determined values of U_c from streamwise correlations of velocity (u_i), pressure (p), and vorticity (ω_i) fields. Fig. 4a shows the profiles of U_c for u_i and p as functions of y, and Fig. 5a shows the profiles of U_c for vorticity (ω_i). Figs. 4b and 5b show the same profiles as functions of y^+.

It is surprising how closely the convection velocities for velocity and vorticity perturbations agree with each other. Moreover, these profiles closely agree with the mean velocity profile, being only slightly lower than mean velocity in the outer region, but being higher than the mean velocity near the wall. There are clear differences between the data presented here and those reported in literature. The convection velocity of pressure in the wall region is consistently higher than those of velocity and vorticity, indicating somewhat the elliptic nature of the pressure field.

Future extensions

(1) To determine V_c in addition to U_c. When correlation in (x and y) is used, the current value of U_c may be somewhat different from that found from the x-correlation alone.
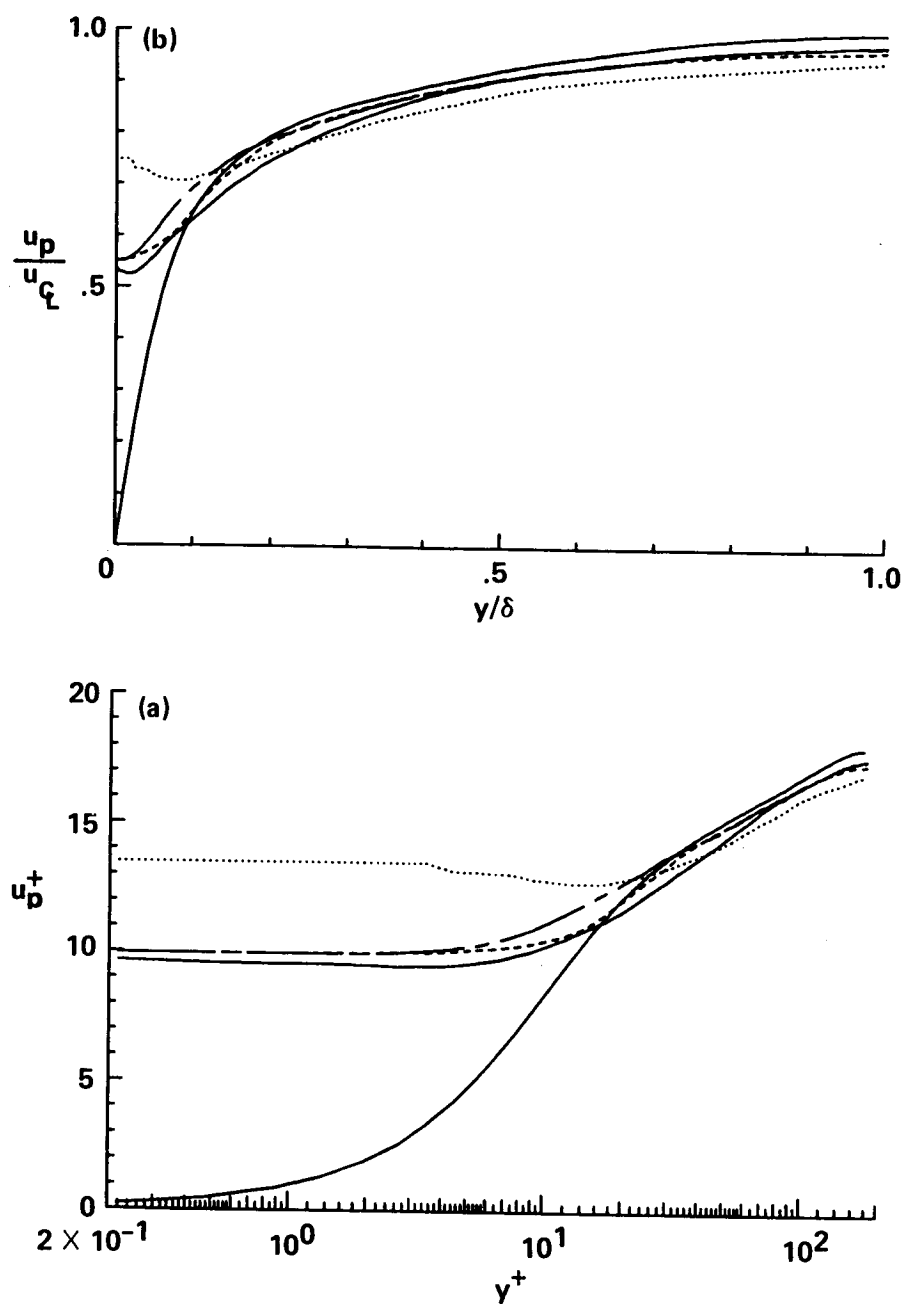
FIGURE 4. Propagation velocity for velocity and pressre (a) in global coordinate, (b) in wall coordinate: ——— , u; - - - - , v; — - — , w; ········· , p.
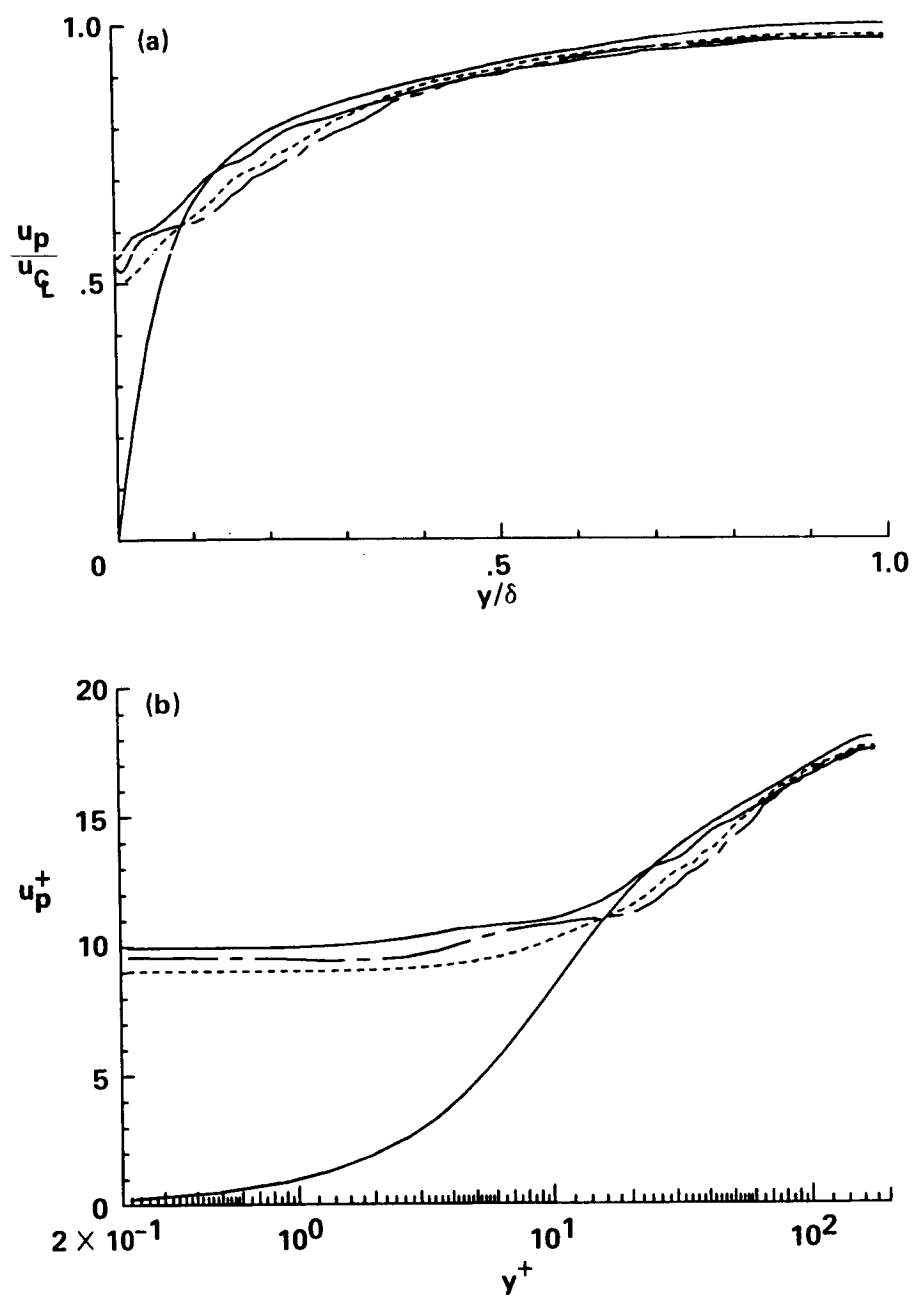
FIGURE 5. Propagation velocity for vorticity (a) in global coordinate, (b) in wall coordinate: ———— , ω_x; - - - - , ω_y; — · — , ω_z.

(2) Determine U_c and V_c for positive and negative ω_z separately.

(3) Determine U_c and V_c values for all variables in the two homogeneous shear flows.

C. Taylor hypothesis

The Taylor hypothesis of frozen turbulence is a common assumption in experimental turbulence for inferring spatial structure of turbulence from temporal data obtained by a stationary probe. It is also commonly invoked for inferring wave number spectrum from measured frequency spectrum as well as in measurements of dissipation and higher-order moments. While there have been extensive discussions of the limitation of the hypothesis, which were obviously known to Taylor himself, no direct test of this hypothesis has been possible yet. The direct numerical simulation databases allow us to make a thorough evaluation of this hypothesis for different flow variables as a function of shear rate.

The hypothesis assumes that

$$D_T \phi = (\frac{\partial}{\partial t} + U_T \frac{\partial}{\partial x})\phi = 0$$

where U_T is the Taylor advection velocity and ϕ can be any of the variables $\{u_i, p, \omega_i, c\}$. The value of U_T used in the literature has varied (Zaman & Hussain, 1981):

$$U_T = U(y), \qquad \text{mean velocity}$$
$$= u(x, y, z), \qquad \text{local velocity}$$
$$= U_c(y), \qquad \text{propagation velocity}$$
$$= u_f(x, y, z), \qquad \text{filtered velocity}$$

We have used the first, second and fourth in the 1987 CTR session. It is seen that both mean and rms values of $D_T \phi$ are small in the outer layer, except very close to the wall. Comparing instantaneous contours of $D_T \phi$ with the smoothed contours of u_i, ω_i, p, it is found that the departure from the hypothesis is not directly associated with large-scale structures.

Future extensions

(1) Compute vorticity fields using Taylor hypothesis and velocity fields, and compare with true vorticity fields.

(2) Determine which choice of U_T produces the minimum error in the use of the Taylor hypothesis.

(3) For situations when there are large values of $D_T \phi$, evaluate the various terms in the convective balance equations of ϕ. Determine which term (and hence which mechanism) produces the maximum contribution to the departure from $D_T \phi = 0$.

REFERENCES

CANTWELL, B. & COLES, D. 1983 An experimental study of entrainment and transport in the turbulent near wake of a circular cylinder . *J. Fluid Mech..* **136**, 321.

HAYAKAWA, M. & HUSSAIN, A.K.M.F. 1985 Eduction of coherent structures in the turbulent plane wake. 5th Symposium on Turbulent Shear Flows, Cornell University, August 7-9, 1985.

HUSSAIN, A.K.M.F. 1980 Lecture Notes in Physics (ed. J. Jimenez), Springer-Verlag, 1980.

HUSSAIN, A.K.M.F. 1983 Coherent structures — Reality and Myth. *Phys. Fluids.* **26.** 2763.

HUSSAIN, A.K.M.F. 1986 Coherent structures and turbulence. *J. Fluid Mech..* **173,** 303.

HUSSAIN, A.K.M.F. & ZAMAN, K.B.M.Q. 1980 Vortex pairing in a circular jet under controlled excitation. Part 2. Coherent structure dyanmics . *J. Fluid Mech..* **101,** 449.

HUSSAIN, A.K.M.F. & ZAMAN, K.B.M.Q. 1985 An experimental study of organized motions in the turbulent mixing layer. *J. Fluid Mech..* **159,** 85.

HUSSAIN, A.K.M.F., KLEIS, S.J. & SOKOLOV, M. 1980 A turbulent spot in an axisymmetric free shear layer. Part 2.. *J. Fluid Mech..* **98,** 97.

KIM, J., MOIN, P. & MOSER, R.D. 1987 Turbulence statistics in fully developed channel flow at low Reynolds number. *J. Fluid Mech..* **177,** 133.

LEE, M.J. & REYNOLDS, W.C. 1985 Numerical experiments on the structure of homogeneous turbulence, Report No. TF-24, Department of Mechanical Engineering, Stanford University, 1985.

METCALFE, R. HUSSAIN, A.K.M.F. & MENON, S. 1985 Coherent structures in a turbulent mixing layer: A comparison between direct numerical simulations and experiments, 5th Symposium on Turbulent Shear Flows, Cornell University, August 7-9, 1985.

MOIN, J. & KIM, J. 1982 Numerical investigation of turbulent channel flow . *J. Fluid Mech..* **118,** 341.

ROGERS, M.R. & MOIN, P. 1987 The structure of the vorticity field in homogeneous turbulent flows. *J. Fluid Mech..* **176,** 33.

SPALART, P. 1987 Direct simulation of a turbulent boundary layer up to $R_\theta = 1410$. NASA Technical Memorandum 89407.

TENNEKES, H. & LUMLEY, J.L. 1972 A First Course in Turbulence, The MIT Press, 1972.

TSO, J. 1983 Ph.D Thesis, The Johns Hopkins University, 1983.

ZAMAN, K.B.M.Q. & HUSSAIN, A.K.M.F. 1981 Taylor hypothesis and large-scale coherent structures. *J. Fluid Mech..* **112,** 379.

ZAMAN, K.B.M.Q. & HUSSAIN, A.K.M.F. 1984 Natural large-scale structures in the axisymmetric mixing layer. *J. Fluid Mech..* **138,** 325.

Inflectional Instabilities in the Wall Region of Bounded Turbulent Shear Flows

By JERRY D. SWEARINGEN,[1] RON F. BLACKWELDER,[1] and PHILIPPE R. SPALART[2]

Objective

The primary thrust of this research was to identify one or more mechanisms responsible for strong turbulence production events in the wall region of bounded turbulent shear flows. Based upon previous work in a transitional boundary layer (Swearingen & Blackwelder 1987), it seemed highly probable that the production events were preceded by an inflectional velocity profile which formed on the interface between the low-speed streak and the surrounding fluid. In bounded transitional flows (Swearingen & Blackwelder 1987, Finlay, Keller & Ferziger 1987), this unstable profile developed velocity fluctuations in the streamwise direction and in the direction perpendicular to the sheared surface. The rapid growth of these instabilities leads to a breakdown and production of turbulence. Since bounded turbulent flows have many of the same characteristics, i.e., strong shear, low-speed regions, oscillatory motions, etc., they may also experience a similar type of breakdown and turbulence production mechanism.

Methodology

From the turbulent-boundary-layer direct numerical simulation of Spalart (1988), the instantaneous velocity, pressure, and vorticity fields were readily available. The first effort was devoted to examining these fields visually through the wonders of the IRIS workstation. The spanwise shear, $\partial u/\partial z$, was examined as well as the related normal vorticity, ω_y. The inflectional profile associated with the shear layer with this orientation may be unstable in the Kelvin-Helmholtz sense and produce u and w fluctuations. Hence, the role of the spanwise velocity fluctuations was deemed to be important. Secondly, these fluctuations were studied to see whether the average structure associated with w indicated turbulence production. A detection method based on w using a VISA and quadrant technique was obtained by modifying existing software programs within the CTR. Thus, the shear $\partial u/\partial z$, etc., could be conditionally averaged to educe the relevant parameters leading up to and associated with the turbulence- production events.

1 U. S. C.

2 NASA Ames Research Center

u′

ω′y
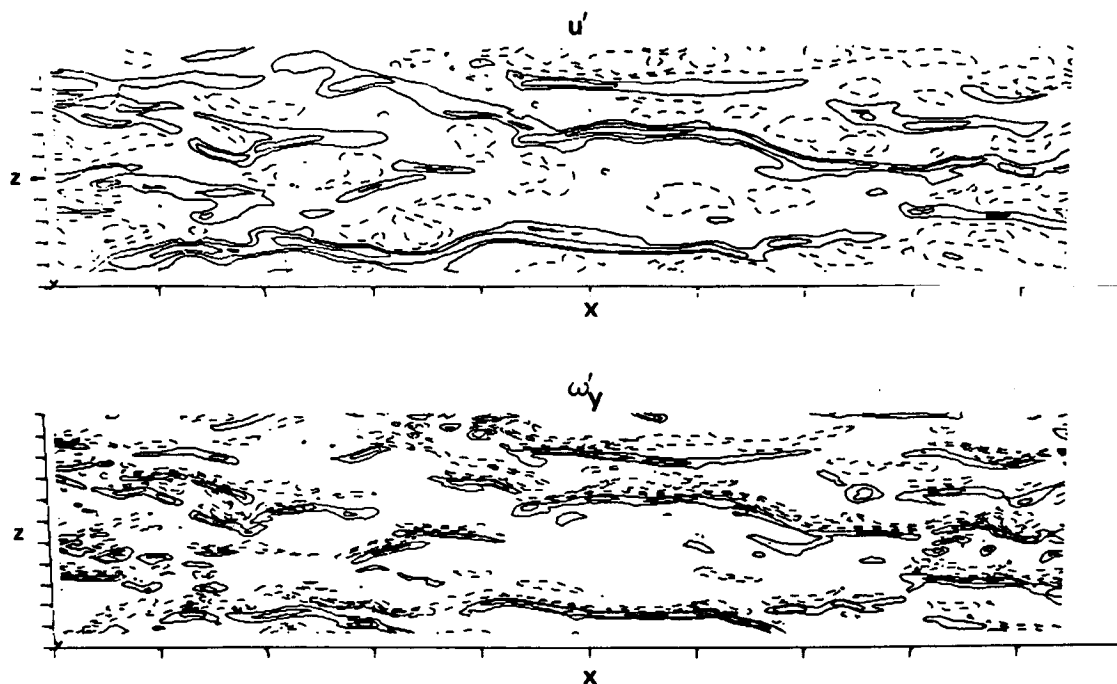
FIGURE 1.   Contours in an $x - z$ plane. a) Streamwise velocity fluctuations u'; b) normal vorticity ω'_y

Results

All of the results reported here were obtained from the boundary-layer-simulation data of Spalart (1988) for $R_\theta = 670$. The visual observations of the instantaneous velocity field near the wall revealed that the low-speed streaks were surrounded by regions of strong shear. On both sides of the streak (see Fig. 1), $|\partial u^+/\partial z^+|$ was typically between 0.2 and 0.5 with opposite signs on the two sides. Above the streaks, $\partial u^+/\partial z^+$ was also large and had similar values. Three-dimensional plots of the modulus

$$\left(\frac{\partial u^{+\,2}}{\partial y^+} + \frac{\partial u^{+\,2}}{\partial z^+}\right)^{1/2}$$

showed that in the region $15 < y^+ < 80$ it had its largest magnitude and was typically beside and above the low-speed streak.

In many instances, the low-speed region undulated, i.e., moved in the spanwise direction with a wavy motion. This movement was similar to those observed by Swearingen & Blackwelder (1987) and Finlay et al. (1987), and had a streamwise wavelength of $100 - 200$ ν/u_τ. As a time sequence of the low-speed region was followed, the undulating motion was seen to grow in amplitude and finally break up into chaotic motion.

Closer study of this motion revealed that the undulation was associated with strong w fluctuations. Data at $y^+ = 15$ were used to examine this aspect of the

low-speed streaks. A quadrant technique program was developed to plot the intense regions in quadrants 2 and 3 of the uw plane; i.e., those regions whose magnitude exceeded $4\,u_\tau^2$ were plotted. The instantaneous field had three important characteristics: first, those spatial regions where quadrant-2 events were occurring had a preferred direction that made an angle with the streamwise direction of 10 to 15° in the $x - z$ plane. Similar quadrant-3 events were aligned at -10 to $-15°$ forming a cone opening downstream and extending over a streamwise extent of 600 to 1200 ν/u_τ. Secondly, the exact locations of the quadrant-2 and -3 events were often aligned with the locations where the low-speed streaks were turning in their undulatory motion; i.e., at the corners where the low-speed streak changes its direction. Thirdly, by plotting the quadrant-2 and -4 uv events (i.e., the high-production events in the Reynolds average sense) from the same data, the uw events were observed to occupy a much larger spatial extent than the corresponding uv events; i.e., the uw events had longer scales.

It was also observed that the corners of the undulating streaks were often in the process of being lifted away from the wall. A similar quadrant technique was used to examine the simultaneous v and w motions; namely, quadrants 1 and 4 in the vw plane. This motion, which had large amplitudes in these quadrants with $v > 0$, were compared with the streaks of the same data. The vw events were much less frequent than either the uw or the vw events. When they occurred, however, they generally denoted regions of the streaks near the corners that had been lifted. As these events were followed visually downstream, they broke up into chaotic motion.

Auxiliary results

If the turbulence production is associated with inflectional velocity profiles, then any disturbance at the inflection point should begin growing where an inflection occurs. The rate of growth is directly proportional to the shear at the inflection point, as described by Drazin & Reid (1984). Thus $U(z)$ data in the $y^+ = 15$ plane were searched for points of inflection, and the value of the gradient $\partial u/\partial z$ was recorded. Similar results were obtained for the values of $\partial u/\partial y$ at the inflection points in the $x - y$ plane in the range $10 < y^+ < 20$. These data were used to construct the conditional probabilities of the shear at the inflection points shown in Fig. 2. The conditional probability of $\partial u/\partial z$ is close to being symmetrical about the origin, consistent with spanwise symmetry, and has peaks at $\pm 0.16\,u_\tau^2/\nu$.

The joint probability distributions of uw, uv, and vw were recorded to ascertain whether the embedded undulating motion described earlier could be detected in the standard statistics. The uw distributions were symmetrical about the $w = 0$ axis, as expected, but were asymmetrical about the $u = 0$ axis. Similar results were obtained for the vw joint distribution.

A preliminary attempt was made to determine where the largest changes in the flow structure occurred as the flow was convected downstream. The convection velocity, U_c, was obtained by comparing two data planes at the same y^+ value but displaced in time by $\Delta t^+ = 9$. The second plane was shifted in the x direction by a distance of $U_c\Delta t$ to form the function $f(x + U_c\Delta t, t_o + \Delta t)$ and the difference $\delta(x)$
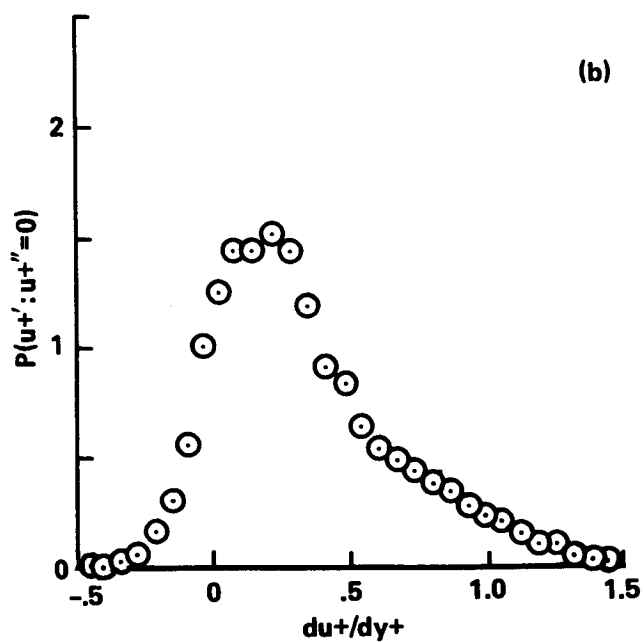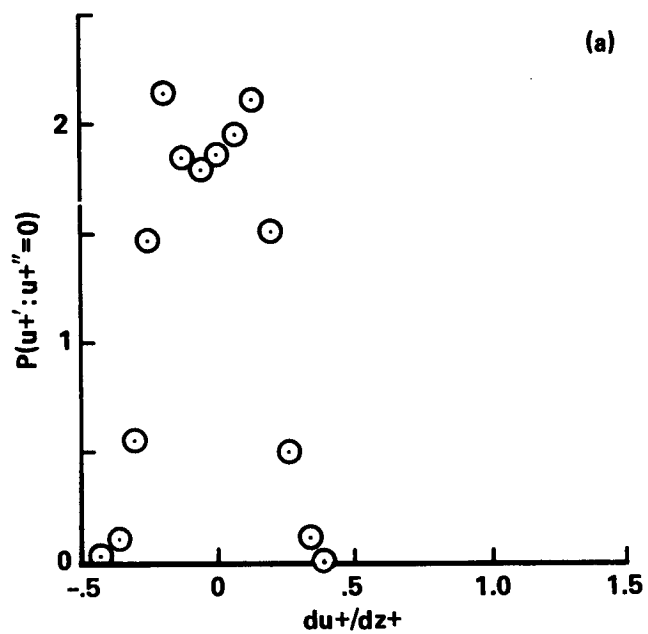
FIGURE 2. Conditional probability distributions at inflection points: a) du^+/dz^+; b) du^+/dy^+

with the first plane $f(x, t_o)$ obtained. The minimization of the mean square of the differences, δ, was used to determine the convection velocity U_c. The convection velocity in the logarithmic and outer region of the flow followed the mean velocity within the accuracy of the calculation. However, for all values of $y^+ < 10$, the convection velocity was constant at $U_c \approx 10 \, u_\tau$ for all flow variables; i.e., the velocities, vorticities, and pressure. This result could be very important for understanding the physics and for modeling and should be pursued further.

Summary

The results support the idea that an inflectional instability may be associated with and responsible for the disintegration of the low-speed streaks in the wall region. There was often a strong shear and an inflectional velocity profile surrounding the low-speed region. The time sequences indicated that this condition persisted up to $60 \, \nu/u_\tau^2$, indicating sufficient time for an instability to develop. The low-speed streaks developed an oscillatory motion which increased as time progressed, also indicative of an instability. The v and w velocity components became large during this motion, in accordance with an instability mechanism. In the last available time frame of the data observed in detail, the undulating portion of the streaks appeared to be breaking up into chaotic motion.

Future work

The work has been based primarily upon a study of the instantaneous data. In the future, one hopes to be able to apply conditional sampling to the data. The 1st and 4th quadrants of vw seemed to be the best detection function to pursue.

The fact that the convection velocity in the wall region was found to be constant at about $10 \, u_\tau$ has important implications for the wall structure, as well as modeling. It is hoped that this work can also be continued in conjunction with J. Kim.

REFERENCES

SWEARINGEN, J. D., AND BLACKWELDER, R. F. 1987 "The Growth and Breakdown of Streamwise Vortices in the Presence of a Wall". To appear in *J. Fluid Mech.*

FINLAY, W. H., KELLER, J. B., AND FERZIGER, J. H. 1987 "Instability and Transition in Curved Channel Flow". Report TF-30, Mech. Engr., Stanford Univ.

SPALART, P. R. 1988 "Direct Simulation of a Turbulent Boundary Layer up to $R_\theta = 1410$". *J. Fluid Mech.*. **187**, 61.

DRAZIN, P. G., AND REID, W. 1984 Hydrodynamic Stability. Cambridge Univ. Press, London.

Active layer model for wall-bounded turbulence

By M. T. Landahl[1] J. Kim[2] and P. R. Spalart[2]

The active-layer model for wall-bounded turbulence hypothesizes that the non-linear terms are large only in a thin layer near the wall, and hence the turbulence in the region outside the active inner layer can be modeled as a linear fluctuating flow driven by the active layer. This hypothesis is tested using data obtained from a direct simulation of turbulent channel flow. It is found that the nonlinear effects are the strongest near the wall with a maximum at around $y^+ = 20$ and, outside the near-wall region, these involve primarily the cascading mechanism leading to dissipation.

1. Introduction

Laboratory experiments and numerical simulation have shown that the turbulent activity in wall-bounded turbulence is the highest in the immediate neighborhood of the wall, in the viscous and buffer layers. Therefore, nonlinear effects may be expected to be strongest in this region. A possible model for the turbulent field might therefore be to consider the turbulence in the region outside an active inner layer as a linear fluctuating flow driven by the active layer (Fig. 1).

2. Analysis

We subdivide the flow field in a parallel mean flow, $U(y)\delta_{i1}$, and a fluctuating field, u, v, w, p. By elimination of the pressure from the momentum equations, making use of the continuity equations in the process, the following equation for the v-component is found (Landahl, 1967):

$$L_{OS}(v) = q \tag{1}$$

where L_{OS} is the (space-time) Orr-Sommerfeld operator,

$$L_{OS}(v) = (\partial/\partial t + U\partial/\partial x)\nabla^2 v - U''\partial v/\partial x - \nu\nabla^4 v \tag{2}$$

and q contains all the nonlinear terms,

$$q = \nabla^2 T_2 - \partial^2 T_i/\partial x_i \partial x_2 \tag{3}$$

where

$$T_i = \partial\tau_{ij}/\partial x_j \tag{4}$$

1 Massachussets Institute of Technology

2 NASA Ames Research Center
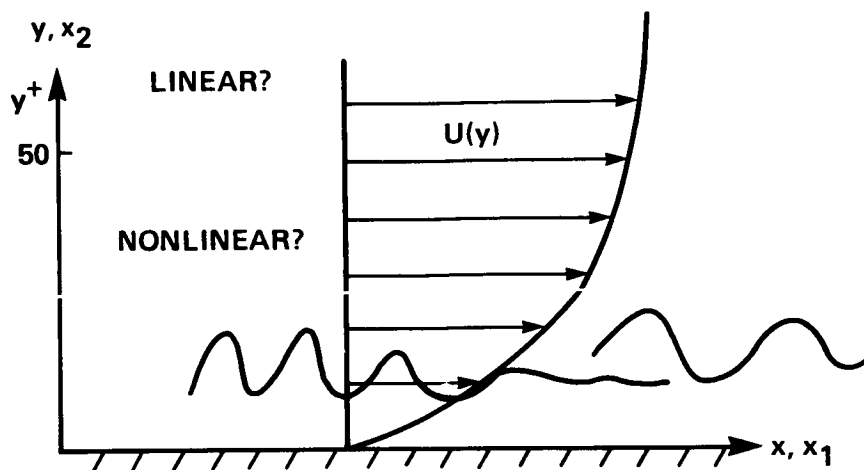
FIGURE 1. A model of wall-bounded turbulence consist of active non-linear inner layer and a linear fluctuating outer layer driven by the active layer.

with

$$\tau_{ij} = -u_i u_j \qquad (5)$$

The solution of (1) assuming q to be given may be determined by applying Fourier transformation in x, z and t, which yields

$$(U - c)(\hat{v}'' - k^2\hat{v}) - U''\hat{v} - (1/ik_x)(d^2/dy^2 - k^2)^2\hat{v} = \hat{q}/ik_x \qquad (6)$$

where the caret denotes a Fourier-transformed quantity, k_x and k_z, denote the x- and z-components of the wave number k, respectively, and $c = \omega/k_x$.

3. Calculation of the Reynolds stress

The basic hypotheses in the active-layer model are that the nonlinear terms are large only in a thin region near the wall and that the flow in the region outside this layer may be found by considering q as a given and driving an outer linear fluctuating flow field. From the statistics of q one may then determine any desired statistical quantity such as the mean Reynolds shear stress,

$$\tau = -\rho < uv > \qquad (7)$$

By applying Fourier transform to the component equations and using Parseval's formula relating quadratic mean quantities to their transforms, one finds, upon neglecting viscous terms, that the wave number spectrum, S_τ, for the Reynolds shear stress, is related to the spectrum for the v-fluctuations through

$$S_\tau' = (k_z/k)^2 \quad (d/dy)(U' S_v^c) + (k_x/k)^2 \quad U'' S_v^c \qquad (8)$$

where S_v^c denotes the spectrum of v in a reference frame convected with the mean velocity $U(y)$, and the prime denotes differentiation with respect to y. From (6), it

follows that for small viscosity the v- fluctuations may receive their largest contributions from the region near $k_x = 0$, in which case the second term in (8) will be negligible, and with $k = k_z$ one finds after integration that

$$S_\tau = U' S_v^c \tag{9}$$

a result that may be shown to be consistent with Prandtl's mixing-length hypothesis.

4. Application to channel flow turbulence

The basic hypothesis on which the present model is based, namely, that the nonlinearities are important only in a thin region near the wall, may be tested with the aid of the numerical turbulence simulations. A fairly extensive data base for turbulent channel flow has been generated in the NASA-Ames numerical simulations, although limited to fairly low Reynolds numbers. From the computed data, the nonlinear terms of (1) may be extracted and appropriate statistical quantities determined. Since the detailed temporal evolution is not so easily accessible because of the way the data are stored, for a preliminary assessment of the soundness of the basic hypothesis of the present model, the spatial mean and power spectrum of a single time realization was determined from the computed velocity field. The results are shown in Figs. 2 and 3. In Fig. 2, the root-mean- square value of q is presented (arbitrary scale). It has a maximum at around $y/h = 0.1$ ($h =$ channel half width), which corresponds to $y^+ = 18$, and drops off to a value of about one tenth of the maximum towards the center of the channel. The spectra shown in Fig. 3 for different distances from the wall are found to be fairly flat in the wall and buffer regions, with the cutoff in k_z at a higher value than for k_x, reflecting the dominance of high streamwise elongation of the dominating structures. The spectrum at $y^+ = 76$ (Figs. 3g and 3h), however, which is well outside the buffer layer, has its main contribution from the high wave-number range (both in k_x and k_z). This probably reflects the nonlinear cascading mechanism involved in dissipation. The production of Reynolds stress resulting from this spectrum is not large, however, since it receives its main contributions from the low k_x-end. The part of the q-spectrum responsible for the production can therefore be expected to be even more concentrated in the near-wall region.

5. Conclusion

The model proposed for wall-bounded turbulence, namely, that the nonlinear driving of the turbulent fluctuations is concentrated in the near-wall region, in the viscous and buffer regions, has been tentatively examined using data from the NASA-Ames channel-flow simulations. The preliminary findings are that the nonlinear effects are the strongest near the wall, with a maximum at around $y^+ = 20$, and that outside the near-wall region they involve primarily the cascading mechanism leading to dissipation. The mean and the spectra were obtained from a single time realization; for a more general treatment, one would need to work with ensemble averages over a large number of realizations, as well as to employ spectra in
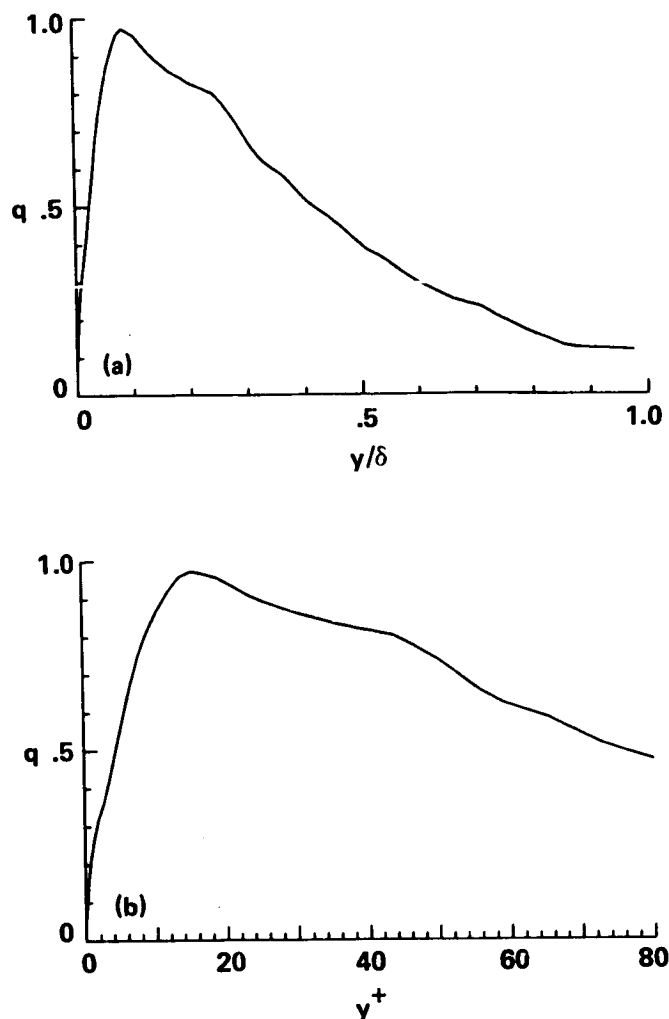
FIGURE 2.   Profiles of the root-mean-square values of q in Eqn. (1).

a frame of reference convected with the local mean velocity. If found to be sound, this model will lead to a reasonably simple procedure for determining the Reynolds stresses and other statistical quantities through a comparatively simple linear calculation making use of a universal model for the nonlinear processes in the near-wall region, the statistics of which may be found from numerical simulations carried out at modest Reynolds numbers.

REFERENCES

LANDAHL, M. T. 1967 A wave-guide model for turbulent shear flow. *J. Fluid Mech.* **29**, 441.
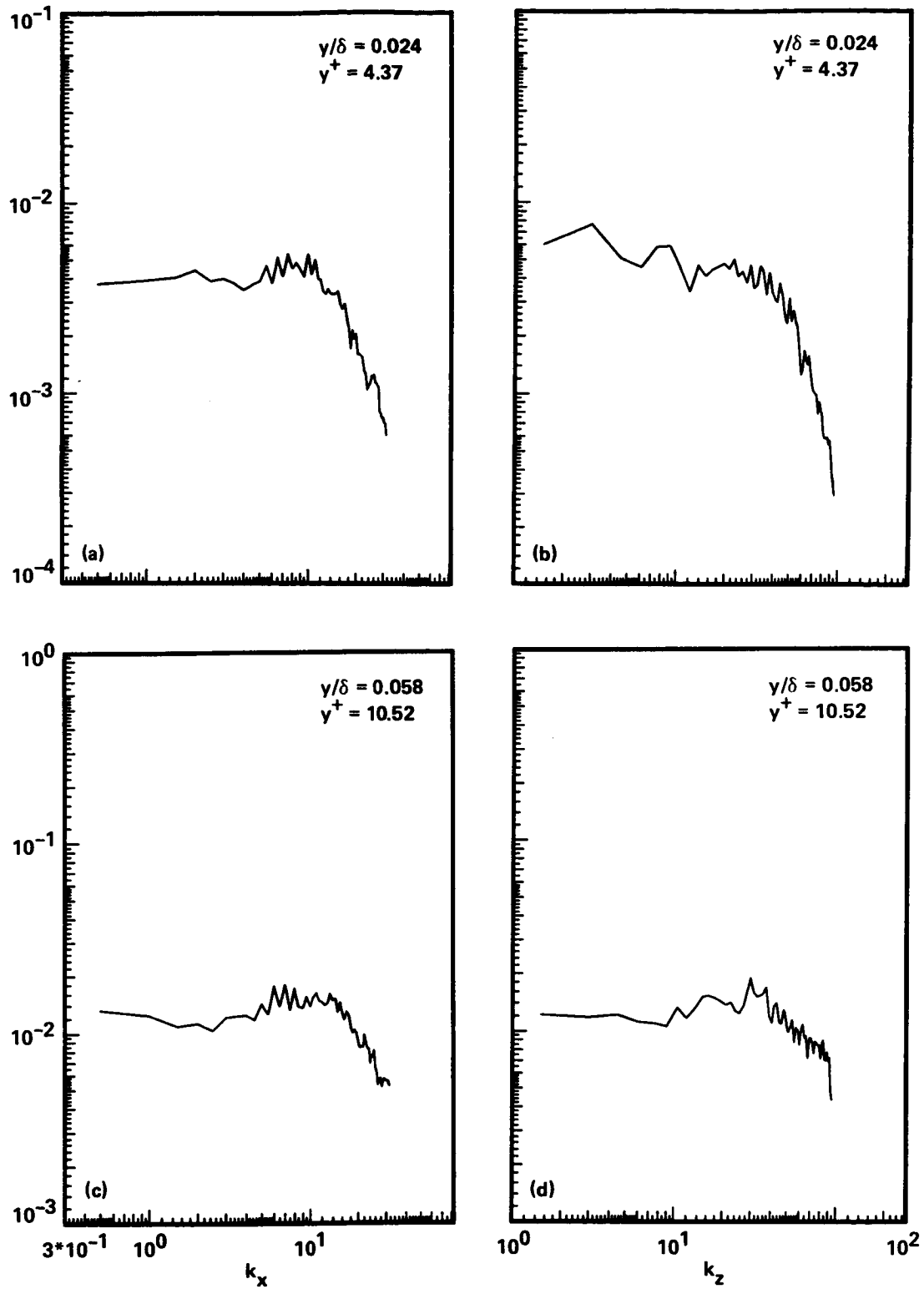
FIGURE 3. Spectra of q at different y-locations.
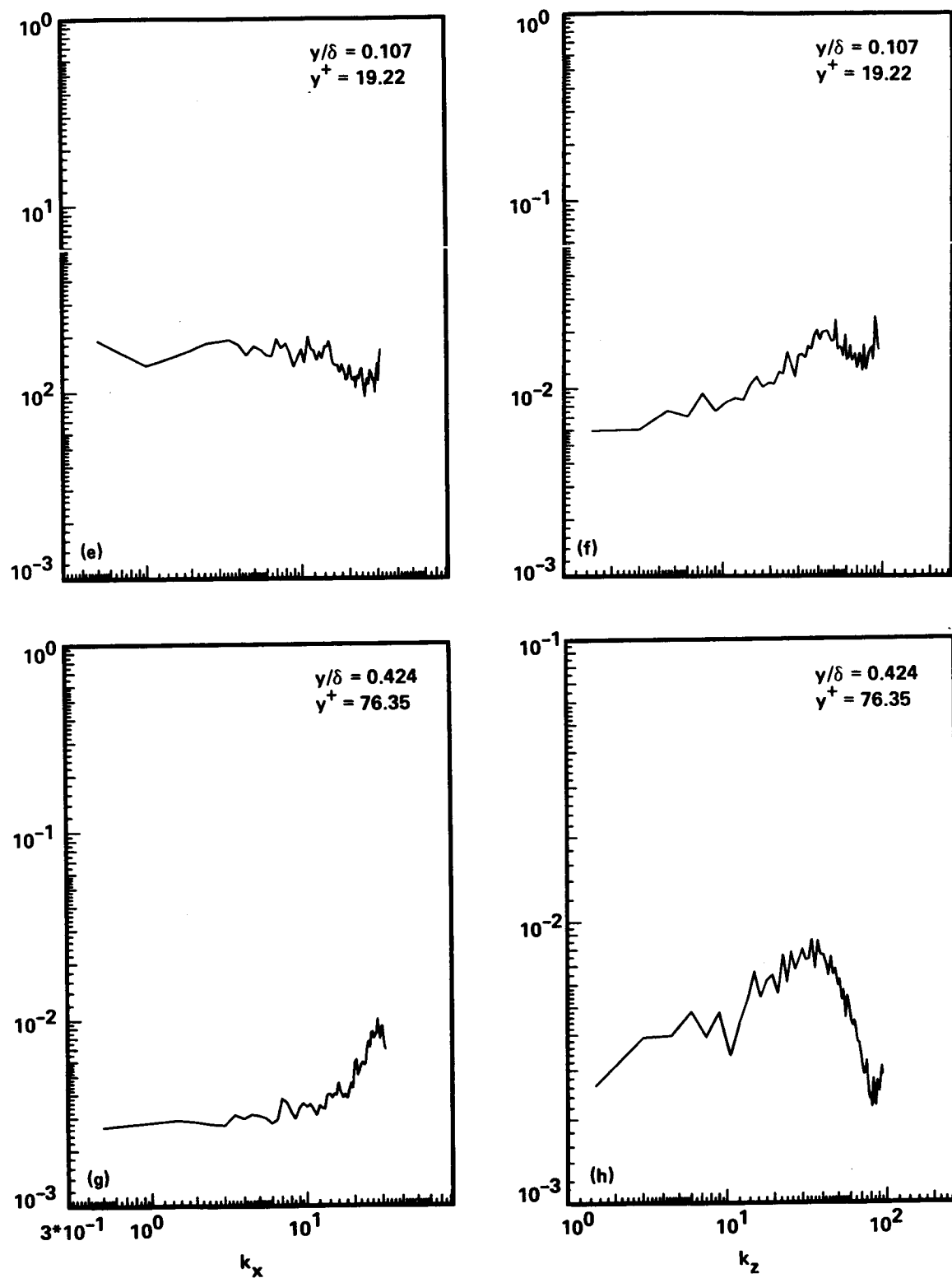
FIGURE 3.   ... continued.

Wave-growth associated with turbulent spot in plane Poiseuille flow

By D. S. Henningson[1], M. T. Landahl[2] and J. Kim[3]

A kinematic wave theory is used to investigate the cause of the rapid growth of waves observed at the wingtip of turbulent spot in plane Poiseuille flow. It is found that the qualitative behavior of the wave motions is well described by Landahl's breakdown criterion as the wave selection procedure. The predicted wave number, wave angle, and phase velocity are in agreement with those values obtained in a direct simulation.

1. Introduction

A localized disturbance in plane Poiseuille flow can develop into a turbulent spot if the Reynolds number ($Re = U_{CL}h/\nu$, where U_{CL} is the center line velocity and h is the half-channel height) is above about 1000. Experiments (Carlson et al. 1982; Alavyoon et al. 1986; Henningson & Alfredsson 1987) have shown that oblique waves develop around the spot as it propagates downstream. Henningson & Alfredsson (1987) observed the waves on the *wingtips*, i.e. the sides of the spot, consisted of the least stable Tollmien-Schlichting (T-S) mode. A recent numerical simulation of a Poiseuille flow spot (Henningson et al. 1987) shows that the wingtip wave-packet extends into the spot where the waves attain very high amplitude before they break down into turbulence. This indicates that the waves do play an important role in the rapid spanwise growth of the spot. In boundary layer spots (Chambers & Chambers 1983), however, waves are not seen to play such a role. This poses the following questions. Is the spreading of the two spots caused by different mechanisms? Are the waves just a passive response to disturbances in the surrounding laminar flow induced by the turbulence fluctuations? As a first step toward resolving these questions the present work addresses the cause of the rapid growth of the waves observed in Poiseuille spots. The related question of wave selection mechanism will also be considered.

2. Analysis

The wave pattern to be analyzed is shown in Fig. 1. Detailed descriptions of the computations can be found in Henningson et al. (1987). In what follows, all dimensional quantities are non-dimensionalized by the centerline velocity, U_{CL},

1 Aeronautical Research Institute of Sweden (FFA)
2 Massachussets Institute of Technology
3 NASA Ames Research Center

and the channel half-width, h, and x, y, and z denote the streamwise, vertical and spanwise directions, respectively. Fig. 1a shows a top view of ± 0.01 contours of the vertical velocity at the channel centerline. The front part of the spot has travelled a distance of about 200 from its generation point at this time, $t = 258$. Fig. 1b shows the modal shape of the waves for the first few amplitude maxima and Fig. 1c shows the corresponding spanwise amplitude variation at the centerline. The waves are seen to grow almost an order of magnitude as they propagate into the spot, while their modal shape still is essentially that of the simplest linear mode, i.e. the T-S wave. The calculations by Henningson et al. (1987) have shown that the phase speed in the streamwise direction of the waves are approximately 0.6, the absolute value of the wave number vector ($k = \sqrt{\alpha^2 + \beta^2}$) about 1.8, and the angle (ϕ) between the wave number vector and the streamwise direction about -65°. The velocity of the spot interface at the wingtip is approximately 0.7 in the streamwise direction and 0.12 in the spanwise direction. (The interface here is taken to be where the vertical velocity exceeds 0.02.)

A plausible explanation of the wave growth seen at the wingtip is interaction between the changing mean profile and the waves. If the time and spatial scales of the mean motion and the waves are widely separated, kinematic wave theory (Witham 1974) is appropriate to analyze their interaction. The starting point of the theory is a wave packet of the form,

$$ae^{i\theta}, \qquad \theta = \alpha x + \beta z - \omega t$$

where a, α, β and ω are assumed to be slowly varying functions of space and time. The waves are assumed to have a known dispersion relation

$$\omega = W(\alpha, \beta, x, z, t)$$

which relates the variation of the angular frequency to the wavenumber vector components. Using the definition of the phase, θ, and the dispersion relation, it can be shown (Witham 1974),

$$\frac{d\alpha}{dt} = -\frac{\partial W}{\partial x}$$

$$\frac{d\beta}{dt} = -\frac{\partial W}{\partial z}$$

$$\frac{d\omega}{dt} = \frac{\partial W}{\partial t}$$

$$\frac{1}{A}\frac{dA}{dt} = -\frac{\partial}{\partial x}\frac{\partial W}{\partial \alpha} - \frac{\partial}{\partial z}\frac{\partial W}{\partial \beta}$$

along the rays defined by

$$\frac{dx}{dt} = \frac{\partial W}{\partial \alpha}$$

$$\frac{dz}{dt} = \frac{\partial W}{\partial \beta}$$
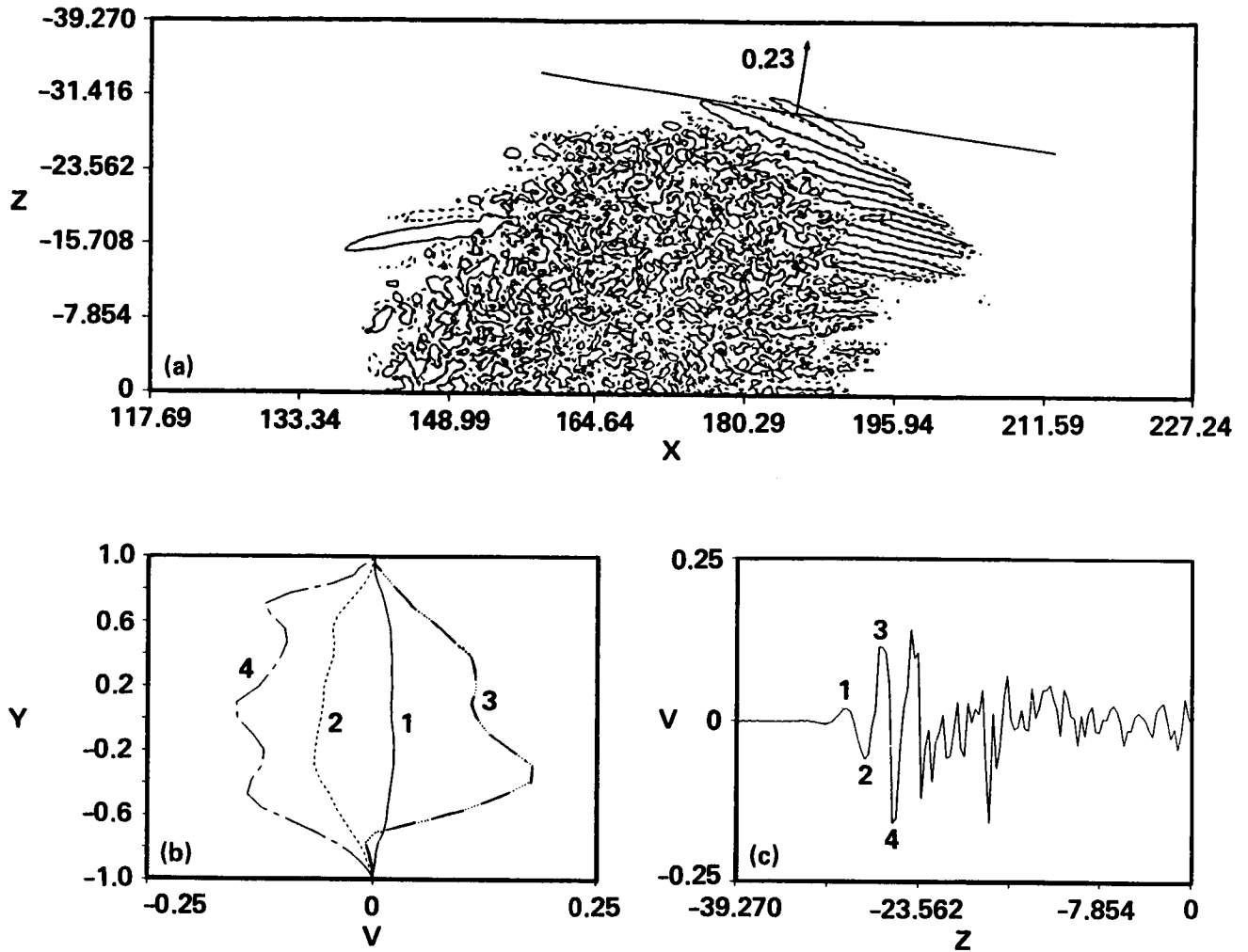
FIGURE 1. (a) A top view of ± 0.01 contours of the vertical velocity at the channel centerline: t=258, Re=1500. (b) Profiles of the vertical velocity for the first few amplitude maxima: ———, x=186, z=-29.8; – – – –, x=186, z=-28.2; ·········, x=186, z=-26.7; — · —, x=186, z=-25.5. (c) Spanwise variations of the vertical velocity at x=186 and y=0.

where A is the wave action density, which is proportional to the square of the wave amplitude. The wave properties are seen to vary along the rays given by the group velocity, $\vec{c}_g = (\partial W/\partial \alpha, \partial W/\partial \beta)$. Landahl (1972) applied the above theory to oblique T-S waves riding on an inhomogeniety consisting of a larger scale locally two-dimensional wave. He was able to integrate the equation for the wave action density along a ray to yield

$$\frac{A}{A_0} = \frac{1}{c_{gn} - c_0}$$

where c_{gn} is the group velocity of the small scale oblique waves normal to the larger

two-dimensional wave, and c_0 is the phase velocity of the two-dimensional wave. Notice when c_{gn} approaches c_0 the wave amplitude will increase dramatically. This is a result of wave energy focusing. When the oblique waves approach the larger wave, their energy piles up on top of the large one since energy is constantly supplied by the incoming waves but no energy can leave, this results in an increase in the amplitude of the oblique waves.

As a first try we shall assume that the edge of the spot, where the waves are found, is locally two-dimensional, and we use the Landahl's breakdown criterion (Landahl 1972): i.e., we will examine if the group velocity of the wingtip waves, for any combination of wave numbers and frequency, is equal to the edge velocity at the wingtip. If the breakdown criterion is satisfied for a specific combination of α, β and ω, then the wave will experience a rapid growth as it approaches the spot edge. Thus, this provides both a mechanism for growth and selection of the waves.

The dispersion relation for the T-S waves are found by solving an extended form of the Orr-Sommerfeld equation (see Henningson et al 1987). The appropriate mean velocity is

$$U(y) + W(y)tan(\phi)$$

where U and W are the mean streamwise and spanwise velocity components, respectively. U and W are found by horizontal averaging and the required combination is fitted to a modified parabola

$$(1 - y^2)(c_0 + c_2 y^2 + c_4 y^4)$$

where c_0, c_2 and c_4 are fitting constants. Profiles are fitted to the velcities seen in Fig. 2 using the appropriate wave angle (only $\phi = 65°$ is shown in the figure). They are obtained from the position indicated at the wingtip in Fig. 1a; the line in Fig. 1a indicates the tangent of the spot edge at this position and the arrow is in the direction of motion. Note that as the wave angle becomes large the departure of the fitted velocity profiles from the parabolic one become greater. This results from the inflectional character of the spanwise mean velocity, which have larger weight for higher wave angles.

When the Orr-Sommerfeld equation is solved, the dispersion relation found is usually complex. This requires a modification of the kinematic wave theory. Landahl (1972) used a simple approach, which involves adding a growth/decay rate term in the equation for the wave action density and the use of the real part of the dispersion relation when the group velocity is calculated. This requires small growth/decay rates and that the development of the wave packet is considered for short times only. Assuming this to be true the breakdown criterion is still valid (Landahl 1982). In the following we will thus use the real part of the dispersion relation in our effort to look for waves that satisfy the breakdown criterion.

3. Results and Discussion

Results from the solution of the Orr-Sommerfeld equation for the position indicated at the wingtip in Fig. 1a can be seen in Figs. 3-5. Contours of the group
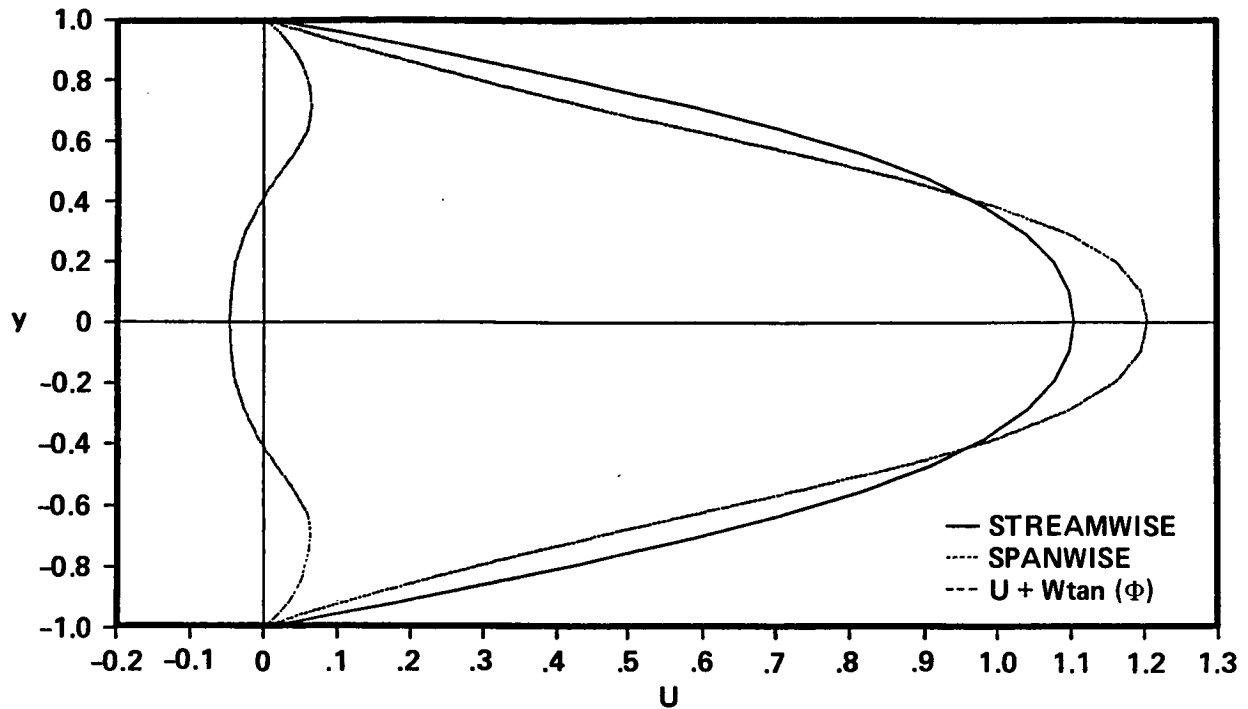
FIGURE 2.   Mean velocity profiles at x=186, z=-30 and $\phi = -65°$.

velocity perpendicular to the spot edge (i.e. in the direction of the arrow in Fig. 1a) are plotted as a function of k and ϕ in Fig. 3. Figs. 4 and 5 show contours of the phase velocity in the streamwise direction and the imaginary part of the dispersion relation. Note that the group velocity attains its maximum of 0.25 for $k = 1.0$ and $\phi = 45°$ (Fig. 3). The edge velocity at this location from the simulation was 0.23. The breakdown criterion is thus seen to be approximately fulfilled for $k = 1.0$ and $\phi = 45°$. This particular wave should grow to large amplitude at the wingtip of the spot. The waves actually observed has both higher wave number, wave angle and phase velocity. However, the waves are damped at this position (see Fig. 5) and only experience exponential growth for higher wave angles. Thus we might expect to find a wave that approximately fulfills the breakdown criterion and at the same time is gowing exponentially. To find such a wave we follow the ridge going from the peak value in Fig. 3 up towards higher wave numbers. At around k=1.7 and $\phi = -65°$, the waves start to grow. This is close to the observed wave parameters. It should be noted here that this is an approximate analysis and that exact agreement cannot be expected. However, it is encouraging to see that the the qualitative behavior of the normal group velocity, with its ridge going through the observed values, is able to select a wave using the breakdown criterion together with the requirement of exponential growth, and thus explain the observed wave motions. It should be an worthwhile effort in a future study to attack the full problem by tracing the wave rays into the spot and calculating the amplitude along them.
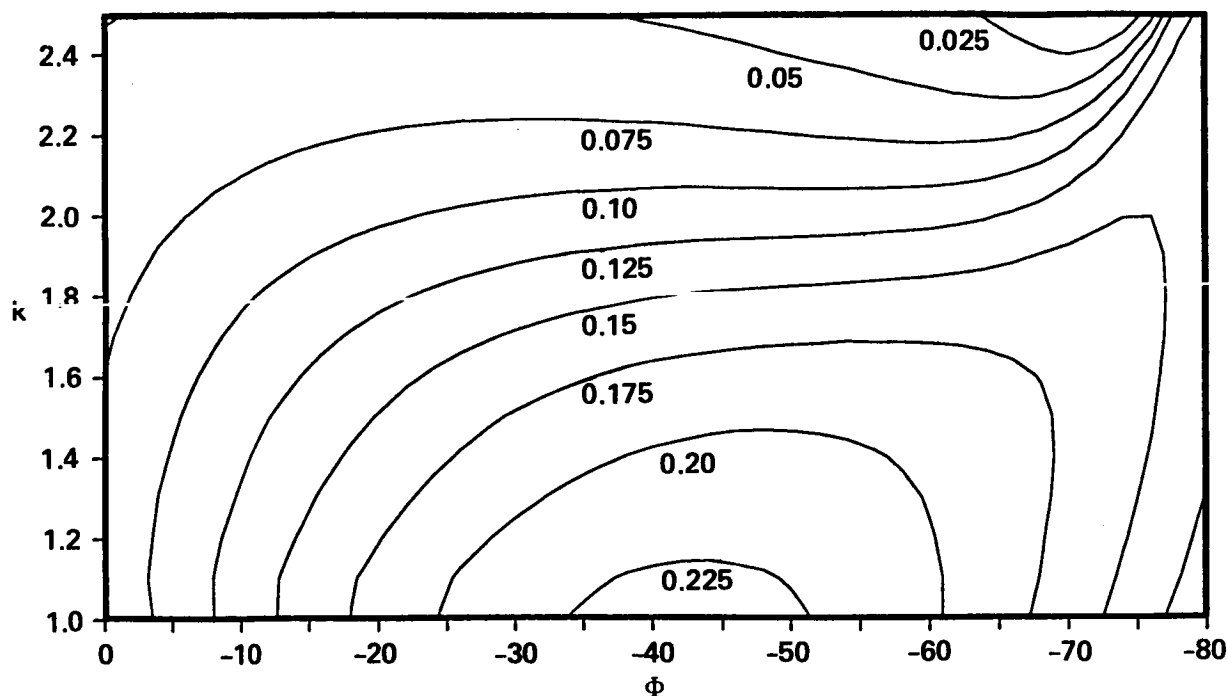
FIGURE 3. Contours of the group velocity perpendicular to the spot edge (i.e. in the direction of the arrow in Fig. 1a).

Finally, the picture that emerges from the present analysis is that the waves outside the spot are first generated by the moving turbulent disturbance, as discussed by for example Li & Widnall (1987), then they experience a growth by the wave energy focusing mechanism and the inflextional character of the effective mean velocity profile.

REFERENCES

F. ALAVYOON, D. S. HENNINGSON, & P. H. ALFREDSSON 1986 Turbulent spots in plane Poiseuille flow - flow visualization. *Phys. Fluids* . **29**, 1328-1331.

D. R. CARLSON, S. E. WIDNALL, & M. F. PEETERS 1982 A flow-visualization study of transition in plane Poiseuille flow. *J. Fluid Mech..* **121**, 487-505.

F. W. CHAMBERS & A. S. W. CHAMBERS 1983 Turbulent spots, wave packets and growth. *Phys. Fluids.* **26**, 1160-1162.

D. S. HENNINGSON & P. H. ALFREDSSON 1987 The wave structure of turbulent spots in plane Poiseuille flow. *J. Fluid Mech..* **178**, 405-421.

D. S. HENNINGSON, P. R. SPALART & J. KIM 1987 Numerical simulations of turbulent spots in plane Poiseuille and boundary layer flows. *Phys. Fluids.* **30**, 2914-2917.

M. T. LANDAHL 1972 Wave mechanics of breakdown. *J. Fluid Mech..* **56**, 775-802.
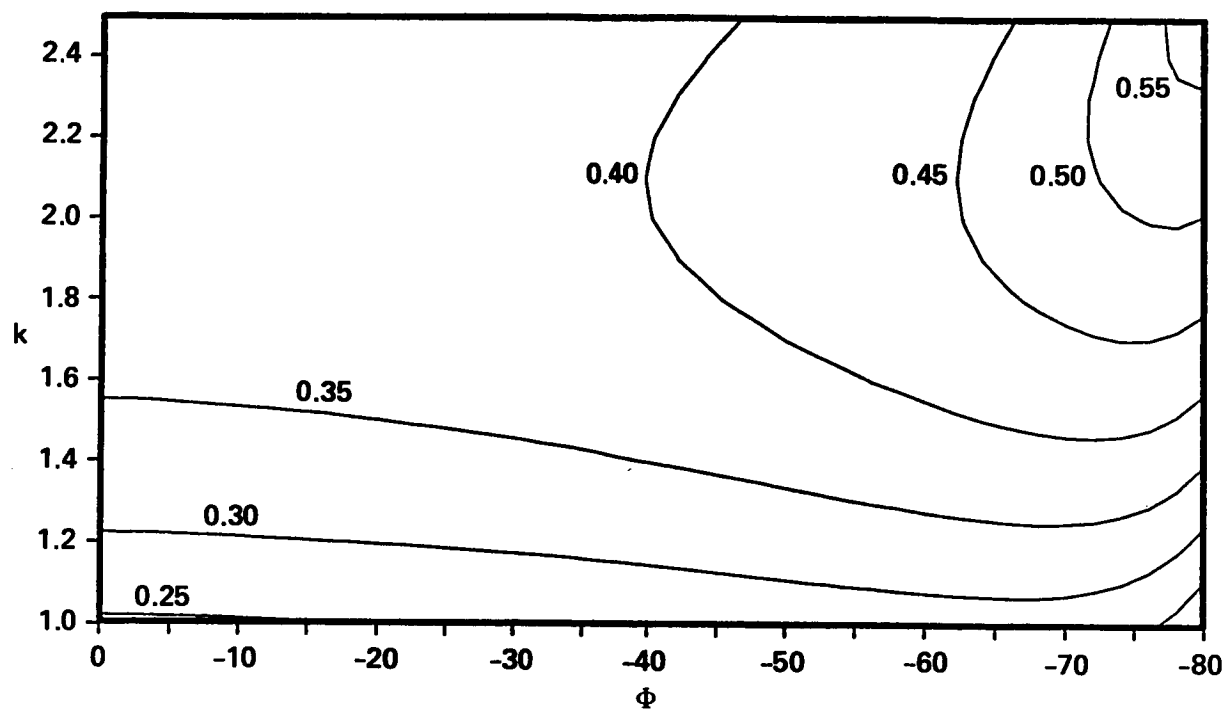
FIGURE 4. Contours of the phase velocity in the streamwise direction.
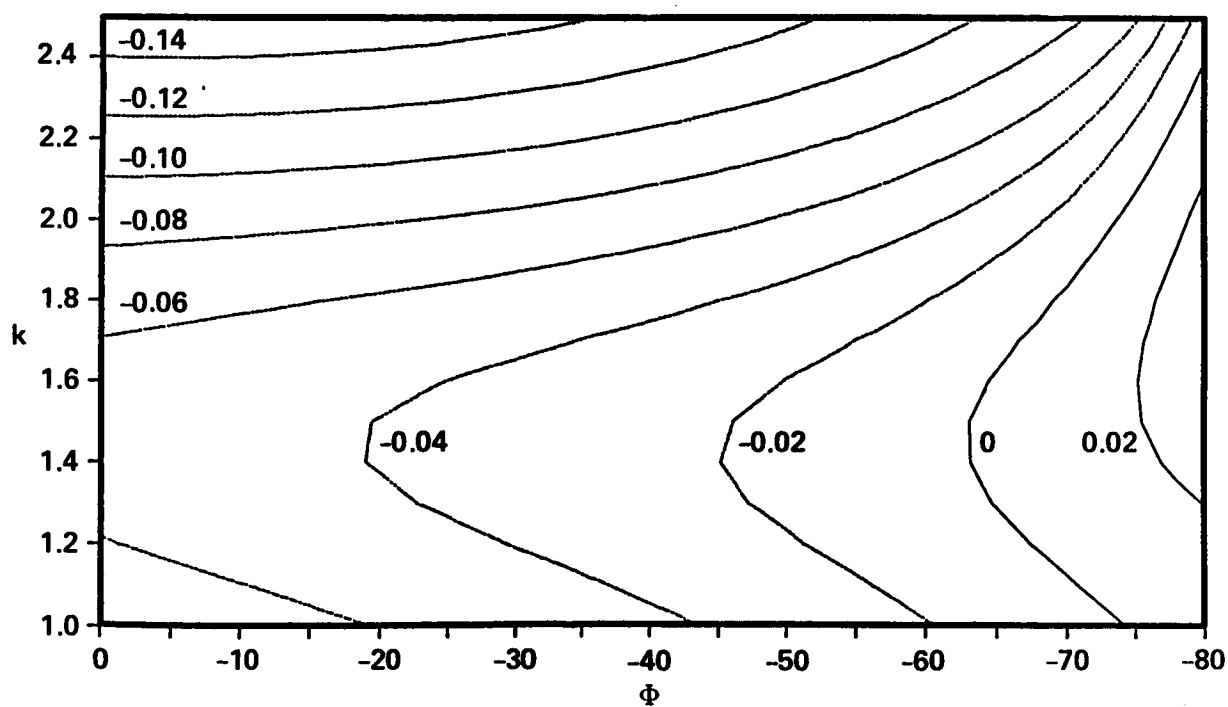
FIGURE 5. Contours of the imaginary part of the dispersion relation.

M. T. LANDAHL 1982 The application of kinematic wave theory to wave trains and packets with small dissipation. *Phys. Fluids.* **25**, 1512-1516.

F. LI & S. E WIDNALL 1987 Wave patterns in plane Poiseuille flow created by concentrated disturbances. Submitted to *J. Fluid Mech.*

G. B. WHITHAM 1974 Linear and nonlinear waves. Wiley.

Appendix

During the summer program a special half day workshop on the role of coherent structures in turbulence modeling was organized by Prof. A. K. M. F. Hussain. The objective was to explore ideas in the use of the knowledge of organized structures in turbulence modeling.

Several participants were asked to make presentations, and five of these prepared written position papers that are included in this appendix. These statements appear as submitted by the authors. While these contain some interesting observations, the organizers of the Summer Program feel that no solution was put forward to the problem of incorporating the coherent structure research in Reynolds stress modeling. This reflects the great difficulty of achieving this integration. Perhaps the views expressed here will be helpful towards this end.

Coherent Structure

By PETER BRADSHAW[1]

Our mental picture of turbulence structure has progressed from the hypothesis that it mimics molecular motion to the belief that turbulence is highly organized though there is some question as to whether there has been an overshoot, i.e., an over-selling of coherent structures in general on the strength of experiences in mixing layers. A brief look at the history is instructive.

- Boussinesq (1883) - "billiard ball" analogy with kinetic theory, leading to the eddy viscosity concept.
- Prandtl (1925) -mixing length "lumps" (apparently inspired by the Ahlborn method of water-surface flow visualization, which forces two-dimensional motion near the surface).
- Theodorsen (1952) - horseshoes of assorted sizes.
- Townsend (1956) - WEAK large eddies with shapes deduced from correlation tails.
- Grant (1958) - STRONG large eddies in boundary layer and wake.
- Bradshaw et al. (1964) - VERY STRONG (but 3D) large eddies in mixing layer.
- Crow &Champagne (1971) - VERY STRONG 2D (but Re-dependent?) orderly structure in mixing layer.
- Brown & Roshko (1971) - confirmed Crow & Champagne picture, with the implication that the 2D vortex roll structure may not be very Re-dependent.

Between 1964 and 1971 Townsend's large eddies grew into orderly structures! Unless the latter term is used to distinguish unusually strong, or unusually long- lived, or unusually two-dimensional large eddies from the norm, it is perhaps a confusing change from Townsend's more descriptive label, at least for discussion of the dominant eddies away from the inner layer of a wall flow. Certainly, the main impression one gets from the last 15 years' research is that large eddies / orderly structures *are* longer-lived than was previously thought - and of course that in the mixing layer the orderly structures are essentially two-dimensional unlike the traditional picture of turbulence. Now the time scale (turbulent kinetic energy)/(dissipation rate) or TKE/(production rate) is always a representative of the energy-containing, shear-stress-carrying eddies. Thus an unusually long eddy lifetime (as deduced from flow visualization, say) implies an unusually small rate of energy transfer (small dissipation rate) in that part of the turbulence - that is, an unusually weak coupling between the long-lived eddy and the rest. This suggests that a two- dimensional eddy may be exceptionally long- lived, simply because it does not share so directly in the vortex- stretching "cascadse" of energy as three- dimensional eddies do. The mixing-layer simulations of Metcalfe et al. (1987) make it clear that a mixing layer with disturbed initial conditions can have a large-eddy structure consisting of long but finite vortex rolls swept back at various angles, presumably strongly interacting with each other and therefore having shorter lives than the parallel two- dimensional rolls observed by Brown & Roshko and others. We need to make sure we are chasing the right, representative eddies! A related point is that our main object in studying any turbulent flow is to improve predictions of shear stress, and we should therefore be studying the eddies that carry, or influence, the shear stress. It seems a good general principle that presentations of educed eddy shapes should be accompanied by an estimate of the fraction of total shear stress that is carried by eddies of that shape.

According to Townsend's large eddy equilibrium hypothesis, turbulent mixing (i.e., shear stress) was supposed to be controlled by large eddies (more or less filling the shear layer but not carrying much of the turbulent energy). This is a paradox - how can eddies be weak in energy, strong in shear stress? "Weakness" of the large eddies was required for the "equilibrium" hypothesis. The result was an eddy viscosity for the smaller, energy-containing eddies. Grant (1958) showed that large eddies in boundary layers and wakes did contain a large fraction of the turbulent energy. This killed the equilibrium hypothesis - but the concept of large eddies as large contributors to mixing should not have been largely ignored for the next 15 years.

The main **questions** about "orderly structures" or "large eddies" are:

(i) How different are they in different shear layers?

---

1 Imperial College, London

(ii) Can we usefully combine a model of the orderly structure with a cruder representation of the small-scale, less-well-ordered eddies as in Townsend's large- eddy equilibrium hypothesis or the Murthy & Hong Large Eddy Interaction Model?

(iii) What about the all-important boundary layer? (Especially the outer layer - engineers *think* they know all they want to about the inner layer.)

Suggested **answers**: -

(i) Large "orderly structure" is just an extreme case of Townsend's large eddies, which were always envisaged as different in different flows. Therefore study of orderly structure is not a route to a universal model (at least at Reynolds-averaged level). The persistence of orderly structure is critical to the success of "zonal average" modeling - if large eddies/orderly structure persist for a long time after a change of zone, the change of empirical coefficients at the edge of a zone will have to be governed by a complicated rate equation.

(ii) Except in the mixing layer and the inner layer of a wall flow, the background turbulence carries a very significant part of $\overline{uv}$ - but maybe we can manage with just a few modes (not necessarily superposable Fourier modes).

(iii) In the outer part of a boundary layer, the large eddies/structures seem to be not-very-well-ordered eruptions, probably horseshoe- or hairpin-like (beware low- Reynolds-number simulations), because the outer structure depends on viscosity up to $Re_\theta = 5000$ (as shown by wake parameter behaviour - see also Murlis et al., *J. Fluid Mech.* **122**, 13, 1982). Since the outer part of the flow presents the biggest challenge to turbulence modeling (provisionally accepting the engineer's view of the inner layer!) study of the more spectacular forms of orderly structure is unlikely to help us with the boundary layer problem. Of course, study of the inner layer is helpful to basic understanding: at least the scaling in the logarithmic region is simpler than usual even if the turbulence is not.

As a final comment, it is still difficult to see how conditionally-sampled data on orderly structures, whether from simulations or from experiments, can actually be used in Reynolds-averaged models, although qualitative understanding is still valuable. However, if we could derive exact transport equations based on some compromise between Reynolds averaging and solution of the time-dependent Navier Stokes equations, we would have a considerably better chance of using our knowledge of orderly structures.

Coherent Structures–Comments on Mechanisms

By J. C. R. HUNT[1]

1. Introductory remarks

There is now overwhelming evidence that in most turbulent flows, despite the flow field being random, there exist regions moving with the flow where the velocity and vorticity have a characteristic "structure." These regions are called "coherent structures" because within them the large-scale distributions of velocity and/or vorticity remain coherent even as these structures move through the flow and interact with other structures. In most flows the sizes of these structures vary but the distributions of velocity/vorticity remain similar. There is also evidence that there is a significant degree of similarity between these distributions in different flows (Hussain 1986).

Since flow enters and leaves the bounding surfaces of these structures, a useful definition, following Hussain (1986), for coherent structures is that they are "open volumes with distinctive large-scale vorticity distributions."

The following schematic remarks are a personal statement about possible fruitful directions for the study of the dynamics of coherent structures (hereafter CS). Most CS research to-date has been concentrated on the measurement and kinematical analysis of CS; there is now a welcome move to examine the dynamics of CS, by a variety of different methods. A few of them will be described here.

2. The origins of coherent structures

Coherent structures arise by two main types of mechanism.

(i) Instability (primary or secondary)

When non-uniform flows are generated at high Reynolds number they are usually unstable, so that some small disturbances to the velocity field amplify. The most unstable disturbances may be small in amplitude but their length scale is usually of the same order as that of the original mean flow. Even as the amplitude of the disturbances grow to the same order as that of the velocity of the original flow, the length scale and flow structure remain similar to that of the original small disturbance, as in the free shear layer (Fig. 1).

Consequently linear stability theory remains of considerable value in analyzing CS and in estimating their consequences, e.g., their effects on noise generation (e.g., Gaster et al. 1985).

Once the primary instabilities have grown secondary instabilities develop, often with vorticity in directions perpendicular to that of the primary instability, for example the "braids" that form in free shear layers with vorticity parallel to the mean flow and that link the primary "roller" vorticities (e.g., Bernal & Roshko 1986).

A general feature of the growth of the primary and secondary instabilities is that they lead to a concentration of vorticity in localized regions in the flow as shown by recent non-linear studies (e.g., Smith 1987). Well-known examples are the rollers and braids in free shear layers, and the spanwise vortices and "horseshoe" vortices in boundary-layer flows. These regions of concentrated vorticity, which occur at Reynolds numbers (based on global or local scales) just great enough for turbulence to persist, are usually found to have characteristics similar to those in coherent structures at high Reynolds numbers.

(ii) Selective amplification of disturbances by the mean field

Consider an initially isotropic homogeneous turbulent velocity field introduced into a shear flow. (This is certainly possible on the computer, e.g., Rogallo 1981, and approximately possible in a wind tunnel, e.g., Champagne et al. 1970; it may broadly approximate the turbulence generated at the wall or at the outer interface in the boundary layer, e.g., Townsend 1970.)

Computations, both non-linear by Rogallo (1981), and linear by Lee et al. (1987), show that the shear stretches and rotates the vorticity in such a way that the eddies become elongated and develop

[1] University of Cambridge
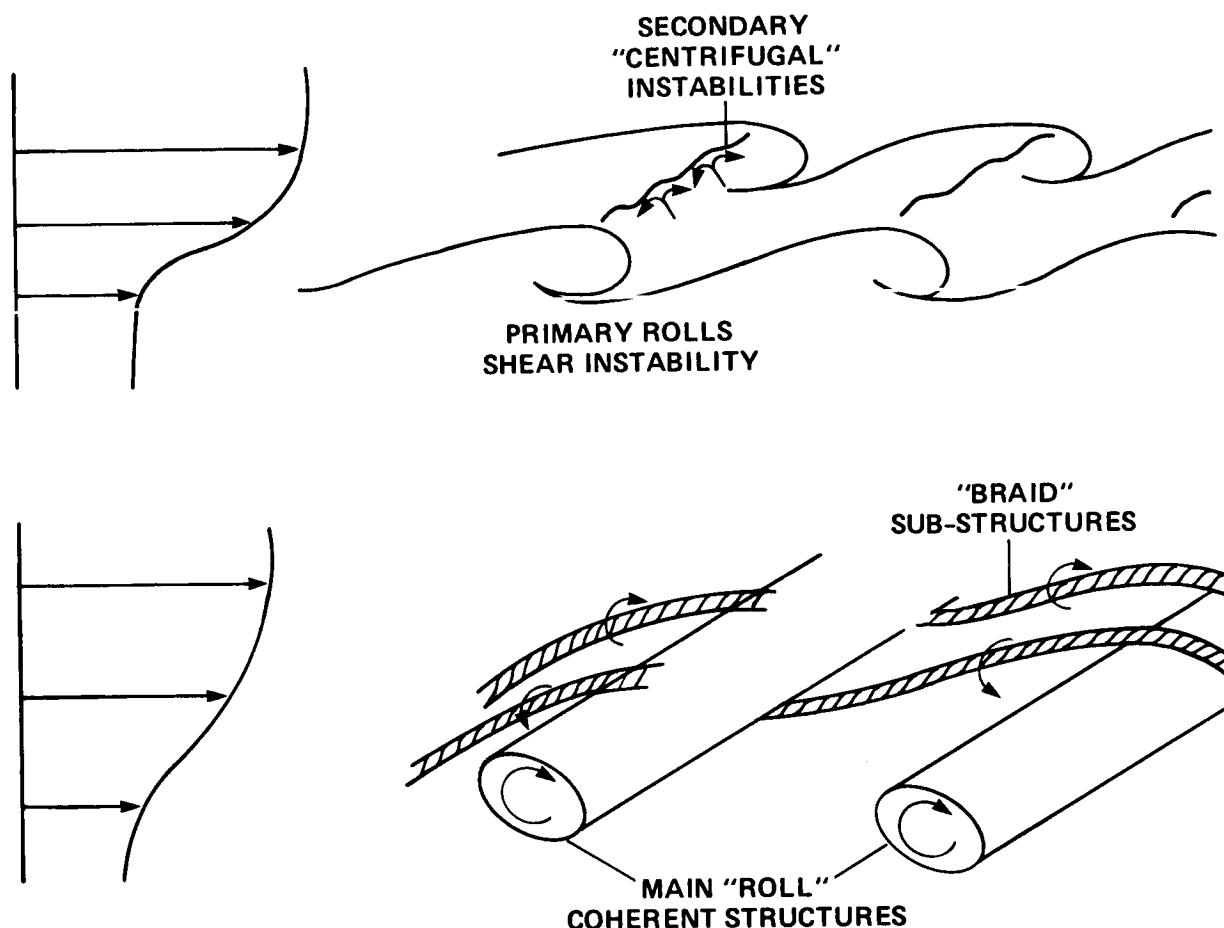
FIGURE 1. Coherent structures generated from instabilities: Primary and secondary instabilities in a free shear layer leading to two kinds of coherent structure — "rolls" and "braids." The latter are also known as "sub-structures."

sharper boundaries (Fig. 2). This is the explanation of the evolution of the velocity spectrum in Rogallo's computations from an exponential decay (indicating very smooth velocity distributions in the eddies) to a k^{-2} decay (indicating discontinuities on the large scale). Linear calculations using Rapid Distortion Theory (RDT) also show these effects; similar coherent structures are found as in the non-linear simulations. (The analysis of the RDT spectra needs to be done.)

3. Interactions between a coherent structure and its surrounding flow

After the formation of a CS, its subsequent existence depends on how it interacts with the surrounding flow. This varies considerably between flows.

(i) Uniform flows

Although CS are not generated in uniform flows, they are often moved by the flow or propagate themselves into regions of approximately uniform velocity; CS in wakes far from the body approximate to this case. The simplest type of CS to consider in this situation is the vortex ring or the vortex pair (Maxworthy 1977). These CS preserve their structure, but they always lose some vorticity as they propagate through the flow (Fig. 3a).

LOW REYNOLDS NUMBER
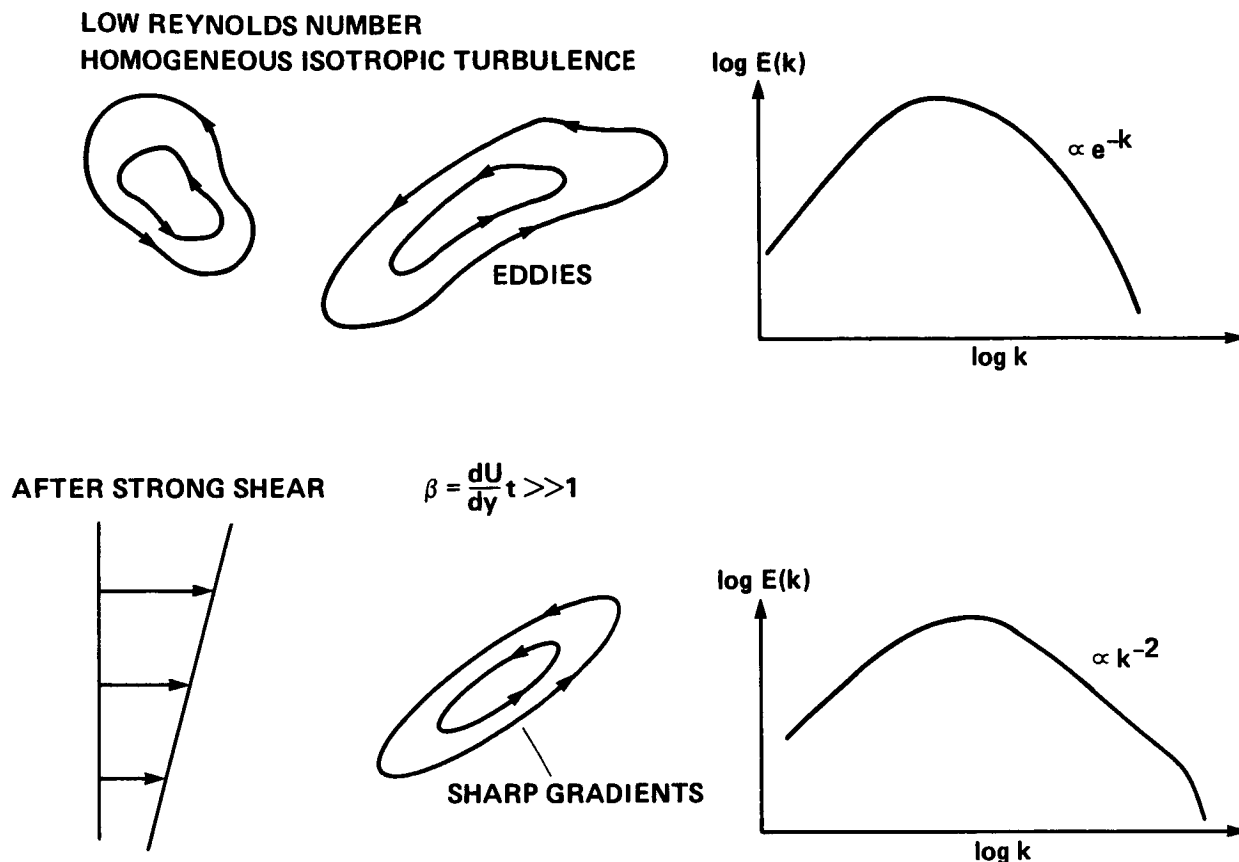**HOMOGENEOUS ISOTROPIC TURBULENCE**

FIGURE 2.   Coherent structures generated by deforming a random velocity field. Distortion of a typical eddy or CS as shear is applied to homogeneous turbulence. Note the change in spectra (Rogallo, 1981; Lee et al., 1987)

(ii) Neighboring structures

In free shear layers, wakes, and jets the CS are formed in thin layers so that the main effect of the surrounding flow on the CS must be caused by adjacent or nearly adjacent CS. This is quite different to boundary layers where each CS is surrounded by other CS (Fig. 3b).

One could characterize these interactions as $1 + 1 + 1 + \ldots$. These kinds of interactions can be idealized by considering the interactions between pairs of vortices. Such studies have yielded useful conservation conditions (Aref 1983), and insights into whether the vortices go round each other or merge or pair (e.g., Kiya et al. 1986).

(iii) Many structures or a mean field?

In turbulent boundary layers each CS is surrounded by others, and also by small-scale incoherent motion. In such cases it is no longer profitable to examine each interaction between the structures; it is more practical to represent the whole velocity field as that of the CS, U, plus a mean velocity field, $\bar{u}$, induced by the vorticity within all the CS, and a random component, u' to represent on the large scale the random locations of the CS, and on the small scale the incoherent motions (Fig. 3c). In other words, $1 + \infty + \infty'$, is equivalent to $U + u + u'$.

At present we understand little about the mechanics of the interaction between a finite volume of fluid containing vorticity and the surrounding flow. Most research on the dynamics of turbulence has been focused on the interaction between small perturbations and various kinds of mean flow, e.g., Townsend (1976) or Landahl & Mollo-Christiansen (1986). This is perhaps surprising since Prandtl's (1925) mixing length theory is based on a qualitative model of how "lumps of fluid" — Flüssigkeit ballen — interact with a shear flow.
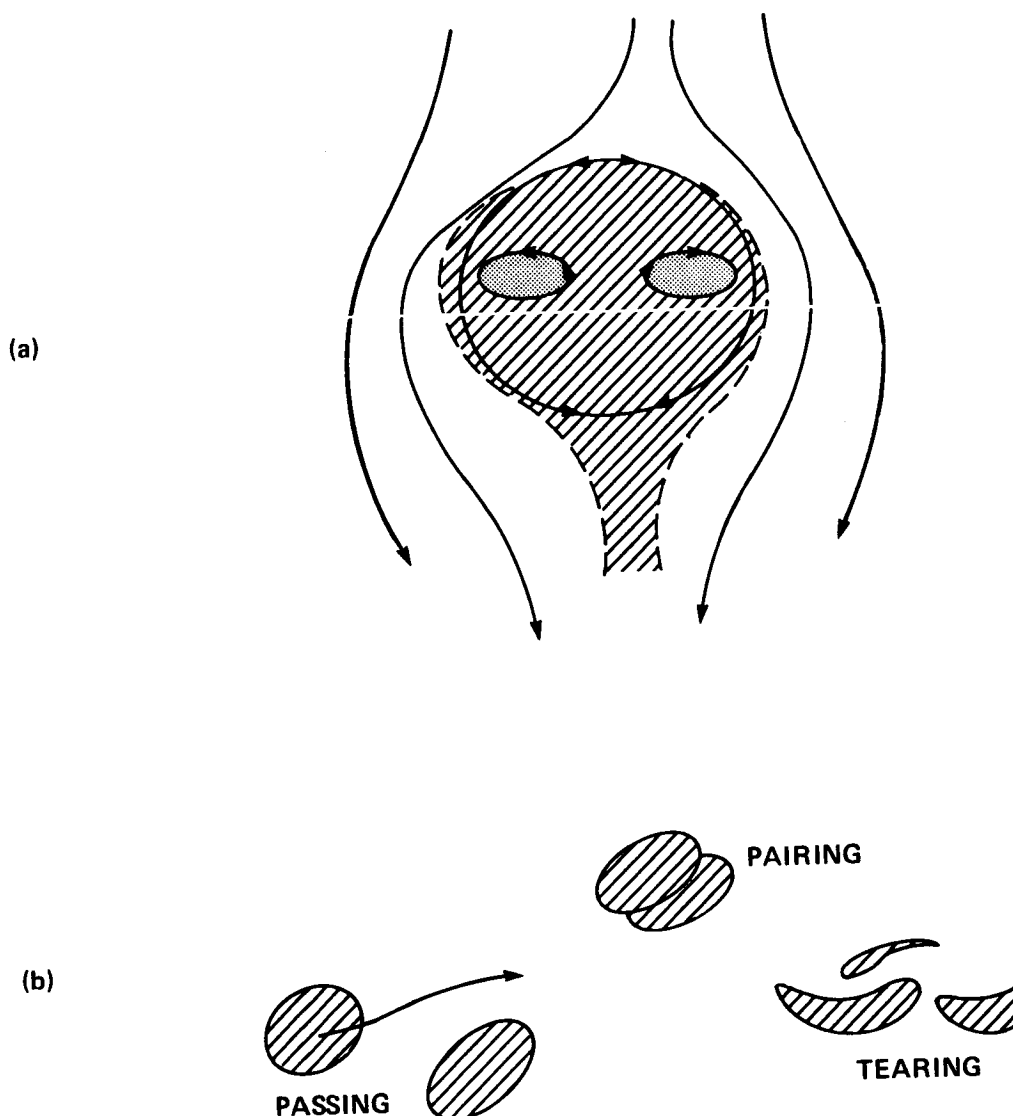
(a)

(b)

PAIRING

PASSING

TEARING

FIGURE 3.   (a) A ring vortex in a uniform flow showing slow shedding of vorticity downstream. (b) Interaction between a Coherent Structure (CS) and neighboring CS (1+1 $\cdots$).

Some general questions about this problem were set out by Hunt (1987):

i) What is the applied force and velocity of a volume V in a non-uniform unsteady flow with velocity u? For inviscid flow (a good idealization for a short time), analytical expressions have recently been obtained for spherical or cylindrical volumes moving in shearing or uniformly straining flows. The initial movements of a lump–or CS– when displaced in a shear flow are largely controlled by inertial forces, in particular the added mass and lift forces. One finds that transverse displacements generate streamwise velocities of the lumps and thence Reynolds stresses–the CS analogy of the small perturbation Reynolds stress found in RDT or second-order calculations (Fig. 3d).

(ii) How does the volume deform as it is accelerated when displaced across a shear flow? Flow visualization of the eddies or CS in a turbulent boundary layer show that as they are ejected from the wall form into "mushroom" shapes. These are very similar to the shapes of vortex sheets surrounding volumes of fluid which are suddenly introduced into jets (Coelho & Hunt 1987). In both cases the vortex sheets roll up into concentrated vortices characteristic of the mushroom
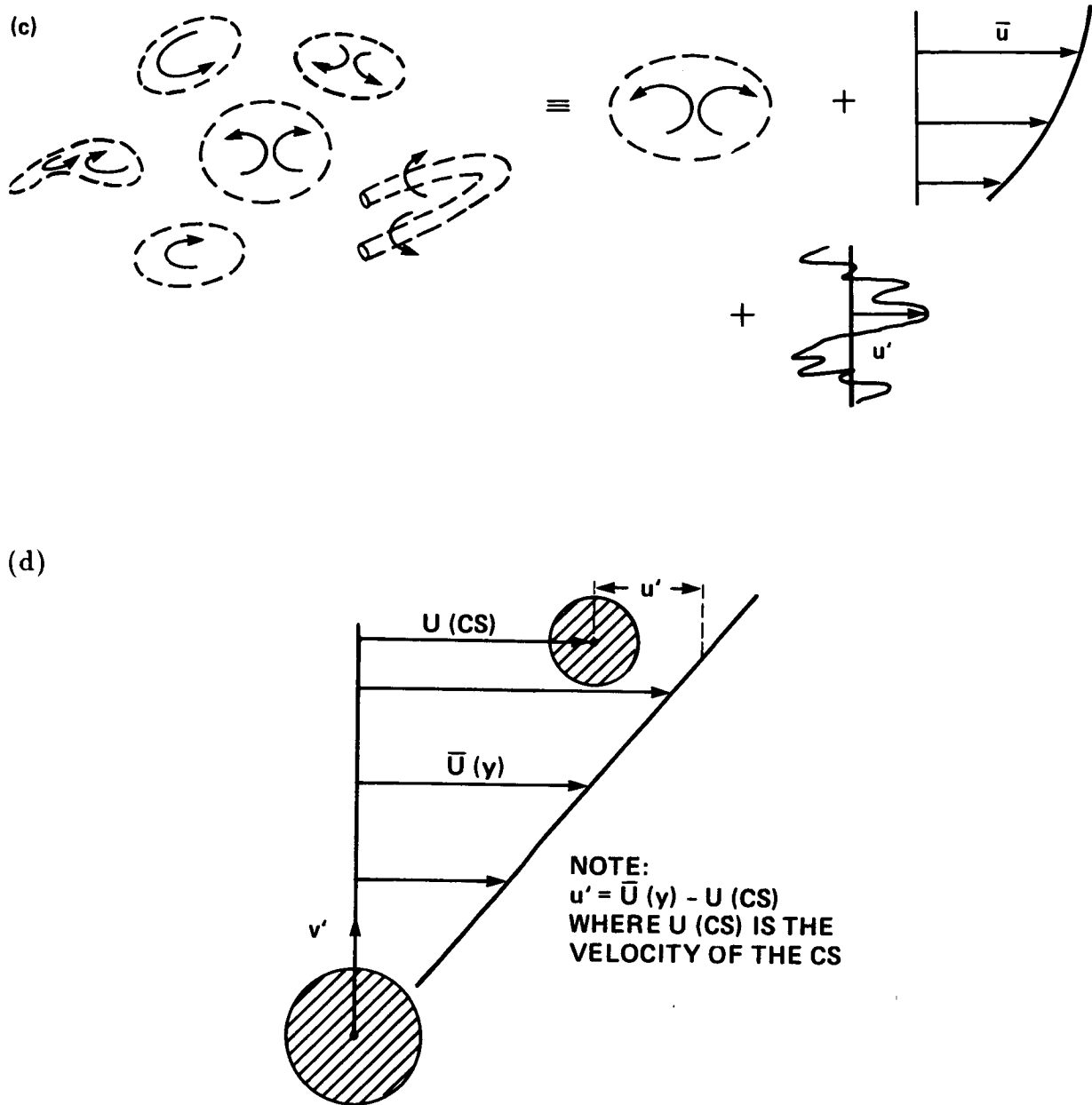
(c)

(d)

FIGURE 3. (c) Interaction between a CS and surrounding CS — equivalent to the interaction with a mean flow u and turbulence u'. (d) Movement of a volume of fluid across a shear flow leading to the generation of Reynolds stress, $-u'v'$ — an idealization of the mechanics of a CS in a shear flow (Hunt 1987).

structures. These vortices appear to have forms that persist–which of course is one of the necessary features of CS.

The other approach to analyzing the dynamics of CS is to take a typical form of the vorticity distribution in a CS and to compute its development in an appropriate shear flow. That has certainly led to some interesting insights (Moin et al. 1986). But it will be necessary to conduct many such computations to obtain general concepts from them.

4. Effects of coherent structures on the whole flow

Since coherent structures are regions of vorticity they induce a velocity field both within them and outside them. Consequently, they affect the mean and the fluctuating components of the velocity field. Because they contain the largest and most energetic scales of motion the CS contribute a significant proportion of the total energy of the turbulence, and the Reynolds stress. The actual proportion depends on the precise definition of the CS (cf. Adrian 1987).

To compute the velocity fields affected by the CS it is necessary to account for all the key dynamical processes that affect the movement and the strength of the CS during its "life." Recent experiments, and detailed analysis of CS found in direct simulations of turbulent shear flows, are beginning to make this possible (Hussain et al. 1987).

Three examples of dynamical processes that need to be considered are: (i) amplification of the small-scale vorticity of the surrounding flow at the stagnation and straining regions around the CS, caused by the relative motion between the CS and the flow. This is similar to the amplification around bluff bodies and cross jets in turbulent flows (Hussain 1986; Hunt 1973) (Fig. 4); (ii) distortion of the vorticity and amplification of the "incoherent" turbulence within the CS, by the internal straining motions and the shear layers on the boundary of the CS. These are particularly important for determining the growth of the CS, i.e., controlling the spreading of the vorticity of the CS. They also largely control (iii) the detrainment of vorticity into the "wake" of the CS. This process has been studied in detail for the simplest type of CS, namely the vortex ring, and the somewhat more complex jet in a cross flow (Maxworthy,1987; Coelho & Hunt 1987). For those CS it was fond that at high enough Reynolds number the shed vorticity produces an unstable velocity distribution similar to that of a bluff body. This is another mechanism whereby one CS can produce another CS and small-scale turbulence in the surrounding flow. This essentially depends on a diffusion process initially, whereas in the free shear layer the secondary structures were produced by inviscid processes.

5. Concluding Remarks

These suggestions for topics of investigation into the dynamics of CS in fact follow many of the lines of study that are being followed at the University of Houston by Prof. Hussain and at the Center for Turbulence Research at Stanford/NASA Ames. There is perhaps one area of significant difference in that at this stage it is not so clear to me how the detailed mechanics of the CS will emerge from interpreting conditionally sampled velocity measurements in terms of conditional joint probability density distributions. This approach may lead to the prediction of certain useful statistics of the flow, but probably not to the dynamics of individual structures. However, the actual conditionally sampled measurements of velocity will help in elucidating the velocity/vorticity distributions in the CS, which is necessary for the dynamical studies outlined here.

REFERENCES

ADRIAN, R. J. 1987 *Lecture at CTR Summer School.*

AREF, H. 1983 *Ann. Rev. Fluid Mech.* **15**, 345- 389.
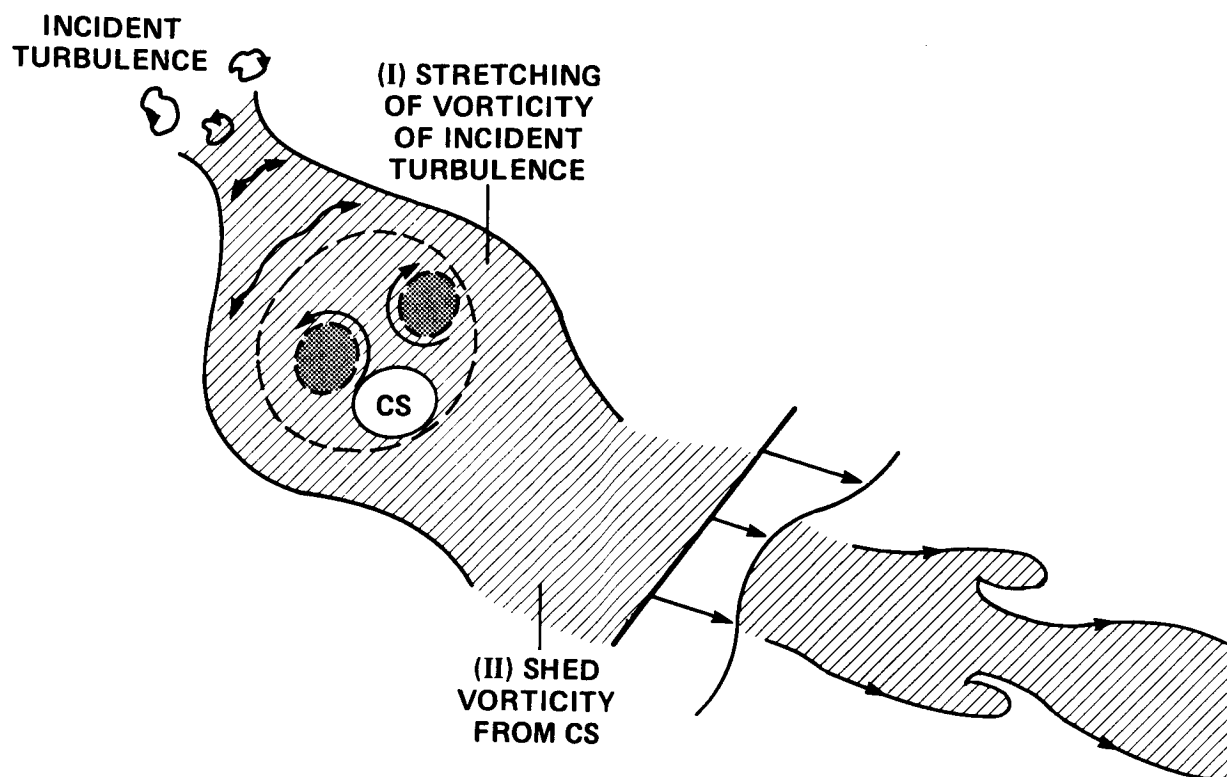
FIGURE 4. Effect of a CS on the surrounding flow in high Reynolds number turbulence. (I) Amplification of turbulence in the surrounding flow. (II) Shedding vorticity which leads to further turbulence in the surroundings.

BERNAL, L. P. & ROSHKO, A. 1986 *J. Fluid Mech.* **170**, 499-525.

CHAMPAGNE, F H., HARRIS, V. G., & CORRSIN, S. 1970 *J. Fluid Mech.* **41**, 81-139.

COELHO, S. L. V., & HUNT, J. C. R. 1987 On the initial deformation of strong jets in cross flows.. *J. Fluid Mech.*. (Submitted).

GASTER, M., KIT, E., & WYGNANSKI, I. 1985 *J. FLuid Mech.* **150**, 23-39.

HUNT, J. C. R. 1973 *J. FLuid Mech.* **61**, 625- 706.

HUNT, J. C. R. 1987 *Trans. Can. Soc. Mech. Eng.* **11**, 21-35.

HUSSAIN, A. M. F. 1986 *J. Fluid Mech.* **173**, 303-356.

HUSSAIN, A. M. F., JEONG, J., & KIM, J. 1987 *Proc., CTR Summer School.*

KIYA, M., OHYAMA, M., & HUNT, J. C. R. 1986 *J. Fluid Mech.* **172**, 1-15.

LANDAHL, M., & MOLLO-CHRISTIANSEN, E. 1986 *Turbulence and Random Processes in Fluid Mechanics.* Cambridge Univ. Press.

MAXWORTHY, T. 1977 *J. Fluid Mech.* **81**, 465-495.

LEE, M. J., KIM, J., & MOIN, P. 1987 *Proc., 6th Turbulent Shear Flows Conf., Toulouse,* pp. 22-6-1 - 22- 6-6.

MOIN, P., LEONARD, A. & KIM, J. 1986 Phys. Fluids . **29. 955-963.**

PRANDTL, L. 1925 . it *Z.A.M.M.* **5**, 136-139.

ROGALLO, R. 1981 *NASA T-M 81315.*

ROTTMAN, J. W., STANSBY, P. K., & SIMPSON, J. E. 1987 *J. Fluid Mech.* **177**, 307-337.

SMITH, F. T. 1987 *Advances in Turbulence*, (Ed., Comte-Bellot & Malthieu), Springer Verlag, pp. 27-36.

TOWNSEND, A. A. 1970 *J. Fluid Mech.* **41**, 13-46.

TOWNSEND, A. A. 1976 *Structure of Turbulent Shear Flow*, Cambridge Univ. Press.

Coherent Structures and Dynamical Systems

By JAVIER JIMENEZ[1]

Any flow of a viscous fluid has a finite number of degrees of freedom, and can therefore be seen as a dynamical system. For a turbulent flow, an upper bound to this number was given by Landau & Lifshitz (1959) and scales as $Re^{9/4}$, which is usually a rather large number. Lower bounds have been computed for some particular turbulent flows, but also tend to be large. In this context, we can think of a coherent structure as a lower dimensional manifold in whose neighborhood the dynamical system spends a substantial fraction of its time. If such a manifold exists, and if its dimensionality is substantially lower than that of the full flow, it is conceivable that the flow could be described in terms of the reduced set of degrees of freedom, and that such a description would be simpler than one in which the existence of structure had not been recognized.

As a trivial example, consider a particular two-dimensional flow for which we can prove that, after some time, most of the vorticity concentrates in a few compact vortices. Such a flow could be described by a few differential equations, and, presumably, easily integrated. Homogeneous, two- dimensional decaying turbulence seems to follow roughly this model (Benzi et al. 1987).

Other examples of the same type are transitional Taylor- Couette flow and Rayleigh-Benard convection. After the initial loss of stability, both systems develop attractors, different from the initial equilibrium, and that can be described in terms of structures (rolls or cells). Although the initial bifurcate states of those flows can hardly be called turbulent, the secondary bifurcations that grow from them can be analyzed, at least for a while, as small perturbations of the initial structures, usually described in terms of their positions and intensities. Technically, we speak of a projection on a central manifold (Demay & Iooss 1984); physically we are talking about describing a turbulent flow in terms of a few degrees of freedom. Another recent example of the same situation is the appearance of disordered states in two-dimensional Poiseuille flow, starting from bifurcations of nonlinear trains of Tollmien Schlichting waves (Jimenez 1987).

The common feature of all these flows is the existence of stable attractors, whose dimensionality is much lower than that of the full flow, and towards which the flow tends after some time. Under those conditions, the flow can be described, up to some level, by the properties of the attractor. Most "attractors" found in nature, are, however, not stable, and cannot be really called attractors at all. The system will approach them for a while, only to be repelled once it gets near the central manifold.

The simplest example of this behavior is the linear differential equation $y_{tt} + sin y = 0$, which represents a circular pendulum. If the system is given proper initial conditions it will approach the position at which the pendulum is pointing "upwards," spend some time near it, and fall back to make a quick revolution across the lower part of its trajectory. Even in this case, the system expends most of its time in the neighborhood of its top (unstable) equilibrium point, and can be described approximately as a being in equilibrium at that position, together with some model for the fast motion in the lower part of its orbit. Perhaps the best example of this situation, in a flow, is the plane temporal mixing layer. Here the "attractor" is a uniform row of compact vortices, and the flow quickly tends towards it. But this solution is itself unstable (mainly through pairing), and is eventually abandoned by the flow, only to converge to a different solution of the same kind. Even so, a model of the flow as a uniform vortex row, with a suitable approximation to the "sudden" pairing process, has been shown to give rough approximations to quantities such as spreading rates (Jimenez 1980) and concentration distributions (Hernan & Jimenez 1982). A more careful perturbation analysis on the lines outlined above has not been attempted, but might be expected to give more accurate results.

Other turbulent flows have phase space structures which are presumably more complicated. The next best plausible candidate for eduction of the complexity of a turbulent flow are the sublayer ejections in wall-bounded turbulence. Recent observations (Jimenez et al. 1987) suggest that the basic structure in that flow is a self-reproducing ejection, that could perhaps be described as an unstable limit cycle. It is not clear, at present, how to treat a dynamical system in the

1 Universidad Politecnica Madrid and IBM Scientific Centre

neighborhood of such a manifold, but any identification of a low dimensional structure which describes a sizeable fraction of the time evolution of a flow, opens the possibility that a local analysis in its neighborhood might give results that capture the qualitative and perhaps even some of the quantitative features of the complete flow.

REFERENCES

BENZI, R., PATARNELLO, S. & SANTANGELO, P. 1987 On the statistical properties of two-dimensional decaying turbulence. *Europhysics Lett..* **3**, 811-818.

DEMAY, Y. & IOOSS, G. 1984 Calcul des solutions bifurcuaees pour le probleme de Couette-Taylor avec les deux cylindres en rotation. *J. Maecanique theor. appl..* **Num. Special,** 193-216.

HERNAN, M. A. & JIMENEZ, J. 1982 Computer analysis of a high speed film of the plane turbulent mixing layer. *J. Fluid Mech.* **119**, 323-345.

JIMENEZ, J. 1980 On the visual growth of a turbulent mixing layer,. *J. Fluid Mech.* **96**, 447-460.

JIMENEZ, J. 1987 Bifurcations and bursting in two- dimensional Couette flow. *Phys. Fluids.* **30**, 3644-3646.

JIMENEZ, J., MOIN, P., R. D. MOSER & KEEFE, L. 1987 Ejection mechanisms in the sublayer of a turbulent channel. *These Proceedings.*

LANDAU, L. D. & LIFSHITZ, E. M. 1959 *Fluid Mechanics.* Pergamon Press, p. 123.

Coherent structures and modeling: some background comments

By S. J. Kline[1]

When Fazle Hussain asked us to discuss how we can use the knowledge of coherent structures in boundary layers in modeling, my first thought was, "I don't know the answer to that, and hence I don't want to give a talk." My second thought was, "The lack of an answer to the question is the most disappointing aspect of the work on coherent structures, which has interested me for a long time." After losing a bit of sleep for three nights, I have to tell you I still don't know the answer to the initial question. However, thinking about the question has led me to some ideas that seem to be worth putting forward. First let me ask, "What are coherent structures in turbulent flows?" in order that we have some mutual understanding of what I am talking about. My personal answer to the question is: "Coherent structures are a sequence of events (identifiable motions) in the flow which convert significant amounts of mechanical energies of the mean flow stream, into turbulent fluctuations."

Since there are other possible definitions, let me call this coherent/p structures. These structures have three identifiable parts in time: (a) creation of coherent/p structures (larger structures) from smaller perturbations; (b) creation of smaller scale motions of many scales from the larger motions; (c) decay of the smaller scaled motions owing to viscosity (Kolmogorov scale). Part (a) is an "anti cascade-like" process; parts (b) and (c) are "cascade-like" processes. Thus cascade theories can describe parts (b) and (c) but not part (a). Cascade-like theories so dominated ideas in turbulence research for many years that when we submitted an article to a leading journal around 1970 describing an anti cascade-like process, the reviewers made us delete the remark on pain of refusing publication. So we seem to have learned at least something in the intervening years in as much as few people in this summer institute would now deny the existence of the anti cascade-like processes. It ought to have been evident all along that something, some energetic process, has to create the larger structures in turbulent flows since otherwise all turbulent motions would die out as the flow goes to downstream infinity, and we know that does not happen in cases like the boundary layer and the mixing layer where a source of energy exists to downstream infinity. In those situations, there are repeatable sequences of events, in a statistical sense, that create quasi-coherent structures from the energy of the mean motion.

If we define an instability to be a qualitative shift in the flow pattern in the advected frame, then type (a) processes appear to be "growth-like" local instabilities and type (b) processes appear to be "breakup" (or breakdown) type local instabilities and are secondary or higher order instabilities. The modifier "local" is used to indicate that the instabilities do not alter the whole flow field, as for example a flow separation often does, but rather only affect energy transfer processes within some localized part of the flow field.

It is important not only to recognize that the two types of instabilities are different, but also that it is particularly difficult to study growth type instabilities, experimentally, analytically or in the computer for a number of reasons. Such instabilities typically grow exponentially, and thus are less apt to satisfy Taylor's hypotheses than other flow structures. They change very rapidly from point to point in the flow, and being instabilities they amplify differences in initial conditions. Thus they tend to have very large "jitter" from realization to realization. For both these reasons they will be hard to identify and measure with fixed probes and will tend to have little if an R_{ij} correlation values at significant probe separations. Moreover, and this has not always been fully appreciated, the ensemble averages of the coherent/p structures will only very rarely, if ever, be seen in individual realizations. The situation with respect to ensemble averaging is precisely analogous to that of the mean velocity profile. As the data of Kim, Kline and Reynolds showed and the movie of Abernathy and other sources reconfirm, profiles of $U(y,t)$ in the boundary all deviate from the very well known mean profile $U(y)$. Not only is the situation precisely analogous for the coherent/p structures, but the implications are perhaps even more important since we are concerned with using the coherent/p structures to tell us about the details of the dynamics and

1 Stanford University

thus the ensemble averages if taken too literally may mislead us. Yann Guezennec's remarks about ways to formulate the ensemble averages by folding structures with "strong left-handed" elements onto those with "strong right-handed" elements are an excellent example of the dangers and what needs to be done about them.

It is also in the nature of growth-like instabilities in hydrodynamics that they respond to a range of perturbations of input parameters with a range of parametric variation in the outputs. Indeed there is now clear evidence, when one begins to put it together, as S. K. Robinson of NASA Ames and I are currently doing, to show quite clearly that there are several (more than four) quite different kinds of perturbations that can set off the growth instabilities involved in the turbulence production in a boundary layer and that at least three kinds of local instabilities occur. It is not yet clear what fraction each of the three contributes to the totality of production of turbulent kinetic energy in the wall layers.

All this suggests that the coherent/p structures are not just an elephant, but are more like a zoo of various animals, each of which occurs with some variation in size and shape. It is easy to deduce examples that demonstrate this fact, but Professor Hussain's strictures on length of this material preclude those details here. In sum the physics of turbulence production in the boundary layer is of truly great complexity, unlike most physical situations in the world which are simple once they are well mapped and understood.

I summarize this "dismal view" of the problem not only because it strongly affects the way we need to conceptualize the physics, but more particularly because for this discussion it implies several things of importance about the utility of structure information in mathematical modeling.

In discussing the use of structure information in modeling, it will be useful to distinguish three "levels of help" that derive from structure information:

1. Qualitative knowledge that helps guide designs including ideas for flow
control: e.g., Riblets, LEBUS, wall curvature, mixing control in jets and cyclones, ...

2. Suggestions about needed precautions in probe measurements, in LES/FTS, and in modeling.

3. Direct use of the features, the sequence of events that create turbulent kinetic energy as the source for mathematical models.

The knowledge of the coherent/p structures has already influenced all the examples of design and control functions listed under 1, and many others not listed, although just how much is hard to say accurately. There is little doubt that the information will continue to serve this function, probably increasingly so as we gain more detailed knowledge.

The knowledge of coherent/p structure at level 2 can, and sometimes has already been critical even though the number of detailed steps involved with that knowledge is small. Some examples include the difficulties with data rate and probe size in lab experiments and grid resolution in FTS that we now know occur as Reynolds number increases owing to the way the coherent/p structures scale.

The most disappointing feature of the several decades of work on coherent/p structures in the boundary layer is the near total absence of use of the information for direct building of mathematical models. So far, outside of some small guidance in the wall model of kuhn and Chapman and important use of the scale information and ensemble average structure model by Perry, Henbest and Chong, there has been very little successful use of the coherent/p information in modeling. Noteworthy attempts have been made by many, including for example Landahl and co-workers, by Beljaars and by Lilley, but thus far these have not led to computations of practical engineering significance. The situation remains that we do most practical modeling via some form of the RANS or equation with closure supplied by models or with even simpler equations such as k-ϵ.

There are then two critical questions. Will this situation continue, or will we be able to build a mathematical model directly on increased information about the coherent/p structures? Second, if we do not build such models, will the coherent/p information be important in the simpler models?

With regard to the first question, I cannot provide an answer, as I noted at the outset; one needs a crystal ball, and mine is cloudy. Only time will tell. One can say this much, the complexities of the problem, some of which are outlined above, mitigate rather strongly against the creation of a complete usable mathematical model built directly on coherent/p information. As we learn more about details in given cases and about a wider range of cases, that becomes clearer and clearer.

However, a little careful thought suggests that even if we do not use the coherent/p information to build a mathematical model directly, that information will be critical in the long run. I have

not seen this argument made, and I am grateful to Professor Hussain for making me think hard enough about the problem to see the results a little more clearly.

We need to remember that the full, unaveraged, honest-to-God Navier-Stokes equations plus continuity (and when necessary the viscous energy equation) are an excellent model of turbulent flows so long as the fluid is Newtonian–at least for all the data we have thus far, and this is quite a lot for many cases. If we utilize simpler equations typically via some form of averaging, then those simple equations *must be insufficient for modeling the totality of turbulent flows precisely to the extent that we have lost information in the averaging or simplifying process*. This follows from the fact that the complete Navier- Stokes equations are a good model not only in the sense that they do describe the motion of Newtonian fluids, but *also that they describe no mode; they do not predict excess information suggesting behavior that cannot occur*. Hence, the losses of information are not trivial. This non-triviality is borne out again and again and again whenever we do careful testing of models as, for example, in the 1968 and 1980-81 AFOSR-Stanford conferences but by no means limited to those examples. An enlightening current example appears in the recent dissertation of S. Tzuoo with J. H. Ferziger and the writer. In this work Tzuoo has been able to show that one can build a "unified zonal model" using the k-e model equations which predicts all the available free-shear layer cases (wakes, jets, mixing layers; near- and far-field, planar and axisymmetric) up to the level of profiles of Reynolds stress with no discrepancy of more than 10data and computer output, IF AND ONLY IF the internal constants in the k-e model equations are made explicit functions of two external non-dimensional governing parameters, a generalized Sabin-Abramovitz parameter and a vortex stretching parameter. These results show quite clearly that the key factor is just the kind of variation in the physics from one "zone" of flow to another suggested by the metaphor above about a "zoo of animals".

This line of thought , and the discussions in the session organized by Professor Hussain, lead me to what seems an important conclusion. The most important use of coherent/p information *may* be in making the critical decisions about what *terms can not be dropped* in forming model equations suitable for particular problems. This information is often relatively small in content, and used only for a moment at one point in a long analysis; its importance is consequently often underestimated. Let me give an example of central importance in fluid mechanics to make the point. Prandtl's derivation of the boundary layer equations, generally accepted as the genesis of modern fluid mechanics, depends critically and explicitly on the use of the empirical information that the shear layer thickness is small compared to its length in the streamwise direction. Mathematicians have sometimes argued this can be justified on mathematical grounds; it cannot. At least all such arguments I have seen are circular in some subtle way, and more important, the Navier-Stokes equations themselves are not mathematical in content, but rather use mathematics to provide a model of the physical world. The relevant underlying theory, including the example, are discussed in detail in my own monograph *Similitude and Approximation Theory*, reprinted in 1986 by Springer-Verlag.

In thinking about the future of our knowledge of coherent/p structures and their uses in the boundary layer, I want to make one more remark before drawing conclusions. Given the complexities of the physics described, IN PART, above it is clear why we have had so much difficulty in finding the details of the dynamics and in reaching agreement in the research community about even the kinematic details. Some years ago a strongly concerned government agency asked me if the time was right for a push on turbulence in order to get through the problem I said, "No!" I did not think so because there were not enough good ideas or research tools, and the added manpower, which could be brought to bear by more money, would not be likely to advance matters significantly faster. If asked that question today, I would give the opposite answer. I would do so precisely because the data bases now available at NASA Ames drastically alter the situation. While it is true that the data bases so far only cover a handful of cases and are restricted to unfortunately low Reynolds Numbers, nevertheless they do provide in central, exemplary cases, a means for investigating questions that lay entirely beyond feasibility a decade ago and equally important they allow this to be done with several orders of magnitude increase in speed and decrease in manpower compared with conventional laboratory work. More specifically, when we bring together the existing knowledge on boundary layer structure available in the various research groups such as those of C. R. Smith at Lehigh, R. E. Falco at Michigan State, R. Blackwelder at USC and H. Eckelmann and others at Gottingen and add in the heat transfer results in the groups of R. J. Moffat at Stanford, H. Kasagi at Tokyo, and M. Khabahkpasheva in Novosibirsk, to mention only a few of the more active groups, some clear questions emerge. When we take these questions to the computer data bases of Spalart and of Moin/Kim, as a number of workers in this

conference, including S. K. Robinson (whose dissertation will focus on these question), have begun to do, answers very quickly begin to emerge. Some of these results answer questions that have been troubling me for a decade or two, and more important, the reasons why we had not been able to resolve them before are also clear. All this is very promising and augurs very well for rapid progress over the next few years on the question of the kinematics and dynamics of coherent/p structures in turbulent boundary layers.

CONCLUSIONS

1. Understanding of the physics cannot hurt. History tells us it almost always "helps" in important, and sometimes surprising ways.

2. "Help" has been and may remain more at levels 1 and 2 than at level 3. But even at level 3, in direct mathematical modeling, the use of coherent/p information may be critical in deciding what terms *can not be dropped* in simplifying model equations for particular flow zones.

3. These potential gains more than justify the current level of research efforts on understanding coherent/p structures.

329

Coherent Structures

By CHARLES G. SPEZIALE[1]

In order to develop more quantitative measures of coherent structures that would have comparative value over a range of experiments, it is essential that such measures be *independent of the observer*. It is only through such a general framework that theories with a fundamental predictive value can be developed. The triple decomposition

$$\phi = \bar{\phi} + \phi_c + \phi_r \tag{1}$$

(where $\bar{\phi}$ is the mean, ϕ_c is the coherent part, and ϕ_r is the random part of any turbulent field ϕ) serves this purpose. For a statistically steady turbulence which possesses coherent structures with a dominant temporal frequency f we can take (see Hussain 1983)

$$\bar{\phi} = \lim_{T \to \infty} \frac{1}{T} \int_0^T \phi(\mathbf{x}, t) dt \tag{2}$$

$$\phi_c = <\phi'> \equiv \lim_{N \to \infty} \frac{1}{N} \sum_{i=1}^{N} \phi'(\mathbf{x}, t + t_i) \tag{3}$$

where $\phi' \equiv \phi - \bar{\phi}, t_i = i/f$, and $< \cdot >$ denotes the phase average. For more general turbulent flows (that are not necessarily statistically steady or do not possess coherent structures with a dominant temporal frequency), on can take

$$\bar{\phi} = \lim_{N \to \infty} \frac{1}{N} \sum_{i=1}^{N} \phi^{(i)}(\mathbf{x}, t) \tag{4}$$

where an ensemble average is taken over N repeated experiments with the same initial and boundary conditions. The coherent part of the turbulence can be taken to be

$$\phi_c = <\phi'|E> \tag{5}$$

where $< \cdot |E>$ denotes a suitable conditional average of ϕ' (i.e., an ensemble average over flow structures subject to the occurrence of some event E. With such triple decompositions, the coherent and random parts of the turbulence will be the same for all observers (see Speziale 1986).

It should be noted that double decompositions (see Hussain 1983, 1986) give rise to coherent and random parts of any turbulent field ϕ that, in general, depend on the observer. Double decompositions should therefore only be used when the mean flow vanishes or is negligibly small compared to the coherent notion (see Speziale 1986). Otherwise, one runs the risk of extracting flow structures that are overly biased by the observer.

The equations of motion for the mean and coherent flow fields, based on the triple decomposition (1), can be written in the form (see Hussain 1983):

$$\frac{D\bar{u}_i}{Dt} = -\frac{\partial \bar{p}}{\partial x_i} + \nu \nabla^2 \bar{u}_i - \frac{\partial}{\partial x_j}(\overline{u_{c_i} u_{c_j}} + \overline{u_{r_i} u_{r_j}}) \tag{6}$$

1 ICASE, NASA Langley Research Center

$$\frac{Du_{c_i}}{Dt} = -\frac{\partial p_c}{\partial x_i} + \nu \nabla^2 u_{c_i} - u_{c_j}\frac{\partial \bar{u}_i}{\partial x_j} - u_{c_j}\frac{\partial u_{c_i}}{\partial x_j}$$

$$-\frac{D\bar{u}_i}{Dt} - \frac{\partial \bar{p}}{\partial x_i} + \nu\nabla^2\bar{u}_i - \frac{\partial}{\partial x_j} < u_{r_i}u_{r_j} > \tag{7}$$

where ν is the kinematic viscosity of the fluid, p is the modified pressure, and $u = \bar{u} + u_c + u_r$ is the velocity field which is subject to the continuity equation which yields the constraints

$$\nabla \cdot \bar{\mathbf{u}} = 0 \tag{8}$$

$$\nabla \cdot \bar{\mathbf{u}}_c = 0 \tag{9}$$

$$\nabla \cdot \bar{\mathbf{u}}_r = 0 \tag{10}$$

In order to achieve closure of the equations of motion (6)- (10), the Reynolds stress terms

$$< u_{r_i}u_{r_j} >, \overline{u_{r_i}u_{r_j}} \tag{11}$$

need to be modeled. The time-averaged Reynolds stress $\overline{u_{r_i}u_{r_j}}$ can be modeled using the currently popular two-equation models or second-order closure models (see Launder, Reece and Rodi 1975 and Lumley 1978). The phase-averaged Reynolds stress $< u_{r_i}u_{r_j} >$ primarily serves as an energy drain on the coherent motion and thus it is plausible that it could be modeled using a gradient transport hypothesis (see Hussain 1983). Hence, eddy viscosity models of the form

$$< u_{r_i}u_{r_j} >= -\nu_T \left(\frac{\partial u_{c_i}}{\partial x_j} + \frac{\partial u_{c_j}}{\partial x_i} \right) \tag{12}$$

can be considered where ν_T is an appropriate eddy viscosity (sufficiently far from solid boundaries, the Smagorinsky model can be tried). This approach, which bears a certain resemblance to large-eddy simulations, has an advantage in that the coherent motion $\mathbf{u}_c$ is calculated directly. Furthermore, the level of computation required is substantially less than that needed for a direct numerical simulation since a coarse mesh can be used (the fine-scale turbulence is modeled) and for some problems (e.g., turbulent mixing layers) the coherent motion is approximately two-dimensional. In my opinion, there is a good chance that such an approach could yield useful new information concerning the nature of coherent structures and it is well worth pursuing future investigations along these lines.

REFERENCES

HUSSAIN, A. K. M. F. 1983 *Phys. Fluids* **26**, 2816.

HUSSAIN, A. K. M. F. 1986 *J. Fluid Mech.***173**, 303.

LAUNDER, B. E., REECE, G. J. & RODI, W. 1975 *J. Fluid Mech.* **68**, 537.

LUMLEY, J. L. 1978 *Adv. Appl. Mech.***18**, 124.

SPEZIALE, C. G. 1986 *Proc. Tenth Symposium on Turbulence,*University of Missouri Rolla, 10:1.